Transactions of the ASME

Technical Editor, L. B. FREUND

Division of Engineering
Brown University
Providence, R.I. 02912

APPLIED MECHANICS DIVISION

Chairman, J. D. ACHENBACH
Secretary, M. M. CARROLL
Associate Editors,
T. BELYTSCHKO
D. B. BOGY
R. M. CHRISTENSEN
R. J. CLIFTON
MAURICE HOLT
W. D. IWAN
W. G. KNAUSS
F. A. LECKIE
L. E. MALVERN
FRANCIS C. MOON
R. P. NORDGREN
R. H. PLAUT
J. R. RICE
R. T. SHIELD
C. T. SUN
J. S. WALKER
G. A. WEMPNER
S. E. WIDNALL

BOARD ON COMMUNICATIONS
Chairman and Vice-President
K. N. REID, JR.

Members-at-Large
W. BEGELL
J. T. COKONIS
W. G. GOTTENBERG
H. C. REEDER
D. KOENIG
M. KUTZ
F. LANDIS
R. E. NICKELL
J. E. ORTLOFF
C. PHILLIPS

President, G. KOTNICK
Exec. Dir.
PAUL ALLMENDINGER
Treasurer, ROBERT A. BENNETT

PUBLISHING STAFF
Mng. Dir., Pub., J. J. FREY
Dep. Mng. Dir., Pub.
JOS. SANSONE
Managing Editor,
CORNELIA MONAHAN
Production Editor, SUZANNE MAGIDA
Prod. Asst., MARISOL ANDINO

The Journal of Applied Mechanics (ISSN 0021-8936) is published quarterly for $100 per year by The American Society of Mechanical Engineers, 345 East 47th Street, New York, NY 10017. Second class postage paid at New York, NY and additional mailing offices. POSTMASTER: Send address changes to The Journal of Applied Mechanics, c/o THE AMERICAN SOCIETY OF MECHANICAL ENGINEERS, 22 Law Drive, Box 2300, Fairfield, NJ 07007-2300. **CHANGES OF ADDRESS** must be received at Society headquarters seven weeks before they are to be effective. Please send old label and new address.

PRICES: *To members, $24.00, annually; to nonmembers, $100.00.* Add $6.00 for postage to countries outside the United States and Canada.

STATEMENT from By-Laws. The Society shall not be responsible for statements or opinions advanced in papers or . . . printed in its publications (B7.1, Par. 3).

COPYRIGHT © 1985 *by the American Society of* Mechanical Engineers. Reprints from this publication may be made on condition that full credit be given the TRANSACTIONS OF THE ASME, JOURNAL OF APPLIED MECHANICS, and the author, and date of publication be stated.

INDEXED by the Engineering Index, Inc.

Journal of Applied Mechanics

Published Quarterly by The American Society of Mechanical Engineers

VOLUME 52 • NUMBER 1 • MARCH 1985

TECHNICAL PAPERS

1 The Application of Kinetic Fracture Mechanics to Life Prediction for Polymeric Materials
R. M. Christensen and R. E. Glaser

6 Use of Statical Indentation Laws in the Impact Analysis of Laminated Composite Plates
T. M. Tan and C. T. Sun

13 Arbitrarily Oriented Cracks in a Reinforced Sheet
C.-C. Chu

19 Stress Field in and Around a Coated Short Fiber in an Infinite Matrix Subjected to Uniaxial and Biaxial Loadings (84-WA/APM-45)
Y. Mikata and M. Taya

25 Estimation of Energy Release Rates: an Alternative to Interpolation
J.-S. Yang

27 Progressing and Oscillatory Waves for Hybrid Synthesis of Source-Excited Propagation and Diffraction
L. B. Felson

33 Reflection and Transmission of Elastic Waves by a Periodic Array of Cracks (85-APM-1)
Y. C. Angel and J. D. Achenbach

42 Elastic Wave Scattering From an Interface Crack in a Layered Half Space
H. J. Yang and D. B. Bogy

51 The Rapid Tearing of a Half Plane (84-WA/APM-51)
J. P. Dempsey and E. B. Smith

57 Analysis of the Reflection of Point Force-Induced Crack Surface Waves by a Crack Edge (84-WA/APM-47)
L. M. Brock and H. P. Rossmanith

62 Flexibility of a Contact Area of an Isotropic Elastic Body
C. M. Szalwinski

67 An Elastic-Plastic Finite Element Model of Rolling Contact Part 1: Analysis of Single Contacts (84-WA/APM-43)
V. Bhargava, G. T. Hahn, and C. A. Rubin

75 An Elastic-Plastic Finite Element Model of Rolling Contact Part 2: Analysis of Repeated Contacts (84-WA/APM-42)
V. Bhargava, G. T. Hahn, and C. A. Rubin

83 The Problem of Minimizing Stress Concentration at a Rigid Inclusion (85-APM-2)
L. Wheeler

87 Antiplane Eigenstrain Problem of an Elliptic Inclusion in a Two-Phase Anisotropic Medium
H. T. Zhang and Y.-T. Chou

91 Elastic Field of an Elliptic Inhomogeneity With Debonding Over an Arc (Anitplane Strain)
B. L. Karihaloo and K. Viswanathan

98 An Elastic Stress-Strain Relation for Sphere Arrays Undergoing Initial Stage Sintering (84-WA/APM-49)
T. L. George, T. C. Kennedy, and K. L. Peddicord

105 Sufficient Conditions for Small Particles to Hold Together Because of Adhesion Forces
M. Fichman and D. Pneuli

109 Moiré Interferometric Study of Dovetail Joints
C. Ruiz, D. Post, and R. Czarnek

115 A Simplified Approach to Elastic-Plastic Response to General Pulse Loads (84-WA/APM-52)
P. S. Symonds and J. M. Mosquera

122 Reliability of Axially Compressed Cylindrical Shells With General Nonsymmetric Imperfections
I. Elishakoff and J. Arbocz

129 Postbuckling Analysis for the Bending of a Long Beam With a Thin, Open, Circular Cross Section (84-WA/APM-46)
R. C. Benson

133 On the Ergodicity Assumption in an Applied Mechanics Problem
A. Scheurkogel and I. Elishakoff

137 Transverse Impact of a Hyperelastic Stretched String
M. F. Beatty and J. B. Haddow

144 The Acoustic Response of a Periodically Rough Elastic Plate (Ice) in Contact With Water
A. Lakhtakia, V. K. Varadan, and V. V. Varadan

149 Free Vibrations of Noncircular Cylindrical Shells Having Circumferentially Varying Thickness (84-WA/APM-50)
K. Suzuki and A. W. Leissa

155 Effects of Geometric Imperfections on Frequency-Load Interaction of Biaxially Compressed Antisymmetric Angle Ply Rectangular Plates (84-WA/APM-44)
D. Hui

(Contents continued on Inside Back Cover)

Downloaded 04 May 2010 to 171.66.16.49. Redistribution subject to ASME license or copyright; see http://www.asme.org/terms/Terms_Use.cfm

CONTENTS (CONTINUED)

163 **Nonlinear Forced Vibrations of Beams**
M. Countryman and R. Kannan

167 **Gravitational Flow Discharge From a Horizontal Duct** (85-APM-4)
P. Chan, T. Han, and W. L. Chow

172 **Chute Flows of Granular Material: Some Computer Simulations**
C. S. Campbell and C. E. Brennen

179 **Clearing Maximum Height With Constrained Kinetic Energy** (85-APM-3)
M. Hubbard and J. C. Trinkle

185 **The Constitutive Theory for Fluid-Filled Porous Materials** (84-WA/APM-48)
N. Katsube

190 **Asymptotic Approximation and Perturbation Stream Functions in Viscous Flow Calculations**
B. S. Berger

193 **Transient Buoyant Convection of a Contained Fluid Driven by the Changes in the Boundary Temperature**
J. M. Hyun

199 ***Directional Sensitivity of Cylindrical Hot-Film Velocity Sensors***
A. Raman, V. S. Krishnan, and R. P. Roy

203 **Boundary Layer Flow Over Long Cylinders With Suction**
B. Bar-Haim and D. Weihs

208 ***Wind-Generated Surface Waves on a Viscous Fluid***
C. Katsis and T. R. Akylas

213 **Hydromagnetic Convective Diffusion Between Parallel Plates With Suction**
N. Annapurna, A. S. Gupta, and B. S. Dandapat

DESIGN DATA AND METHODS

216 **Elastic Stress Concentration Phenomena in an Axially Stressed Rectangular Plate With a Central Circular Hole and Other Related Problems**
D. Shilkrut and E. Ben-Gad

BRIEF NOTES

Rayleigh Revisited
D. A. Johnson — 220

Wave Propagation in Semi-Infinite Elastic Bars With Randomly Varying Elastic Modulus
Dr. S. K. Roy Choudhuri — 222

Thermoelastic Stress due to Surface Parallelpiped Inclusions
S. Lee and C. C. Hsu — 225

Design of an Adhesive Lap Joint
P. Czarnocki and K. Piekarski — 228

Stability of Short Columns Subjected to Distributed Axial Loads
B. P. Shastry and G. Venkateswara Rao — 229

230 Response Cell Probabilities for Nonlinear Random Systems
T. T. Soong and L. L. Chung

232 Stability of Wide Strips Under Locally Distributed Forces
G. Baker and M. N. Pavlović

234 A Pathological Situation in Micropolar Elasticity
R. S. Lakes

235 Effect of Debonding on the Stability of Fiber-Reinforced Composites
J. Barber and N. Triantafyllidis

237 Crack Growth Prediction of Subsurface Crack in Yielded Material
D. Y. Tzou and G. C. Sih

DISCUSSIONS

239 Discussion on previously published papers by **H. C. Sih and N. P. Suh and G. M. T. D'Eleuterio and P. C. Hughes**

BOOK REVIEWS

241 ***Boundary Element Techniques. Theory and Applications in Engineering*** by **C. A. Brebbia, J. C. F. Telles,** and **L. C. Wrobel** . . . Reviewed by **S. Mukherjee**

Elastic Instability Phenomena by **J.M.T. Thompson and G. W. Hunt** . . . Reviewed by **V. Tvergaard**

242 ***Problems of Mixed Mode Crack Propagation*** by **E. E. Gdoutos** . . . Reviewed by **L. M. Brock**

Numerical Simulation of Non-Newtonian Flow by **M. J. Crochet, A. R. Davies, and K. Walters** . . . Reviewed by **R. I. Tanner**

243 ***Computer Aided Analysis and Optimization of Mechanical System Dynamics*** edited by **E. J. Haug** . . . Reviewed by **R. L. Huston**

Books Received by the office of the Technical Editor

240, 246 Worldwide Mechanics Meeting List

18, 41, 56, 74, 82, 86 Applied Mechanics Symposium Proceedings

97, 136, 162, 178, 184, 207 Applied Mechanics Symposium Proceedings

61 Change of Address Form

245 Postdoctoral Research Awards

Downloaded 04 May 2010 to 171.66.16.49. Redistribution subject to ASME license or copyright; see http://www.asme.org/terms/Terms_Use.cfm

The Application of Kinetic Fracture Mechanics to Life Prediction for Polymeric Materials[1]

R. M. Christensen

R. E. Glaser

Lawrence Livermore National Laboratory,
P.O. Box 808,
Livermore, Calif. 94550

A recently developed theory of kinetic crack growth is applied to the problem of the time-dependent failure of polymeric materials subject to a timewise constant state of stress. The theory is generalized to include a rather complete treatment of statistical variability. When restricted to the power law range of behavior, it is found that an assumption of a Weibull distribution of static strengths implies rigorously that the corresponding lifetime distributions are also Weibully distributed. In fact, an extremely simple interrelation is found wherby the shape parameter for lifetime is equal to the product of the shape parameter for static strength times the magnitude of the log stress versus log lifetime slope of the scale parameter for the lifetime distribution. These theoretical predictions are compared with the experimental results available from the testing of a particular polymeric fiber composite material, Kevlar 49/epoxy. The theoretical prediction for the lifetime distribution compares favorably with the observed data.

Introduction

The present work is concerned with the time-dependent failure of composite materials. In particular, we seek a physically motivated and developed theory in order to quantify a growing state of damage in the material, which ultimately causes total failure. We will not attempt to apply forms of utmost generality, rather we will examine a rather specific, but very important problem in the class of the time-dependent failure of polymeric materials. Before describing the specific problem of interest, let us place the work in a general perspective.

With regard to the failure of polymeric materials, a general distinction can be drawn between materials at temperatures far above or far below their glass transition temperatures. As classes of behavior, these are either elastomers, or rather glassy materials. Interest centers here on the latter, the glassy class, as load bearing materials. Glassy polymers exhibit rigid and sometimes very brittle behavior. Failure occurs at low strain levels, without large changes in compliance as a precursor to failure. Typically, such materials show scatter in the data of ultimate tensile strength and it is necessary to employ statistical characterizations. As with certain brittle metals and ceramics, Weibull-type statistical distributions generally suffice to model the data. Of course, the success of Weibull statistics relates to its relevance for describing the fracture-type failure induced by isolated inherent flaws in the interior or on the surfaces of test specimens.

With glassy, rigid polymeric materials one might expect that knowledge of the static strength provides the complete knowledge of its failure property. Such is not the case. At load levels below those of short time static strength, but sustained in duration, failure can occur in the time spectrum. The situation is somewhat akin to that of fatigue in metals. However, in polymers, even when the loads and stresses are completely constant in time, failure can still occur. Although to outward appearance and dimensional measurement such materials are inert and unchanging, clearly, internal microscale mechanisms of damage growth in effect, ultimately lead to failure. Polymeric materials exhibit this complex time envelope of failure. The situation is much more complicated than that of static failure. Normally, the timewise scatter in the failure data is orders of magnitude broader than the scatter in static strengths.

The problem of interest here is the tensile failure of unidirectional composite materials. A theoretical method for damage accumulation and time-dependent failure will be evaluated with respect to a large body of data for a Kevlar 49/epoxy composite. The loading program is that of the application of load that is maintained constant in time, up until material failure. The theoretical method follows the derivation of Christensen [1], whereby the composite is idealized as being effectively homogeneous, such that time and rate-dependent fracture mechanics can be applied to model the failure process. Before describing this approach, however, we should mention that this is but one of many different possible approaches and levels of idealization. For example, Morgan, Pruneda, and Steele [2] have obtained

[1]Work performed under the auspices of the U.S. Department of Energy by the Lawrence Livermore National Laboratory under contract number W-7405-ENG-78.

Contributed by the Applied Mechanics Division for publication in the JOURNAL OF APPLIED MECHANICS.

Discussion on this paper should be addressed to the Editorial Department, ASME, United Engineering Center, 345 East 47th Street, New York, N.Y. 10017, and will be accepted until two months after final publication of the paper itself in the JOURNAL OF APPLIED MECHANICS. Manuscript received by ASME Applied Mechanics Division, September, 1983; final revision, April, 1984.

Copyright © 1985 by ASME
Downloaded 02 May 2010 to 171.66.16.54. Redistribution subject to ASME license or copyright; see http://www.asme.org/terms/Terms_Use.cfm

extensive information about the molecular structure of Kevlar 49 fibers. This information, from spectroscopy and other sources, provides fundamental insights on failure beginning at the molecular scale of chain scission and bond rupture. Another entirely different level of idealization involves the detailed modeling of fiber matrix interaction, with load transfer around broken fibers, etc. This approach has been extensively pursued by Phoenix and Wu [3]. The approach here is yet one of a completely different nature; it invokes a macroscopic idealization of damage and failure.

Fracture mechanics has been enormously successful in explaining and characterizing the static failure of ideally brittle materials. Particularly when combined with Weibull statistics, fracture mechanics provides a virtually complete description of failure for such materials. It is logical to seek an extension of static, time-independent fracture mechanics to model the time-dependent behavior of polymers. We follow the approach of Christensen [1] in generalizing elastic fracture mechanics to include time and rate-dependent effects. However, there are several different approaches to this problem, some of which are noted in reference [1]. See Knauss [6] for a comprehensive account of the line-damage zone approach to the problem. Actually, although these various approaches appear to differ greatly in mathematical detail, they differ little in concept. All of these approaches generalize the elastic fracture mechanics methdology to model the viscoelastic effects of polymers through the replacement of the elastic modulus or compliance by the viscoelastic relaxation function or creep function. Of course this process is not a direct replacement of the elastic property by the viscoelastic property, in the literal sense. Rather the proper mathematical procedures must be found for generalization to viscoelasticity. The end result of the derivation in reference [1] involves the replacement of the elastic compliance by the viscoelastic creep function whose argument is ρ/c. Variable c is the time-dependent crack velocity, while ρ is a length parameter characteristic of the crack tip region. In the present work, ρ is treated as a constant to be normalized to experimental data. This probably represents the simplest possible generalization of elastic fracture mechanics to a time-dependent form, consistent with a rational theory. In the following, this approach will be referred to as flaw growth theory.

The work in the following section merely recalls appropriate theoretical results from reference [1] and then applies them to the problem of interest here. The main concern here is with the statistical scatter in the time-dependent failure of the composite material. It is not just coincidental that both static strength and time-dependent failure exhibit statistical scatter. Even though the scatter in the time domain is much greater than the scatter for static strength, these cannot be independent, uncorrelated phenomena. Obviously, the same inherent mechanisms for damage growth must control both effects. We believe that a realistic physical/mathematical model of failure kinetics should bridge the gap between these two seemingly disparate manifestations of failure. Our specific objective is to begin with an assumption of Weibull statistics for static strength, and use kinetic fracture mechanics (flaw growth theory) to deduce the proper statistical forms for lifetime distributions under stress rupture conditions. A secondary objective is to evaluate the theory with respect to the data base mentioned in the foregoing.

Theoretical Forms

We begin by recalling certain theoretical forms. The basis of the flaw growth method for life prediction is the kinetic form relating applied stress to the velocity of crack growth. Several appropriate kinetic forms will be noted here from the work of Christensen [1]. The generalization of elastic fracture mechanics to viscoelasticity is given by

$$\sigma^2 = \frac{2\Gamma/h}{(1-\nu^2)J(\rho/c)} \tag{1}$$

where σ is the opening mode applied stress, ν is the constant Poisson's ratio, $J(\ )$ is the uniaxial creep function, c is crack velocity, ρ is a characteristic length in the crack region, Γ is the surface energy/work of crack creation, and $h(t)$ is the time-dependent characteristic size of the crack. Parameter ρ is treated as a fixed constant to be found from normalizing data. Reference should be made to [1] for a more detailed definition of these terms. To render (1) solvable for crack velocity, a specific representation must be taken for the creep function. The most general form of $J(t)$ is taken as

$$J(t) = \frac{J_0(1+\gamma_1 t^n)}{(1+\gamma_2 t^n)} \tag{2}$$

where n is the power law exponent, $0 \le n \le 1$. Substituting (2) into (1) gives a form that can be solved for c as

$$c^n = \frac{2\Gamma\,\gamma_2\rho^n - \sigma^2 J_0\gamma_1\rho^n h}{\sigma^2 J_0 h - 2\Gamma} \tag{3}$$

with the Poisson's ratio termed neglected. Under the restriction to the power law range of behavior, we get

$$c = \rho\left(\frac{\gamma_1 h}{h_0}\right)^{1/n}\left(\frac{\sigma}{\sigma_i}\right)^{2/n} \tag{4}$$

subject to

$$\frac{2\Gamma\,\gamma_2}{hJ_0\gamma_1} \ll \sigma^2 \ll \frac{2\Gamma}{J_0 h} \tag{5}$$

where

$$\sigma_i = \sqrt{\frac{2\Gamma}{h_0 J_0}} \tag{6}$$

The form (6) is defined as the "intrinsic strength" of the material since it is governed by the initial value of the creep function J_0 and the initial crack size h_0. This intrinsic strength is what we conventionally interpret as static strength in time-dependent materials. We refer to this as the intrinsic/static strength.

Using the crack velocity $c = dh/dt$ in (4), the variables can be separated, and the lifetime under applied stress history can be found. The lifetime is defined as the time span from first application of stress, until the crack size, $h(t)$, grows to the critical size at which material instability commences. From (4) it is found that the nondimensional lifetime is given as

$$\tau = \int_1^{\frac{1}{\tilde{\sigma}^2}} \frac{d\zeta}{\tilde{\sigma}^{\frac{2}{n}}\zeta^{\frac{1}{n}}} \tag{7}$$

where

$$\tilde{\sigma} = \frac{\sigma}{\sigma_i}$$

$$\tau = \frac{t}{t_0} \tag{8}$$

$$t_0 = \frac{h_0}{\gamma_1^{\frac{1}{n}}\rho}$$

When the applied stress is taken to be constant, equation (7) gives the lifetime in the power law region, restricted by (5), as

Downloaded 02 May 2010 to 171.66.16.54. Redistribution subject to ASME license or copyright; see http://www.asme.org/terms/Terms_Use.cfm

$$\tau = \frac{1}{\left(\frac{1}{n} - 1\right)\tilde{\sigma}^{\frac{2}{n}}} \tag{9}$$

Our attention is restricted to the power law region of behavior given by (9), although the more general case is discussed in [1].

At this point we wish to generalize the lifetime form (9) to model statistical variability. Begin by assuming the static strength is Weibully distributed. Specifically, take the complement of the distribution function for strength as

$$F(\sigma') = e^{-\left(\frac{\sigma'}{\sigma_s}\right)^m} \tag{10}$$

where $F(\sigma')$ is the probability that σ_i exceeds σ', m is the shape parameter, and σ_s is the scale parameter, with the intrinsic/static strength, σ_i, being taken to be a random variable. Since from (8) and (9) nondimensional lifetime τ may be expressed in terms of the Weibully distributed strength variable, σ_i, as $\tau = \lambda \sigma_i^{\theta}$, where $\theta = 2/n$ and $\lambda = [(1/p - 1)\sigma^{2/n}]^{-1}$, it follows that τ has a Weibull distribution with shape parameter $m/\theta = mn/2$ and scale parameter $\lambda \sigma_s^{\theta} = (\sigma_s/\sigma)^{2/n}/(1/n - 1)$. Similarly, the explicit time variable t is Weibully distributed with complementary distribution function

$$G(t') = e^{-\left(\frac{t'}{t_s}\right)^r} \tag{11}$$

where $G(t')$ is the probability that the lifetime, t, exceeds t', r is the shape parameter

$$r = \frac{mn}{2} \tag{12}$$

and t_s is the scale parameter

$$t_s = \left(\frac{\sigma_s}{\sigma}\right)^{2/n}\left(\frac{t_0}{\frac{1}{n} - 1}\right) \tag{13}$$

Furthermore, since the pth quantile of σ_i is

$$\sigma_p = \sigma_s[-Ln(1-p)]^{1/n} \tag{14}$$

it follows that the pth quantile of lifetime t is

$$t_p = t_s[-Ln(1-p)]^{1/r} = \left(\frac{\sigma_s}{\sigma}\right)^{2/n}\left(\frac{t_0}{\frac{1}{n} - 1}\right)\left[-Ln(1-p)\right]^{\frac{2}{mn}} \tag{15}$$

Thus, we have shown that the lifetimes are Weibully distributed. Furthermore, this theory predicts the very simple relationship (12) between the shape parameter of intrinsic/static strength, m, and the shape parameter of life, r. Specifically, the scale parameter for lifetime (13) has a power law form with exponent $2/n$ in $t \sim \sigma^{-2/n}$, thus the shape parameter for lifetime is given by the shape parameter for intrinsic/static strength, divided by the power law exponent $2/n$. The latter quantity, $2/n$, is just the absolute value of the reciprocal of the slope on a plot of log stress versus log lifetime scale parameter. This is the prime result of the present work; the flaw growth theory, under conditions of constant stress, and in the power law range of behavior, predicts that if the intrinsic/static strength is Weibully distributed, then the lifetimes are also Weibully distributed, with the shape and scale parameters of one interrelated to those of the other by (12) and (13). These basic results will be tested by a large data base, but first a generalization of the theory just examined will be given.

Table 1 Breaking load of individual Kevlar/epoxy strands. Multiply by 158.0 to convert to MPa

Specimen no.	Load (lb)	Specimen no.	Load (lb)
1	22.0	28	22.2
2	22.0	29	22.7
3	22.0	30	22.7
4	21.6	32	22.5
5	21.6	32	22.2
6	22.0	33	22.5
7	22.0	34	22.0
8	20.9	35	20.5
9	22.5	36	22.5
10	22.7	37	21.1
11	22.9	38	22.2
12	22.0	39	21.4
13	22.5	40	22.5
14	22.5	41	21.4
15	21.6	42	21.6
16	21.8	43	22.0
17	22.0	44	21.4
18	22.0	45	21.4
19	21.8	46	22.7
20	22.9	47	21.6
21	21.8	48	21.6
22	23.1	49	22.7
23	22.9	50	21.8
24	22.0	51	22.0
25	22.2	52	22.2
26	22.5	53	22.0
27	21.4		

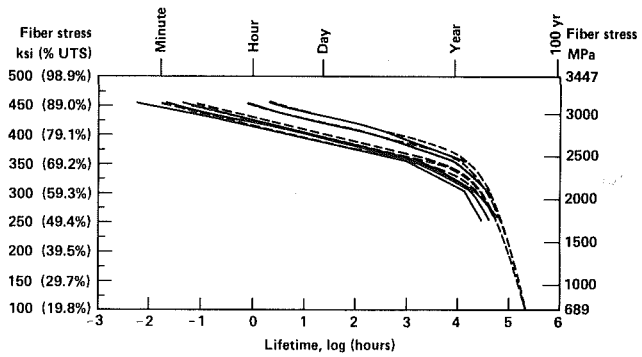


Fig. 1 Annual chemical degradation rate: 5 percent. Quantiles: 2.e-02, 5.e-02, 8.e-02, 5.e-01, and 9.e-01.

In reference [1], the flaw growth theory just described was generalized to include a mechanism of chemical degradation. The instrinsic/static strength, σ_i, of the flaw growth theory was taken to be time-dependent in accordance with first-order reaction rate theory. Specifically, σ_i, was, and is here taken as

$$\sigma_i = \hat{\sigma}\, e^{-t/t_c} \tag{16}$$

where $\hat{\sigma}$ is the initial intrinsic/static strength and t_c is the time constant of any dominant mechanism of chemical degradation. Again, we wish to generalize to statistical conditions, and we take a Weibully distributed complement of the distribution function for the random variable, $\hat{\sigma}$, as

$$F(\sigma') = e^{-\left(\frac{\sigma'}{\sigma_s}\right)^m}, \quad \text{the probability that } \hat{\sigma} \text{ exceeds } \sigma', \tag{17}$$

where as before, m is the shape parameter and σ_s is the scale parameter. Using the Weibull form (17), the estimated lifetime under constant stress can be made. The details may be found in reference [1]. Equation (46) of reference [1] has the form

Downloaded 02 May 2010 to 171.66.16.54. Redistribution subject to ASME license or copyright; see http://www.asme.org/terms/Terms_Use.cfm

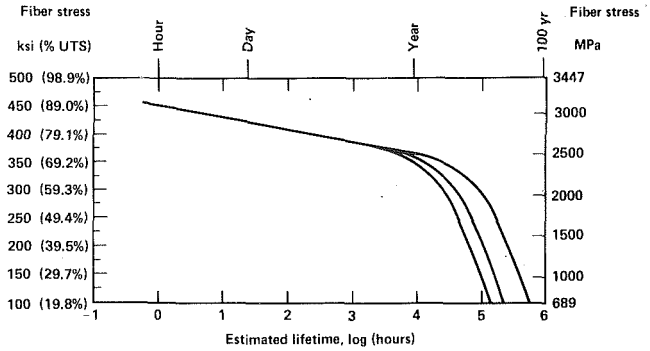


Fig. 2 Quantile: 5.e-01. Annual chemical degradation rates (percent): 8, 5, 2.

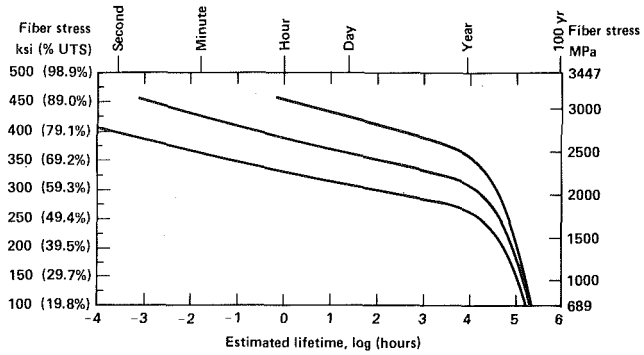


Fig. 3 Annual chemical degradation rate: 5 percent. Quantiles: 1.e-06, 1.e-03, and 5.e-01.

$$t=\frac{nt_c}{2}Ln\left[\frac{2}{nt_c}\left(\frac{t_0}{\frac{1}{n}-1}\right)\left(\frac{\hat{\sigma}}{\sigma}\right)^{2/n}+1\right] \tag{18}$$

It follows from (17) and (18) that the distribution function of lifetime, t, has the complement

$$G(t')=\exp\left[-\left(\frac{2t_s}{nt_c}\right)^{-r}\left(e^{\frac{2t'}{nt_c}}-1\right)^{r}\right]$$

$$=\exp\left\{-\left(\frac{\sigma}{\sigma_s}\right)^{m}\left[\frac{nt_c}{2}\left(\frac{\frac{1}{n}-1}{t_0}\right)\right]^{mn/2}\left(e^{\frac{2t'}{nt_c}}-1\right)^{mn/2}\right\} \tag{19}$$

where $G(t')$ is the probability that lifetime t exceeds t'. The corresponding pth quantile is

$$t_p=\frac{n}{2}t_cLn\left\{\frac{2t_s}{nt_c}\left[Ln(1-p)\right]^{1/r}+1\right\}$$

$$=\frac{n}{2}t_cLn\left\{\frac{2}{nt_c}\left(\frac{t_0}{\frac{1}{n}-1}\right)\left(\frac{\sigma_s}{\sigma}\right)^{2/n}\left[-Ln(1-p)\right]^{2/mn}+1\right\} \tag{20}$$

From this result it can be seen that the complementary distribution function has the form

$$G\sim e^{-(e^{t'}-1)^k}$$

which is certainly not a Weibull form. Thus, in contrast to the situation involving purely mechanical flaw growth, the generalization involving an interactive chemical degradation mechanism does not result in simple Weibull forms for lifetimes to failure. Nevertheless, the general forms (19) and (20) will be evaluated with respect to a large data base in the next section.

Evaluation

We evaluate the theory outlined in the preceding section against an unusually large and significant data base. T. T. Chiao and R. L. Moore, along with various coworkers conceived, implemented, and monitored the constant stress rupture testing of 553 strands of an aramid fiber, epoxy matrix composition. The fiber phase was Kevlar 49, and the volume fraction was close to 0.7. Specimens at seven different stress levels and at room temperature involved loading with dead weight mechanisms. Times to failure were recorded. The testing times extended over a 10-year period. Also, 53 specimens were quickly tested to failure in testing machines in order to establish the corresponding data base for static strength. The stress rupture specimens and the static strength specimens had fiber compositions not only from the same manufacturer's batch, but even from the same spool. The epoxy composition was Union Carbide 2258/ZZL 0820. The Kevlar fiber, being of polymeric constitution, is of a time-dependent nature in its mechanical properties. The present flaw growth theory is applied to model the strand data base, under the assumption that the strand response is fiber dominated, with resin content being secondary.

The static strengths of the 53 specimens are shown in Table 1, from Penn [4]. The method of maximum likelihood is used to estimate the corresponding Weibull parameters. Indeed, the experimental distribution is found to be well modeled by the Weibull form with the shape and scale parameters

$$m=46.3$$

$$\sigma_s=3524\ \text{MPa}$$

The 95 percent confidence interval for the shape parameter is [38.4, 58.2]. The 95 percent confidence interval for the scale parameter is extremely narrow.

The lifetime stress rupture experimental data are shown by the solid line segments in Fig. 1. The data are arranged in the following quantiles of failure: 2, 5, 8, 50, and 90 percent. Straight line segments are used to connect the statistical failure quantiles at the seven stress levels. The form in Fig. 1 involves a linear scale for stress level versus a $\log_{10}$ time scale for lifetime to failure. If the scales were both of logarithmic nature, a power law form would give a straight line representation. In fact, the data in the upper portion of Fig. 1 exhibit a power law behavior. However, there is a strong downturn in the data, which is suggestive of a separate chemical degradation mechanism. This has, in fact, been shown to be the case (Chiao [5]), and this matter was discussed at length in reference [1]. As mentioned there, independent data suggest a degradation of static strength of about 5 percent a year due to ultraviolet light radiation exposure. The 5 percent per year level (first year) is taken as the base line level to be used in the present theory. The time constant t_c in (16) and (18)–(20) is adjusted to provide various levels of interactive chemical degradation.

The theoretical predictions are shown as the dashed curves in Fig. 1. These predictions are obtained in the following manner. The experimental data at levels above 80 percent of static strength (intrinsic/static strength scale parameter) show a predominantly power law behavior. Accordingly, the

Downloaded 02 May 2010 to 171.66.16.54. Redistribution subject to ASME license or copyright; see http://www.asme.org/terms/Terms_Use.cfm

corresponding parameters in (18) and (19) are estimated to fit these upper level data. The method of maximum likelihood is used. The parameter, t_c, is adjusted as previously described to model the downturn due to the chemical degradation. The shape parameter for lifetimes above the 80 percent level is estimated to be

$$r = 0.960$$

with 95 percent confidence interval [0.891, 1.04]. The power law exponent is estimated to be

$$\frac{2}{n} = 45.6$$

The theoretical predictions in Fig. 1 at the 5 percent chemical degradation rate fit the experimental data quite well with the exception of the 2 and 5 percent quantiles at the lowest stress levels. However, these experimental data points involve only a few specimens and they are thereby the results with the least certainty. Overall, the theoretical model fits the data with considerable facility.

Next, we come to the critical test of the theory, namely the evaluation of the theoretical prediction relating the parameters of static strength to the parameters of the lifetime. This evaluation is, of course, only appropriate to the upper power law region of the data in Fig. 1. Using relation (12), we use the intrinsic/static strength shape parameter, m, and the power law slope $(-n/2)$ to predict the lifetime shape parameter as

$$r = \frac{46.3}{45.6} = 1.02$$

This should be compared with the close value of 0.960 obtained from the maximum likelihood treatment of the lifetime data. We thus have used the flaw growth theory to establish the connection between the parameters of static strength, and the parameters of stress rupture lifetimes. The Kevlar strand data base corroborates the theoretical prediction. Extension of this basic result to other systems and other conditions remains to be investigated. We now are in a position to understand the reason why the lifetime scatter is so much broader than the static strength scatter. From relation (12), the Weibull shape parameter for life involves the product of the static strength shape parameter and the slope of the power law relation on log-log scales. This slope is always small in magnitude, for common data sets. Thus a small lifetime shape parameter ensues, giving very broad scatter to the lifetime data.

As a matter of interest, other rates of chemical degradation can be investigated. Figure 2 shows the estimated 50 percent quantile of lifetime for rates of chemical degradation of 2, 5, and 8 percent. It is seen that only the later stages of lifetimes are affected by varying parameter t_c, and thereby the rate of chemical degradation.

The main purpose of any theory is to make predictions outside the range of accessible data. Figure 3 shows the use of the present theory to extend the data base to examine extreme reliability levels. Failure quantiles of 10^{-6}, 10^{-3}, and 0.5 reveal the associated lifetimes at these reliability specifications, as a function of stress level. For example, at about 50 percent of static strength load level, the 10^{-6} quantile gives an estimated lifetime of a little more than a year. It is seen that at the longer times the chemical degradation mechanism begins to overtake the purely mechanical effect of damage growth and the spread between the various reliability levels diminishes relative to the log scale.

It is worth noting that the theory can be used to remove the effect of U.V. degradation from the data base in order to make reliability predictions in the absence of chemical degradation. In this case, the general lifetime form (20) reverts back to the simple statistical form involving the power law, equation (15). In terms of plots of log applied stress level versus log lifetime, the various quantiles of failure are parallel straight lines. Corresponding lifetimes at low stress levels are much greater than those shown in Fig. 1.

Finally, it should be mentioned that a large number of references have dealt with the problem of the statistics of time-dependent failure. Knauss [7] has observed some general features of distribution functions. Coleman [8] assumed an exponential distribution for constant stress lifetime and derived distributions for other stress histories from this. Halpin, Jerina, and Johnson [9] also assumed an exponential distribution for constant stress lifetime and derived corresponding distributions for fatigue type loading programs. The latter work, known in the composite material literature as the "wearout model," is based on a postulated form for damage kinetics and the assumed exponential distribution for constant stress lifetime. The present work makes no assumption about the lifetime distribution or the kinetics. In fact the lifetime distribution is derived from the static strength distribution and the end result is not exponential. Nevertheless the present approach and the wearout model share the philosophy of attempting to relate the statistics of static strength to those of lifetime behavior.

References

1 Christensen, R. M., "Interactive Mechanical and Chemical Degradation in Organic Materials," UCRL-88459, 1983, Lawrence Livermore National Laboratory, *Int. J. Solids and Structures* (in press).

2 Morgan, R. J., Pruneda, C. O., and Steele, W. J., "The Relationship Between the Physical Structure and the Microscopic Deformation and Failure Processes of Poly (p-phenylene terephthalamide) Fibers," *Journal of Polymer Science*: Polymer Physics Edition, Vol. 21, 1983.

3 Phoenix, S. L., and Wu, E. M., 'Statistics of the Time-Dependent Failure of Kevlar 49/Epoxy Composites: Micromechanical Modeling and Data Interpretation," *Mechanics of Composite Materials, Recent Advances*, Hashin, Z., and Herakovich, C. T., eds., Pergamon Press, New York, 1983.

4 Penn, L., "Stress-Rupture Data for Kevlar 49/Epoxy Strands," UCID-17738, 1978, Lawrence Livermore National Laboratory.

5 Chiao, T. T., "No-Stress Aging of Kevlar 49/Epoxy Composites," Memorandum, 1982, Lawrence Livermore National Laboratory.

6 Knauss, W. G., "On the Steady Propagation of a Crack in a Viscoelastic Sheet: Experiments and Analysis," *Deformation and Fracture of High Polymers*, Kausch, H. H., Hassell, J. A., and Jaffee, R. I., eds., Plenum Press, 1973.

7 Knauss, W. G., "Fracture of Solids Possessing Deformation Rate Sensitive Material Properties," *The Mechanics of Fracture*, AMD-Vol. 19, ASME, 1976.

8 Coleman, B. D., "Time Dependence of Mechanical Breakdown Phenomena," *J. Appl. Physics*, Vol. 27, 1956, p. 862.

9 Halpin, J. C., Jerina, K. L., and Johnson, T. A., "Characterization of Composites for the Purpose of Reliability Evaluation," ASTM, STP521, 1973, p. 5.

Downloaded 02 May 2010 to 171.66.16.54. Redistribution subject to ASME license or copyright; see http://www.asme.org/terms/Terms_Use.cfm

T. M. Tan[1]
Post-Doctoral Research Associate.

C. T. Sun
Professor.
Mem. ASME

School of Aeronautics and Astronautics,
Purdue University,
W. Lafayette, Ind. 47907

Use of Statical Indentation Laws in the Impact Analysis of Laminated Composite Plates

The low-velocity impact response of graphite/epoxy laminates was investigated theoretically and experimentally. A nine-node isoparametric plate finite element in conjunction with an empirical contact law was used for the theoretical investigation. Theoretical results are in good agreement with strain-gage experimental data. The results of the investigation indicate that the present theoretical procedure describes the impact response of laminate for low-impact velocities.

Introduction

Advanced fiber-reinforced composite materials such as graphite/epoxy have been successfully employed as structural materials in space vehicles, aircrafts, and missiles. The performance of these composites has shown their superiority over metals in applications requiring high strength, high stiffness, as well as low weight. However, their relatively poor resistance to the impact loadings has become one of the major concerns in recent years. To analyze the impact response problems, it is obvious that an accurate account of the contact behavior is one of the most important steps. The classical contact law between an elastic sphere and an elastic half-space derived by Hertz [1] has been used by many authors for the study of impact on homogeneous isotropic materials [2]. In studying impact responses of laminated composites, however, the problem becomes more complicated. One may easily realize that the Hertzian contact law, which was derived based on homogeneous isotropic materials, may not be adequate in describing the contact behavior of laminated composites due to their anisotropic and nonhomogeneous properties. Moreover, most of the laminated composites in use are quite thin and cannot be represented by a half-space. In the existing analytical work [3], loadings to the laminates were assumed known, and the responses of the laminates were assumed elastic.

Willis [4] has obtained some explicit formulas for contact of a rigid sphere and a transversely isotropic half-space. It was shown that

$$F=k\alpha^n \tag{1}$$

with $n = 3/2$ is valid for the contact force F and the indentation α, where k is a contact coefficient whose value depends on the material properties of the target and the sphere, and the radius of sphere. Recently Yang and Sun [5] have conducted static indentation tests on the [0 deg/45 deg /0 deg/ −45 deg/0 deg]$_{2s}$ graphite/epoxy laminate using spherical steel indenters of 6.35 mm (0.25 in.) and 12.7 mm (0.5 in.) diameters. The results were fitted into equation (1) and were found that the 3/2 power is valid. In addition, it was also observed that even for a small amount of load there could be significant permanent indentations. This indicates that the unloading curve has to be different from the loading curve. To account for the permanent deformation, the equation

$$F=F_m\left(\frac{\alpha-\alpha_0}{\alpha_m-\alpha_0}\right)^q \tag{2}$$

proposed by Crook [6] was used in [5] to model the unloading path. In equation (2), F_m is the contact force at which unloading begins, α_m is the indentation corresponding to F_m, and α_0 denotes the permanent indentation in an unloading cycle. This equation can be rewritten as

$$F=s(\alpha-\alpha_0)^q \tag{3}$$

in which

$$s=F_m/(\alpha_m-\alpha_0)^q \tag{4}$$

is an unloading rigidity.

Some practical difficulties in performing the indentation tests were mentioned in [5] and [7]. Since the indentation was measured step-by-step using a dial gage and readings on the gage were taken about 10–20 sec after the load was increased by one step, the creep effect may cause an appreciable error to the results. Another difficulty lies in the measurement of the permanent indentation using the dial gage. To overcome these problems, a Linear Variable Differential Transformer (LVDT) was used in this study which allowed more accurate estimation of the permanent indentation and the effect of loading rate.

Statical Indentation Test

Specimens and Experimental Procedures. Two groups of beam specimens were prepared from a [0 deg/45 deg/0 deg/ −

[1]Present affiliation: Department of Mechanical Engineering, Drexel University, Philadelphia, Pa. 19104.

Contributed by the Applied Mechanics Division for publication in the JOURNAL OF APPLIED MECHANICS.

Discussion on this paper should be addressed to the Editorial Department, ASME, United Engineering Center, 345 East 47th Street, New York, N.Y. 10017, and will be accepted until two months after final publication of the paper itself in the JOURNAL OF APPLIED MECHANICS. Manuscript received by ASME Applied Mechanics Division, June, 1983; final revision, March, 1984.

Copyright © 1985 by ASME
Downloaded 02 May 2010 to 171.66.16.54. Redistribution subject to ASME license or copyright; see http://www.asme.org/terms/Terms_Use.cfm

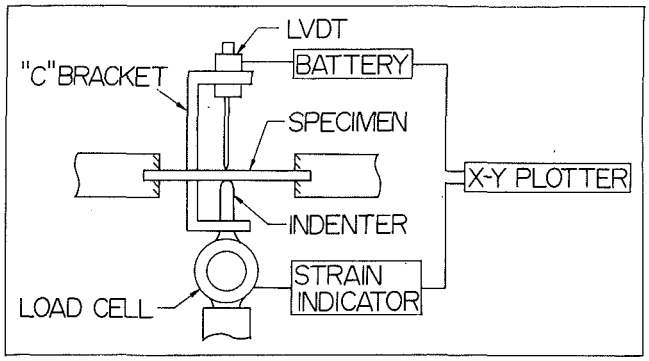


Fig. 1 Schematic diagram for the indentation set-up

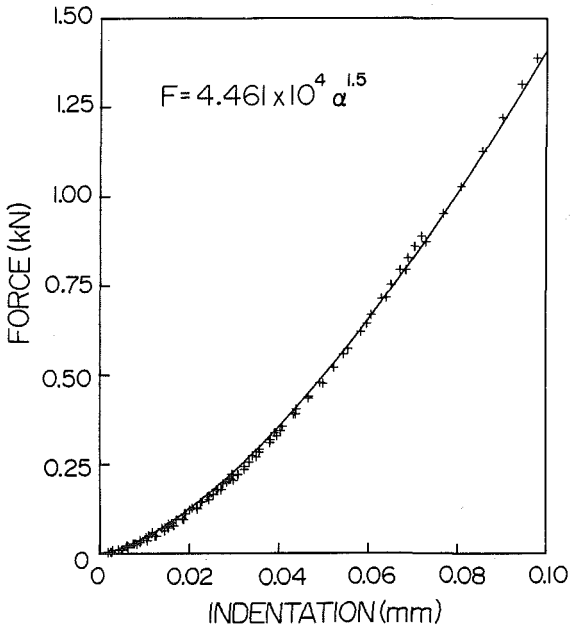


Fig. 2 Loading curve of [0 deg/45 deg/0 deg/ − 45 deg/0 deg]$_{2s}$ specimens with 12.7 mm indenter

45 deg/0 deg]$_{2s}$ graphite/epoxy laminate with the following ply properties:

$$E_1 = 120 \text{ GPa } (17.5 \times 10^6 \text{ psi})$$

$$E_2 = 7.9 \text{ GPa } (1.15 \times 10^6 \text{ psi})$$

$$G_{12} = 5.5 \text{ GPa } (0.8 \times 10^6 \text{ psi}) = G_{13} = G_{23}$$

$$\nu_{12} = 0.30$$

$$\rho = 1582 \text{ Kg/m}^3 \ (3.069 \text{ slug/ft}^3)$$

where E_1 and E_2 are the longitudinal and transverse strengths, respectively, G_{12} is the inplane shear modulus, ν_{12} is the Poisson's ratio for contraction in the transverse direction when loading is in the longitudinal direction, and ρ is the mass density. They were cut in the manner such that the longitudinal direction of the beam specimen of the first group was parallel to the 0 deg fiber direction while the second one was perpendicular to it. The latter then became [90 deg/45 deg/90 deg/ − 45 deg/90 deg]$_{2s}$ laminated beams. The thickness of the beam was 2.7 mm (0.106 in.) and the width was approximately 32 mm (1.25 in.). In all tests, the specimens were clamped at both ends. It was shown in [5] that the span of the specimen in the range of 50 mm–150 mm (2–6 in.) has little effect on the contact law. Hence, only one span, i.e., 50 mm (2 in.), was used in the test.

The experimental set-up is shown schematically in Fig. 1. The LVDT was mounted on a "*C*" bracket fixed to the loading piston so that only the relative movement between the indenter and the specimen was recorded. The load was applied pneumatically by a cylinder with a sphere cap and was measured using a load cell and a strain indicator. Outputs from the LVDT and the strain indicator were fed into an *X-Y* plotter so that a continuous force-indentation curve could be obtained. Two spherical steel indenters of diameters 12.7 mm (0.5 in.) and 19.1 mm (0.75 in.) were used.

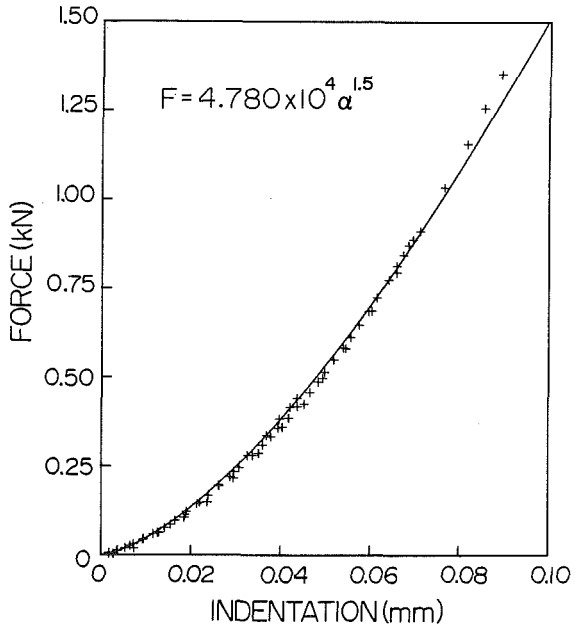


Fig. 3 Loading curve of [90 deg/45 deg/90 deg/ − 45 deg/90 deg]$_{2s}$ specimens with 12.7 mm indenter

Experimental Results

Loading Curves. The experimental curves were first digitized into discrete data points and then fitted into equation (1) using least-squares method. Figures 2 and 3 show the test data and the fitted curves for a 12.7 mm- (0.5 in.) diameter indenter. It can be seen from these figures that the 3/2 power index gives very good results. However, the contact coefficient k for the [0 deg/45 deg/0 deg/ − 45 deg/0 deg]$_{2s}$ specimen is less than the one for the [90 deg/45 deg/90 deg/ − 45 deg/90 deg]$_{2s}$ specimen by about 7 percent. During the test, larger deflections were observed for the second group of specimens due to their lower flexural rigidity. This means that the contact area was also larger and the indentation under the same amount of loading should be smaller comparing with the first group of specimens. Consequently, the higher value of k for the [90 deg/45 deg/90 deg/ − 45 deg/90 deg]$_{2s}$ specimens is reasonable.

The results for 19.1 mm- (0.75 in.) diameter indenter are presented in Figs. 4 and 5. Again, good agreement between the experimental data and fitted curves indicates that the 3/2 power index is valid for loading. The values of k for both indenters are summarized in Table 1. It should be noted that the average value of k obtained from the two groups of specimens was used later for the finite element analysis on the impact response of a laminated plate.

Unloading Curves. By choosing a suitable value for q, it can be seen from equation (4) that once the relation between α_0 and α_m is established, the unloading rigidity s is then determined. Test results showed that the permanent indentation α_0 and the corresponding maximum indentation α_m exhibit a rather linear relationship. The equation given by

$$\alpha_0 = s_p (\alpha_m - \alpha_p) \tag{5}$$

Downloaded 02 May 2010 to 171.66.16.54. Redistribution subject to ASME license or copyright; see http://www.asme.org/terms/Terms_Use.cfm

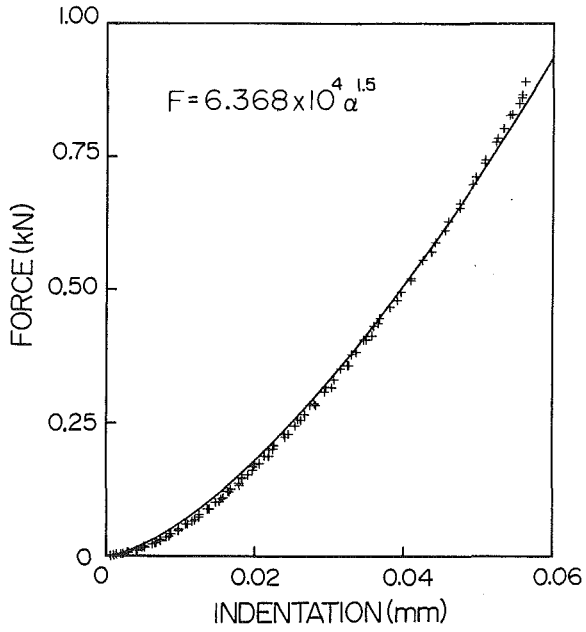


Fig. 4 Loading curve of [0 deg/45 deg/0 deg/ − 45 deg/0 deg]$_{2s}$ specimens with 19.1 mm indenter

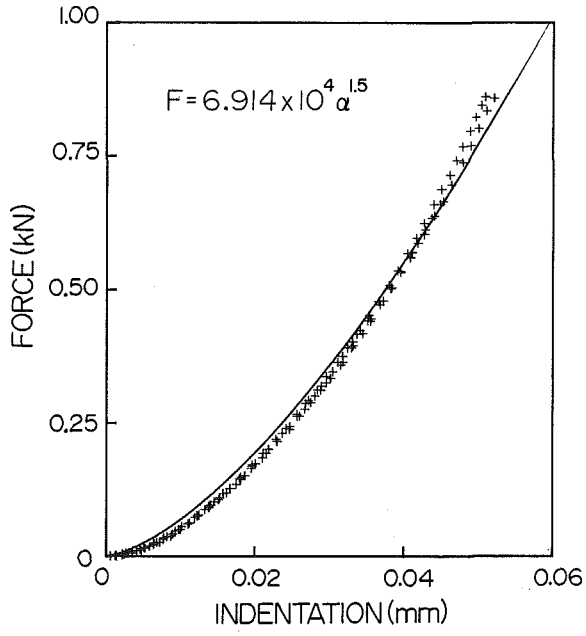


Fig. 5 Loading curve of [90 deg/45 deg/90 deg/ − 45 deg/90 deg]$_{2s}$ specimens with 19.1 mm indenter

with $s_p = 0.094$ and $\alpha_p = 0.0167$ mm (6.564 × 10^{-4} in.) was obtained from the test data for both sizes of indenters using least-squares fitting method, and are plotted in Fig. 6. In equation (5), α_p can be considered as a critical value of indentation beyond which permanent deformation will occur.

Substitution of equations (5) and (1) into equation (4) yields

$$s = \frac{k\alpha_m^{3/2}}{[(1-s_p)\alpha_m + s_p\alpha_p]^q} \quad \text{if} \quad \alpha_m \geq \alpha_p$$

$$s = \frac{k\alpha_m^{3/2}}{\alpha_m^{q}} \quad \text{if} \quad \alpha_m < \alpha_p \qquad (6)$$

These two equations along with equation (3) were used to fit the experimental unloading curves in finding the value of q.

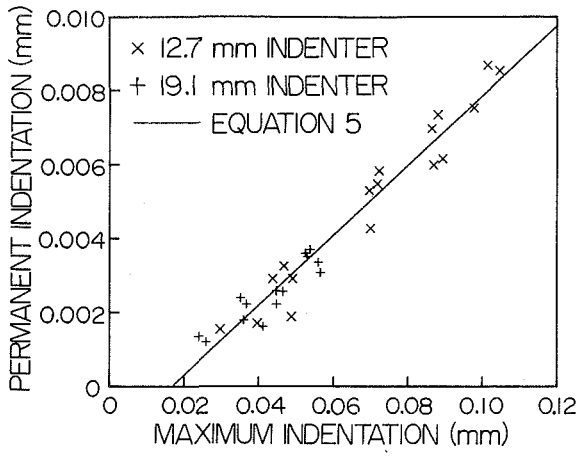


Fig. 6 Relation between permanent indentation and maximum indentation

Table 1 Contact coefficient k of loading law $F = k\alpha^{1.5}$

Size of indenter (mm)	12.7		19.1	
Specimen group	1[a]	2[b]	1[a]	2[b]
$k(10^4$ N/mm$^{1.5})$	4.461	4.780	6.368	6.914
Average k	4.621		6.641	
Reference [7]	3.368			

[a] [0 deg/45 deg/0 deg/ − 45 deg/0 deg]$_{2s}$ specimens
[b] [90 deg/45 deg/90 deg/ − 45 deg/90 deg]$_{2s}$ specimens

Yang and Sun [5] have shown that $q = 2.5$ fitted the test results for both 6.35 mm (0.25 in.) and 12.7 mm (0.5 in.) indenters quite well. In this study, however, the values of 2.2 and 1.8 were found to give the best fitting for 12.7 mm (0.5 in.) and 19.1 mm (0.75 in.) indenters, respectively, using the aforementioned method. For convenience, $q = 2.5$ was used for 12.7 mm (0.5 in.) indenter while $q = 2.0$ was chosen for 19.1 mm (0.75 in.) indenter. Some of the results are presented in Figs. 7 and 8. Further discussion on the unloading law will be given in the next section.

Discussion. As mentioned before, the loading rate may affect the contact law (i.e., the value of k). A series of tests with different loading rates were performed to examine this point. The maximum loading rate that the test equipment could apply without exceeding its capacity was about 200 N/sec (45 lb/sec). It was found that in the range of 20 N/sec–200 N/sec the values of k showed very little scatter, and the effect due to local material nonhomogeneity in the composite might be even greater than that due to the loading rate. However, an appreciable decrease of the value of k was observed when the loading rate was lower than 5 N/sec. In some extreme cases where loadings were applied as low as 1 N/sec, the average value of k for 12.7 mm (0.5 in.) indenter was very close to the one obtained previously by Yang and Sun [5] using dial gage. In this study, the loading rates for all tests were approximately equal to 40 N/sec.

Unlike the exponent n of the loading law for which the value of 3/2 seemed to yield good agreement with all experimental data, the exponent q of the unloading law (equation (2) or (3)) revealed much wider deviation for different sizes of indenter. The value of $q = 3/2$ corresponding to an elastic recovery according to the Hertzian theory was previously used by Crook [6] in a study of impacts between metal bodies. The experimental results from [5] and present study showed that the value of q varied from 1.5–2.5. Local

Downloaded 02 May 2010 to 171.66.16.54. Redistribution subject to ASME license or copyright; see http://www.asme.org/terms/Terms_Use.cfm

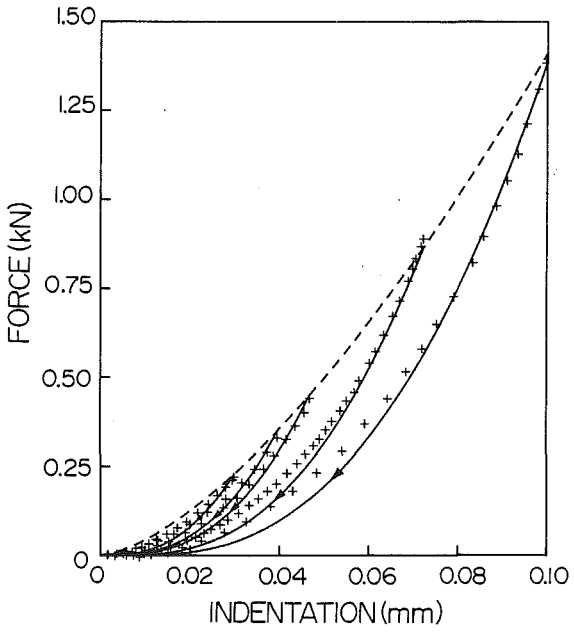


Fig. 7 Unloading curves of [0 deg/45 deg/0 deg/ – 45 deg/0 deg]$_{2s}$ specimens with 12.7 mm indenter according to equations (3) and (6) (q = 2.5, s_p = 0.094, α_p = 0.0167 mm)

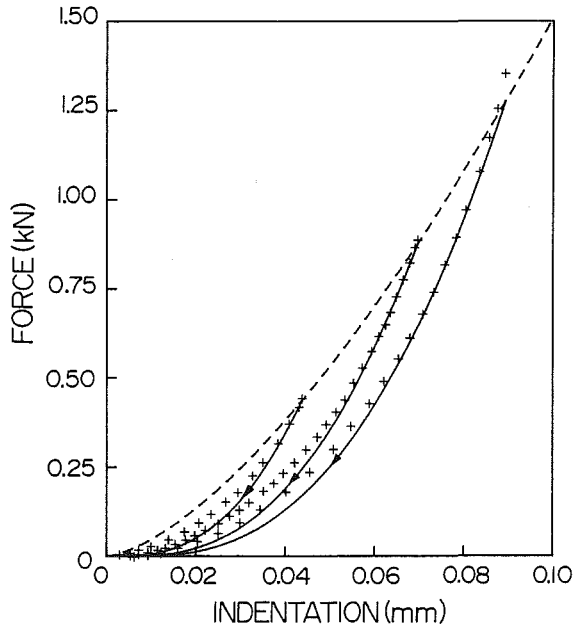


Fig. 8 Unloading curve of [90 deg/45 deg/90 deg/ – 45 deg/90 deg]$_{2s}$ specimens with 12.7 mm indenter according to equations (3) and (6) (q = 2.5, s_p = 0.094, α_p = 0.0167 mm)

plastic deformation, anisotropic properties of composite material, and unloading rate were all possible causes for this deviation. Obviously, an analytical study to determine the value of q as a function of the aforementioned factors is impracticable. Since the purpose of this study is to establish a contact law that can be used in the analysis of impact, the validity of this law must be verified from impact experiment. This will be investigated in the next section.

From equation (2) or (3) it can be seen that α_0 plays an essential role in the unloading law and hence the value of it must be estimated accurately. To simplify the modeling of the unloading law, it was assumed in [5] that the value of s for all the unloading curves remained the same. Consequently, a constant α_{cr} given by

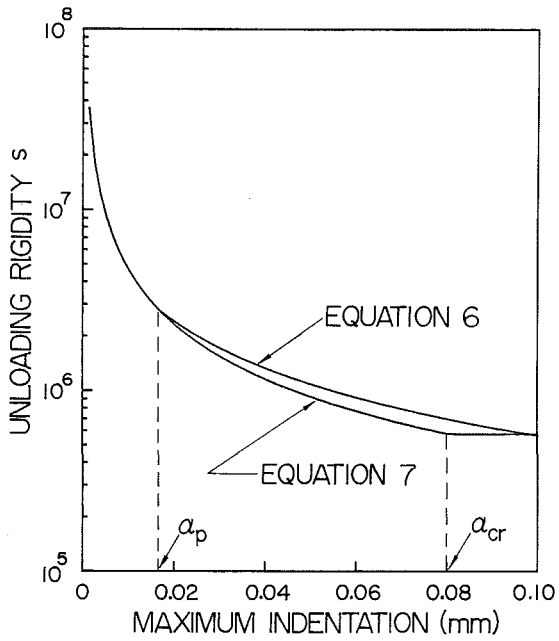


Fig. 9 Unloading rigidity s as function of maximum indentation according to equations (6) and (7)

$$\alpha_{cr} = k/s \tag{7}$$

was introduced. By choosing $q = 5/2$, the relation between the permanent indentation α_0 and the maximum indentation α_m was obtained as

$$\alpha_0/\alpha_m = 1 - (\alpha_{cr}/\alpha_m)^{2/5} \quad \text{as} \quad \alpha_m > \alpha_{cr}$$
$$\alpha_0 = 0 \quad \text{as} \quad \alpha_m \le \alpha_{cr} \tag{8}$$

Equations (8) and (6) were obtained experimentally, in which α_{cr} and α_p were considered to be material constants and were determined using α_0 and α_m from test data. For comparison, the relations between unloading rigidity s and maximum indentation α_m using equation (7) with α_{cr} = 0.0803 mm [5] and equation (6) with α_p = 0.0167 mm, respectively, are plotted in Fig. 9. It is interesting to see that these two equations give almost the same values of s up to α_m = 0.1 mm (4×10^{-3} in.) which is approximately the maximum indentation before failure could occur to the specimen. The advantage of using equation (7) for the formulation of the unloading law is that the value of s is constant for any α_m once the indentation passes α_{cr}, and only one unloading test is necessary to determine α_{cr} provided that load is high enough to produce permanent indentations. The use of equation (6) needs performing many tests to obtain a proper relation between α_0 and α_m according to equation (5). However, it should be noted that equation (7) is valid only if q = 5/2 is used in the unloading equation (3), while equation (6) has no such restriction.

Impact Experiments

Wang [8] has performed a number of impact tests on graphite/epoxy laminated beams and plates. It was shown that the strain responses calculated using the finite element method and the statically determined contact laws from [5] agreed with the experimental measurements quite well. This indicates that the statical indentation law is reasonably adequate in the dynamical impact analysis. It was also suggested that the contact force should be measured experimentally to provide an additional basis for comparison with the finite element solution which could allow further evaluation of the applicability of the contact laws in impact analysis. In this study, an attempt was made to obtain the

Downloaded 02 May 2010 to 171.66.16.54. Redistribution subject to ASME license or copyright; see http://www.asme.org/terms/Terms_Use.cfm

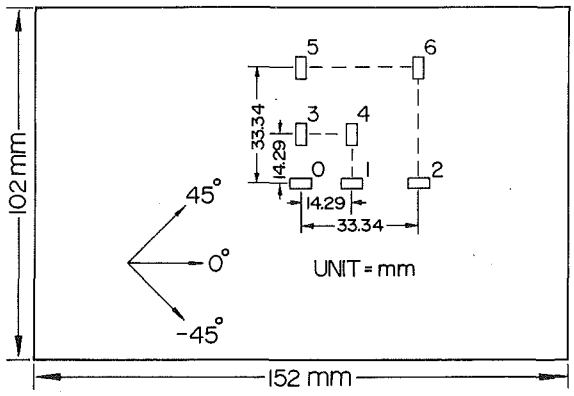


Fig. 10 Laminate dimension and strain gage locations

contact force directly. The contact force history and strain responses at various points on the plate were measured by means of an impact-force transducer and surface strain gages, respectively, and were compared with the predictions of finite element analysis using the present contact law.

Experimental Procedure. A 152 mm by 102 mm (6 in. by 4 in.) laminated plate cut from a [0 deg/45 deg/0 deg/ −45 deg/ 0 deg]$_{2s}$ graphite/epoxy panel was used as the impact target. The 0 deg-direction was arranged to parallel the long side of the plate. Seven strain gages (Micro Measurement Company, TYPE EA-13 – 062 AQ 350) were placed at different locations as shown in Fig. 10 to record the dynamic strain histories. One of the gages was placed on the surface directly opposite to the impact point to trigger the oscilloscope. This plate was hung with two strings at two corners to achieve the free boundary condition. The impactor was a 25.4 mm-(1 in.) long bullet-like steel mass which had a spherical head of 19.1 mm (0.75 in.) diameter, and with an impact-force transducer fixed in the middle. This mass was then attached to a thin rod to form a pendulum that could produce impact velocities up to 4 m/sec (160 in./sec). The total mass of the impactor was 0.0317 Kg (0.00217 slug). Signals from gages and transducer were amplified by a 3A9 Textronix amplifier and displayed on the screen of an oscilloscope.

Calibration of Impact-Force Transducer. The impact-force transducer used was Modal 200A05 marketed by PCB Piezotronics Inc. The structure of this transducer contains two thin quartz disks operating in a thickness compression mode and sandwiched between hardened steel cylindrical members. A built-in amplifier was used to reduce the high impedance of the voltage from the quartz element and to provide an output voltage, which was read out on oscilloscope, recorder etc. [9]. The impact force was then computed using the equation,

$$F = V_F / c_F \tag{9}$$

whee V_F is the output voltage and c_F is the sensitivity of the transducer. Since the value of c_F (1.0 mV/lb) provided by [9] was obtained under quasistatic conditions, it must be verified under impact conditions first so that later the results from the impact experiment can be correctly interpreted.

A circular cylindrical steel rod of 50 mm (2 in.) in diameter and 30.2 m (1.19 in.) long hung on strings was used as the impact target to calibrate the transducer. The acceleration of the rod was measured by using a Model 302A accelerometer, which was mounted on the end of the rod opposite to the impacted end. The total weight of the target was 4.915 N (1.105 lb).

Using equation (9) and

$$a = V_a / c_a \tag{10}$$

$$F = ma \tag{11}$$

the value of c_F can be obtained as

$$c_F = (c_a / m)\,(V_F / V_a) \tag{12}$$

where V_a and c_a are the output voltage and the sensitivity of the accelerometer, respectively, a is the acceleration of the target, and m is the mass of the target.

When impacting a metal impactor on a metal target with no pad on the impact surface, a high-frequency ringing can be heard at the output of the transducer. To obtain smooth output curves, a thin soft pad was placed on the impact region of the target to eliminate the high-frequency ringing. The cause of this ringing phenomenon will be discussed later. The output voltages from the transducer (V_F) and the accelerometer (V_a) were recorded on an oscilloscope simultaneously. Values of V_F were then plotted versus the corresponding values of V_a taken from these two curves at several discrete points in time and then fitted into a straight line. The slope of this line represents the ratio of V_F/V_a which was then substituted in equation (12) to calculate the sensitivity c_F.

By using equation (12) and the test data, the average value of c_F was calculated to be 0.494 mV/lb. A comparison with the value 1.0 mV/lb given by [9] showed that the test result had approximately 50 percent error. However, since the quartz elements were located at the center of the impactor while the impact force was applied at the end, the force history picked up by the quartz elements was not the real history of the impact force. A simple analysis on the propagation of stress wave in a 25.4 mm- (1 in.) long steel rod with free-free boundary condition was performed, and the result showed that with an impulse loading function similar to the experimental loading history applied at the end of the rod, the average ratio of the stress resultant at the midpoint of the rod to the applied loading was approximately 0.498, which is very close to the value of c_F obtained previously. On the other hand, the accelerations everywhere in the rod were almost the same. This indicated that the accelerometer did measure the real acceleration of the target while the impact-force transducer only picked up the force history at its own position. In other words, the wave motion in the impactor cannot be neglected in interpreting the measurements using force transducer.

It was also observed that the ringing phenomenon mentioned before was caused by the stress wave traveling back-and-forth in the rod. Repeating the previous analysis by changing the shape of the impulse loading showed that the initial slope of the impulse forcing function would affect the amplitude of ringing. The steeper the initial slope was (or, the harder the impact surface was), the higher the amplitude of ringing would be. When impacting the steel impactor on graphite/epoxy surface, this ringing phenomenon was also observed.

Finite Element Analysis

Plate Finite Element. A nine-node isoparametric plate finite element developed by Yang [10] based on the laminate theory of Whitney and Pagano [11] was used to model the dynamic motion of the laminated plate. At each node there are five degrees of freedom, i.e., displacement components of mid-plane in the x, y, and z directions, and rotations of the cross sections perpendicular to the x and y axis. For symmetric laminates, the flexural deformation is uncoupled from the inplane extensional and shear deformations, and hence, the degrees of freedom corrresponding to the inplane displacement components can be neglected in the transverse impact problem. The stiffness and mass matrices were obtained by a numerical integration using Gauss quadrature. Following standard finite element procedures, the system

Downloaded 02 May 2010 to 171.66.16.54. Redistribution subject to ASME license or copyright; see http://www.asme.org/terms/Terms_Use.cfm

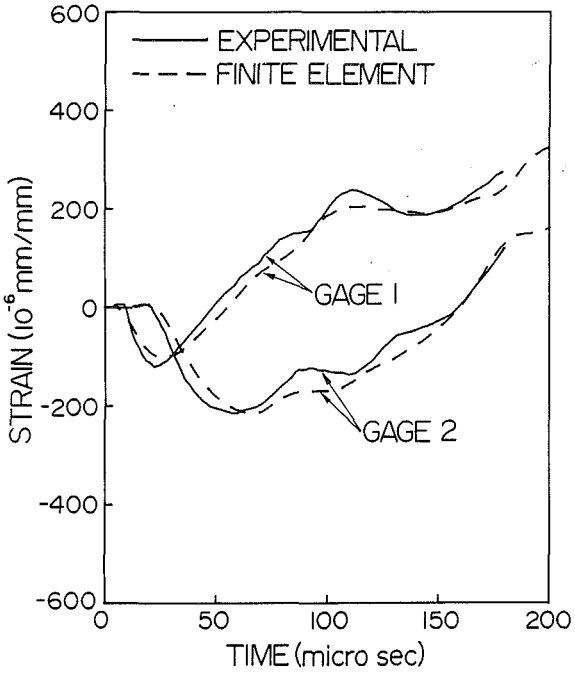


Fig. 11 Strain response histories of laminate at gages 1 and 2

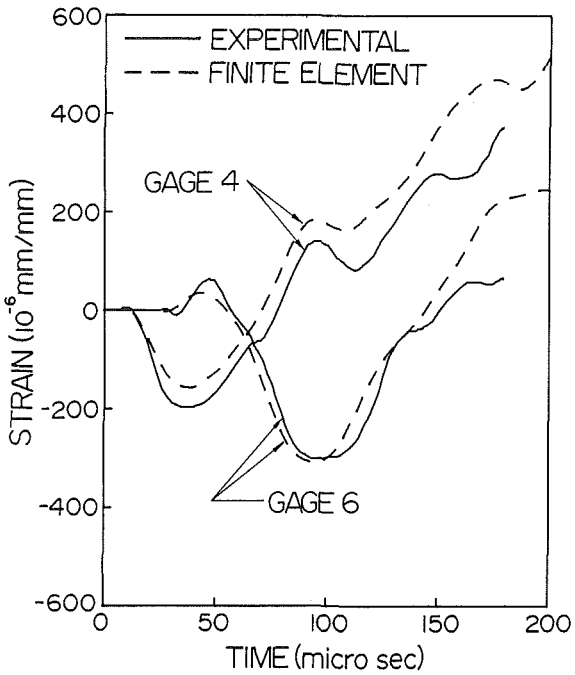


Fig. 13 Strain response histories of laminate at gages 4 and 6

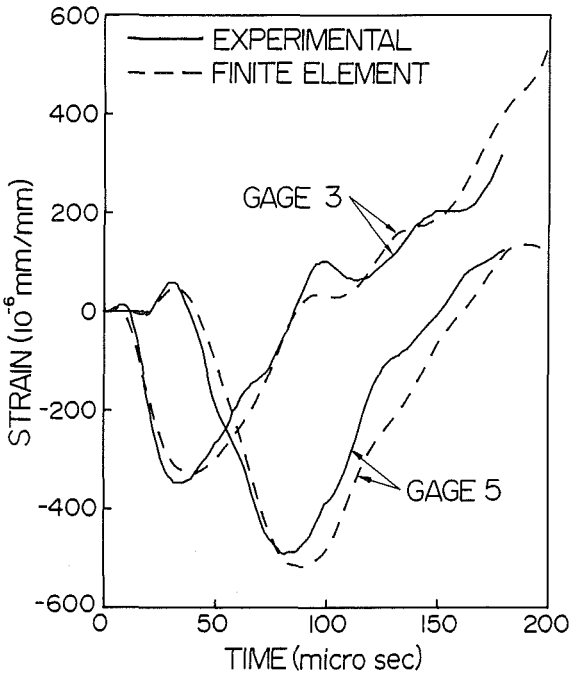


Fig. 12 Strain response histories of laminate at gages 3 and 5

stiffness matrix $[K_p]$ and mass matrix $[M_p]$ were assembled from the element matrices. The equations of motion were expressed in matrix form as

$$[M_p]\{\ddot{q}_p\} + [K_p]\{q_p\} = \{P_p\} \tag{13}$$

where $\{q_p\}$ is the assembled global displacement vector, and

$$\{P_p\}^T = \{0, \ldots, F, \ldots, ,0\} \tag{14}$$

is the force vector in which F is the contact force associated with the degree of freedom corresponding to the w-displacement at the impact point.

Modeling of Impactor. It has been shown that to correctly interpret the experimental transducer response, it is necessary to treat the impactor as an elastic body. A high-order rod finite element developed by Yang and Sun [12] was used to model the impactor. This element has two degrees of freedom at each node, namely the axial displacement u and its first derivative $\partial u/\partial x$. It has been shown that this higher-order element is far more superior than the elements with less degrees of freedom in the analysis of dynamic problems. Following the usual finite element formulation, the equation of motion of the impactor was obtained as

$$[M_r]\{\ddot{q}_r\} + [K_r]\{q_r\} = \{P_r\} \tag{15}$$

where

$$\{P_r\}^T = \{F, 0, \ldots, ,0\} \tag{16}$$

in which F is the contact force applied at the impacting end of the impactor.

Results and Discussion

The 152 mm by 102 mm (6 in. by 4 in.) graphite/epoxy laminate was modeled by 140 (14 × 10 mesh) plate elements while the impactor was modeled by 20 rod elements. The two sets of equations (13) and (15) along with the contact laws given by equations (1) and (2) were solved simultaneously. The finite difference method with $\Delta t = 0.2$ μsec was used to integrate the time variable. A coarser finite element mesh for plate was used and it was found that the present mesh yielded converged solutions. A three-dimensional analysis using 112 axisymmetric finite elements to model the impactor was also performed, and the results showed that the response at the midpoint of the impactor had no significant difference compared with the one obtained by using rod elements.

An impact velocity of 2.92 m/sec (115 in./sec) was used in the experiment. Figures 11–13 show the strain response histories at the six locations picked up by the strain gages. The results obtained using the finite element methods and the contact laws are also shown in these figures. It is evident that the finite element solutions agree with the experimental data very well.

In Fig. 14, the experimental transducer responses and the computed transducer responses using finite element are plotted against time as curve *I* and curve *II*, respectively. The

Downloaded 02 May 2010 to 171.66.16.54. Redistribution subject to ASME license or copyright; see http://www.asme.org/terms/Terms_Use.cfm

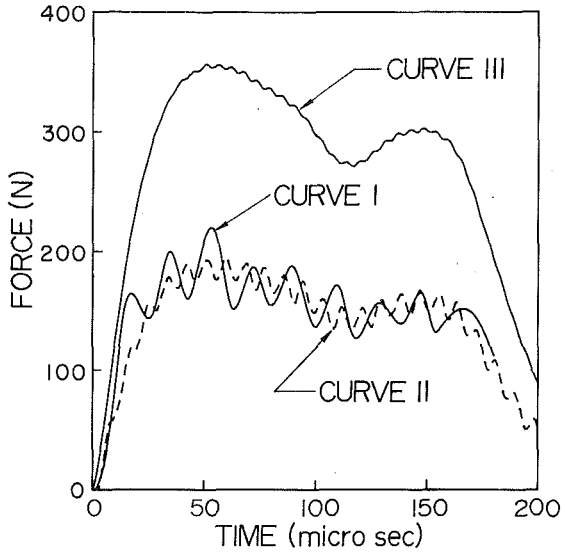


Fig 14 Experimental and computed transducer responses (curve *I* and *II*) and computed contact force history (curve *III*)

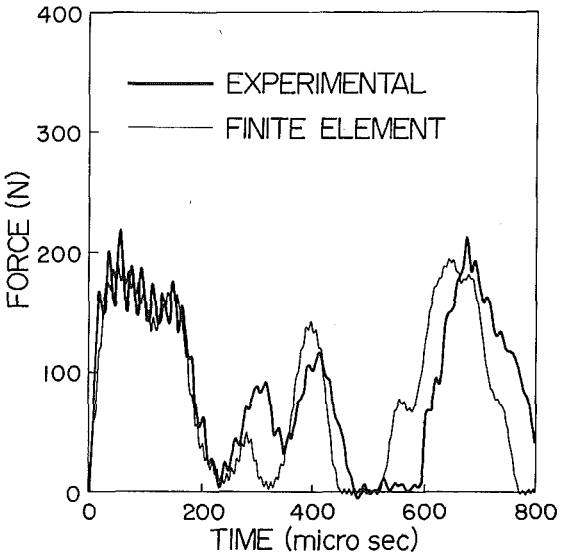


Fig. 15 Experimental and computed (finite element) transducer response histories up to 800 μsec

computed contact force history is also plotted as curve *III*. It can be seen that the magnitudes of curves *I* and *II* agree fairly well. The frequencies of ringing for these two curves, however, are quite different. For the finite element results, the time interval between two consecutive peaks of ringing is approximately equal to the time that the longitudinal stress wave needs to travel over the impactor. This indicates that these ringings are simply caused by the transient wave traveling back-and-forth in the impactor.

From Fig. 14 it can be seen that curve *I* has exactly nine peaks in 180 μsec, and the time interval between two consecutive peaks is about 20 μsec. It is noted that this transducer has a rise time of 10 μsec [9], which is the time for it to reach the maximum response. Any input signal with period smaller than twice this value, will be smoothed out by the transducer, and the output signal may appear to have lower frequency. In other words, the period of the output signal will be at least 20 μsec. This explains the lower frequency of ringing in the output voltage from the transducer.

The total duration of contact for this impact test was about 800 μsec, and multiple contact was also observed from the test data. Figure 15 shows the experimental transducer response and the computed transducer response up to 800 μsec. Although these two results do not match very well in phase after the end of the first contact, it is evident that the finite element analysis does predict the magnitude, contact duration, and the multiple contact phenomenon.

Summary

The contact laws for the 12.7 mm-(0.5 in.) and 19.1 mm-(0.75 in.) spherical steel indenters and the graphite/epoxy laminate were determined experimentally by means of a statical indentation test. The beam specimens were clamped at both ends. Loading and unloading curves were fitted into power equations. A linear relation was found between the permanent indentation and the maximum indentation at unloading, which was seen to be independent of the size of indenters. This relation was used to determine the coefficient of the unloading law. Test results showed loading curves followed the 1.5 power laws very well, while the power indices for unloading curves varied from 1.5–2.5.

The statically determinend contact laws were incorporated into an existing nine-node isoparametric plate finite element program to study the dynamic response of a graphite/epoxy laminated plate subjected to impact of a hard object. An impact experiment was conducted on a graphite/epoxy laminated plate with free-end boundary conditions to verify the validity of statical contact laws in the dynamical impact analysis. It was shown that the strain responses predicted using the finite element method agreed very well with the test results. It was also demonstrated that the finite element solution for the contact force history matched very well with the measured contact force obtained using an impact-force transducer.

Acknowledgment

This work supported by a NASA Lewis Center Grant No. NSG 3185. The authors are grateful to Professor J. F. Doyle for his valuable suggestions and help.

References

1 Hertz, H., "Uber die Beruhrung fester Elastischer Korper," *Journal Reine Angle Math*, Crelle, Vol. 92, 1881, p. 155.

2 Goldsmith, W., *Impact*, Edward Arnold, London, 1960.

3 *Foreign Object Impact Damage to Composite*, ASTM STP 568, American Society for Testing and Materials, 1973.

4 Willis, J. R., "Hertzian Contact of Anisotropic Bodies," *Journal of Mechanics and Physics of Solids*, Vol. 14, 1966, pp. 163–176.

5 Yang, S. H., and Sun, C. T., "Indentation Law for Composite Laminates," *Composite Materials: Testing and Design*, ASTM STP 787, American Society for Testing and Materials, 1982, pp. 425–449.

6 Crook, A. W., "A Study of Some Impacts Between Metal Bodies by a Piezoelectric Method," *Proceedings of the Royal Society*, London, Series *A*, Vol. 212, 1952, p. 377.

7 Sun, C. T., Sankar, B. V., and Tan, T. M., "Dynamic Response of SMC to Impact of a Steel Ball," *Advances in Aerospace Structures and Materials*, The Winter Annual Meeting of the American Society of Mechanical Engineers, Washington, D.C., 1981, pp. 99–107.

8 Wang, T., "Dynamic Response and Damage of Hard Object Impact on a Graphite/Epoxy Laminate," Ph.D. Dissertation, Purdue University, West Lafayette, Ind., 1982.

9 *Operating Instructions*, Model No. 200A05 Transducer, PCB Piezotronics, INC.

10 Yang, S. H., "Static and Dynamic Contact Behavior of Composite Laminates," Ph.D. Dissertation, Purdue University, West Lafayette, Ind., 1981.

11 Whitney, J. M., and Pagano, N. J., "Shear Deformation in Heterogeneous Anisotropic Plates," ASME JOURNAL OF APPLIED MECHANICS, Vol. 37, 1970, pp. 1031–1036.

12 Yang, T. Y., and Sun, C. T., "Finite Elements for the Vibration of Framed Shear Walls," *Journal of Sound and Vibration*, Vol. 27, No. 3, 1973, pp. 297–311.

Downloaded 02 May 2010 to 171.66.16.54. Redistribution subject to ASME license or copyright; see http://www.asme.org/terms/Terms_Use.cfm

Arbitrarily Oriented Cracks in a Reinforced Sheet

C.-C. Chu
Engineering and Research Staff,
Ford Motor Company,
Dearborn, Mich. 48121

The elastic interaction between a crack and a fiber is studied for various loading conditions. Generalized from earlier work by Greif and Sanders, the present formulation is valid for arbitrary relative orientation between the crack and the fiber. Helpful design information, such as the critical loading condition and the critical fiber orientation to trigger a certain failure mode, is therefore attainable. The fundamental solutions, each associated with proper parameters and proper boundary conditions, can also be superposed to model more realistic problems.

1 Introduction

During the past few years, fiber-reinforced composite materials have become among the most actively studied materials, especially in the aerospace and automotive industries. Despite these efforts, a great deal of difficulty in performing failure analyses for such materials remains. This is mainly due to the strong heterogeneity of these materials. The complexity of observed failure phenomena involves having multiply failure modes that trigger and interact with one another (see, for example, [1]), suggesting that analyses on the microscopic as well as the macroscopic level are necessary to help understand the fracture behavior of composites.

On the microscopic level, a significant amount of information has been obtained via the application of linear elastic fracture mechanics to the composite field. For example, the stress intensity factor (K), which represents the crack tip stress field, was utilized to predict the strength of a notched laminate [2]. There are also analytical models to calculate K in a layered composites [3–6]. While these layered models help us gain rather complete insight into the crack-tip stress field in composites, they seem to be inadequate in analyzing the effects of an approaching crack on the fibers.

This paper will investigate the effects of fibers on the crack tip stress field, and vice versa, by considering linear elastic fibers in an otherwise homogeneous isotropic linear elastic matrix. A special case of the problem with the crack running normal to a fiber and subject to a tensile load coaxial with the fiber at infinity was studied by Greif and Sanders [7]. In [7], the dependence of the mutual influence on the geometric and material parameters was emphasized. Here attention will be primarily focused on the generalization and application of the solution method. Also to be examined is the importance of load orientation, relative to the fiber and to the crack, on the fiber-crack interaction.

The formulation of this generalized problem, emphasizing the differences between the current treatment and that in [7], is presented in Section 2. Results for single-fiber problems are shown in Section 3. In the last section, an attempt is made to extract some useful design information from the fundamental solutions.

2 Formulation

As shown in Fig. 1, the problem considered is a crack of length $\bar{l}_c$ contained in an infinite sheet strenghthened by a single fiber. The angle between the crack and the fiber is denoted by θ. The normal distance between the fiber and the closer crack tip a is denoted by $\bar{l}$. The stress field at infinity is indicated by a superscript ∞. For $\theta = \pi/2$, the problem reduces to that studied in [7].

By assuming the sheet thickness to be very small relative to other dimensions, approximate plane stress conditions prevail. Therefore, we can formulate the problem in terms of the displacement potentials of Muskhelishvili [8]. By normalizing variables, i.e., length with respect to $\bar{l}$, stress field with respect to $\bar{\sigma}^{\infty}_{xx}$ and the displacement potentials with

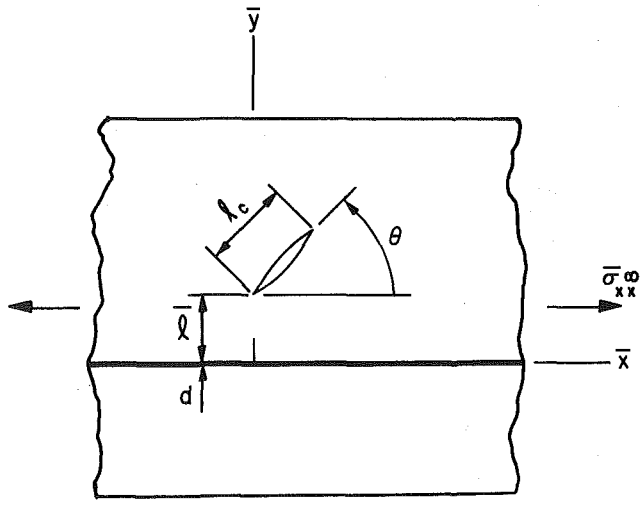


Fig. 1 A sketch of the cracked sheet reinforced by a single fiber

Contributed by the Applied Mechanics Division for publication in the JOURNAL OF APPLIED MECHANICS.

Discussion on this paper should be addressed to the Editorial Department, ASME, United Engineering Center, 345 East 47th Street, New York, N.Y. 10017, and will be accepted until two months after final publication of the paper itself in the JOURNAL OF APPLIED MECHANICS. Manuscript received by ASME Applied Mechanics Division, December, 1983; final revision, May, 1984.

Copyright © 1985 by ASME
Downloaded 02 May 2010 to 171.66.16.54. Redistribution subject to ASME license or copyright; see http://www.asme.org/terms/Terms_Use.cfm

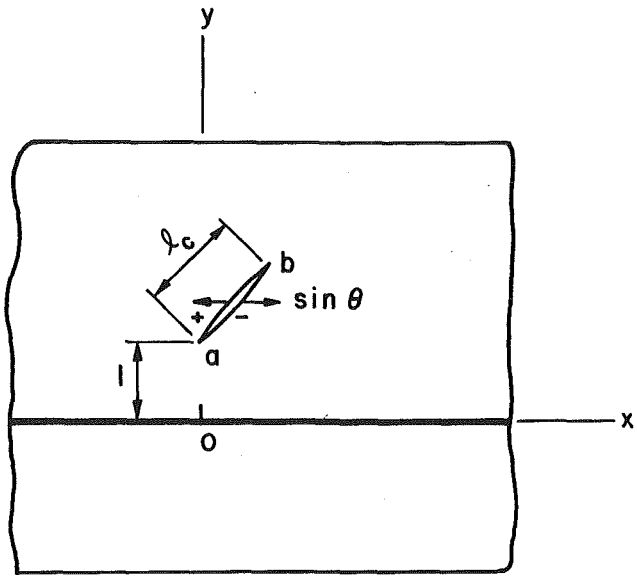


Fig. 2 A sketch of the simplified problem with normalized parameters

respect to the product $(\bar{l}\bar{\sigma}^{\infty}_{xx})$, the displacement and stress components are given by the analytic functions ϕ and ψ in the complex z-plane $(z=x+iy)$ as follows:

$$E(u-iv)=(3-\nu)\phi-(1+\nu)(\bar{z}\phi'+\psi) \tag{1a}$$

$$\sigma_{xx}-\sigma_{yy}-2i\sigma_{xy}=-2(\bar{z}\phi''+\psi') \tag{1b}$$

$$\sigma_{xx}+\sigma_{yy}=2(\phi'+\bar{\phi}') \tag{1c}$$

where u and v are the normalized displacements in the x and y-directions, respectively. The parameters E and ν are Young's modulus and Poisson's ratio of the material, respectively. Also in equations (1), $(\ )'$ denotes the differentiation of a complex function with respect to its argument z, and $(\bar{\ })$ denotes the complex conjugate of a complex function.

It is common practice to decompose a linear elastic crack problem into (*a*) an uncracked sheet having a uniform stress state and (*b*) a crack sheet subject to normalized horizontal traction (T_x,T_y) $[=(-\sin\theta,0)$ for the geometry shown in Fig. 1] along the crack surface, and zero traction at infinity. The problem is thus transformed to the one shown in Fig. 2.

Note that the boundary conditions at infinity in Fig. 1 can be easily generalized to allow nonzero σ^{∞}_{xy} and σ^{∞}_{yy}. In that case, the scale of normalization for the stress field and displacement potentials must be clarified. For example, here we define $(\sigma^{\infty}_{xx},\ \sigma^{\infty}_{xy}) = \sigma^{\infty}$ $(\sin\gamma,-\cos\gamma)$ and $(\sigma^{\infty}_{xy},\ \sigma^{\infty}_{yy}) = \sigma^{\infty}(-\sin\gamma,\cos\gamma)$ for the stress field prescribed at $|x|=\infty$ and $|y|=\infty$, respectively, and use σ^{∞} as the normalizing scale. The angle γ is used later as the geometric parameter indicating the direction of the loading axis.

Following the approach in [7], if the fiber is assumed to be comparatively thin and the displacement continuous (or the bonding between the fiber and the material perfect), the inhomogeneity condition due to the existence of the fiber can be approximated by a special boundary condition along $y=0$ which can be obtained by equilibrating the force along the fiber axis; namely,

$$\frac{\partial^2 u}{\partial x^2}+\frac{\bar{l}\sigma^{\infty}}{dE_f}\left(\sigma^{+}_{xy}-\sigma^{-}_{xy}\right)=0 \tag{2}$$

where E_f is Young's modulus of the fiber, d is the width of the fiber, and the superscripts $+$ and $-$ are used to indicate the value (of σ_{xy}) at $(x,0)$ when the line $y=0$ is approached from the upper and lower half planes, respectively.

The traction boundary condition along the crack is

$$\bar{z}\phi'+\psi+\bar{\phi}=-i(T_x-iT_y)r+C \tag{3}$$

where r is the distance to a point on the crack from crack tip a, and C is a complex constant. The right-hand side of equation (3) is easily obtained from integrating the constant complex traction $-i(T_x-iT_y)$ along the crack. As will be noted later, equation (3) specifies only the boundary condition along the $(+)$ side of the crack (Fig. 2). The other half of it is enforced by requiring the traction prescribed on the $(-)$ side to be of the same magnitude but of opposite sign as that on the $(+)$ side.

Now the problem is to find the displacement potentials ϕ and ψ satisfying the aforementioned traction conditions and vanishing at infinity. Two sets of Green's functions, due to a source load at ζ along the crack, which satisfy equation (2) and zero stress conditions at infinity are obtained as:

$$\begin{cases}\phi=\dfrac{1}{z-\zeta}+\dfrac{1}{2}\phi_1\\[2ex] \psi=\dfrac{1}{2}\psi_1=-\dfrac{1}{2}\left(\dfrac{1}{\alpha}\phi_1+z\phi_1'\right)\end{cases} \tag{4}$$

with

$$\phi_1=-\frac{\alpha\bar{\zeta}}{(z-\bar{\zeta})^2}+(1+\alpha+i\lambda\alpha\bar{\zeta})I(z,\bar{\zeta})$$

and

$$\begin{cases}\phi=\dfrac{1}{2}\phi_2\\[2ex] \psi=\dfrac{1}{z-\zeta}+\dfrac{1}{2}\psi_2=\dfrac{1}{z-\zeta}-\dfrac{1}{2}\left(\dfrac{1}{\alpha}\phi_2+z\phi_2'\right)\end{cases} \tag{5}$$

with

$$\phi_2=\alpha I(z,\bar{\zeta})$$

where

$$I(z,\bar{\zeta})=i\lambda e^{-i\lambda z}\int^{z}d\xi\,\frac{e^{i\lambda\xi}}{\xi-\bar{\zeta}}-\frac{1}{z-\bar{\zeta}}$$

and

$$\alpha=\frac{1+\nu}{3-\nu}$$

$$\lambda=\frac{\bar{l}E}{dE_f}\frac{4}{(1+\nu)(3-\nu)}.$$

The lower limit of the integral $I(z,\bar{\zeta})$ can be chosen as $c+i\,\infty$, with c being any real number, to satisfy the conditions that $\phi\to 0$ and $\psi\to 0$ as $z\to\infty$. Note that equations (4) and (5) are the general forms of the Green's functions obtained in [2]. The parameter λ, as it is defined, can be used to indicate the mutual influence between the fiber and the crack. For instance, a decrease in $\bar{l}/d$ or E/E_f that gives smaller λ is likely to result in a crack-tip field more disturbed from the homogeneous solution.

The displacement potentials now can be obtained as a superposed result of the fundamental solutions, equations (4) and (5), in terms of unknown intensity functions f and g along the crack surface:

$$\phi=\int_0^{l_c}d\eta\left[f(\eta)\left(\frac{1}{z-\zeta}+\frac{1}{2}\phi_1(z,\zeta)\right)+\frac{1}{2}g(\eta)\phi_2(z,\zeta)\right]$$

$$\psi=\int_0^{l_c}d\eta\left[\frac{1}{2}f(\eta)\psi_1(z,\zeta)+g(\eta)\left(\frac{1}{z-\zeta}+\frac{1}{2}\psi_2(z,\zeta)\right)\right]. \tag{6}$$

Here the point ζ along the crack is related to the integration parameter η by $\zeta=i+\eta\,e^{i\theta}$. This is the same relationship between r and z as, for example, in equation (3).

Downloaded 02 May 2010 to 171.66.16.54. Redistribution subject to ASME license or copyright; see http://www.asme.org/terms/Terms_Use.cfm

As mentioned earlier, the tractions on two sides of the crack are of the same magnitude but of opposite sign. It can be shown that as a result the intensity functions f and g can be related to one another. First, we write out the stress components in terms of the displacement potentials as

$$\sigma_{nn} - i\sigma_{nt} = \phi' + \bar{\phi}' + (\bar{z}\phi'' + \psi')e^{2i\theta}. \tag{7}$$

Here subscripts n and t denote the components in directions normal and tangent to the crack surface, respectively. The aforementioned traction condition can then be stated as

$$(\sigma_{nn} - i\sigma_{nt})_+ = (\sigma_{nn} - i\sigma_{nt})_-. \tag{8}$$

By substituting equations (6) and (7) into equation (8), it is noted that only the singular terms of the integrand contribute differently to the stresses when the point along the crack is approached from the (+) and the (−) side. Therefore, to satisfy equation (8) only these singular terms need to be considered. By employing the Plemelj formulas, we obtain that

$$g(\eta) = \bar{f}(\eta)e^{2i\theta} - \bar{\zeta}f'(\eta)e^{-i\theta}. \tag{9}$$

To have the stresses at crack tips no more singular than $R^{-1/2}$, where R is the radial distance away from the tips, f is also required to satisfy

$$f(0) = f(l_c) = 0. \tag{10}$$

By substituting equations (4), (5), (6) and (9) into equation (3), the latter is transformed into the following singular integral equation:

$$\int_0^{l_c} d\eta \left\{ \frac{2\bar{f}e^{i\theta}}{r-\eta} + \frac{1}{2} f X_1 + \frac{1}{2} \bar{f} X_2 + \frac{1}{2}\left(fe^{-2i\theta} + \bar{f}e^{2i\theta}\right) X_3 \right\} = -i\left(T_x - iT_y\right) r + c \tag{11}$$

with

$$X_1 = \bar{z}\phi_1' + \psi_1 + \bar{\zeta}e^{-i\theta}\frac{d}{d\eta}\left(\bar{z}\phi_2' + \psi_2\right)$$

$$X_2 = \bar{\phi}_1 + \zeta e^{i\theta}\frac{d}{d\eta}\bar{\phi}_2$$

$$X_3 = \bar{z}\phi_2' + \psi_2 + \bar{\phi}_2.$$

Subject to the end conditions (equations (10)), equation (11) can be solved for f. The method used here is taken from Erdogan and Gupta's paper [9]. New parameters $\hat{r}$ and $\hat{\eta}$ are first defined as

$$\hat{r} = \frac{2}{l_c} r - 1 \qquad \text{and} \qquad \hat{\eta} = \frac{2}{l_c}\eta - 1$$

so that equation (11), now having $[-1,1]$ as the integration interval, remains valid for all $\hat{r}$ in the same interval.

Since in this approach the presence of the fiber is viewed as a disturbance (via the special condition along the fiber axis, equation (2)) to the otherwise homogeneous material, it is expected that the same $(1-\hat{\eta}^2)^{-1/2}$-type of singularity in stress components as in the homogeneous case also holds here. Correspondingly, f can be written as $F(\hat{\eta})\sqrt{1-\hat{\eta}^2}$. Using this form of f in equation (11), the integral, according to [9], can be approximated by a summation of addends of identical forms as those of the integrand if the nodal points are chosen properly. With a little manipulation the result is a set of $(n+1)$ algebraic equations for n F's and the constant C:

$$\sum_{k=1}^{n} \frac{1-\hat{\eta}_k^2}{n+1}\left\{ \frac{2\bar{F}_k e^{i\theta}}{\hat{r}_i - \hat{\eta}_k} + \frac{1}{2}\left[F_k X_{1ik} + \bar{F}_k X_{2ik} + \left(F_k e^{-2i\theta} + \bar{F}_k e^{2i\theta}\right) X_{3ik}\right]\right\} = -i\left(T_x - iT_y\right)\frac{l_c}{2}\left(\hat{r}_i + 1\right) + C \qquad i = 1,2,\ldots(n+1) \tag{12}$$

where the nodal points $\hat{r}_i$ and $\hat{\eta}_k$, and accordingly $\hat{z}_i$ and $\hat{\zeta}_k$, are selected as

$$\hat{r}_i = \cos\frac{(2i-1)\pi}{2(n+1)} \qquad i = 1,2,\ldots,(n+1)$$

and

$$\hat{\eta}_k = \cos\frac{k\pi}{n+1} \qquad k = 1,2,\ldots,n.$$

The subscripts i and k in equations (12) indicate the location $(\hat{z}_i, \hat{\zeta}_k)$ where a function is evaluated.

Equations (12) can be solved numerically with little difficulty. The results are presented in the following section.

3 Results for the Single-Fiber Case

The numerical solutions are found to converge rapidly with increasing n. The results presented in this section are obtained by taking $n = 20$. The accuracy of the solutions is examined by comparing the current results for $\theta = \pi/2$ with those in [2]; very good agreement is found. (Note that due to minor differences in formulating the problem, $(1 + l_c \sin\theta)^{-1}$ and $(1 + l_c \sin\theta)\lambda$ are the corresponding values for a_{GS} and λ_{GS}, respectively.) Hereafter, the subscript GS is used to denote the parameters defined by Greif and Sanders in [7].

In [7], the dependence of the crack-tip field and the load carried by the fiber on parameters a_{GS} and λ_{GS} was typically illustrated. Here the effects on the stress field from the direction of the crack and that of the applied force, relative to the fiber axis, is emphasized.

The crack-tip field is represented by stress intensity factors K. Three forms of K are included; namely, K_I and K_{II}, the mode I and mode II intensity factors, and K^*, which is obtained by assuming that the crack will grow along the radial plane from the crack tip which has the highest tensile stress (and thus the lowest shear stress) [10]. The K's are presented as ratios to K_{I0}, the value of K_I for a homogeneous material.

The critical stress in the fiber at the point closest to the crack, which is the origin in Fig. 2, is measured by the magnification factor L, defined as the ratio of the axial stress in the fiber to the stress applied at infinity, σ^∞. By resorting to the assumptions that the displacements are continuous across the matrix-fiber interface and that the axial stress of the fiber can be simply approximated by $E_f\,(\partial u)/(\partial x)$, L is obtained from equations (1a), (4), and (5) as

$$L = Re\left(\int_0^{l_c} \left\{ \frac{-2\frac{1-\nu}{1+\nu} f + fe^{-2i\theta} + \bar{f}e^{2i\theta}}{(z-\zeta)^2} + \frac{2(\bar{\zeta}-\bar{z})f}{(z-\zeta)^3} + \frac{1}{\alpha}\left(fe^{-2i\theta} + \bar{f}e^{2i\theta} + f\bar{\zeta}e^{-i\theta}\frac{d}{d\eta}\right)\left[\phi_2' + \frac{\alpha(z-\bar{z})}{2}\phi_2''\right] + \frac{f}{\alpha}\left[\phi_1' + \frac{\alpha(z-\bar{z})}{2}\phi_1''\right] \right\}(1+\nu)\,d\eta \right). \tag{13}$$

Here z denotes the point at which the critical load is predicted to occur.

The shear stress at the fiber-matrix interface, which may indicate the propensity for debonding, can be calculated from equations (1b), (4), and (5). The magnification factor L_τ, defined as the ratio of this shear stress to σ^∞, can be calculated by

$$L_\tau = Im\left(\int_0^{l_c} \left\{ -\frac{fe^{-2i\theta} + \bar{f}e^{2i\theta}}{(z-\zeta)^2} + \frac{2(\bar{z}-\bar{\zeta})f}{(z-\zeta)^3} + \frac{f}{2}\left((\bar{z}-z)\phi_1'' - \frac{\beta}{\alpha}\phi'\right) + \frac{1}{2}\left(fe^{-2i\theta} + \bar{f}e^{2i\theta} + \bar{\zeta}fe^{-i\theta}\frac{d}{d\eta}\right)\left((\bar{z}-z)\phi_2'' - \frac{\beta}{\alpha}\phi_2'\right) \right\} d\eta \right).$$

Downloaded 02 May 2010 to 171.66.16.54. Redistribution subject to ASME license or copyright; see http://www.asme.org/terms/Terms_Use.cfm

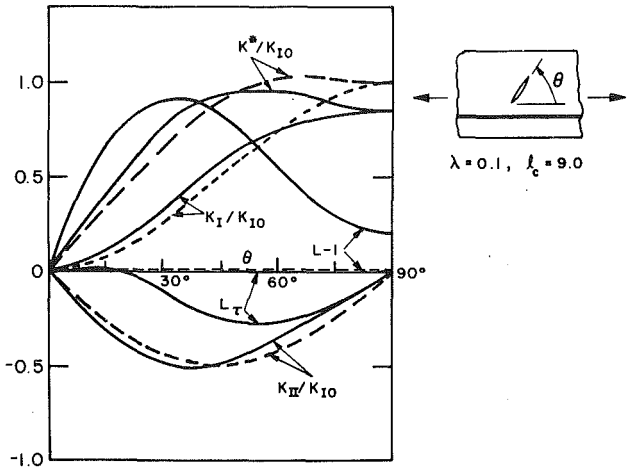


Fig. 3 Results of K/K_{I0} and L as a function of crack angle θ for cases in which the load is coaxial with the fiber axis

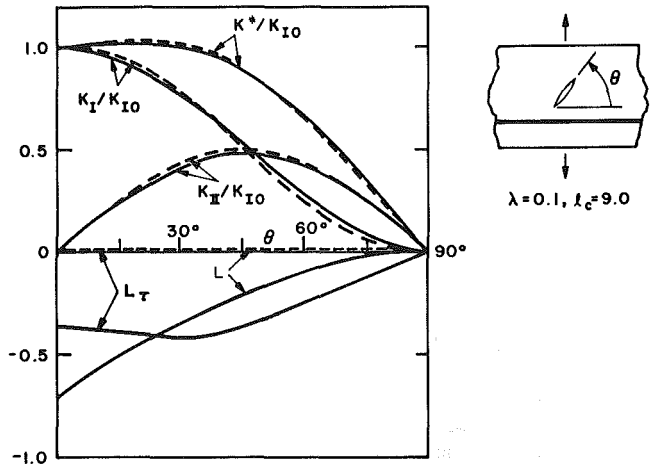


Fig. 4 Results of K/K_{I0} and L as a function of crack angle θ for cases in which the load is perpendicular to the load axis

In all the following examples, Poisson's ratio is assumed to be 1/3. Values of l_c and λ used in the calculations are specified in the figures. Figure 3 shows the effects of different crack orientations when the applied load is assumed to be coaxial with the fiber. In Fig. 3, as well as in the following figures, solid curves for (K/K_{I0}) are for crack tip a. The counterparts for a homogeneous medium are plotted as dashed curves. The latter can be easily obtained from classical elasticity solutions. For example, under the loading condition prescribed in Fig. 3, $K_I/K_{I0} = \sin\vartheta \cos\theta$, $K_{II}/K_{I0} = -\cos^2\theta$ and $K^*/K_{I0} = \max_{\text{w.r.t.}\delta}$ [$\cos\delta/2$ ($\sin\theta \cos\theta \cos^2\delta/2 + 3/2 \cos^2\theta \sin\delta$)]. The differences between the two sets of curves represent the perturbations of the crack-tip fields from homogeneous solutions due to the existence of the fiber and, therefore, can be used as a measure of the effectiveness of the fiber reinforcement. Since the fiber is expected to have more influence on the field of the nearer crack tip, curves for the farther crack tip b must fall between the two sets displayed.

Also displayed in the figures are the effects of crack and load orientations on the magnification factors L and L_τ. The solid curves are for the present problem and the dashed curves are straightforward results from an uncracked sheet. The difference between these two sets of curves thus shows the influence of an approaching crack on the axial stress in the fiber and the shear stress at the fiber-matrix interface.

It can be observed from Fig. 3, and later from Figs. 4 to 6, that the fiber is not always reinforcing since the stress intensity factors can be found higher than their counterparts in

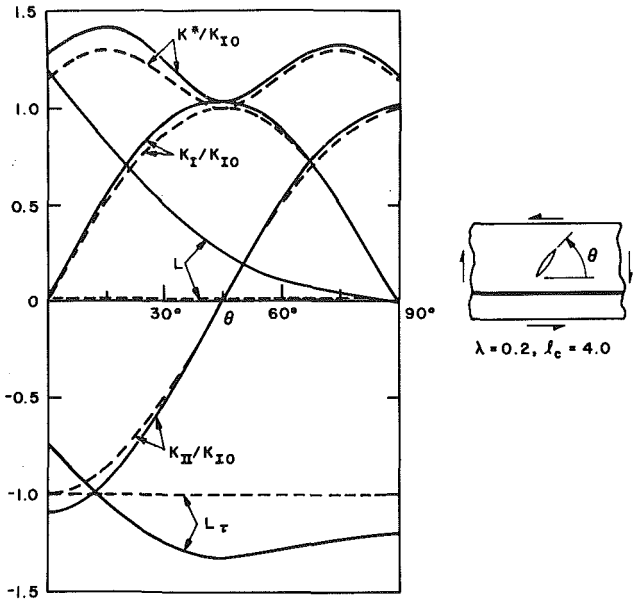


Fig. 5 Results of K/K_{I0} and L as a function of crack angle θ when the sheet is under pure shear

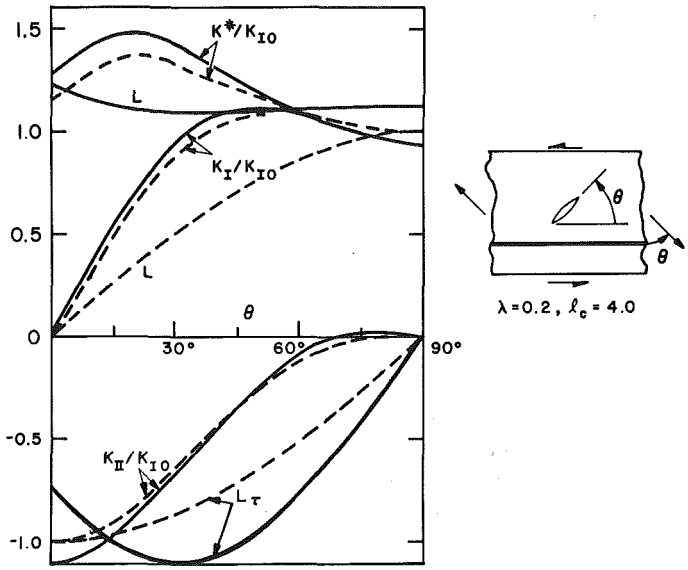


Fig. 6 Results of K/K_{I0} and L as a function of crack angle θ when the load is perpendicular to the crack surface and the relative orientation of the fiber varies

a homogeneous material. It is also noticed that the peak value of each curve is generally reached at different crack orientations. The critical geometric arrangement to be considered in a design process, therefore, depends on the adopted criteria, such as the threshold stress intensity factor for crack propagation in the matrix (K/K_{I0}), the fiber strength (L), and the fiber-matrix bonding strength (L_τ).

Since the failure phenomena under compression are different from those under tension, it is important to note that the magnification factors change signs when the loading at infinity is reversed. That means magnified compressive force can be induced in the fiber, which deserves design consideration as well [11].

Solutions for the mutual effects between a fiber and a crack under the other two basic loading conditions, transverse loading and pure shear loading, are shown in Figs. 4 and 5. Figure 4 reveals that under transverse loading the fiber has practically no effect on the crack tip stress field. On the other

Downloaded 02 May 2010 to 171.66.16.54. Redistribution subject to ASME license or copyright; see http://www.asme.org/terms/Terms_Use.cfm

Table 1 Results for a reinforced plate, containing a crack parallel to the fiber direction, loaded β deg away from the fiber axis

β	0 deg	15 deg	30 deg	45 deg	60 deg	75 deg	90 deg
K_{I_c}	0.02	0.28	0.67	0.71	0.87	0.96	0.99
L	1.22	0.99	0.70	0.35	−0.01	−0.39	−0.72
L_τ	0.44	0.44	0.40	0.34	0.26	0.15	0.04
σ_c(ksi)	69.3	5.02	2.07	1.94	1.60	1.44	1.40

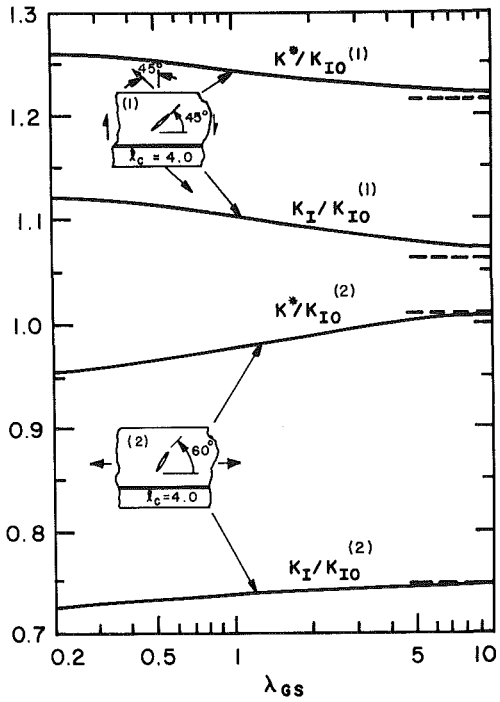


Fig. 7 Variation of K/K_{I0} with parameter λ_{GS}

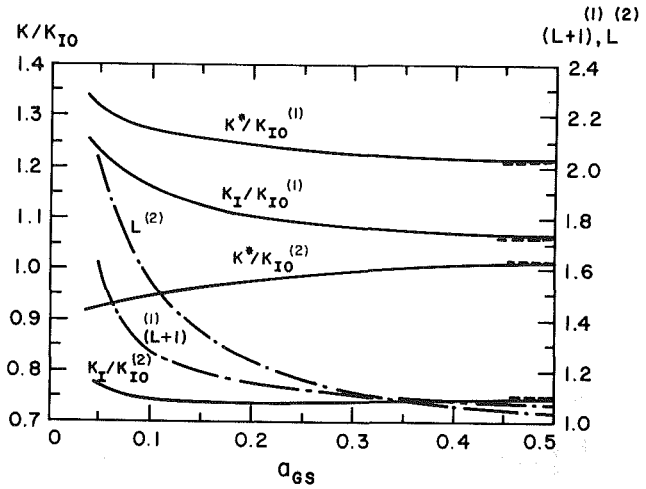


Fig. 8 Variation of K/K_{I0} and L with parameter a_{GS}

hand, both the stress in the fiber and the stress along the fiber-matrix interface can be significantly influenced by the approaching crack, as indicated by L and L_τ in Figs. 3–5.

By superposing results in Figs. 3, 4, and 5, the stress state under a general loading condition can be constructed. One example is shown in Fig. 6 for cases in which the load is kept at a constant angle, 90 deg, with respect to the crack while the fiber changes its orientation.

Finally in Figs. 7 and 8 two examples are plotted to show the dependence of the aforementioned effects on the parameters a_{GS} and λ_{GS}. As reported in [7], when a_{GS} or λ_{GS} increases, the mutual influence between the fiber and the crack decreases; that is, the solutions for a homogeneous material are approached. The curve rises or falls from the homogeneous solution as a_{GS} or λ_{GS} decreases depending on the positive or negative effects the fiber and the crack have on one another.

4 Some Application Examples and Discussions

In this section the applicability of the current approach to more realistic situations is discussed. First it is noted that problems with multiple cracks and/or multiple fibers can be solved by superposing fundamental (single-crack and single-fiber) solutions associated with proper parameters l_c and λ and properly modified boundary conditions along the crack surface (equation (3)) and/or along the fiber axis (equation (2)). The technique inevitably gets more and more tedious when the number of cracks (or fibers) increases. However, as shown in Figs. 7 and 8, the mutual influence between the fiber and the crack decays rapidly as the distance between them increases, which therefore suggests that models with a limited numbers of cracks and fibers in a representative homogeneous matrix may be sufficient for stress analyses of real composites.

In the following, the dependence of composite tensile strength on fiber orientation predicted from the present fundamental model is compared with existing results from other models. The first comparison is between results shown in Fig. 6 with those obtained through finite element anlayses in [12] for single-edge-notched plates subjected to simple tension. In these cases, the crack forms an angle θ with the fiber and remains normal to the tensile axis. If a critical mode I stress intensity factor (K_{I_c}) is considered sufficient to trigger a tensile failure, as assumed in [12], and according to Fig. 6, the mode I stress intensity factor is higher in the reinforced plate than in a homogeneous material for $\theta<60$ deg, then the tensile strength of the composite is expected lower than that of the homogeneous material for $\theta<60$ deg. On the other hand, for $\theta>60$ deg, higher composite strength than the homogeneous strength is expected to result from the fiber reinforcement. Furthermore, there exists a critical fiber angle $\theta\cong 50$ deg, where mode I stress intensity factor reaches a maximum, which gives the lowest tensile strength. These findings agree very well with those shown in Fig. 5 in [12].

The second example involves a reinforced plate containing a crack paralllel to the fiber direction subjected to simple tension. The angle between the loading axis and the fiber is β. Listed in Table 1 are results for different values of β. If the mode I stress intensity factor is again the criterion, then as shown in the last row of Table 1, the critical tensile stress (σ_c) of the plate decreases rapidly as β increases. The critical tensile stress is obtained by assuming a K_{I_c}-value such that the strength derived from it for $\beta=90$ deg matches with the experimental data [13]. The predicted tensile strength when plotted against β falls between the results obtained by Sih et al. [5] from the anisotropic model and the matrix model.

In summary, it is seen that even the fundamental solution as presented here can provide helpful design information such as

Downloaded 02 May 2010 to 171.66.16.54. Redistribution subject to ASME license or copyright; see http://www.asme.org/terms/Terms_Use.cfm

the most critical loading condition and the most critical flaw orientation for a reinforced plate. It is reasonable to believe that when other failure criteria, such as the fiber strength, are used the current microscale study can also help analyze complicated failure mechanisms.

References

1 Zweben, C., "Fracture Mechanics and Composite Materials: A Critical Analysis," *Analysis of The Test Methods for High Modulus Fibers and Composites*, ASTM STP521, 1973, pp. 65-97.

2 Whitney, J. M., and Nuismer, R. J., "Stress Fracture Criteria for Laminated Composites Containing Stress Concentrations," *Journal of Composite Materials*, Vol. 8, 1974, pp. 253-265.

3 Erdogan, F., and Gupta, G., "The Stress Analysis of Multi-Layered Composites With a Flaw," *Int. Journal of Solids and Structures*, Vol. 7, 1971, pp. 39-61.

4 Hilton, P. D., and Sih, G. C., "A Laminate Composite with a Crack Normal to the Interfaces," *Int. Journal of Solids and Structures*, Vol. 7, 1971, pp. 913-930.

5 Sih, G. C., Chen, E. P., Huang, S. L., and McQuillen, E. J., "Material Characterization on the Fracture of Filament-Reinforced Composites," *Journal of Composite Materials*, Vol. 9, 1975, pp. 167-186.

6 Omoike, G., and Vilmann, C. R., "Arbitrarily Oriented Cracks in a Layered Media," *Journal of Composite Materials*, Vol. 17, 1983, pp. 316-329.

7 Greif, R., and Sanders, J. L., "The Effect of a Stringer on the Stress in a Cracked Sheet," ASME JOURNAL OF APPLIED MECHANICS, Vol. 32, 1965, pp. 59-66.

8 Muskhelishvili, N. I., *Some Basic Problems of the Mathematical Theory of Elasticity*, P. Noordhoff, Amsterdam, The Netherlands, 1953.

9 Erdogan, F., and Gupta, G. D., "On the Numerical Solution of Singular Integral Equations," *Quarterly of Applied Mathematics*, Jan. 1972, pp. 525-534.

10 Erdogan, F., and Sih, G. C., "On the Crack Extension in Plates under Plane Loading and Transverse Shear," ASME *Journal of Basic Engineering*, Vol. 85, 1963, pp. 519-527.

11 Greszezuk, L. B., "Compressive Strength and Failure Modes of Unidirectional Composites," *Analysis of The Test Methods for High Modulus Fibers and Composites*, ASTM STP 521, 1973, pp. 192-217.

12 Mandell, J. F., McGarry, F. J., Wang, S. S., and Im, J., "Stress Intensity Factors for Anisotropic Fracture Test Specimens of Several Geometries," *Journal of Composite Materials*, Vol. 8, 1974, pp. 106-116.

13 Wu, E. M., and Reuter, R. C., "Crack Extension in Fiber-Glass Reinforced Plastics," University of Illinois TAM Report No. 275, 1965.

Downloaded 02 May 2010 to 171.66.16.54. Redistribution subject to ASME license or copyright; see http://www.asme.org/terms/Terms_Use.cfm

Stress Field in and Around a Coated Short Fiber in an Infinite Matrix Subjected to Uniaxial and Biaxial Loadings

Y. Mikata
Graduate Student.

M. Taya
Associate Professor.
Mem. ASME.

Department of Mechanical and Aerospace Engineering,
University of Delaware,
Newark, Del. 19716

The stresses induced in and around a coated short-fiber composite are investigated by use of the Boussinesq-Sadowsky stress function. The coated fiber is assumed to consist of two confocal spheroids and it is embedded in an infinite body. The major parameters in this analysis are the fiber aspect ratio, the coating thickness-to-fiber radius ratio, the coating-to-matrix stiffness ratio and the fiber-to-matrix stiffness ratio. It is found in the analysis that the stiffness and thickness of the coating and the fiber aspect ratio have some effect on the stress field in and around the coating in a coated short-fiber composite.

1 Introduction

Recently coating on fibers is becoming important in fabricating various composite materials, especially metal matrix composites and electrical composites for electrostatic discharge (ESD) and electromagnetic interference (EMI) shield. If we look at a coated short-fiber composite from the mechanics viewpoint, we are much concerned with the stress field induced in and around a coated fiber in an infinite body subjected to a far-field applied stress.

Thus the foregoing problem is reduced to "an inhomogeneity problem" in general. The main task in an inhomogeneity problem is to calculate the stresses induced in and around the inhomogeneity in an infinite body subjected to the far-field applied stress. If the inhomogeneity is ellipsoidal and one-phase (not coated), a number of the related problems have already been solved [1-5]. The case of two ellipsoidal inhomogeneities embedded in an infinite body was also solved by Moschovidis and Mura [6]. The method of analysis used in these studies is based on either the classical three stress function approach originated by Boussinesq [7] or the equivalent inclusion method proposed by Eshelby [4, 5]. The problem of a single ellipsoidal inhomogeneity embedded in an infinite body is easily solved by the use of the Eshelby's equivalent inclusion method. However, when the body surrounding the ellipsoidal inhomogeneity is finite, the Eshelby's method is not applicable. Then, the more complicated method, such as the classical stress function approach must be used. For example, Tsuchida and Uchiyama [8] solved the problem of spheroidal cavity in a cylinder under tension by use of Dougall's stress function approach.

In this paper a coated short fiber in a matrix is modeled as two confocal spheroids surrounded by the infinite matrix. Thus we have three phase-materials in the composite: the fiber, the coating layer, and the matrix. The present problem cannot be solved by the Eshelby's method, hence, we will use the classical three stress function method originated by Boussinesq and extended by Sadowsky (the Boussinesq-Sadowsky stress functions).

The formulation of the problem is given in Section 2, the numerical results and discussion are in Section 3 followed by the conclusions in Section 4.

2 Formulation of the Problem

Consider two confocal spheroids in an infinite solid subjected to uniaxial loads in the z-direction, σ_0 as shown in Fig. 1. Without loss of generality we set $\sigma_0 = 1$. Let us denote the surrounding infinite solid, the region between the outer spheroid and the inner spheroid, the inner spheroid as 1, 2, 3, respectively. Here we take prolate spheroidal coordinates (α, β, γ) as shown in Fig. 2. The relation between cartesian coordinates and the prolate spheroidal coordinates is given by

$$\begin{aligned} x &= \bar{q}\,\bar{p}\cos\gamma \\ y &= \bar{q}\,\bar{p}\sin\gamma \\ z &= qp \end{aligned} \tag{1}$$

where the auxiliary parameters q ($\bar{q}$) and p ($\bar{p}$) are defined as

$$\begin{aligned} q &= \cosh\alpha, \quad \bar{q} = \sinh\alpha = \sqrt{q^2-1} \\ p &= \cos\beta, \quad \bar{p} = \sin\beta = \sqrt{1-p^2} \end{aligned} \tag{2}$$

The applied external stress field of the problem is

$$\sigma_x{}^0 = \sigma_y{}^0 = 0,\ \sigma_z{}^0 = \sigma_0 = 1,\ \tau_{xy}{}^0 = \tau_{yz}{}^0 = \tau_{zx}{}^0 = 0. \tag{3}$$

The displacement field that can be derived from (3) is written as

Contributed by the Applied Mechanics Division and presented at the Winter Annual Meeting, New Orleans, La., December 9-14, 1984 of THE AMERICAN SOCIETY OF MECHANICAL ENGINEERS.

Discussion on this paper should be addressed to the Editorial Department, ASME, United Engineering Center, 345 East 47th Street, New York, N.Y. 10017, and will be accepted until two months after final publication of the paper itself in the JOURNAL OF APPLIED MECHANICS. Manuscript received by ASME Applied Mechanics Division, October, 1983; final revision, May, 1984. Paper No. 84-WA/APM-45.

Copies will be available until August 1985.

Copyright © 1985 by ASME
Downloaded 02 May 2010 to 171.66.16.54. Redistribution subject to ASME license or copyright; see http://www.asme.org/terms/Terms_Use.cfm

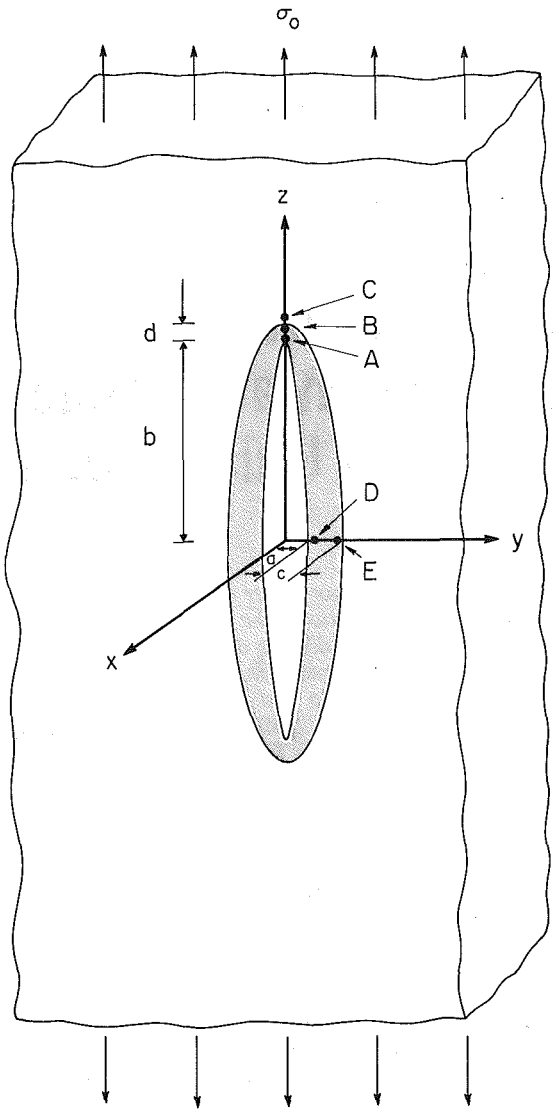


Fig. 1 A theoretical model for a coated short fiber composite

$$u^0 = -\frac{1}{2G_1}\frac{\nu_1}{1+\nu_1}x$$
$$v^0 = -\frac{1}{2G_1}\frac{\nu_1}{1+\nu_1}y \quad (4)$$
$$w^0 = \frac{1}{2G_1}\frac{1}{1+\nu_1}z$$

The boundary conditions for the problem are, at infinity (when $q \to \infty$):

$$\sigma_z{}^1 \to 1,\ \sigma_x{}^1,\ \sigma_y{}^1,\ \tau_{xy}{}^1,\ \tau_{yz}{}^1,\ \tau_{zx}{}^1 \to 0 \quad (5)$$

on $q = q_1$ (on the outer interface between Regions 1 and 2):

$$u_\alpha{}^1 = u_\alpha{}^2,\quad u_\beta{}^1 = u_\beta{}^2,\quad u_\gamma{}^1 = u_\gamma{}^2 \quad (6)$$
$$\sigma_\alpha{}^1 = \sigma_\alpha{}^2,\quad \tau_{\alpha\beta}{}^1 = \tau_{\alpha\beta}{}^2,\quad \tau_{\alpha\gamma}{}^1 = \tau_{\alpha\gamma}{}^2 \quad (7)$$

on $q_1 = q_2$ (on the inner interface between Regions 2 and 3):

$$u_\alpha{}^2 = u_\alpha{}^3,\quad u_\beta{}^2 = u_\beta{}^3,\quad u_\gamma{}^2 = u_\gamma{}^3 \quad (8)$$
$$\sigma_\alpha{}^2 = \sigma_\alpha{}^3,\quad \tau_{\alpha\beta}{}^2 = \tau_{\alpha\beta}{}^3,\quad \tau_{\alpha\gamma}{}^2 = \tau_{\alpha\gamma}{}^3 \quad (9)$$

The external uniform displacement field (equation (4)) and the corresponding applied stress field (equation (3)) are reexpressed in spheroidal coordinates as

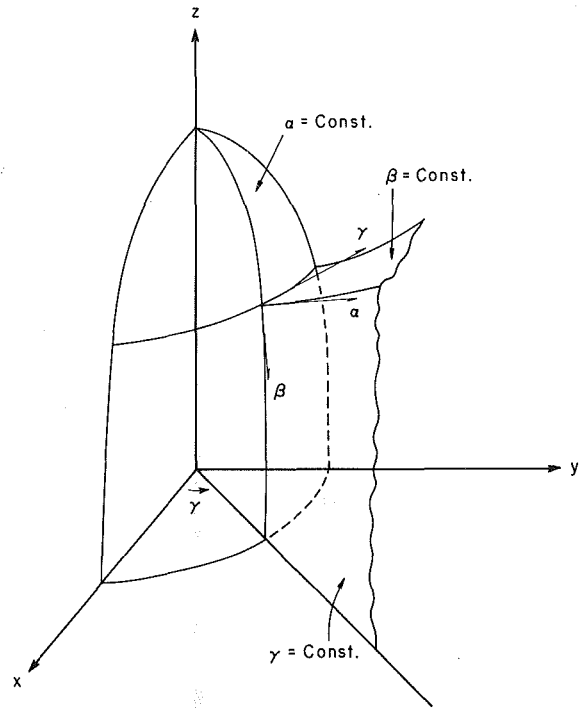


Fig. 2 The definition of spheroidal coordinates α, β, and γ

$$u_\alpha{}^0 = \frac{hq\bar{q}}{2G_1(1+\nu_1)}[(1+\nu_1)p^2-\nu_1]$$
$$u_\beta{}^0 = \frac{hp\bar{p}}{2G_1(1+\nu_1)}[\nu_1-(1+\nu_1)q^2]$$
$$\sigma_\alpha{}^0 = -\bar{q}^2+h^2q^2\bar{q}^2$$
$$\sigma_\beta{}^0 = q^2-h^2q^2\bar{q}^2 \quad (10)$$
$$\sigma_\gamma{}^0 = 0$$
$$\tau_{\alpha\beta}{}^0 = -h^2q\bar{q}p\bar{p}$$
$$\tau_{\alpha\gamma}{}^0 = \tau_{\beta\gamma}{}^0 = 0$$

where

$$h^2 = \frac{1}{q^2-p^2}, \quad (11)$$

and G_1, ν_1 are the shear modulus and the Poisson ratio of the material 1, respectively.

Using the Boussinesq-Sadowsky stress functions [1, 3], and noting that the present problem is axisymmetric, we can set the displacement fields as

$$[u^i, v^i, w^i] = \frac{1}{2G_i}\,grad\,\phi + \frac{z}{2G_i}\,grad\,\lambda - \left[0,0,\frac{3-4\nu_i}{2G_i}\lambda\right] + [u^0, v^0, w^0]\delta_{1i} \quad (12)$$

where ϕ and λ are harmonic functions, i stands for Region i, and δ_{1i} is Kronecker's delta. By use of equation (12), the displacement and the stress fields are expressed in spheroidal coordinates as [1, 3],

$$u_\alpha{}^i = \frac{h}{2G_i}\bar{q}\,\phi_q + \frac{h}{2G_i}[q\lambda_q-(3-4\nu_i)\lambda]p\bar{q}+u_\alpha{}^0\delta_{1i}$$
$$u_\beta{}^i = -\frac{h}{2G_i}\bar{p}\phi_p + \frac{h}{2G_i}[-p\lambda_p+(3-4\nu_i)\lambda]\bar{p}q+u_\beta{}^0\delta_{1i} \quad (13)$$
$$u_\gamma{}^i = \frac{1}{2G_i}\frac{\phi_\gamma}{\bar{p}\bar{q}} + \frac{1}{2G_i}\frac{pq}{\bar{p}\bar{q}}\lambda_\gamma + u_\gamma{}^0\delta_{1i},$$

Downloaded 02 May 2010 to 171.66.16.54. Redistribution subject to ASME license or copyright; see http://www.asme.org/terms/Terms_Use.cfm

$$
\begin{aligned}
\sigma_\alpha{}^i &= h^2\bar{q}^2\phi_{qq} + h^4\bar{p}^2(q\phi_q - p\phi_p) + h^2(q\lambda_{qq} - 2\lambda_q)p\bar{q}^2 \\
&\quad - 2\nu_i h^2(q\bar{p}^2\lambda_p - p\bar{q}^2\lambda_q) \\
&\quad + h^4(q\lambda_q - p\lambda_p)pq\bar{p}^2 + \sigma_\alpha{}^0\delta_{1i} \\
\sigma_\beta{}^i &= h^2\bar{p}^2\phi_{pp} + h^4\bar{q}^2(q\phi_q - p\phi_p) + h^2(p\lambda_{pp} - 2\lambda_p)q\bar{p}^2 \\
&\quad + 2\nu_i h^2(q\bar{p}^2\lambda_p - p\bar{q}^2\lambda_q) \\
&\quad + h^4(q\lambda_q - p\lambda_p)pq\bar{q}^2 + \sigma_\beta{}^0\sigma_{1i} \\
\sigma_\gamma{}^i &= \frac{\phi_{\gamma\gamma}}{\bar{p}^2\bar{q}^2} + h^2(q\phi_q - p\phi_p) + \frac{pq\lambda_{\gamma\gamma}}{\bar{p}^2\bar{q}^2} \\
&\quad + (1-2\nu_i)h^2pq(q\lambda_q - p\lambda_p) \\
&\quad - 2\nu_i h^2(q\lambda_p - p\lambda_q) + \sigma_\gamma{}^0\delta_{1i} \qquad (14) \\
\tau_{\alpha\beta}{}^i &= [-h^2\phi_{pq} + h^4(q\phi_p - p\phi_q)]\bar{p}\bar{q} + h^2[(1-2\nu_i) \\
&\quad (p\lambda_p + q\lambda_q) - pq\lambda_{pq}]\bar{p}\bar{q} \\
&\quad + h^4p\bar{p}q\bar{q}(q\lambda_p - p\lambda_q) + \tau_{\alpha\beta}^0\delta_{1i} \\
\tau_{\alpha\gamma}{}^i &= \frac{h}{\bar{p}\bar{q}^2}(\bar{q}^2\phi_{q\gamma} - q\phi_\gamma) + \frac{hp}{\bar{p}}\left[q\lambda_{q\gamma}\right. \\
&\quad \left. - \left(2 - 2\nu_i + \frac{1}{\bar{q}^2}\right)\lambda_\gamma\right] + \tau_{\alpha\gamma}{}^0\delta_{1i} \\
\tau_{\beta\gamma}{}^i &= -\frac{h}{\bar{p}^2\bar{q}}(\bar{p}^2\phi_{p\gamma} + p\phi_\gamma) + \frac{hq}{\bar{q}}\left[-p\lambda_{p\gamma}\right. \\
&\quad \left. + \left(2 - 2\nu_i - \frac{1}{\bar{p}^2}\right)\lambda_\gamma\right] + \tau_{\beta\gamma}^0\delta_{1i} \\
&\quad i = 1, 2, 3
\end{aligned}
$$

where ϕ and λ are determined such that those terms including ϕ and λ in equations (13) and (14) will vanish at infinity ($q \to \infty$).

Noting that the problem is axisymmetric, we can assume the haromonics ϕ and λ as follows:

$$
\phi = \sum_{m=0}^{\infty} A_m^1 Q_m(q) P_m(p), \qquad \lambda = \sum_{m=0}^{\infty} A_m^2 Q_m(q) P_m(p)
$$

in Region 1 (15)

$$
\left.
\begin{aligned}
\phi &= \sum_{m=0}^{\infty} [B_m^1 Q_m(q) + B_m^2 P_m(q)] P_m(p) \\
\lambda &= \sum_{m=0}^{\infty} [B_m^3 Q_m(q) + B_m^4 P_m(q)] P_m(p)
\end{aligned}
\right\} \text{in Region 2} \qquad (16)
$$

$$
\phi = \sum_{m=0}^{\infty} C_m^1 P_m(q) P_m(p), \qquad \lambda = \sum_{m=0}^{\infty} C_m^2 P_m(q) P_m(p)
$$

in Region 3 (17)

where A_m^1, A_m^2, B_m^1, B_m^2, B_m^3, B_m^4, C_m^1, and C_m^2 are the unknown coefficients that will be determined by the boundary conditions, equations (5)–(9), and P_m and Q_m are the Legendre function of the first and the second kind of order m, respectively. It should be noted here that equations (14) and (15) are constructed so as to satisfy the far-field boundary condition (equation (5)). Hence the boundary conditions to be satisfied are equations (6) to (9).

It is found that the boundary conditions associated with γ-surface, $u_\gamma^1 = u_\gamma^2$, $\tau_{\alpha\gamma}^1 = \tau_{\alpha\gamma}^2$, $u_\gamma^2 = u_\gamma^3$ and $\tau_{\alpha\gamma}^2 = \tau_{\alpha\gamma}^3$ (equations (6)–(9)) are automatically satisfied since they vanish. Thus, we are left with eight boundary conditions (see equations (6)–(9)) that are to be satisfied. The eight boundary conditions will be used for solving for eight unknown coefficients, $A_m^1, A_m^2, B_m^1, B_m^2, B_m^3, B_m^4, C_m^1$, and C_m^2. The subscript m in these coefficients is integer varying from zero to infinity as defined in equations (15)–(17). For the purpose of computation, we will truncate the infinite series at $m = N$, then the number of the unknowns becomes $8(N+1)$.

3 Numerical Results and Discussion

The $8(N+1)$ simultaneous algebraic equations for unknown coefficients will be solved numerically. The truncation number N will be determined such that the change in the numerical values of the coefficients from the case of the truncation number N to $N+1$ becomes within 1 percent.

First the numerical results are compared with the Eshelby's solution [4, 5]. To this end the following data are chosen:

fiber aspect ratio $b/a = 5$
coating thickness to the fiber radius ratio $c/a = 0.05$
coating to matrix stiffness ratio $G_2/G_1 = 4.8$
fiber to matrix stiffness ratio $G_3/G_1 = 5$
Poisson's ratios $\nu_1 = \nu_2 = \nu_3 = 0.3$

where a and b are the semiaxes of the inner spheroid in the radial direction and in the z-direction, respectively. C is the thickness of Region 2 in the radial direction (or along the x-y plane, see Fig. 1). Since the two spheroids are confocal, it is only required to specify the aspect ratio of the inner spheroid b/a and the thickness ratio c/a. It is noted in Fig. 1 that the thickness of the coating at poles (along the z-axis), d is smaller than that at equators, c due to the assumption of confocal spheroids. If we set $c/a = 0$ and $G_2/G_1 = G_3/G_1$ to make a single inhomogeneity problem, which was solved by Edwards [3] and Eshelby [4, 5], then the truncated algebraic equations in the present formulation becomes singular. There are two reasons for this. One is that we have assumed infinite terms for the harmonics ϕ and λ in equations (14)–(16), whereas the single inhomogeneity problem can be solved with finite terms [1–3]. The other is that even the finite number of equations set up for the single inhomogeneity problem are linearly dependent of each other, thus a set of linearly independent equations must be chosen out of them [1–3]. In the test case, therefore, we have chosen c/a and G_2/G_1 such that the effect of the second phase (Region 2) is minimized. The numerical results based on the present method on the stresses σ_z and σ_r along the z-axis are shown as a solid line in Fig. 3(a) where the Eshelby's solutions inside the inhomogeneity are denoted by a dotted line and the stress σ_r just outside the matrix-fiber interface is denoted by an open circle. A similar comparison is made on the stress σ_z along the radial direction (the x or y-axis) and the results are given in Fig. 3(b), where the results on σ_r are not shown since the values are very small. It follows from Figs. 3(a) and 3(b) that a good agreement between the present results and the Eshelby's solutions is obtained.

Next a number of parametric studies are made for a coated short-fiber composite. To this end the following data are used:

fiber aspect ratio $b/a = 5, 10, 20$
coating thickness to the fiber radius ratio $c/a = 0.05, 0.1, 0.2$
coating to matrix stiffness ratio $G_2/G_1 = 2, 5$
fiber to matrix stiffness ratio (fixed) $G_3/G_1 = 10$
Poisson's ratios (fixed) $\nu_1 = \nu_2 = \nu_3 = 0.3$

Some of the numerical results are shown in Figs. 4–7 where all the stresses are normalized by the applied stress σ_0.

The results on σ_r and σ_z along the z-axis for the case of a short fiber ($b/a = 20$) with thin coating ($c/a = 0.1$) and $G_2/G_1 = 2$ are shown in Fig. 4. It is noted in this figure that the magnitude of σ_r is too small to be plotted in the fiber and

Downloaded 02 May 2010 to 171.66.16.54. Redistribution subject to ASME license or copyright; see http://www.asme.org/terms/Terms_Use.cfm

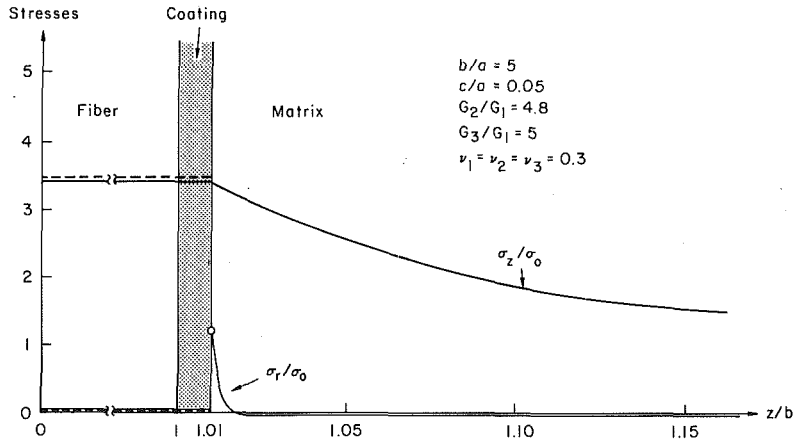


Fig. 3(a) The present results (solid line) compared with the Eshelby's solutions (dotted line and open circle) for σ_z along the r-axis

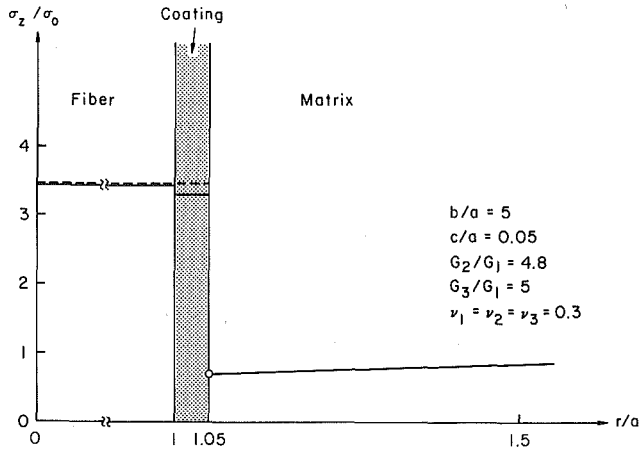


Fig. 3(b) The present results (solid line) compared with the Eshelby's solutions (dotted line and open circle) for σ_r and σ_z along the z-axis

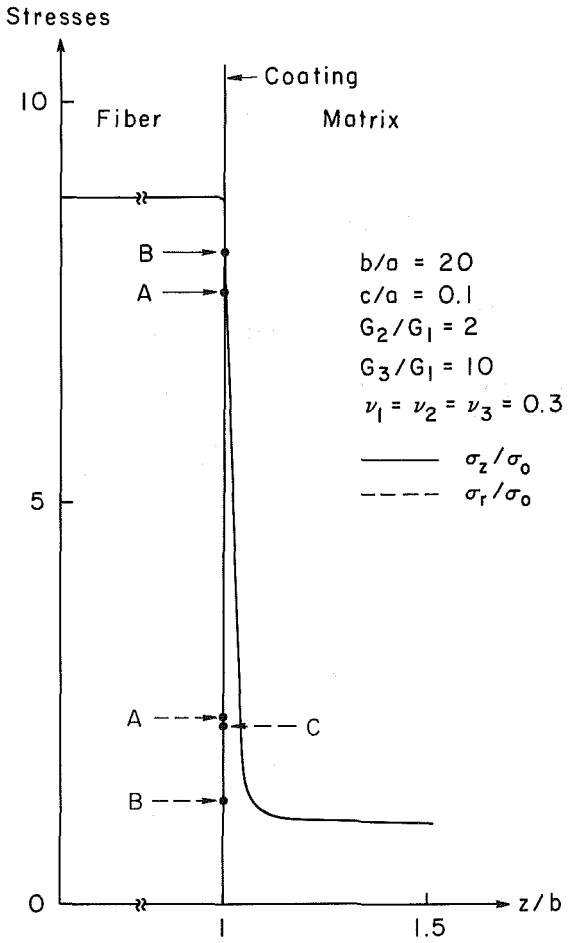


Fig. 4 The results of σ_r and σ_z along the z-axis

matrix domains, but it has some value in the thin coating (points A and B) as well as just outside the coating (point C) and the values of σ_r at these points are plotted as a filled circle.

The results on σ_z along the radial direction (y-axis in Fig. 1) are plotted as a solid line in Fig. 5 where data $b/a = 20$, $c/a = 0.1$, and $G_2/G_1 = 2$ are used. Again the magnitude of σ_r is too small to be plotted. It is easily seen from Fig. 5 that the value of σ_z in each region is roughly proportional to that of the shear modulus G in the corresponding region, i.e., 10 (8.8) in fiber, 2 (1.8) in coating, and 1 (0.9) in matrix where the values in the bracket are the stresses (σ_z) of the corresponding region. This proportionality between σ_z and the stiffness becomes exact as b/a approaches to infinity. It can be concluded from Figs. 4 and 5 that the high magnitude of the stress σ_z at the fiber-ends (at the poles) may result in a fiber-end cracking. A possibility of such a fiber-end cracking was discussed for the case of a noncoated fiber composite [9].

To examine the effect of thickness (c) and stiffness (G_2) of the coating on the stress field, we have plotted the averaged value of σ_z ($\bar{\sigma}_z$) over the coating thickness at poles (AB) and at equators (DE) as a function G_2/G_1 for various values of c/a in Fig. 6 where the other data are kept fixed, $b/a = 10$, $G_3/G_1 = 10$, and $\nu_1 = \nu_2 = \nu_3 = 0.3$. The stress $\bar{\sigma}_z$ at the poles has some sensitivity to c/a, but it does not change much with G_2/G_1. While magnitude of the stress $\bar{\sigma}_z$ at the equators is proportional to G_2/G_1, but it is not sensitive to c/a. Next the effect of fiber aspect ratio (b/a) was studied for various values of c/a and the results on σ_z averaged over the coating zone at poles (AB) and equators (DE) are plotted in Fig. 7 where the other data are kept fixed, $G_2/G_1 = 2$, $G_3/G_1 = 10$, $\nu_1 = \nu_2 = \nu_3 = 0.3$. It follows from Fig. 7 that the stress $\bar{\sigma}_z$ at the poles is sensitive to both b/a and c/a, whereas $\bar{\sigma}_z$ at the equators is not much sensitive to b/a and almost insensitive to c/a. We can conclude by summarizing the results of Figs. 6 and 7 that the stress at poles increases with the fiber aspect ratio, but decreases with the coating thickness and it is insensitive to the stiffness of the coating, while the stress σ_z at equators increases with the stiffness of the coating and the fiber aspect ratio, but it is insensitive to the coating thickness.

Downloaded 02 May 2010 to 171.66.16.54. Redistribution subject to ASME license or copyright; see http://www.asme.org/terms/Terms_Use.cfm

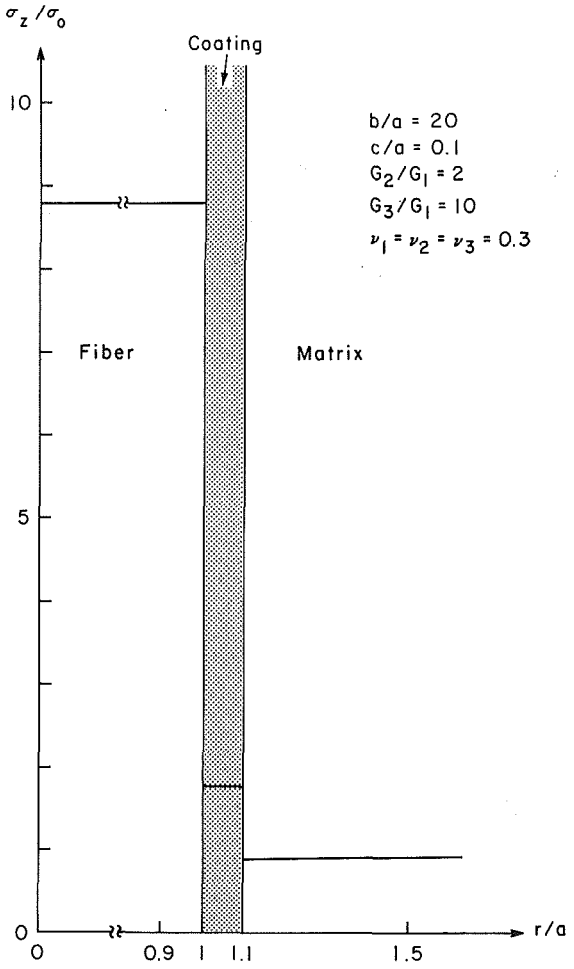


Fig. 5 The results of σ_z along the r-axis

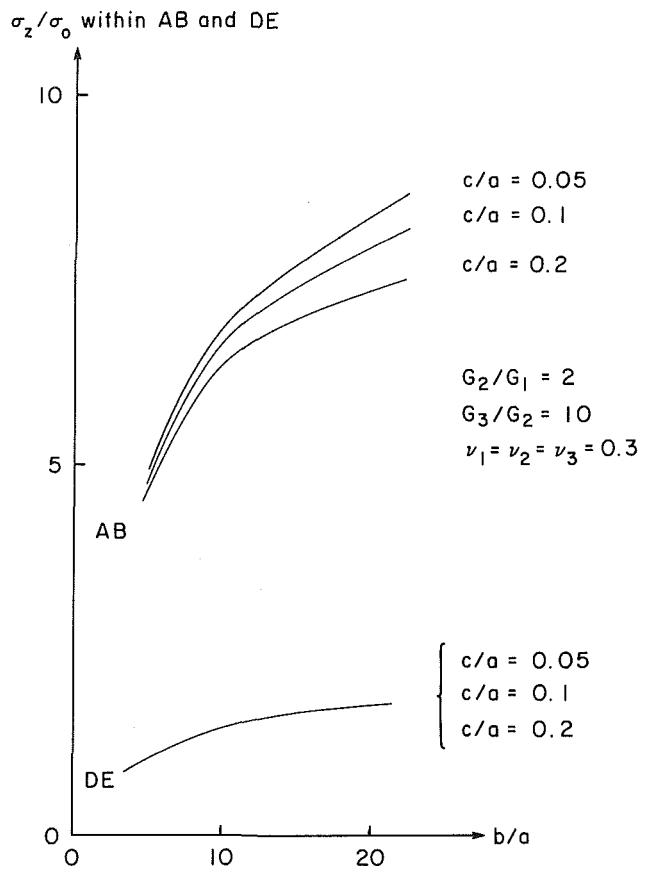


Fig. 6 The results of σ_z within *AB* and *DE* versus G_2/G_1 for various values of *c/a*

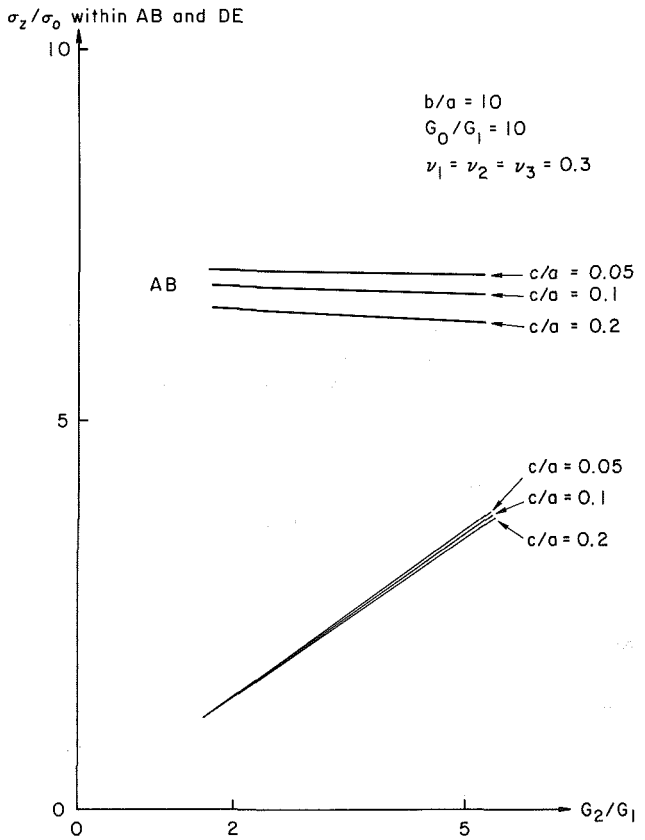


Fig. 7 The results of σ_z within *AB* and *DE* versus *b/a* for various values of *c/a*

The foregoing results seem to suggest that thicker coating is advantageous to reduce the magnitude of the already high stress σ_z at poles. However, the application of thicker coating may be hindered by two reasons: the industrial process of thicker coating is costly, and the thicker coating, once it becomes brittle due to the reaction with the matrix metal, would give rise to a crack of the size equal to the coating thickness. For the crack of larger size is more likely to propagate under the applied stress. A similar argument can be applied to a crack in the brittled coating at equators [10, 11].

We have extended the present formulation to another axisymmetric loading case, biaxial transverse loading, $\sigma_x^0 = \sigma_y^0 = 1$, $\sigma_z^0 = \tau_{xy}^0 = \tau_{yz}^0 = \tau_{zx}^0 = 0$. To demonstrate the results, the following data are used:

fiber aspect ratio $b/a = 5$
coating thickness to the fiber radius ratio $c/a = 2$
coating to matrix stiffness ratio $G_2/G_1 = 2$
fiber to matrix stiffness ratio $G_3/G_1 = 4$
Poisson's ratios $\nu_1 = \nu_2 = \nu_3 = 0.3$

The distribution of the stresses along the radial direction (y-axis) is shown by a solid (σ_r), dotted (σ_θ) and dash-dot line (σ_z) in Fig. 8, and that along the z-axis is given in Fig. 9. It is noted from Figs. 8 and 9 that the thickness of the coating along the z-axis is a bit smaller than that along the radial axis. This is due to the fact that a coated short fiber is simulated by two confocal spheroids.

4 Conclusions

The mechanics of a coated short fiber composite was investigated under two axisymmetric loading conditions,

Downloaded 02 May 2010 to 171.66.16.54. Redistribution subject to ASME license or copyright; see http://www.asme.org/terms/Terms_Use.cfm

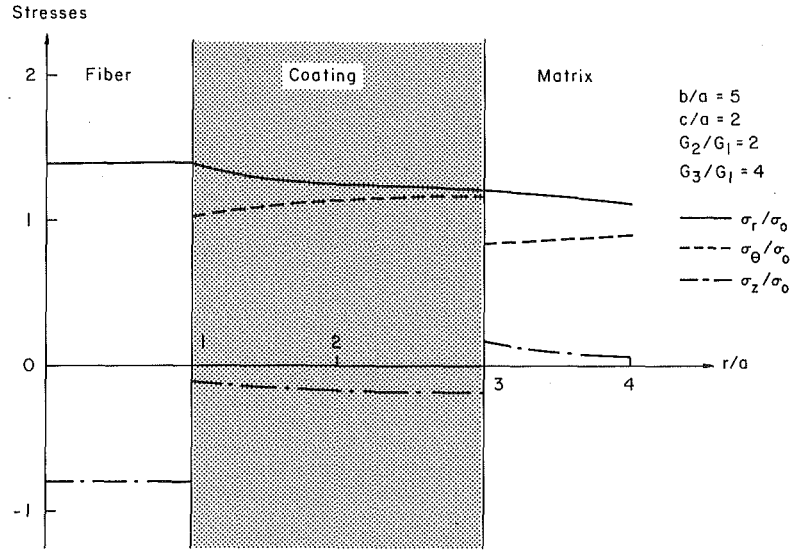


Fig. 8 The distribution of the stresses σ_r, σ_θ, and σ_z along the r-axis for biaxial loading

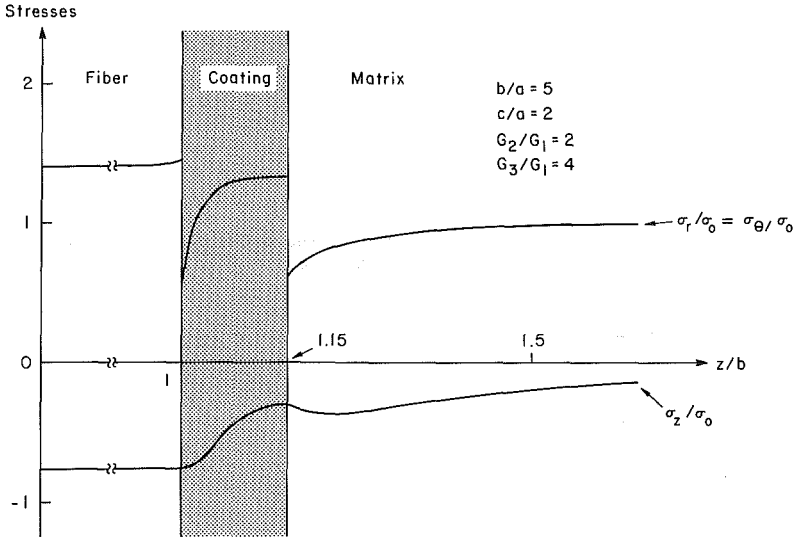


Fig. 9 The distribution of the stresses σ_r, σ_θ, and σ_z along the z-axis for biaxial loading

uniaxial and biaxial tension. It was found that the stiffness and thickness of the coating and the fiber aspect ratio has some effect on the stresses induced in and around the coated short fiber.

Acknowledgments

The financial support from Honda R & D Co., Ltd. was greatly appreciated. The discussions with Dr. E. Tsuchida of Saitama University, Japan are acknowledged.

References

1 Sadowsky, M. A., and Sternberg, E., "Stress Concentration Around an Ellipsoidal Cavity in an Infinite Body Under Arbitrary Plane Stress Perpendicular to the Axis of Revolution of Cavity," ASME JOURNAL OF APPLIED MECHANICS, Vol. 14, Sept. 1947, pp. A191–A201.

2 Sadowsky, M. A., and Sternberg, E., "Stress Concentration Around a Triaxial Ellipsoidal Cavity," ASME JOURNAL OF APPLIED MECHANICS, Vol. 16, June 1949, pp. 149–157.

3 Edwards, R. H., "Stress Concentrations Around Spheroidal Inclusions and Cavities," ASME JOURNAL OF APPLIED MECHANICS, Vol. 18, Mar. 1951, pp. 19–30.

4 Eshelby, J. D., "The Determination of the Elastic Field of an Ellipsoidal Inclusion, and Related Problems," *Proceedings of the Royal Society*, London, Series *A*, Vol. 241, 1957, pp. 376–386.

5 Eshelby, J. D., "The Elastic Field Outside an Ellipsoidal Inclusion," *Proceedings of the Royal Society*, London, Series *A*, Vol. 252, 1959, pp. 561–569.

6 Moschovidis, Z. A., and Mura, T., "Two-Ellipsoidal Inhomogeneities by the Equivalent Inclusion Method," ASME JOURNAL OF APPLIED MECHANICS, Vol. 42, Dec. 1975, pp. 847–852.

7 Boussinesq, J., *Application des Potentiels*, Ganthier-Villars, 1885.

8 Tsuchida, E., and Uchiyama, T., "Stresses in an Elastic Circular Cylinder with a Prolate Spheroidal Cavity Under Tension," *Bulle. JSME*, Vol. 22, No. 166, Apr. 1979, pp. 476–482.

9 Taya, M., and Mura, T., "On Stiffness and Strength of an Aligned Short-Fiber Reinforced Composite Containing Fiber-End Cracks Under Uniaxial Applied Stress," ASME JOURNAL OF APPLIED MECHANICS, Vol. 48, 1981, pp. 361–367.

10 Metcalfe, A. G., and Klein, M. J., "Effect of the Interface on Longitudinal Tensile Properties," in *Composite Materials*, Vol. 1, Broutmann and Krock, eds., Academic Press, New York, 1974, pp. 125–168.

11 Ochiai, S., and Murakami, Y., "Tensile Strength of Composites with Brittle Reaction Zone at Interfaces," *J. Mater. Sci.*, Vol. 14, 1979, pp. 831–840.

Downloaded 02 May 2010 to 171.66.16.54. Redistribution subject to ASME license or copyright; see http://www.asme.org/terms/Terms_Use.cfm

J-S. Yang
College of Engineering,
Michigan State University,
East Lansing, Mich. 48824

Estimation of Energy Release Rates: an Alternative to Interpolation

Introduction

The central theoretical quantity behind nonlinear fracture mechanics for rate-independent materials under monotonic loading is the J-integral. It can be regarded as a measure of the intensity of the crack-tip singularity fields. It also represents the energy release rate in nonlinearly elastic solids. (See for example the recent survey article, Hutchinson [1].)

The estimation of J for elastic-plastic crack problems is usually achieved by interpolating between the values of J corresponding to linearly elastic and pure power-law materials (e.g., Shih [2]). The interpolation scheme involves coefficients that are determined through a finite element analysis. Moreover, different constitutive descriptions (e.g., a Ramberg-Osgood material as against a piecewise power-law material) require different interpolation schemes.

It appears that the analytical estimation procedure suggested by Abeyaratne [3], does not suffer from these drawbacks. The results for J obtained by that scheme are appropriate for general constitutive relations (and are very accurate under certain conditions). Consequently the need to interpolate between particular materials can be avoided. This important observation is not made in [3] and it is this point that we wish to draw attention to in this paper. We use a center-cracked strip in Mode *III* to illustrate this.

2 Formulation and Solution

Consider a center-cracked strip whose cross section D in the (x_1, x_2) plane has a width of $2b$ and infinite length in the x_2-direction. The strip has a traction-free crack of length $2a$ $(a<b)$ in the plane $x_2=0$, and traction-free sides at $x_1=\pm b$. Suppose we load the strip at infinity by an antiplane simple shear parallel to the crack faces. If $\tau=\tau(k)$ represents the response function of the homogeneous, isotropic, incompressible material in simple shear, the corresponding secant, tangent, and infinitesimal shear moduli (all positive) are

$$\mu(k)=\frac{\tau(k)}{k},\ \tau'(k)=\frac{d\tau(k)}{dk},\ \mu_0=\tau'(0). \tag{1}$$

The boundary-value problem governing the out-of-plane displacement $u(x_1, x_2)$ consists of the equilibrium equation

$$[\mu(|\nabla u|)u_{,1}]_{,1}+[\mu(|\nabla u|)u_{,2}]_{,2}=0 \quad \text{on} \quad D, \tag{2}$$

with the boundary conditions

$$\begin{aligned}
&\sigma_{32}=\mu(|\nabla u|)u_{,2}=0 && \text{on} && x_2=0\pm, |x_1|<a,\\
&\sigma_{31}=\mu(|\nabla u|)u_{,1}=0 && \text{on} && x_1=\pm b, |x_2|<\infty,\\
&u\sim k_\infty x_2 && \text{as} && x_2\to\pm\infty, |x_1|<b,
\end{aligned} \tag{3}$$

where σ_{31}, σ_{32} are the Cauchy stress components. The associated energy release rate can be written in the form of a line integral, J,

$$J=\int_C [W(|\nabla u|)n_1-\sigma_{3\alpha}n_\alpha u_{,1}]ds, \tag{4}$$

where C is any simple closed contour that encloses the right crack-tip in its interior but does not include the left one; n_α are the components of the unit outward normal to C, and W denotes the strain energy density. Our purpose is to estimate J.

In the absence of the crack, the deformation of the body is one of simple shear and the associated displacement field is $u=k_\infty x_2$. Following [3], if we assume that the presence of the crack causes only a small disturbance of this crack-free equilibrium state, we would have

$$u(x_1, x_2)=k_\infty x_2+\tilde{u}(x_1, x_2), \qquad \text{where} \quad |\nabla\tilde{u}|<<1. \tag{5}$$

While such a hypothesis is undoubtedly invalid in the vicinity of the crack, it seems reasonable to assume that it would be true at points distant from the crack tips. Since our interest here lies solely in the computation of the path-independent integral J, and since for this purpose we may consider a path that is essentially far removed from the crack tips (provided the crack length $2a>0$ is not too close to the strip width $2b$), the errors introduced by such an assumption are probably small.

Therefore we now assume that the displacement field is given by (5). The nonlinear boundary-value problem (2), (3) can then be linearized to give

$$\begin{aligned}
&\mu(k_\infty)\tilde{u}_{,11}+\tau'(k_\infty)\tilde{u}_{,22}=0 && \text{on} && D,\\
&\tilde{u}_{,2}=-\tau_\infty/\tau'(k_\infty) && \text{on} && x_2=0\pm, |x_1|<a,\\
&\tilde{u}_{,1}=0 && \text{on} && x_1=\pm b, |x_2|<\infty,\\
&\tilde{u}\to 0 && \text{as} && |x_2|\to\infty, |x_1|<b.
\end{aligned} \tag{6}$$

Here τ_∞ is the remotely applied shear stress, $\tau_\infty=\tau(k_\infty)$. The corresponding linearized version of J is

Contributed by the Applied Mechanics Division for publication in the JOURNAL OF APPLIED MECHANICS.
Discussion on this paper should be addressed to the Editorial Department, ASME, United Engineering Center, 345 East 47th Street, New York, N.Y. 10017, and will be accepted until two months after final publication of the paper itself in the JOURNAL OF APPLIED MECHANICS. Manuscript received by ASME Applied Mechanics Division, April, 1984; Final revision, July, 1984.

Copyright © 1985 by ASME
Downloaded 02 May 2010 to 171.66.16.54. Redistribution subject to ASME license or copyright; see http://www.asme.org/terms/Terms_Use.cfm

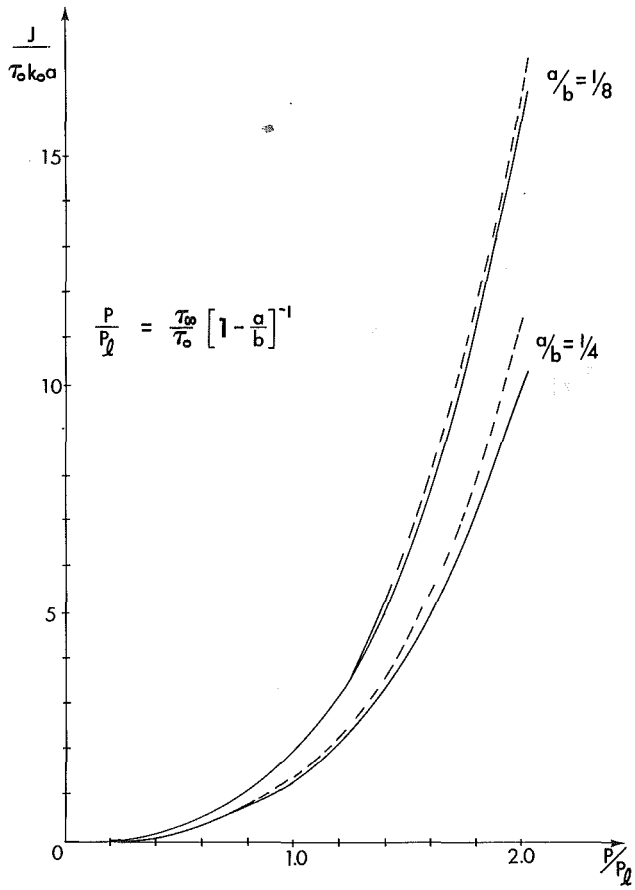


Fig. 1 Variation of J with load for a Ramberg-Osgood material with $n=3$, $\alpha=3/7$. Solid curve corresponds to the formula (18) derived here; dashed curve corresponds to interpolation formula (17).

$$J=\int_C 1/2[-\mu(k_\infty)\tilde{u}_{,1}^2 n_1+\tau'(k_\infty)\tilde{u}_{,2}^2 n_1 - 2\tau'(k_\infty)\tilde{u}_{,1}\tilde{u}_{,2}n_2]ds. \tag{7}$$

The linear boundary-value problem (6) may be further simplified by the scaling $\xi_1=x_1$, $\xi_2=mx_2$, $m^2=\mu(k_\infty)/\tau'(k_\infty)$ and by setting

$$U(\xi_1,\xi_2)=\tilde{u}(x_1,x_2)+k_\infty m^2 x_2. \tag{8}$$

This leads to

$$\begin{aligned} &\nabla^2 U(\xi_1,\xi_2)=0 && \text{on} \quad D,\\ &U_{,2}=0 && \text{on} \quad \xi_2=0\pm,\ |\xi_1|<a,\\ &U_{,1}=0 && \text{on} \quad \xi_1=\pm b,\ |\xi_2|<\infty,\\ &U\sim(k_\infty m)\xi_2 && \text{on} \quad \xi_2\to\pm\infty,\ |\xi_1|<b, \end{aligned} \tag{9}$$

which is identical to the linear elasticity problem governing the mode *III* center-cracked strip problem. Accordingly, we have

$$U\sim 2\frac{K_{III}}{\mu/m}\sqrt{\frac{r}{2\pi}}\sin\frac{\theta}{2} \quad \text{as} \quad r\to 0, \quad -\pi<\theta<\pi, \tag{10}$$

where $r\cos\theta=\xi_1-a$, $r\sin\theta=\xi_2$, and

$$K_{III}=\tau_\infty\sqrt{\pi a}\left[\frac{2b}{\pi a}\tan\left(\frac{\pi a}{2b}\right)\right]^{1/2}. \tag{11}$$

Thus on using (8) and (10) we may evaluate the J integral (7) (see [3] for details) to obtain

$$J=\frac{1}{2}\frac{K_{III}^2}{\sqrt{\mu(k_\infty)\tau'(k_\infty)}}, \tag{12}$$

which in view of (11), gives *the result*

$$J=\frac{1}{2}\frac{\tau_\infty^2}{\sqrt{\mu(k_\infty)\tau'(k_\infty)}}\pi a\left[\frac{2b}{\pi a}\tan\left(\frac{\pi a}{2b}\right)\right], \tag{13}$$

where $\mu(k_\infty)$ and $\tau'(k_\infty)$ are the values of the secant and tangent moduli far from the crack.

3 Discussion

In the case of a linear material, $k/k_0=\tau/\tau_0$, we find from (13) the ("small scale yielding") expression

$$\frac{J}{\tau_0 k_0 a}=1/2\left(\frac{\tau_\infty}{\tau_0}\right)^2\pi\left[\frac{2b}{\pi a}\tan\left(\frac{\pi a}{2b}\right)\right]. \tag{14}$$

On the other hand, in the case of a pure power-law material described by $k/k_0=\alpha(\tau/\tau_0)^n$, (13) yields (the "fully plastic solution")

$$\frac{J}{\tau_0 k_0 a}=\frac{\alpha}{2}\left(\frac{\tau_\infty}{\tau_0}\right)^{1+n}\sqrt{n}\pi\left[\frac{2b}{\pi a}\tan\left(\frac{\pi a}{2b}\right)\right]. \tag{15}$$

If one were now interested in a, say, Ramberg-Osgood material,

$$k/k_0=\tau/\tau_0+\alpha(\tau/\tau_0)^n, \tag{16}$$

the traditional procedure for determining J has been to interpolate between (14) and (15). (The need for such a procedure stems from the fact that (14) and (15) are usually found directly, by exploiting certain special features of those materials, rather than from a more general result (such as (13)): No such direct method has been available to study more general materials (such as (16)).) The interpolation formula proposed by Shih [2] for the Ramberg-Osgood material is

$$\frac{J}{\tau_0 k_0 a}=\left(\frac{\tau_\infty}{\tau_0}\right)^2\frac{f_1(a/b,1)}{(1-a/b)}+\alpha\left(\frac{\tau_\infty}{\tau_0}\right)^{n+1}\frac{f_1(a/b,n)}{(1-a/b)^n}, \tag{17}$$

where the function $f_1(a/b,n)$ is determined numerically through a finite element analysis (see Table 1 in [2]). Improvements to (17), based on the notion of an effective crack length, have also been proposed in [2].

The advantage of the present procedure is that the result (13) is not restricted to a particular constitutive law. For a Ramberg-Osgood material one obtains, from (16) and (13), the expression (in the "elastic-plastic range")

$$\frac{J}{\tau_0 k_0 a}=1/2\left(\frac{\tau_\infty}{\tau_0}\right)^2\left[1+\alpha(n+1)\left(\frac{\tau_\infty}{\tau_0}\right)^{n-1}+\alpha^2 n\left(\frac{\tau_\infty}{\tau_0}\right)^{2n-2}\right]^{1/2}\frac{2b}{a}\tan\left(\frac{\pi a}{2b}\right). \tag{18}$$

Figure 1 shows the variation of the energy release rate $J/\tau_0 k_0 a$ with the applied load τ_∞/τ_0 (in the case $n=3$, $\alpha=3/7$ and for $a/b=1/8$ and $1/4$). The solid curve corresponds to the formula (18) derived here. The dashed curve describes the result according to the interpolation formula (17). The agreement is seen to be good.

Acknowledgments

The author is grateful to Professor Rohan Abeyaratne for his comments. The results reported here were obtained in the course of an investigation supported by the U.S. National Science Foundation under Grant CME 81-06581.

References

1 Hutchinson, J. W., "Fundamentals of the Phenomenological Theory of Nonlinear Fracture Mechanics," ASME JOURNAL OF APPLIED MECHANICS, Vol. 50, 1983, pp. 1042–1051.

2 Shih, C. F., "J-Integral Estimates for Strain Hardening Materials in Antiplane Shear Using Fully Plastic Solution," in: *Mechanics of Crack Growth*, ASTM STP 590, 1976, pp. 3–22.

3 Abeyaratne, R., "On the Estimation of Energy Release Rates," ASME JOURNAL OF APPLIED MECHANICS, Vol. 50, 1983, pp. 19–23.

Downloaded 02 May 2010 to 171.66.16.54. Redistribution subject to ASME license or copyright; see http://www.asme.org/terms/Terms_Use.cfm

Progressing and Oscillatory Waves for Hybrid Synthesis of Source-Excited Propagation and Diffraction

L. B. Felsen
Department of Electrical Engineering and Computer Science/ Microwave Research Institute, Polytechnic Institute of New York, Route 110, Farmingdale, N.Y. 11735

Time-harmonic and transient propagation and diffraction phenomena can be described alternatively by progressing and oscillatory waves that express the wave motion in terms of direct and multiple wavefronts or rays, and in terms of resonances or modes, respectively. Each description is convenient and physically appealing when it requires few contributing elements. It is inconvenient and physically less transparent when it requires many elements, and it would then be desirable to combine many inconvenient elements into fewer convenient ones. For a variety of propagation environments, including layered or other guiding regions, this can be done by expressing a group of rays collectively in terms of modes, or a group of modes collectively in terms of rays. When this ray-mode equivalence is invoked selectively, there emerges a hybrid representation that combines ray fields and modal fields in uniquely defined proportions. The theory is based on Poisson summation and on alternative treatments of wave spectra. It has been applied to electromagnetics, underwater acoustics, and SH elastic motion, and is now being extended to general propagation in elastic media.

Introduction

Two principal methods of analyzing wave propagation in a finite volume utilize progressing (traveling wave) and oscillatory (standing wave) descriptions. In the former, the wave motion is organized along wavefronts that travel away from the source region along trajectories called rays. In the latter, the wave motion is synthesized by phase coherent oscillations that occupy the entire propagation volume and, in the absence of dissipation or radiation, maintain themselves without continuous excitation. Wavefronts reaching an observer convey *local* information about the propagation environment along the ray path that connects source and receiver either directly or via reflections at boundaries or scattering centers. Changes in source and receiver locations generally change the ray path and therefore the local information delivered. Wavefronts are useful at short observation times since, due to causality, their number is then relatively small, and the fields carried on and behind them are readily resolvable. The converse is true at long observation times, when many wavefronts have arrived, making isolation of their fields difficult and summation inconvenient. The oscillatory or resonant fields, on the other hand, convey *global* information independent, except for excitation amplitude, of source and receiver arrangements. They generally are effective at long observation times when the environment has fully responded to the incident disturbance. At short observation times, when the disturbance has not as yet traversed the entire propagation volume, resonances are inconvenient because only by destructive interference due to many of them, can the quiescent condition in the unexcited portion be satisfied. Progressing and oscillatory descriptions are therefore complementary in that one is convenient, and therefore also physically more transparent, when the other is not. Analogous considerations can be brought to bear on the time-harmonic regime where equiphase surfaces replace wavefronts and normal modes replace resonances. Moreover, in regions with one distinctive (guiding) coordinate, oscillatory solutions may be defined in the transverse domain to yield guided instead of volume resonant modes.

While progressing and oscillatory events lead to independent alternative descriptions of the propagation and scattering process, they are related in that either expresses the collective effects of the other. The relation is formalized by the Poisson sum formula which represents a group of elements as a sum of its Fourier transforms. Since rays and modes are essentially one another's Fourier transforms [1], Poisson summation has been employed to transform a ray field formulation into a modal field formulation, and vice versa. But rays (wavefronts) alone or modes (resonances) alone are not convenient for *all* observation ranges of interest. Therefore, one has had to switch from the one to the other in a suitable overlapping domain where neither is excessively inconvenient. This disjoint procedure has motivated the search for a *hybrid* formulation that combines rays (wavefronts) and modes (resonances) self-consistently, with the number of elements retained in the one uniquely determined by the number of elements retained in the other, and the need for switching eliminated [2, 3]. In spectral terms, this

Contributed by the Applied Mechanics Division for publication in the JOURNAL OF APPLIED MECHANICS.
Discussion on this paper should be addressed to the Editorial Department, ASME, United Engineering Center, 345 East 47th Street, New York, N.Y. 10017, and will be accepted until two months after final publication of the paper itself in the JOURNAL OF APPLIED MECHANICS. Manuscript received by ASME Applied Mechanics Division, February, 1984; final revision, June, 1984.

Copyright © 1985 by ASME
Downloaded 02 May 2010 to 171.66.16.54. Redistribution subject to ASME license or copyright; see http://www.asme.org/terms/Terms_Use.cfm

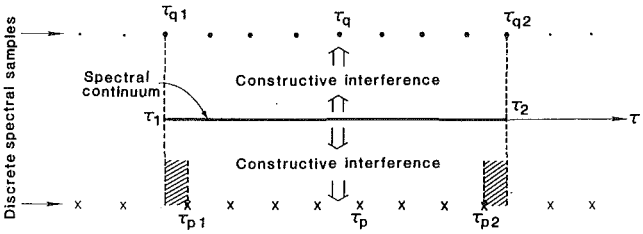


Fig. 1 Ray-mode equivalence by alternative constructive spectral interference. Finite spectral wavenumber interval $\tau_1 \le \tau \le \tau_2$ is filled completely with rays $\tau_{q_1} \le \tau \le \tau_{q_2}$ (dark dots), with $\tau_{q_{1,2}} = \tau_{1,2}$. The equivalent mode group $\tau_{p_1} \le \tau_p \le \tau_{p_2}$ (dark crosses), with $\tau_{p_{1,2}} \neq \tau_{1,2}$, does not fill the interval completely. The spectral voids (shaded) are filled with spectral remainders. Light dots and crosses identify ray fields and mode fields outside the spectral interval.

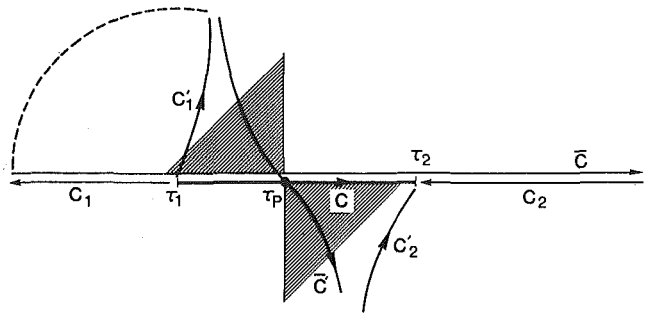


Fig. 2 Contours for spectral integral in complex τ-plane. The initial contour C is expressed as $C = \bar{C} + C_1 + C_2$, with subsequent deformation into $\bar{C}'$(*SDP*), C_1' and C_2' into valleys corresponding to the saddle point τ_p. For several saddle points in the interval $\tau_1 < \tau_p < \tau_2$, there is a corresponding multiplicity of valley regions.

implies that a given finite spectral wave number or wave slowness interval is to be filled either with ray fields or with mode fields plus a remainder to take care of any "spectral voids" near the edges. The ray or mode descriptions then express two distinctive alternative orderings of the constructive interference between the spectral constituents [4, 5].

The hybrid method was first developed for electromagnetic and acoustic pressure fields [6–15], but has subsequently been applied to wave motion in elastic media, under time-harmonic and transient conditions [16–19]. The principles of the method, and its extension to layered multiwave media, are described in the next section.

The Ray-Mode Equivalent

(*A*) The Poisson Sum Formula. As mentioned in the foregoing, a hybrid formulation is based on the ability to express a group of ray or wavefront fields collectively as a group of mode or resonant fields, and vice versa. This, in turn, implies an ordering of waves in a finite *continuous* spectrum interval by alternative *discrete* constructive interference processes, as schematized in Fig. 1. The formalization of this procedure is based on the Poisson sum formula applied to a finite group of elements [20]

$$\sum_{q=q_1}^{q_2} f_q = \frac{1}{2} f_{q_1} + \frac{1}{2} f_{q_2} + \sum_{p=-\infty}^{\infty} F_p(q_1, q_2) \tag{1}$$

where

$$F_p(q_1, q_2) = \frac{1}{2\pi} \int_{\tau_1}^{\tau_2} f(\tau) e^{ip\tau} d\tau$$

$$= F_p + \hat{F}_p(q_1) + \hat{F}_p(q_2) \tag{2}$$

Here (see Fig. 2)

$$\hat{F}_p\left(q_{\frac{1}{2}}\right) = \pm \frac{1}{2\pi} \int_{\mp\infty}^{\tau_{\frac{1}{2}}} f(\tau) e^{ip\tau} d\tau, \quad \tau_{1,2} = 2\pi q_{1,2} \tag{3a}$$

and

$$F_p = \frac{1}{2\pi} \int_{-\infty}^{\infty} f(\tau) e^{ip\tau} d\tau \tag{3b}$$

In (2), the continuous function $f(\tau)$ is obtained from f_q on replacing the discrete index q by the continuous variable $(\tau/2\pi)$. It is assumed that f_q is properly continuable. The interval $\tau_1 \le \tau \le \tau_2$ defines the domain of the generic continuous spectrum. In what follows, f_q refers to wavefronts or rays, and F_p refers to resonances or modes.

(*B*) Asymptotic Approximations. The formula in (1) is exact. Its physical implication within the present context is demonstrated first in the frequency domain by applying it to asymptotic approximations for the ray fields f_q rather than to the exact generalized ray integrals that generate the asymptotic forms. Accordingly, we assume that the f_q behave in the manner of a "local plane wave" that permits identification of a slowly varying amplitude a_q and a rapidly varying phase $k\psi_q$, where k is a (large) reference wave number:

$$f_q = a_q \exp(ik\psi_q) \tag{4}$$

When (4) is continued to $f(\tau)$ and substituted into (2), one may evaluate the integral asymptotically by the method of saddle points. Stationary (saddle) points τ_p of the composite phase $k\psi_p$ are solutions of

$$\frac{d\Psi_p}{d\tau} = 0 \quad \text{at} \quad \tau_p, \qquad \Psi_p = \psi(\tau) + p\tau/k. \tag{5}$$

Principal contributions to the integral arise from those τ_p that lie on the interval $\tau_1 < \tau_p < \tau_2$ and also from the endpoints $\tau_{1,2}$. Assuming the saddle points to be separated from one another and from endpoints or singularities (if any) of $f(\tau)$, one may evaluate the integral F_p in (3*b*) along the steepest descent path $\bar{C}'$ (*SDP*) in the complex τ-plane (see Fig. 2) to obtain [21]

$$F_p(\tau_p) \sim A_p(\tau_p) e^{ik\Psi(\tau_p)} \tag{6}$$

where

$$A_p(\tau) = \frac{1}{2\pi} a_p(\tau_p) \sqrt{\frac{2\pi i}{k\Psi_p''(\tau_p)}} \tag{7}$$

with a prime denoting the derivative with respect to the argument.

Endpoint contributions to the integrals in (3*a*), when isolated from a saddle point and from singularities (if any) of $f(\tau)$, yield asymptotically by integration along C_2' and C_1' in Fig. 2 [21],

$$\hat{F}_p\left(q_{\frac{2}{1}}\right) = \frac{1}{2\pi} \int_{C_{\frac{2}{1}}'} f(\tau) e^{ip\tau} d\tau \sim$$

$$\pm \frac{f(\tau_{2,1}) \exp(ip\tau_{2,1})}{2\pi i k \Psi_p'(\tau_{2,1})} = \mp \frac{i/2\pi}{k\psi'(\tau_p) + p} f_{q_{2,1}} \tag{8}$$

i.e., the limiting elements of the *original* series, but with a modified amplitude. The p-series in (1), with (8), can be summed into closed form via the formula

$$\sum_{p=-\infty}^{\infty} \frac{1}{v-p} = \pi \cot(v\ \pi) \tag{9}$$

whence

$$\sum_{p=-\infty}^{\infty} \hat{F}_p(q_{2,1}) \sim \pm \frac{1}{2} \Delta_{q_{2,1}} f_{q_{2,1}},$$

$$\Delta_{q_{2,1}} = i \cot[\pi k \psi'(\tau_{2,1})] \tag{10}$$

When these results are collected, one finds

$$\sum_{q=q_1}^{q_2} f_q \sim \sum_{p=p_1}^{p_2} F_p U(\tau_2 - \tau_p) U(\tau_p - \tau_1) + \bar{f}_{q_1} + \bar{f}_{q_2} \tag{11}$$

where

Downloaded 02 May 2010 to 171.66.16.54. Redistribution subject to ASME license or copyright; see http://www.asme.org/terms/Terms_Use.cfm

$$\bar{f}_{q_{2,1}} = \frac{1}{2}(1 \pm \Delta_{q_{2,1}}) f_{q_{2,1}} \tag{11a}$$

and $U(\tau) = 0$, $\tau < 0$, but $U(\tau) = 1$, $\tau > 0$. The formulation in (11) expresses the original group of (ray) elements f_q in terms of a series of its Fourier transformed elements F_p (subsequently shown to be modal local plane waves) plus elements $\bar{f}_{q_{2,1}}$, which are the collectively weighted last and first elements, respectively, in the original group. These "collective" (ray) elements, expressive of the truncation of the original set, account for the spectral voids $(\tau_{p1} - \tau_1)$ and $(\tau_2 - \tau_{p2})$ left unfilled by the (modal) F_p elements, where τ_{p2} and τ_{p1} denote the saddle points closest to τ_2 and τ_1, respectively, and contained within the interval $\tau_1 < \tau_p < \tau_2$ (see Fig. 2).

The elements f_q and F_p generally depend also on other parameters that determine the distribution and location of the saddle points τ_p. Should it happen that the f_q set and F_p set fill the spectral interval $\tau_1 < \tau < \tau_2$ completely (i.e., $\tau_{p1} = \tau_1$, $\tau_{p2} = \tau_2$), implying coincident saddle points and endpoints, then the endpoint contributions $F_p(q_{2,1})$ equal (1/2) of the saddle point contributions $F_p(\tau_{2,1})$ [21], so that (10) may be rewritten in the symmetric form

$$\sum_{q=q_1}^{q_2} \epsilon_q f_q \sim \sum_{p=p_1}^{p_2} \epsilon_p F_p \tag{12}$$

which exhibits the bilateral equivalence of the truncated sets f_q and F_p. Here, $\epsilon_{q_{1,2}} = 1/2$ while $\epsilon_q = 1$, $q \neq q_{1,2}$, and similarly for ϵ_p. Alternatively, when an endpoint lies approximately midway between the last included and the first excluded saddle point, then $\cot[\pi k \psi'(\tau_1)]$ and (or) $\cot[\pi k \psi'(\tau_2)]$ in (10) is small. By setting $\Delta_{q1} \approx 0$ and (or) $\Delta_{q2} \approx 0$ in (10), one thereby obtains a different simplification of (11). Finally, when the saddle point τ_{p2} approaches the endpoint τ_2, the simple asymptotic formulas in (6) and (7) must be replaced by the uniform formula involving a Fresnel integral [21]

$$F_p(q_2) \sim \frac{e^{ik\Psi(\tau_{p_2})}}{2\pi} a(\tau_{p_2}) h_p Q(s_e) + \frac{e^{-s_e^2}}{2s_e}[a(\tau_2) h_e - a(\tau_{p_2}) h_p] \tag{13}$$

Here

$$Q(y) = \int_y^\infty e^{-x^2} dx, \quad s_e = [ik(\Psi(\tau_{p_2}) - \Psi(\tau_2))]^{1/2}, \tag{13}$$

$$h_e = \frac{-s_e}{ik\Psi'(\tau_2)}, \quad h_p = \sqrt{\frac{-2}{ik\Psi''(\tau_{p_2})}} \tag{13a}$$

where $\arg h_p = \arg(d\tau)\tau_{p2}$, $d\tau$ being an element along the steepest descent path SDP through τ_{p2}, and $\arg s_e$ is defined so that $h_e \to h_p$ as $s_e \to 0$. With (13), passage of the saddle point τ_{p2} and therefore the corresponding element F_{p2} out of the spectral interval, or transition of a previously external saddle point τ_p and therefore the corresponding element F_p into the spectral interval, may be tracked smoothly and continuously. Since the (modal) elements F_p in (6) also have a local plane wave form, it is evident that the same procedure may be applied to a sum of the F_p, with $p_1 \leq p \leq p_2$. This generates a sum of f_q(ray) elements plus (modal) collective remainders $\bar{F}_{p_{1,2}}$, thereby demonstrating the bilateral equivalence, but with a choice of collective elements, either $\bar{f}_{q_{1,2}}$ or $\bar{F}_{p_{1,2}}$. Details may be found in [4, 5].

To demonstrate that the wave fields F_p synthesize a guided mode if the wave fields f_q represent rays, we consider the simple example of a region bounded by two plane parallel boundaries at $x = 0$ and $x = a$ (Fig. 3). A line source at $S = (x', 0)$ radiates harmonic waves that reach the observer at

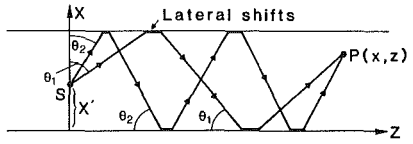


Fig. 3 Ray paths with departure angles $\theta_q = \theta_q(x,z;x')$, $q = 1,2$ from S to P in a parallel plane waveguide. The index q is related to the number of reflections. The lateral shifts arise from the contribution of the boundary reflection coefficient phases $\Phi_{0,a}$ to the stationary phase condition in (15).

$P = (x,z)$ via direct and multiple reflected ray paths. Along each ray, the field has the form in (4), with the index q referring to the number of reflections. The phase along a typical ray depicted in Fig. 3 is

$$\psi_q(\zeta_q) = \Omega(\zeta_q) + q\,\Phi(\zeta_q)/k, \tag{14}$$

where

$$\Omega(\zeta_q) = \zeta_q z + \xi_q(x_> - x_<), \quad \xi_q = (1 - \zeta_q^2)^{1/2} \tag{14a}$$

$$\Phi(\zeta) = 2ka\xi_q + \Phi_0(\zeta_q) + \Phi_a(\zeta_q) \tag{14b}$$

Here, $x_>$ and $x_<$ denote the greater and lesser of the values of x and x', respectively, and $\Phi_{0,a}(\zeta_q)$ are the phases of the plane wave reflection coefficients at $x = 0$ and $x = a$, respectively. The ray parameter $\zeta_q = \sin\theta_q$, where θ_q is the ray departure angle at the source (with respect to the x direction), renders the phase stationary along the path:

$$\frac{d\psi_q}{d\zeta_q} = 0 \tag{15}$$

The amplitude of the ray field,

$$a_q(\zeta_q) = \frac{1}{4\xi_q}\left[\frac{2i}{\pi k \psi_q''(\zeta_q)}\right]^{1/2} \tag{16}$$

follows from conventional ray theory [22] if the line source field is normalized to represent the asymptotic form of the two-dimensional free-space Green's function $(i/4)H_0^{(1)}(k\rho)$, where ρ is the distance from the source.

With (14) and (16) substituted into (4) and (1), one is led via (5) to the stationary phase condition

$$\frac{\partial \psi[\tau, \zeta(\tau)]}{\partial \tau} + \frac{p}{k} = 0 \text{ at } \tau_p \tag{17}$$

since $(d/d\tau) = (\partial/\partial\tau) + (\partial\psi/\partial\zeta)\,(\partial\zeta/\partial\tau)$, and $(\partial\psi/\partial\zeta) = 0$ from (15). It has here been recognized that ψ depends on τ explicitly through $q \to \tau/2\pi$ and implicitly through $\zeta_q \to \zeta(\tau)$. Thus, from (14) and (17)

$$\frac{1}{2\pi}\Phi(\zeta_p) = -p, \quad \zeta_p \equiv \zeta(\tau_p) \tag{18}$$

which relation expresses the resonance condition for the guided modes in the plane parallel waveguide. Following through to (6), one may show that

$$F_p = \frac{\exp[ik\Omega(\zeta_p)]}{2i\Phi'(\zeta_p)\xi_p} \tag{19}$$

This wave field is the partial mode excited by the source, and corresponds to those rays that leave S and arrive at P in the upward direction. Conversion of the remaining three ray species to make up the totality of ray fields leaving S upward or downward and arriving at P from above or below then synthesizes the complete conventional guided modes [5, 7]. The collective ray field is given in (11a), with $\Delta_{q_{1,2}} = i\cot[\Phi(\zeta_{1,2})/2]$, $\zeta_{1,2} \equiv \zeta_{q_{1,2}}$.

Hybrid Representation

(A) Formal Decomposition. The hybrid ray-mode representation is generated by partitioning the total set of f_q elements,

Downloaded 02 May 2010 to 171.66.16.54. Redistribution subject to ASME license or copyright; see http://www.asme.org/terms/Terms_Use.cfm

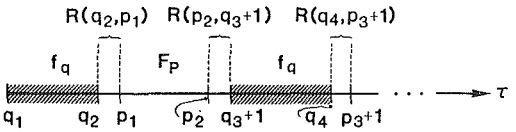


Fig. 4 Partitioning of spectral range for hybrid formulation. q_i and p_i denote spectral values delimiting intervals occupied by f_q and F_p elements, respectively. $R(q,p)$ and $R(p,q)$ are remainders accounting for spectral voids.

$$G=\sum_{q=q_1}^{\infty} f_q \tag{20}$$

into N subgroups

$$G=\Big(\sum_{q_1}^{q_2}+\sum_{q_2+1}^{q_3}+\cdots\cdots+\sum_{q_N+1}^{\infty}\Big)f_q. \tag{21}$$

Subgroups with favorable convergence properties are to be retained intact; those with unfavorable convergence properties are to be converted into F_p groupings. This yields alternating groupings of f_q and F_p elements, with collective elements $\bar{f}_q$ and $\bar{F}_p$ added to fill any spectral voids between adjacent groups. A hybrid representation appears typically as

$$G=\sum_{q_1}^{q_2} f_q+\sum_{p_1}^{p_2} F_p+\sum_{q_3+1}^{q_4} f_q+\cdots\cdots+\sum_{p_j}^{\infty} F_p +R(q_2,p_1)+R(p_2,q_3+1) +R(q_4,p_3+1)+\cdots\cdots+R(q_N,p_j) \tag{22}$$

where $R(q,p)$ and $R(p,q)$ denote collective elements pertaining to the spectral interval between $\tau_{q,p}$ and $\tau_{p,q}$ (see Fig. 4).

(*B*) Construction From a Rigorous Spectral Integral. The ray-mode equivalent and hybrid formulation of a wave field may be constructed also by manipulating a rigorous spectral integral representation rather than asymptotic constituents. This is illustrated here on the Green's function for the configuration in Fig. 3. Retaining only the wave category described by the phase function in (14), one may construct the corresponding partial Green's function in the form of a spectral integral representation [7, 22]

$$G^g=\frac{i}{4\pi}\int_{-\infty}^{\infty}\frac{\exp[ik\Omega(\zeta)]}{\xi[1-R(\zeta)]}d\zeta,\quad R(\zeta)\equiv\exp[i\Phi(\zeta)] \tag{23}$$

with $\Phi(\zeta)$ defined in (14*b*). The integration path in (23) avoids the pole singularities at the zeros ζ_p of the denominator of the integrand, the modal resonances in (18), by indentations into the second and fourth quadrants.

Various alternative formulations can be extracted from the Green's function representation in (23). Power series expansion of the resonant denominator

$$\frac{1}{1-R(\zeta)}=\sum_{q=0}^{\infty}[R(\zeta)]^q, \tag{24}$$

and interchange of the order of summation and integration in (23) generates the ray series, but with elements f_q expressed as (exact) generalized ray integrals instead of the asymptotic approximations in (4), with (14) and (16). A normal mode series may be derived by contour deformation about the pole singularities and use of the residue theorem. A hybrid formulation in terms of generalized rays and normal modes follows from partial series expansion of the resonant denominator

$$\frac{1}{1-R}=\frac{1-R^{q_1}}{1-R}+\sum_{q=q_1}^{q_2-1}R^q+\frac{R^{q_2}}{1-R} \tag{25}$$

which, upon substitution into (23), yields a group of generalized ray integrals with multiple reflections identified

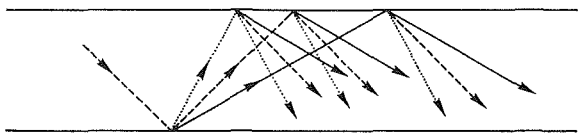


Fig. 5 Coupling in a layer with three wave species ($M=3$). A ray in one of the species, incident on the bottom boundary, gives rise to $M^2=9$ incident rays after one reverberation.

by the index $q_1\le q\le(q_2-1)$, plus remainder terms. The first remainder term can be subdivided as follows:

$$\frac{1-R^{q_1}}{1-R}=\frac{1}{1-R}-\frac{1}{2}R^{q_1}-\frac{1}{2}\frac{1+R}{1-R}R^{q_1},$$

$$\frac{1+R}{1-R}=i\cot\Big[\frac{\Phi(\zeta)}{2}\Big] \tag{26}$$

The first term on the right-hand side of (26), when inserted into (23), evidently furnishes the original integral but this can, by contour deformation into the upper half plane and residue evaluation at the poles, be expressed as a sum over *all* of the guided modes (propagating and evanescent) having a form as in (19). The second term in (26) yields just $(-1/2)$ times the q_1th generalized ray integral. The third term in (26) has a phase term like the q_1th generalized ray integral and an additional amplitude function $(-\frac{1}{2})\,(1+R)\,(1-R)^{-1}$. This integral can be made more rapidly convergent by deforming the integration path into the steepest descent path through the saddle point for the q_1th generalized ray (cf. (15)), account being taken of residues at those ζ_p poles that are intercepted during the deformation. The contribution from the last term in (25) may be treated in the same manner. When all of these results are combined, one obtains an exact hybrid formulation wherein the fields within the spectral intervals $-\infty<\zeta<\zeta_1$ and $\zeta_2<\zeta<\infty$ are expressed in terms of guided modes, while the spectral interval $\zeta_1<\zeta<\zeta_2$ is filled with generalized rays, with collective ray remainders filling out the spectral voids between these separate representations just as in (11) and (22). When the exact generalized ray and remainder integrals are evaluated asymptotically by the saddle point method, one recovers the explicit results derived previously in (11), with (10) and (19).

Extension to Elastic and General Multiwave Media

When a propagation environment can support multiple wave species (for example, compressional and shear waves in an elastic medium), the description of signal transmission is complicated by the coupling, in general, between these species at inhomogeneities and boundaries. Thus, in a plane parallel multiwave waveguide supporting M wave species, a ray in one of the species generates, in general, M reflected rays at each encounter with a boundary surface (Fig. 5). This feature not only complicates the ray tracing problem, due to rapid proliferation of the ray fields, but it also introduces fundamental difficulties into the formulation of a ray-mode equivalent. To overcome these difficulties, a new method for propagation in layered multiwave media has been proposed recently. Details may be found in reference [19], but the salient underlying principles are summarized here for the simplest case of a single multiwave layer (for example, an elastic plate). In a single multiwave layer, of width a, the time-harmonic (two-dimensional) potential functions, from which the wave fields in the various species can be derived via the field equations, can be arranged to form elements in an M-dimensional potential vector $\hat{\mathbf{V}}(x,x';z)$, where (x,z) is the observation point and $(x',0)$ is the location a forcing line distribution, with $0<x'<a$. In a plane wave spectral representation, $\hat{\mathbf{V}}$ is expressed as the Fourier integral

$$\hat{\mathbf{V}}(x,x';z)=\int_{-\infty}^{\infty}\mathbf{V}(x,x';\zeta)e^{ik\zeta z}d\zeta \tag{27}$$

Downloaded 02 May 2010 to 171.66.16.54. Redistribution subject to ASME license or copyright; see http://www.asme.org/terms/Terms_Use.cfm

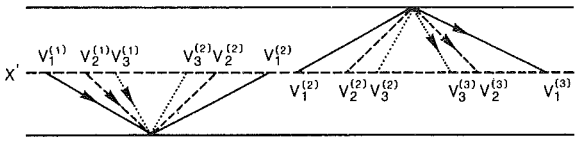


Fig. 6(*a*) Wave potential basis. At the reference level x', $\mathbf{V}^{(3)} = \underline{\mathbf{F}} \cdot \mathbf{V}^{(1)}$, where the potential vector V contains as elements the three wave species potentials. $\underline{\mathbf{F}}$ is the reverberation matrix.

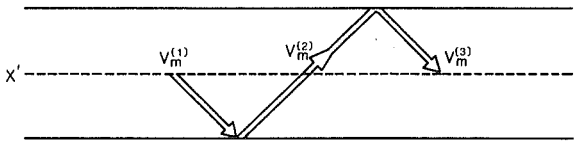


Fig. 6(*b*) Eigenray basis. Each eigenelement $V_m(m=1,2,3)$ of V transforms like a scalar, $V_m^{(3)} = \lambda_m V_m^{(1)}$. $\lambda_m(m=1,2,3)$ are the eigenvalues of $\underline{F}$.

Fig. 6 Schematization of reverberation process in wave potential and eigenray bases, for specified spectral wavenumber ζ. $M=3$.

where

$$\mathbf{V}(x,x';\zeta) = \underline{\mathbf{G}}(x,x';\zeta) \cdot \mathbf{S}(\zeta) \tag{27a}$$

and

$$\underline{\mathbf{G}}(x,x';\zeta) = \underline{\mathbf{T}}(x,x';\zeta) \cdot [\underline{\mathbf{I}} - \underline{\mathbf{F}}(\zeta)]^{-1} \tag{27b}$$

Here, **V** and **S** are M-dimensional vectors whose elements represent, respectively, the plane wave potentials and the excitation functions for these potentials, in the spectral wavenumber space ζ. $\underline{\mathbf{G}}$, $\underline{\mathbf{T}}$, and $\underline{\mathbf{F}}$ are $M \times M$ element matrices (dyadic operators), $\underline{\mathbf{I}}$ is the identity operator, and superscript (-1) denotes the inverse operator. The Green's operator $\underline{\mathbf{G}}$ is composed of the translation operator $\underline{\mathbf{T}}$, which connects wave processes at x' with those at x, and the reverberation operator

$$\underline{\mathbf{F}}(\zeta) = \underline{\mathbf{R}}_u(\zeta) \cdot \underline{\mathbf{R}}_d(\zeta) \tag{28}$$

containing ordered products of operators $\underline{\mathbf{R}}_u$ and $\underline{\mathbf{R}}_d$ that account for reflections at the upper and lower boundaries, respectively. Due to wave coupling at the boundaries, the matrix representations of $\underline{\mathbf{R}}_u$ and $\underline{\mathbf{R}}_d$ and therefore of $\underline{\mathbf{F}}$ are filled out.

The spectral integral in (27) is the matrix generalization of the scalar integral in (23) for the single-wave layer. A ray expansion as in (24) now involves powers $\underline{\mathbf{F}}^q$ of the reverberation operator $\underline{\mathbf{F}}$, and each of the $\underline{\mathbf{F}}^q$ terms must be expanded further to yield a generalized ray integral. This leads to the proliferation of ray fields mentioned earlier. A guided mode representation is obtained by residue evaluation at the zeros ζ_p of the "resonant denominator," i.e., the poles of the integrand in (27),

$$\det[\underline{\mathbf{I}} - \underline{\mathbf{F}}(\zeta_p)] = 0, \qquad p = 1,2, \ldots \tag{29}$$

Because of the multiplicity of rays, ray-mode conversion is tedious and definition of a *ray-mode equivalent* for a *finite* spectral interval ambiguous.

The cause of the difficulty, namely coupling between individual wave species at the boundaries, may be removed by diagonalization of the reverberation opertor $\underline{\mathbf{F}}$. This is accomplished via the eigenvalue problem

$$\underline{\mathbf{F}}(\zeta) \cdot \mathbf{e}_m(\zeta) = \lambda_m(\zeta)\mathbf{e}_m(\zeta), \qquad m = 1 \ldots M \tag{30}$$

where each of the M elements of an eigenvector $\mathbf{e}_m$ represents combinations of the original M wave species in such proportion that after one reverberation, $\mathbf{e}_m$ repeats itself except for multiplication by a common constant factor, the eigenvalue λ_m (see Fig. 6). These eigencombinations of the original M wave species will be called *eigenrays*. The *eigenmodes* of the waveguide are generated from the eigenrays by the constraint

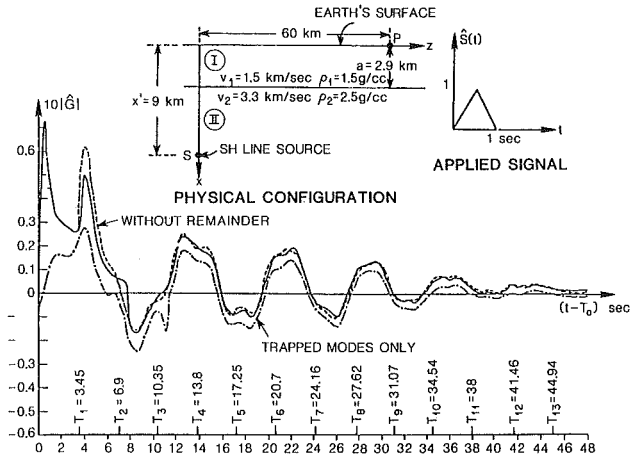


Fig. 7 *SH* Motion $\hat{G}(t)$ in a two-layer earth model with a homogeneous sedimentary layer of width a and a homogeneous bedrock half space. A line source of *SH* waves, with source function $\hat{S}(t)$, is shown in the figure. Solid curve: exact (reference) solution obtained by summing Cagniard-DeHoop rays. The number of rays depends on the observation time, with T_q denoting the arrival time of the qth ray. For a time span of 48 secs from the first arrival at time $T_0 = 19.99$ secs, one finds $Q_{max} = 13$ (i.e., 14 rays). The hybrid solution: first two Cagniard rays $q = 0,1$, two trapped modes excited by evanescent tunneling, and a collective ray remainder. Result coincides with reference solution to within the accuracy of the drawing. Dashed curve: hybrid solution without the remainder. Dot-dash curve: contribution from the two trapped modes only.

$$\lambda_m(\zeta) = 1, \zeta = \zeta_{pm}, \quad m = 1 \ldots M, \quad p = 1,2 \ldots \tag{31}$$

which expresses the requirement of phase coherence after one reverberation that distinguishes a (source-free) guided mode field. One may show, in fact, that the totality of solutions ζ_{pm} in (31) is the same as that obtained from (29).

The eigenvectors $\mathbf{e}_m$ and their adjoints can be employed to define a new basis, the eigenbasis, for representation of the vectors and operators in (27*a*). In the eigenbasis, *operation* by $\underline{\mathbf{F}}$ or a function of $\underline{\mathbf{F}}$ implies *scalar multiplication* by λ_m or the corresponding function of λ_m. In particular,

$$\underline{\mathbf{F}}^q \leftrightarrow \lambda_m^q, \quad (\underline{\mathbf{I}} - \underline{\mathbf{F}})^{-1} \leftrightarrow \frac{1}{1-\lambda_m} \tag{32}$$

thereby scalarizing (decoupling) the original coupled wave problem. The resulting integrals then resemble the one in (23), with $\lambda_m(\zeta)$ taking the place of $R(\zeta)$. Each of these integrals may now be manipulated as in the discussion on Hybrid Representation to furnish an eigenray-eigenmode equivalent, hybrid eigenray-eigenmode representation, etc. After the manipulations have been performed in the eigenbasis, one transforms back to the original wave potential basis in the spectral (ζ) domain and performs the inversion to physical space via (27). Full details of the procedure, its comparison with the conventional method (without diagonalization of $\underline{\mathbf{F}}$), and its application to P-SV propagation in an elastic plate are given in reference [19].

Applications

The ray-mode equivalents and resulting hybrid field representations have been applied to a variety of time-harmonic and transient propagation and scattering problems in electromagnetics, tropospheric propagation, underwater acoustics, and seismology (see References). The applications have stressed: (*a*) propagation along curved boundaries, convex and concave; (*b*) layered guiding environments with homogeneous and inhomogeneous transverse velocity profiles and also with longitudinal dependence of the medium parameters and (or) layer boundaries; (*c*) transmission through, and reflection from, curved and tapered layers, with

Downloaded 02 May 2010 to 171.66.16.54. Redistribution subject to ASME license or copyright; see http://www.asme.org/terms/Terms_Use.cfm

collective ray treatment of internal multiple reflections; and (*d*) transient scattering by obstacles and layered media. In each case, the ray-mode equivalent and hybrid formulation have been employed to remedy some defect in a field representation that includes either only wavefronts (rays) or only resonances (modes). Such defects include poor convergence, in which event one seeks to replace the slowly convergent ray or mode elements by more favorably behaved mode or ray elements (plus collective remainders), respectively. Deficiencies of an approximate representation may also be repaired by the hybrid scheme. Thus, failure of asymptotic ray theory in transition regions near caustics, shadow boundaries, critical reflection, etc. can be repaired by eliminating the troublesome transitional rays and filling the spectral interval vacated by them with modes.

Details of the analysis and numerical implementations pertaining to these applications may be found in the cited references. Here, for illustration, we present only one of the results, involving a two-layer half-space excited by a transient source [16]. The parameters pertain to a seismic environment, modeling a homogeneous sedimentary surface layer above a semi-infinite homogeneous bedrock with a line source of SH motion located in the bedrock, and the resulting SH motion observed at the earth's surface (Fig. 7). An exact reference solution for observation times from 0-48 secs after the first arrival was generated by summing up to 14 Cagniard rays and convolving these with the triangular source function. The hybrid solution, likewise exact, consists of two Cagniard rays, the first two modes trapped inside the surface layer (other modes were found to be insignificant), and a remainder integral. These constituents were evaluated numerically and are seen to agree completely with the Cagniard ray sum. Also shown for comparison is the effect of omitting the collective ray remainder. This introduces some distortion near the arrival time of the second ray because the ray series is truncated there. At later times, the influence of the remainder diminishes. The motion was calculated also by including only the two trapped modes. This description clearly fails at early times but predicts the motion well at later times; the small discrepancy there is most likely due to omission of the continuous mode spectrum, which has not been included but turns out to be non-negligible here.

Conclusions

Rigorously phrased ray-mode or wavefront-resonance equivalents as discussed here furnish the building blocks for a rigorous hybrid theory for time-harmonic and transient propagation and diffraction in difficult environments. The hybrid formulation can make numerical calculations more efficient because integrals, when they appear, are defined along steepest descent paths, on which the integrands decay and have only weak oscillations; integrands in the original spectral integrals (see (23) and (27)) are usually highly oscillatory. Asymptotic approximations are often useful to reduce the integrals analytically and to provide thereby numerical simplification as well as fundamental insights into the interplay between traveling and oscillatory wave processes. How to combine these processes most effectively depends on the problem at hand. The information sought, and the given physical parameters, play a decisive role in the strategy for choosing the hybrid mix. However, once a decision has been made that it is desirable, for instance, to retain two rays as in the example of Fig. 7, the modes to be included, as well as the collective remainders, are determined uniquely.

The hybrid approach lends greater flexibility to the analysis of propagation and diffraction problems than is available when only one particular description is invoked. Thus, diffraction in a guiding environment – for example, by a crack in a solid plate – could be formulated in terms of an incident guided mode field but diffracted fields that contain both rays and modes combined so as to optimize calculation of the detected signal. Since ray fields and mode field convey different (local versus global) information, the hybrid method bears also on the inversion of scattering data to infer properties of the scatterer. These intriguing aspects remain to be further explored.

Acknowledgment

The research forming the basis of this paper was sponsored by the Office of Naval Research under Contracts No. N-00014-79-C-0013 and N-00014-83-K-0214, by the National Science Foundation under Grant No. EAR-8213147, by the Army Research Office under Contract No. DAAG29-82-K-0097, and by the Joint Services Electronics Program under Contract No. F-49620-82-C-0084.

References

1 Gao, T. F., and Shang, E. C., "The Transformation Between the Mode Representation and the Generalized Ray Representation of a Sound Field," *J. Sound Vib.*, Vol. 80, 1982, pp. 105–115.

2 Felsen, L. B., "Hybrid Ray-Mode Fields in Inhomogeneous Waveguides and Ducts," *J. Acoust. Soc. Am.*, Vol. 69, 1981, pp. 352–361.

3 Kamel, A., and Felsen, L. B., "On the Ray Equivalent of a Group of Modes," *J. Acoust. Soc. Am.*, Vol. 71, 1982, pp. 1445–1452.

4 Felsen, L. B., "Progressing and Oscillatory Waves for Hybrid Synthesis of Source-Excited Propagation in Layered Media," to be published in *Geophys. J. Roy. Astron. Soc.*

5 Felsen, L. B., "Progressing and Oscillatory Fields for Propagation and Scattering," invited paper, to be published in *IEEE Transactions Antennas and Propagation*, 1984.

6 Ishihara, T., Felsen, L. B., and Green, A., "High Frequency Fields Excited by a Line Source Located on a Perfectly Conducting Concave Cylindrical Surface," *IEEE Transactions on Antennas and Propagation*, Vol. AP-26, 1978, pp. 757–767.

7 Felsen, L. B., and Kamel, A., "Hybrid Ray-Mode Formulation of Parallel Plane Waveguide Green's Functions," *IEEE Transactions on Antennas and Propagation*, Vol. AP-29, 1981, pp. 637–649.

8 Niver, E., Cho, S. H., and Felsen, L. B., "Rays and Modes in an Acoustic Channel with Exponential Velocity Profile," *Radio Science*, Vol. 16, 1981, pp. 963–970.

9 Migliora, C. G., Felsen, L. B., and Cho, S. H., "High Frequency Propagation in an Elevated Tropospheric Duct," *IEEE Transactions on Antennas and Propagation*, Vol. AP-30, 1982, pp. 1107–1120.

10 Heyman, E., and Felsen, L. B., "Creeping Waves and Resonances in Transient Scattering by Smooth Convex Objects," *IEEE Transactions on Antennas and Propagation*, Vol. AP-31, 1983, pp. 426–437.

11 Heyman, E., and Felsen, L. B., "Traveling Wave and Oscillatory Formulations of Scattering Problems," to be published in *Handbook on Acoustic, Electromagnetic and Elastic Wave Scattering—Theory and Experiment*, 1984.

12 Einziger, P. D., and Felsen, L. B., "Rigorous Asymptotic Analysis of Transmission Through a Curved Dielectric Slab," *IEEE Transactions on Antennas and Propagation*, Vol. AP-31, 1983, pp. 863–870.

13 Einziger, P. D., and Felsen, L. B., "Ray Analysis of Two-Dimensional Radomes," *IEEE Transactions on Antennas and Propagation*, Vol. AP-31, 1983, pp. 870–884.

14 Kamel, A., and Felsen, L. B., "Spectral Theory of Sound Propagation in an Ocean Channel With Weakly Sloping Bottom," *J. Acoust. Soc. Am.*, Vol. 73, 1983, pp. 1120–1130.

15 Arnold, J. M., and Felsen, L. B., "Rays and Local Modes in a Wedge-Shaped Ocean," *J. Acoust. Soc. Am.*, Vol. 73, 1983, pp. 1105–1119.

16 Kamel, A., and Felsen, L. B., "Hybrid Ray-Mode Formulation of SH Motion in a Two-Layer Half Space," *Bull. Seismol. Soc. Am.*, Vol. 71, 1981, pp. 1763–1781.

17 Kamel, A., and Felsen, L. B., "Hybrid Green's Function for SH Motion in a Low Velocity Layer," *Wave Motion*, Vol. 5, 1983, pp. 83–97.

18 Niver, E., Kamel, A., and Felsen, L. B., "Modes to Replace Transitional Ray Fields in a Vertically Inhomogeneous Earth Model," to be published in *Geophys. J. Roy. Astron. Soc.*

19 Lu, I. T., Felsen, L. B., and Kamel, A., "Eigenreverberations, Eigenmodes and Hybrid Combinations: A New Approach to Propagation in Layered Multiwave Media," to be published in *Wave Motion*, 1984.

20 Papoulis, A., *Signal Analysis*, McGraw-Hill, New York, 1977, Section 3.3.

21 Felsen, L. B., and Marcuvitz, N., *Radiation and Scattering of Waves*, Prentice-Hall, Englewood Cliffs, N.J., 1973, Sections 4.1 and 4.6.

22 Ibid., Sections 1.6 and 1.7.

Downloaded 02 May 2010 to 171.66.16.54. Redistribution subject to ASME license or copyright; see http://www.asme.org/terms/Terms_Use.cfm

Reflection and Transmission of Elastic Waves by a Periodic Array of Cracks

Y. C. Angel[1]
Mem. ASME

J. D. Achenbach
Fellow ASME

Department of Civil Engineering,
Northwestern University,
Evanston, Ill. 60201

The interaction of elastic waves with a planar array of periodically spaced cracks of equal length is investigated. For normal incidence, reflection and transmission of longitudinal and transverse wave has been considered. Application of finite Fourier transform techniques reduces the solution of the mixed-boundary value problem for a typical strip to that of a singular integral equation. The solution has been obtained numerically. The reflected and transmitted far-field displacements are shown to be superpositions of a finite number of propagating body-wave modes. The numerical results have been checked by an application of the balance of rates of energies. The reflection coefficients have been plotted versus both the frequency and the ratio of crack length to crack spacing. The results according to exact elastodynamic theory have been compared with two approximations. Good agreement is observed at low frequencies.

1 Introduction

Scattering of elastic waves by a single crack has been studied in considerable detail (see e.g., Achenbach et al. [1]). In the present paper we investigate the interaction of elastic waves with a planar array of periodically spaced cracks of equal length. Normal incidence of longitudinal and transverse waves is considered.

The total field in the solid has been analyzed as the superposition of the incident field in an uncracked space and the scattered field in the cracked space. The scattered field is generated by surface tractions on the crack faces which are equal in magnitude, but opposite in sign, to the tractions corresponding to the incident wave. The periodicity of the geometry implies that only a typical strip of the solid needs to be considered. By the use of Fourier series expansions, the mixed-boundary value problem for such a typical strip has been reduced to a singular integral equation of the first kind for the dislocation density across the crack faces. The integral equation has been solved numerically. There are certain frequencies for which the integral equation does not hold. At these frequencies, a pair of integral equations, rather than a single equation, is needed to describe the behavior of the system properly.

The reflected and transmitted fields are easily computed once the dislocation density is known. It is found that at some distance from the plane of the crack the displacement fields appear as superpositions of a finite number of reflected and transmitted plane-wave propagating modes. The reflection and transmission coefficients, corresponding to the propagating mode of order zero, have been investigated for various values of the frequency and the ratio of crack length to crack spacing. The balance of rates of energies, which involves the incident wave as well as the reflected and transmitted propagating modes, has been obtained for all frequencies, and it has been used to check the accuracy of the computations. It is of interest that the results are comparable to those obtained for scattering of elastic waves by periodic surfaces (see Jungman et al. [2] and Fokkema and Van den Berg [3]).

Apart from its own intrinsic interest for applications to quantitative nondestructive evaluation and seismology, the results of this paper are also relevant to reflection of elastic waves by a flaw plane. In general, a flaw plane may be viewed as a region where separation zones and contact zones can both exist, and friction may be significant over the contact zones. Achenbach and Norris [4] have proposed a set of nonlinear flaw-plane conditions to account for the separation and friction effects. Other conditions, of a linear type, have been discussed by Thompson and Fiedler [5]. Another approach has been pursued by Comninou and Dundurs [6, 7]; they have considered the interaction of elastic waves with an interface between two half-spaces that cannot transmit tensile tractions and where frictional slip may or may not be significant. The possible zones of separation are not known beforehand. A paper by Miller and Tran [8] has extended the results of [6, 7] to a broad class of friction laws, under the condition that separation does not occur. In the present paper the separation

[1] Present address: Department of Mechanical Engineering and Materials Science, Rice University, P.O. Box 1892, Houston, Texas 77251.

Contributed by the Applied Mechanics Division for presentation at the 1985 Joint ASME/ASCE Applied Mechanics, Fluids Engineering and Bioengineering Conference, Albuquerque, N. Mex., June 24-26, 1985 of THE AMERICAN SOCIETY OF MECHANICAL ENGINEERS.

Discussion on this paper should be addressed to the Editorial Department, ASME, United Engineering Center, 345 East 47th Street, New York, N.Y. 10017, and will be accepted until two months after final publication of the paper itself in the JOURNAL OF APPLIED MECHANICS. Manuscript received by ASME Applied Mechanics Division, January, 1984. Paper No. 85-APM-1.

Copies will be available until February, 1986.

Copyright © 1985 by ASME
Downloaded 02 May 2010 to 171.66.16.54. Redistribution subject to ASME license or copyright; see http://www.asme.org/terms/Terms_Use.cfm

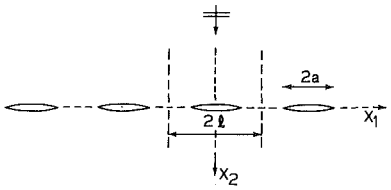


Fig. 1 Incidence of a plane time-harmonic wave on a periodic array of cracks of length 2a and period 2l

zones (the cracks) are known and they remain stress-free under the action of the incident wave. The displacements as well as the stresses are continuous over the plane regions between the cracks. Hence, the configuration models an interface with predetermined separation zones and rough contact zones.

In the final section the exact results are compared with results according to two approximate theories. The first approximation is a static limit to the dynamic theory. In the second one, which is due to Thompson and Fiedler [5], the array of cracks is replaced by an equivalent spring-layer. Both approximations agree with the exact theory at low frequency.

2 Formulation of the Problem

We consider a homogeneous, isotropic, linearly elastic, unbounded solid that contains a periodic array of cracks of length $2a$, as shown in Fig. 1. The cracks lie in the plane $x_2 = 0$ and extend to infinity in the direction perpendicular to the plane of the figure. The period of the crack-array is $2l$. Let μ and ν denote the shear modulus and Poisson's ratio of the solid. The slownesses of longitudinal and transverse waves will be referred to as s_L and s_T, respectively; their ratio is $\epsilon = s_L/s_T$.

An incident time-harmonic body wave travels in the direction of the positive x_2 axis. Let u_0 and ω denote an amplitude factor and the frequency of the incident wave. The steady state term $\exp(-i\omega t)$, which is common to all field variables, has been omitted in the sequel.

The displacements generated by an incident longitudinal wave are

$$u_1 = 0, \qquad u_2 = u_0 \exp(i\omega s_L x_2). \tag{1a}$$

For an incident transverse wave, we have

$$u_1 = u_0 \exp(i\omega s_T x_2), \qquad u_2 = 0. \tag{1b}$$

The stresses associated with the incident wave are readily obtained by using Hooke's law. In the plane of the cracks ($x_2 = 0$), we have

$$\sigma_{12} = 0, \qquad \sigma_{22} = i\mu u_0 \omega s_L/\epsilon^2, \tag{2a}$$

$$\sigma_{12} = i\mu u_0 \omega s_T, \qquad \sigma_{22} = 0, \tag{2b}$$

where (2*a*) and (2*b*) correspond to an incident longitudinal wave and an incident transverse wave, respectively.

The total field in the solid can be analyzed as the superposition of the incident field in an uncracked solid and the scattered field in the cracked solid. The scattered field can be thought of as being generated by prescribed surface tractions on the faces of the cracks. These tractions are equal in magnitude, but opposite in sign, to the tractions of equation (2). The scattered field corresponding to an incident longitudinal wave is *physically* symmetric with respect to the x_1 axis, as well as with respect to axes $x_1 = nl$ ($n = 0, \pm 1, \ldots \pm\infty$). Similarly, the scattered field corresponding to an incident transverse wave is *physically* antisymmetric with respect to those axes. Hence, the scattered fields can be determined from the solutions of two mixed-boundary value problems for the typical strip defined by $x_2 \geq 0$, $0 \leq x_1 \leq l$.

For the case of an incident longitudinal wave, the boundary conditions on the faces of the strip are

$$\sigma_{12} = 0, \qquad 0 \leq x_1 \leq l, \qquad x_2 = 0, \tag{3a}$$

$$\sigma_{22} = -i\mu u_0 \omega s_L/\epsilon^2, \qquad 0 < x_1 < a, \qquad x_2 = 0, \tag{3b}$$

$$u_2 = 0, \qquad a \leq x_1 \leq l, \qquad x_2 = 0, \tag{3c}$$

$$\sigma_{12} = 0, \qquad x_1 = 0, \qquad x_1 = l, \; 0 \leq x_2 < \infty, \tag{3d}$$

$$u_1 = 0, \qquad x_1 = 0, \qquad x_1 = l, \; 0 \leq x_2 < \infty. \tag{3e}$$

For an incident transverse wave, we have

$$\sigma_{22} = 0, \qquad 0 \leq x_1 \leq l, \qquad x_2 = 0, \tag{4a}$$

$$\sigma_{12} = -i\mu u_0 \omega s_T, \qquad 0 < x_1 < a, \qquad x_2 = 0, \tag{4b}$$

$$u_1 = 0, \qquad a \leq x_1 \leq l, \qquad x_2 = 0, \tag{4c}$$

$$\sigma_{11} = 0, \qquad x_1 = 0, \qquad x_1 = l, \; 0 \leq x_2 < \infty, \tag{4d}$$

$$u_2 = 0, \qquad x_1 = 0, \qquad x_1 = l, \; 0 \leq x_2 < \infty. \tag{4e}$$

3 Singular Integral Equation

In this section the formulation of the problem is reduced to a singular integral equation of the first kind. First we define the finite cosine and sine transforms of order r of a function $f(x_1, x_2)$ by

$$f_r^{\{c\atop s\}}(x_2) = \int_0^l f(x_1, x_2) \begin{Bmatrix} \cos \\ \sin \end{Bmatrix} (r\xi x_1) dx_1, \tag{5}$$

where $\xi = \pi/l$. The corresponding inverse relations are

$$lf(x_1, x_2) = f_0^c(x_2) + 2\sum_{r=1}^{\infty} f_r^c(x_2)\cos(r\xi x_1), \tag{6}$$

$$lf(x_1, x_2) = 2\sum_{r=1}^{\infty} f_r^s(x_2)\sin(r\xi x_1). \tag{7}$$

The fields in the strip defined in the preceding section are sought in the form of infinite series of the types (6) or (7). In particular, the series (7) will be used in such a way that the boundary conditions (3*d*,*e*) and (4*d*,*e*) are identically satisfied.

The solutions to the displacement equations of motion are written in terms of the two Green-Lamé potentials ϕ and ψ, which satisfy simple wave equations. When the incident wave is longitudinal, the potential ϕ takes the general form (6) and ψ takes the form (7). The coefficients ϕ_r^c and ψ_r^s are

$$\phi_r^c = M_r e^{-\beta_L x_2}, \; \psi_r^s = N_r e^{-\beta_T x_2}; \qquad \beta_L^2(r) = r^2\xi^2 - \omega^2 s_L^2,$$
$$\beta_T^2(r) = r^2\xi^2 - \omega^2 s_T^2, \tag{8}$$

where M_r and N_r are constants to be determined from the boundary conditions. Next we introduce the function $a_L(u)$ such that

$$u_2(x_1, 0^+) = \begin{cases} -\int_{x_1}^{a} a_L(u)\,du, & 0 \leq x_1 < a \\ 0, & a \leq x_1 \leq l \end{cases}. \tag{9}$$

For every function a_L integrable in the interval $[0,a]$, $u_2(x_1, 0^+)$ is continuous in $[0,l]$ and the boundary condition (3*c*) is satisfied. Taking the cosine transform of equation (9) and the sine transform of the boundary condition (3*a*), and making use of Hooke's law, we obtain a system of two equations for the constants M_r and N_r. The solution of this system yields M_r and N_r in terms of the function a_L.

When the incident wave is transverse, the potential ϕ takes the general form (7) and ψ takes the form (6). Now we need to introduce a function $a_T(u)$ such that

Downloaded 02 May 2010 to 171.66.16.54. Redistribution subject to ASME license or copyright; see http://www.asme.org/terms/Terms_Use.cfm

$$u_1(x_1,0^+)=\begin{cases}-\int_{x_1}^{a} a_T(u)\,du, & 0\le x_1<a\\ 0, & a\le x_1\le l\end{cases}. \quad (10)$$

Then the fields are expressed in terms of the function a_T. Observe that a_L and a_T can be interpreted as dislocation densities across the faces of the cracks.

Next we define

$$\Sigma_\alpha(x_1,0)=\begin{cases}\sigma_{22}(x_1,0), & \alpha=L\\ \sigma_{12}(x_1,0), & \alpha=T\end{cases}, \quad (11)$$

and we find that ($\alpha = L$ or T, no sum on α)

$$\Sigma_\alpha(x_1,0)=\bar{R}(0)\bar{J}_\alpha/\bar{\beta}_\alpha(0)$$
$$+2\sum_{r=1}^{\infty}\bar{R}(r)\bar{I}_\alpha(r)\cos(r\xi x_1)/[r\xi\bar{\beta}_\alpha(r)], \quad (12)$$

where

$$\bar{R}(r)=(2r^2\xi^2-\omega^2 s_T^2)^2-4r^2\xi^2\bar{\beta}_L(r)\bar{\beta}_T(r), \quad (13)$$

$$\bar{J}_\alpha=\int_0^a u a_\alpha(u)\,du, \qquad \bar{I}_\alpha(r)=\int_0^a a_\alpha(u)\sin(r\xi u)\,du. \quad (14)$$

The integral equations for a_L and a_T follows now from equation (12) and from the boundary conditions (3*b*) and (4*b*), respectively. Observe, however, that

$$\bar{R}(r)/[r\xi\bar{\beta}_\alpha(r)]=-2\omega^2(s_T^2-s_L^2)+0(r^{-2}), \qquad \text{as } r\to\infty. \quad (15)$$

Thus, special care must be exercised in interchanging the summation and integration in equation (12). The final form of the integral equations is obtained by using the Riemann–Lebesgue Lemma (see Churchill and Brown [9], page 88), together with the following results

$$2\sum_{r=1}^{m}\sin(ru)=\cot(u/2)-\cot(u/2)\cos(mu)+\sin(mu), \quad (16)$$

$$\sum_{r=1}^{\infty}\cos(ru)/r=-\mathrm{Log}\,|2\sin(u/2)|, \quad u\neq 2k\pi, \quad (17)$$

$$(\xi/2)\int_0^a\cot[\xi(u-x_1)/2]du=\mathrm{Log}\,|\sin[\xi(a-x_1)/2]$$
$$/\sin(\xi x_1/2)|, \quad 0<x_1<a, \quad (18)$$

where the integration is performed in the principal-value sense. In dimensionless form the singular integral equations are obtained as

$$\int_0^1\tilde{a}_\alpha(\gamma)[\cot[\xi a(\gamma-x)/2]+\cot[\xi a(\gamma+x)/2]$$
$$+i\gamma\tilde{a}A_\alpha-2S_\alpha(\gamma,x)]d\gamma=i\tilde{u}_0A_\alpha, \quad (19)$$

where $0<x<1$, $\alpha = L$ or T (no sum on α), and

$$\tilde{a}_\alpha(\gamma)=a_\alpha(\gamma a), \quad x=x_1/a, \quad \tilde{a}=a/l,$$
$$\tilde{u}_0=u_0/a, \quad \xi=\pi/l, \quad (20)$$

$$A_L=A_T/\epsilon, \quad A_T=-\tilde{s}_T/[\tilde{a}(1-\epsilon^2)], \quad \tilde{s}_T=\omega s_T a, \quad (21)$$

$$S_\alpha(\gamma,x)=2\sum_{r=1}^{\infty}\bar{S}_\alpha(r)\sin(r\xi a\gamma)\cos(r\xi a x),$$
$$\bar{S}_\alpha(r)=1+R(r)/[2(1-\epsilon^2)r\Lambda\beta_\alpha]. \quad (22)$$

In equation (22) we have

$$\Lambda=\xi/\omega s_T, \quad \beta_L^2(r)=r^2\Lambda^2-\epsilon^2, \quad \beta_T^2(r)=r^2\Lambda^2-1,$$
$$R(r)=(2r^2\Lambda^2-1)^2-4r^2\Lambda^2\beta_L\beta_T. \quad (23)$$

Observe that $\bar{S}_\alpha(r)$ becomes infinite when $\beta_\alpha(r)$ vanishes. Hence, the series $S_\alpha(\gamma,x)$ is undefined when there is an integer r_α, ($\alpha = L$ or T), such that

$$\begin{cases}r_L\Lambda/\epsilon=1, & \alpha=L\\ r_T\Lambda=1, & \alpha=T\end{cases}, \quad (C)$$

where $\epsilon = s_L/s_T$. Whenever condition (*C*) is satisfied, equation (19) cannot be used, and we must derive another set of equations. This is done in the next section.

4 Integral Equations When Condition (*C*) Holds

We assume here that $\beta_\alpha(r_\alpha)=0$, ($\alpha = L$ or T), for some integer $r_\alpha > 0$. Then we may proceed as in the preceding sections to obtain the following equations

$$\begin{cases}\int_0^1\tilde{a}_\alpha(\gamma)\,[\cot[\xi a(\gamma-x)/2]+\cot[\xi a(\gamma+x)/2]\\ +i\gamma\tilde{a}A_\alpha-2S'_\alpha(\gamma,x)]d\gamma+B_\alpha\cos(\tilde{s}_\alpha x)\,b_\alpha=i\tilde{u}_0A_\alpha, & (24)\\ \int_0^1\tilde{a}_\alpha(\gamma)\sin(\tilde{s}_\alpha\gamma)\,d\gamma=0, & (25)\end{cases}$$

where $0<x<1$, $\alpha = L$ or T (no sum on α), and

$$S'_\alpha(\gamma,x)=2\sum_{\substack{r=1\\ r\neq r_\alpha}}^{\infty}\bar{S}_\alpha(r)\sin(r\xi a\gamma)\cos(r\xi a x), \quad \tilde{s}_\alpha=\omega s_\alpha a, \quad (26)$$

$$B_L=(2\epsilon^2-1)B_T, \quad B_T=2\tilde{s}_T^2/(1-\epsilon^2). \quad (27)$$

The remaining quantities are defined in equations (20)–(23). Equations (24) and (25) represent a pair of equations for the dislocation density $\tilde{a}_\alpha(\gamma)$ and the constant b_α.

5 Method of Solution

The singular integral equation (19) is solved numerically by using the methods developed by Erdogan et al. in references [10, 11]. The details of this procedure for equations of the type (19) can be found in Angel and Achenbach [12, 13]. We recall here that the dislocation densities $\tilde{a}_\alpha(x)$ can be written in the form

$$\tilde{a}_\alpha(x)=\phi_\alpha(x)/(1-x)^{1/2}, \quad (\alpha=L \text{ or } T), \quad (28)$$

where ϕ_α is bounded in the interval [0,1]. We also define the bounded function $V(\gamma-x)$ by

$$\cot[\xi a(\gamma-x)/2]\equiv 2/[\xi a(\gamma-x)]+V(\gamma-x). \quad (29)$$

Then we can proceed in a way entirely analogous to that of references [12, 13]. Equation (19) yields the following system

$$\sum_{j=1}^{n}Q_\alpha(\beta_j,\zeta_k)\,\phi_\alpha(\beta_j)=i\tilde{u}_0g_\alpha, \qquad (k=1,\ldots,n), \quad (30)$$

where $\alpha = L$ or T (no sum on α), n is the number of quadrature points in the integration formulas, and

$$\beta_j=\cos^2[(2j-1)\pi/(4n)], \qquad \zeta_k=\cos^2[2k\pi/(4n+2)],$$
$$g_\alpha=n\tilde{a}A_\alpha/2. \quad (31)$$

The function Q_α is given by (no sum on j)

$$Q_\alpha(\beta_j,\zeta_k)/\beta_j^{1/2}=W_j(\zeta_k)+U_\alpha(\beta_j,\zeta_k), \quad (32)$$

where

$$W_j(\zeta_k)=2n[T_j(\zeta_k)/(2n+1)-\tilde{\Delta}_j/\pi]/(\zeta_k\beta_j^{1/2})-(\beta_j-\zeta_k)^{-1}$$
$$+(\xi a/2)\cot[\xi a(\beta_j-\zeta_k)/2]+(\xi a/2)\cot[\xi a(\beta_j+\zeta_k)/2], \quad (33)$$

$$U_\alpha(\beta_j,\zeta_k)=i\pi\tilde{a}^2A_\alpha\beta_j/2-\pi\tilde{a}S_\alpha(\beta_j,\zeta_k), \quad (34)$$

$$T_j(\zeta_k)=\sum_{l=1}^{n}\alpha_l^{3/2}\Delta_j(\alpha_l)/(\alpha_l-\zeta_k),$$

Downloaded 02 May 2010 to 171.66.16.54. Redistribution subject to ASME license or copyright; see http://www.asme.org/terms/Terms_Use.cfm

$$\bar{\Delta}_j = \int_0^1 \Delta_j (1-u^2)du,$$

$$\Delta_j(x) = \Delta_j^*(x)/\Delta_j^*(\beta_j), \quad \text{(no sum)}, \tag{35}$$

$$\alpha_l = \cos^2[(2l-1)\pi/(4n+2)], \tag{36}$$

$$\Delta_j^*(x) = (x-\beta_1)\ldots(x-\beta_{j-1})(x-\beta_{j+1})\ldots(x-\beta_n). \tag{37}$$

Equation (30) represents a linear system of n equations for the n complex-valued unknowns $\phi_\alpha(\beta_j)$. This system is solved numerically.

It suffices to prescribe the values of four dimensionless parameters: Poisson's ratio of the solid, ν; the ratio of the crack length to the period of the crack-array, $\bar{a} = a/l$; the amplitude of the incident wave, $\bar{u}_0 = u_0/a$; and the frequency of the incident wave, $\bar{\omega} \equiv 2l/\lambda_T = \Lambda^{-1}$; where $\lambda_T = 2\pi/\omega s_T$ is the wavelength of transverse waves in the solid. All other dimensionless parameters can be written in terms of these four basic parameters.

The numerical method to solve equations (24) and (25) follows the same steps. We need only record the equation obtained from equation (25)

$$\sum_{j=1}^{n} \beta_j^{1/2} \sin(\bar{s}_\alpha \beta_j)\, \phi_\alpha(\beta_j) = 0, \qquad (\alpha = L \text{ or } T, \text{ no sum}). \tag{38}$$

Equations (24) and (25) yield a linear system of $(n+1)$ equations for the $(n+1)$ complex-valued unknowns $\phi_\alpha(\beta_j)$, $(j = 1, \ldots, n)$, and b_α.

6 Far-Field Displacements

To investigate the wave motion at a large distance from the plane of the cracks ($x_2 = 0$), we first give the exact expressions for the scattered displacements in the solid. These displacements take the form of Fourier series of the type (6) or (7), in which the coefficients depend on the dislocation densities. We have

$$\bar{u}_{\alpha\delta}(x,y) = E_{\alpha\delta} J_\alpha e^{i\bar{s}_\alpha y} + \sum_{r=1}^{\infty} H_{\alpha\delta}(r,x,y) I_\alpha(r), \tag{39}$$

where $\alpha = L$ or T (no sum on α), $\delta = 1$ or 2, and

$$x = x_1/a, \; y = x_2/a, \quad \bar{u}_{\alpha\delta}(x,y) = u_{\alpha\delta}(ax,ay)/a, \tag{40}$$

$$J_\alpha = \int_0^1 \gamma \bar{a}_\alpha(\gamma)\, d\gamma, \quad I_\alpha(r) = \int_0^1 \bar{a}_\alpha(\gamma) \sin(r\xi a\gamma)\, d\gamma, \tag{41}$$

$$H_{\alpha\delta}(r,x,y) = \bar{H}_{\alpha\delta}(r,y) \begin{matrix}\sin\\ \cos\end{matrix}(r\xi a x), \qquad (\alpha = L\colon \delta = \tfrac{1}{2}), \quad (\alpha = T\colon \delta = \tfrac{2}{1}), \tag{42}$$

$$\bar{H}_{\alpha\delta}(r,y) = P_{\alpha\delta} \exp(-\bar{s}_T \beta_L y) + R_{\alpha\delta} \exp(-\bar{s}_T \beta_T y), \tag{43}$$

$$P_{L1} = 2\Lambda(2r^2\Lambda^2 - 1)/(\pi\beta_L), \quad R_{L1} = -4\Lambda\beta_T/\pi, \quad P_{L2} = R_{T1} = 2(2r^2\Lambda^2 - 1)/(r\pi), \tag{44}$$

$$R_{L2} = P_{T1} = -4r\Lambda^2/\pi, \quad P_{T2} = 4\Lambda\beta_L/\pi, \quad R_{T2} = -2\Lambda(2r^2\Lambda^2 - 1)/(\pi\beta_T), \tag{45}$$

$$E_{L1} = E_{T2} = 0, \quad E_{L2} = E_{T1} = -\bar{a}. \tag{46}$$

All other quantities appearing in equations (40)–(46) have been defined in equations (20), (21), and (23). When condition (C) holds, the displacements take the following form

$$\bar{u}_{\alpha\delta}(x,y) = F_{\alpha\delta} \sin(\bar{s}_\alpha x)\, b_\alpha + E_{\alpha\delta} J_\alpha e^{i\bar{s}_\alpha y} + \sum_{\substack{r=1 \\ r \neq r_\alpha}}^{\infty} H_{\alpha\delta}(r,x,y) I_\alpha(r), \tag{47}$$

where

$$F_{L1} = -2\bar{s}_L \bar{a}, \quad F_{L2} = F_{T1} = 0, \quad F_{T2} = 2\bar{s}_T \bar{a}. \tag{48}$$

Next we discuss the nature of the scattered displacements for large values of the variable y. Observe that, depending on the values of r and Λ, the quantities β_L and β_T may take real or purely imaginary values. The choice of branches for β_α, ($\alpha = L$ or T), is such that $Im(\beta_\alpha) < 0$ whenever β_α^2 is negative. This ensures that the requirement of outgoing waves is satisfied (see Lamb [14] for further details).

Assuming that condition (C) does not hold, we can find two integer numbers r_L and r_T such that

$$r_L\Lambda/\epsilon < 1 < (r_L+1)\Lambda/\epsilon, \quad r_T\Lambda < 1 < (r_T+1)\Lambda, \tag{49}$$

for Λ in the interval $(0,\infty)$. When $\Lambda > 1$, we have $r_T = 0$, and when $\Lambda > \epsilon$, we have $r_L = 0$.

It follows that

$$\beta_L(r) = \begin{cases} -i\sqrt{\epsilon^2 - (r\Lambda)^2}, & 0 \le r \le r_L \\ \sqrt{(r\Lambda)^2 - \epsilon^2}, & r > r_L \end{cases}$$

$$\beta_T(r) = \begin{cases} -i\sqrt{1 - (r\Lambda)^2}, & 0 \le r \le r_T \\ \sqrt{(r\Lambda)^2 - 1}, & r > r_T \end{cases} \tag{50}$$

It is then convenient to define the angles $\theta_L(r)$ and $\theta_T(r)$ by

$$\sin\theta_L = \sqrt{1 - (r\Lambda/\epsilon)^2} = i\beta_L/\epsilon, \; \cos\theta_L = r\Lambda/\epsilon, \quad 0 \le r \le r_L, \tag{51}$$

$$\sin\theta_T = \sqrt{1 - (r\Lambda)^2} = i\beta_T, \quad \cos\theta_T = r\Lambda, \quad 0 \le r \le r_T. \tag{52}$$

Also we can write

$$r\xi a = r\pi\bar{a} = r\Lambda\bar{s}_T = \begin{cases} \bar{s}_L \cos\theta_L, & 0 \le r \le r_L \\ \bar{s}_T \cos\theta_T, & 0 \le r \le r_T \end{cases}. \tag{53}$$

Observe that θ_L and θ_T are in the interval $(0,\pi/2]$, and that both approach $\pi/2$ as Λ tends to zero (or $\omega \to \infty$), for fixed $r > 0$.

The displacements of equation (39) appear as a sum of terms that either decay exponentially with y or oscillate, without decay, as functions of y. In the far-field, only the oscillating terms are significant. We find then that the far-field displacements generated by an incident longitudinal wave can be written in the form

$$\overset{\infty}{\mathbf{u}}{}^L = u_{L0}^L(0)\mathbf{X}^L(\pi/2) + \sum_{r=1}^{r_L} u_{L0}^L(r)[\mathbf{X}^L(\theta_L) - \mathbf{X}^L(\pi-\theta_L)] + \sum_{r=1}^{r_T} u_{L0}^T(r)[\mathbf{X}^T(\theta_T) + \mathbf{X}^T(\pi-\theta_T)]. \tag{54}$$

For an incident transverse wave, we have

$$\overset{\infty}{\mathbf{u}}{}^T = u_{T0}^T(0)\mathbf{X}^T(\pi/2) + \sum_{r=1}^{r_L} u_{T0}^L(r)[\mathbf{X}^L(\theta_L) + \mathbf{X}^L(\pi-\theta_L)] + \sum_{r=1}^{r_T} u_{T0}^T(r)[\mathbf{X}^T(\theta_T) - \mathbf{X}^T(\pi-\theta_T)]. \tag{55}$$

Note that the summations are ignored when the upper limit (r_L or r_T) is zero. The quantities introduced in equations (54) and (55) are obtained directly from equations (39)–(46). We have

$$\mathbf{X}^L(\theta) = \{\begin{matrix}\cos\theta\\ \sin\theta\end{matrix}\}\exp[i\bar{s}_L\chi(\theta)], \quad \mathbf{X}^T(\theta) = \{\begin{matrix}-\sin\theta\\ \cos\theta\end{matrix}\}\exp[i\bar{s}_T\chi(\theta)], \tag{56}$$

where

$$\chi(\theta) = x\cos\theta + y\sin\theta. \tag{57}$$

The displacements $\mathbf{X}^L(\theta)$ correspond to a longitudinal wave

Downloaded 02 May 2010 to 171.66.16.54. Redistribution subject to ASME license or copyright; see http://www.asme.org/terms/Terms_Use.cfm

of amplitude unity traveling at an angle θ from the x_1 axis, in the direction of the positive x_2-axis if $0 < \theta < \pi$. The displacements $\mathbf{X}^T(\theta)$ correspond to a transverse wave traveling in the same direction. The amplitudes in equations (54) and (55) are

$$u^L_{L0}(0) = -\tilde{a}J_L, \qquad u^T_{T0}(0) = \tilde{a}J_T, \tag{58}$$

$$u^L_{L0}(r) = (2r^2\Lambda^2 - 1)I_L(r)/(r\pi\sin\theta_L),$$

$$u^T_{L0}(r) = -2\Lambda I_L(r)/\pi, \tag{59}$$

$$u^L_{T0}(r) = -2\epsilon\Lambda I_T(r)/\pi,$$

$$u^T_{T0}(r) = -(2r^2\Lambda^2 - 1)I_T(r)/(r\pi\sin\theta_T). \tag{60}$$

The integrals J_α and $I_\alpha(r)$ are defined in equation (41).

It can be seen from equation (54) that, for $\Lambda > 1$, the far-field displacements correspond to those of a longitudinal wave traveling in the same direction as the longitudinal incident wave. An analogous statement applies to equation (55), provided that "longitudinal" is replaced by "transverse." As the value of Λ decreases, successive longitudinal and transverse propagating modes appear in the far-field. In fact, each mode corresponds to a pair of waves propagating symmetrically with respect to the x_2 axis. The transverse mode of order r emerges at an angle $\theta_T(r) = 0$ when Λ becomes equal to $1/r$; as Λ decreases, the angle $\theta_T(r)$ increases and approaches the value $\pi/2$ in the limit as $\Lambda \to 0$. Similarly, the longitudinal mode of order r emerges at an angle $\theta_L(r) = 0$ when Λ becomes equal to ϵ/r, and the angle $\theta_L(r)$ behaves like $\theta_T(r)$ as Λ decreases. In qualitative terms, we can say that there will be more and more transverse and longitudinal modes in the far-field as Λ decreases. It actually follows from equation (49) that the numbers r_L and r_T can be made as large as one wishes by choosing a sufficiently small value of Λ.

Now assume that the incident wave is longitudinal and that condition (C) holds. Then there are two integer numbers r_L and r_T such that

$$r_L\Lambda/\epsilon = 1, \quad r_T\Lambda \le 1 < (r_T+1)\Lambda. \tag{61}$$

The dislocation density $\tilde{a}_L(x)$ and the constant b_L are obtained from equations (24) and (25), and the exact displacements are those of equation (47), where $\alpha = L$. The far-field displacements are given by equation (54), except that

$$u^L_{L0}(r_L) = i\pi r_L\tilde{a}^2 b_L, \qquad \theta_L(r_L) = 0. \tag{62}$$

If the incident wave is transverse and condition (C) holds, we can find two integer numbers r_L and r_T such that

$$r_L\Lambda/\epsilon \le 1 < (r_L+1)\Lambda/\epsilon, \qquad r_T\Lambda = 1. \tag{63}$$

The equations for the dislocation density $\tilde{a}_T(x)$ and the constant b_T are equations (24) and (25); the exact displacements are given by equation (47), where $\alpha = T$. The far-field displacements are given by equation (55), except that

$$u^T_{T0}(r_T) = -i\pi r_T\tilde{a}^2 b_T, \qquad \theta_T(r_T) = 0. \tag{64}$$

Finally, recall that, for all values of Poisson's ratio ν in the interval $[0,1/2]$, the ratio $\epsilon = s_L/s_T$ takes its values in the interval $(0,1/\sqrt{2}]$. Hence, the integer numbers r_L and r_T of equation (49) must be such that $0 \le r_L \le r_T$; those of equation (61) are such that $1 \le r_L \le r_T$; and those of equation (63) must satisfy $0 \le r_L < r_T$. Since all possible situations are encompassed by these three cases, we always have $r_L \le r_T$.

7 Transmitted and Reflected Fields and Balance of Rates of Energies

At a large distance from the plane of the cracks ($x_2 = 0$), on the side $x_2 > 0$, the total displacements are equal to the sum of the displacements (54) and (1a), or (55) and (1b), depending on the type of incident wave. We define the transmitted displacements $\mathbf{u}^\alpha_{tr}$ by

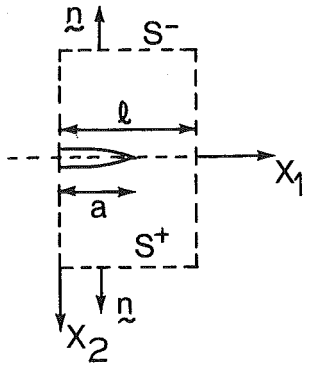


Fig. 2 Rectangular region bounded by two surfaces S^+ and S^- for computation of the balance of rates of energies

$$\mathbf{u}^L_{tr} = \mathbf{u}^L_{in} + \overset{\infty}{\mathbf{u}}{}^L, \qquad \mathbf{u}^T_{tr} = \mathbf{u}^T_{in} + \overset{\infty}{\mathbf{u}}{}^T, \tag{65}$$

where the dimensionless form of the incident wave $\mathbf{u}^\alpha_{in}$ is

$$\mathbf{u}^L_{in} = \tilde{u}_0\mathbf{X}^L(\pi/2), \qquad \mathbf{u}^T_{in} = -\tilde{u}_0\mathbf{X}^T(\pi/2). \tag{66}$$

The reflected displacements $\mathbf{u}^\alpha_{re}$ at large negative values of x_2 follow directly from equations (54) and (55) by using the symmetries of the problem. We find that

$$\mathbf{u}^L_{re} = u^L_{L0}(0)\mathbf{X}^L(-\pi/2) + \sum_{r=1}^{r_L} u^L_{L0}(r)[\mathbf{X}^L(-\theta_L) + \mathbf{X}^L(\theta_L - \pi)]$$

$$+ \sum_{r=1}^{r_T} u^T_{L0}(r)[-\mathbf{X}^T(-\theta_T) + \mathbf{X}^T(\theta_T - \pi)], \tag{67}$$

$$\mathbf{u}^T_{re} = u^T_{T0}(0)\mathbf{X}^T(-\pi/2) + \sum_{r=1}^{r_L} u^L_{T0}(r)[-\mathbf{X}^L(-\theta_L) + \mathbf{X}^L(\theta_L - \pi)]$$

$$+ \sum_{r=1}^{r_T} u^T_{T0}(r)[\mathbf{X}^T(-\theta_T) + \mathbf{X}^T(\theta_T - \pi)]. \tag{68}$$

The transmitted, reflected, and incident fields satisfy a balance of rates of energies. We recall from Achenbach et al. [1] (see section 2.5) that, for time-harmonic waves, in the absence of body forces, the time-averaged power flux $< \mathcal{P} >$ through a closed surface S is equal to zero. Here we apply this result to a rectangular box bounded by the two planes $x_1 = 0$, l and the surfaces S^+ and S^- (see Fig. 2). The depth in the direction perpendicular to the plane (x_1, x_2) is unity. It follows from the boundary conditions (3d, e) and (4d, e) that the power flux through the surfaces $x_1 = 0$, l vanishes. The assumption of plane-strain causes the power flux to vanish also through the surfaces parallel to the plane of the figure. There remains to calculate the time-averaged power fluxes $< \mathcal{P} >^+$ and $< \mathcal{P} >^-$ through S^+ and S^-, respectively.

It is useful to record the stresses associated with the waves of equation (56). Using the notation $\mathbf{\Sigma}$ for the vector of components σ_{12} and σ_{22}, we find that

$$\mathbf{\Sigma}^L(\theta) = i\rho\omega c_L \begin{Bmatrix} \epsilon^2\sin(2\theta) \\ 1 - 2\epsilon^2\cos^2(\theta) \end{Bmatrix} \exp[i\bar{s}_L\chi(\theta)], \tag{69a}$$

$$\mathbf{\Sigma}^T(\theta) = i\rho\omega c_T \begin{Bmatrix} \cos(2\theta) \\ \sin(2\theta) \end{Bmatrix} \exp[i\bar{s}_T\chi(\theta)], \tag{69b}$$

where $\chi(\theta)$ is defined by equation (57) and c_L and c_T represent the speeds of longitudinal and transverse waves, respectively. The transmitted, incident, and reflected (σ_{12}, σ_{22}) stress fields are obtained by replacing the symbol $\mathbf{X}$ by $\mathbf{\Sigma}$ in equations (65)–(68), (54), and (55).

When the surfaces S^+ and S^- are at a large distance from the plane $x_2 = 0$, it follows from Achenbach et al. [1] (section 2.5) that

Downloaded 02 May 2010 to 171.66.16.54. Redistribution subject to ASME license or copyright; see http://www.asme.org/terms/Terms_Use.cfm

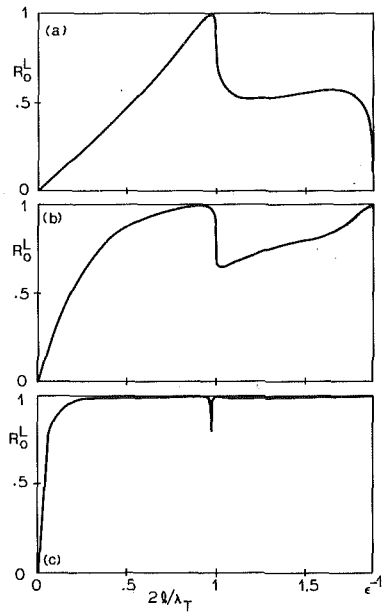


Fig. 3 Reflection coefficient versus frequency for: (a) $a/l = 0.5$, (b) 0.8, and (c) 0.9999999; $\nu = 0.3$, $\epsilon^{-1} \cong 1.87$; incident longitudinal wave

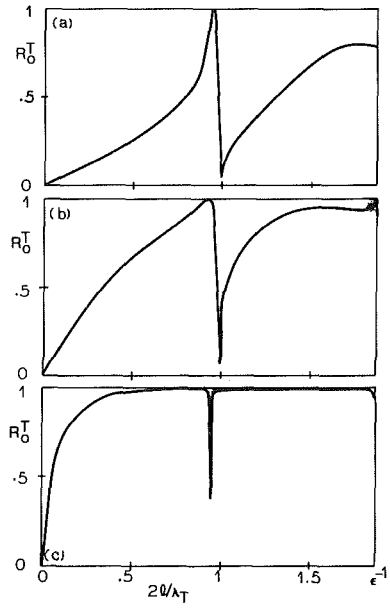


Fig. 4 Reflection coefficient versus frequency for: (a) $a/l = 0.5$, (b) 0.8, and (c) 0.9999999; $\nu = 0.3$, $\epsilon^{-1} \cong 1.87$; incident transverse wave

$$2<\mathcal{P}>_\alpha^+ = \omega Re\left[ia^3 \int_0^{l/a} \mathbf{u}_{tr}^{\alpha *} \cdot \boldsymbol{\Sigma}_{tr}^{\alpha} dx\right], \tag{70}$$

$$2<\mathcal{P}>_\alpha^- = -\omega Re\left[ia^3 \int_0^{l/a} [\mathbf{u}_{in}^{\alpha *} + \mathbf{u}_{re}^{\alpha *}] \cdot [\boldsymbol{\Sigma}_{in}^{\alpha} + \boldsymbol{\Sigma}_{re}^{\alpha}] dx\right], \tag{71}$$

where $x = x_1/a$, $\alpha = L$ or T (no sum), the superscript * denotes the complex conjugate, and the unit normals on S^+ and S^- are shown in Fig. 2. Observe that $<\mathcal{P}>^+$ and $<\mathcal{P}>^-$ have the dimension of power per unit length.

In the computation of the various integrals in equations (70) and (71), the following results have been used

$$\int_0^{l/a} \cos(x\tilde{s}_\alpha \cos\theta_\alpha) dx = 0, \quad \text{(no sum)}, \tag{72}$$

$$c_T(\cos\theta_L \cos 2\theta_T + \sin\theta_L \sin 2\theta_T) + c_L[-\epsilon^2 \sin\theta_T \sin 2\theta_L + (1 - 2\epsilon^2 \cos^2\theta_L)\cos\theta_T] = 0. \tag{73}$$

These results are readily obtained from equations (51)–(53). For an incident longitudinal wave, we find that

$$2<\mathcal{P}>_L^+ / (\rho\omega^2 l a^2) = -c_L |\bar{u}_0 + u_{L0}^L(0)|^2$$

$$-2c_L \sum_{r=1}^{r_L} \sin\theta_L |u_{L0}^L(r)|^2 - 2c_T \sum_{r=1}^{r_T} \sin\theta_T |u_{L0}^T(r)|^2, \tag{74a}$$

$$2<\mathcal{P}>_L^- / (\rho\omega^2 l a^2) = c_L \bar{u}_0^2 - c_L |u_{L0}^L(0)|^2$$

$$-2c_L \sum_{r=1}^{r_L} \sin\theta_L |u_{L0}^L(r)|^2 - 2c_T \sum_{r=1}^{r_T} \sin\theta_T |u_{L0}^T(r)|^2. \tag{74b}$$

When the incident wave is transverse, we have

$$2<\mathcal{P}>_T^+ / (\rho\omega^2 l a^2) = -c_T |-\bar{u}_0 + u_{T0}^T(0)|^2$$

$$-2c_L \sum_{r=1}^{r_L} \sin\theta_L |u_{T0}^L(r)|^2 - 2c_T \sum_{r=1}^{r_T} \sin\theta_T |u_{T0}^T(r)|^2, \tag{75a}$$

$$2<\mathcal{P}>_T^- / (\rho\omega^2 l a^2) = c_T \bar{u}_0^2 - c_T |u_{T0}^T(0)|^2$$

$$-2c_L \sum_{r=1}^{r_L} \sin\theta_L |u_{T0}^L(r)|^2 - 2c_T \sum_{r=1}^{r_T} \sin\theta_T |u_{T0}^T(r)|^2. \tag{75b}$$

The amplitudes appearing in the expressions (74) and (75) are defined in equations (58)–(60), (62), and (64). Finally, we write the balance of rates of energies as

$$<\mathcal{P}>_\alpha^+ + <\mathcal{P}>_\alpha^- = 0, \quad \alpha = L \text{ or } T. \tag{76}$$

When the incident wave is longitudinal, this yields

$$\bar{u}_0^2 = |u_{L0}^L(0)|^2 + |\bar{u}_0 + u_{L0}^L(0)|^2 + 4\sum_{r=1}^{r_L} \sin\theta_L |u_{L0}^L(r)|^2 + 4\epsilon \sum_{r=1}^{r_T} \sin\theta_T |u_{L0}^T(r)|^2. \tag{77}$$

For an incident transverse wave, the result is

$$\bar{u}_0^2 = |u_{T0}^T(0)|^2 + |-\bar{u}_0 + u_{T0}^T(0)|^2 + (4/\epsilon)\sum_{r=1}^{r_L} \sin\theta_L |u_{T0}^L(r)|^2 + 4\sum_{r=1}^{r_T} \sin\theta_T |u_{T0}^T(r)|^2. \tag{78}$$

8 Discussion of Numerical Results

Numerical results are presented in Figs. 3–6. These results were computed for Poisson's ratio $\nu = 0.3$, which yields $\epsilon \equiv s_L/s_T \cong 0.535$. The number n of quadrature points (see Section 5) is $n = 15$ when the dimensionless frequency $\bar{\omega} \equiv 2l/\lambda_T$ satisfies $\bar{\omega} \leq 1$, and $n = 20$ when $\bar{\omega} > 1$.

For convenience, we define the reflection and transmission coefficients of order zero, R_0^α and T_0^α ($\alpha = L$ or T is used as a label for the type of incident wave), as

$$R_0^L = |u_{L0}^L(0)|/\bar{u}_0, \qquad T_0^L = |\bar{u}_0 + u_{L0}^L(0)|/\bar{u}_0, \tag{79}$$

$$R_0^T = |u_{T0}^T(0)|/\bar{u}_0, \qquad T_0^T = |-\bar{u}_0 + u_{T0}^T(0)|/\bar{u}_0. \tag{80}$$

For an incident longitudinal wave, Fig. 3 shows the reflection coefficient R_0^L versus $\bar{\omega}$ for three values of $\bar{a} = a/l$—the ratio of the crack length to the period of the crack-array. In Fig. 4 the reflection coefficient R_0^T for an incident

Downloaded 02 May 2010 to 171.66.16.54. Redistribution subject to ASME license or copyright; see http://www.asme.org/terms/Terms_Use.cfm

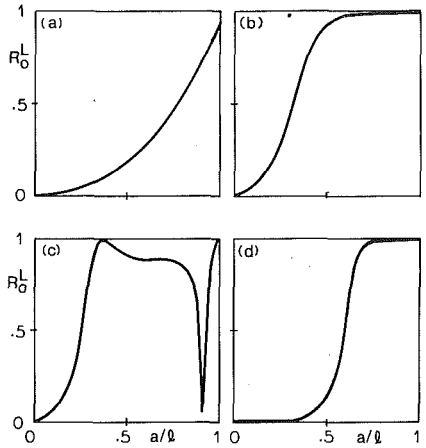


Fig. 5 Reflection coefficient versus ratio of crack length to crack spacing for: (a) $2l/\lambda_T = 0.2$, (b) 0.9, (c) 1.0, and (d) ϵ^{-1}; $\nu = 0.3$, $\epsilon^{-1} \cong 1.87$; incident longitudinal wave

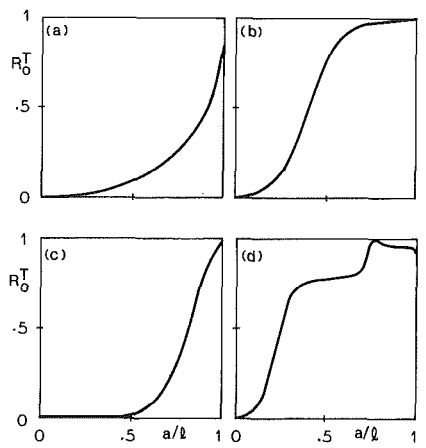


Fig. 6 Reflection coefficient versus ratio of crack length to crack spacing for: (a) $2l/\lambda_T = 0.2$, (b) 0.9, (c) 1.0, and (d) ϵ^{-1}; $\nu = 0.3$, $\epsilon^{-1} \cong 1.87$; incident transverse wave

transverse wave is shown versus $\bar{\omega}$ for the same three values of $\bar{a}$: $\bar{a} = 0.5$, 0.8, and 0.9999999.

The range of values of $\bar{\omega}$ that has been considered is $0 < \bar{\omega} \leq 1/\epsilon$ ($1/\epsilon \cong 1.87$). The value $\bar{\omega} = 1$ corresponds to the emergence of the first transverse propagating mode, and $\bar{\omega} = 1/\epsilon$ to that of the first longitudinal propagating mode. Therefore, the values of r_α ($\alpha = L$ and T) that must be used in the balance of rates of energies [equation (77) or (78)] are such that $r_L = r_T = 0$, if $0 < \bar{\omega} < 1$; $r_L = 0$ and $r_T = 1$, if $1 \leq \bar{\omega} < 1/\epsilon$; $r_L = r_T = 1$, if $\bar{\omega} = 1/\epsilon$. Observe that in the range $0 < \bar{\omega} \leq 1$ the transmission coefficients T_0^L and T_0^T can easily be obtained from the reflection coefficients and the balance of rates of energies.

When the incident wave is longitudinal, condition (C) is satisfied at $\bar{\omega} = 1/\epsilon$ for $r_L = 1$, and the behavior of the system is governed by equations (24) and (25). Similarly, for the case of an incident transverse wave, condition (C) is satisfied at $\bar{\omega} = 1$ for $r_T = 1$, and equations (24) and (25) must be used at that frequency.

Figures 3 and 4 show that the reflection coefficient vanishes in the limit as $\bar{\omega} \to 0$. This is a direct consequence of the vanishing of the stresses in equation (2) for $\omega = 0$. When $\bar{a} = 0.9999999$, there are only thin strings of solid material connecting the cracks to each other, and the reflectipn coefficient is expected to approach its maximum value of unity. The numerical results of Figs. 3(c) and 4(c) bear out this prediction. There is, however, a sharp dip at $\bar{\omega} = 0.96$ (Fig. 3(c)) and at $\bar{\omega} = 0.9401$ (Fig. 4(c)). This suggests that the thin strings of material between the cracks can still transmit a considerable amount of incident energy at certain frequencies. For $\bar{a} = 0.5$ and 0.8, the value of the reflection coefficient climbs from zero at $\bar{\omega} = 0$ to values close to unity at $\bar{\omega} = 0.97$ (Fig. 3(a)), $\bar{\omega} = 0.93$ (Fig. 3(b)), $\bar{\omega} = 0.95$ (Fig. 4(a)), and $\bar{\omega} = 0.93$ (Fig. 4(b)). When the incident wave is transverse, the maximum reflection is followed by a sharp dip, which reduces the reflection coefficient to a value of 0.019 at $\bar{\omega} = 0.9999999$ (Fig. 4(a)) and of 0.06 at $\bar{\omega} = 0.985$ (Fig. 4(b)).

Figures 5(a, b, c, d) show the reflection coefficient versus the ratio $\bar{a} = a/l$ for four values of the dimensionless frequency $\bar{\omega}$; the incident wave is longitudinal. The analogous curves for an incident transverse wave are shown in Figs. 6(a, b, c, d). The four values of the dimensionless frequency are $\bar{\omega} = 0.2$, 0.9, 1.0, and $1/\epsilon$ ($\cong 1.87$). The reflection coefficient decreases as $\bar{a}$ approaches zero, because the cracks then occupy only a small area of the plane $x_2 = 0$. In Fig. 5(c) the reflection coefficient becomes equal to 0.996 at $\bar{a} = 0.38$, and in Fig. 6(d) it takes the value 0.999 at $\bar{a} = 0.76$. The other curves climb monotonically from the value zero at $\bar{a} = 0$ to their maximum value at $\bar{a} = 1$. The closest value to unity that was used for $\bar{a}$ in the computations was $\bar{a} = 0.9999999$.

The balance of rates of energies has been verified to hold for all numerical calculations. In the range $0 < \bar{\omega} \leq 1$, it is found that the quantity

$$1 - (R_0^\alpha)^2 - (T_0^\alpha)^2, \qquad (\alpha = L \text{ or } T), \tag{81}$$

is less than 1.3×10^{-12} in absolute value. When the frequency is such that $1 < \bar{\omega} \leq 1/\epsilon$, the quantity analogous to that of equation (81), which is obtained from the balance of rates of energies after transposition to the left-hand side and division by $\bar{u}_0^2$, decreases as the number of quadrature points, n, increases. For instance, when $\bar{\omega} = 1.1$ and $\bar{a} = 0.8$, the result is of the order 10^{-3} for $n = 20$ and of the order 10^{-7} for $n = 40$. The value of this quantity also decreases, for fixed values of n and $\bar{\omega}$, as the ratio $\bar{a}$ decreases. We find that, for $n = 20$ and $\bar{\omega} = 1.5$, the order of magnitude is 10^{-4} when $\bar{a} = 0.9999999$ and 10^{-15} when $\bar{a} = 0.001$.

9 Approximate Results

The results of the preceding section are compared with those obtained from two approximate theories. The first approximation will be referred to as the "static" approximation, and the second one as the "spring-layer" approximation.

In the first approximation, we compute the *static* crack-face displacements $\bar{u}_{\alpha\delta}(x,0^+) - \alpha = L,T$, $\delta = 1,2$ – when the crack faces are subjected to prescribed tractions that are equal in magnitude, but opposite in sign, to the tractions of equation (2). These displacements follow directly from the results of Tada et al. [15] (page 7.1, together with equations (39) and (56) of Part I). Using the dimensionless notation of equation (40), we find that

$$\bar{u}_{L1}(x,0^+) = 0, \ \bar{u}_{L2}(x,0^+) = i\bar{u}_0(\bar{\omega}/\epsilon)L(x), \qquad |x| < 1, \tag{82a}$$

$$\bar{u}_{T1}(x,0^+) = i\bar{u}_0\bar{\omega}Lx, \ \bar{u}_{T2}(x,0^+) = 0, \qquad |x| < 1, \tag{82b}$$

where (82a) and (82b) correspond to an incident longitudinal wave and an incident transverse wave, respectively; and

$$L(x) = 2(1-\nu)\cosh^{-1}[\cos(\pi\bar{a}x/2)/\cos(\pi\bar{a}/2)]. \tag{83}$$

Then it follows from equations (58), (41), (40), (20), (10), and (9) that

$$u_{L0}^L(0) = \bar{a}\int_0^1 \bar{u}_{L2}(x,0^+)dx = i\bar{u}_0\bar{\omega}(\bar{a}/\epsilon)\int_0^1 L(x)\,dx, \tag{84a}$$

$$u_{T0}^T(0) = -\bar{a}\int_0^1 \bar{u}_{T1}(x,0^+)dx = -i\bar{u}_0\bar{\omega}\bar{a}\int_0^1 L(x)\,dx. \tag{84b}$$

The reflection coefficients $R_0^L = |u_{L0}^L(0)|/\bar{u}_0$ and $R_0^T = |u_{T0}^T(0)|/\bar{u}_0$ follow from equations (84a,b), once the function

Downloaded 02 May 2010 to 171.66.16.54. Redistribution subject to ASME license or copyright; see http://www.asme.org/terms/Terms_Use.cfm

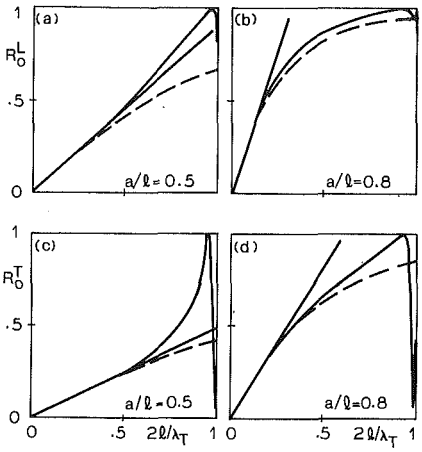


Fig. 7 Reflection coefficient versus frequency for an incident longitudinal wave (*a,b*) and an incident transverse wave (*c,d*); straight solid lines: static approximation; dashed lines: spring-layer approximation; curved solid lines: exact results; $\nu = 0.3$

$L(x)$ is integrated numerically. It is noted that R_0^L and R_0^T are linear functions of the dimensionless frequency $\bar{\omega}$. The corresponding straight lines are shown in Fig. 7 for $\bar{a} = 0.5$ and 0.8. For convenience, the curves of Figs. 3(*a*), 3(*b*), 4(*a*), and 4(*b*) have been reproduced in Figs. 7(*a*), 7(*b*), 7(*c*), and 7(*d*), respectively. It is seen that the two sets of curves cannot be distinguished for small values of $\bar{\omega}$. The agreement extends to larger values of $\bar{\omega}$ for $\bar{a} = 0.5$ than for $\bar{a} = 0.8$.

In the second approximation, the array of cracks is replaced by an equivalent layer of springs. This method has been used by Thompson and Fiedler [4] to model the array of cracks as a reflector.

First consider two elastic half-spaces connected by a layer of massless springs along the plane $x_2 = 0$. Choose a system of coordiantes as in Fig. 1, and let an incident wave of the type (1*a*) or (1*b*) be traveling in the upper half-space in the direction of the positive x_2 axis. The incident wave induces a transmitted wave of amplitude T^α ($\alpha = L$ or T) and a reflected wave of amplitude R^α. The transmitted and reflected waves are of the same type as the incident wave. Let k_α denote the spring constants. Then the following boundary conditions must be satisfied for an incident longitudinal wave

$$\sigma_{22}(x_1,0^+) = \sigma_{22}(x_1,0^-), \tag{85}$$

$$\sigma_{22}(x_1,0^+) = k_L[u_2(x_1,0^+) - u_2(x_1,0^-)]. \tag{86}$$

When the incident wave is transverse, we have

$$\sigma_{12}(x_1,0^+) = \sigma_{12}(x_1,0^-), \tag{87}$$

$$\sigma_{12}(x_1,0^+) = k_T[u_1(x_1,0^+) - u_1(x_1,0^-)]. \tag{88}$$

Equations (85) and (86) yield a system of two equations for the two complex-valued unknowns R^L and T^L. Similarly, equations (87) and (88) yield a system of equations for R^T and T^T. The reflection coefficients $R_0^\alpha = |R^\alpha|/u_0$ ($\alpha = L$ or T) follow from the solution of these systems; they can be written in the form

$$R_0^\alpha = \frac{\bar{\omega}}{(\bar{\omega}^2 + K_\alpha^2)^{1/2}}, \quad (\alpha = L \text{ or } T), \tag{89}$$

where

$$K_L = 2\epsilon l k_L/(\pi\mu), \qquad K_T = 2lk_T/(\pi\mu). \tag{90}$$

Next we compute the constant k_α of the spring-layer that produces the same *static* displacements as the array of cracks, when the solid is subjected to uniform tension (case of an incident longitudinal wave) or uniform shear (incident transverse wave). Once k_α is determined, the reflection coefficient is readily obtained from equation (89).

Consider two elastic half-spaces connected by springs, and apply uniform tension $\sigma_{22} = \sigma$, or uniform shear $\sigma_{12} = \tau$, at a distance L on either side of the plane $x_2 = 0$. For the case of uniform tension, the distance $2L$ becomes $2L + \Delta L^L$; and, when uniform shear is applied, two points of initial coordinates (x_1, L) and $(x_1, -L)$ find their x_1 coordinates moved a distance ΔL^T apart. The elongation ΔL^α, ($\alpha = L$ or T), is caused by the deformation of the elastic solid together with the extension of the springs. We find, if λ denotes Lamé's constant,

$$\Delta L^L = u_2(L) - u_2(-L) = 2L\sigma/(\lambda+2\mu) + \sigma/k_L, \tag{91a}$$

$$\Delta L^T = u_1(L) - u_1(-L) = 2L\tau/\mu + \tau/k_T. \tag{91b}$$

Now replace the elastic layer by the array of cracks. The configuration is that of Fig. 1. Apply the same uniform tension field, or shear field, as before. The distance ΔL^α is given by Tada et al. [15] (see equation *B*8) in the form

$$\Delta L = \frac{\partial U}{\partial Q} + \frac{\partial}{\partial Q}\int_0^A \mathcal{G}\,dA, \tag{92}$$

where $\mathcal{G}$ is the energy made available per unit increase of the crack area (on one side) and U is the strain energy due to applying loading forces with no crack present.

For mode *I* and mode *II* deformations, we find from equation (*B*4), equation (18) (Part I), and page 7.1 of reference [15] that

$$\begin{Bmatrix} \mathcal{G}_I \\ \mathcal{G}_{II} \end{Bmatrix} = \begin{Bmatrix} \sigma^2 \\ \tau^2 \end{Bmatrix} l(1-\nu)\tan\left(\frac{\pi a}{2l}\right)/\mu. \tag{93}$$

In equation (92) we take the upper limit of integration, A, as the crack-area per unit length in the direction perpendicular to the (x_1, x_2) plane-$A = 2a$. The load Q with respect to which the differentiation is performed is $Q = 2l\begin{Bmatrix}\sigma\\ \tau\end{Bmatrix}$. Then equation (92) yields

$$\Delta L^L = 2L\sigma/(\lambda+2\mu) + 2\sigma l/(\pi\mu K), \tag{94a}$$

$$\Delta L^T = 2L\tau/\mu + 2\tau l/(\pi\mu K), \tag{94b}$$

where

$$1/K = -2(1-\nu)\,\mathrm{Log}\left|\cos\left(\frac{\pi a}{2l}\right)\right|. \tag{95}$$

There remains to equate the values of ΔL^α given by equations (91*a*), (94*a*), and by equations (91*b*), (94*b*). This yields the values of K_L and K_T, defined in equation (90), as

$$K_L = \epsilon K, K_T = K. \tag{96}$$

For $\bar{a} = 0.5$ and 0.8, the curves for the reflection coefficients R_0^L and R_0^T of equation (89) are the dashed lines of Fig. 7. These results agree with those of the preceding section, and also with those of the static approximation, for small values of the dimensionless frequency $\bar{\omega}$. In Figs. (7*b*) and (7*d*), which correspond to $\bar{a} = 0.8$, the curves for the spring approximation and those of the previous section have the same curvature over a large range of values of $\bar{\omega}$.

Acknowledgments

The work reported here was carried out under Contract DE-AC02-83ER13036.A002 with the Department of Energy, Office of Basic Energy Sciences, Engineering Research Program. The authors would like to acknowledge helpful discussions with Dr. Ronald Roberts.

References

1 Achenbach, J. D., Gautesen, A. K., and McMaken, H., *Ray Methods for Waves in Elastic Solids*, Pitman, Boston, London, Melbourne, 1982.

2 Jungman, A., Adler, L., Achenbach, J. D., and Roberts, R., "Reflection from a Boundary With Periodic Roughness: Theory and Experiment," *J. Acoust. Soc. Am.*, Vol. 74, 1983, pp. 1025–1032.

Downloaded 02 May 2010 to 171.66.16.54. Redistribution subject to ASME license or copyright; see http://www.asme.org/terms/Terms_Use.cfm

3 Fokkema, J. T., and Van den Berg, P. M., "Elastodynamic Diffraction by a Periodic Rough Surface (Stress-Free Boundary)," *J. Acoust. Soc. Am.*, Vol. 62, 1977, pp. 1095-1101.

4 Achenbach, J. D., and Norris, A. N., "Loss of Specular Reflection Due to Nonlinear Crack-Face Interaction," *J. Nondestructive Evaluation*, Vol. 3, 1982, pp. 229-239.

5 Thompson, R. B., and Fiedler, C. J., "The Effects of Crack Closure on Ultrasonic Scattering Measurements," *Review of Progress in QNDE 3A*, Thompson, D. O., and Chimenti, D. E., eds., Plenum, New York, 1984, pp. 207-215.

6 Comninou, M., and Dundurs, J., "Reflection and Refraction of Elastic Waves in Presence of Separation," *Proceedings, Royal Society*, London, Series *A*, Vol. 356, 1977, pp. 509-528.

7 Comninou, M., and Dundurs, J., "Interaction of Elastic Waves With a Unilateral Interface," *Proceedings, Royal Society*, London, Series *A*, Vol. 368, 1979, pp. 141-154.

8 Miller, R. K., and Tran, H. T., "Reflection, Refraction, and Absorption of Elastic Waves at a Frictional Interface: *P* and *SV* Motion," ASME JOURNAL OF APPLIED MECHANICS, Vol. 48, 1981, pp. 155-160.

9 Churchill, R. V., and Brown, J. W., *Fourier Series and Boundary Value Problems*, 3rd Ed., McGraw-Hill, New York, 1978.

10 Erdogan, F., and Gupta, G. D., "On the Numerical Solution of Singular Integral Equations," *Quarterly of Applied Mathematics*, Vol. 30, 1972, pp. 525-534.

11 Erdogan, F., Gupta, G. D., and Cook, T. S., "Numerical Solution of Singular Integral Equations," *Methods of Analysis and Solutions to Crack Problems*, Sih, G. C., ed., Noordhoff, Groningen, 1972.

12 Angel, Y. C., and Achenbach, J. D., "Reflection and Transmission of Obliquely Incident Rayleigh Waves by a Surface-Breaking Crack," *J. Acoust. Soc. Am.*, Vol. 75, 1984, pp. 313-319.

13 Angel, Y. C., and Achenbach, J. D.,"Stress-Intensity Factors for 3-D Dynamic Loading of a Cracked Half-Space," *Journal of Elasticity*, to appear.

14 Lamb, H., "On the Propagation of Tremors Over the Surface of an Elastic Solid," *Philosophical Transactions, Royal Society*, London, Series *A*, Vol. 203, 1904, pp. 1-42.

15 Tadas, H., Paris, P., and Irwin, G., *The Stress Analysis of Cracks Handbook*, Del Research Corporation, St. Louis, Mo., 1973.

Downloaded 02 May 2010 to 171.66.16.54. Redistribution subject to ASME license or copyright; see http://www.asme.org/terms/Terms_Use.cfm

Elastic Wave Scattering From an Interface Crack in a Layered Half Space

H. J. Yang

D. B. Bogy

Mem. ASME

Department of Mechanical Engineering,
University of California,
Berkeley, Calif. 94720

Many applications in industry utilize a layered elastic structure in which a relatively thin layer of one material is bonded to a much thicker substrate. Often the fabrication process is imperfect and cracks occur at the interface. This paper is concerned with the plane strain, time-harmonic problem of a single elastic layer of one material on a half space of a different material with a single crack at the interface. Green's functions for the uncracked medium are used with the appropriate form of Green's integral theorem to derive the scattered field potentials for arbitrary incident fields in the cracked layered half space. These potentials are used in turn to reduce the problem to a system of singular integral equations for determining the gradients of the crack opening displacements in the scattered field. The integral equations are analyzed to determine the crack tip singularity, which is found, in general, to be oscillatory, as it is in the corresponding static problem of an interface crack. For many material combinations of interest, however, the crack tip singularity in the stress field is one-half power, as in the case of homogeneous materials. In the numerical work presented here attention is restricted to this class of composites and the integral equations are solved numerically to determine the Mode I and Mode II stress intensity factors as a function of a dimensionless wave number for various ratios of crack length to layer depth. The results are presented in graphical form and are compared with previously published analyses for the special cases where such results are available.

1 Introduction

In this paper we are concerned with a problem of considerable practical importance in various engineering and seismological applications. Many structures, both man-made and of natural origin, are composed of different elastic materials formed in layers. Often the layers are bonded together along common faces, but it can happen that the bonding is not perfect and flaws occur as cracks or regions of poor bonding in the interface. It is of importance to be able to detect these interface cracks, and one of the most practical methods for accomplishing this, in the cases of engineering interest, utilizes the scattering of elastic waves and the subsequent detection of these scattered waves by appropriate transducers. The goal of this paper is to contribute to the theoretical basis for detecting the interface flaw by these means.

The previously published works that bear directly on this problem are those of Neerhoff [1], which considered the corresponding problem for the case of antiplane strain, and the paper by Keer et al. [2], which was concerned with the plane strain problem of a crack parallel to the boundary in a homogeneous half space. Therefore, the problem considered in reference [2] is the same as the problem considered here for the special case in which the layer and substrate are made of the same materials. Also the paper by Farnell and Adler [3] which studied the various types of free surface waves that can exist in a half space with a single layer on top, as well as the paper by Bogy and Gracewski [4] on the same topic, are of major significance to this work. This paper is based on the Ph.D. dissertation of Yang [10].

The method utilized here to solve the plane strain interface flaw problem is similar to that used by Neerhoff [1] for the antiplane problem. First we formulate the problem in Section 2, where the elastic field is separated into the incident and scattered fields. The incident field is left arbitrary in the analysis until a particular choice is made later for the purpose of obtaining numerical results. In Yang [10] the Green's functions were derived for dilatational and rotational sources in the layer as well as the substrate. These Green's functions are used in conjunciton with the appropriate form of Green's integral theorem, in Section 3, to reduce the problem to a system of singular integral equations. These integral equations are analyzed in Section 4 to determine the order of singularity in the stress field at the crack tip, and it is found that this singularity is of the oscillatory type, except for a certain class of composites. The methods of Muskhelishvill [5] and Erdogan and Gupta [6] are utilized in Section 5 to reduce

Contributed by the Applied Mechanics Division for publication in the JOURNAL OF APPLIED MECHANICS.

Discussion on this paper should be addressed to the Editorial Department, ASME, United Engineering Center, 345 East 47th Street, New York, N.Y. 10017, and will be accepted until two months after final publication of the paper itself in the JOURNAL OF APPLIED MECHANICS. Manuscript received by ASME Applied Mechanics Division, March, 1984.

Copyright © 1985 by ASME

Downloaded 02 May 2010 to 171.66.16.54. Redistribution subject to ASME license or copyright; see http://www.asme.org/terms/Terms_Use.cfm

these singular integral equations to a system of algebraic equations suitable for numerical solution.

These equations are solved numerically in Section 6 for several sets of composities, and the results are presented in the form of Mode *I* and Mode *II* stress intensity factors plotted as functions of dimensionless wave number for various ratios of layer depth to crack length. To obtain these numerical results, the incident field and material combinations have to be specified. We choose the incident field as that which would occur in the uncracked layered half space due to a harmonic uniform normal traction applied to the boundary of the half space. Also we choose three material combinations that can be considered as belonging to the special class of composities with the half power crack tip singularity. These are nickel/iron, aluminum/zinc, and nickel/gold. For each of the material combinations, each material is considered in turn as the layer and as the substrate. Finally a discussion of the results is presented in Section 7.

2 Problem Formulation

We consider the steady time-harmonic plane-strain problem for the cracked layered elastic half space shown in Fig. 1. The layered half space is composed of a single isotropic layer of thickness d that is bonded at its lower surface to the surface of an isotropic elastic half space of a different material, except in the region $|x| < a$, $z=d$, where the crack faces are assumed to be free of traction. The density, shear modulus and Poisson's ratio of the layer are denoted by ρ, μ, and σ, while those for the half space are ρ', μ', and σ', respectively.

The time-reduced form of the displacement equations of motion for an isotropic media is

$$(\lambda+\mu)\,\nabla\nabla\cdot\mathbf{u}+\mu\nabla^2\mathbf{u}+\rho\omega^2\mathbf{u}=-\rho\mathbf{f}, \tag{2.1}$$

in which $\mathbf{u}$ and $\mathbf{f}$ are the time-reduced, complex valued displacement vector and the body force vector fields, respectively, and ω is the frequency. The Lame constant, λ, is related to μ, σ by $\lambda = 2\mu\sigma/(1-2\sigma)$. If these vectors are decomposed into their Helmholtz resolutions according to

$$\mathbf{u}=\nabla\phi+\nabla\times\Psi, \qquad \mathbf{f}=\nabla c+\nabla\times\mathbf{b}, \tag{2.2}$$

then ϕ and Ψ must satisfy the equations,

$$(\nabla^2+k_L^2)\,\phi=-\frac{1}{\lambda+2\mu}\,c, \qquad (\nabla^2+k_L^2)\,\Psi=-\frac{1}{\mu}\,b, \tag{2.3}$$

in which

$$k_L^2=\rho\omega^2/\lambda+2\mu, \qquad k_L^2=\rho\omega^2/\mu, \tag{2.4}$$

and where the scalars Ψ and b are related to the corresponding vectors by

$$\Psi=\Psi\mathbf{e}_2, \qquad \mathbf{b}=b\mathbf{e}_2, \tag{2.5}$$

for the case of plane strain.

The boundary and continuity conditions are

$$\begin{aligned}
&\tau_{zx}=T_x,\ \tau_{zz}=T_z; \quad z=0,-\infty<x<\infty,\\
&\tau_{zx}=\tau_{zz}=\tau'_{zx}=\tau'_{zz}=0; z=d,\ |x|<a,\\
&\tau_{zx}=\tau'_{zx},\ \tau_{zz}=\tau'_{zz},\ u_x=u'_x,\ u_z=u'_z; z=d,\ |x|>a,
\end{aligned} \tag{2.6}$$

in which T_x and T_z denote applied tractions. We also impose the radiation condition of outgoing scattered energy in the far field, $|x|\to\infty$.

The displacement and stress can be decomposed into the sum of incident and scattered parts according to

$$\mathbf{u}=\mathbf{u}^{(I)}+\mathbf{u}^{(s)}, \qquad \tau=\tau^{(I)}+\tau^{(s)}, \tag{2.7}$$

where the incident displacement and stress fields $\mathbf{u}^{(I)}$ and $\tau^{(I)}$ correspond to the solution of the problem defined by equations (2.6) in the absence of the crack, i.e., for the case when the crack length a equals zero. Therefore, the incident field solution satisfies

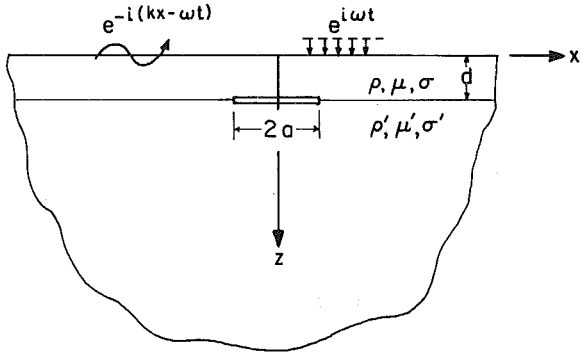


Fig. 1 Layered half space with interface crack and incident surface or plane waves

$$\begin{aligned}
&\tau_{zx}^{(I)}=T_x,\ \tau_{zz}^{(I)}=T_z; z=0,\ -\infty<x<\infty,\\
&\tau_{xz}^{(I)}=\tau_{zx}'^{(I)},\ \tau_{zz}^{(I)}=\tau_{zz}'^{(I)},\ u_x^{(I)}=u_u'^{(I)},\ u_z^{(I)}=u_z'^{(I)};\\
&\qquad z=d,\ -\infty>x<\infty,
\end{aligned} \tag{2.8}$$

while the scattered field solution satisfies

$$\begin{aligned}
&\tau_{zx}^{(s)}=\tau_{zz}^{(s)}=0; z=0,\ -\infty<x<\infty,\\
&\tau_{zx}^{(s)}=\tau_{zx}'^{(s)}=-\tau_{zx}^{(I)},\ z_{zz}^{(s)}=\tau_{zz}'^{(s)}=-\tau_{zz}^{(I)}; z=d,\ |x|<a,\\
&\tau_{zx}^{(s)}=\tau_{zx}'^{(s)},\ \tau_{zz}^{(s)}=\tau_{zz}'^{(s)},\ u_x^{(s)}=u_x'^{(s)},\ u_z^{(s)}=u_z'^{(s)};\\
&\qquad z=d,\ |x|>a.
\end{aligned} \tag{2.9}$$

The relationships between u_x, u_z, τ_{zz} and the potentials ϕ and Ψ are

$$\begin{aligned}
&u_x=\phi_{,x}-\Psi_{,z},\ u_z=\phi_{,z}+\Psi_{,x},\\
&\tau_{zx}=\mu(2\phi_{,xz}-\Psi_{,zz}+\Psi_{,xx}),\\
&\tau_{zz}=(\lambda+2\mu)\,\nabla^2\phi-2\mu(\phi_{,xx}-\Psi_{,xz}).
\end{aligned} \tag{2.10}$$

The solution of the scattered field problem formulated here is obtained in the following sections by a method of integral equations in a manner similar to that used for the corresponding antiplane problem in reference [1]. This method utilizes Green's functions corresponding to point sources in the uncracked layered half space. These Green's functions were derived in reference [10].

3 Reduction of the Problem to a System of Integral Equations

In this section we make use of the Green's functions derived in reference [10] for the uncracked layered half space to reduce the problem formulated in Section 2 for the cracked layered half space to a system of integral equations. For this purpose we make use of Green's (divergence) theorem in the following form (for three-dimensional elasticity solutions).

$$\iint_D (u_i^A\tau_{ij,j}^B-u_i^B\tau_{ij,j}^A)\,dA=\oint_{\partial D}(u_i^A\tau_{ij}^B-u_i^B\tau_{ij}^A)\,n_j\,dS, \tag{3.1}$$

where ∂D denotes the boundary of the region D and $\mathbf{n}$ is the outward unit normal to ∂D. Letting $\mathbf{u}^A=\mathbf{u}^{(s)}$, $\mathbf{u}^B=\mathbf{u}_L$ and $\mathbf{u}^A=\mathbf{u}^{(s)}$, $\mathbf{u}^B=\mathbf{u}_T$, respectively, where $\mathbf{u}^{(s)}$ is the displacement of the scattered field of equation (2.7) and $\mathbf{u}_L$, $\mathbf{u}_T$ denote the dilatational and rotational wave fields associated with the Green's functions derived in reference [10], we can derive the potentials $\phi^{(s)}(\mathbf{x}_p)$, $\Psi^{(s)}(\mathbf{x}_p)$ for the scattered field. ($\mathbf{x}_p$ denotes the location of the point source.)

Recall that (for $\mathbf{u}^A=\mathbf{u}^{(s)}$ and $\mathbf{u}^B=\mathbf{u}_L$)

$$\begin{aligned}
&\nabla\cdot\mathbf{u}^{(s)}=\nabla^2\phi^{(s)}=-k_L^2\phi^{(s)},\\
&\nabla\times\mathbf{u}^{(s)}=-\nabla^2\Psi^{(s)}=k_T^2\Psi^{(s)}
\end{aligned} \tag{3.2}$$

and also, when $0<z_p<d$

$$\begin{aligned}
&(\nabla^2+k_L^2)\,\phi_L=\delta(\mathbf{x}-\mathbf{x}_p), \quad (\nabla^2+k_T^2)\,\Psi_L=0, \quad 0<z<d\\
&(\nabla^2+k_L'^2)\phi_L'=0, \quad (\nabla^2+k_T'^2)\Psi_L'=0, \quad d<z<\infty.
\end{aligned} \tag{3.3}$$

Downloaded 02 May 2010 to 171.66.16.54. Redistribution subject to ASME license or copyright; see http://www.asme.org/terms/Terms_Use.cfm

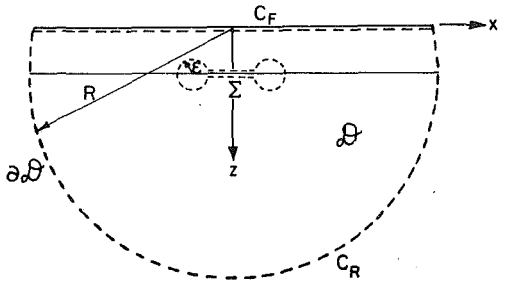


Fig. 2 Domain to which divergence theorem, equation (3.1) is applied

where the subscript L or T on the potentials ϕ and Ψ correspond to the type of source.

With these one can obtain from the left-hand side of equation (3.1)

$$\iint_D (u_i^{(s)} \tau_{ij,j}^L - u_i^L \tau_{ij,j}^{(s)})\, dA = -\mu k_T^2 \phi^{(s)}(\mathbf{x}_p), \qquad 0<z_p<d \tag{3.4}$$

Next consider the right-hand side of equation (3.1) and let D and ∂D be as shown in Fig. 2., i.e.,

$$\partial D = C_F \cup C_R \cup \Sigma$$

On C_F:

$$\tau_{zx} = \tau_{zx}^{(I)} = T_x, \quad \tau_{zz} = \tau_{zz}^{(I)} = T_z$$
$$\tau_{zx}^{(s)} = \tau_{zx}^L = 0, \quad \tau_{zz}^{(s)} = \tau_{zz}^L = 0 \tag{3.5}$$

On Σ:

$$\tau_{zx} = \tau'_{zx} = \tau_{zz} = \tau'_{zz} = 0$$
$$\tau_{zx}^L = \tau_{zx}'^L, \quad \tau_{zz}^L = \tau_{zz}'^L, \quad u_x^L = u_x'^L, \quad u_z^L = u_z'^L \tag{3.6}$$

and on C_R the radiation conditions insure that τ_{ij}^L and $\tau_{ij}^{(s)}$ vanish as $R \to \infty$. Using these results we obtain

$$\oint_{\partial D} (u_i^{(s)} \tau_{ij}^L - u_i^L \tau_{ij}^{(s)})\, \eta_j dS = \int_{-a}^{a} \{[u_x^{(s)}]\tau_{zx}^L + [u_z^{(s)}]\tau_{zz}^L dx\} \tag{3.7}$$

in which

$$[u_x^{(s)}] = \lim_{z\to d^+} u_x^{(s)} - \lim_{z\to d^-} u_x'^{(s)},$$
$$[u_z^{(s)}] = \lim_{z\to d^+} u_z^{(s)} - \lim_{z\to d^-} u_z'^{(s)}, \tag{3.8}$$

By a similar analysis we treat the case $d < z_p < \infty$. Then, by letting $\mathbf{u}_A = \mathbf{u}^{(s)}$ and $\mathbf{u}_B = \mathbf{u}^T$ and repeating the process we finally obtain the result

$$\phi^{(s)}(\mathbf{x}_p) = \begin{cases} -\dfrac{1}{\mu k_T^2} \displaystyle\int_{-a}^{a} \left\{[u_x^{(s)}]\tau_{zx}^L + [u_z^{(s)}]\tau_{zz}^L\right\} dx, & 0<z_p<d \\ -\dfrac{1}{\mu' k_T'^2} \displaystyle\int_{-a}^{a} \left\{[u_x^{(s)}]\tau_{zx}^L + [u_z^{(s)}]\tau_{zz}^L\right\} dx, & d<z_p<\infty \end{cases}$$

$$\psi^{(s)}(\mathbf{x}_p) = \begin{cases} -\dfrac{1}{\mu k_T^2} \displaystyle\int_{-a}^{a} \left\{[u_x^{(s)}]\tau_{zx}^T + [u_z^{(s)}]\tau_{zz}^T\right\} dx, & 0<z_p<d \\ -\dfrac{1}{\mu' k_T'^2} \displaystyle\int_{-a}^{a} \left\{[u_x^{(s)}]\tau_{zx}^T + [u_z^{(s)}]\tau_{zz}^T\right\} dx, & d<z_p<\infty \end{cases} \tag{3.9}$$

in which the integrals are taken along the crack and therefore the quantities τ_{zx}^L, etc. are evaluated along $z = d$. Equations (3.9) express the wave potentials of the scattered field in terms of the unknown crack opening displacements of the scattered field and the interface traction associated with the Green's functions for the uncracked layered half space.

We next compute the interface tractions corresponding to the scattered wave potential of equations (3.9), and then we impose the traction-free conditions on the crack face to obtain integral equations for determining the unknown crack-opening displacments. From equations (2.10) we obtain:

$$\tau_{zx}^{(s)}(\mathbf{x}_p) = \mu[2\phi^{(s)}_{,x_p z_p} - \Psi^{(s)}_{,z_p z_p} + \Psi^{(s)}_{,x_p x_p}],$$
$$\tau_{zz}^{(s)}(\mathbf{x}_p) = (\lambda+2\mu)\nabla^2_{\mathbf{x}_p}\phi^{(s)} + 2\mu(\Psi^{(s)}_{,x_p z_p} - \phi^{(s)}_{,x_p x_p}). \tag{3.10}$$

The substitution of equations (3.9) into equations (3.10) and with use of results from reference [10], yields

$$\tau_{zx}^{(s)}(\mathbf{x}_p)\Big|_{z_p\to d} = \frac{1}{2\pi k_T^2}\int_{-a}^{a}\Big\{\Big(\int_{-\infty}^{\infty}[(2k^2-k_T^2)S_T + i2k\,S_{L,z_p}]_{z_p\to d}\exp[ik(x-x_p)]dk\Big)[u_x^{(s)}] + \Big(\int_{-\infty}^{\infty}[(2k^2-k_T^2)N_T + i2k\,N_{L,z_p}]\Big|_{z_p\to d}\exp[ik(x-x_p)]dk\Big)[u_z^{(s)}]\Big\}dx,$$

$$\tau_{zz}^{(s)}(\mathbf{x}_p)\Big|_{z_p\to d} = \frac{1}{2\pi k_T^2}\int_{-a}^{a}\Big\{\Big(\int_{-\infty}^{\infty}[(k_T^2-2k^2)S_L + i2k\,S_{T,z_p}]\Big|_{z_p\to d}\exp[ik(x-x_p)]dk\Big)[u_x^{(s)}] + \Big(\int_{-\infty}^{\infty}[(k_T^2-2k^2)N_L + i2k\,N_{T,z_p}]\Big|_{z_p\to d}\exp[ik(x-x_p)]dk\Big)[u_z^{(s)}]\Big\}dx. \tag{3.11}$$

in which N and S denote the Fourier transforms with resepct to x of τ_{zz} and τ_{zx}, respectively, and they are derived in reference [10]. They are listed here in the Appendix.

If we now define $p_1(k), p_2(k)$ by

$$p_1(k) = \frac{\Delta}{\mu\mu' k_T^2}[(2k^2-k_T^2)S_T + 2ikS_{L,z_p}]\Big|_{z_p\to d}$$
$$p_2(k) = \frac{\Delta}{\mu\mu' k_T^2}[(2k^2-k_T^2)N_T + 2ikN_{L,z_p}]\Big|_{z_p\to d}, \tag{3.12}$$

where Δ is given in Appendix, then, in view of the symmetry properties of N_T, S_T and N_L, S_L we have

$$p_1^*(k) = \frac{\Delta}{\mu\mu' k_T^2}[(k_T^2-2k^2)N_L + i2kN_{T,z_p}]\Big|_{z_p\to d}$$
$$p_2^*(k) = \frac{\Delta}{\mu\mu' k_T^2}[(2k^2-k^2{}_T)S_L - i2kS_{T,z_p}]\Big|_{z_p\to d} \tag{3.13}$$

where the relation between $p_\alpha(k)$ and $p_\alpha^*(k)$ will be given at the end of equations (3.15). With this equations (3.11) can be written as

Downloaded 02 May 2010 to 171.66.16.54. Redistribution subject to ASME license or copyright; see http://www.asme.org/terms/Terms_Use.cfm

$$\tau_{zx}^{(s)}(x_p)=\frac{\mu\mu'}{2\pi}\int_{-a}^{a}\left\{\left[\int_{-\infty}^{\infty}\frac{p_1(k)}{\Delta(k)}\exp[ik(x-x_p)]dk\right][u_x^{(s)}]\right.$$
$$\left.+\left[\int_{-\infty}^{\infty}\frac{p_2(k)}{\Delta(k)}\exp[ik(x-x_p)]dk\right][u_z^{(s)}]\right\}dx,$$
$$\tau_{zz}^{(s)}(x_p)=\frac{\mu\mu'}{2\pi}\int_{-a}^{a}\left\{\left[\int_{-\infty}^{\infty}\frac{-p_2^*(k)}{\Delta(k)}\exp[ik(x-x_p)]dk\right][u_x^{(s)}]\right.$$
$$\left.+\left[\int_{-\infty}^{\infty}\frac{p_1^*(k)}{\Delta(k)}\exp[ik(x-x_p)]dk\right][u_z^{(s)}]\right\}dx. \tag{3.14}$$

in which

$$p_1(k)=-\frac{i\mu\gamma_L'k_T'^2}{4k^2\gamma_L\gamma_T}[(k_T^2-2k^2)^4$$
$$+16k^4\gamma_L^2\gamma_T^2]\sin(\gamma_L d)\sin(\gamma_T d)$$
$$+\mu' k_T^2[(k_T'^2-2k^2)^2+4k^2\gamma_L'\gamma_T']$$
$$\left[\frac{(k_T^2-2k^2)^2}{4k^2\gamma_T}\cos(\gamma_L d)\sin(\gamma_T d)\right.$$
$$\left.+\gamma_L\sin(\gamma_L d)\cos(\gamma_T d)\right]$$
$$+i2\mu\gamma_L'k_T'^2(k_T^2-2k^2)^2[\cos(\gamma_L d)\cos(\gamma_T d)-1],$$
$$p_2(k)=\mu[(k_T'^2-2k^2)-2\gamma_L'\gamma_T']\left\{i2k(k_T^2\right.$$
$$-2k^2)^2[\cos(\gamma_L d)\cos(\gamma_T d)-1]$$
$$\left.-\frac{i}{4k\gamma_L\gamma_T}[(k_T^2-2k^2)^4+16k^4\gamma_L^2\gamma_T^2]\sin(\gamma_L d)\sin(\gamma_T d)\right\}$$
$$+\mu'[(k_T'^2-2k^2)^2+4k^2\gamma_L'\gamma_T']$$
$$\left\{\frac{i(k^2-2k^2)}{2k}(k_T^2-4k^2)[\cos(\gamma_L d)\cos(\gamma_T d)\cos(\gamma_T d)-1]\right.$$
$$\left.+\frac{i}{4k\gamma_L\gamma_T}[(k_T^2-2k^2)^3-8k^2\gamma_L^2\gamma_T^2]\sin(\gamma_L d)\sin(\gamma_T d)\right\}$$
$$p_\alpha^*(\gamma_L,\gamma_T,\gamma_L',\gamma_T')=p_\alpha(\gamma_T,\gamma_L,\gamma_T',\gamma_L'),\quad \alpha=1,2. \tag{3.15}$$

If we observe that $p_1(k)$ and $\Delta(k)$ are symmetric and $p_2(k)$ is antisymmetric in k then we can integrate equation (3.14) by parts and make use of equations (3.5) and (2.7) to obtain the following pair of integral equations

$$\int_{-a}^{a}\left\{\left[\int_0^{\infty}\frac{p_1(k)}{\Delta(k)k}\sin[k(x-x_p)]dk\right][u_x^{(s)}]'(x)\right.$$
$$\left.-\left[\int_0^{\infty}\frac{ip_2(k)}{\Delta(k)k}\cos[k(x-x_p)]dk\right][u_z^{(s)}]'(x)\right\}dx$$
$$=\frac{\pi}{\mu\mu'}\tau_{zx}^{(I)}(x_p) \tag{3.16}$$
$$\int_{-a}^{a}\left\{\left[\int_0^{\infty}\frac{ip_2^*(k)}{\Delta(k)k}\cos[k(x-x_p)]dk\right][u_x^{(s)}]'(x)\right.$$
$$\left.+\left[\int_0^{\infty}\frac{p_1^*(k)}{\Delta(k)k}\sin[k(x-x_p)]dk\right][u_z^{(s)}]'(x)\right\}dx$$
$$=\frac{\pi}{\mu\mu'}\tau_{zz}^{(I)}(x_p),\quad -a<x_p<a.$$

where

$$[u_x^{(s)}]'(x)=\frac{d}{dx}[u_x^{(s)}(x)],\ \text{etc.} \tag{3.17}$$

and where

$$\int_{-a}^{a}[u_x^{(s)}]'(s)\,ds=0,\quad \int_{-a}^{a}[u_z^{(s)}]'(x)\,dx=0. \tag{3.18}$$

The problem has therefore been reduced to the system of integral equations in equations (3.16), which need to be solved for $[u_x^{(s)}]'$ and $[u_z^{(s)}]'$ for prescribed $\tau_{zx}^{(I)}$, $\tau_{zz}^{(I)}$, and subject to the resultant conditions in equations (3.18). In the next section we analyze the kernels of the integral equations to determine the nature of their singularities.

4 Analysis of the Integral Equations

The integral equations, equations (3.16), appear to be of the first kind but the kernal functions contain infinite integrals that may have singularities. We know that the function $\Delta(k)$ has zeros corresponding to the propagating surface modes of the type studied in reference [3]. These roots may occur on or off the real k-axis and they determine poles in the complex k-plane of the integrands in the kernels. We must determine their locations for given geometry, material parameters, and frequency and take them into account in our numerical solution to be obtained in the next section.

In addition to the zeros of $\Delta(k)$, we must investigate the behavior of the kernel integrands in the limit $k\to\infty$ and $k\to 0$. Also, the multivalued functions γ_L, γ_T, γ_L', and γ_T', have branch points at $\pm k_L$, $\pm k_T$, $\pm k_L'$ and $\pm k_T'$, respectively. We choose the branches such that $\mathrm{Re}(\gamma_L)\geq 0$, $\mathrm{Re}(\gamma_T)\geq 0$ on the path of integration. With this choice we can obtain the following asymptotic expansions in the limit $k\to\infty$.

$$\gamma_L=(k_L^2-k^2)^{1/2},\quad k<k_L$$
$$\gamma_L=i\left[k-\frac{k_L^2}{2k}-\frac{k_L^4}{8k^3}+0(k^{-5})\right],\quad k>k_L \tag{4.1}$$
$$\sin(\gamma_L d)\to\frac{i}{2}\exp(kd),\quad \cos(\gamma_L d)\to\frac{1}{2}\exp(kd)$$

Using these results in $\Delta(k)$, as defined in the Appendix, and in $p_1(k)$, $p_2(k)$, as defined in equations (3.15), we obtain as $k\to\infty$:

$$\Delta(k)\to-\frac{k^2(k_L^2-k_T^2)}{4\gamma_L\gamma_T}\exp(2kd)\,\delta_0,$$
$$p_1(k)\to-\frac{k^3(k_L^2-k_T^2)}{4\gamma_L\gamma_T}\exp(2kd)\,\delta_1, \tag{4.2}$$
$$p_1(k)\to\frac{ik^3(k_L^2-k_T^2)}{4\gamma_L\gamma_T}\exp(2kd)\,\delta_2,$$

where

$$\delta_0=\frac{1}{2}\mu'^2(k_L^2+k_T^2)(k_L'^2-k_T'^2)+\frac{1}{2}\mu^2(k_L'^2+k_T'^2)(k_L^2-k_T^2)$$
$$-\mu\mu'(k_L^2k_L'^2+k_T^2k_T'^2), \tag{4.3}$$
$$\delta_1=\mu k_T'^2(k_L^2-k_T^2)+\mu' k_T^2(k_L'^2-k_T'^2),$$
$$\delta_2=\mu'(k_L'^2-k_T'^2)k_L^2-\mu(k_L^2-k_T^2)k_L'^2.$$

It follows that the kernel integrands in equations (3.16) have the limits as $k\to\infty$,

$$\frac{p_1(k)}{\Delta(k)k}\to\frac{\delta_1}{\delta_0}=0(1),\frac{p_2(k)}{\Delta(k)k}\to\frac{-i\delta_2}{\delta_0}=0(1). \tag{4.4}$$

Next consider the limit $k\to 0$ in which we obtain

$$\frac{p_1(k)}{\Delta(k)k}\to\frac{\eta_1}{k},\quad \eta_1=\frac{-ik_T^2k_T'^2\sin(\gamma_T d)}{i\mu\gamma_T k_T'^2\cos(\gamma_T d)+\mu'\gamma_T'k_T^2\sin(\gamma_T d)}$$
$$=0(1) \tag{4.5}$$
$$\frac{p_2(k)}{\Delta(k)k}=0(1)$$

In the kernel integrals of equation (3.16) the p_1 expression is a coefficient of $\sin[k(x-x_p)]$ while the p_2 expression is a coefficient of $\cos[k(x-x_p)]$. Therefore, and from equations (4.5), the integrands are regular at $k=0$.

Downloaded 02 May 2010 to 171.66.16.54. Redistribution subject to ASME license or copyright; see http://www.asme.org/terms/Terms_Use.cfm

We next make use of the asymptotic expressions in equations (4.4) to remove the singularities from the kernels . First we recall the results

$$\int_0^\infty \sin[k(x-x_p)]dk = \frac{1}{x-x_p}$$

$$\int_0^\infty \cos[k(x-x_p)]dk = \pi\delta(x-x_p) \tag{4.6}$$

in which $\delta(x-x_p)$ represents the Dirac delta function. With these results we may write

$$\int_0^\infty \frac{p_1(k)}{\Delta(k)k}\sin[k(x-x_p)]dk = L(x_p,x) + \frac{\delta_1}{\delta_0}\frac{1}{(x-x_p)}$$

$$\int_0^\infty \frac{p_2(k)}{\Delta(k)k}\cos[k(x-x_p)]dk = M(x_p,x) - i\pi\frac{\delta_2}{\delta_0}\delta(x-x_p) \tag{4.7}$$

where

$$L(x_p,x) = \int_0^\infty \left[\frac{p_1(k)}{\Delta(k)k} - \frac{\delta_1}{\delta_0}\right]\sin[k(x-x_p)]dk$$

$$M(x_p,x) = \int_0^\infty \left[\frac{p_2(k)}{\Delta(k)k} + i\frac{\delta_1}{\delta_0}\right]\cos[k(x-x_p)]dk \tag{4.8}$$

Introducing a shorthand notation,

$$f_x(x) = [u_x^{(s)}]'(x), \quad f_z(x) = [u_z^{(s)}]'(x) \tag{4.9}$$

and using equations (4.8) in equations (3.16), we obtain the following integral equations

$$-\frac{\pi\delta_2}{\delta_0}f_z(x_p) + \frac{\delta_1}{\delta_0}\int_{-a}^{a}\frac{f_x(x)}{x-x_p}dx + \int_{-a}^{a}L(x_p,x)f_x(x)dx$$

$$-i\int_{-a}^{a}M(x_p,x)f_z(x)dx = \frac{\pi}{\mu\mu'}\tau_{zx}^{(I)}(x_p), \tag{4.10}$$

$$\frac{\pi\delta_2}{\delta_0}f_x(x_p) + \frac{\delta_1}{\delta_0}\int_{-a}^{a}\frac{f_z(x)dx}{x-x_p} + i\int_{-a}^{a}M(x_p,x)f_x(x)dx$$

$$+\int_{-a}^{a}L^*(x_p,x)f_z(x)dx = \frac{\pi}{\mu\mu'}\tau_{zz}^{(I)}(x_p).$$

The kernels $L(x_p,x)$, $M(x_p x)$ are regular, which means that the system, equations (4.10), has only Cauchy singularities.

We next analyze the singular integral equations to determine the order of singularity in the solution functions $f_x(x)$ and $f_z(x)$. Here we follow the technique in reference [5] and define $F_x(x)$, $F_z(x)$ through

$$f_x(x) = F_x(x)/(a^2-x^2)^\alpha, \quad f_z(x) = F_z(x)/(a^2-x^2)^\alpha, \quad |x| < a \tag{4.11}$$

where $Re(\alpha) < 1$ and F_x,F_z are Hölder continuous. Using the result

$$\phi(x_p) = \frac{1}{\pi}\int_{-a}^{a}\frac{f_x(x)}{x-x_p}dx = \frac{F_x(-a)\cot(\pi\alpha)}{(2a)^\alpha(a+x_p)^\alpha} - \frac{F_x(a)\cot(\pi\alpha)}{(2a)^\alpha(a-x_p)^\alpha} \tag{4.12}$$

together with a similar result for $f_z(x)$, and equation (4.11), we obtain from equations (4.10), by analyzing the dominant part and taking the limit $x_p \to a$ (or $x_p \to -a$),

$$\delta_1 F_x(a)\cot(\pi\alpha) + \delta_2 F_z(a) = 0$$

$$\delta_2 F_x(a) - \delta_1 F_z(a)\cot(\pi\alpha) = 0 \tag{4.13}$$

This system requires, for a nontrivial solution,

$$\left(\frac{\delta_2}{\delta_1}\right)^2 \sin^2(\pi\alpha) + \cos^2(\pi\alpha) = 0, \tag{4.14}$$

which is the same as the equation that determines the stress singularity at the tip of an interface crack in static problems (see reference [7]). In fact, it can be shown that (for plane strain)

$$\frac{\delta_2}{\delta_1} = \beta = \frac{\mu'(1-2\sigma) - \mu(1-2\sigma')}{2\mu'(1-\sigma) + 2\mu(1-\sigma')} \tag{4.15}$$

which is one of the composite parameters introduced in reference [8].

The solution to equation (4.14) is

$$\alpha = \frac{1}{2} \pm \frac{i}{\pi}\tanh^{-1}(\beta) = \frac{1}{2} \pm \frac{i}{2\pi}ln\left(\frac{1+\beta}{1-\beta}\right). \tag{4.16}$$

Therefore, the well-known oscillating singularity occurs in the solution of the integral equations, equations (4.10), unless $\beta = 0$. if $\beta = 0$, the crack tip singularity is 1/2, as in the case of a homogeneous material. We will restrict our numerical solution of the integral equations to this case.

5 Algebraic System Obtained from the Singular Integral Equations

In this section we approximate the system of integral equations, equations (4.10), by a corresponding set of algebraic equations. First we introduce dimensionless variables as follows:

$$\tilde{x} = x/a, \quad \tilde{k} = ka, \quad \tilde{d} = d/a, \quad \tilde{\mu} = \mu'/\mu,$$

$$\tilde{p}_\gamma(\tilde{k}_{(s)}) = \frac{1}{\mu}p_\gamma(k_{(s)}), \quad \tilde{\Delta}(\tilde{k}_{(s)}) = \frac{1}{\mu^2}\Delta(k_{(s)}),$$

$$\tilde{\delta}_\gamma = \delta_\gamma/\mu, \quad \tilde{\delta}_0 = \delta_0/\mu^2,$$

$$\tilde{f}_\alpha(\tilde{x}_p) = f_\alpha(x_p), \quad \tilde{\tau}_{\alpha\beta}(\tilde{x}_p) = \tau_{\alpha\beta}^{(I)}(x_p)/\mu',$$

$$\tilde{L}(\tilde{x}_p,\tilde{x}) = \mu L(x_p,x), \quad \tilde{M}(\tilde{x}_p,\tilde{x}) = \mu M(x_p,x),$$

$$\alpha = x,z, \quad \gamma = 1,2. \tag{5.1}$$

We also decompose the problem into its physically symmetric and antisymmetric parts with respect to x. Superscripts S and A will henceforth denote elements of this decomposition. It is easily shown that $\tilde{f}_x^A$, $\tilde{f}_z^S$, $\tilde{\tau}_{xz}^A$, $\tilde{\tau}_{zz}^S$ are mathematically even functions of x while $\tilde{f}_x^S$, $\tilde{f}_z^A$, $\tilde{\tau}_{xz}^S$, $\tilde{\tau}_{zz}^A$ are odd functions of x. After introducing the nondimensional variables according to equations (5.1), and then decomposing the problem into its physically symmetric and antisymmetric parts, we obtain (after dropping the " ~ " from all terms).

$$-\pi\frac{\delta_2}{\delta_0}f_z^L(x_p) + \frac{\delta_1}{\delta_0}\int_{-1}^{1}\frac{f_x^L(x)dx}{x-x_p} + \int_{-1}^{1}L(x_p,x)f_x^L(x)dx$$

$$-i\int_{-1}^{1}M(x_p,x)f_z^L(x)dx = \pi\tau_{zx}^L(x_p),$$

$$\pi\frac{\delta_2}{\delta_0}f_x(x_p) + \frac{\delta_1}{\delta_0}\int_{-1}^{1}\frac{f_z(x)dx}{x-x_p} + i\int_{-1}^{1}M(x_p,x)f_x^L(x)dx$$

$$+\int_{-1}^{1}L^*(x_p,x)f_z(x)dx = \pi\tau_{zz}^L(x_p), \quad L = S, A. \tag{5.2}$$

Next we use the methods described by Erodgan and Gupta [6], to obtain the algebraic system of equations corresponding to equations (5.2). This analysis is presented in detail in reference [10] so it need not be repeated here. The solution is straightforward, except for the singularities in the integrands of the integrals that define the kernels $L(x_p,x)$, $M(x_p,x)$ in equations (4.8). These singularities are poles that occur in the complex k-plane at the zeros of $\Delta(k)$. It was shown by Farnell and Adler [3] that in the "loading" case, for which the shear wave velocity of the layer is less than that of the substrate, only one Rayleigh-type pole occurs, and it is on the real k-axis. However, for the "stiffening" case, for which the substrate shear wave velocity is greater, more than one such

Downloaded 02 May 2010 to 171.66.16.54. Redistribution subject to ASME license or copyright; see http://www.asme.org/terms/Terms_Use.cfm

Table 1 Values used for material parameters in the composites

Material	Poisson's ratio σ	Shear modulus $\mu(N/m^2)$	Density $\rho(g/cm^3)$	c_L (km/s)	c_T (km/s)	c_R (km/s)
Gold (Au)	0.42	28	19.3	3.24	1.20	1.14
Nickel (Ni)	0.31	66.5	8.8	5.24	2.75	2.55
Aluminum (Al)	0.34	26.5	2.7	6.36	3.13	2.92
Zinc (Zn)	0.25	41.4	7.1	4.18	2.41	1.22
Iron (Fe)	0.28	77	7.7	5.72	3.16	2.92

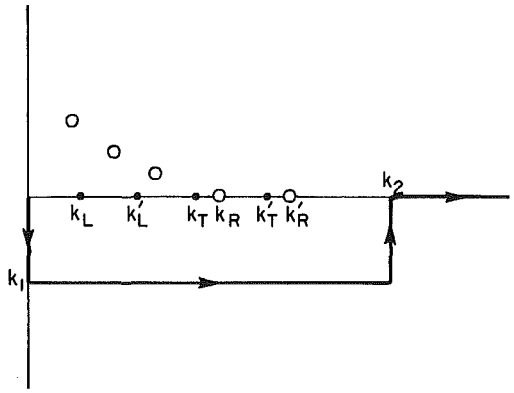


Fig. 3 Path of integration for evaluating semi-infinite integrals as in equations (4.8)

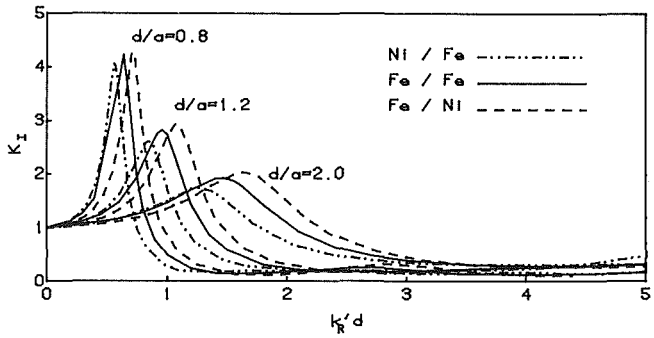


Fig. 4 Mode I stress intensity factor as a function of dimensionless wave numbers for various ratios of layer thickness to crack half length. Materials are nickel and iron, layer/substrate.

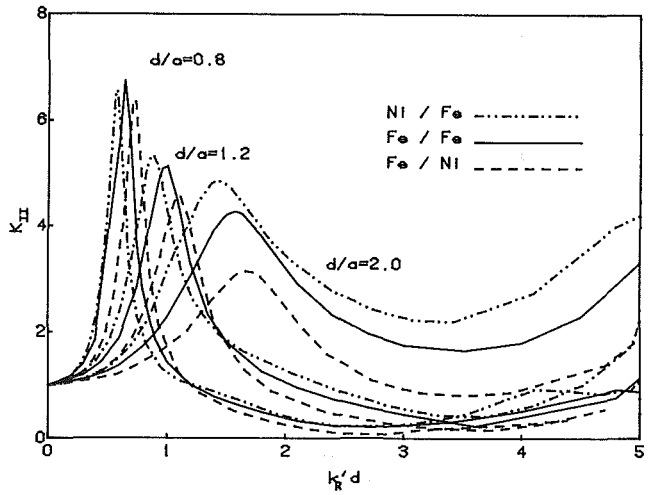


Fig. 5 Mode II stress intensity factor as a function of dimensionless wave number for various ratios of layer thickness to crack half length. Materials are nickel and iron, layer/substrate.

pole may occur, depending on the frequency. In both cases, it is found (see Bogy and Gracewski [4]), that the poles never occur in the fourth quadrant ($Re(k) > 0$, $Im(k) < 0$) of the k-plane.

Two different ways have been used by others for dealing with these poles in the integrations in equations (4.8). Kundu and Mal [9] use a technique of removing the singularities from the integrands. The other technique, used by Neerhoff [1] and Keer et al. [2], merely deforms the contour of integration below the real k-axis, as shown in Fig. 3, so that no poles occur on the path of integration. In order to optimize accuracy and computation time, judicious choices of the two parameters k_1 and k_2, that determine the deformed path, are required. k_2 must be chosen beyond the Rayleigh poles corresponding to the two materials, and hence it depends on frequency. The value of k_1 needs to be large enough to offset the path sufficiently from the singular points but not too large because the magnitudes of the hyperbolic functions increase rapidly with the imaginary part of k. In our calculations we usually chose the value $k_1 = 1$ and k_2 depended on ω, d and c_T/c'_T.

6 Numerical Results

Various numerical results can be obtained from our analysis. We will restrict the presentation here to the dynamic stress intensity factors K_I and K_{II}, at the crack tips, due to an incident wave resulting from a harmonic uniform normal traction applied at the boundary $z = 0$. Therefore, the incident wave is determined by the boundary conditions in equations (2.8), where

$$T_x = 0, \quad T_z = 1. \tag{6.1}$$

The solution to this incident wave problem is presented in reference [10], and it yields the following results for the $\tau_{\alpha\beta}$ needed for the integral equations, equations (5.2)

$$\tau_{zx}^{(I)} = 0, \quad \frac{1}{\mu'}\tau_{zz}^{(I)}(x) = \frac{\varkappa}{\varkappa\cos(k_L d) - i\sin(k_L d)}, \tag{6.2}$$

in which

$$\varkappa = \rho' c'_L / \rho c_L. \tag{6.3}$$

The stress intensity factors K_I and K_{II} are defined by

$$K_I = \lim_{x\to a}\ [\sqrt{2(x-a)}\,\tau_{zz}(x,d)],$$
$$K_{II} = \lim_{x\to a}\ [\sqrt{2(x-a)}\,\tau_{xz}(x,d)]. \tag{6.4}$$

These expressions can be evaluated from equations (5.2) and (5.3) and they yield the results (in which $\tilde{K}_I = K_I/\mu a^{1/2}$, etc. and after dropping the tilde)

$$K_I = \frac{\delta_1}{\delta_0}F_z(1), \quad K_{II} = \frac{\delta_1}{\delta_0}F_x(1). \tag{6.5}$$

Numerical calculations were carried out for three different material pairs: nickel/iron, aluminum/zinc, and nickel/gold. Both materials were considered as layer and substrate in each case. The material parameters were slightly adjusted in each case in order to satisfy the condition $\beta = 0$, where β is given in equation (4.15). It will be recalled that this condition is necessary for the singularity power α to be one-half as shown

Downloaded 02 May 2010 to 171.66.16.54. Redistribution subject to ASME license or copyright; see http://www.asme.org/terms/Terms_Use.cfm

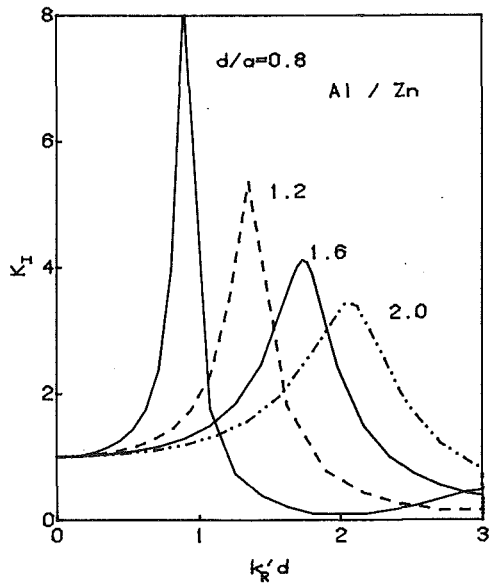


Fig. 6 Same as Fig. 4 but with the materials aluminum/nickel

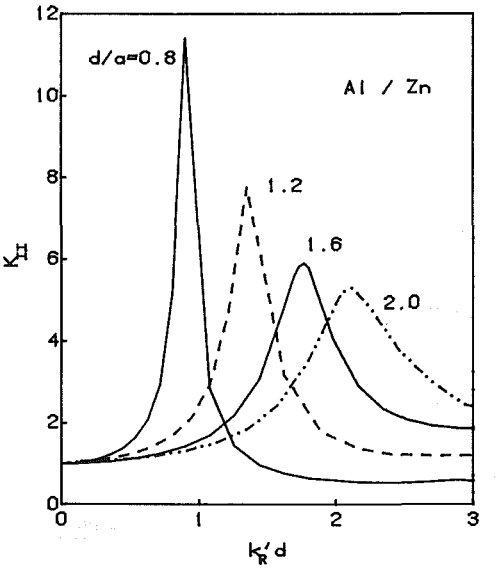


Fig. 7 Same as Fig. 5 but with the materials aluminum/nickel

in equation (4.16). The actual values for the material parameters used are given in Table 1.

Figure 4 shows three sets of K_I versus $k_R'd$ curves of the type presented in Keer et al. [2] for a single material. Here one set is for a nickel layer with iron substrate, one set is for iron layer with iron substrate (and hence, is the same as in reference [2]), and the third set is for an iron layer on a nickel substrate. The material parameters for these two materials are not very different and the computations for this case caused less difficulties than for other cases in which the materials are radically different. Figure 5 gives K_{II} corresponding to the K_I shown in Fig. 4.

Figures 6 and 7 show K_I and K_{II}, respectively, as functions of $k_R'd$ for various values of d/a for the case of an aluminum layer on a zinc substrate. Figures 8 and 9 show the corrresponding results for a zinc layer on an aluminum substrate.

Finally, Figs. 10 and 11 show K_I and K_{II}, respectively, as functions of $k_R'd$ for various values of d/a for the case of a nickel layer on a gold substrate. Figures 12 and 13 show the corresponding results for a gold layer on a nickel substrate.

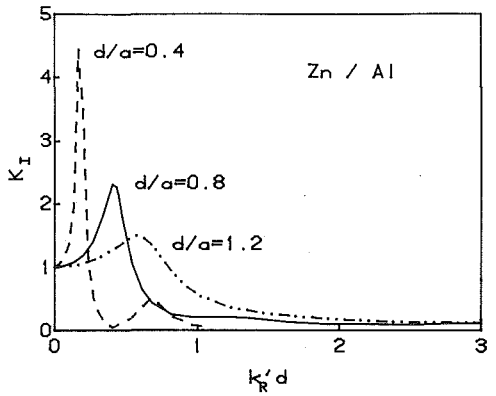


Fig. 8 Same as Fig. 4 but with the materials zinc/aluminum

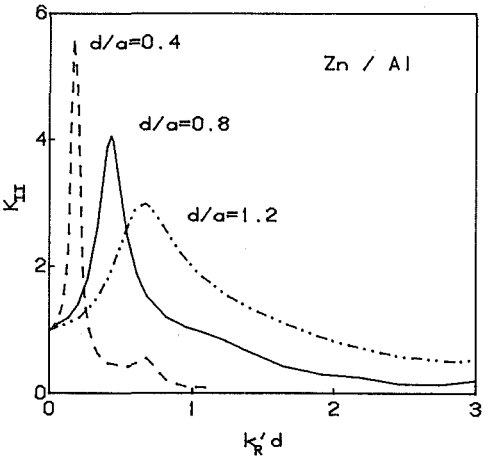


Fig. 9 Same as Fig. 5 but with the materials zinc/aluminum

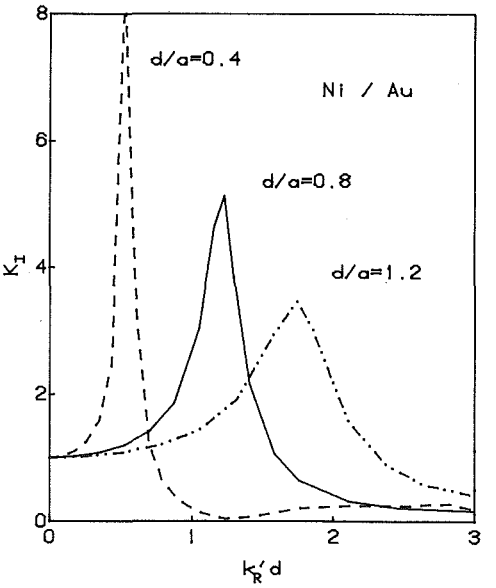


Fig. 10 Same as Fig. 4 but with the materials nickel/gold

This pair of materials had the greatest mismatch of material parameters of the three pairs considered.

7 Discussion

We have presented the plane strain solution for the problem of elastic wave scattering from an interface crack in a layered half space for the case of a single layer. The stress field has an

Downloaded 02 May 2010 to 171.66.16.54. Redistribution subject to ASME license or copyright; see http://www.asme.org/terms/Terms_Use.cfm

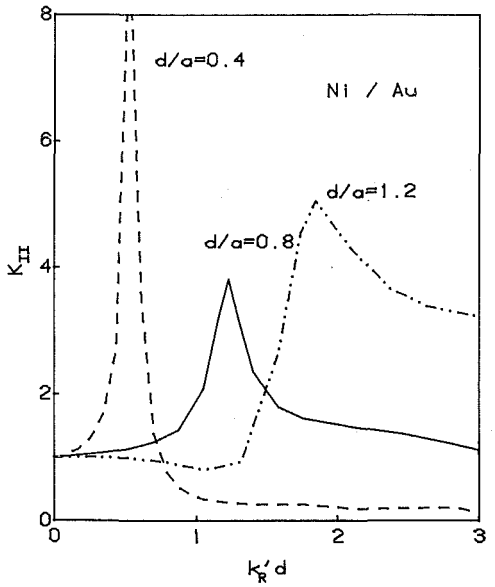


Fig. 11 Same as Fig. 5 but with the materials nickel/gold

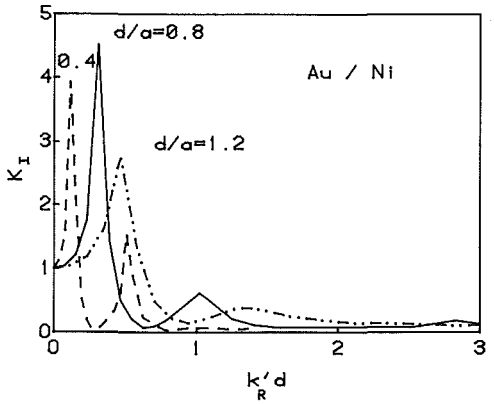


Fig. 12 Same as Fig. 4 but with the materials gold/nickel

oscillatory singularity, in general, at the crack tips, but it is a nonoscillatory square root singularity in the class of composites for which $\beta = 0$ in equation (4.16). The numerical solution to the integral equations was restricted to this class of composites and to the case when the incident wave is generated by harmonic uniform normal tractions on the boundary.

The stress intensity factors K_I and K_{II} show resonances at specific values of $k'_R d$ and the locations as well as peak values of these resonances depend on the material combinations. As shown in Figs. 4 and 5 the $k'_R d$ value for resonance is smaller, for a pair of materials, in the loading case ($c_T < c'_T$) than it is in the stiffening case ($c_T > c'_T$).

Some difficulties were encountered in the numerical computations, especially when the material parameters for the layer and substrate were quite different and for the larger values of $k'_R d$. Further work is planned to investigate these problems in more detail.

References

1 Neerhoff, F. L., "Diffraction of Love Waves by a Stress-Free Crack of Finite Width in the Plane Interface of a Layered Composite," *Applied Scientific Research*, Vol. 35, 1979, pp. 265-315.

2 Keer, L. M., Lin, W., and Achenbach, J. D., "Resonance Effects for a Crack Near a Free Surface," ASME JOURNAL OF APPLIED MECHANICS, Vol. 51, 1984, pp. 65-70.

3 Farnell, G. W., and Adler, E. L., "Elastic Wave Propagation in Thin Layers," in *Physical Acoustics*, Vol. 9, Academic Press, New York, 1972, pp. 35-127.

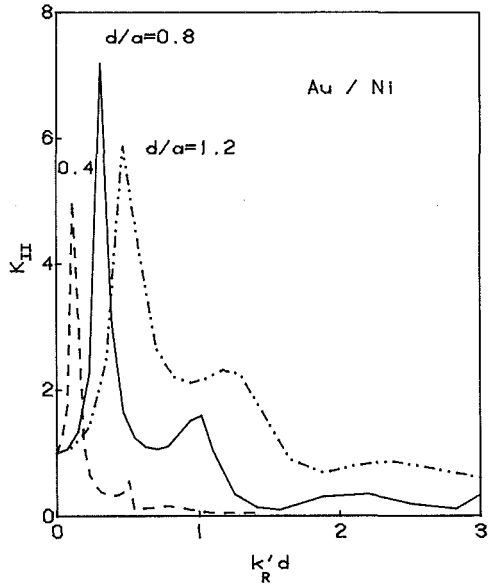


Fig. 13 Same as Fig. 5 but with the materials gold/nickel

4 Bogy, D. B., and Gracewski, S. M., "On the Plane-Wave Reflection Coefficient and Nonspecular Reflection of Bounded Beams for Layered Half-Spaces Underwater," *J. Acoust. Soc. Am.*, Vol. 74, 1983, pp. 591-599.

5 Muskhelishvili, N. I., *Singular Integral Equations*, Noordhoff International, 1977.

6 Erodgan, F., and Gupta, G. D., "On the Numerical Solution of Singular Integral Equations," *Quarterly Appl. Math.*, Vol. 30, 1972, pp. 525-534.

7 Bogy, D. B., "Two Edge-Bonded Elastic Wedges of Different Materials and Wedge Angels Under Surface Tractions," ASME JOURNAL OF APPLIED MECHANICS, Vol. 38, 1971, pp. 377-386.

8 Dundurs, J., Discussion, ASME JOURNAL OF APPLIED MECHANCIS, Vol. 36, 1969, p. 650.

9 Kundu, T., and Mal, A. K., "Calculation of the Surface Response of a Layered Solid to a Point Dislocation Source," private communication.

10 Yang, Huey-Ju Pearl, *Elastic Wave Scattering from an Interface Crack in a Layered Half Space*. Ph.D. Dissertation, University of California, Berkeley, Feb., 1984.

APPENDIX

The functions N_L, N_T, S_L, and S_T first appearing in equations (3.11) are derived in reference [10] and their needed limiting values are listed here for completeness.

For $0 < z_p < d$ (source in layer). $z \to d$,

$$N_L = \frac{\mu\mu' k_T^2}{\Delta}\left(-i\mu\gamma'_T(k_T^2-2k^2)k_T'^2\cos[\gamma_L(d-z_p)]\right.$$

$$+\frac{(k_T^2-2k^2)}{2\gamma_L}\left\{\mu(k^2{}_T-2k^2)(k_T'^2-2k^2-2\gamma'_L\gamma'_T)\right.$$

$$\left.\left.-\mu'[(k_T'^2-2k^2)^2+4k^2\gamma'_L\gamma'_T]\right\}\sin[\gamma_L(d-z_p)]\right.$$

$$+\frac{i\mu\gamma'_T(k_T^2-2k^2)k_T'^2}{4k^2\gamma_L\gamma_T}\left\{4k^2\gamma_L\gamma_T\cos(\gamma_T d)\cos(\gamma_L z_p)\right.$$

$$\left.-(k_T^2-2k^2)^2\sin(\gamma_T d)\sin(\gamma_L z_p)\right\}$$

$$+\frac{1}{4k^2\gamma_L}\left\{2\mu k^2(k_T'^2-2k^2-2\gamma'_L\gamma'_T)\right.$$

$$\left.+\mu'[(k_T'^2-2k^2)^2+4k^2\gamma'_L\gamma'_T]\right\}$$

$$\times[(k_T^2-2k^2)^2\cos(\gamma_T d)\sin(\gamma_L z_p)$$

Downloaded 02 May 2010 to 171.66.16.54. Redistribution subject to ASME license or copyright; see http://www.asme.org/terms/Terms_Use.cfm

$$+4k^2\gamma_L\gamma_T\sin(\gamma_T d)\cos(\gamma_L z_p)]\Big)$$

$$S_L=\frac{\mu\mu' k_T^2}{\Delta}\Big(\frac{\mu\gamma_L'(k_T^2-2k^2)^2}{2k\gamma_L}k_T'^2\sin[\gamma_L(d-z_p)]$$

$$+\frac{i(k_T^2-2k^2)}{2k}\Big\{2\mu k^2(k_T'^2-2k^2-2\gamma_L'\gamma_T')$$

$$+\mu'[(k_T'^2-2k^2)^2+4k^2\gamma_L'\gamma_T']\Big\}\cos[\gamma_L(d-z_p)]$$

$$+\frac{\mu\gamma_L' k_T'^2}{2k\gamma_L}[4k^2\gamma_L\gamma_T\sin(\gamma_T d)\cos(\gamma_L z_p)$$

$$+(k_T^2-2k^2)^2\cos(\gamma_T d)\sin(\gamma_L z_p)]$$

$$+\frac{i}{4k\gamma_L\gamma_T}\Big\{\mu(k_T^2-2k^2)(k_T'^2-2k^2-2\gamma_L'\gamma_T')$$

$$-\mu'[(k_T'^2-2k^2)+4k^2\gamma_L'\gamma_T']\Big\}$$

$$\times[(k_T^2-2k^2)^2\sin(\gamma_T d)\sin(\gamma_L z_p)$$

$$-4k^2\gamma_L\gamma_T\cos(\gamma_T d)\cos(\gamma_L z_p)]\Big),$$

$$N_T=S_L^*,\quad S_T=-N_L^*. \tag{A.1}$$

For $d<z_p<\infty$ (source in substrate), $z\to d$,

$$N_L=\frac{\mu\mu' k_T'^2}{\Delta}\exp[i\gamma_L'(z_p-d)]$$

$$\times\Big(\frac{i\gamma_T'}{4k^2\gamma_L\gamma_T}\sin(\gamma_L d)\sin(\gamma_T d)\Big\{2\mu' k^2[8k^2\gamma_L^2\gamma_T^2$$

$$-(k_T^2-2k^2)^3]-\mu[(k_T^2-2k^2)^4+16k^4\gamma_L^2\gamma_T^2]\Big\}$$

$$+\frac{\mu'(k_T'^2-2k^2)}{4k^2\gamma_L}k_T^2[(k_T^2-2k^2)^2\sin(\gamma_L d)\cos(\gamma_T d)$$

$$+4k^2\gamma_L\gamma_T\sin(\gamma_T d)\cos(\gamma_L d)]$$

$$+i\gamma_T'(k_T^2-2k^2)[\cos(\gamma_L d)\cos(\gamma_T d)-1]$$

$$[2\mu(k_T^2-2k^2)+\mu'(4k^2-k_T^2)]\Big),$$

$$S_L=\frac{\mu\mu'}{\Delta}k_T'^2\exp[i\gamma_L'(z_p-d)]$$

$$\times\Big(\frac{i}{4k\gamma_L\gamma_T}\sin(\gamma_L d)\sin(\gamma_T d)\Big\{\mu[16k^4\gamma_L^2\gamma_T^2$$

$$+(k_T^2-2k^2)^4]+\mu'(k_T'^2-2k^2)[8k^2\gamma_L^2\gamma_T^2-(k_T^2-2k^2)^3]\Big\}$$

$$-\frac{\mu'\gamma_T'}{2k\gamma_T}k_T^2[(k_T^2-2k^2)^2\sin(\gamma_T d)\cos(\gamma_L d)$$

$$+4k^2\gamma_L\gamma_T\sin(\gamma_L d)\cos(\gamma_T d)]$$

$$+\frac{i(k_T^2-2k^2)}{2k}[1-\cos(\gamma_L d)\cos(\gamma_T d)][4\mu k^2(k_T^2-2k^2)$$

$$+\mu'(k_T'^2-2k^2)(k_T^2-4k^2)]\Big),$$

$$N_T=S_L^*,\quad S_T=-N_L^*. \tag{A.2}$$

The generalized Rayleigh function Δ is given by

$$\Delta=\mu'^2[(k_T'^2-2k^2)^2+4k^2\gamma_L'\gamma_T']$$

$$\times\Big\{\Big[\frac{(k_T^2-2k^2)^2}{4k_L k_T}+\gamma_L\gamma_T\Big]\sin(\gamma_L d)\sin(\gamma_T d)$$

$$-\Big[\frac{(k_T^2-2k^2)^2}{4k^2}+k^2\Big]\cos(\gamma_L d)\cos(\gamma_T d)-(k_T^2-2k^2)\Big\}$$

$$+i\mu\mu'\gamma_L'\gamma_T k_T^2 k_T'^2\Big[\cos(\gamma_L d)\sin(\gamma_T d)$$

$$+\frac{(k_T^2-2k^2)^2}{4k^2\gamma_L\gamma_T}\sin(\gamma_L d)\cos(\gamma_T d)\Big]$$

$$+i\mu\mu'\gamma_L\gamma_T' k_T^2 k_T'^2\Big[\sin(\gamma_L d)\cos(\gamma_T d)$$

$$+\frac{(k_T^2-2k^2)^2}{4k^2\gamma_L\gamma_T}\cos(\gamma_L d)\sin(\gamma_T d)\Big]$$

$$+\mu\mu'[(k_T'^2-2k^2)-2\gamma_L'\gamma_T']$$

$$\times\Big\{(k_T^2-2k^2)(k_T^2-4k^2)[1-\cos(\gamma_L d)\cos(\gamma_T d)]$$

$$+\Big[4k^2\gamma_L\gamma_T-\frac{(k_T^2-2k^2)^3}{2\gamma_L\gamma_T}\Big]\sin(\gamma_L d)\sin(\gamma_T d)\Big\}$$

$$-\mu^2(k^2+\gamma_L'\gamma_T')\Big\{2(k_T^2-2k^2)^2[\cos(\gamma_L d)\cos(\gamma_T d)-1]$$

$$-\Big[4k^2\gamma_L\gamma_T+\frac{(k_T^2-2k^2)^4}{4k^2\gamma_L\gamma_T}\Big]\sin(\gamma_L d)\sin(\gamma_T d)\Big\}; \tag{A.3}$$

Downloaded 02 May 2010 to 171.66.16.54. Redistribution subject to ASME license or copyright; see http://www.asme.org/terms/Terms_Use.cfm

The Rapid Tearing of a Half Plane

J. P. Dempsey
Assistant Professor.
Assoc. Mem. ASME

E. B. Smith[1]
Graduate Student.

Department of Civil and Environmental Engineering,
Clarkson University,
Potsdam, N.Y. 13676

The surface of an elastic half space is subjected to sudden antiplane mechanical disturbances. Crack initiation and subsequent crack instability are examined via two idealized problems; the first is concerned with instantaneous crack bifurcation and the second with instantaneous skew crack propagation. In either problem, crack propagation occurs at a constant subsonic velocity under an angle $\kappa\pi$ with the normal to the surface. For the externally applied disturbances that are considered here, and for contstant crack-tip velocities, the particle velocity and $\tau_{\theta z}$ are functions of r/t and θ only, which allows Chaplygin's transformation and conformal mapping to be used. The problems can then be solved using analytic function theory. For various values of the angle of crack propagation, the dependence of the elastodynamic stress intensity factors on the crack propagation velocity is investigated. For certain specific geometries, fully analytical solutions are derived to provide check cases.

1 Introduction

Crack bifurcation and crack branching is observed frequently in brittle materials. However, the elastodynamic analysis of the inplane problems is especially difficult. Only recently have the associated Mode *III* solutions been obtained, for an initially stationary crack loaded dynamically, by Burgers and Dempsey [1], Burgers [2], and Dempsey et al. [3]. Solutions such as these solve some of the difficulties found in attempting the mixed-mode problems, thereby setting the stage for the solution of more relevant problems. They also serve as check cases for numerical techniques, such as the finite element method. Moreover, the solutions aid in the formulation of a criterion for the observed crack instability, in order that crack branching can be reliably predicted.

In the present paper time-varying, discontinuous, antiplane mechanical disturbances are applied to the surface of a half plane. The material is homogeneous, isotropic, and elastic. The sudden loading gives rise to singularities in the shear stress. In the case of applied surfaces tractions, for instance, the loading discontinuity gives rise to a logarithmic singularity. A static analysis similar to that employed by Williams [4], but necessarily modified to treat stresses of order lnr (see [5]), confirms the foregoing singular behavior as does the study by Achenbach [6]. The singular stresses are assumed to promote the rapid tearing of the half plane at the point of load discontinuity.

Under perfectly antisymmetric loading conditions, the tearing should first give rise to crack propagation normal to the surface. Since the speed of crack propagation in brittle materials is high, inertia effects are important. Crack bifurcation is then to be expected, due to higher elastodynamic stress intensity factors or greater energy flux into the crack tip along alternate paths. Another possibility exists if there is the presence of a preexisting very small flaw, or of a weak plane, at an oblique angle. Skew crack propagation is then to be expected.

Two particular idealized cases are treated here; the first is symmetric crack bifurcation and the second is skew crack propagation. In either case, crack propagation occurs at a constant, subsonic velocity v, under an angle $\kappa\pi$ with the normal to the surface, at the instant that the mechanical disturbances are applied to the surface of the half space.

The method used in this paper takes advantage of dynamic similarity of the particle velocity of the diffracted field, which occurs when appropriate conditions on the incident wave and the geometry are satisfied. The tearing of a half plane, and subsequent skew crack propagation, was formulated almost a decade ago by Achenbach and Varatharajulu [7]. Unfortunately the analytic function they chose to satisfy the boundary conditions in the ζ-plane is not complete (compare equation (34) in [7] to equations (2.4), (3.2), and (3.3) in this paper).

The treatment here is largely analytical, except in the final stages where certain integrals must be computed numerically. In several cases, however, fully analytical solutions are obtained and these provide valuable check cases.

2 Crack Bifurcation

Problem 1: Prescribed Surface Tractions. An isotropic, linearly elastic half space is subjected to sudden antiplane strain loading applied at time $t=0$. Upon application of the uniform stress to the surface of the half plane, two cracks emanate from the origin and propagate with subsonic velocity v under angle $\pm\ \kappa\pi$ with the x-axis (Fig. 1). The three loading cases studied in this paper are now defined. Case (a):

[1] Now with Applied Research Associates, South Royalton, Vt. 05068.

Contributed by the Applied Mechanics Divison and presented at the Winter Annual Meeting, New Orleans, La., Decemer 9-14, 1984 of THE AMERICAN SOCIETY OF MECHANICAL ENGINEERS.

Discussion on this paper should be addressed to the Editorial Department, ASME, United Engineering Center, 345 East 47th Street, New York, N.Y. 10017, and will be accepted until two months after final publication of the paper itself in the JOURNAL OF APPLIED MECHANICS. Manuscript received by ASME Applied Mechanics Division, April, 1983; final revision, December, 1983. Paper No. 84-WA/APM-51.

Copies will be available until August, 1985.

Copyright © 1985 by ASME
Downloaded 02 May 2010 to 171.66.16.54. Redistribution subject to ASME license or copyright; see http://www.asme.org/terms/Terms_Use.cfm

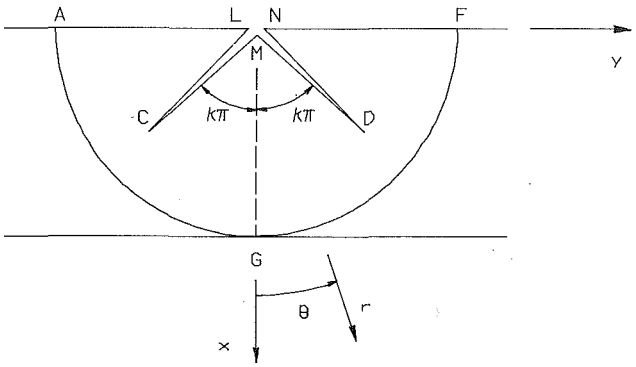


Fig. 1 Bifurcation of a half plane subjected to dynamic loading in antiplane strain

$\tau_{\theta z} = \tau_0 H(t)$ on the half-plane surface, $\tau_{\theta z} = 0$ on the cracks; Case (*b*): same surface loading as in Case (*a*), but $\tau_{\theta z} = -\tau_0 H(t)$ on the cracks; Case (*c*): $\tau_{\theta z} = 0$ on the half-plane surface, same loading on the cracks as in Case (*b*). $H(t)$ is the Heaviside function. The solution for Case (*c*) is obtained by the appropriate superposition of Cases (*a*) and (*b*).

Since no fundamental length enters the formulation, and because of the loading considered in this paper, the particle velocity is self-similar. A new variable $s = r/t$ is introduced so that $\dot{w}$ is a function of s and θ. The use of Chaplygin's transformation $\beta = \cosh^{-1}(c/s)$, in which $c^2 = \mu/\rho$, maps the quartercircle *MGFN* of the physical problem into a semi-infinite strip in the γ-plane, where $\gamma = \beta + i\theta$. The governing equation of motion, expressed in polar coordinates, and rewritten in terms of the preceding transformation, reveals that the particle velocity $\dot{w}$ (β,θ) satisfies Laplace's equation in β and θ. Therefore $\dot{w}$ can be taken as the real part of an analytic function $\dot{w} = Re\, G(\gamma)$ and the Schwarz-Christoffel transformation can be used to map the semi-infinite strip onto the upper half of the ζ-plane (Fig 2), where $\zeta = \xi + i\eta$. Now $\dot{w} = Re\, F(\zeta)$, where

$$\gamma = \kappa \cosh^{-1}\left(\frac{1+\xi_M\zeta}{\zeta+\xi_M}\right) + (1/2-\kappa)\cosh^{-1}\left(\frac{1-\xi_N\zeta}{\zeta-\xi_N}\right) + i\pi/2 \tag{2.1}$$

in which

$$\cosh^{-1}(c/v) = \kappa \cosh^{-1}(1/\xi_M) + (1/2-\kappa)\cosh^{-1}(1/\xi_N), \tag{2.2a}$$

$$\kappa\, \xi_N/(1-\xi_N^2)^{1/2} = (1/2-\kappa)\,\xi_M/(1-\xi_M^2)^{1/2}. \tag{2.2b}$$

Since κ and v/c are given quantities, (2.2*a*,*b*) may be used to compute the values of ξ_M and ξ_N. The boundary conditions for Cases (*a*) or (*b*) in the γ-plane on the real axis ($\eta = 0$) are

$$-\infty < \xi < -1: \quad \dot{w} = c\,\tau_0/\mu, \quad \partial\dot{w}/\partial\xi = 0, \tag{2.3a}$$

$$-1 < \xi < -\xi_M: \quad \dot{w} = 0, \quad \partial\dot{w}/\partial\xi = 0, \tag{2.3b}$$

$$-\xi_M < \xi < 1: \quad \dot{\tau}_{\theta z} = 0, \quad \partial\dot{w}/\partial\eta = 0, \tag{2.3c}$$

$$1 < \xi < \infty: \quad \dot{w} = c\,\tau_0/\mu, \quad \partial\dot{w}/\partial\xi = 0. \tag{2.3d}$$

An analytic function $F'(\zeta)$ must be found to satisfy the boundary conditions given in (2.3). The question of completeness is important since the function may satisfy the boundary conditions, for instance, but may not give the correct crack tip singularity. Following the procedure in [3] (see equations (3.19)–(3.23) therein) an asymptotic analysis along the line $\theta = \kappa\pi$ in the ζ-plane for $|\zeta| << 1$ reveals that a singularity of order $(r-vt)^{-1/2}$ in the particle velocity corresponds to a singularity of order ζ^{-1} in $F(\zeta)$. The appropriate form for $F'(\zeta)$ is thus

$$F'(\zeta) = F_1'(\zeta) + F_2'(\zeta), \tag{2.4}$$

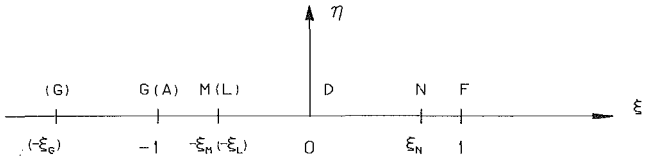


Fig. 2 The $\zeta = \xi + i\eta$-plane for crack bifurcation

where

$$F_1'(\zeta) = iA\{2(1-\xi_M)/(\zeta-1)(\zeta+\xi_M)\}^{1/2}/(\zeta+1), \tag{2.5}$$

$$F_2'(\zeta) = iA\,(B/\zeta + C/\zeta^2)/(\zeta-1)^{1/2}(\zeta+\xi_M)^{1/2}. \tag{2.6}$$

$F_1'(\zeta)$ satisfies the boundary conditions; the jump in particle velocity at $\xi = -1$ gives $A = c\tau_0/\mu\pi$. The integration of $F_2'(\zeta)$ gives rise to arc sin terms, which in turn give rise to a logarithmic singularity in the particle velocity near the crack tip; to exclude this singularity it is necessary that $B = (1-\xi_M)C/2\xi_M$—see [1] for a similar, more detailed, treatment.

To determine C and then the stress intensity factor, the stress ahead of the crack tip is needed. Following the procedure used in equations (3.30)–(3.37) of [3], the shear stress may be written in the form

$$\tau_{\theta z}(s,\theta) = -\{(\mu/s)(1-s^2/c^2)^{1/2} Im F_2(\zeta) + \mu I(s,\theta)\}H(c-s) + \tau_0 \mathrm{sgn}(\theta)\sin(\theta)H(c-s\cos(\theta)), \tag{2.7}$$

where

$$I(s,\theta) = I_3(s,\theta) - C\, I_4(s,\theta), \tag{2.8a}$$

$$I_3 = Im\int_s^c \frac{1}{s'^2} F_1'(\zeta)\,\frac{d\zeta}{d\gamma}\,ds', \tag{2.8b}$$

$$CI_4 = Im\int_s^c F_2(\zeta)\,\frac{ds'}{s'^2\sqrt{1-s'^2/c^2}}, \tag{2.8c}$$

$$F_2(\zeta) = iAC(\zeta-1)^{1/2}(\zeta+\xi_M)^{1/2}/\zeta\xi_M. \tag{2.9}$$

To evaluate the constant C observe that the regular part of $\tau_{\theta z}$ in (2.7) for $\theta = \kappa\pi$ and $(r-vt) \to 0^+$ must be equal to the loading on the new crack faces for $\theta = \kappa\pi$ and $(r-vt) \to 0^-$. Thus, in loading Case (*a*), $\lim_{s\to v}(-\mu I + \tau_0 \mathrm{sgn}(\kappa\pi)\sin(\kappa\pi)) = 0$, hence

$$C^a I_4(v,\kappa\pi) = I_3(v,\kappa\pi) - (\tau_0/\mu)\mathrm{sgn}(\kappa\pi)\sin(\kappa\pi). \tag{2.10}$$

$$C^b I_4(v,\kappa\pi) = C^a I_4(v,\kappa\pi) - (\tau_0/\mu). \tag{2.11}$$

The elastodynamic Mode *III* stress intensity factor is defined as

$$K_{III} = \lim_{r\to vt}\,(2\pi)^{1/2}(r-vt)^{1/2}\tau_{\theta z}(r>vt, \theta=\kappa\pi). \tag{2.12}$$

By the use of (2.7)–(2.12),

$$K_{III}^q = \tau_0(ct)^{1/2} H\{I_3(v,\kappa\pi) - (\tau_0/\mu)\mathrm{sgn}(\kappa\pi)\sin(\kappa\pi)\}/I_4(v,\kappa\pi), \tag{2.13}$$

in which

$$H = -\{(c/v)(1-v^2/c^2)^{3/2} h/\pi\xi_M\}^{1/2}, \tag{2.14}$$

$$h = \kappa(1-\xi_M^2)^{1/2}/\xi_M^2 + (1/2-\kappa)(1-\xi_N^2)^{1/2}/\xi_N^2. \tag{2.15}$$

By superposition, $K_{III}^b = K_{III}^a + K_{III}^c$. Here it is necessary to state only K_{III}^c:

$$K_{III}^c = -\tau_0(ct)^{1/2} H(\tau_0/\mu)/I_4(v,\kappa\pi). \tag{2.16}$$

Problem 2: Prescribed Surface Displacements. Traction-free crack bifurcation under the applied, discontinuous, surface displacements defined in the following is considered here:

$$\theta = \pm\pi/2, \quad r>0: \quad w = \pm W_0 t\, H(t), \tag{2.17}$$

Downloaded 02 May 2010 to 171.66.16.54. Redistribution subject to ASME license or copyright; see http://www.asme.org/terms/Terms_Use.cfm

The boundary conditions in the ζ-plane are:

$$-\infty<\xi<-\xi_G: \quad \dot{w}=W_0, \quad \partial\dot{w}/\partial\xi=0, \quad (2.18a)$$

$$-\xi_G<\xi<-\xi_M: \quad \dot{w}=0, \quad \partial\dot{w}/\partial\xi=0, \quad (2.18b)$$

$$-\xi_M<\xi<\xi_N: \quad \dot{\tau}_{\theta z}=0, \quad \partial\dot{w}/\partial\eta=0, \quad (2.18c)$$

$$\xi_N<\xi<\infty: \quad \dot{w}=W_0, \quad \partial\dot{w}/\partial\xi=0. \quad (2.18d)$$

For this problem the form for $F'(\zeta)$, noting (2.4), is given by

$$F_1'(\zeta)=iA\{(1-\xi_M)(1+\xi_N)/(\zeta+\xi_M)(\zeta-\xi_N)\}^{1/2}/(\zeta+1), \quad (2.19)$$

$$F_2'(\zeta)=iA(B/\zeta+C/\zeta^2)/(\zeta+\xi_M)^{1/2}(\zeta-\xi_N)^{1/2}, \quad (2.20)$$

$$A=W_0/\pi, \qquad B=C(\xi_N-\xi_M)/2\xi_M\xi_N. \quad (2.21)$$

The elastodynamic crack bifurcation stress intensity factor for prescribed displacements is now given by (2.13) with (τ_0/μ) replaced by (W_0/c), and with (2.19)–(2.21) used in (2.8*b*,*c*).

3 Skew Crack Propagation

On applying a sudden antiplane mechanical disturbance to the half plane, one crack is assumed to propagate from the surface with constant velocity v making an angle $\kappa\pi$ with the normal to the surface (Fig. 1—the points C and M are assumed to coalesce to point L). The similarities with the analysis in Section 2 are used here to abbreviate this skew crack treatment.

The mapping from the physical plane to the γ-plane is again accomplished using Chaplygin's transformation, while that from the γ-plane to the ζ-plane is accomplished using the Schwarz-Christoffel transformation given in equations (25)–(28) of [7], in which $\xi_p \equiv \xi_L$, $\xi_Q \equiv \xi_N$.

Problem 3: Prescribed Surface Tractions. The boundary conditions in the ζ-plane for loading Cases (*a*) and (*b*) are

$$-\infty<\xi<-\xi_G: \quad \dot{w}=c\,\tau_0/\mu, \quad \partial\dot{w}/\partial\xi=0, \quad (3.1a)$$

$$-\xi_G<\xi<-1: \quad \dot{w}=-c\,\tau_0/\mu, \quad \partial\dot{w}/\partial\xi=0, \quad (3.1b)$$

$$-1<\xi<1: \quad \dot{\tau}_{\theta z}=0 \quad \partial\dot{w}/\partial\eta=0, \quad (3.1c)$$

$$1<\xi<\infty: \quad \dot{w}=c\,\tau_0/\mu, \quad \partial\dot{w}/\partial\xi=0. \quad (3.1d)$$

The appropriate form for $F'(\zeta)$, noting (2.4), is given by

$$F_1'(\zeta)=iA(\xi_G^2-1)^{1/2}/(\zeta+\xi_G)(\zeta^2-1)^{1/2}, \quad (3.2)$$

$$F_2'(\zeta)=iAC/\zeta^2(\zeta^2-1)^{1/2}. \quad (3.3)$$

The boundary conditions determine that $A=2c\tau_0/\mu\pi$. The constant C is again determined by the regular part of the stress ahead of the crack tip. Equations (2.7) and (2.8), along with (3.3), are used. The elastodynamic skew crack stress intensity factors for loading Cases (*a*) and (*c*) are again given by (2.13) and (2.16), respectively, although here

$$H=-2\{(c/v)(1-v^2/c^2)^{3/2}h/\pi\}^{1/2}, \quad (3.4)$$

$$h=(1/2+\kappa)(1-\xi_L^2)^{1/2}\xi_L^2+(1/2-\kappa)(1-\xi_N^2)^{1/2}/\xi_N^2. \quad (3.5)$$

and (3.2) and (3.3) are now used to define (2.8*b*,*c*).

Problem 4: Prescribed Surface Displacements. Traction-free skew crack propagation under the applied, discontinuous, surface displacements defined in (2.17) is considered here. The boundary conditions in the ζ-plane are:

$$-\infty<\xi<-\xi_G: \quad \dot{w}=W_0, \quad \partial\dot{w}/\partial\xi=0, \quad (3.6a)$$

$$-\xi_G<\xi<-\xi_L: \quad \dot{w}=-W_0, \quad \partial\dot{w}/\partial\xi=0, \quad (3.6b)$$

$$-\xi_L<\xi<\xi_N: \quad \dot{\tau}_{\theta z}=0, \quad \partial\dot{w}/\partial\eta=0, \quad (3.6c)$$

$$\xi_N<\xi<\infty: \quad \dot{w}=W_0, \quad \partial\dot{w}/\partial\xi=0. \quad (3.6d)$$

Noting (2.4), $F'(\zeta)$ is given here by

$$F_1'(\zeta)=iA\{(\xi_G-\xi_L)(\xi_G+\xi_N)/(\zeta+\xi_L)(\zeta-\xi_N)\}^{1/2}/(\zeta+\xi_G), \quad (3.7)$$

$$F_2'(\zeta)=iA(B/\zeta+C/\zeta^2)/(\zeta+\xi_L)^{1/2}(\zeta-\xi_N)^{1/2}, \quad (3.8)$$

$$A=2W_0/\pi, \quad B=C(\xi_N-\xi_L)/2\xi_L\xi_N. \quad (3.9)$$

The elastodynamic skew crack stress intensity factor for prescribed displacements is now given by (2.13) with (τ_0/μ) replaced by (W_0/c), with H as defined in (3.4), and with (3.7)–(3.9) being used to define (2.8*b*,*c*).

4 Analytical Solutions and Numerical Analysis

In Sections 2 and 3 expressions for the elastodynamic stress intensity factors for the rapid tearing of a half plane and subsequent crack bifurcation or skew crack propagation under prescribed surface tractions and displacements are derived. The evaluation of these stress intensity factors for given values of κ and v/c generally involves numerical computation, since the relationship between $\gamma=\cosh^{-1}(ct/r)+i\theta$ and $\zeta=\xi+i\eta$ is rarely invertible. In these rare instances, explicit expressions for ζ in terms of r/t and θ allow fully analytical solutions to be obtained. These closed-form solutions in turn can be used to reveal the weight functions appropriate for the numerical evaluation of I_3 and I_4 in (2.8*b*,*c*). In addition, they provide check cases for the numerical treatment of those geometries for which the Schwarz-Christoffel mapping is not invertible.

Prescribed Surface Tractions. The simplest problem that can be treated analytically is now discussed. Consider the half-plane surfaces dynamically loaded by $\tau_{\theta z}=\tau_0 H(t)$, but with no ensuing crack propagation. The mapping (2.1) can be inverted in this case:

$$\zeta=\operatorname{sech} 2(\gamma-i\pi/2), \quad (4.1)$$

and $F'(\zeta)$ is now given by $F_1'(\zeta)$ in (2.5). Noting that $\dot{w}=Re\,F(\zeta)$, and that $\dot{\tau}_{\theta z}=-(u/r)\,Im[F'(\zeta)\zeta'(\gamma)]$, it can be shown that

$$\dot{\tau}_{\theta z}=2^{3/2}(c\,\tau_0/\pi r)\,Im\,\zeta^{1/2}/(1+\zeta)^{1/2} \quad (4.2)$$

The shear stress is therefore given by, using (4.1) and (4.2),

$$\tau_{\theta z}=2\left(\frac{\tau_0}{\pi}\right)\cos(\theta)\int_{r/c}^{t}\frac{(x^2-r^2/c^2)^{1/2}}{[x^2-(r^2/c^2)\cos^2(\theta)]}dx + \tau_0\,\mathrm{sgn}(\theta)\sin(\theta)H[t-(r/c)\cos(\theta)]. \quad (4.3)$$

After integrating the preceding integral

$$\tau_{\theta z}=2\left(\frac{\tau_0}{\pi}\right)\cos(\theta)\cosh^{-1}(ct/r)H(t-r/c) + \tau_0\,\mathrm{sgn}(\theta)\sin(\theta)H[t-(r/c)\cos(\theta)] + \left(\frac{\tau_0}{\pi}\right)\mathrm{sgn}(\theta)\sin(\theta)H(t-r/c)\left\{\sin^{-1}\left(\frac{r-ct\cos(\theta)}{ct-r\cos(\theta)}\right) - \sin^{-1}\left(\frac{ct\cos(\theta)+r}{ct+r\cos(\theta)}\right)\right\}. \quad (4.4)$$

Note that the shear stress is logarithmically singular as $t/r\to\infty$; this behavior is not unexpected since the logarithmic nature of the singularity occurs in both the static case, as revealed by the method of Williams [4, 5], and in a related transient analysis [6]. The use of $F_2'(\zeta)$ in (2.6) would give rise to behavior that is too singular for the deformation considered in the foregoing.

The second case considered is crack propagation normal to the half-plane surface ($\kappa=0$ in Fig. 1) upon application of the loading considered previously. The inversion of (2.1) now gives

$$\zeta=\frac{1+\xi_N\cosh 2(\gamma-i\pi/2)}{\xi_N+\cosh 2(\gamma-i\pi/2)}, \quad (4.5)$$

Downloaded 02 May 2010 to 171.66.16.54. Redistribution subject to ASME license or copyright; see http://www.asme.org/terms/Terms_Use.cfm

where $\xi_N = (2c^2/v^2 - 1)^{-1}$, $\xi_M = 0$. The appropriate choice of $F'(\zeta)$ is given by (2.4)–(2.6) with $C = 0$. It follows that

$$\dot{\tau}_{\theta z} = 2(c\,\tau_0/\pi r)[1-\xi_N^2]^{-1/2} Im\{[2^{1/2}\zeta + B(\zeta+1)](\zeta-\xi_N)/\zeta^{3/2}(1+\zeta)\}. \quad (4.6)$$

The explicit dependence of ζ on r/t and θ is given by (4.5), from which it can be determined that for $r > vt$ and $\theta = 0$,

$$\zeta = \xi = -(s^2 - v^2)/[(c^2 - s^2) + (c^2 - v^2)], \quad (4.7)$$

where $s = r/t$. Hence $\dot{\tau}_{\theta z}(r > vt,\ \theta = 0)$ is singular as $(r-vt)^{-3/2}$, because of the $\zeta^{-3/2}$ term in (4.6). The appropriate traveling crack-tip singularity is therefore present; the preceding requirement that $C = 0$ in (2.6) again precludes the presence of physically unrealistic singular behavior.

At this point it is appropriate to observe that for $\kappa = 0$, $\zeta \sim (r-vt)$ near the crack tip, but for $\kappa \neq 0$, $\zeta \sim (r-vt)^{1/2}$. The term C/ζ^2 is included in each of the $F_2'(\zeta)$'s defined in this paper to give the appropriate crack-tip singularity for $\kappa \neq 0$. Since the analysis in [7] does not include either of the terms B/ζ or C/ζ^2, their results cannot be correct for $\kappa = 0$ or $\kappa \neq 0$, respecively, as is verified in the following.

The shear stress ahead of the crack tip, obtained using (4.6) and (4.7), is given by

$$\tau_{\theta z}(r > vt, \theta = 0) = 2(\tau_0/\pi)(1 - v^2/c^2)^{1/2}(c/v)^2[-2B(r/ct)\,(c^2t^2 - r^2)^{1/2}/(r^2 - v^2t^2)^{1/2} + (v/c)^2 F(p,q) + 2B\,E(p,q)], \quad (4.8)$$

in which $F(p,q)$ and $E(p,q)$ are incomplete elliptic integrals of the first and second kind, respectively, and

$$q = (1 - v^2/c^2)^{1/2}, \quad p = \sin^{-1}\{(1 - r^2/c^2t^2)^{1/2}/q\} \quad (4.9)$$

Note the $(r-vt)^{1/2}$ singularity present in $\tau_{\theta z}(r > vt, \theta = 0)$. $F(\pi/2, q) = K(q)$ and $E(\pi/2, q) = E(q)$ are complete elliptic integrals of the first and second kind, respectively; for definitions of these integrals, see Gradshteyn and Ryzhik [8]. Consistent with the loading Cases (*a*) and (*b*) treated in Sections 2 and 3 we require that the regular part of $\tau_{\theta z}$ in (4.8) $\to 0$, $-\tau_0$, respecively, as $(r-vt) \to 0^+$ on $\theta = 0$. This determines B for each loading case; loading Case (*c*) is solved by using superposition. Finally, the stress intensity factors may be obtained, using (2.12), as

$$K_{III}^q(\kappa = 0) = \tau_0(ct)^{1/2} 2\pi^{-1/2}(v/c)^{1/2}(1 - v^2/c^2)K(q)/E(q), \quad (4.10)$$

$$K_{III}^c(\kappa = 0) = \tau_0(ct)^{1/2}\pi^{1/2}(v/c)^{1/2}(1 - v^2/c^2)^{1/2}/E(q), \quad (4.11)$$

while $K_{III}^b = K_{III}^q + K_{III}^c$.

The bifurcation stress-intensity factor for prescribed surface tractions, given in Section 2, in the limit as $\kappa \to 0$ is expected from consideration of energy flux into the crack tip regions, to be $2^{-1/2}$ times the values given in (4.10) and (4.11) for crack propagation with no bifurcation. Also, the skew crack stress intensity factor for prescribed surface tractions, given in Section 3, should agree exactly with those in (4.10) and (4.11) for $\kappa = 0$.

The final case considered is symmetric bifurcation with $\kappa = \pm 1/4$. Again (2.1) is invertible, giving

$$\zeta^2 = 1 - (1 - \xi_N^2)\tanh^2 2(\gamma - i\pi/2), \quad (4.12)$$

where $\xi_N = \xi_M = (v^2/c^2)/(2 - v^2/c^2)$. $F'(\zeta)$ is given by (2.4)–(2.6). The shear stress ahead of the crack tip is

$$\tau_{\theta z}(r > vt, \theta = \pi/4) = (\tau_0/\pi)(2 - v^2/c^2)(1 - v^2/c^2)^{-1/2}(c/v)^2[B\,E(p,q) + 2(2 - v^2/c^2)^{-1/2}(1 - v^2/c^2)^{1/2}(v/c)^2\{F(p,q) - \Pi(p, -q^2, q)\} - B(r/ct)\,(c^2t^2 - r^2)^{1/2}/(r^2 - v^2t^2)^{1/2}] + \tau_0/2^{1/2}, \quad (4.13)$$

in which

$$\Pi(\phi, n, k) = \int_0^{\sin\phi} \frac{dx}{(1 - nx^2)(1 - x^2)^{1/2}(1 - k^2x^2)^{1/2}}. \quad (4.14)$$

Note that $\Pi(\phi, n, k)$ in [8] should be defined as in (4.14). The constant B is obtained by considering the behavior of the regular part of $\tau_{\theta z}$ as $(r-vt) \to 0^+$ on $\theta = \pi/4$, as discussed earlier. Finally, it is found that

$$K_{III}^a(\kappa = 1/4) = \tau_0(ct)^{1/2}(2/\pi)^{1/2}(v/c)^{1/2}(1 - v^2/c^2)^{1/2}\{2^{1/2}(2 - v^2/c^2)^{1/2}[K(q) - \Pi(\pi/2, -q^2, q)] + \pi/2\}/E(q), \quad (4.15)$$

$$K_{III}^c(\kappa = 1/4) = \tau_0(ct)^{1/2}\pi^{1/2}(v/c)^{1/2}(1 - v^2/c^2)^{1/2}/E(q). \quad (4.16)$$

The dependence of the elastodynamic stress intensity factors on the velocity of crack-tip motion v/c and different crack angles $\kappa\pi$ is shown in Figs. 3 and 4 for crack bifurcation and skew crack propagation, respectively, under loading Case (*a*). The general expression in (2.13) is evaluated using either (2.5), (2.6), and (2.14), (2.15) for crack bifurcation or (3.2)–(3.5) for skew crack propagation. Guass-Jacobi quadrature [9] is used to compute the integrals. The analytical solutions in (4.10) and (4.15) provided invaluable checks on the accuracy. As indicated in Figs. 3 and 4, the stress intensity factor behaves as $(v/c)^{1/2}$ for each κ; this factor is evident in (4.10) and (4.15). The lack of the inverse-square-root crack-tip singularity in $\tau_{\theta z}$ for the uncracked half plane, as shown in (4.4), necessitates the foregoing behavior, since for any length of crack the singularity exists.

The stress intensity factors given by the curve $\kappa = 0$ in Fig. 3 for crack propagation normal to the half plane under prescribed surface tractions agree with those given by Brock and Achenbach [10] (see the solid curve in Fig. 3 of [10] for $k = m = 1$ and note that the stress intensity factors differ in definition by a factor of $(2\pi)^{1/2}$). These results do not agree with those in Fig. 4 of [7].

From Figs. 3 and 4 it is evident that the stress intensity factors tend to zero both as the crack tip velocity vanishes and as the tip velocity approaches the shear wave speed, c. The maximum values occur for $v \approx 0.4c$ and increase in magnitude as κ tends toward the value $\kappa = 1/2$—that is, as the branching angle increases. Apparently crack propagation just under the surface is the most likely failure mode.

Prescribed Surface Displacements. The half plane subjected to the antiplane displacement loading $w = \pm W_0 t\,H(t)$, with no ensuing crack propagation, is examined first. The mapping is again given by (4.1), and $F'(\zeta)$ is equal to $F_1'(\zeta)$ in (2.19) (note that $\xi_M = \xi_N = \xi_D = 0$). In this problem

$$\tau_{\theta z} = 2\left(\frac{\mu W_0}{\pi c}\right)(c^2t^2/r^2 - 1)^{1/2} H(t - r/c) + \left(\frac{\mu W_0}{c}\right)\mathrm{sgn}(\theta)\sin(\theta)\,H[t - (r/c)\cos(\theta)] + \left(\frac{\mu W_0}{\pi c}\right)\mathrm{sgn}(\theta)\sin(\theta)\,H(t - r/c)\left\{\sin^{-1}\left(\frac{r - ct\cos(\theta)}{ct - r\cos(\theta)}\right) + \sin^{-1}\left(\frac{r + ct\cos(\theta)}{ct + r\cos(\theta)}\right) - \pi\right\}. \quad (4.17)$$

As $t/r \to \infty$, the shear stress is singular as t/r; this behavior is not unexpected since the continuity of displacements as $r \to 0$ is not maintained.

The second geometry considered is crack propagation normal to the half plane surface ($\kappa = 0$ in Fig. 1) upon application of the previous loading. The mapping is given by

Downloaded 02 May 2010 to 171.66.16.54. Redistribution subject to ASME license or copyright; see http://www.asme.org/terms/Terms_Use.cfm

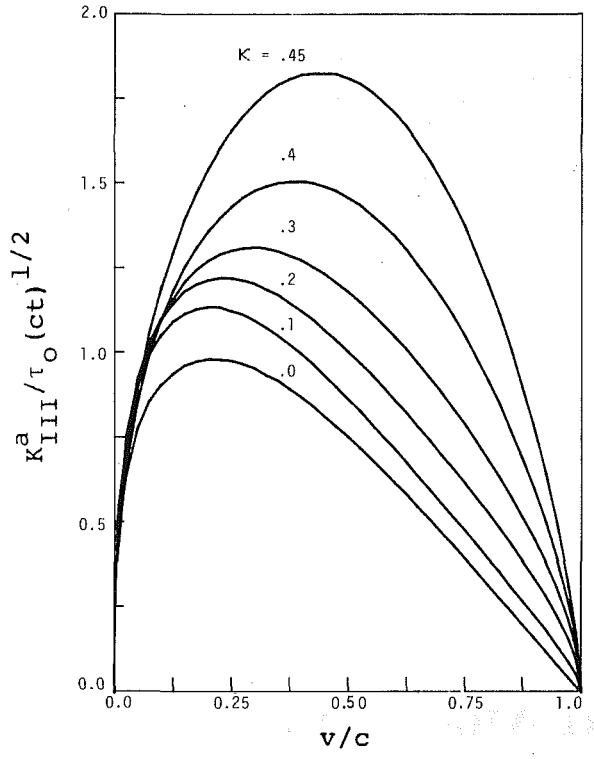


Fig. 3 Stress intensity factors for crack bifurcation under prescribed surface tractions: loading Case (a)

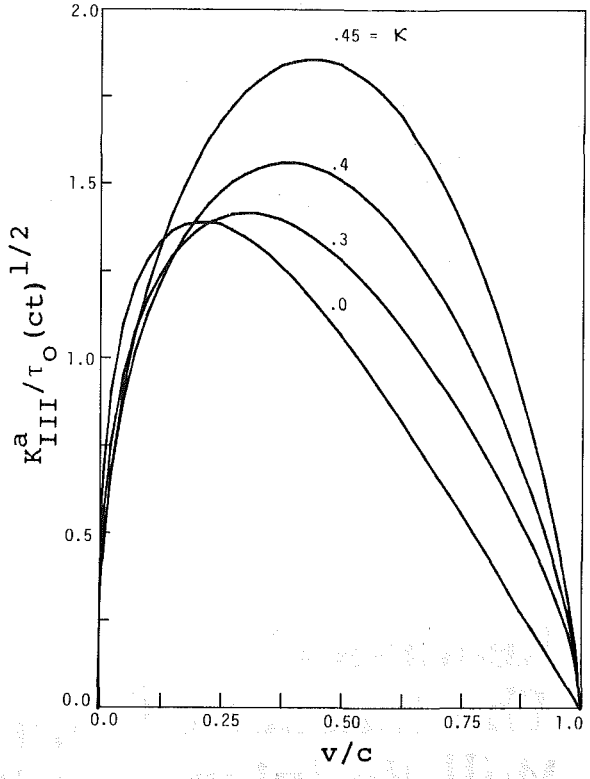


Fig. 4 Stress intensity factors for skew crack propagation under prescribed surface tractions: loading case (a)

(4.4) ($\xi_M = 0$), and $F'(\zeta)$ is defined in (2.4) and (2.19)–(2.21) with $C = 0$. The shear stress ahead of the crack tip is

$$\tau_{\theta z}(r > vt, \theta = 0) = 2\mu\left(\frac{W_0}{\pi}\right)\left(1 - \frac{v^2}{c^2}\right)^{1/2}$$

$$\times\left\{-B\,2^{1/2}(2 - v^2/c^2)^{1/2}(c/v^2)\left(\frac{c^2t^2 - r^2}{r^2 - v^2t^2}\right)^{1/2}\right.$$

$$\left. + \left[1 + B\,2^{1/2}\left(2 - \frac{v^2}{c^2}\right)^{1/2}(c/v)^2\right]\right.$$

$$\left.\times\left(\frac{2}{c}\right)\left(1 + \frac{v}{c}\right)^{-1}[2\Pi(\lambda,\rho,\rho) - F(\lambda,\rho)]\right\}, \quad (4.18)$$

in which $\Pi(\lambda,\rho,\rho)$ is defined in (4.14) and $F(\lambda,\rho)$ in [8], where

$$\lambda = \sin^{-1}\left\{\frac{(c+v)(ct-r)}{(c-v)(ct+r)}\right\}^{1/2}, \quad \rho = \frac{c-v}{c+v}. \quad (4.19)$$

For the problem being examined here, the elastodynamic stress intensity factor is found to be given by

$$K_{III}(\kappa = 0) = (\mu W_0/c)(ct)^{1/2}2\pi^{-1/2}(1 - v^2/c^2)(v/c)^{-1/2}. \quad (4.20)$$

The preceding expression for crack propagation normal to half-plane surfaces that are subjected to discontinuous surface displacements is remarkably simple and indicates clearly that the stress intensity factors for different $\kappa\pi$ do not remain bounded as the crack tip velocity vanishes. This behavior is expected since the shear stress in (4.17) is more singular than $(t/r)^{1/2}$ as $t/r \to \infty$. The results in Fig. 5 of [7] do not indicate this behavior, further evidence of the importance of the additional terms $F_2'(\zeta)$.

It is important to note that the nonintegrable strain-energy density evident in (4.17) as $(t/r) \to \infty$ makes any discussion of an untorn state, under the displacements prescribed, unrealistic in the realm of brittle fracture mechanics. In fact, the energy flux F into the crack tip (defined in [11]) for crack propagation normal to the half plane is given by $F = (2\mu W_0/\pi)(1 - v^2/c^2)^{3/2}t$. This expression is finite for zero crack tip velocity! A more physical situation is to have displacement loading of the type considered but in the presence of a preexisting very small flaw, which may be oblique to the half-plane surface. After propagating to several times its initial length, the information contained in (4.20) should be "accurate." The latter observation, which essentially relates a self-similar solution to a nonself-similar problem, is substantiated by the work of Rose [12, 13].

For symmetric bifurcation and $\kappa = 1/4$ the expression for the stress intensity factor is lengthy and is not presented here. Moreover, the strong initial singularity present in this prescribed surface displacement problem so dominates the stress and particle velocity fields that little variation with κ is observed. In fact, the slight varation of the stress intensity factors with the branching angle $\kappa\pi$ is perhaps best understood by noting that the singular term in the expression for $\tau_{\theta z}$ with no tearing (4.17) contains no θ variation. The analytical solution for $\kappa = 1/4$ is very useful, however, since it provides the only check case for nonero κ.

In conclusion, the bifurcation stress-intensity factor for prescribed surface displacements, in the limit as $\kappa \to 0$ is $2^{-1/2}$ times the value given in (4.20) for crack propagation with no bifurcation. Also, the skew crack stress intensity factor is given by (4.20) for $\kappa = 0$. Because of the lack of variation of the stress intensity factors with κ, no figures showing the results of the numerical analysis for different κ are included here.

References

1 Burgers, P., and Dempsey, J. P., "Two Analytical Solutions for Dynamic Crack Bifurcation in Antiplane Strain," ASME JOURNAL OF APPLIED MECHANICS, Vol. 49, 1982, pp. 366–370.

Downloaded 02 May 2010 to 171.66.16.54. Redistribution subject to ASME license or copyright; see http://www.asme.org/terms/Terms_Use.cfm

2 Burgers, P., "Dynamic Propagation of a Kinked or Bifurcated Crack in Antiplane Strain," ASME JOURNAL OF APPLIED MECHANICS, 1982, Vol. 49, pp. 371–376.

3 Dempsey, J. P., Kuo, M.-K., and Achenbach, J. D., "Mode III Crack Kinking under Stress-Wave Loading," *Wave Motion*, Vol. 4, 1982, pp. 181–190.

4 Williams, M. L., "Stress Singularities Resulting From Various Boundary Conditions in Angular Corners of Plates in Extension," ASME JOURNAL OF APPLIED MECHANICS, Vol. 19, 1952, pp. 526–528.

5 Dempsey, J. P., "The Wedge Subjected to Tractions: A Paradox Resolved," *J. Elasticity*, Vol. II, 1981, pp. 1–10.

6 Achenbach, J. D., "Transient Shear Waves in Two Joined Elastic Quarter-Spaces," ASME JOURNAL OF APPLIED MECHANICS, Vol. 36, 1969, pp. 491–496.

7 Achenbach, J. D., and Varatharajulu, V. K., "Elastodynamic Stress Intensity Factors for Tearing of a Half Plane," ASME JOURNAL OF APPLIED MECHANICS, Vol. 41, 1974, pp. 1099–1105.

8 Gradshteyn, I. S., and Ryzhik, I. M., *Table of Integrals, Series, and Products*, Academic Press, New York, 1980.

9 A. H. Stroud and D. Secrest, *Gaussian Quadrature Formulas*, Prentice-Hall, Englewood Cliffs, N.J.

10 Brock, L. M., and Achenbach, J. D., Rapid Tearing Along an Interface, *J. Appl. Math. Phys. (ZAMP)*, Vol. 25, 1974, pp. 331–345.

11 Achenbach, J. D., "Wave Propagation, Elastodynamic Stress Singularities, and Fracture," *Proc. 14th IUTAM Congress, Delft, The Netherlands*, W. T. Koiter, ed., 1976.

12 Rose, L. R. F., "Recent Theoretical and Experimental Results on Fast Brittle Fracture," *Int. J. Fracture*, Vol. 12, 1976, pp. 799–813.

13 Rose, L. R. F., "On The Initial Motion of a Griffith Crack," *Int. J. Fracture*, Vol. 12, 1976, pp. 829–841.

Downloaded 02 May 2010 to 171.66.16.54. Redistribution subject to ASME license or copyright; see http://www.asme.org/terms/Terms_Use.cfm

Analysis of the Reflection of Point Force-Induced Crack Surface Waves by a Crack Edge

L. M. Brock
Department of Engineering Mechanics,
University of Kentucky,
Lexington, Ky. 40506

H. P. Rossmanith
Institute of Mechanics,
Technical University of Vienna,
Karlsplatz 13,
A-1040 Vienna, Austria

Dynamic stress fields near cracks follow in part from the reflection of crack surface waves by the crack edges. To gain insight into the reflection process, the problem of stationary normal and tangential point forces applied to one surface of a stationary semi-infinite crack is considered, and analytical expressions for the crack surface reflection-generated particle velocity waves presented. Study of these expressions shows that the dominant reflected wave is singular at its wave front, travels at the Rayleigh speed, and is generated by the reflection of a singular Rayleigh wave. However, the reflection process "moves" the singularity from the velocity component parallel to the particular force to the component normal to it.

Introduction

The dynamic field generated at one edge of a finite internal crack by stress wave loading arises eventually from crack surface waves reflected from the other edge. Similarly, the single edge of a crack in a material boundary generates a dynamic field in part by reflecting waves produced along the crack surfaces by boundary disturbances.

From the fracture mechanics viewpoint, these reflections influence the stress state and, therefore, the possibility of fracture at the crack edges [1, 2]. From the viewpoint of nondestructive testing, the dynamic field generated by the crack edge scattering and reflection of ultrasonic waves [3, 4] provides information for crack detection and characterization.

Analysis of the reflection process, however, can be complicated. Finite element and finite difference studies of such situations [5] do not always allow a complete wave signal identification. Yet, photoelastic results [6] show that a crack edge stress field induced by crack-elastic wave interaction is sensitive to individual signals, a conclusions confirmed by analysis [1, 7] specifically of interaction due to wave reflection.

This paper therefore provides insight into the reflection of crack surface waves at a crack edge by examining the two-dimensional problem of stationary tangential and normal point forces (line loads in the out-of-plane direction) applied suddenly to one surface of a stationary semi-infinite crack. This problem exhibits all three (dilatational, rotational, Rayleigh) possible wave speeds, as well as a characteristic length (the point force-crack edge separation). The problem analysis is exact, as opposed to studies involving time-harmonic incident waves of no specific source or high-frequency approximations, e.g., [3, 4].

The problem analysis is given in the next section, and the solution, whose basic ingredients can be found in [7], is briefly outlined. The results are then used to derive explicit formulas for the particle velocities generated on both crack surfaces by the reflection of the point force-induced waves. The various signals comprising the velocities are identified and studied. The velocities at various crack surface locations are then plotted versus a time parameter, and comparison is made with the point force-induced velocities.

Problem Formulation

As seen in Fig. 1(*a*), a semi-infinite crack in an unbounded, isotropic, homogeneous, linearly elastic solid is defined in terms of the Cartesian coordinates (x,y) by $y=0$, $x<0$. For $s<0$, where s = (dilatational wave speed) x (time), the solid is at rest. For $s>0$ normal (N) and tangential (S) point forces are applied to the lower crack surface $y=0-$ at $x=-h$. We then have for $y=0$

$$x<0: \quad \mathbf{j}\cdot\boldsymbol{\sigma}^{+}=0; \quad \mathbf{j}\cdot\boldsymbol{\sigma}^{-}=-(S,N)\,\delta(x+h)\,H(s) \tag{1}$$

$$x>0: \quad \mathbf{u}^{-}-\mathbf{u}^{+}=\mathbf{0} \tag{2}$$

where $(\mathbf{u},\boldsymbol{\sigma})$ are the two-dimensional displacement vector and stress tensor, $\mathbf{j}$ is the basis vector parallel to y, $(\cdot)$ denotes the inner product, (δ,H) are the Dirac and Heaviside functions, and the arrangement $(\ldots,\ldots)$ often denotes the (x,y)-components of a vector. For $\pm y>0$, Hooke's Law and the displacement equations of motion in the absence of body force terms hold when $s>0$, while $\mathbf{u}\equiv\mathbf{0}$ for $s\leq 0$ [7].

When (S,N) are applied, the wave-front pattern shown in Fig. 1(*a*) is generated in the half-plane $y<0$ for $s<h$. For $s>h$, the pattern is diffracted at the crack edge, i.e., its surface intersection is reflected at the crack edge. Figure 1(*b*) shows the resulting wave pattern after the point force-induced

Contributed by the Applied Mechanics Division and presented at the Winter Annual Meeting, New Orleans, La., December 9-14, 1984 of THE AMERICAN SOCIETY OF MECHANICAL ENGINEERS.

Discussion on this paper should be addressed to the Editorial Department, ASME, United Engineering Center, 345 East 47th Street, New York, N.Y. 10017, and will be accepted until two months after final publication of the paper itself in the JOURNAL OF APPLIED MECHANICS. Manuscript received by ASME Applied Mechanics Division, September, 1983; final revision, May, 1984. Paper No. 84-WA/APM-47.

Copies will be available until August, 1985.

Copyright © 1985 by ASME
Downloaded 02 May 2010 to 171.66.16.54. Redistribution subject to ASME license or copyright; see http://www.asme.org/terms/Terms_Use.cfm

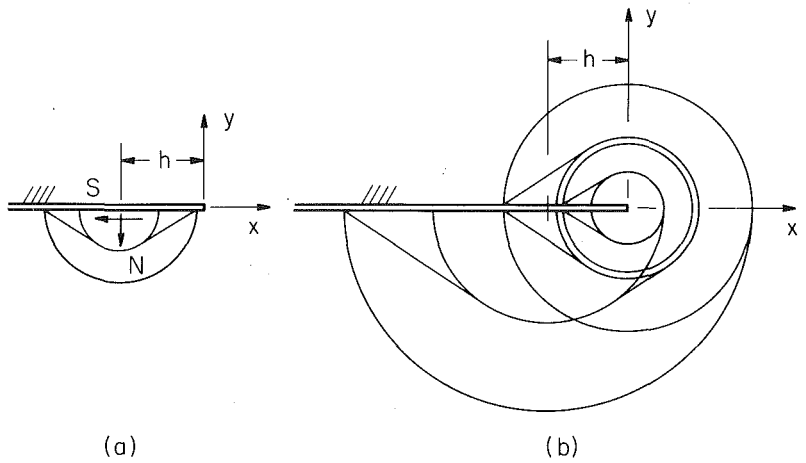


Fig. 1 (*a*) Point force application and wave pattern for $0 < s < h$, and (*b*) wave pattern for $s > mh$

rotational wave has reached the crack edge ($s > mh$). In this paper, all speeds are non-dimensionalized by dividing by the dilatational wave speed. Thus, the constant $1/m$ is the nondimensionalized rotational wave speed, and $m > 1$.

Problem Solution

As noted in [7], the characteristic length h makes a direct problem solution difficult. Instead, then, the problem is viewed as a superposition of the two Lamb's problems [8] obtained by relaxing (2), i.e., separating the two half-planes for all $y = 0$, and the problem of displacement discontinuities propagating ahead of a stationary stress-free crack, which exactly cancels the difference in the two Lamb's problem surface displacements for $x > 0$.

Clearly, the Lamb's problem solution for the half-plane $y > 0$ vanishes identically. The Lamb's problem for the half-plane $y < 0$ has no characteristic length and is readily solved [7] for the surface displacement

$$\pi\mu \mathbf{u}_L^- = N\int_1^{s/X} Im\left(\mp q\frac{P}{R},\ \frac{a}{R}m^2\right)dq$$

$$+S\int_1^{s/X} Im\left(\frac{b}{R}m^2,\ \pm q\frac{P}{R}\right)dq \tag{3}$$

$$P = T - 2ab,\ R = T^2 + 4q^2ab,\ T = b^2 - q^2 \tag{4}$$

where μ is the shear modulus, $X = |x+h|$, integration is along the lower side of the $Re(q)$-axis, $\pm$ denotes the sign of $x+h$, and

$$a = a_+a_-,\quad b = b_+b_-,\quad a_\pm = \sqrt{(1\pm q)},\quad b_\pm = \sqrt{(m\pm q)} \tag{5}$$

The radicals $(a_\pm, b_\pm)$ are defined in the q-plane cut along $Im(q) = 0,\ \pm Re(q) > (-1, -m)$ so that $Re(a_\pm, a), Re(b_\pm, b) \geq 0$. Here R is the Rayleigh function with zeroes $q = \pm n$, where $1/n$ is the nondimensionalized Rayleigh speed and $n > m > 1$.

Equation (3) shows that $\mathbf{u}_L^-$ is a function of the ratio X/s, where $0 \leq X/s < 1$. Thus, for a given value $X/s = c$, the corresponding value $\mathbf{u}_L^-(c)$ in effect travels away from the point $x = -h$ with the nondimensionalized "speed" c. It reaches the point $x = 0$ at $s_0 = h/c$. Conversely for an $x = 0$ arrival to occur at a given s, we must have $c = h/s$. Based on these observations, the stress-free crack problem can be solved by a procedure devised in [1]. As used in [7], this procedure first considers the problem of a uniform discontinuity Δ in the displacement $\mathbf{u}$ along $y = 0$ appearing ahead of the crack edge at $s = 0$ and propagating ahead of it with a constant nondimensionalized speed c, where $0 < c < 1$. That is, (S,N) vanish in (1) while (2) is replaced by

$$\mathbf{u}^- - \mathbf{u}^+ = \Delta H(cs - x) \tag{6}$$

for $x > 0$. This new problem has no characteristic length, and so is readily solved. It can be shown that any scalar field variable in the solution has the form $\Delta \cdot \mathbf{f}(x,y,s,c)$. If the discontinuity appears at the crack-edge at $s_0 = h/c$ and Δ is replaced by $-d\mathbf{u}_L^-(c)$, then this form becomes $-d\mathbf{u}_L^-(c) \cdot \mathbf{f}(x,y,s-s_0,c)$. In view of the preceding discussion, this new form can be summed with respect to c over $h/s < c < 1$ to give the corresponding scalar field variable for the stress-free crack problem. Thus, if (F, F_L, F_C) are corresponding scalar field variables for, respectively, the original, Lamb's and stress-free crack problem, then

$$F^\pm = F_L^\pm + F_C^\pm H(s-h),\quad F_L^+ \equiv 0 \tag{7}$$

$$F_C^\pm = \int_{h/s}^1 \mathbf{f}(x,y,s-h/c,c) \cdot \frac{d\mathbf{u}_L^-(c)}{dc}\,dc \tag{8}$$

for $\pm y > 0$. The form of (7) shows that the stress-free crack problem solutions are in fact the solutions generated by the crack surface wave reflections. Subsequently, then, our attention is focused on (8).

Particle Velocities Due to Reflections

For the tangential and normal components of the nondimensionalized particle velocity $\dot{\mathbf{u}}_C^\pm$ generated on the crack surfaces $\pm y = 0, x < 0$ by reflection, it is readily shown that the functions $\mathbf{f}(x,0,s-h/c,c)$ in (8) are

$$2\pi|x|\mathbf{f} = Im\left[\frac{H(q-1)}{(q-n)(q+k)G_-}\left(\pm C_x b_-, -\frac{C_y}{m^2}\frac{qP}{a_+}\right)\right] \tag{9}$$

$$2\pi|x|\mathbf{f} = Im\left[\frac{H(q-1)}{(q-n)(q+k)G_-}\left(\frac{C_x}{m^2}\frac{qP}{b_+}, \pm C_y a_-\right)\right], \tag{10}$$

respectively. Here $(\cdot)$ denotes s-differentiation,

$$a_+(k)C_x = (k+n)G_+(k),\ |x|q = s - kh, k = 1/c \tag{11}$$

$$lnG_\pm(q) = -\frac{1}{\pi}\int_1^m \frac{1}{w\pm q}\tan^{-1}\left(\frac{4w^2|a|b}{T^2}\right)dw, \tag{12}$$

C_y follows from C_x by replacing a_+ with b_+ and the right-hand side of (9) and (10) are evaluated along the upper side of the $Re(q)$-axis. From (3)

$$\pi\mu c^2\frac{d\mathbf{u}_L^-(c)}{dc} = -NIm\left(k\frac{P}{R}, \frac{a}{R}m^2\right)H(1-c)$$

$$+SIm\left(-\frac{b}{R}m^2, k\frac{P}{R}\right)H(1-c) \tag{13}$$

where the right-hand side is a function of k evaluated along

Downloaded 02 May 2010 to 171.66.16.54. Redistribution subject to ASME license or copyright; see http://www.asme.org/terms/Terms_Use.cfm

the lower side of the $Re(k)$-axis. Substitution of (9)–(13) into (8) gives formal expressions for $\dot{\mathbf{u}}_C^{\pm}$. For purposes of analysis and computation, however, more explicit results are needed. To obtain these, we integrate with respect to the variable k in (8) and introduce the dimensionless parameters

$$\tau = s/h, \quad z = |x|/h \tag{14}$$

By varying (τ,z) and studying the resulting alignment of integration limits and integrand branch cuts and poles along the $Re(k)$-axis, the formal integrations for $\dot{\mathbf{u}}_C^{\pm}$ can easily be written as simple combinations of real integrals. In carrying out this process, it is helpful to note that the Riemann sheets chosen for $(a_{\pm},\ b_{\pm})$ imply that quantities in (9)–(13) evaluated along opposite sides of the $Re(q,k)$-axes are complex conjugates, and that the relation $2Im(A)Im(B) = Re[B(\bar{A}-A)] = Re[A(\bar{B}-B)]$ aids in extracting residues due to the Rayleigh functions $R(q), R(k)$. Here $(\bar{\ })$ denotes the complex conjugate.

Expressions for Reflection-Generated Particle Velocities

Carrying out this process on (8)–(14) yields the expression

$$\mu h \dot{\mathbf{u}}_C^{+} = N(u_N, v_N) + S(u_S, v_S) \tag{15}$$

for the reflection-generated particle velocities on the crack surface $y = 0+$. In (15)

$$\begin{aligned} 4\pi z u_N = {} & (B_1C_1 - C_mA_1)_1 + (C_mB_m - A_1C_1)_{1m} \\ & + (C_mA_1 - A_mC_1)_{m1} + (A_mC_1 - C_mB_m)_m \\ & BD(q_n)[A_m(q_n)H(k_m - n) - B_1(q_n)H(k_1 - n)] \\ & + AzD(k_n)[B_m(k_n)H(k_n - m) - A_1(k_n)H(k_n - 1)] \end{aligned} \tag{16}$$

$$\begin{aligned} 4\pi z u_S = {} & (C_mC_m - B_1B_1)_1 + (B_1A_m - C_mC_m)_{1m} \\ & + (A_mB_1 - C_mC_m)_{m1} + (C_mC_m - A_mA_m)_m \\ & + AzD(k_n)C_m(k_n)[H(k_n - 1) - H(k_n - m)] \\ & + AD(q_n)C_m(q_n)[H(k_1 - n) - H(k_m - n)] \end{aligned} \tag{17}$$

where v_N and v_S follow from u_S and u_N, respectively, by interchanging the symbols A and B, C_1, and C_m. In (16) and (17)

$$a_+(n)A = b_+(n)B = \frac{n}{G_-(n)}[T(n) - 2|a(n)\|b(n)|] \tag{18}$$

$$k_\alpha = \tau - \alpha z, \quad zq = \tau - k, \quad zq_n = \tau - n \tag{19}$$

where it is noted that $k_1 > k_m > k_n$. The subscripted operators in (16) and (17) involve the simple real-line integration

$$(fg)_{\alpha\beta} = \frac{2}{\pi} m^2(1-m^2)\int_\alpha^{k_\beta} fgQdkH(k_\beta - \alpha),$$

$$Q = \frac{(k+n)D(k)(q+n)D(q)}{q+k} \tag{20}$$

where $(fg)_{\alpha\alpha} \equiv (fg)_\alpha$ and it is understood that the first and second factors in the integral are always functions of q and k, respectively. As written as functions of q, the real quantities appearing in (16)–(20) have the forms

$$A_1 = T^2\sqrt{(q-1)}, \quad B_1 = 4b^2q^2\sqrt{\left(\frac{1+q}{m+q}\right)}\sqrt{(q-1)},$$

$$C_1 = 2Tq\sqrt{(1+q)}\sqrt{(q-1)}\sqrt{|q-m|} \tag{21}$$

$$A_m = T^2\sqrt{|q-m|}, \quad B_m = 4a^2q^2\sqrt{\left(\frac{m+q}{1+q}\right)}\sqrt{|q-m|},$$

$$C_m = \sqrt{\left(\frac{m+q}{1+q}\right)}C_1 \tag{22}$$

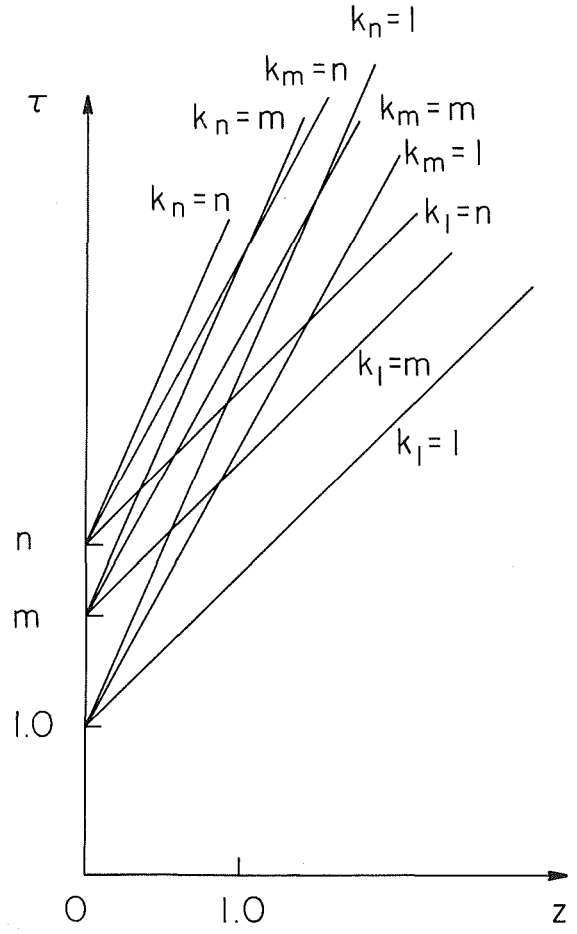


Fig. 2 Trajectories in τz-plane

$$(T^4 - 16q^4a^2b^2)D = G_+ \tag{23}$$

where it is noted that D has a first-order singularity at n.

The corresponding expressions for $\dot{\mathbf{u}}_C^{-}$ follow from (15) merely by appending the minus $(-)$ sign to the definitions of the subscripted (A,B)-terms when they are functions of q or q_n.

Examination of (16)–(23) and their v-counterparts shows that the integrands in (20) vanish in square-root fashion at their integration limits and are continuous in between—except when $k_\beta \geq n$ or $k_n \geq \alpha$. When $k_\beta = n$, the $D(k)$-singularity at $k = n$ coincides with the limit k_β and the integrand is now square-root singular and, thus, still integrable. When $k_\beta > n$, the singularity moves into the integration range, prompting integration in the Cauchy Principal Value sense. Analogous statements hold for $k_n \geq \alpha$ because of the singular behavior of $D(q)$ at $q = n(k = k_n)$. It follows that the integration does not exist when the singularities coincide within the integration range, i.e. $k_n = n$.

Study of the individual (q_n,k_n)-terms in (16) and (17) shows that they are almost always continuous in the regions of existence in the τz-plane defined by the Heaviside functions that appear with them, and vanish when the Heaviside arguments vanish. The exception occurs when $k_n = n$; then, the terms are first-order singular due to $D(q_n)$ or $D(k_n)$.

Analysis of Wave Response

How the mathematical behavior indicated in the foregoing is manifested in the wave propagation nature of the reflection-generated crack surface particle velocities can be seen by examining the behavior in terms of the τz-plane. This plane is shown schematically in Fig. 2, where it is clear that the eight

Downloaded 02 May 2010 to 171.66.16.54. Redistribution subject to ASME license or copyright; see http://www.asme.org/terms/Terms_Use.cfm

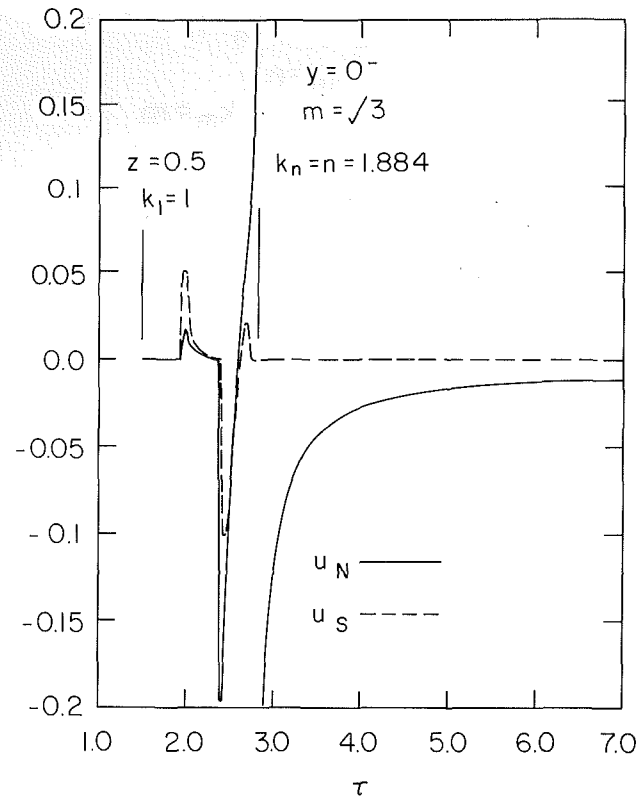


Fig. 3 Reflection-generated particle velocity components for $z = 0.5$

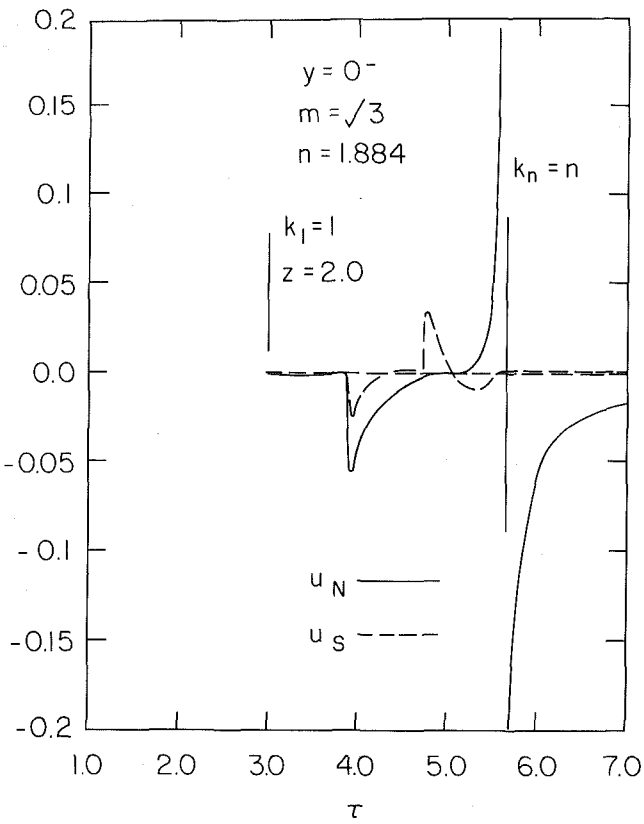


Fig. 4 Reflection-generated particle velocity components for $z = 2.0$

Heaviside arguments in (16) and (17) and the singularity relation $k_n = n$ represent the nine discernible wave-front trajectories $k_1 = (1,m,n)$, $k_m = (1,m,n)$ and $k_n = (1,m,n)$. In particular, the terms (k_1,k_m,k_n) represent reflection wave fronts that travel with, respectively, the dilatational, rotational, and Rayleigh wave speeds, while the terms $(1,m,n)$ denote that a given wave front arose due to the reflection of incident wave fronts moving with, respectively, the dilatational, rotational, and Rayleigh wave speeds.

It follows that the integration operators defined by (20) represent four reflection signals that travel at the dilatational or rotational wave speed, and which were generated by the reflection of signals traveling with these speeds. The wave fronts of these signals can be seen in Fig. 1(*b*). The *PV*-integrations and limit-singularity coincidence conditions which occur in the integral operators as well as the (q_n,k_n)-terms represent signals that travel at the dilatational or rotational wave speed and which are generated by the reflection of Rayleigh-speed signals, or vice-versa. Finally, the integral nonexistence and unbounded (q_n,k_n)-term behavior occurring when $k_n = n$ represents Rayleigh-speed signals that were generated by the reflection of Rayleigh-speed signals.

The mathematical behavior of (15)–(17) suggests that all but one of the nine discernible types of signals mentioned in the foregoing exhibit wave-front continuity in the reflection-generated crack surface particle velocities. The exception is the aforementioned $k_n = n$ signal. From (3) we have

$$\mu h \dot{\mathbf{u}}_L^- = N(U_N,V_N) + S(U_S,V_S) \tag{24}$$

$$\pi Z U_N = -\pi Z V_S = 2m^2 q|a|b\,\frac{T}{|R|^2}\,H(p-1)H(m-p) \tag{25}$$

$$\pi Z U_S = m^2\left|\frac{b}{R}\right|H(p-m) - 4m^2|a|b^2\,\frac{q^2}{|R|^2}\,H(p-1))H(m-p) \tag{26}$$

$$\pi Z V_N = -m^2\left|\frac{a}{R}\right|H(p-m) + m^2|a|\,\frac{T^2}{|R|^2}\,H(p-1)H(m-p) \tag{27}$$

$$Z = |1-z|, \quad q = \tau/(1-z), \quad p = |q|, \tag{28}$$

which indicates that the crack surface incident wave particle velocities are first-order singular at the Rayleigh wave fronts $|q| = n$. Thus, we conclude that the crack edge acts to transmit the singular wave-front behavior to its Rayleigh-speed reflection.

Illustration of Reflection-Generated Wave Response

To illustrate the behavior discussed in the foregoing, the reflection-generated particle velocity terms u_N and u_S for $y = 0-$ are plotted in Figs. 3 and 4 versus τ at locations between the crack edge and point forces ($z = 0.5$) and outside the point forces ($z = 2.0$). The parameter m is given the typical value $\sqrt{3}$, which means that $n \sim 1.884$. The first and last wave-front arrivals in each case are indicated by vertical bars. In order of appearance, the arrival of all the discernible reflection wavefronts are

$\tau = 1.5$ $(k_1 = 1)$	$\tau = 3.0$ $(k_1 = 1)$
$\tau = 1.866$ $(k_m = 1)$	$\tau = 3.732$ $(k_1 = m)$
$\tau = 1.942$ $(k_n = 1)$	$\tau = 3.884$ $(k_1 = n)$
$\tau = 2.232$ $(k_1 = m)$	$\tau = 4.464$ $(k_m = 1)$
$\tau = 2.384$ $(k_1 = n)$	$\tau = 4.768$ $(k_n = 1)$
$\tau = 2.598$ $(k_m = m)$	$\tau = 5.196$ $(k_m = m)$
$\tau = 2.674$ $(k_n = m)$	$\tau = 5.348$ $(k_m = n)$
$\tau = 2.75$ $(k_m = n)$	$\tau = 5.5$ $(k_n = m)$
$\tau = 2.826$ $(k_n = n)$	$\tau = 5.652$ $(k_n = n)$

for $z = 0.5$ and $z = 2.0$, respectively. As noted earlier, the four

Downloaded 02 May 2010 to 171.66.16.54. Redistribution subject to ASME license or copyright; see http://www.asme.org/terms/Terms_Use.cfm

Rayleigh-related wave fronts $(k_1,k_m)=n$ and $k_n=(1,m)$ are nonsingular. Comparison of the preceding tabular list with Figs. 3 and 4 shows that their arrivals do, however, cause distinct peaks that dominate the particle velocity components in an order-of-magnitude fashion. This comparison also illustrates the overtaking of slower-traveling wave fronts by faster ones. This overtaking, which is simply a manifestation of the intersecting trajectories seen in Fig. 2, may partly explain the sign reversal seen in corresponding wave portions on opposite sides of the point force location $z=1.0$.

Although not shown, plots for v_S and v_N are similar to Figs. 3 and 4 with, as might be expected from the form of $\dot{\mathbf{u}}_C^{\pm}$, (v_S,v_N) exhibiting behavior similar to that of (u_N,u_S), respectively. Moreover, the responses of all four quantities on $y=0^+$ and $y=0^-$ are similar. In this light, the fact that Figs. 3 and 4 and equation (26) show Rayleigh-speed wave-front singularities in (u_N,V_N) but not (v_N,U_N) indicates that the aforementioned crack edge reflection singularity transmission occurs when the singularity from the particle velocity component parallel to the generating point force "moves" to the component normal to that force.

Figures 3 and 4 do not show, of course, the complete particle velocity response for $y=0-$. The incident wave components defined by (24) were not included since they would, except at the Rayleigh wave front, obscure the details of the reflection-generated wave response with which this analysis is chiefly concerned.

Discussion

The results illustrated in the foregoing show that the reflection-generated crack surface particle velocity exhibits a series of well-defined peaks, either moving with the Rayleigh speed, or arising from the reflection of an incident Rayleigh wave. However, the dominant response is an infinite discontinuity whose speed and that of its associated incident wave are the Rayleigh speed. Thus, a crack surface point at some distance ($x<-h$ in Fig. 1(a)) from the point force will essentially experience a pair of Rayleigh-speed singularities: the first arrives directly from the point force, while the second is generated by crack edge reflection. Because of the force/velocity direction relations noted in the foregoing, this pair between them affect both velocity components.

From another viewpoint, the traveling peak/singularity nature of the particle velocity would tend to justify a high-frequency approximate analysis [3, 4]. Moreover, that the most noticeable (singular) effects both incident and reflected-travel at the Rayleigh speed would tend to justify an analysis that considers only Rayleigh-speed crack surface disturbances [9].

In closing, it should be noted that performing the problem analysis here in the time domain allowed attention to remain focused on the complicated wave propagation nature of the process. The difficulty of the analysis arose largely due to the characteristic length h. This difficulty was overcome by following a scheme used in [7] and developed in [1]. Further development of the scheme can also be found in [10].

Acknowledgment

The numerical data used in this work was prepared by L.M.B. while at the Naval Research Laboratory in Washington, D.C. in the 1983 Navy/ASEE Summer Faculty Research Program.

References

1 Freund, L. B., "The Stress Intensity Factor Due to Normal Impact Loading of the Faces of a Crack," *International Journal of Engineering Science*, Vol. 12, 1974, pp. 179–190.

2 Brock, L. M., "Effects of Secondary Diffractions on the Stress Intensity Factors Generated for a Finite Crack by a Shear Wave," *International Journal of Engineering Science*, Vol. 13, 1975, pp. 851–859.

3 Achenbach, J. D., and Gautesen, A. K., "Elastic Surface Waves Guided by the Edge of a Slit," *Journal of Sound and Vibration*, Vol. 53, 1977, pp. 407–416.

4 Norris, A. N., and Achenbach, J. D., "Mapping of a Crack Edge by Ultrasonic Methods," *Journal of the Acoustical Society of America*, Vol. 72, 1982, pp. 264–272.

5 Mall, S., "Finite Element Analysis of Stationary Cracks in Time-Dependent Stress Fields," in *Numerical Methods in Fracture Mechanics*, Owen, D. R. J., and Luxmore, A. R., eds., Pineridge Press, Swansea, 1980, pp. 539–551.

6 Rossmanith, H. P., "How 'Mixed' is Dynamic Mixed-Mode Crack Propagation?—a Dynamic Photoelastic Study," *Journal of the Mechanics and Physics of Solids*, Vol. 31, 1983, pp. 251–260.

7 Brock, L. M., "Shear and Normal Impact Loadings on One Face of a Narrow Slit," *International Journal of Solids and Structures*, Vol. 18, 1982, pp. 467–477.

8 Lamb, H., "On the Propagation of Tremors Over the Surface of an Elastic Solid," *Philosophical Transactions of the Royal Society of London*, Series *A*, Vol. 203, 1904, pp. 1–42.

9 Freund, L. B., "The Oblique Reflection of a Rayleigh Wave From a Crack Tip," *International Journal of Solids and Structures*, Vol. 7, 1971, pp. 1199–1210.

10 Abou-Syed, I. S., "Some Novel Problems in Dynamic Crack Propagation," Ph.D. Dissertation, Division of Engineering, Brown University, Providence, R.I.

Downloaded 02 May 2010 to 171.66.16.54. Redistribution subject to ASME license or copyright; see http://www.asme.org/terms/Terms_Use.cfm

Flexibility of a Contact Area of an Isotropic Elastic Body

C. M. Szalwinski
Alex Tobias Associates Ltd,
194 Wilson Ave.,
Toronto M5M 3A1, Canada

From Cerruti's solution to the problem of the plane and Cattaneo's traction distributions, instantaneous and secant flexibilities are derived for an elliptical contact area which includes a region of slip. The results apply to force histories where the tangential component is constantly directed. Some of the results differ from those reported by Mindlin and Deresiewicz [4]. Ellipticity affects normal and tangential flexibilities differently but is independent of the extent of slip.

1 Introduction

The problem of two identical bodies slipping over one another has been solved for cases where their contact area is circular [1]. This is useful for assemblages of nearly identical, nearly spherical particles, which, in soil mechanics, is a rather special case. Particles within an assemblage of soil exhibit significant variations in size, shape, and angularity. The empirically established importance of the latter [2] suggests that the problem of slip over an elliptical contact area deserves attention.

The present study augments the work of Cattaneo [3], Mindlin [1], Mindlin and Deresiewicz [4], and Deresiewicz [5] on the contact problem. Mindlin [1] investigated elliptical contact areas with no slip as well as circular contact areas with slip. Mindlin and Deresiewicz [4] investigated the effects of different loading histories on instantaneous tangential flexibilities for circular contact areas with slip. Deresiewicz [5] showed that the form of the expression for displacement in the direction of tangential force remains unaltered in a substitution of elliptical for circular contact area in the special case where tangential force is directed along one of the axes of the ellipse. Here, an elliptical contact area with slip is investigated for loading histories where the tangential component is constantly directed with respect to the axes of the contact area. Secant as well as instantaneous flexibilities are derived.

2 Mathematical Description of the Model

Dimensions of the contact area are small in comparison with those of the body itself. The model under investigation is illustrated in Fig. 1. Two bodies in contact possess a common tangent plane. The reference system $\{x, y, z\}$ is such that $\{x, y, 0\}$ defines the tangent plane and (0,0,0) corresponds to the point where the bodies touch in an unloaded condition. With the application of a force, P_z, normal to this plane, the contact point grows into a finite area, S. This area, according to Hertz, takes the form of an ellipse with semiaxes a and b (in x and y, respectively). We chose x and y such that $a \leq b$, assume $P_z > 0$, consider the body that lies to side $z > 0$, and introduce an additional force, (P_x, P_y), embedded in plane $\{x, y, -0\}$ and of constant direction there:

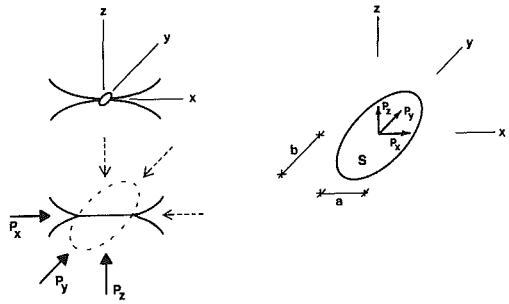


Fig. 1 Model under investigation

$$P_x/p = P_y/q = \pm P_t \pm \tag{1a}$$

$$p^2 + q^2 = 1. \tag{1b}$$

p and q are constants and $\pm P_t \pm$ denotes the magnitude of (P_x, P_y). We require, first, an expression for the displacement of (0,0,0)[1] and for the normal and tangential flexibilities associated with any loading increment in a history where p and q remain constant.

The theory of elasticity provides some solutions of the equations of equilibrium for an isotropic body with a given boundary [6;art.157ff.]. In particular, Cerruti's solution for a body bounded by a plane and subject to a prescribed set of tractions is as follows.

Let $(\bar{x}, \bar{y}, \bar{z})$ denote coordinates of a point within a body such that $\bar{z} = 0$ defines its bounding plane and the body lies on side $\bar{z} > 0$. Let (x, y, z) denote coordinates of another point within the body and r the distance from it to $(\bar{x}, \bar{y}, \bar{z})$. The displacement field (u, v, w) due to a traction distribution (U, V, W) on $\bar{z} = 0$ is given by

Contributed by the Applied Mechanics Division for publication in the JOURNAL OF APPLIED MECHANICS.

Discussion on this paper should be addressed to the Editorial Department, ASME, United Engineering Center, 345 East 47th Street, New York, N.Y. 10017, and will be accepted until two months after final publication of the paper itself in the JOURNAL OF APPLIED MECHANICS. Manuscript received by ASME Applied Mechanics Division, January, 1983; final revision, February, 1984.

[1] Although much of the mathematics in Sections 2-4 is similar to that in [1], it is not identical. It is presented in full for completeness, and readers familiar with [1] may wish to omit the details and turn directly to the result (equation 15).

Copyright © 1985 by ASME
Downloaded 02 May 2010 to 171.66.16.54. Redistribution subject to ASME license or copyright; see http://www.asme.org/terms/Terms_Use.cfm

$$u(x,y,z) = (1/2\pi\mu)F_{,zz} - (1/4\pi\mu)H_{,zx} + (\sigma/2\pi\mu)(F_{,x}+G_{,y}+H_{,z})_{,x} - (1/4\pi\mu)z(F_{,x}+G_{,y}+H_{,z})_{,zx}, \quad (2a)$$

$$v(x,y,z) = (1/2\pi\mu)G_{,zz} - (1/4\pi\mu)H_{,zy} + (\sigma/2\pi\mu)(F_{,x}+G_{,y}+H_{,z})_{,y} - (1/4\pi\mu)z(F_{,x}+G_{,y}+H_{,z})_{,zy}, \quad (2b)$$

$$w(x,y,z) = (1/4\pi\mu)H_{,zz} + ((1-2\sigma)/4\pi\mu)(F_{,x}+G_{,y}+H_{,z})_{,z} - (1/4\pi\mu)z(F_{,x}+G_{,y}+H_{,z})_{,zz}. \quad (2c)$$

σ and μ denote Poisson's ratio and shear modulus, respectively. F, G, and H are harmonic functions:

$$\nabla^2 F = 0, \quad \nabla^2 G = 0, \quad \nabla^2 H = 0 \quad (3)$$

defined by the surface integrals

$$F(x,y,z) = \iint U(\bar{x},\bar{y})[z\ln(z+r) - r]d\bar{x}d\bar{y}, \quad (4a)$$

$$G(x,y,z) = \iint V(\bar{x},\bar{y})[z\ln(z+r) - r]d\bar{x}d\bar{y}, \quad (4b)$$

$$H(x,y,z) = \iint W(\bar{x},\bar{y})[z\ln(z+r) - r]d\bar{x}d\bar{y}. \quad (4c)$$

These equations, apart from several substitutions including $\bar{z}=0$, may be found in Love [6;art.166].

In our problem, S, the contact area, is a portion of the tangent plane enclosed by an ellipse. The portion outside but in the neighborhood of S, is free of tractions. This confines evaluation of (4) to S. For convenience, we introduce a trigonmetric set in place of $(\bar{x}, \bar{y})$, letting s be the distance from (x, y) to $(\bar{x}, \bar{y})$ on S $(s \equiv r|_{z=0})$, and θ an angular measure, such that

$$s\cos\theta = \bar{x} - x, \quad (5a)$$

$$s\sin\theta = \bar{y} - y. \quad (5b)$$

Substituting (5) into (4), evaluating the partial derivatives of F, G, and H, and then substituting them along with (3) into (2), we obtain expressions for the displacement field on the tangent plane $(z=0)$:

$$u(x,y,0) = ((2-\sigma)/4\pi\mu)\int U\,ds d\theta + (\sigma/4\pi\mu)\int U\cos 2\theta + V\sin 2\theta\; ds d\theta - ((1-2\sigma)/4\pi\mu)\int W\cos\theta\; ds d\theta, \quad (6a)$$

$$v(x,y,0) = ((2-\sigma)/4\pi\mu)\int V\,ds d\theta + (\sigma/4\pi\mu)\int U\sin 2\theta - V\cos 2\theta\; ds d\theta - ((1-2\sigma)/4\pi\mu)\int W\sin\theta\; ds d\theta, \quad (6b)$$

$$w(x,y,0) = ((1-\sigma)/2\pi\mu)\int W\,ds d\theta - ((1-2\sigma)/4\pi\mu)\int U\cos\theta + V\sin\theta\; ds d\theta; \quad (6c)$$

U, V and W have to be specified and the integrals are evaluated over S.

The normal tractions are given by Hertz [6],

$$W = D[1-(\bar{x}/a)^2 - (\bar{y}/b)^2]^{1/2} \quad \text{on } S, \quad (7)$$

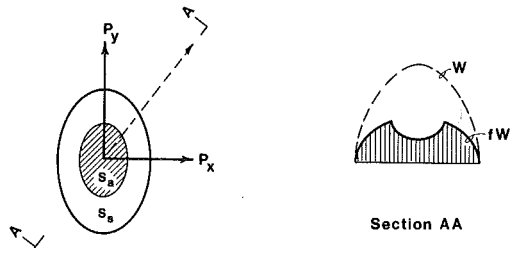


Fig. 2 Cattaneo's traction distributions

where

$$D = 3P_z/(2\pi ab), \quad (8)$$

and a and b are each proportional to the cube root of P_z, so that

$$da/a = db/b = dP_z/3P_z, \quad (9)$$

and D/a is a constant.

3 Cattaneo's Traction Distributions

According to Cattaneo [3], S contains two zones: S_a and S_s, bounded by homothetic ellipses (Fig. 2). On S_a, of semiaxes (a',b'), the bodies adhere. On S_s, of semiaxes (a,b) and (a',b'), they slip with $(U^2+V^2)^{1/2} = fW$. f is the coefficient of friction. U and V are as follows[2].

$$U = pfD[1-(\bar{x}/a)^2 - (\bar{y}/b)^2]^{1/2} \quad \text{on } S_s, \quad (10a)$$

$$= pfD\{[1-(\bar{x}/a)^2 - (\bar{y}/b)^2]^{1/2} - Q'[1-(\bar{x}/a')^2 - (\bar{y}/b')^2]^{1/2}\} \quad \text{on } S_a, \quad (10b)$$

$$V = (q/p)U. \quad (10c)$$

Cattaneo's assumption of homothetic ellipses,

$$Q' = (b'/b) = (a'/a), \quad 0 \le Q' \le 1 \quad (11)$$

ensures that u and v are constant on S_a. Q' measures the extent of S_a: Q' is unity for perfect adhesion and vanishes for full sliding.

The traction distributions are required in terms of (s, θ). Substitution of (5) into (7) and (10) (with $(x,y) = (0,0)$) yields

$$U(s,\theta) = pfD(1-s^2/A^2)^{1/2} \quad \text{on } S_s, \quad (12a)$$

$$U(s,\theta) = pfD[(1-s^2/A^2)^{1/2} - Q'(1-s^2/A'^2)^{1/2}] \quad \text{on } S_a, \quad (12b)$$

$$V(s,\theta) = (q/p)U, \quad (12c)$$

$$W(s,\theta) = D(1-s^2/A^2)^{1/2}; \quad (12d)$$

where

$$A = (a^{-2}\cos^2\theta + b^{-2}\sin^2\theta)^{-1/2}, \quad (13a)$$

$$A' = (a'^{-2}\cos^2\theta + b'^{-2}\sin^2\theta)^{-1/2} = Q'A. \quad (13b)$$

A and A' are not functions of s.

4 Integration of Traction Distributions

An ellipse of semiaxes (a,b) is described by $s = A$, and so, the intervals of integration for s are $[0, A]$ and $[0, A']$ on S and S_a, respectively, while the interval for θ is $[0, 2\pi]$. Substitution of (12) into (6) followed by integration about s yields the displacement of S_a:

$$u_a = ((2-\sigma)pfD(1-Q'^2)/16\mu)\int_0^{2\pi} A\,d\theta + (\sigma pfD(1-Q'^2)/16\mu)\int_0^{2\pi} A\cos 2\theta\,d\theta$$

[2] These expressions contain an approximation to Coulomb friction: on S_s the direction of slip is not identical to the direction of traction [4].

Downloaded 02 May 2010 to 171.66.16.54. Redistribution subject to ASME license or copyright; see http://www.asme.org/terms/Terms_Use.cfm

$$+(\sigma qfD(1-Q'^2)/16\mu)\int_0^{2\pi} A\sin 2\theta\, d\theta$$

$$-((1-2\sigma)D/16\mu)\int_0^{2\pi} A\cos\theta\, d\theta, \tag{14a}$$

$$v_a = ((2-\sigma)qfD(1-Q'^2)/16\mu)\int_0^{2\pi} A\, d\theta$$

$$-(\sigma qfD(1-Q'^2)/16\mu)\int_0^{2\pi} A\cos 2\theta\, d\theta$$

$$+(\sigma pfD(1-Q'^2)/16\mu)\int_0^{2\pi} A\sin 2\theta\, d\theta$$

$$-((1-2\sigma)D/16\mu)\int_0^{2\pi} A\sin\theta\, d\theta, \tag{14b}$$

$$w_a = ((2-2\sigma)D/16\mu)\int_0^{2\pi} A\, d\theta$$

$$-((1-2\sigma)pfD(1-Q'^2)/16\mu)\int_0^{2\pi} A\cos\theta\, d\theta$$

$$-((1-2\sigma)qfD(1-Q'^2)/16\mu)\int_0^{2\pi} A\sin\theta\, d\theta. \tag{14c}$$

To simplify integration over $[0, 2\pi]$, divide the interval into two parts: $[0, \pi]$ and $[\pi, 2\pi]$. Since $A(\theta) = A(\theta+\pi)$, $\cos(\theta) = -\cos(\theta+\pi)$ and $\sin(\theta) = -\sin(\theta+\pi)$, integrals containing $\cos\theta$ and $\sin\theta$ vanish over $[0, 2\pi]$. Moreover, integrals containing $\sin 2\theta$ vanish over $[0, \pi]$. Finally, for $a \le b$,

$$u_a = (pfD/4\mu)(1-Q'^2)a(2-\sigma)K(1+N), \tag{15a}$$

$$v_a = (qfD/4\mu)(1-Q'^2)a(2-\sigma)K(1-N), \tag{15b}$$

$$w_a = (D/2\mu)a(1-\sigma)K; \tag{15c}$$

where

$$K = \int_0^{\pi/2} (1-(1-(a/b)^2)\sin\theta)^{-1/2}\, d\theta, \tag{16a}$$

$$E = \int_0^{\pi/2} (1-(1-(a/b)^2)\sin^2\theta)^{+1/2}\, d\theta, \tag{16b}$$

$$N = [\sigma/(2-\sigma)][1-2(1-E/K)/(1-(a/b)^2)]. \tag{16c}$$

Since a/b and σ are constants, K, E, and N are constants. (K and E denote complete elliptic integrals of the first and second kind in argument $(\pi/2, a/b)$.)

Note that, if (P_x, P_y) is not directed along one of the axes of the ellipse, then, unless $\sigma = 0$, $N \neq 0$ and there is a nonzero component of displacement orthogonal to the direction of application of (P_x, P_y). (This result was obtained by Bryant and Kerr [8] independently.)

Since b is proportional to the cube root of P_z, the normal flexibility is

$$F_{zz} = dw_a/dP_z = 2(1-\sigma)M, \tag{17}$$

where

$$M \equiv K/4\pi\,\mu b. \tag{18}$$

5 Initial Loading With (a', b') Continuous

Consider an initial program of $(0, 0, 0) -> (0, 0, >0) -> (P_x, P_y, P_z)$. Assume that (a', b') evolve continuously.[3] For equilibrium,

$$|P_t| = \int_S (U/p)\, sds d\theta = fdY(1-Q'^3), \tag{19a}$$

$$P_z = \int_S W\, sds d\theta = DY; \tag{19b}$$

where

$$Y = \int_S (1-s^2/A^2)^{1/2} sds d\theta = \int_0^{2\pi} (A^2/3) d\theta. \tag{20}$$

Hence,

$$Q' = (1-|P_t|/fP_z)^{1/3}. \tag{21}$$

There is perfect adhesion during $(0, 0, 0) -> (0, 0, >0)$ and a continuous drop in its extent during $(0, 0, >0) -> (P_x, P_y, P_z)$.

For a simultaneous change in $|P_t|$ and P_z, let

$$\beta \equiv dP_z/d|P_t|. \tag{22}$$

Then

$$dQ' = -(\tfrac{1}{3}fP_zQ'^2)(1-\beta|P_t|/P_z)d|P_t|. \tag{23}$$

Differentiation of (15), noting that

$$da/a = f\beta d|P_t|/3P_z, \tag{24}$$

$$d|P_t| = pdP_x + qdP_y, \tag{25}$$

yields[4]

$$F_{xx} \equiv \partial u_a/\partial P_x = p^2(2-\sigma)M(1+N)\xi', \tag{26a}$$

$$F_{xy} \equiv \partial u_a/\partial P_y = pq(2-\sigma)M(1+N)\xi', \tag{26b}$$

$$F_{yx} \equiv \partial v_a/\partial P_x = qp(2-\sigma)M(1-N)\xi', \tag{26c}$$

$$F_{yy} \equiv \partial v_a/\partial P_y = q^2(2-\sigma)M(1-N)\xi', \tag{26d}$$

where

$$\xi' = f\beta + (1-f\beta)/Q'. \tag{26e}$$

The expression for $F_{xx}|_{a=b, \beta=0, q=0}$ is the same as that reported in [1; equation (103)] for circular contact areas and constant P_z.

6 Differential Form of the Traction Distributions

Whenever, in a given loading increment, the extent of adhesion exceeds that established in the preceding increment, there is a jump in (a', b'). In such cases, it is necessary to start with the differential form of the traction distributions.

Differentiation of (12), with (s, θ) held constant, yields

$$dU = pfD(1-s^2/A^2)^{-1/2} da/a \quad \text{on } S_s, \tag{27a}$$

$$= pfD[(1-s^2/A^2)^{-1/2} da/a - Q'(1-s^2/A'^2)^{-1/2} da'/a'] \quad \text{on } S_a, \tag{27b}$$

$$dV = (q/p)dU, \tag{27c}$$

$$dW = D(1-s^2/A^2)^{-1/2} da/a. \tag{27d}$$

Equation (27b) ensures perfect adhesion on S_a. For equilibrium,

$$d|P_t| = \int_S (dU/p) sds d\theta = 3fDY[da/a - Q'^3 da'/a'], \tag{28a}$$

$$dP_z = \int_S (dW) sds d\theta = 3DY da/a. \tag{28b}$$

Substitution of (28b) and (19b) into (28a) yields

$$d|P_t| = f(1-Q'^3)dP_z - 3fP_zQ'^2 dQ'.$$

Initially, $Q' = Q'_{+0}$, where $_{+0}$ refers to the start of the increment. For small changes in Q', $3Q'^2_{+0}dQ' = Q'^3 - Q'^3_{+0}$, and so

$$Q'^3 = (1-1/f\beta_{+0})dP_z/P_z + Q'^3_{+0}(1-dP_z/P_z). \tag{29}$$

[3] Conditions for continuity are established in the next section.

[4] The partials indicate that β and either P_x or P_y are held constant.

Downloaded 02 May 2010 to 171.66.16.54. Redistribution subject to ASME license or copyright; see http://www.asme.org/terms/Terms_Use.cfm

Equations (27)–(29) are valid for (a', b') continuous as well as discontinuous.

For (a', b') discontinuous, $dQ' = 0$[5], and so $Q' = Q'_{+0}$. From (29),

$$Q'_{+0} = (1 - 1/f\beta_{+0})^{1/3}. \tag{30}$$

Since the extent of adhesion is greater than it was in the preceding increment ($Q'_{+0} > Q'_{-0}$ where $_{-0}$ refers to the end of the preceding increment), $\beta_{+0} > \beta_{1cr}$, where

$$\beta_{1cr} \equiv 1/f(1 - Q'^3_{-0}) \quad \geq 1/f. \tag{31}$$

β_{1cr} is the critical obliquity beyond which Q' evolves discontinuously. Applying the method of Section 4, the associated changes in u and v are found to be

$$du_a = (pfD/2\mu)(1 - Q'^2)(2 - \sigma)K(1 + N)da, \tag{32a}$$

$$dv_a = (qfD/2\mu)(1 - Q'^2)(2 - \sigma)K(1 - N)da. \tag{32b}$$

((Equation (32) may also be obtained by differentiation of (15) with Q' held constant.) It follows that the instantaneous flexibilities are given by (26), but now, with Q' defined by (30).

For (a', b') continuous, $Q'_{+0} = Q'_{-0}$. Here, the extent of adhesion does not increase ($Q' \leq Q'_{-0}$) and so, from (29), $\beta_{+0} \leq \beta_{1cr}$. If $\beta_{+0} = \beta_{1cr}$, the extent remains constant ($da'/a' = da/a$); the contribution to (U_0, V_0) is such that a' is an infinitesimal distance ($= Q'da$) from a'_{-0}. If $0 < \beta_{+0} < \beta_{1cr}$, the extent diminishes slowly with a' less than infinitesimal distance ($< Q'da$) from a'_{-0} but nevertheless greater than a'_{-0}. If $\beta_{+0} = 0$, $a' = a'_{-0}$. If $\beta_{+0} < 0$, $dP_z < 0$, and so, $da < 0$. In this case, the extent of adhesion diminishes noticeably as a' is more than an infinitesimal distance from a'_{-0} ($da' < Q'da < 0$). As S contracts, dU on S_s is of opposite sign to $d|P_t|$, removing enough of (U_0, V_0) to keep the friction law satisfied on S_s. The amount removed is added to (U_0, V_0) on S_a ensuring that equilibrium is maintained.

If β is continuous over a series of infintesimal increments, then so is Q' and, since (a, b) are continuous from physical requirements, so are (a', b'). It follows (from (22)) that a sufficient condition for continuity is that (P_x, P_y, P_z) are C^1-continuous. The necessary condition is that $\beta_{+0} \leq \beta_{1cr}$.

In the case of initial loading, (a', b') is continuous if $\beta_{+0} \leq P_z/|P_t|$.

7 Secant Flexibilities

Assume that (P_x, P_y, P_z) are C^1-continuous throughout a loading increment described by $\beta(a)$ over the interval $]a_0, a]$. Since $a_{-0} = a_{+0}$, the notation a_0 suffices. Here, β is C^0-continuous as are Q' and (a', b').

Integration on (27) over $]a_0, a]$ yields the changes in traction distributions:

$$\Delta U = pfD[R - (a_0/a)R_0 - Q'R' + (a_0/a)Q'_{+0}R'_{+0}], \tag{33a}$$

$$\Delta V = (q/p)\Delta U, \tag{33b}$$

$$\Delta W = D[R - (a_0/a)R_0]; \tag{33c}$$

where

$$Q'_{+0} = a'_{+0}/a_0 = b'_{+0}/b_0, \tag{34a}$$

$$R = (1 - s^2/A^2)^{1/2} \qquad 0 < s < A, \tag{34b}$$

$$R' = (1 - s^2/A'^2)^{1/2} \qquad 0 < s < A', \tag{34c}$$

$$R_0 = (1 - s^2/A_0^2)^{1/2} \qquad 0 < s < A_0, \tag{34d}$$

$$R'_{+0} = (1 - s^2/A'^2_{+0})^{1/2} \qquad 0 < s < A'_{+0}, \tag{34e}$$

$$A_0 = (a_0/a)A, \tag{34f}$$

$$A'_{+0} = Q'_{+0}A_0, \tag{34g}$$

[5] Setting $da' = 0$ would remove the second term in (27b) and produce microslip on S_a.

with R, R', R_0, and R'_{+0} vanishing outside the noted limits. For equilibrium,

$$\Delta|P_t| = \int_S (\Delta U/p)sdsd\theta = fDY(1 - Q'^3 - (a_0/a)^3 + (a_0/a)^3 Q'^3_{+0}), \tag{35a}$$

$$\Delta P_z = \int_S (\Delta W)sdsd\theta = DY(1 - (a_0/a)^3), \tag{35b}$$

and so

$$Q'^3 = (1 - 1/f\bar{\beta})(\Delta P_z/P_z) + Q'^3_{+0}(1 - \Delta P_z/P_z), \tag{36}$$

where

$$\bar{\beta} \equiv \Delta P_z/\Delta|P_t|. \tag{37}$$

The overscore $^-$ denotes secant value of. The change in the displacements follows directly from (15):

$$\Delta u_a = (pfD/4\mu a)(2 - \sigma)K(1 + N)[a^2(1 - Q'^2) - a_0^2(1 - Q'^2_{+0})], \tag{38a}$$

$$\Delta v_a = (qfD/4\mu a)(2 - \sigma)K(1 - N)[a^2(1 - Q'^2) - a_0^2(1 - Q'^2_{+0})], \tag{38b}$$

$$\Delta w_a = (D/2\mu a)(1 - \sigma)K(a^2 - a_0^2). \tag{38c}$$

After some algebraic manipulation, the secant flexibilities are found to be

$$\bar{F}_{xx} \equiv \Delta u_a/\Delta P_x = p^2(2 - \sigma)\bar{M}(1 + N)\bar{\xi}', \tag{39a}$$

$$\bar{F}_{xy} \equiv \Delta u_a/\Delta P_y = pq(2 - \sigma)\bar{M}(1 + N)\bar{\xi}', \tag{39b}$$

$$\bar{F}_{yx} \equiv \Delta v_a/\Delta P_x = qp(2 - \sigma)\bar{M}(1 - N)\bar{\xi}', \tag{39c}$$

$$\bar{F}_{yy} \equiv \Delta v_a/\Delta P_y = q^2(2 - \sigma)\bar{M}(1 - N)\bar{\xi}', \tag{39d}$$

$$\bar{F}_{zz} \equiv \Delta w_a/\Delta P_z = 2(1 - \sigma)\bar{M}, \tag{39e}$$

where

$$\bar{M} \equiv (3K/8\pi\mu b_0)(m + 1)/(m^2 + m + 1), \tag{39f}$$

$$\bar{\xi}' \equiv f\bar{\beta} + (1 - f\bar{\beta})[(m^2 + m + 1)(m' + 1)/((m + 1)(m'^2 + m' + 1))]/Q'_{+0}, \tag{39g}$$

$$m = (1 + \Delta P_z/P_{z0})^{1/3}, \tag{39h}$$

$$m' = [(1 - 1/f\bar{\beta})(\Delta P_z/P_{z0}) + Q'^3_{+0}]^{1/3}. \tag{39i}$$

Equation (39) is valid for any increment throughout which β has been continuous. The initial extent of adhesion depends upon β_{+0}:

$$Q'_{+0} = Q'_{-0}, \qquad \beta_{+0} \leq \beta_{1cr} \tag{40a}$$

$$= (1 - 1/f\beta_{+0})^{1/3}. \qquad \beta_{+0} > \beta_{1cr} \tag{40b}$$

Note that the increment could have been described by $(\Delta P_z, \bar{\beta})$ with an initial condition of (P_{z0}, Q'_{-0}).

Expressions for instantaneous flexibilities are obtained by letting ΔP_z vanish. Then, $m = 1$, $m' = Q'_{+0}$, $\bar{M} = M$ and $\bar{\xi}' = \xi'$. Evidently, expressions (26) are valid for any loading provided that Q' is determined using (40).

8 Special Loading Programs

Consider those programs where either of P_z or $|P_t|$ is held constant with the initial condition given by (P_{z0}, Q'_{-0}).

(a) Tangential force constant, normal force increasing ($\Delta|P_t| = 0$, $\Delta P_z > 0$): Here, $\beta_{+0} > \beta_{1cr}$ (unless $Q'_{-0} = 1$). Initially, there is perfect adhesion ($Q'_{+0} = 1$). As loading increases, perfect adhesion is maintained (from (36), $Q' = 1$). Since $m' = m$ and $\bar{\xi}' = 1$,

$$\bar{F}_{xx} = p^2(2 - \sigma)\bar{M}(1 + N).$$

This is the elastic, no slip, secant flexibility [1; equation (140)].

(b) Tangential force constant, normal force decreasing

Downloaded 02 May 2010 to 171.66.16.54. Redistribution subject to ASME license or copyright; see http://www.asme.org/terms/Terms_Use.cfm

$(\Delta\,|P_t|=0,\ \Delta P_z<0)$: Here, $\beta_{+0}<\beta_{|cr}$. Initially, the extent of adhesion is that established in the preceding increment $(Q'_{+0}=Q'_{-0})$. As loading increases, the extent diminishes $(Q'^3=Q'^3_{+0}+(1-Q'^3_{-0})\,\Delta P_z/P_z)$. Unless there was perfect adhesion before, the tangential flexibilities are undefined and

$$\Delta u_a=p(2-\sigma)\bar{\bar{M}}(1+N)\{1-[(m^2+m+1)(m'+1)/((m+1)(m'^2+m'+1)Q'_{-0})]\}f\Delta P_z.$$

But if there was perfect adhesion $(Q'_{-0}=1)$, then $m'=m$, $\bar{\bar{\xi}}'=1$ and

$$\bar{\bar{F}}_{xx}=p^2(2-\sigma)\bar{\bar{M}}(1+N):$$

the response is perfectly elastic.

(*c*) Tangential force increasing, normal force constant $(\Delta\,|P_t|>0,\ \Delta P_z=0)$: Here, $0=\beta_{+0}<\beta_{|cr}$. Initially, the extent of adhesion is that established in the preceding increment $(Q'_{+0}=Q'_{-0})$. As loading increases, the extent diminishes $(Q'^3=Q'^3_{-0}-\Delta\,|P_t|/fP_{z0})$. Moreover, $m=1$ and $m'=Q'$, yielding

$$\bar{\bar{F}}_{xx}=p^2(2-\sigma)M(1+N)[3(1-Q'^2)/(2(1-Q'^3)Q'_{-0})]. \qquad (41)$$

If there was perfect adhesion in the preceding increment $(Q'_{-0}=1)$, then the instantaneous flexibility is the elastic one. But, if $\Delta\,|P_t|$ is finite, the elastic expression is only anapproximation to (41).

9 Comparison With Published Results

Mindlin and Deresiewicz [4] reported $F_{xx\,|a=b}$ for a variety of loading programs. Expression (26*a*) with (40) embodies their cases 3, 7, 8, and 14 (oblique loading with β constant). The present results differ from those in [4; cases 7, 14] for $\beta_{+0}>1/f$.

According to Johnson [7], there is a paradox in case 14 for $\beta_{+0}>1/f$: although the derivations assume slip, the results show that the friction law $(U=pfW)$ is satisfied nowhere in S. By assuming perfect adhesion throughout S, he obtained the same results but without the paradox.

The source of the paradox is in case 7. For $\beta_{+0}>1/f$, $(\Delta P_z,\ \Delta\,|P_t|)$ are not applied simultaneously. $(\Delta P_z,\ 0)$ is applied first and is followed by $(0,\ \Delta\,|P_t|)$. During $(\Delta P_z,0)$ $Q'=1$ and $\Delta u_a=0$. This produces an initial condition of perfect adhesion for the second process $(0,\ \Delta\,|P_t|)$, during which, Q'^3 diminishes from unity as $\Delta\,|P_t|$ increases from 0. Thus, $F_{xx|a=b}$ is the elastic flexibility [4; equation (26)]. To obtain this result, it is necessary to proceed to a limit twice: once for $\Delta\,|P_t|->0$ and once for $\Delta P_z->0$. The latter keeps a_0+da within an infinitesimal distance of a_0, while the former keeps a' within an infinitesimal distance of a_0+da. For any finite value of $\bar{\beta}$, this force forces $d\,|P_t|$ to be doubly small; that is $d\,|P_t|<<fdP_z$. The net effect is that the width of the slip annulus is constrained to being infinitesimally small which is the elastic solution.

This solution is valid for $\Delta\,|P_t|<<f\,\Delta P_z$, but leaves the problem of $\Delta\,|P_t|$ less than $f\Delta P_z$, yet finite, unresolved. Since double limits are likewise taken in the solution for oblique loading, the problem remains unresolved. (Note that [4; equation (54)] is the same as [7; equation (10)]).

The present investigation provides the missing link. Since, for $\beta_{+0}>\beta_{|cr}$, tangential flexibilities are functions of loading obliquity (β), a procedure that simply accumulates linear contributions is not suitable. A procedure like the one outlined in Section 6 has to be used instead of the one outlined in [4; case 7].

10 Ellipticity of the Contact Area

For $\sigma\neq 0$ and an elliptical contact area with no slip, Mindlin [1] showed that the ratio of tangential flexibility to normal flexibility is a function of a/b being greater than unity but less than 2. From the present results, this conclusion may be extended to elliptical contact areas with slip. The ratio is $[(2-\sigma)(1\mp N)/2(1-\sigma)]\,\xi'$. Since $\xi'>1$, the ratio is not less than unity but has no absolute upper bound.

The ratio is a product of two mutually independent terms – a shape factor associated with the material and a slip factor associated with the extent of partial slip. One might infer that, for loosely packed samples of soil (where interlocking does not play an important role) expressions for the ratio of shear modulus to bulk modulus ought to contain an angularity constant and a slip function, both as scalar multipliers.

Acknowledgments

The author is grateful to the Soil Mechanics Group of Cambridge University for providing necessary facilities during preparation of this paper. The work reported here was initially sponsored by the Transport and Road Research Laboratories of the Department of the Environment.

References

1 Mindlin, R. D., "Compliance of Elastic Bodies in Contact," ASME JOURNAL OF APPLIED MECHANICS, Vol. 16, 1949, pp. A259–A268.

2 Hardin, B. O., and Black, W. L., "Sand Stiffness under Various Triaxial Stresses," *Proc. ASCE*, Vol. 92, SM2, 1966, pp. 27–42.

3 Cattaneo, C., "Sul Contatto di due Corpi Elastici: Distribuzione Locale degli sforzi," *Rendiconti, Accademia Nationale dei Lincei*, Series 6, Vol. 27, 1938, pp. 342–348; 434–436; 474–478.

4 Mindlin, R. D., and Deresiewicz, H., "Elastic Spheres in Contact Under Varying Oblique Forces," ASME JOURNAL OF APPLIED MECHANICS, Vol. 20, 1953, pp. 327–344.

5 Deresiewicz, H., "Oblique Contact of Nonspherical Elastic Bodies," ASME Journal of Applied Mechanics, Vol. 24, 1957, pp. 623–624.

6 Love, A. E. H., *A Treatise on the Mathematical Theory of Elasticity*, 4th Ed., Dover, New York, 1944.

7 Johnson, K. L., "Energy Dissipation at Spherical Surfaces in Contact Transmitting Oscillating Forces," *J. Mech. Eng. Sci.*, Vol. 3, No. 4, 1961, pp. 362–368.

8 Bryant, M. D., and Keer, L. M., "Rough Contact Between Elastically and Geometrically Identical Curved Bodies," ASME JOURNAL OF APPLIED MECHANICS, Vol. 49, 1982, pp. 345–352.

Downloaded 02 May 2010 to 171.66.16.54. Redistribution subject to ASME license or copyright; see http://www.asme.org/terms/Terms_Use.cfm

An Elastic-Plastic Finite Element Model of Rolling Contact

Part 1: Analysis of Single Contacts

V. Bhargava
Graduate Student.

G. T. Hahn
Professor.

C. A. Rubin
Associate Professor.
Mem. ASME

Department of Mechanical and Materials Engineering,
Vanderbilt University,
Nashville, Tenn. 37235

This paper describes a two-dimensional (plane strain) elastic-plastic finite element model of rolling contact that embodies the elastic-perfectly plastic, cycle and amplitude-independent material of the Merwin and Johnson theory, but is rigorous with respect to equilibrium and continuity requirements. The rolling contact is simulated by translating a semielliptical pressure distribution. Both Hertzian and modified Hertzian pressure distributions are used to estimate the effect of plasticity on contact width and the continuity of the indentor-indentation interface. The model is tested for its ability to reproduce various features of the elastic-plastic indentation problem and the stress and strain states of single rolling contacts. This paper compares the results derived from the finite element analysis of a single, frictionless rolling contact at $p_0/k = 5$ with those obtained from the Merwin and Johnson analysis. The finite element calculations validate basic assumptions made by Merwin and Johnson and are consistent with the development of "forward" flow. However, the comparison also reveals significant differences in the distribution of residual stress and strain components after a single contact cycle.

Introduction

The most detailed analysis of repeated two-dimensional rolling contact – that of Merwin and Johnson [1] – is an idealized, plane strain analysis and contains a number of untested assumptions. The analysis treats a rigid cylinder in contact with an elastic-perfectly plastic Von Mises material. The cyclic shear resistance, $k = \sigma_0/\sqrt{3}$, is isotropic and independent of the strain amplitude and the number of load cycles. The analysis makes three important assumptions:

(*i*) It assumes that the contact width and pressure distribution remain Hertzian after the body begins to deform plasitcally. The Hertzian distribution is $p = p_0[(1 - x^2/a^2)]^{0.5}$, where p is the pressure, p_0 is the peak pressure, and $2a$ is the contact width.

(*ii*) The treatment assumes that the sums of the elastic and plastic strain components are the same as the Hertzian elastic strains.

(*iii*) Since no attempt is made to satisfy equilibrium requirements while rolling, the stress components acting at any depth below the surface are uncoupled from those acting at any other depth; thus any region that remains elastic is devoid of residual stresses. Equilibrium for a plane surface free from traction is attained at the end of every contact sequence by completely relaxing elastically the radial and shear residual stresses.

The Merwin and Johnson analysis is, nonetheless, powerful, offering valuable insights into the stress and strain states attending repeated rolling contact. The treatment defines the bounds of three characteristic deformation regimes in terms of p_0/k, the relative, Hertzian peak pressures:

$p_0/k < 3.1$	continuing elastic deformation
$3.1 < p_0/k < 4.0$	transient plastic deformation (shakedown)
$p_0/k > 4.0$	continuing elastic-plastic deformation

The analysis also predicts values of (1) the stresses and elastic and plastic strain components in the contact region, (2) residual stresses away from the contact, and (3) the steady states and accumulated forward flow in the elastic-plastic regime. Attempts to test these predictions and the three underlying assumptions by way of experiments encounter serious difficulties. This is because the shear resistance of materials that strain harden least and are most nearly perfectly-plastic, are likely to be the most strain amplitude and cycle-dependent. For example, measurements of cyclic plasticity of steel by Stone and Park [2] and Thielen, Fine, and Fournelle [3] show that the value of k appropriate for plastic strain amplitudes in the range, $10^{-4} < \Delta\epsilon p/2 < 10^{-3}$

Contributed by the Applied Mechanics Division and presented at the Winter Annual Meeting, New Orleans, La., December 9–14, 1984 of THE AMERICAN SOCIETY OF MECHANICAL ENGINEERS.

Discusison on this paper should be addressed to the Editorial Department, ASME, United Engineering Center, 345 East 47th Street, New York, N.Y. 10017, and will be accepted until two months after final publication of the paper itself in the JOURNAL OF APPLIED MECHANICS. Manuscript received by ASME Applied Mechanics Division, September, 1983. Paper No. 84-WA/APM-42.

Copies will be available until August, 1985.

Copyright © 1985 by ASME
Downloaded 02 May 2010 to 171.66.16.54. Redistribution subject to ASME license or copyright; see http://www.asme.org/terms/Terms_Use.cfm

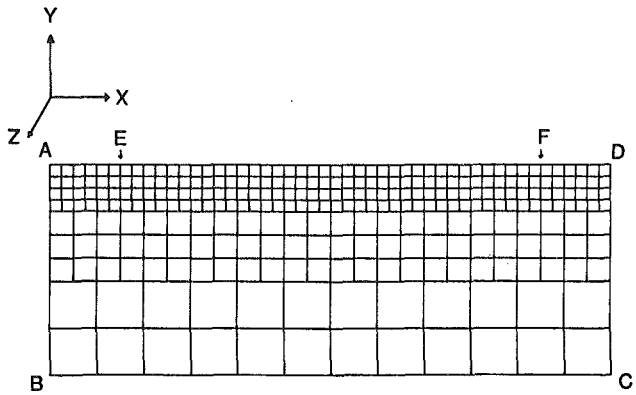


Fig. 1 Finite-element mesh for the elastic-plastic, semi-infinite half plane. The smallest dimension of the mesh = 0.2 mm.

produced by rolling contact is 0.9 to 0.5 times the value of k for monotonic loading, depending on the number of cycles. This is further complicated by the fact that the amplitudes and numbers of cycles relevant to the steady state differ from but are influenced by those involved in the initial cycles that shape the residual stresses. As a result, it is difficult to assign a single, meaningful value of k to the material with which to test the Merwin and Johnson theory. Evidence for this is contained in the measurements of forward flow [4] and the apparent absence of a steady state [5].

Rigorous numerical analyses offer an alternative route for testing either the Merwin and Johnson analysis [1] or the Johnson and Jefferis [6] version that incorporates a shear traction and friction. Hills and Ashelby [7] have determined the elastic, shakedown and load limits for other contact geometries. Dumas and Baronet [8] have examined an elastic-plastic, plane strain, finite element model of a rigid cylinder indenting (but not rolling on) an elastic-plastic half space. They determined the exact contact width and contact pressure distribution that accompanies such indentation. Both elastic [9, 10] and elastic-plastic [11, 12] finite element analyses have been used to investigate stresses in railroad wheels in contact with rails. However, the bulk of these are concerned with the effects of thermal [9, 11] and both thermal and mechanical [10, 12] loading in regions far removed from the contact. So far only three finite element analyses have attempted to treat the plastic deformation in the rim. Martin and Hay [13] developed a three-dimensional finite element model that closely follows the Merwin and Johnson assumptions (*i*) and (*ii*) of contact geometry and elastic-plastic strains. However, this three-dimensional treatment case does not lend itself to comparison with the Merwin and Johnson analysis. Garg, et al. [14] used a finite element technique to analyze elastic-plastic rolling contact by predicting the elastic limit, shakedown, and collapse. A very coarse mesh is used which cannot give detailed information in the contact region. Another investigation by Suh [15, 16] examines the deformation and stresses produced by a single, idealized sliding contact. Studies of residual stress, cyclic loading, and the effect of plasticity on contact width are not included.

This paper describes a two-dimensional (plane strain) elastic-plastic finite element model of rolling contact that embodies the elastic-perfectly plastic, cycle and amplitude-independent material of the Merwin and Johnson theory, but is rigorous with respect to equilibrium and continuity requirements. The rolling contact is simulated by translating a semielliptical pressure distribution. Both Hertzian and modified Hertzian distributions are used to estimate the effect of plasticity on the contact width and the continuity of the indentor-indentation interface. Translation requirements for simulating steady state conditions are examined. This paper

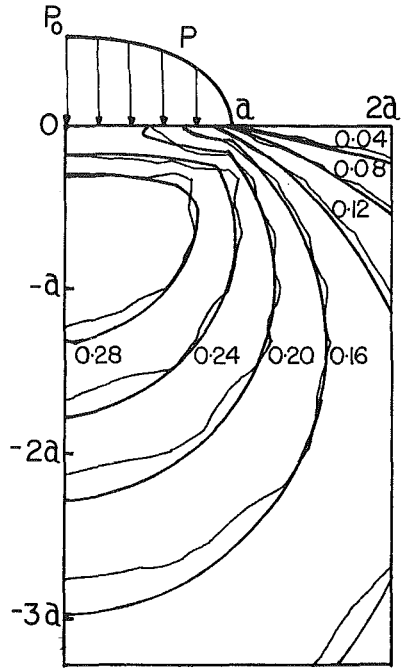


Fig. 2(*a*) Comparison of contours of constant values of $\sqrt{J_2}/p_0$. Sharp lines = finite element analysis, smooth lines = theoretical values.

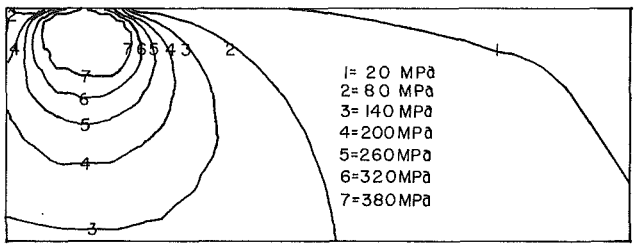


Fig. 2(*b*) Contours of Mises equivalent stress $\sqrt{3J_2}$ with the pressure distribution near one end. The boundaries are almost transparent to the contours.

Fig. 2 Elastic field of indentation

compares results derived from the finite element analysis with the Merwin-Johnson predictions, for a single, frictionless contact. A companion paper [17], describes results for repeated contacts. The comparison reveals significant differences in the distribution of stress and strain components below the rim.

Description of the Model

Rolling of a Hertzian cylinder on an elastic-perfectly plastic, semi-infinite body is simulated by translating a semielliptical pressure distribution over a finite element mesh representing a semi-infinite body. The semi-infinite body is represented by a finite sized mesh by appropriately displacing its three side boundaries (*AB*, *BC*, and *CD* in Fig. 1). For the purpose of calculating displacements at the boundaries, the semielliptical distribution is represented by 200 concentrated forces indenting an elastic half plane. The displacements on the finite boundary points are calculated for each of the concentrated forces and superposed. All displacements are with reference to a point at the bottom of the mesh directly under the center of the modified semielliptical pressure distribution. Comparison of normalized Mises equivalent stress ($\sqrt{J_2}/p_0$) produced under a Hertzian pressure distribution with those predicted by the Hertzian analysis Fig. 2(*a*), indicates that the finite sized mesh with displaced boundaries is an adequate representation of an elastic semi-

Downloaded 02 May 2010 to 171.66.16.54. Redistribution subject to ASME license or copyright; see http://www.asme.org/terms/Terms_Use.cfm

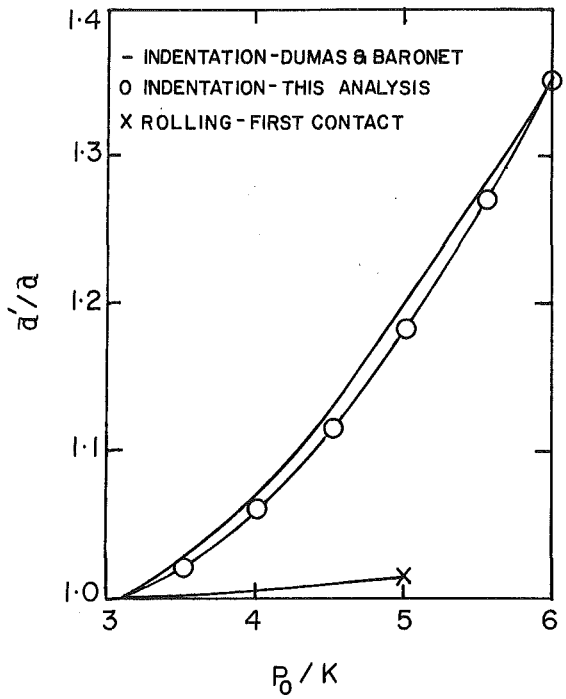


Fig. 3 Dependence on p_0/k of the relative contact widths for indentation and a single rolling contact. (Note: Values for Dumas and Baronet curve were transcribed from a figure and are approximate.)

infinite body. The elastic field in Fig. 2(*b*) appears to be unaffected by the mesh boundaries, showing that the finite mesh successfully represents the semi-infinite body.

Initial elastic-plastic finite element calculations for indentation loading (without rolling) of a finite element mesh with a Hertzian pressure distribution showed that the vertical displacements, d, under the center of contact are substantially larger than that predicted by the Hertzian Theory. For example, the parameter $\rho_i = a^2/2rd$, where r is the radius of the indenting cylinder, is ~2.6. Continuity of the indentor-indenting interface requires ρ_i to be unity. This larger displacement must be accompanied by an increase in the contact width in order to maintain continuity of the contacting surfaces. The Hertzian pressure distribution was modified to provide a degree of continuity. the semielliptical form of the distribution and, P, the total; load applied to the cylinder were not altered.

$$P = \int_{-a'}^{a'} p_0' [1 - (x^2/a'^2)]^{0.5}\, dx = \pi p_0' a'/2 = \pi p_0 a/2 \qquad (1)$$

However, the contact width was increased to the value a' (the peak pressure is correspondingly reduced to the value p_0') which produced continuity of the cylinder and the half space surfaces at the center edges of the contact.[1]

The modified Hertzian pressure distribution and the three-point continuity are features of the model of rolling that were adopted to simplify and improve the rigor of the calculations. An alternate way of simulating rolling with continuity over the entire contacting surfaces would be to translate the appropriate displacement distribution. However, the corresponding nonelliptical pressure distribution and total load cannot be known in advance and would have to be calculated for each increment of translation. This complicates the task of displacing the side boundaries of the mesh and the simulation of rolling at constant load.

[1] In other words, the vertical displacement difference of points on the surface of the half space at the center and edges of the contact and the vertical displacement difference of points on the surface of the cylinder at the center and edges are required to be the same. This requirement fixes the value of a'.

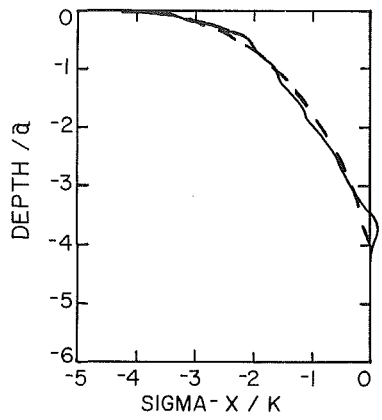


Fig. 4(*a*) Normalized circumferential stress

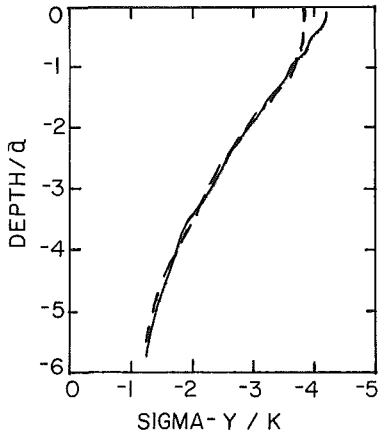


Fig. 4(*b*) Normalized radial stress

Fig. 4 Comparison of normalized stresses obtained on the plane of symmetry under indentation. Dashed lines = Dumas and Baronet; solid lines = this analysis. (Note: a^* is the elastic contact width at yield.)

To test the adequacy of the simplified approach, the modified Hertzian three-point continuity model incorporating the mesh shown in Fig. 1, was used to perform calculations of the Hertzian cylinder indenting an elastic-plastic half space. The appropriate values of a' were obtained by a series of iterations. The results obtained in Fig. 3 are compared with the finite element calculations of Dumas and Baronet, which accurately model the displacement distribution produced by the indenting cylinder. The comparisons demonstrate that the contact widths (Fig. 3) and the circumferential and radial stresses (Figs. 4(*a*) and (*b*)) obtained with the present model agree with the results obtained with the more exact displacement distribution.

In this paper, the semielliptical three-point continuity model is used to simulate a single sequence of frictionless rolling. Calculations were made using the mesh in Fig. 1 with eight-noded, isoparametric, plane strain elements for $p_0/k = 5.0$ with a rigid cylinder of radius 50 mm, Young's modulus $E = 207$ GPa, $\nu = 0.3$, and a relative shear resistance $[k(1-\nu^2)]/E = 10^{-3}$ for the half space. The modified pressure distribution was applied incrementally $2.4a$ from one end (E in Fig. 1), translated incrementally a distance of $14.4a$ in increments of $0.2a$ to the other end and unloaded incrementally a distance of $2.4a$ from the other end (F in Fig. 1). The three boundaries of the mesh are appropriately displaced at each increment. Calculations referred to as modified-1 were performed using a preliminary estimate of a' derived from

Downloaded 02 May 2010 to 171.66.16.54. Redistribution subject to ASME license or copyright; see http://www.asme.org/terms/Terms_Use.cfm

Table 1 Summary of results

Analysis	p_0/k	p_0'/k	a (mm)	a'/a	p_0 (MPa)	p_0'/p_0	δ μm	y_0	ρ_i	ρ_r
Merwin & Johnson	5	5.0	0.50	1	1137.35	1	0.70	$-2a$	—	—
Unmodified FE-8	5	5.0	0.50	1	1137.35	1	0.26	$-2.49a$	0.39	0.91
Modified 1 FE-8	5	4.23	0.50	1.18	1137.35	0.85	−0.62	$-2a$	1.05	1.48
Modified 2 FE-8	5	4.35	0.50	1.15	1137.35	0.87	−0.74	$-2a$	~0.95	~1.3
Modified 2 FE-4	5	4.35	0.50	1.15	1137.35	0.87	−0.73	$-2.2a$	1.02	1.34
Modified 2 FE8-2x	5	4.35	0.50	1.15	1137.35	0.87	−0.71	$-2a$	0.85	1.28
Merwin & Johnson	6	6.0	0.60	1	1364.82	1	1.5	$-2.6a$	—	—
Modified 1 FE-8	6	4.44	0.60	1.35	1364.82	0.74	−0.78	$-2.33a$	1.17	1.88
Modified 2 FE-8	6	4.68	0.60	1.28	1364.82	0.78	−0.65	−2.74	0.88	1.66

FE-4 = Finite element model with four-noded elements
FE-8 = Finite element model with eight-noded elements
$2x$ = Finite element model with twice the translation increment
δ = The net "forward" displacment at the surface
y_0 = Depth of the plastic zone
$\rho_i = a^2/2rd$ while indenting
$\rho_r = a^2/2rd$ while rolling

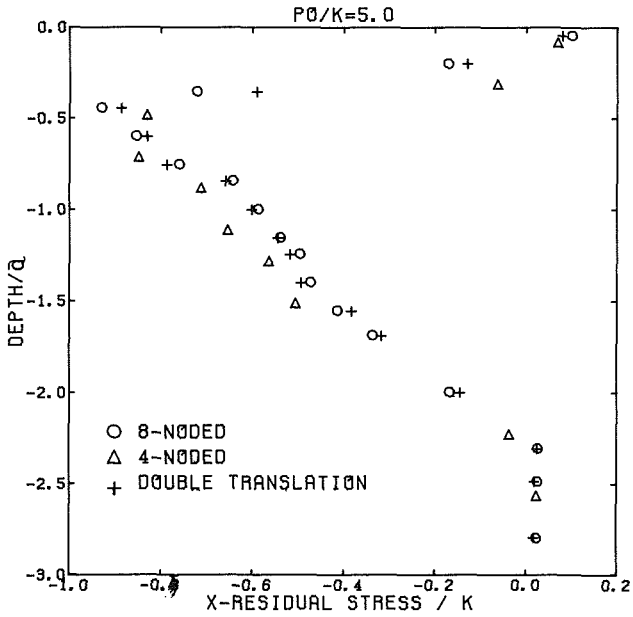


Fig. 5 Influence of model refinement on residual circumferential stress. Comparison of normalized circumferential stress as a function of depth, obtained using eight-noded elements, four-noded elements, and eight-noted elements with twice the translation increment step of the first two analyses

Fig. 3. It was found that while this estimate of a' was appropriate for indenting, it grossly overestimated the correction when the pressure distribution is translated. Calculations referred to as modified-2 employ the more reliable estimate of a' that can be derived from the surface of modified-1 after conditions associated with rolling are achieved (see Fig. 3). Modified-2 calculations provide better continuity during indentation; however during rolling a smaller correction, closely approximating the unmodified calculations (employing the Hertzian width and pressure distribution) provides better model continuity. These calculations are the finite element equivalent of the Merwin-Johnson analysis devoid of their assumptions.

One calculation for $p_0/k = 5$ was repeated replacing eight-noded elements; with four-noded elements, another with eight-noded elements was repeated using double the translation increments. The residual circumferential stresses obtained from the three analyses are compared in Fig. 5; other results are shown in Table 1. These results suggest that further refinement of the mesh and incrementation is not warranted at this time.

The finite element modeling for this project was done on the multipurpose finite element package "ABAQUS." Typical CPU time for a single contact sequence involving the quoted translations is 7–20 hours on a VAX 11/780 computer.

Results

Results of the different calculations are summarized in Table 1. Figures 6–11 show the results obtained using eight-noded quadrilateral elements, and an unmodified pressure distribution for $p_0/k = 5$. The displacements of the mesh during rolling are shown in Fig. 5. Figure 6(*a*) shows the displaced mesh after the pressure distribution is applied at one end. Figure 6(*b*) shows the same mesh after the pressure distribution has been translated to the center of the mesh. Figures 6(*c*) and (*d*) show the displaced meshes with the contact pressure distribution at the other end just before unloading and the residual displacements after unloading. The dashed lines represent the original mesh; the solid lines, the displaced mesh with the displacements magnified by the factor noted in each figure. The distortion in the vertical lines of the meshes are an indication of the displacements occurring in the rim and show both "forward" and "backward" flow.

To the extent that the rolling process is viewed as rotation of two bodies about fixed centers of rotation, the "forward" or rolling direction is indicated by an arrow in Fig. 6. Figures 7 and 8 show the residual Mises equivalent stresses and the residual plastic equivalent strains, respectively, after the model has been totally unloaded. First principles require that the residual shear stresses, the residual circumferential strains, and residual radial stresses be zero and residual radial strains be small. These stresses and strains obtained from the finite element calculations are zero or very small compared to the peak stresses and strains. The stresses are ~ 1–5 percent of the peak Hertzian stress or less than 50 MPa.

The residual stresses and strains obtained from the various

Downloaded 02 May 2010 to 171.66.16.54. Redistribution subject to ASME license or copyright; see http://www.asme.org/terms/Terms_Use.cfm

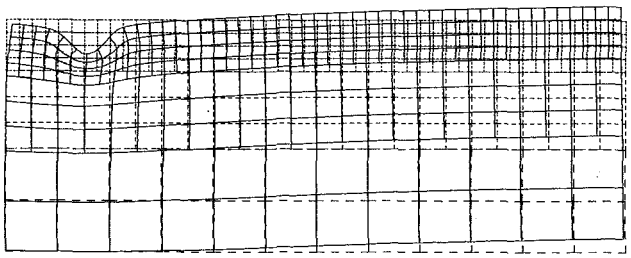


Fig. 6(*a*) The pressure distribution at one end, mag. factor = 54.2

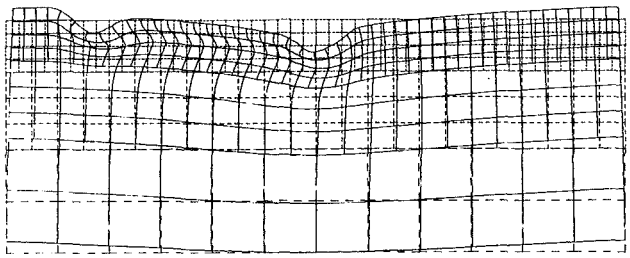


Fig. 6(*b*) The pressure distribution translated to the center, mag. factor = 72.0

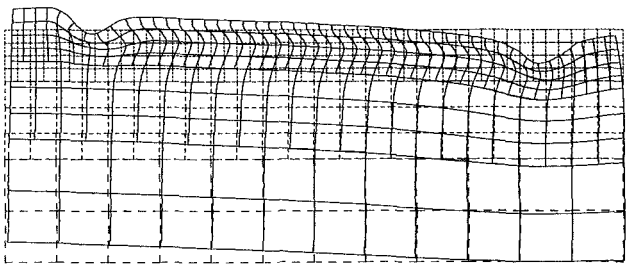


Fig. 6(*c*) The pressure distribution at the other end, mag. factor = 78.3

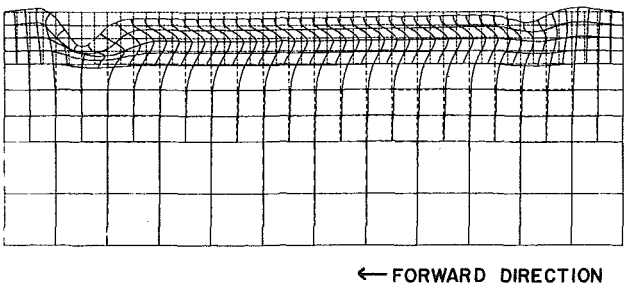


Fig. 6(*d*) The residual displacement with the load removed, mag. factor = 117.8

Fig. 6 Examples of the displaced meshes for unmodified $p_0/k = 5$. Solid lines = displaced mesh, dashed lines = original mesh.

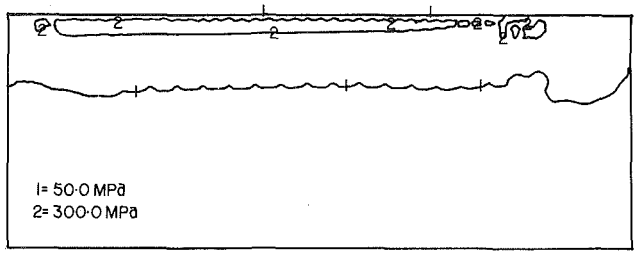


Fig. 7 The residual Mises equivalent stresses for $p_0/k = 5$

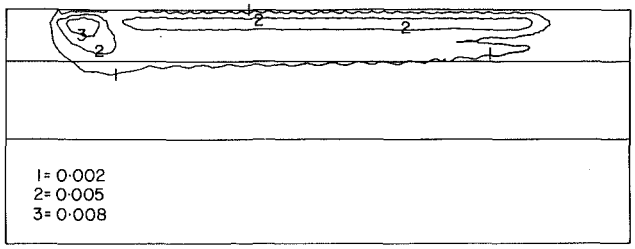


Fig. 8 The residual equivalent plastic strain for $p_0/k = 5$

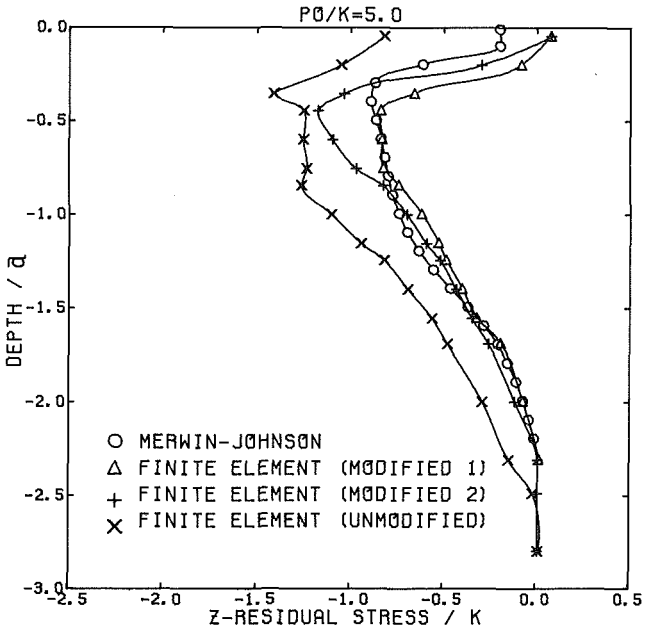


Fig. 9 Comparison of the normalized axial stress as a function of depth obtained from the various analyses for unmodified $p_0/k = 5$

analyses are compared to those obtained from the Merwin and Johnson analysis. Figures 9 and 10 compare the normalized residual axial and circumferential stresses obtained from the central region as a function of normalized depth. The stresses are normalized with respect to shear resistance, k, and the depth with respect to the contact width, a. Figure 11 compares the normalized residual shear strains, $(\gamma xyG/k)$, as a function of normalized depth. The residual shear strains obtained using an unmodified pressure distribution are very different from those obtained from the Merwin and Johnson analysis. The negative residual shear strains, strains that account for the "forward" flow in the rim, are much larger than those predicted by the Merwin and Johnson analysis. Also, while there is only a hint of positive residual strains or "backward" flow in the Merwin and Johnson analysis, the finite-element results show a region of substantial backward flow. Consequently the displacements in the rim are very different from those obtained in the Merwin and Johnson analysis. The residual peak strains and strain gradients in the y-direction vary inversely with and are very sensitive to modifications of the contact width.

Figures 6(*d*)–8, clearly show three distinct regions. On the left is the indentation region. This is followed by a region in which the stresses and strains produced by rolling are relatively insensitive to the translation distance, and on the right the region in which the indentor is lifted. The results show that a region associated with rolling is produced $\sim 6.4a$ away from the center of indentation and is distinctly different from the region of indentation. This region extends $\sim 4.5a$ and gives way to another transient region of $\sim 3.5a$, a region associated with the lifting of the indentor.

Downloaded 02 May 2010 to 171.66.16.54. Redistribution subject to ASME license or copyright; see http://www.asme.org/terms/Terms_Use.cfm

Table 2 Summary of results for alternative interpretation

P_0/K	r (mm)	a (mm)	P_0 MPa	δ	ρ_i	ρ_r	$(G\delta/P_0a)_{FE}$	$(G\delta/P_0a)_{MJ}$
4.23	69.62	0.59	964	−0.62	0.76	1.07	−0.087	−0.0015
4.35	66.125	0.575	989	−0.74	0.65	0.96	−0.104	0.0068
4.44	91.125	0.81	1011	−0.78	0.64	1.03	−0.076	0.0145
4.68	81.92	0.768	1066	−0.65	0.54	1.01	−0.063	0.0377
5.0	50.0	0.5	1137	+0.26	0.39	0.91	0.036	0.0704

$(G\delta/P_0a)_{FE}$ = normalized forward displacement—Finite Element
$(G\delta/P_0a)_{MJ}$ = normalized forward displacement—Merwin and Johnson
r = radius of the indentor
δ = the net "forward" displacement at the surface
$\rho_i = a^2/2rd$ while indenting
$\rho_r = a^2/2rd$ while rolling

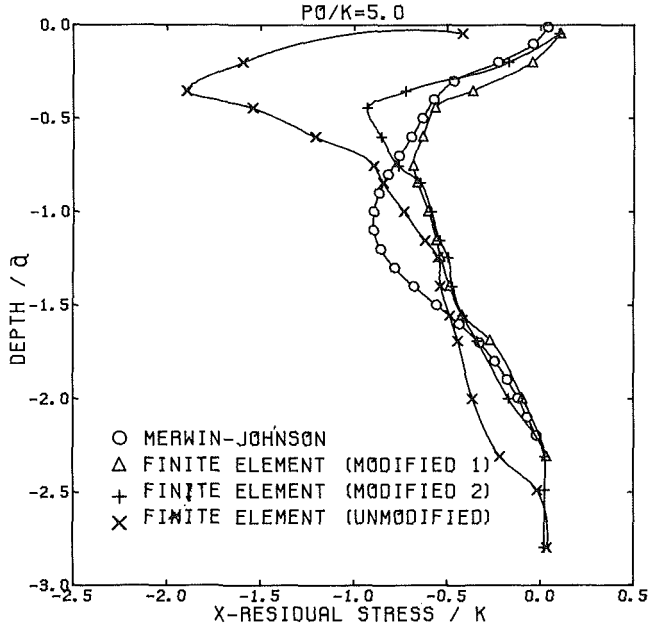


Fig. 10 Comparison of the normalized circumferential stresses as a function of depth obtained from the various analysis for $p_0/k = 5$

The parameter ρ_i (Table 1) is very sensitive to modification of the contact width. However, once rolling is in effect the parameter ρ_r is relatively less sensitive to changes in the contact width and tends toward unity for contact widths close to those predicted by the Hertzian analysis. The displacements in the rim of the finite element model (Fig. 6(*d*)) appear to be the sum of a "forward" component (negative shear strain) and a "backward" component (positive shear strain) with the former dominating near the surface: $0 \geq y \geq -0.8a$, and the latter below the surface: $-0.8 \geq y \geq -2.4a$ (see Fig. 11). The net displacement at the surface, δ, is "forward" but much smaller than that predicted by the Merwin and Johnson analysis. The values of the depth of the plastic zone, y_0, for the various analyses are in reasonable agreement. The value of p/σ_0, where p is the average pressure over the contact width, is ~ 2.27 for $p_0/k = 5$. For $p_0k = 6$ the value of p/σ_0 is ~ 2.72 and as expected produces large displacements under the contact during indentation giving rise to problems involvilng convergence.

Discussion

The modified Hertzian, three-point continuity finite element model has been shown to reproduce five features of the rolling contact problem:

(*i*) The elastic field is accurately reproduced.

(*ii*) The finite-element model reproduces the plastic field of an indentation with resonable accuracy.

(*iii*) The saturation of $\bar{p}/\sigma_0$ value in the range $2 < \bar{p}/\sigma_0 < 3$ is consistent with the well-known slipline field for indentation in bulk which yields at $p/\sigma_0 = 3$.

(*iv*) The pressure distribution has been translated a significant distance from the point of indenting.

(*v*) Model refinement appears to be adequate. The extent of the model in the translation direction is not large enough to produce well-defined steady state values. While further refinements of the mesh and increase the size of the model are possible, such refinements will make the calculation of repeated rolling contact more cumbersome and time-consuming.

The results obtained by the Merwin and Johnson analysis and the present authors apply strictly to a cylinder rolling on a half space of infinite radius with the same elastic properties as the cylinder. However, the normalized results can be applied to other radii and moduli combinations loaded to the same p_0/k ratios. This is true because the elliptical nature of the Hertzian pressure distribution is independent of the radii and the elastic properties of the contacting bodies. The elliptical distribution is fully defined by the applied load, geometry, and elastic properties of the two bodies as defined by (1) and (2):

$$p_0 = [\{P/(\pi(1-\nu^2))\}[(1/R_1)+(1/R_2)]/[(1/E_1)+(1/E_2)]]^{0.5} \quad (2)$$

As a consequence, the analysis does not depend on whether the cylinder is elastic or rigid, as long as the radius of the contacting rigid cylinder is twice that of the elastic cylinder. Also, for the same reasons, the modified-2 calculations, which failed to achieve continuity for a radius of 50 mm and values of p_0/k shown in Table 1, can be interpreted differently as shown in Table 2. These values of p_0/k and radius of indentor then represent a Hertzian distribution and a fair degree of continuity is attained while rolling. The half space can be viewed as a cylinder rotating counterclockwise; the rolling or "forward" direction corresponds with the negative x-direction (see Fig. 1) and is opposite to the direction in which the pressure distribution translates. The curvatures of the two contacting cylinders affect the stress state under the rim. The curvature of the second cylinder introduces a residual radial stress. However, as long as the radius of the cylinder is large compared to the depth of the plastic zone, the radial stress introduced would be negligibly small [1].

The validity of the first two assumptions made by Merwin and Johnson can be tested by comparing the scaled results

Downloaded 02 May 2010 to 171.66.16.54. Redistribution subject to ASME license or copyright; see http://www.asme.org/terms/Terms_Use.cfm

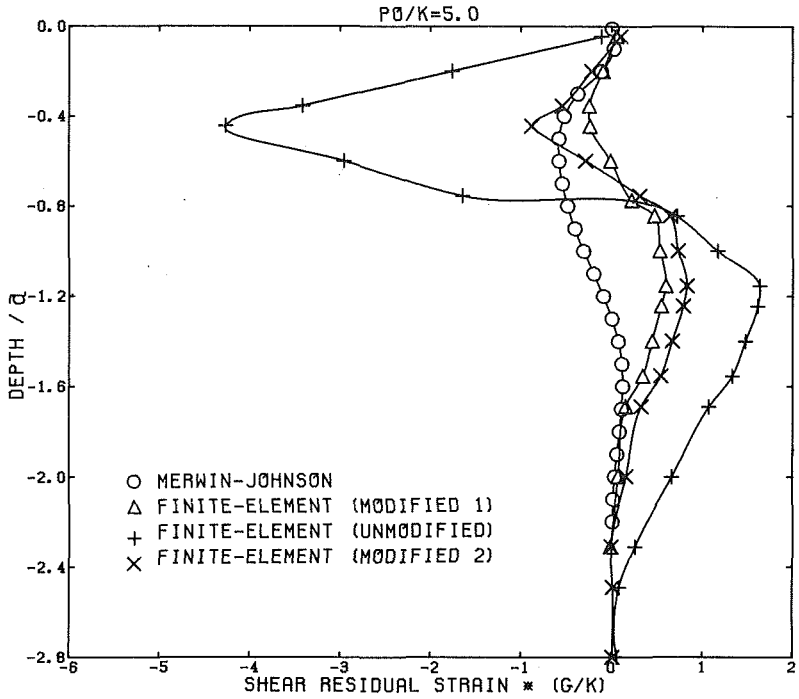


Fig. 11 Comparison of the residual shear strain as a function of depth obtained from the various analyses for $p_0/k = 5$

with those of the unmodified finite element calculations. While the assumptions do not look good while indenting, the correction to the contact width is only marginal while rolling. However, there are substantial differences. While the "backward" component of the displacement is negligible in the Merwin and Johnson analysis of a single contact; the "backward" .component in the finite element analysis is comparable to the forward component (see Fig. 11). These findings are not necessarily inconsistent with the steady state description developed by Merwin and Johnson. A finite element simulation of multiple contacts, reported in the companion paper [17], does show that δ and the "forward" component of residual displacement are increased by the second rolling contact, while the "backward" component is essentially unchanged. It is not yet clear whether the "backward" flow is a rolling phenomenon that has not been observed previously, or whether it is caused by the initial indentation of the finite element model. The fact that there is no plasticity, and thus no "forward" or "backward" flow, incorporated into the boundaries may also contribute to these results. These complications will bear further study, and indicate that the direction of future work should be in the development of a model for which (1) continuity can be obtained both during the indentation and the rolling process, or finding a method of avoiding the initial indentation altogether and (2) plasticity can be incorporated into the boundary conditions.

The assumption that $k = \sigma_0/\sqrt{3}$ with σ_0 taken as the monotonic yield stress, is not generally valid for cyclic loading with plastic strain amplitudes of the order of those produced by rolling contact. For most materials, the appropriate values of σ_0 and k will vary with distance from the rim and depend on the character of the stress-strain cycle. Consequently, the present analysis may overstate or understate the plastic efforts in real solids. Efforts are now underway to incorporate cyclic strain hardening and softening into the finite element analysis.

Conclusions

1. The semielliptical pressure distribution three-point continuity finite element model reproduces the elastic and plastic fields of indentation.

2. The pressure distribution and contact width appropriate for simulation of rolling contact are close to Hertzian.

3. During the first contact-sequence, there is "forward" flow near the surface and "backward" flow under the surface.

4 The residual stress and strain states after one contact are different from those predicted by Merwin and Johnson, with the computed peak residual shear strains significantly larger.

5. The depth to which the plastic zone extends is approximately the same for all cases.

Acknowledgments

This material is based on work supported by the National Science Foundation under Grant No. (DMR-8108500). The authors are grateful to Hibbitt, Karlsson & Sorensen, Inc. for use of their multipurpose finite-element program ABAQUS. The authors would like to thank Dr. K. L. Johnson, Dr. G. C. Martin, and Mr. Rainer Hoff for their helpful discussions. They also acknowledge Ms. C. Wieger's contribution to the preparation of the manuscript.

References

1 Merwin, J. E., and Johnson, K. L., "An Analysis of Plastic Deformation in Rolling Contact," *Proc. Inst. Mech. Engs.*, Vol. 177, 1963, p. 667.

2 Stone, D. M., and Park, Y. S., "Cyclic Plasticity of Class A and Class B Heat Treated Wheel Steels," ASME App. Mech. Div., Vol. 40, Nov. 1980, p. 157.

3 Thielen, P. N., Fine, M. E., and Fonrnelle, R. A., "Cyclic Stress Strain Relations and Strain Controlled Fatigue of 4140 Steel," *Acta Metallurgica*, Vol. 24, 1976, pp. 1-10.

4 Hamilton, G. M., "Plastic Flow in Rollers Loaded Above the Yield Point," *Proc. Inst. Mech. Engs.*, Vol. 177, 1963, p. 667.

5 Fujita, K., and Yoshida, A., "Macroscopic and Microscopic Changes in the Surface Layers of Annealed and Cast Hardened Steel Rollers Due to Rolling Contact," *Wear*, Vol. 48, 1977, p. 301.

6 Johnson, K. L., and Jefferis, J. A., "Plastic Flow and Residual Stresses in Rolling and Sliding Contact," *Proc. Symp. on Fatigue in Rolling Contact, Inst. Mech. Engr. London*, 1963, Papers.

7 Hills, D. A., and Ashelby, D. W., "The Influence of Residual Stresses on Contact Load Bearing Capacity," *Eng. Fracture Mech.*, Vol. 13, pp. 69-78.

Downloaded 02 May 2010 to 171.66.16.54. Redistribution subject to ASME license or copyright; see http://www.asme.org/terms/Terms_Use.cfm

8 Dumas, G., and Baronet, C. N., "Elastoplastic Indentation of a Half-Space by an Infinitely Long Rigid Circular Cylinder," *Int. J. Mech. Sci.*, Pergamon Press, 1071, Vol. 13, pp. 519–530.

9 Wetenkamp, M. R., and Kipp, R. M., "Thermal Damage and Rail Load Stresses in a 33-inch Railroad Car Wheel," ASME *Journal of Engineering for Industry*, Vol. 100, 1978, pp. 363–369.

10 Hooper, A. T., Sampath, S. G., and Stonesifer, R. B., "The Elastic Finite Element Analysis of CM-36 Railcar Wheel under Mechanical and Thermal Loads," Rusin, T. M., Kleeschuti, D. G., and Conghin, J. M., "Application of the Finite Element Method in the Development of Improved Railroad Car Wheel Designs," ASME *Journal of Engineering In Industry*, Vol. 101, 1979, pp. 378–384.

11 Johnson, M. R., and Young, K. S., "Applications of Finite Element Analysis to the Study of Railroad Wheel Failure Phenomena," *Track/Train Dynamics and Design, Advanced Techniques*, Moyer, Pikley, Pikey, Eds., Pergamon Press, New York, p. 384.

12 Johnson, M. R., Welch, R. E., and Young, K. S., "Analysis of Thermal Stresses and Residual Stress Changes in Railroad Wheels Caused by Sevcor Drag Boaking," ASME *Journal of Engineering for Industry*, 1977, pp. 18–23.

13 Martin, G. C., and Hay, W. W., "The Influence of Wheel-Rail Contact-Forces on the Formation of Rail Steels," Paper 72-WA/RT-8, ASME, New York, 1972.

14 Garg, V. K., et al., "Elastic-Plastic Analysis of a Wheel Rolling on a Rigid Track," *IJSS*, Vol. 10, No. 9B, pp. 945–950.

15 Suh, Nam P., "An Overview of the Delamination Theory of Wear," *Wear*, Vol. 44, 1977, p. 1.

16 Suh, Nam P., Jahanmir, S., Fleming, J., Abrahamson, E. P., Saka, N., and Teixeira, J. P., "The Delamination Theory of Wear-II," Progress Report to the Department of Defense, Sept. 1975.

17 Bhargava, V., Hahn, G. T., and Rubin, C. A., "An Elastic-Plastic Finite Element Model of Rollilng Contact Part 2: Analyses of Repeated Contacts," ASME JOURNAL OF APPLIED MECHANICS, Vol. 51, 1984, pp.

Downloaded 02 May 2010 to 171.66.16.54. Redistribution subject to ASME license or copyright; see http://www.asme.org/terms/Terms_Use.cfm

V. Bhargava
Professor.

G. T. Hahn
Professor.

C. A. Rubin
Associate Professor.
Mem. ASME

Department of Mechanical and Materials Engineering.
Vanderbilt University,
Nashville, Tenn. 37235

An Elastic-Plastic Finite Element Model of Rolling Contact

Part 2: Analysis of Repeated Contacts

This paper presents finite element analyses of two-dimensional (plane strain), elastic-plastic, repeated, frictionless rolling contact. The analysis employs the elastic-perfectly plastic, cycle and strain-amplitude-independent material used in the Merwin and Johnson analysis but avoids several assumptions made by these workers. Repeated rolling contacts are simulated by multiple translations of a semielliptical Hertzian pressure distribution. Results at $p_0/k = 3.5$, 4.35, and 5.0 are compared to the Merwin and Johnson prediction. Shakedown is observed at $p_0/k = 3.5$, but the comparisons reveal significant differences in the amount and distribution of residual shear strain and forward flow at $p_0/k = 4.35$ and $p_0/k = 5.0$. The peak incremental, shear strain per cycle for steady state is five times the value calculated by Merwin and Johnson, and the plastic strain cycle is highly nonsymmetric.

Introduction

There are only two detailed analyses of the stress and strain states in an elastic-plastic rim subjected to repeated rolling contact: (*i*) The classical elastic, quasiplastic, two-dimensional (plane-strain) analysis which was employed by Merwin and Johnson [1] and Johnson and Jefferis [2], and (*ii*) a three-dimensional, elastic-plastic finite element analysis by Martin and Hay [3]. Both analyses treat a rigid cylinder rolling on an semi-infinite half plane. They simulate rolling by translating a Hertzian pressure distribution along the half space with and without (frictionless rolling) surface tractions [2, 3]. The analyses are carried out for an elastic-perfectly plastic, Von Mises material with a cyclic shear resistance $k = \sigma_0/\sqrt{3}$ (σ_0 is the yield strength) that is assumed to be isotropic and independent of the strain amplitude and the number of load cycles. A rigorous elastic-plastic finite element analysis of a single cycle of frictionless rolling by the present authors [4] verifies that, $2a$, the appropriate contact width, for a relative peak pressure of up to at least $p_0/k = 5$, is close to the Hertzian value even after the half plane begins to deform plastically. This, together with the Dumas and Baronet work [5], implies that the pressure distribution is not affected significantly by plastic flow.

The finite element analysis also provides a basis for examining the other assumptions made by Merwin and Johnson. One is that the sums of elastic and plastic strain components are the same as the Hertzian elastic strains after the half plane begins to yield. In addition, because equilibrium is not maintained throughout the contact cycle, their computations predict extraneous stresses at the end of each contact cycle. The assumption that equilibrium can be restored and the stress-strain history described by superposing a stress state designed to eliminate the extraneous stresses, is not borne out in all respects. For example, the residual shear strain distribution and the amount of forward flow calculated by Merwin and Johnson for a single contact depart from those obtained in the finite element analysis [4].

As noted in Part 1 [4], the Merwin and Johnson analysis of repeated frictionless rolling contact predicts that a steady state is quickly attained, usually within the first few cycles for $p_0/k > 4.0$. Further load cycles produce continuing, partially reversed stress-strain cycles with small plastic strain amplitudes that lead to accumulating residual shear strain and forward flow. Such accummulating strains can produce cyclic hardening or softening and have a bearing on the life of the component. No other analytical forward flow predictions have been forthcoming, and the experimental evidence is contradictory [6–8]. The Martin and Hay study treats a three-dimensional model and is primarily interested in the stresses and strains in the transverse plane (the cross-sectional plane that is perpendicular to the Merwin-Johnson plane strain model) after steady state has been reached. Thus, this study does not lend itself to comparison with the Merwin and Johnson analysis.

Neither of these analyses examines the complication that the flow properties of structural alloys are cycle and strain-amplitude-dependent. Measurements of cyclic plasticity of steel by Stone and Park [9] and Thielen, Fine and Fournelle [10] show the values of k appropriate for fully reversed cycles

Contributed by the Applied Mechanics Division and presented at the Winter Annual Meeting, New Orleans, La., December 9–14, of THE AMERICAN SOCIETY OF MECHANICAL ENGINEERS.

Discussion on this paper should be addressed to the Editorial Department, ASME, United Engineering Center, 345 East 47th Stret, New York, N.Y. 10017, and will be accepted until two months after final publication of the paper itself in the JOURNAL OF APPLIED MECHANICS. Manuscript received by ASME Applied Mechanics Division, January, 1984; final revision, May, 1984. Paper No. 84-WA/APM-43.

Copies will be available until August, 1985.

Copyright © 1985 by ASME
Downloaded 02 May 2010 to 171.66.16.54. Redistribution subject to ASME license or copyright; see http://www.asme.org/terms/Terms_Use.cfm

Table 1 Summary of results (steady state)

p_0/k	r (mm)	a (mm)	p_0 (MPa)	δ (μm)	$(G\delta/p_0a)_{FE}$	$(G\delta/p_0a)_{MJ}$
3.5	50.0	0.350	796	0.0	0.0	0.0
4.35	66.1	0.575	989	0.3	0.04	0.01
5.0	50.0	0.500	1137	2.7	0.38	0.06
5.0(*)	50.0	0.500	1137	2.9	0.41	0.06

p_0/k = relative peak pressure
r = radius of the indentor
$2a$ = steady state contact widths
δ = steady state forward displacement per cycle
$(G\delta/p_0a)_{FE}$ = steady state normalized forward displacement = Finite Element
$(G\delta/p_0a)_{MJ}$ = steady state normalized forward displacement = Merwin and Johnson

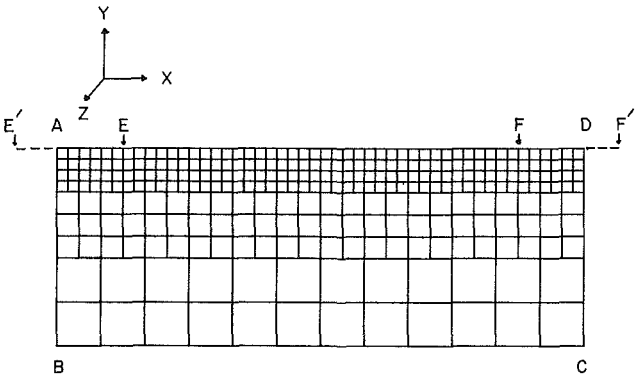


Fig. 1 Finite element mesh for the elastic-plastic semi-infinite half plane. The smallest dimension of the mesh = 0.2 mm for calculations at p_0/k = 4.35 and 5.0. The smallest dimension = 0.14 for p_0/k = 3.5.

with plastic strain amplitudes in the range $10^{-4} < \Delta\epsilon p/2 < 10^{-3}$ is 0.9–0.5 times the value of k for monotonic loading and depends on the number of cycles. Neither Merwin and Johnson [1] nor Martin and Hay [3] incorporated a strain-amplitude-dependent value of k in the contact calculation.

This paper applies a two-dimensional, plane strain, finite element model of rolling contact that it fully described in a comparison paper [4] to examine repeated contacts. It employs the elastic-perfectly plastic, cycle and strain-amplitude-independent material used in the Merwin and Johnson analysis. The calculations are, however, rigorous with respect to equilibrium requirements. Repeated rolling contacts are simulated by multiple translations of a semielliptical Hertzian pressure distribution. The results are compared with the predictions of the Merwin and Johnson analysis for repeated frictionless rolling contact and serve to validate a finite element model that will be used in the future to examine the effects of strain-amplitude-dependent cyclic flow properties.

Description of the Model

Rolling of a Hertzian cylinder is simulated by translating a semielliptical pressure distribution over an elastic-plastic semi-infinite half space. The half space is represented by a finite-sized mesh (Fig. 1) whose three side boundaries are consistant with the elastic deformation. The features of the model are described in reference [4].

Rolling is simulated using two methods. In the first method, the pressure distribution is applied incrementally at E (Fig. 1) and translated incrementally to the point F near the other end and then unloaded. The boundaries are displaced appropriately at each increment. For each consecutive cycle the pressure distribution is again applied incrementally translated incrementally, and unloaded. The boundaries are displaced appropriately at each increment. In the second method, an attempt is made to minimize the indenting for one case, with $p_0/k = 5$ (to be referred to as $p_0/k = 5.0^*$). The boundaries of the mesh are displaced consistant with the pressure distribution being applied incrementally on the left side of the left boundary at an imaginary point (E' in Fig. 1). The pressure distribution was then incrementally moved on to the mesh, over it, and beyond the boundary on the other side to an imaginary point (F' in Fig. 1). The boundaries were displaced appropriately at each increment. The pressure distribution was then removed incrementally and the

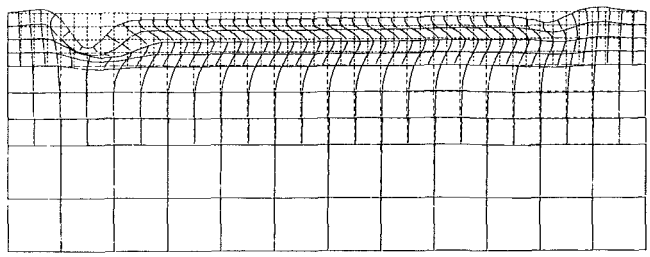


Fig. 2(a)

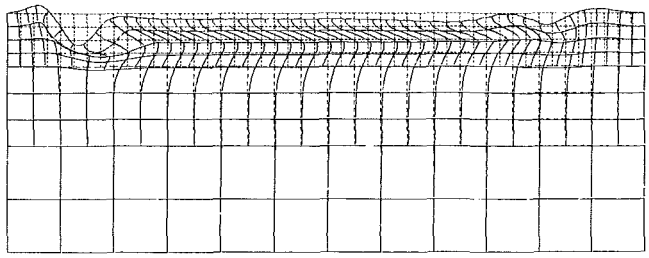


Fig. 2(b)

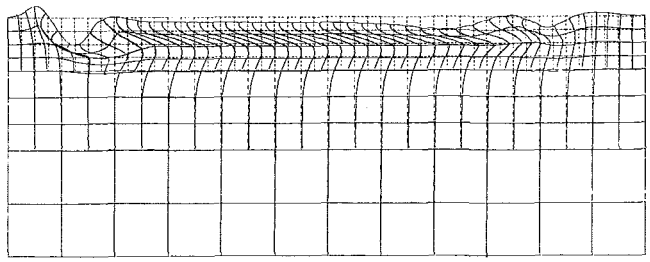


Fig. 2(c)

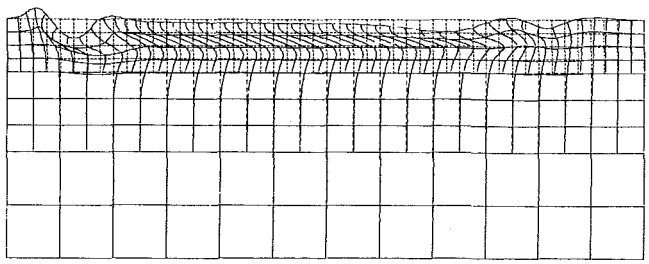


Fig. 2(d)

Fig. 2 The displaced meshes for p_0/k = 5.0 after each contact cycle (a) after the first contact cycle, mag. factor = 117.8, (b) after the second contact cycle, mag. factor = 107.4, (c) after the third contact cycle, mag. factor = 90.3, and (d) after the fourth contact cycle, mag. factor = 63.1

Downloaded 02 May 2010 to 171.66.16.54. Redistribution subject to ASME license or copyright; see http://www.asme.org/terms/Terms_Use.cfm

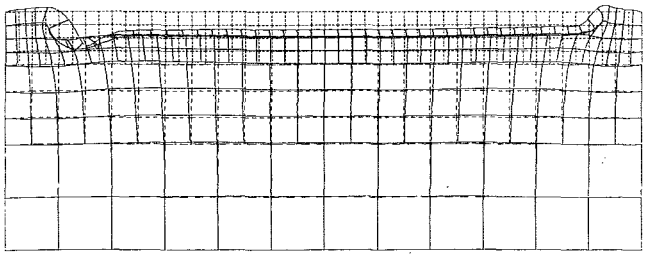


Fig. 3(a)

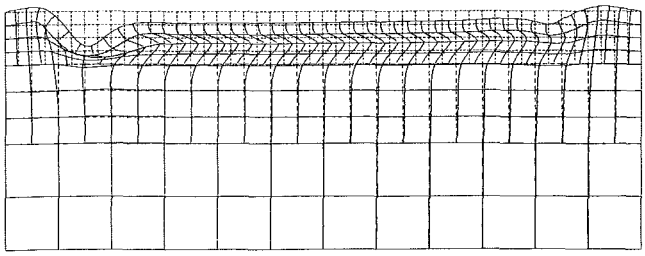


Fig. 3(b)

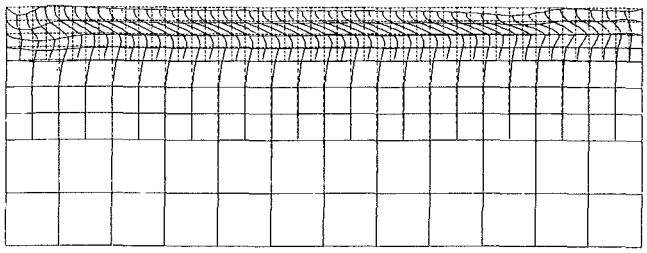


Fig. 3(c)

Fig. 3 Examples of the displaced meshes after the final contact cycle (a) for p_0/k = 3.5 after the second contact cycle, mag. factor = 6000, (b) for p_0/k = 4.35 after the third contact cycle, mag. factor = 332.2, and (c) for p_0/k = 5.0* after the third contact cycle, mag. factor = 55.

boundaries forced to their original positions. Calculations were made using the mesh in Fig. 1 with eight-noded, isoparametric, plane strain elements with a rigid cylinder of radius 50 mm, Young's modulus E = 207 GPa, ν = 0.3, and a relative shear resistance $[k(1-\nu^2)]/E = 10^{-3}$ for the half space.

The finite element modeling for this project employed the multipurpose finite element package "ABAQUS." Typical CPU time for a single contact sequence is ~ 7–24 hours on a VAX 11/780 computer. A more detailed description of the finite element model can be found in reference [4].

Results

Results of the different calculations are summarized in Table 1. Calculations were carried out for p_0/k = 3.5, 4.35, 5.0, and 5.0*; the corresponding Hertzian contact widths are 0.35 mm, 0.575 mm, 0.5 mm, and 0.5 mm. Figure 2 shows the distorted mesh for p_0/k = 5.0 after each cycle. The dashed lines represent the original mesh; the solid lines the displaced mesh, with the displacements being magnified by the factor noted in each figure. The distortions of the vertical lines represent the forward or backward flow. Figure 2(*a*) shows the distorted mesh after the first cycle and indicates forward flow near the surface along with substantial backward flow under it. Consecutive cycles produce increases in the forward flow only. Figure 3 shows the displaced meshes after the final contact sequences for p_0/k = 3.5, 4.35, and 5.0*. Figure 3(*a*) indicates no forward or backward flow at p_0/k = 3.5. Figure 3(*b*) shows the forward flow for p_0/k = 4.35. Figure 3(*c*) shows the distortions under the surface for p_0/k = 5.0*. Since no indenting was done for 5.0*, there is a smaller

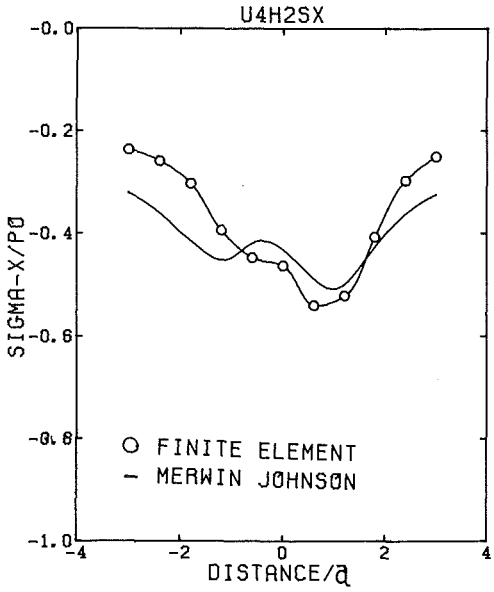


Fig. 4(a)

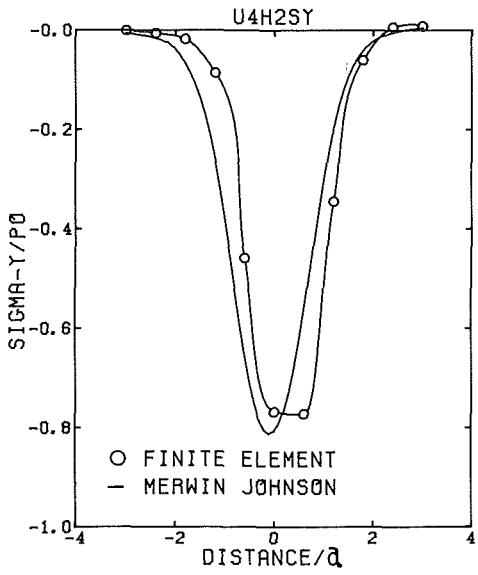


Fig. 4(b)

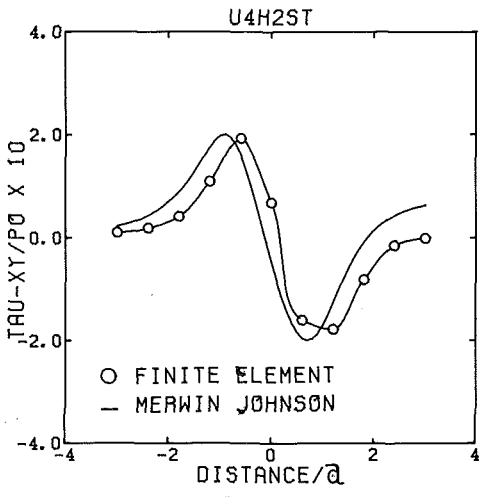


Fig. 4(c)

Fig. 4 Comparison of normalized stress history of a point at depth = 0.755a for p_0/k = 5.0 (a) σ_x/p_0 (b) σ_y/p_0, and (c) τ_{xy}/p_0

Downloaded 02 May 2010 to 171.66.16.54. Redistribution subject to ASME license or copyright; see http://www.asme.org/terms/Terms_Use.cfm

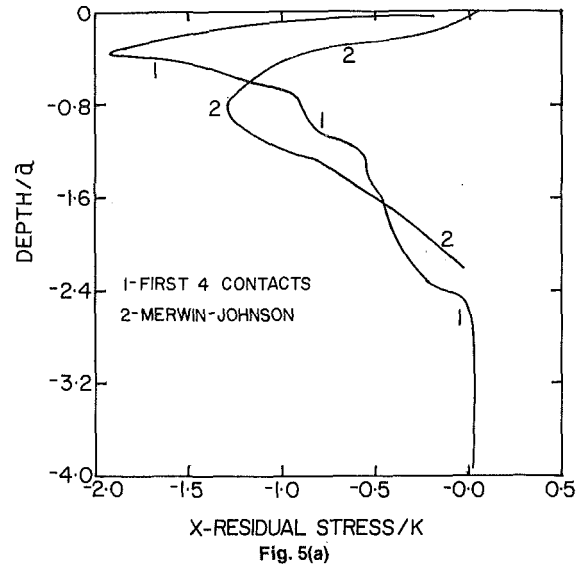


Fig. 5(a)

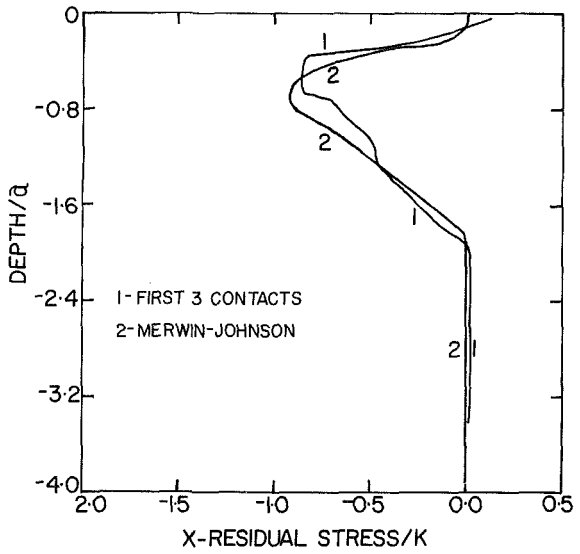


Fig. 5(b)

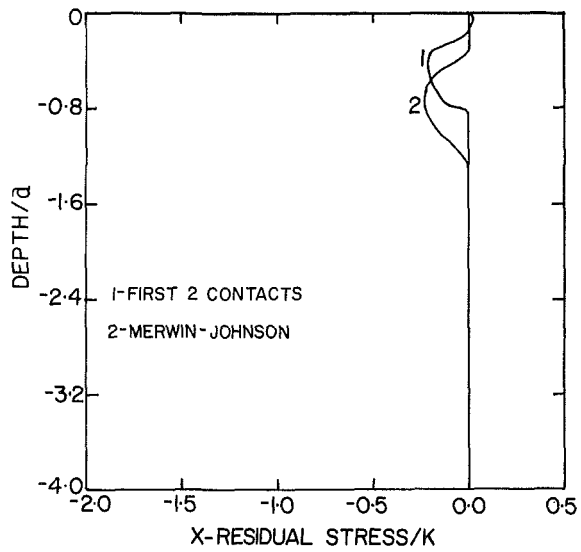


Fig. 5(c)

Fig. 5 Comparison of normalized residual circumferential stresses as a function of depth (*a*) $p_0/k = 5.0$, (*b*) $p_0/k = 4.35$, and (*c*) $p_0/k = 3.5$. Where results for successive repeated contacts were not significantly different, they are represented by a single curve.

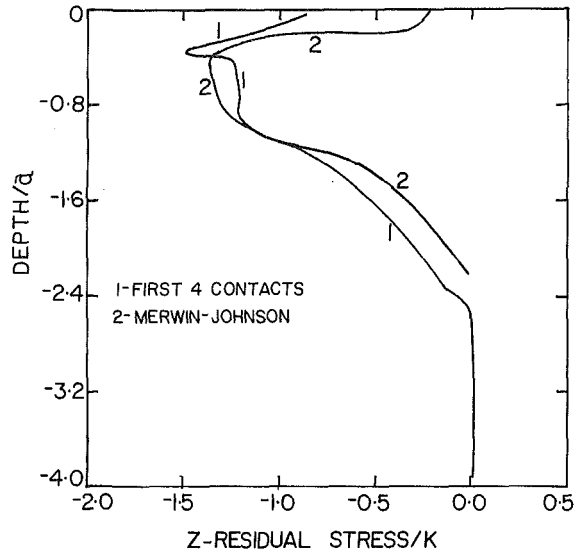


Fig. 6(a)

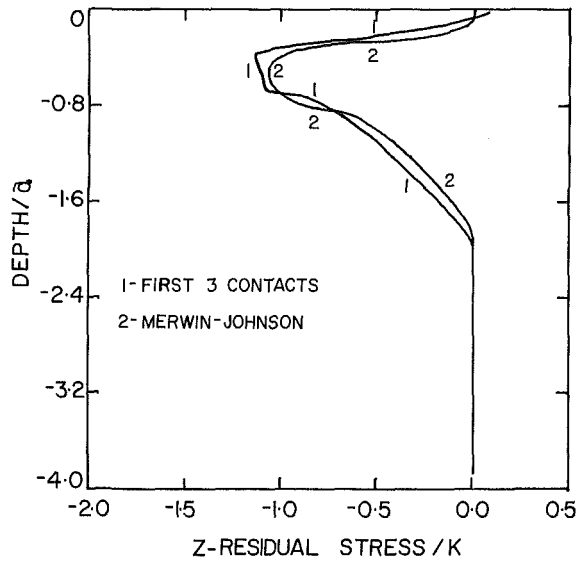


Fig. 6(b)

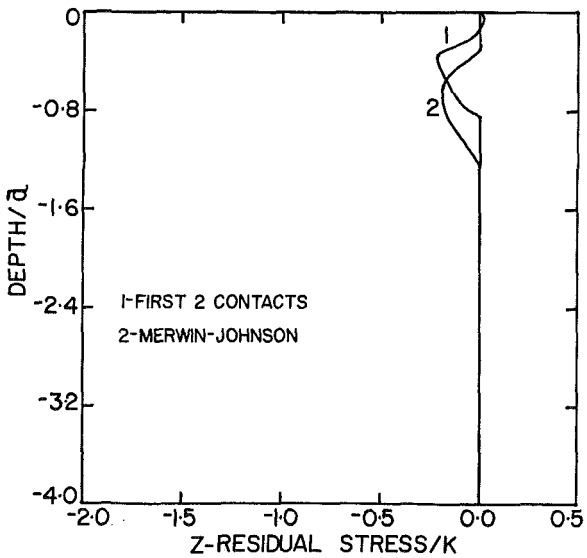


Fig. 6(c)

Fig. 6 Comparison of normalized residual axial stress as a function of depth (*a*) $p_0/k = 5.0$, (*b*) $p_0/k = 4.35$, and (*c*) $p_0/k = 3.5$. Where results for successive repeated contacts were not significantly different, they are represented by a single curve.

Downloaded 02 May 2010 to 171.66.16.54. Redistribution subject to ASME license or copyright; see http://www.asme.org/terms/Terms_Use.cfm

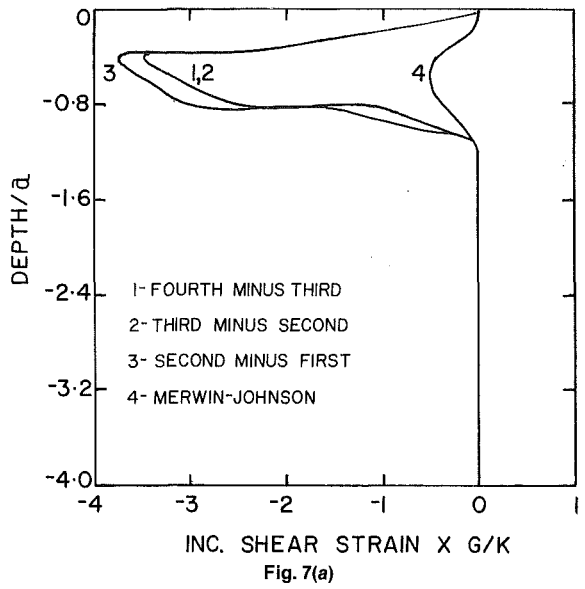


Fig. 7(a)

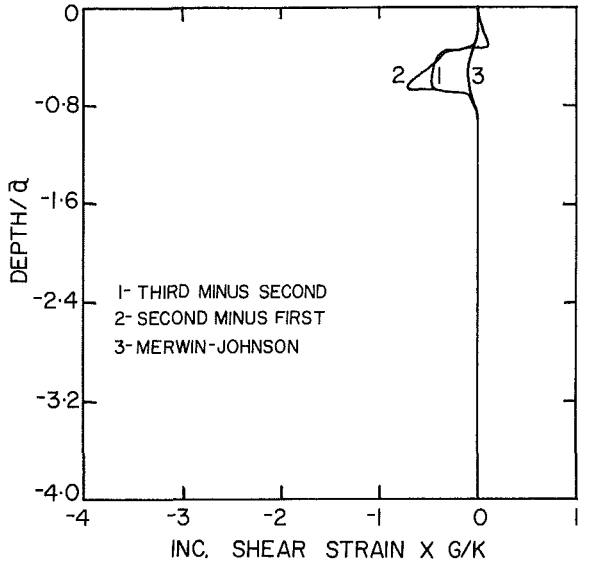


Fig. 7(b)

Fig. 7 Comparison of normalized residual shear strain increment as a function of depth (a) $p_0/k = 5.0$ and (b) $p_0/k = 4.35$. The incremental shear strain is the residual shear strain after the nth contact minus the residual shear strain after the $(n-1)$th contact.

buckling of the top surfaces as compared to the case where the load was applied directly onto the mesh. This is because the boundaries are made rigid at the end of the cycle and cannot accommodate forward flow. The amounts of forward flow per cycle for both cases are the same.

Figure 4 compares the stress history of a point at a depth of $0.755a$ and $p_0/k = 5$, obtained from the finite element analysis to those obtained from the Merwin and Johnson analysis. The basic characteristics of the stress history are the same in both cases. Figures 5–7 compare the normalized residual stress and incremental residual shear strain per cycle as a function of depth with those obtained from the Merwin and Johnson analysis. The stresses are normalized with respect to k, the strains with respect to k/G, and depth with respect to a. The comparisons are made for $p_0/k = 3.5$, 4.35, and 5.0. Figure 5 compares the normalized residual circumferential stress σ_x/k. The peak stresses predicted by the finite element analysis occur closer to the surface and are greater than those predicted by Merwin and Johnson for p_0/k

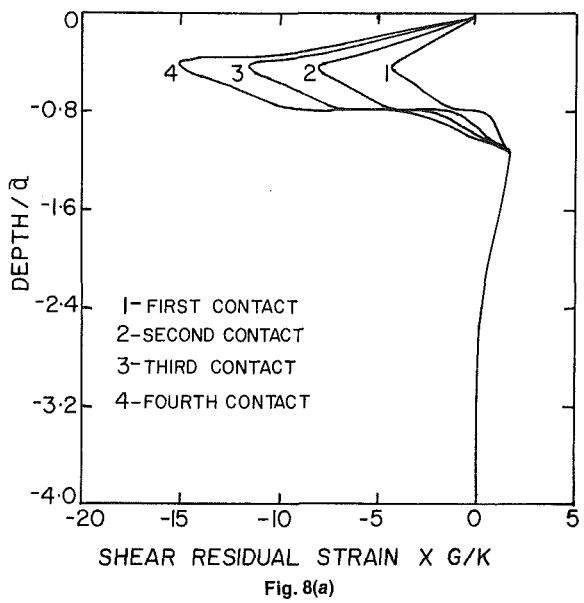


Fig. 8(a)

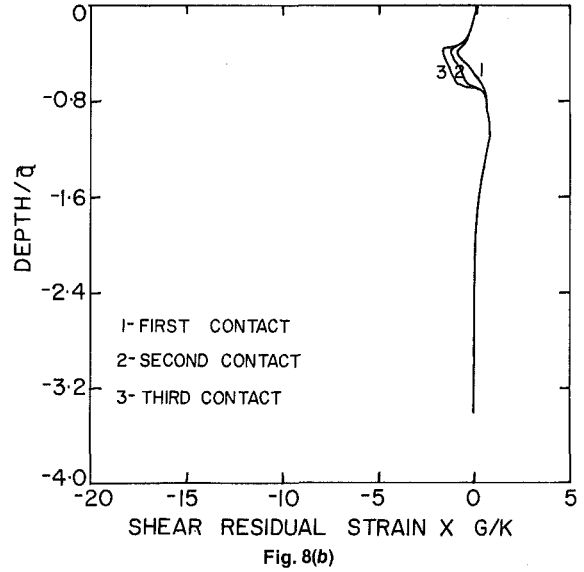


Fig. 8(b)

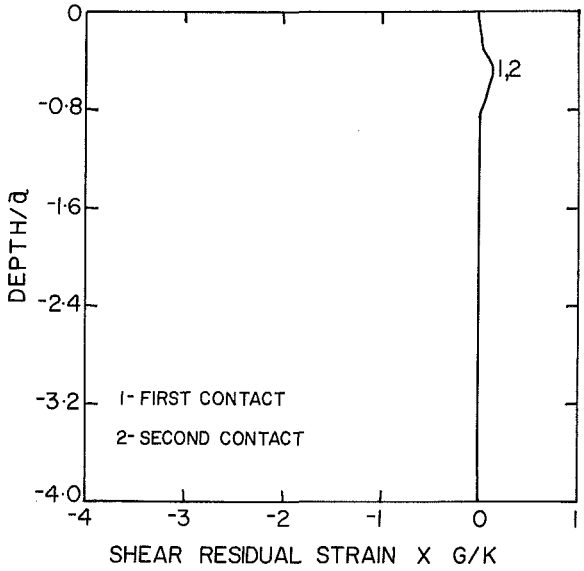


Fig. 8(c)

Fig. 8 Normalized residual shear strain after each contact cycle as a function of depth (a) $p_0/k = 5.0$, (b) $p_0/k = 4.35$, and (c) $p_0/k = 3.5$

Downloaded 02 May 2010 to 171.66.16.54. Redistribution subject to ASME license or copyright; see http://www.asme.org/terms/Terms_Use.cfm

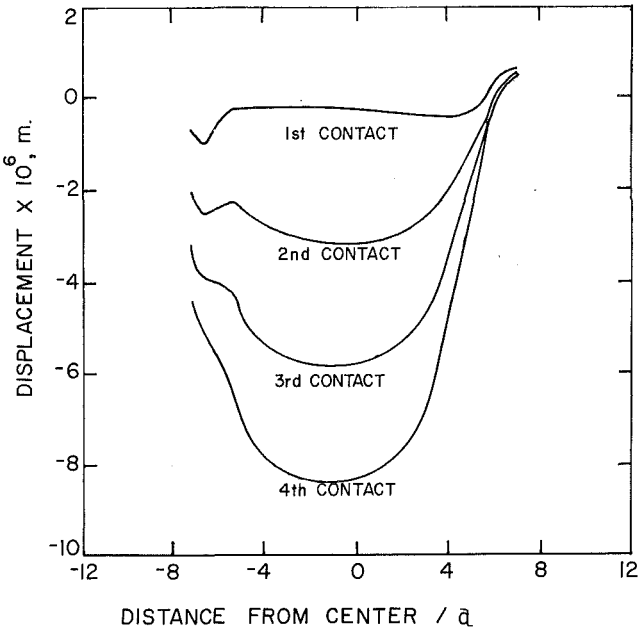


Fig. 9 Forward flow after each cycle as a function of relative distance from the center of the mesh for $p_0/k = 5.0$

$= 5.0$. For $p_0/k = 4.35$ and 3.5 the peak values are almost equal. Figure 6 compares the normalized residual axial stresses. Again the peaks occur closer to the surface than predicted by Merwin and Johnson. Figure 7 compares the normalized residual shear strain increment per cycle. The increase in residual shear strain and hence forward flow per cycle is much larger than that preidcted by Merwin and Johnson. Both analyses predict no increment of residual shear strain at $p_0/k = 3.5$.

Figure 8 shows the normalized residual shear strain after each contact sequence. Consistent with the distorted mesh (Fig. 2(*a*)), a significant amount of backward flow is observed after the first cycle for $p_0/k = 5.0$ and 4.35. However, consecutive cycles produce only forward flow. For $p_0/k = 3.5$, shakedown is observed.

To examine the effect of indenting at the beginning of the cycle on the backward flow and the residual stress and strain state, the results obtained from $p_0/k = 5.0$ were compared to those from $p_0/k = 5.0^*$. While the indent in the case of $p_0/k = 5.0^*$ is much smaller, the amount of backward flow after the first cycle was essentially the same in both cases. The residual stresses, shear strains, and plastic equivalent strains after the fourth cycle are also the same in both cases, indicating that the effect of indenting is negligible.

Figure 9 shows the distribution of forward flow across the surface for $p_0/k = 5.0$ after each cycle. To examine whether the stresses and strains are independent of the translation distance in the central region of the mesh, residual stresses and strains for $p_0/k = 5.0$ were compared from three different sections in the central region. A comparison of the residual stresses, shear strains, and plastic equivalent strains after the fourth cycle shows no significant difference among the three sections. Figure 10 shows the stress strain cycle of points at various depths in the rim. The cycles are highly nonsymmetric. Figure 11 compares the predictions of the normalized forward flow per cycle. Consistent with the prediction of larger residual shear strains, the amounts of forward flow per cycle obtained with the finite element analysis are much larger than predicted by the Merwin and Johnson analysis.

Discussion

The adequacy of the finite element mesh, its ability to

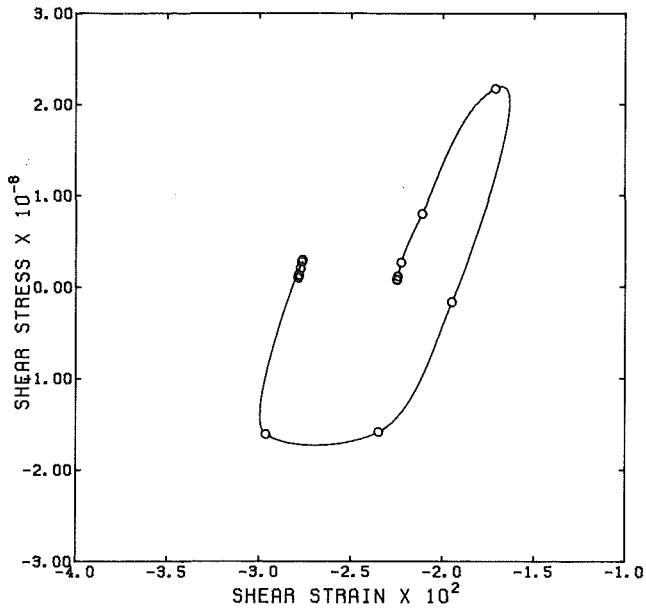


Fig. 10(*a*)

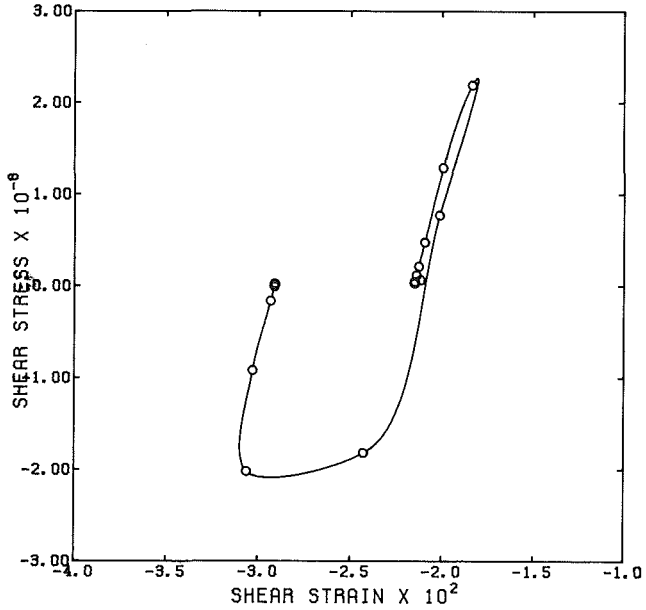


Fig. 10(*b*)

Fig. 10 The shear stress strain cycle at various depths (*a*) depth = 0.355*a*, (*b*) depth = 0.755*a*

reproduce various features representative of the rolling contact problem, and the justification for using the Hertzian pressure distribution to represent the contact stresses were discussed in a previous paper [4] which deals with a single contact cycle. With repeated rolling contacts, little change is observed in the residual axial and circumferential stresses produced by successive contacts after the first cycle. The residual shear strain increment per cycle also becomes constant after the first two contact cycles. Further cycles produce no change in either the residual stress state or the shear strain increment per cycle. A steady state can be said to have been attained within the first two cycles. This is assuming the flow properties are not cycle and amplitude-dependent.

Comparison of the residual stress and strain states of the two simulation methods, (*i*) with the pressure distribution first indented onto the mesh and (*ii*) with the pressure distribution slowly eased onto the mesh, shows that the effect of in-

Downloaded 02 May 2010 to 171.66.16.54. Redistribution subject to ASME license or copyright; see http://www.asme.org/terms/Terms_Use.cfm

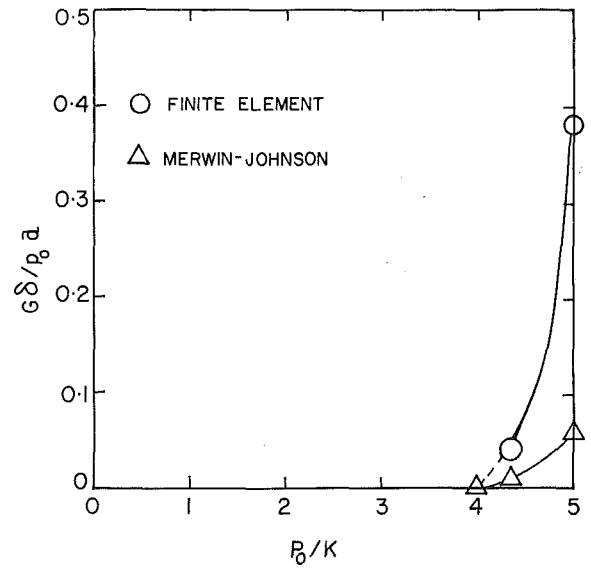


Fig. 11 Comparison of normalized forward flow per cycle as a function of relative peak pressure

dentation, in spite of indentation size, is negligible in the central region of the mesh. Also the comparison of stresses and strains at three different sections in the central region indicates that the residual stresses and strains are largely independent of the translation distance. The amount of forward flow at the surface varies with distance (Fig. 9). Only the region in the center can accommodate forward flow since the forward flow must go to zero at each end. This might have some effect on the value of forward flow in the central region, and the effect may increase with every cycle, however, the effect would propably underestimate rather than overestimate the forward flow. The elastic deformation of the boundaries is larger than the accumulated forward flow hence the effect, of displacing the boundaries elastically should be small at the center. A longer mesh will be used to examine this constraining effect and possible ways of positioning the boundaries for plasticity are being sought.

In general, the results of the finite element analyses are in accord qualitatively with those of the Merwin and Johnson analysis and even quantitatively in some respects. The basic features of the stress history and the residual stress state are similar. Shakedown is predicted by both analyses to occur at $p_0/k = 3.5$ and since the residual stress states at $p_0/k = 4.35$ of the two analyses are quite similar, it is expected that the shakedown limit of $p_0/k = 4.0$, calculated by Merwin and Johnson, is appropriate. Some significant differences are observed when the residual stresses at $p_0/k = 5.0$ are compared with the Merwin and Johnson predictions. The largest differences are observed in the amounts and distribution of the residual shear strain increment per cycle. The peak residual shear strain increments at steady state are up to five times larger than the Merwin and Johnson values. Consequently the forward flow near the rim surface is also up to five times larger than that predicted by Merwin and Johnson. The backward flow observed during the first cycle is absent during consecutive cycles.

The measurements of forward flow by Hamilton [6] for cold-worked copper are in better agreement with the smaller values calculated by Merwin and Johnson. For 1018 steel [8], the measured forward flow is even smaller than the values that Merwin and Johnson predict. While steady state is predicted within the first few cycles, Johns and Davies [7] observe that the residual stresses continue to change with the number of cycles. The reasons for this are not clear; it is possible that these discrepancies are all related to the fact that cyclic flow properties may be quite different from the monotonic flow properties.

It is difficult to estimate the errors Merwin and Johnson introduced by assuming: (1) that elastic-plastic strains are the same as in the purely elastic case and (2) that equilibrium is maintained throughout the cycle. The predictions of residual shear strains show the largest differences between the two analyses. This is not surprising for two reasons. First, by assuming an equality between the Hertzian (elastic strains which fully reverse) and total (elastic plus plastic) strains, Merwin and Johnson tend to limit the magnitude of the residual shear strain that is not reversing. Secondly, the assumption that the extraneous residual shear stress produces an equivalent amount of elastic residual shear strain may be inappropriate for a nonlinear system.

Neither the Merwin and Johnson theory nor the present finite element model account for a cycle and amplitude-dependent cyclic shear resistance. The peak amplitude of the cyclic shear strain is $\Delta\gamma_p \sim 0.01$ at $p_0/k = 5.0$ and the strain cycle can be highly nonsymmetric at small depths (Fig. 10). The implication of the large values of the cyclic strain amplitude is that rolling contact can produce cyclic strain hardening as well as cyclic strain softening further altering the residual stress and strain gradients. Evidence of this can be found in reference [8]. A finite element model employing cycle and amplitude-dependent flow is presently being developed.

Conclusions

1. With repeated rolling contacts, a steady state is usually attained within the first two cycles, provided the flow stress does not change.

2. The basic features of the stress history experienced by a point are similar in both the Merwin and Johnson and the finite element analysis.

3. The values of peak residual and circumferential residual stresses obtained here are similar to the values reported by Merwin and Johnson except the peak circumferential residual stress at $p_0/k = 5.0$ is $\sim$ 30 percent larger in the finite element analysis.

4. The residual shear strain increments per cycle at steady state are up to five times larger than values predicted by Merwin and Johnson. Consequently, the forward flow at the surface is also correspondingly larger.

5. In view of the large peak values of the cyclic strain amplitudes, both strain hardening and cyclic softening may take place in the rim depending on the particular stress-strain cycle experienced at each depth.

6. The backward flow is only associated with the first cycle, and subsequent cycles produce only forward flow.

7. In one calculation at $p_0/k = 3.5$, shakedown was observed.

Acknowledgments

This material is based on work supported by the National Science Foundation under Grant No. (DME-8108500). The authors are grateful to Hibbitt, Karlsson & Sorensen, Inc. for the use of their multipurpose finite element program ABAQUS. The authors would like to thank Mr. Rainer Hoff for many helpful suggestions and discussions. They also acknowledge Ms. C. Wieger's contribution to the preparation of the manuscript.

Downloaded 02 May 2010 to 171.66.16.54. Redistribution subject to ASME license or copyright; see http://www.asme.org/terms/Terms_Use.cfm

References

1 Merwin, J. E., and Johnson, K. L., "An Analysis of Plastic Deformation in Rolling Contact," *Proc. Inst. Mech. Eng.*, Vol. 177, 1963, p. 667.

2 Johnson, K. L., and Jefferis, J. A., "Plastic Flow and Residual Stresses in Rolling and Sliding Contact," *Proc. Symp. on Fatigue in Rolling Contact*, Inst. Mech. Eng. London, 1963.

3 Martin, G. C., and Hay, W. W., "The Influence of Wheel-Rail Contact-Forces on the Formation of Rail Steels," Paper 72-WA/RT-8, ASME, New York, 1972.

4 Bhargava, V., Hahn, G. T., and Rubin, C. A., "An Elastic-Plastic Finite Element Model of Rolling Contact: Part 1: Analysis of Single Contacts," ASME JOURNAL OF APPLIED MECHANICS, Vol. 51, 1984, pp. 00-00.

5 Dumas, G., and Baronet, C. N., "Elastoplastic Indentation of a Half-Space by an Infinitely Long Rigid Circular Cylinder," *Int. J. Mech. Sci.*, Pergamon Press, 1071, Vol. 13, pp. 519-530.

6 Hamilton, G. M., "Plastic Flow in Rollers Loaded Above the Yield Point," *Proc. Inst. Mech. Eng.*, Vol. 177, 1963, p. 667.

7 Johns, T. G., and Davies, K. B., "A Preliminary Description of Stresses in Railroad Rail," Federal Rail Road Administration Report FRA-ORD-76-294, Nov. 1976, p. 24.

8 Bhargava, V., Rubin, C., and Hahn, G. T., "Analysis of Rolling Contact Failure," *Proceedings of the Workshop on Mechanics of Fracture and Damage*, Nov. 1982, Stone Mountain Ga., p. 17.

9 Stone, D. M., and Park, Y. S., "Cyclic Plasticity of Class A and Class B Heat-Treated Wheel Steels," ASME App. Mech. Div., Vol. 40, Nov. 1980, p. 157.

10 Thielen, P. N., Fine, M. E., and Fournelle, R. A., "Cyclic Stress Strain Relations and Strain Controlled Fatigue of 4140 Steel," *Acta Metallurgica*, Vol. 24, 1976, pp. 1-10.

Downloaded 02 May 2010 to 171.66.16.54. Redistribution subject to ASME license or copyright; see http://www.asme.org/terms/Terms_Use.cfm

L. Wheeler
Department of Mechanical Engineering,
University of Houston,
Houston, Texas 77004

The Problem of Minimizing Stress Concentration at a Rigid Inclusion

With the objective of minimizing stress concentration, the plane-strain problem of the optimum shape for a rigid inclusion in an elastic matrix of unbounded extent is investigated. It is shown rigorously that the underlying variational problem is reducible to a more elementary problem which can be solved by conventional methods to arrive at the optimum shape, which is a suitably proportioned ellipse.

Introduction

The object of this paper is an optimization problem aimed at finding the best shape for a rigid inclusion imbedded in an elastic matrix of infinite extent, if the stress concentration is to be minimized. The matrix is governed by the linear theory for homogeneous and isotropic solids in a state of plane deformation. Stress is applied at infinity, while the inclusion remains free of externally applied forces. The precise statement of the corresponding boundary-value problems is given in Section 1.

Section 2 is devoted to the formulation of the optimization problem. Here we adopt a measure of stress concentration appropriate to materials that fail by yielding in accordance with the von Mises criterion.

Section 3 concerns the reduction of the optimization problem to a kind of inverse problem which appears to be more elementary than the optimization problem. At this stage appears the main result of the paper, the determination of a set of conditions under which this reduction is justified mathematically.

In Section 4, the final section, we discuss actual solutions of the inverse problem, which are readily found in the form of ellipses.

1 The Plane Strain Problem of a Rigid Inclusion Bonded to an Elastic Matrix

Let D designate a plane domain formed by the deletion of a bounded region, and denote by C the boundary of D. We are concerned with the state of stress within D arising from the application of stress at infinity when an elastic material (the matrix) occupies D and a rigid material (the inclusion) is situated in the complement of D (see Fig. 1).

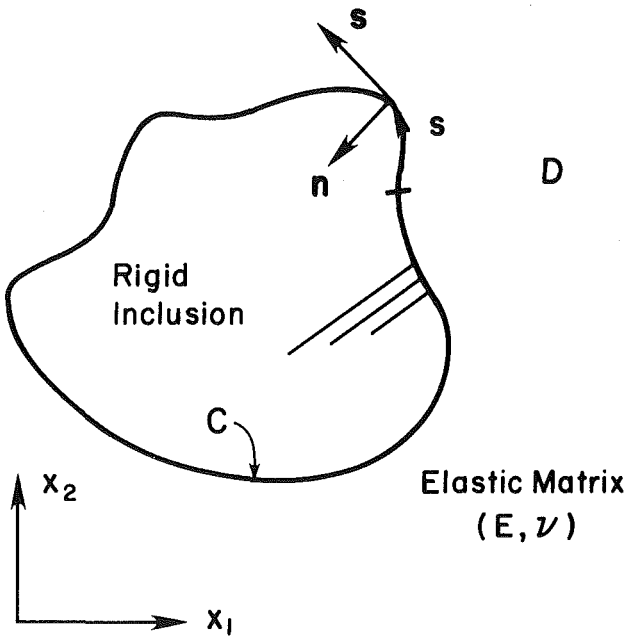


Fig. 1

For plane deformation, the stresses[1] $\sigma_{\alpha\beta}$ and displacements u_α are governed by the equations of equilibrium

$$\sigma_{\alpha\beta,\beta} = 0 \quad \text{on} \quad D, \tag{1.1}$$

and the displacement-stress relations

$$u_{(\alpha,\beta)} = \frac{1+\nu}{E}[\sigma_{\alpha\beta} - \nu\sigma_{\gamma\gamma}\delta_{\alpha\beta}], \tag{1.2}$$

where the subscripts enclosed in parentheses refer to the symmetric part, E denotes Young's modulus and ν Poisson's ratio. Since the inclusion is rigid and perfectly bonded, the displacements have the form

$$u_\alpha = a_\alpha + be_{\alpha\beta}x_\beta \quad \text{on} \quad C, \tag{1.3}$$

where a_α, b are constants and $e_{\alpha\beta}$ denote the components of the two-dimensional alternator

[1] Greek letter subscripts have the range {1,2}, summation is understood where they are repeated, and those following a comma indicate differentiation with respect to the corresponding cartesian coordinates.

Contributed by the Applied Mechanics Division for presentation at the 1985, Joint ASME/ASCE Applied Mechanics, Fluids Engineering and Bioengineering Conference, Albuquerque, N. Mex., June 24-26, 1985 of THE AMERICAN SOCIETY OF MECHANICAL ENGINEERS.

Discussion on this paper should be addressed to the Editorial Department, ASME, United Engineering Center, 345 East 47th Street, New York, N.Y. 10017, and will be accepted until two months after final publication of the paper itself in the JOURNAL OF APPLIED MECHANICS. Manuscript received by ASME Applied Mechanics Division, October, 1983; final revision, May, 1984. Paper No. 85-APM-2.

Copies will be available until May, 1984.

Copyright © 1985 by ASME
Downloaded 02 May 2010 to 171.66.16.54. Redistribution subject to ASME license or copyright; see http://www.asme.org/terms/Terms_Use.cfm

$$e_{\alpha\beta}=\begin{cases}1 & \alpha=1,\quad \beta=2\\ -1 & \alpha=2,\quad \beta=1\\ 0 & \alpha=\beta\end{cases}\qquad(1.4)$$

The resultant force and moment on the inclusion are required to vanish, so that

$$\int_C \sigma_{\alpha\beta}n_\beta ds=0,\quad \int_C e_{\alpha\beta}x_\alpha\sigma_{\beta\gamma}n_\gamma ds=0,\qquad(1.5)$$

where n_α denote the components of the unit normal directed outward from D. Finally, the boundary-value problem is completed by the requirement

$$\sigma_{\alpha\beta}\to\overset{\infty}{\sigma}_{\alpha\beta}\qquad\text{as}\quad r=(x_\alpha x_\alpha)^{1/2}\to\infty,\qquad(1.6)$$

where $\overset{\infty}{\sigma}_{\alpha\beta}$ are the given stresses acting at infinity.

It is assumed that the displacements u_α are twice continuously differentiable on D and that the elastic constants obey

$$-1<\nu<1/2,\quad E>0.\qquad(1.7)$$

We close this section with certain properties of the solution that are needed in the sequel. In particular, if

$$\Theta=\sigma_{\alpha\alpha}\qquad\text{on}\quad D\qquad(1.8)$$

and Δ stands for the two-dimensional Laplace operator, we have the familiar result

$$\Delta\Theta=0\qquad\text{on}\quad D,\qquad(1.9)$$

which follows from (1.1), (1.2).

Let s_α stand for the components of the unit tangent vector to C, oriented as in Fig. 1, and let σ_N and σ_{SN} denote the normal and shearing components of traction acting on the matrix at points of C, so that

$$\sigma_N=n_\alpha n_\beta\sigma_{\alpha\beta},\quad \sigma_{SN}=s_\alpha n_\beta\sigma_{\alpha\beta}.\qquad(1.10)$$

Further, let σ_s stand for the stress

$$\sigma_S=s_\alpha s_\beta\sigma_{\alpha\beta}\qquad\text{on}\quad C.\qquad(1.11)$$

Then, at points of C,

$$\sigma_S=\nu\Theta,\quad \sigma_N=(1-\nu)\Theta.\qquad(1.12)$$

To see this, we first note that if s stands for arc-length along C, then $s_\alpha = dx_\alpha/ds$, so that (1.3) yields

$$u_{\alpha,\beta}s_\beta=be_{\alpha\beta}s_\beta.\qquad(1.13)$$

Accordingly, and since $e_{\alpha\beta}$ is skew,

$$u_{(\alpha,\beta)}s_\alpha s_\beta=0\qquad\text{on}\quad C.\qquad(1.14)$$

Therefore, (1.2) furnishes

$$\sigma_s=\nu\Theta\qquad\text{on}\quad C.\qquad(1.15)$$

The desired conclusion $(1.12)_2$ now follows from the fact that Θ is invariant,

$$\Theta=\sigma_{\alpha\alpha}=\sigma_S+\sigma_N.$$

2 The Optimization Problem

To formulate the problem of minimum stress concentration, we need to decide how to define its magnitude. The definition has to fulfill certain mathematical requirements and at the same time measure the severity of stress states in a practical and physically acceptable manner. Here, for the sake of simplicity and to fix ideas, we base our work on the yield criterion of von Mises. It will become readily apparent that certain generalizations are possible.

The von Mises criterion involves the function

$$f(\sigma)=\frac{1}{2}\sigma'_{ij}\sigma'_{ij},\qquad(2.1)^2$$

where σ'_{ij} denote the deviatoric components

$$\sigma'_{ij}=\sigma_{ij}-\frac{1}{3}\sigma_{kk}\delta_{ij}.\qquad(2.2)$$

For plane deformation normal to the x_3-axis,

$$\sigma_{3\alpha}=\sigma_{\alpha 3}=0,\qquad \sigma_{33}=\nu\sigma_{\gamma\gamma}.\qquad(2.3)$$

Accordingly,

$$2f(\sigma)=\sigma_{\alpha\beta}\sigma_{\alpha\beta}+\frac{1}{3}(2\nu^2-2\nu-1)(\sigma_{\gamma\gamma})^2.\qquad(2.4)$$

For our purposes, it is convenient to introduce a stress norm[3]

$$\sigma=\sqrt{2f(\sigma)}.\qquad(2.5)$$

According to the yield criterion of von Mises, the material is on or beyond the verge of yielding if

$$\sigma=\sqrt{\frac{2}{3}}\,Y,\qquad(2.6)$$

but remains elastic if

$$\sigma<\sqrt{\frac{2}{3}}\,Y,\qquad(2.7)$$

where Y denotes the yield strength in simple tension.

We are led naturally to the idea of an optimal shape for an elastic solid as one for which the largest value of σ within the solid is rendered a minimum. More precisely, let

$$\sigma_{\mathfrak{M}}[D]=\sup_{\mathbf{x}\in D}\ \sigma(\mathbf{x}).\qquad(2.8)$$

The problem of optimum shape for the von Mises stress norm σ is to find a domain D_m such that

$$inf\ \sigma_{\mathfrak{M}}[D]=\sigma_{\mathfrak{M}}[D_m]\overset{def}{=}\sigma_m,\qquad(2.9)$$

where the infimum is taken over all doubly connected exterior domains. A domain D_m is said to be optimal (with respect to von Mises effective stress), if (2.9) holds, and σ_m is called the optimum stress.

3 Solution to the Optimization Problem as an Inverse Problem

The purpose of this section is to establish conditions under which the solution of a more tangible problem involving unknown shapes furnishes a solution to the optimization problem. In this new problem, which is often referred to as an inverse problem [1], a domain D^* is sought such that on C^*, the stresses σ^*_N and σ^*_S are constant, while σ^*_{NS} vanishes. We mention that if (1.5) fails to hold, then the existence of such a solution is precluded.

Such inverse problems have received considerable attention in the literature in connection with optimization problems where, in contrast to the rigid inclusions presently under consideration, the matrix contains a *void*, which is either traction free or pressurized [1–3]. It was remarked in [1] that a rigorous optimality proof was evidently yet to be found. Subsequently, a proof appeared in [4], followed shortly by [5], in which essentially the same ideas were used to handle more realistic failure criteria. The actual solution of the inverse problem for a single inclusion or void is elementary. A discussion is left for Section 4. The case of multiple voids, including periodic arrays, was dealt with in [1]. Neuber [6, 7]

[2] Latin letter subscripts have the range {1,2,3}.

[3] The function defined in (2.5) is actually a norm on the subspace of traceless symmetric tensors.

Downloaded 02 May 2010 to 171.66.16.54. Redistribution subject to ASME license or copyright; see http://www.asme.org/terms/Terms_Use.cfm

has given examples where the boundary extends continuously to infinity. An optimality proof appears in [8].

In a series of papers [9–13], Bjorkman and Richards introduce an interesting class of two-dimensional inverse problems also aimed at finding shapes of minimum stress concentration, and describe a systematic method of solution involving complex variables. In one of these, [12], they solve a problem for a rigid inclusion, and arrive at the same family of ellipses derived by a different method in Section 4 of the present paper.

While there is a certain degree of overlap between the work described in [9–13] and [1, 2, 4–7] on the matter of inverse problems and methods of solving them, there are significant differences between the present work and that of [12] concerning the underlying optimization problem and its reduction to an inverse problem, especially regarding concepts of stress concentration. In particular, [12] deals with the minimization of $\sup\sigma_N(\mathbf{x})$ and $\sup\sigma_S(\mathbf{x})$ where $\mathbf{x}$ is restricted to boundary points.

A theorem follows in which we establish the connection between the optimization problem and the inverse problem. First we discuss a result from potential theory which enables us to exploit the fact that $\Delta\Theta=0$.

Lemma: Let ϕ be a solution of

$$\Delta\phi=0 \quad \text{on} \quad D, \tag{3.1}$$

where D is a doubly connected exterior domain. Assume that ϕ is continuous on the closure of D and that

$$\phi\to c \quad \text{as} \quad r\to\infty, \tag{3.2}$$

where c is a constant. Then:

(a) either $|\phi|$ exceeds $|c|$ at a point of C or $\phi\equiv c$ on $D\cup C$;

(b) if ϕ is constant on C, $\phi=c$ on $D\cup C$.

These results are easily established by subjecting D to an inversion in a circle lying within the complement of $D\cup C$. This transformation [14, p. 248] takes ϕ into a function that is harmonic on a bounded region and assumes the value c at an interior point. Since the boundary values of this new function are the same as those assumed by ϕ, (a) follows from the maximum principle, whereas (b) is a consequence of the uniqueness theorem.

Theorem: Assume that the stresses $\overset{\infty}{\sigma}_{\alpha\beta}$ obey the inequality

$$[\nu^2+(1-\nu)^2](\overset{\infty}{\sigma}_{\gamma\gamma})^2\geq\overset{\infty}{\sigma}_{\alpha\beta}\overset{\infty}{\sigma}_{\alpha\beta}. \tag{3.3}$$

Let D^* be a domain that solves the inverse problem, i.e., such that on C^*, the stresses σ_S^* and σ_N^* are constant, and $\sigma_{SN}^*\equiv 0$. Let D be a given doubly connected exterior domain. Then,

$$\sigma_{\mathfrak{M}}[D]\geq\sigma_{\mathfrak{M}}[D^*]. \tag{3.4}$$

Thus, D^* is an optimal domain and $\sigma_{\mathfrak{M}}[D^*]$ is the optimum stress

$$\sigma_m=\sigma_{\mathfrak{M}}[D^*]. \tag{3.5}$$

Further, $\sigma_{\mathfrak{M}}[D^*]$ is given by

$$\sigma_{\mathfrak{M}}[D^*]=\sqrt{\frac{2}{3}}(1-2\nu)|\overset{\infty}{\sigma}_{\gamma\gamma}|. \tag{3.6}$$

Proof: Since Θ^* assumes the constant value

$$\Theta^*=\sigma_N^*+\sigma_S^* \quad \text{on} \quad C, \tag{3.7}$$

it follows from Part (b) of the Lemma that

$$\Theta^*=\overset{\infty}{\sigma}_{\gamma\gamma} \quad \text{on} \quad D\cup C. \tag{3.8}$$

Therefore, and by (1.1), (1.2),

$$\Delta\sigma_{\alpha\beta}^*=0 \quad \text{on} \quad D^*. \tag{3.9}$$

By (2.5), (2.4), and in view of (3.8),

$$(\sigma^*)^2=\sigma_{\alpha\beta}^*\sigma_{\alpha\beta}^*+\frac{1}{3}(2\nu^2-2\nu-1)(\overset{\infty}{\sigma}_{\gamma\gamma})^2. \tag{3.10}$$

From (3.8) and (3.9), we infer that $(\sigma^*)^2$ is a subharmonic function. Accordingly, and in view of (1.12), (2.4), and (2.5)

$$(\sigma_{\mathfrak{M}}[D^*])^2=max\left\{\left[\nu^2+(1-\nu)^2+\frac{1}{3}(2\nu^2-2\nu-1)\right](\overset{\infty}{\sigma}_{\gamma\gamma})^2,\right.$$

$$\left.\overset{\infty}{\sigma}_{\alpha\beta}\overset{\infty}{\sigma}_{\alpha\beta}+\frac{1}{3}(2\nu^2-2\nu-1)(\overset{\infty}{\sigma}_{\gamma\gamma})^2\right\}, \tag{3.11}$$

which, because of the condition (3.3) yields (3.6).

Now consider a competing domain D. From Part (a) of the Lemma and (3.8) we infer

$$\sup_C\Theta^2\geq(\overset{\infty}{\sigma}_{\gamma\gamma})^2=(\Theta^*)^2. \tag{3.12}$$

Therefore, and in view of (2.4), (2.5), (2.8), (1.12), we have

$$\begin{aligned}(\sigma_{\mathfrak{M}}[D])^2\geq\sup_C\sigma^2 &= \sup_C\left\{\sigma_S^2+\sigma_N^2+2\sigma_{NS}^2+\frac{1}{3}(2\nu^2-2\nu-1)\Theta^2\right\}\\ &\geq \sup_C\left\{\sigma_S^2+\sigma_N^2+\frac{1}{3}(2\nu^2-2\nu-1)\Theta^2\right\}\\ &= \left\{\nu^2+(1-\nu)^2+\frac{1}{3}(2\nu^2-2\nu-1)\right\}\sup\Theta^2\\ &> \left\{\nu^2+(1-\nu)^2+\frac{1}{3}(2\nu^2-2\nu-1)\right\}(\Theta^*)^2\\ &= (\sigma_{\mathfrak{M}}[D^*])^2.\end{aligned}$$

The proof is now complete.

4 Solution to the Inverse Problem

The solution to the inverse problem may be found with the aid of complex analysis [12]. It is also derivable by simple arguments from results given somewhat earlier in [1, 2]. Although [1] is concerned primarily with multiple voids, it contains as a special case a result for a single pressurized elliptic void which by an obvious choice of the pressure leads at once to the solution for a rigid inclusion.

For the traction free-void, it was shown in [2] that an elliptic hole furnishes a surface at points of which the hoop stress is constant, provided the principal axes are parallel to those of the principal stresses acting at infinity and form a ratio equal to that of the corresponding principal stresses. Since the results of [2] concern a traction-free void, one must first subtract a suitable state of stress to apply their results. Accordingly, we find that in the present context if the axes x_1-x_2 are principal axes for the ellipse and the applied stress, then

$$\frac{a_1}{a_2}=\frac{\overset{\infty}{\sigma}_1-(1-\nu)(\overset{\infty}{\sigma}_1+\overset{\infty}{\sigma}_2)}{\overset{\infty}{\sigma}_2-(1-\nu)(\overset{\infty}{\sigma}_1+\overset{\infty}{\sigma}_2)}, \tag{4.1}$$

where a_1, a_2 are the semimajor axes of the ellipse, so that

$$\left(\frac{x_1}{a_1}\right)^2+\left(\frac{x_2}{a_2}\right)^2=1, \tag{4.2}$$

and $\overset{\infty}{\sigma}_1$, $\overset{\infty}{\sigma}_2$ denote the corresponding principal stresses.

Considering that a_1/a_2 must be positive, we see that the stresses $\overset{\infty}{\sigma}_1$, $\overset{\infty}{\sigma}_2$ cannot be prescribed arbitrarily. It is easy to show that with Poisson's ratio in the range

$$0<\nu<1/2, \tag{4.3}$$

a necessary and sufficient condition for $a_1/a_2>0$ is that neither $\overset{\infty}{\sigma}_1$, $\overset{\infty}{\sigma}_2$ be zero and

$$\frac{\nu}{1-\nu}<\frac{\overset{\infty}{\sigma}_1}{\overset{\infty}{\sigma}_2}<\frac{1-\nu}{\nu}. \tag{4.4}$$

Downloaded 02 May 2010 to 171.66.16.54. Redistribution subject to ASME license or copyright; see http://www.asme.org/terms/Terms_Use.cfm

Set $\xi = \sigma_1/\sigma_2$, and put

$$f(\xi) = \frac{1+\xi^2}{(1+\xi)^2}.$$

Then, f has the properties

$$f'(\xi) = 0 \Rightarrow \xi = 1, \qquad f'(\xi) < 0 \qquad \text{for} \quad \xi < 1,$$

$$f'(\xi) = 0 \qquad \text{for} \quad \xi > 1,$$

$$f\left(\frac{\nu}{1-\nu}\right) = f\left(\frac{1-\nu}{\nu}\right) = \nu^2 + (1-\nu^2),$$

from which it follows that (4.4) is equivalent to (3.3). Thus, the inequality (3.3) is also necessary and sufficient condition for the existence of a solution of the inverse problem.

Acknowledgment

Support for this work was provided by a contribution from the Shell Companies Foundation to the University of California in support of the research of Professor M. M. Carroll. To Professor Carroll and the Shell Foundation, I wish to extend by sincerest thanks.

References

1 Cherepanov, G. P., "Inverse Problems of the Plane Theory of Elasticity," *PMM*, Vol. 38, No. 6, 1974.

2 Durrelli, A. J., and Murray, W. M., "Stress Distribution Around an Elliptic Discontinuity in Any Two-Dimensional, Uniform, and Axial System of Combined Stress," *Experimental Stress Analysis Proceedings*, Vol. 1, No. 1, 1943, pp. 19–31.

3 Wheeler, L. T., and Kunin, I. A., "On Voids of Minimum Stress Concentration," *Int. J. Solids and Structures*, Vol. 18, 1982, pp. 85–89.

4 Wheeler, L., "On the Role of Constant Stress Surfaces in the Problem of Minimizing Elastic Stress Concentration," *Int. J. Solids and Structures*, Vol. 12, 1976, pp. 779–789.

5 Banichuk, N. V., "Optimality Conditions in the Problem of Seeking the Hole Shapes in Elastic Bodies," *PMM*, Vol. 41, No. 5, 1977, pp. 920–925.

6 Neuber, H., "Der zugbeanspruchte Flachstab mit Optimalem Querschnittubeigang, *Forsch. Ingenieurwesen*, Vol. 35, No. 1, 1969, pp. 29–30.

7 Neuber, H., "Zur Optimierung der Spannungskonzentration," in *Continuum Mechanics and Related Problems of Analysis*, Nauka, Moscow, 1972, pp. 375–380.

8 Wheeler, L., "On Optimum Profile for the Minimization of Elastic Stress Concentration, *ZAMM*, 1978, pp. T235–T236.

9 Bjorkman, G. S., Jr., and Richards R., Jr., "Harmonic Holes—An Inverse Problem in Elasticity," ASME JOURNAL OF APPLIED MECHANICS, Vol. 43, No. 3, 1976, pp. 414–418.

10 Bjorkman, G. S., Jr., and Richards, R., Jr., "Optimum Shapes for Unlined Tunnels and Cavities," *Engineering Geology*, Vol. 12, 1978, pp. 171–179.

11 Bjorkman, G. S., Jr., and Richards, R., Jr., "Harmonic Holes for Nonconstant Fields," ASME JOURNAL OF APPLIED MECHANICS, Vol. 46, No. 3, 1979, pp. 573–576.

12 Bjorkman, G. S., Jr., and Richards, R., Jr., "Harmonic Shapes and Optimum Design," *Journal of the Engineering Mechanics Division*, ASCE, Vol. 106, 1980, pp. 1125–1134.

13 Bjorkman, G. S., Jr., and Richards, R., Jr., "Neutral Holes; Theory and Design," *Journal of the Engineering Mechanics Division*, ASCE, Vol. 108, 1982, pp. 945–960.

14 Kellogg, O. D., *Foundations of Potential Theory*, Springer-Verlag, 1929.

Downloaded 02 May 2010 to 171.66.16.54. Redistribution subject to ASME license or copyright; see http://www.asme.org/terms/Terms_Use.cfm

H. T. Zhang[1]

Y. T. Chou

Department of Metallurgy and Materials Engineering, Lehigh University, Bethlehem, Pa. 18015

Antiplane Eigenstrain Problem of an Elliptic Inclusion in a Two-Phase Anisotropic Medium

An antiplane eigenstrain problem of an elliptic inclusion in a two-phase anisotropic medium is analyzed based on the line-force concept. Explicit expressions for the stress field and strain energy are obtained under a given symmetry. The results are used to determine the stress singularity coefficient for a flat inclusion. When the tip of the inclusion is located at the interface boundary, the stress singularity coefficient $\mathcal{S}'$ varies according to the formula $\mathcal{S}' = (1+K)\,\mathcal{S}^\circ$ where K is the elastic inhomogeneity factor and $\mathcal{S}^\circ$ is the stress singularity coefficient for a homogeneous medium ($K = 0$).

1 Introduction

Inclusion problems, as in the notion of Eshelby [1, 2], have not been treated for multiphase composite materials because of mathematical complexity. However, Masumura and Chou [3] recently solved the antiplane eigenstrain problem of an elliptic inclusion in an anisotropic half-space. Their analysis stimulated the present study of a similar problem in which the semi-infinite matrix is replaced by a two-phase infinite composite. As shown in the following, closed-form solutions are obtainable by using the result of the antiplane line force and the method of conformal mapping.

2 Analysis and Results

The innovation in Eshelby's treatment of inclusion problems is the use of the point-force concept. To determine the elastic field of a system of which a portion (the inclusion) undergoes an eigenstrain transformation, Eshelby introduces the following hypothetical operations: first, the inclusion is cut from the matrix and allowed to achieve a stress-free deformation (eigenstrain) E_{ij}°. Second, a surface traction ($-T_i = -P_{ij}^\circ n_j$) is applied to restore the inclusion to its original form, i.e., one that generates an elastic deformation $-E_{ij}^\circ$ and stress $-P_{ij}^\circ$. Third, the stressed inclusion again is inserted into the cavity and rejoined with the matrix across the cut. At this time, the matrix is unstressed and the inclusion is under a stress field ($-P_{ij}^\circ$), while the applied surface traction ($-T_i$) remains in the medium as a layer of body force spread over the interface S. Fourth, this layer of body force subsequently is removed by applying equal and opposite point forces distributed over S, which, upon integration, generate a constrained stress field (P_{ij}) in the entire region.

Thus, at the end of the transformation process, the medium is internally stressed by an amount of $P_{ij} - P_{ij}^\circ$ in the inclusion and P_{ij} in the matrix, both of which can be explicitly determined. Eshelby further shows that for a uniform eigenstrain in an ellipsoidal inclusion, the stress inside the inclusion is also uniform. This leads to an easy path of extension to the inhomogeneity problem, as detailed in his original work [1, 2].

Thus, for an eigenstrain transformation problem, the key steps are (1) to obtain the stress field of a unit point-force in the medium (line-force in the two-dimensional analysis), and (2) to calculate the resulting field through integration of the point-force distribution along the boundary of the inclusion. These are essentially the steps to be performed in the present analysis.

Consider an infinite anisotropic elastic medium composed of two distinct half-spaces (phase I and phase II) joined along the plane $x_1 = 0$ of a cartesian coordinate system $Ox_1x_2x_3$. Denote the elastic constants of phase I by C_{ij} and those of phase II by C'_{ij}. For simplicity, assume that both phases possess a two-fold rotation symmetry about the x_3 axis. This implies that for an antiplane strain system only three elastic constants ($C_{44} = C_{2323}$, $C_{55} = C_{1313}$, and $C_{45} = C_{2313}$) will be involved in the analysis.

For the preceding elastic system, the elastic field of an antiplane line-force per unit length has been reported by Chou [4]. In the forms of complex functions, the stress components at $x = x_1 + ix_2$, due to a line force F_3 at $y = y_1 + iy_2$ in phase I, can be written in two parts:

(i) in phase I ($x_1 \geq 0$)

$$P_{3j} = Re\left\{\lambda_j F_3 \left(\frac{1}{D_1} - \frac{K}{D_2}\right)\right\}, \qquad j = 1,2, \tag{1}$$

where Re stands for the real part of a complex function,

$$\lambda_j = -(C_{3j31} + \mu\, C_{3j32})/\pi L \tag{2}$$

$$K = \frac{L' - L}{L' + L} \tag{3}$$

$$L = (C_{44}C_{55} - C_{45}^2)^{1/2} \tag{4}$$

[1] On leave from the Department of Physics, Lanzhou University, Lanzhou, China.

Contributed by the Applied Mechanics Division for publication in the JOURNAL OF APPLIED MECHANICS.

Discussion on this paper should be addressed to the Editorial Department, ASME, United Engineering Center, 345 East 47th Street, New York, N.Y. 10017, and will be accepted until two months after final publication of the paper itself in the JOURNAL OF APPLIED MECHANICS. Manuscript received by ASME Applied Mechanics Division November, 1983.

Copyright © 1985 by ASME

Downloaded 02 May 2010 to 171.66.16.54. Redistribution subject to ASME license or copyright; see http://www.asme.org/terms/Terms_Use.cfm

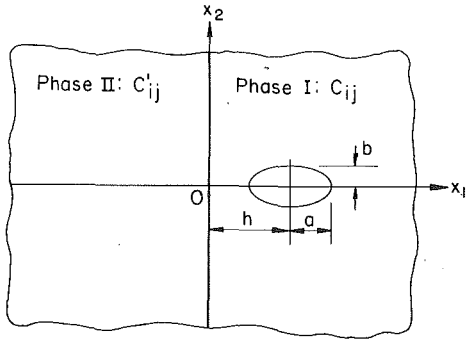


Fig. 1 An elliptic inclusion in a two-phase medium

$$L' = (C'_{44}C'_{55} - C'^{2}_{45})^{1/2} \tag{5}$$

$$D_1 = (x+\bar{x}) - i\mu(x-\bar{x}) - (y+\bar{y}) + i\mu(y-\bar{y}) \tag{6}$$

$$D_2 = (x+\bar{x}) - i\mu(x-\bar{x}) + (1+\mu\epsilon_1)(y+\bar{y}) + i\mu(y-\bar{y}) \tag{7}$$

$$\mu = -(C_{45} - iL)/C_{44} \tag{8}$$

$$\epsilon_1 = 2\,C_{45}/C_{55} \tag{9}$$

and a bar denotes the complex conjugation. For convenience, the parameter K defined by equation (3) is called the inhomogeneity factor

(*ii*) in phase II $(x_1 \le 0)$

$$p'_{3j} = (1+K)\mathrm{Re}\left\{\frac{\lambda'_j F_3}{D'}\right\}, \qquad j = 1,2 \tag{10}$$

where

$$\lambda'_j = -(C'_{3j31} + \mu'\ C'_{3j32})/\pi L' \tag{11}$$

$$D' = (x+\bar{x}) - i\mu'(x-\bar{x}) - (\epsilon_2 + \mu'\ \epsilon_3)(y+\bar{y}) + i\mu'(y-\bar{y}) \tag{12}$$

$$\mu' = -(C'_{45} - iL')/C'_{44} \tag{13}$$

and

$$\epsilon_2 = \frac{C'_{45}L}{C_{55}L'}, \qquad \epsilon_3 = \frac{C'_{45}L}{C_{55}L'} - \frac{C_{45}}{C_{55}} \tag{14}$$

Now consider an elliptic inclusion in phase I, with its cylindrical axis parallel to the x_3 axis (Fig. 1). The boundary of the inclusion is described by $(x_1-h)^2/a^2 + x_2{}^2/b^2 = 1$ where a and b are semiaxes, respectively, and h is the distance from the center of the inclusion to the interface boundary $x_1 = 0$. Inside the inclusion the antiplane eigenstrains E°_{13} and E°_{23} are prescribed and the corresponding stresses are

$$P^\circ_{23} = 2(C_{44}E^\circ_{23} + C_{45}E^\circ_{13}) \tag{15a}$$

$$P^\circ_{13} = 2(C_{45}E^\circ_{23} + C_{55}E^\circ_{13}) \tag{15b}$$

The elastic field in the inclusion and the matrix can be determined by integrating the field of the line force along the contour of the ellipse, using the same method employed by Masumura and Chou in the case of a half-space [3]. The results obtained are given in the following subsections.

2.1 Stress Field of the Eigenstrain System.

(*i*) in phase I $(x_1 \ge 0)$

$$P_{3j} = Re\left\{-\frac{\lambda_j}{2}\Omega\right\}, \qquad j = 1,2 \tag{16}$$

where

$$\Omega = P^\circ_{23}(I+J) + iP^\circ_{13}(I-J) \tag{17}$$

$$I = I_1 - K\,I_2 \tag{18}$$

$$J = J_1 - K\,J_2 \tag{19}$$

$$I_1 = \oint \frac{dy}{D_1}, \quad I_2 = \oint \frac{dy}{D_2} \tag{20}$$

$$J_1 = \oint \frac{d\bar{y}}{D_1}, \quad J_2 = \oint \frac{d\bar{y}}{D_2} \tag{21}$$

In equations (20) and (21) the contour integrations are taken counterclock-wise along the boundary of the inclusion. These integrals have been evaluated by Masumura and Chou [3], and their resutls are

$$I_1 = -i\,\pi\frac{a+b}{(a-i\mu\ b)} \tag{22a}$$

$$J_1 = -i\,\pi\frac{a-b}{(a-i\mu\ b)} \tag{22b}$$

for the region inside the inclusion,

$$I_1 = -\gamma_1(1+i\mu)S_1(x) \tag{23a}$$

$$J_1 = \gamma_1(1-i\mu)S_1(x) \tag{23b}$$

for the region outside the inclusion and

$$I_2 = \gamma_2(\alpha - i\mu)S_2(x) \tag{24a}$$

$$J_2 = -\gamma_2(\alpha + i\mu)S_2(x) \tag{24b}$$

for both inside and outside the inclusion. In the previous equations,

$$\gamma_1 = i\pi\frac{ab}{(a^2+\mu^2b^2)} \tag{25}$$

$$\gamma_2 = i\pi\frac{ab}{(\alpha^2a^2+\mu^2b^2)} \tag{26}$$

$$\alpha = 1 + \mu\ \epsilon_1 \tag{27}$$

$$S_1(x) = 1 - \frac{x_1 + \mu\ x_2 - h}{[(x_1+\mu x_2 - h)^2 - (a^2+\mu^2b^2)]^{1/2}} \tag{28}$$

and

$$S_2(x) = 1 - \frac{x_1 + \mu\ x_2 + \alpha\ h}{[(x_1+\mu x_2 + \alpha h)^2 - (\alpha^2a^2+\mu^2b^2)]^{1/2}} \tag{29}$$

It is seen that equations (16)–(21) reduce to the expressions for a homogeneous single phase medium at $K = 0$ and for a half-space at $K = -1$. Furthermore, since I_2 and J_2 vary with x in the entire region, the stresses in the inclusion are, therefore, nonuniform, an unfortunate result that invalidates an easy path from the eigenstrain problem to the inhomogeneity problem taken previously [1, 2, 5, 6].

(*ii*) in phase II $(x_1 \le 0)$

$$P'_{3j} = (1+K)Re\left\{-\frac{\lambda'_j}{2}\Omega'\right\}, \qquad j = 1,2 \tag{30}$$

where

$$\Omega' = P^\circ_{23}(I'+J') + i\,P^\circ_{13}(I'-J') \tag{31}$$

$$I' = \oint \frac{dy}{D'} \tag{32}$$

$$J' = \oint \frac{d\bar{y}}{D'} \tag{33}$$

and D' is defined by equation (12). The contour integrations in equations (32) and (33) were evaluated by employing a mapping technique with the aid of the Marden theorem [7]. We obtained

$$I' = \gamma'(\nu' - i\mu')S'(x) \tag{34}$$

$$J' = -\gamma'(\nu' + i\mu')S'(x) \tag{35}$$

with

$$\gamma' = i\pi\frac{ab}{(\nu'^2a^2+\mu'^2b^2)} \tag{36}$$

$$\nu' = -(\epsilon_2 + \mu'\epsilon_3) \tag{37}$$

Downloaded 02 May 2010 to 171.66.16.54. Redistribution subject to ASME license or copyright; see http://www.asme.org/terms/Terms_Use.cfm

and

$$S'(x)=1-\frac{x_1+\mu' x_2+\nu' h}{[(x_1+\mu' x_2+\nu' h)^2-(\nu'^2 a^2+\mu'^2 b^2)]^{1/2}} \tag{38}$$

It is interesting to note that if the primes are deleted in equations (34)–(38) and $\nu' = -1$, we recover I_1 and J_1 of equations (22); and if $\nu' = \alpha$, we have I_2 and J_2 of equations (24).

2.2 Strain Energy. According to Eshelby [1], the strain energy per unit length of a two-dimensional eigenstrain system can be calculated by the general tensor expression

$$E=-\frac{1}{2}\int(P_{ij}-P^{\circ}_{ij})E^{\circ}_{ij}dS \tag{39}$$

where the areal integration is taken over the cross section. Equation (39) is also valid for a multiphase composite system, provided that all tractions and displacements are continuous across the interface boundaries. However, to effect a simple result for illustration, we will relax the degree of symmetry imposed on the medium, namely, that both phase *I* and phase *II* now possess a four-fold rotational symmetry about the x_3 axis, instead of a two-fold symmetry assumed in the foregoing. (A typical example is the <100> axis of cubic crystals.) Under this condition, $C_{44} = C_{55}$, $C_{45} = 0$ in phase *I* and $C'_{44} = C'_{55}$, $C'_{45} = 0$ in phase *II*. Another situation that would result in the same conclusions is when both the x_3 and x_1 (or x_2) axes are two-fold, such as the <110> axis of a cubic lattice.

For comparison, it is convenient to express the total strain energy in two separate terms, i.e.,

$$E=E^{\infty}+E' \tag{40}$$

The first term E^{∞} corresponds to the energy per unit thickness of the infinite medium as if it were a homogeneous phase. (Phase *I* and phase *II* become indistinguishable and $K = 0$). The expression is given by

$$E^{\infty}=2\pi ab\ C_{44}\left[\frac{a}{a+b}E^{\circ 2}_{13}+\frac{b}{a+b}E^{\circ\ 2}_{23}\right] \tag{41}$$

which can also be obtained from equation (31) in reference [8].[2] The second term E' represents the contribution due to the inhomogeneitu effect. Its expression is much more complex. For the sake of illustration, we will examine two special cases.

2.2.1 Strain Energy for a Circular Inclusion. For a circular inclusion ($a = b$), a simple expression for E is obtainable,

$$E=\left(1+\frac{K}{4t^2}\right)E^{\infty} \tag{42}$$

where

$$E^{\infty}=\pi\ ab\ (E^{\circ\ 2}_{13}+E^{\circ\ 2}_{23}) \tag{43}$$

and

$$t=\frac{h}{a} \tag{44}$$

It is readily seen that $E \to E^{\infty}$ as $t\to\infty$. The contribution due to the inhomogeneity effect in fact becomes very small (<1 percent) when $t>4$. The inhomogeneity effect continuously increases as t decreases and reaches a maximum at $t = 1$. At this position, the system has a strain energy $E = (1 \pm 0.25)\ E^{\infty}$ at $K = \pm 1$, giving a maximum variation of $\pm$ 25 percent.

2.2.2 Strain Energy for a Flat Inclusion. For a flat inclusion, two distinct cases are of interest, $b << a$ and $a << b$.

(*i*) For $b << a$ (a flat inclusion situated perpendicular to the interface), we obtained

$$E^{\infty}=2\ \pi\ \text{ab}\ C_{44}\left[E^{\circ\ 2}_{13}+\frac{b}{a}E^{\circ\ 2}_{23}\right] \tag{45}$$

$$E'=2\ \pi\ ab\ C_{44}[E^{\circ\ 2}_{13}+E^{\circ\ 2}_{23}]\frac{b}{a}K(A-1) \tag{46}$$

where

$$A=\frac{2}{\pi}\int_{-1}^{1}\frac{(x+2t)\sqrt{1-x^2}}{\sqrt{(x+2t)^2-1}}dx, \qquad 1\le t\le\infty \tag{47}$$

is an elliptical integral and can be readily evaluated by a numerical method. It is seen that A is a monotone-decreasing function of t. At $t=1$, $A=1.273$ and at $t=\infty$, $A=1$. Furthermore, the total variation of A over the range (4, ∞) is found to be less than 1 percent.

When the eigenstrain has only one component $E_{13}=0$ and $E^{\circ}_{23}=0$, we have at $t=1$

$$E=(1+0.273K)E^{\infty} \tag{48}$$

where

$$E^{\infty}=2\ \pi\ ab\ C_{44}\left(\frac{b}{a}\right)E^{\circ\ 2}_{23} \tag{49}$$

The variation of E due to the inhomogeneity effect is, therefore, very similar to the case of a circular inclusion. On the other hand, if $E^{\circ}_{13}\neq 0$ and $E^{\circ}_{23}=0$, we have $t = 1$

$$E=\left(1+0.273K\frac{b}{a}\right)E^{\infty} \tag{50}$$

where

$$E^{\infty}=2\ \pi\ ab\ C_{44}E^{\circ\ 2}_{13} \tag{51}$$

In this case, the inhomogeneity effect is very small due to the factor b/a.

(*ii*) For $a << b$ (a flat inclusion situated parallel to the interface), we have

$$E^{\infty}=2\pi\ ab\ C_{44}\left[\frac{a}{b}E^{\circ\ 2}_{13}+E^{\circ\ 2}_{23}\right] \tag{52}$$

and

$$E'=2\pi\ ab\ C_{44}\left[E^{\circ\ 2}_{13}+E^{\circ\ 2}_{23}\right]\frac{a}{b}K(1-B) \tag{53}$$

where

$$B=Re\left\{\frac{2}{\pi}\int_{-1}^{1}\frac{(ix+2h/b)\sqrt{1-x^2}}{\sqrt{(ix+2h/b)^2+1}}dx\right\} \tag{54}$$

Obviously, when $h\to\infty$, $B\to 1$, and $E'\to 0$. When $t = 1$, i.e., the vertical flat inclusion meets the interface at the origin, the inhomogeneity effect is maximized. For one-component eigenstrain system in which $E_{13}\neq 0$, the total energy at $t = 1$ is given by

$$E=(1+K)E^{\infty} \tag{55}$$

where

$$E^{\infty}=2\pi\ ab\ C_{44}\left(\frac{a}{b}\right)E^{\circ\ 2}_{13} \tag{56}$$

On the other hand, when $E_{23}{}^{\circ}\neq 0$, the total energy at $t = 1$ is

$$E=\left(1+\frac{a}{b}K\right)E^{\infty} \tag{57}$$

where

$$E^{\infty}=2\pi\ ab\ C_{44}E^{\circ\ 2}_{23} \tag{58}$$

Thus, the inhomogeneity effects on E are basically similar in case (*i*) and case (*ii*). The effect is large if the eigenstrain is parallel to the inclusion, and is small if it is perpendicular to the inclusion.

[2] In a corresponding expression given by equation (28) in reference [3], the factor of 1/2 should be dropped. Also in the expression for $\bar{D}$ in equations (3) of the same reference, a factor of $(1+\mu\epsilon_1)$ should be added before $(\gamma+\bar{\gamma})$.

Downloaded 02 May 2010 to 171.66.16.54. Redistribution subject to ASME license or copyright; see http://www.asme.org/terms/Terms_Use.cfm

2.3 Stress Singularity Coefficient. As a useful application, let us examine the stress concentration effect due to the eigenstrain transformation discussed in the foregoing. It is interesting to note that with the near-field formalism, there is associated a square-root stress singularity at the tip of a flat inclusion.

For $b \ll a$, the shear stress near the tip of the flat inclusion can be found from equations (16)–(21) to be

$$P_{23} = \left(\frac{b}{a}\right) P_{23}^{\circ} \left\{ \frac{a}{\pm 2[x_1 - (h \pm a)]} \right\}^{1/2}, \qquad a \ll h \tag{59}$$

where the "+" sign refers to the near field at the right of the inclusion and the "−" sign refers to that at the left. Clearly, a square-root stress singularity is located at $x_1 = h - a$ and at $x_1 = h + a$.

For convenience in reference, it is useful to define a new terminology, the "stress singularity coefficient," $\mathcal{S}^{\circ}$, by

$$\mathcal{S}^{\circ} = \left(\frac{b}{a}\right) P_{23}^{\circ} \sqrt{\pi a}, \qquad a \ll h \tag{60}$$

As will be shown in the following, $\mathcal{S}^{\circ}$ is also the stress singularity coefficient for a flat inclusion in a homogeneous matrix ($K = 0$). At the moment, $\mathcal{S}^{\circ}$ has no connection with other physical properties. It should not therefore be confused with the term "the stress intensity factor" used in fracture mechanics.

As the flat inclusion is approaching the interface boundary ($h \to a$, $t \to 1$), so also is the stress singularity. In equations (30)–(38), the stress in front of the tip of the inclusion is

$$P'_{23} = \left(\frac{b}{a}\right)(1+K) P_{23}^{\circ} \sqrt{\frac{a}{-2x_1}}, \qquad x_1 < 0, \quad x_2 = 0 \tag{61}$$

and the corresponding stress singularity coefficient is

$$\mathcal{S}' = \left(\frac{b}{a}\right)(1+K) P_{23}^{\circ} \sqrt{\pi a} \tag{62}$$

$$= (1+K)\mathcal{S}^{\circ}$$

Equation (62) is also applicable for a vertical flat inclusion ($a \ll b$), if a and b are interchanged and P_{23}° is replaced by P_{13}°.

It is seen that when $K = 0$ (a homogeneous matrix,) equation (62) reduces to equation (60); when $K \to 1$ (a rigid phase *II*), $\mathcal{S}' \to 2\mathcal{S}^{\circ}$.

3 Conclusions

By using the line-force method, closed-form solutions for the stresses and energy in the antiplane eigenstrain problem of an elliptic inclusion in a two-phase anisotropic medium were obtained. The stress singularity coefficient for a flat inclusion was calculated. When the tip of the inclusion lies at the interface boundary, the stress singularity coefficient is given by the formula, $\mathcal{S}' = (1+K)\,\mathcal{S}^{\circ}$, where K is the inhomogenity factor and $\mathcal{S}^{\circ}$ is the stress singularity coefficient for a homogeneous matrix.

Acknowledgment

The work was supported by the National Science Foundation under Grant DMR-7915799.

References

1 Eshelby, J. D., "The Determination of the Elastic Field of an Ellipsoidal Inclusion, and Related Problems," *Proceedings of the Royal Society*, London, Series *A*, Vol. 241, 1957, pp. 376–396.

2 Eshelby, J. D., "The Elastic Field Outside an Ellipsoidal Inclusion," *Proceedings of the Royal Society*, London, Series *A*, Vol. 252, 1959, pp. 561–569.

3 Masumura, R. A., and Chou, Y. T., "Antiplane Eigenstrain Problem of an Elliptic Inclusion in an Anisotropic Half Space," ASME JOURNAL OF APPLIED MECHANICS, Vol. 49, 1982, pp. 52–54.

4 Chou, Y. T., "On Antiplane Line Force in a Two-Phase Anisotropic Medium," *Physics Status Solidi*, Vol. 34, 1976, pp. 645–650.

5 Yang, H. C., and Chou, Y. T., "Generalized Plane Problems of Elastic Inclusions in Anisotropic Solids," ASME JOURNAL OF APPLIED MECHANICS, Vol. 43, 1976, pp. 424–430.

6 Yang, H. C. and Chou, Y. T., "On Rigid Elliptical Inclusions in Orthotropic Solids," ASME JOURNAL OF APPLIED MECHANICS, Vol. 45, 1978, pp. 683–685.

7 Marden, M., *Geometry of Polynomials*, 2nd Ed., American Mathematical Society, 1966, pp. 194–197.

8 Yang, H. C., and Chou, Y. T., "Antiplane Strain Problems of an Elliptic Inclusion in an Anisotropic Medium," ASME JOURNAL OF APPLIED MECHANICS, Vol. 44, 1977, pp. 437–441.

Downloaded 02 May 2010 to 171.66.16.54. Redistribution subject to ASME license or copyright; see http://www.asme.org/terms/Terms_Use.cfm

B. L. Karihaloo
Professor,
Department of Civil
Engineering and Surveying,
University of Newcastle,
New South Wales, Australia 2308
Mem. ASME

K. Viswanathan
Principal Scientific Officer,
Defence Science Centre,
Metcalfe House,
Delhi, India 110054

Elastic Field of an Elliptic Inhomogeneity With Debonding Over an Arc (Antiplane Strain)

This paper describes the elastic field of an elliptic inhomogeneity that has debonded over an arc of its common boundary with a different elastic material in which it is embedded. Eshelby's method of equivalent inclusion with a stress-free eigenstrain is employed. The solution is facilitated by the properties of Green's functions. Only the antiplane strain case is treated for illustrating the procedure. Numerical results are presented for the stress intensity factors at the tips of the debonded arc, as well as for the relative displacements across the debond.

1 Introduction

The elastic field induced in a matrix by the presence of inhomogeneities (inclusions, voids, etc.) plays an important role in the behavior of composite materials. In a classical paper, Eshelby [1], developed a method for treating a single inhomogeneity in the form of an ellipsoidal inclusion. Using the concepts of stress-free "eigenstrain" and "equivalent inclusion," he arrived at an elegant solution to this complex problem. Ever since, there has been considerable activity in extending Eshelby's approach to a variety of practical problems, such as the interaction of two ellipsoidal inhomogeneities (Moschovidis and Mura [2]), the behavior of hybrid composites (Taya and Chou [3]), and the analysis of composites with cracks at the ends of reinforcing fibers (Taya and Mura [4]), to cite only a few examples.

However, it seems that no attempt has been made at extending Eshelby's technique to the problem of solving the elastic field induced by a partially debonded inclusion, apart from the paper by Taya and Patterson [5] who considered the simpler case of a completely debonded inhomogeneity. On the other hand, several authors have attempted the boundary-value problem of a rigid inclusion with one or two cracks along the interface [6, 7] and employed the analytic-function theory (or what is referred to as Muskhelishvili's technique). This technique suits only two-dimensional problems, and it is, therefore, of great interest to try to extend Eshelby's method to the partially debonded inclusion case, as it is likely to render three-dimensional problems amenable to mathematical treatment.

In the present paper, we describe the extension of Eshelby's technique with respect to the simple example of a two-dimensional elliptic inclusion in antiplane strain. The field due to an elliptic inhomogeneity with debonding over an arc is considered. The geometry of the inclusion and the coordinate axes, together with the debonded arc are shown in Fig. 1. The treatment of the plane-strain case and of the three-dimensional ellipsoidal inclusion will be reported in future communications.

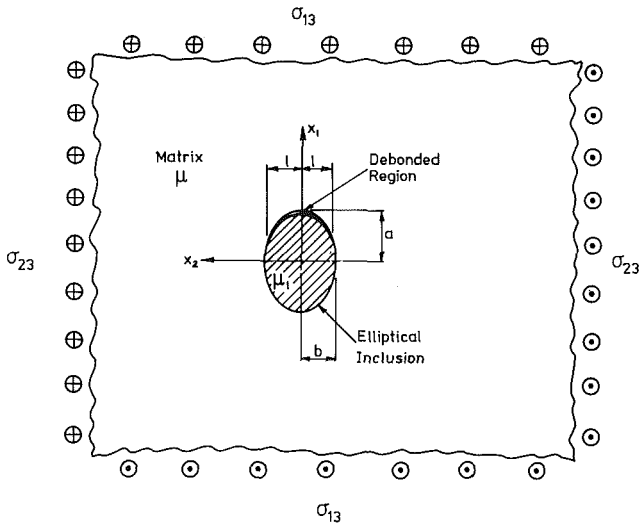


Fig. 1 The debonded elliptical inhomogeneity, showing the coordinate axes and remote stress field

2 Basic Equations and Their Solution Using Green's Function

For the antiplane strain case, the elastic displacement w is in the direction normal to the plane of the elliptic inclusion (Fig. 1). The nonvanishing components of the stress tensor are

$$\sigma_{13} = \mu \frac{\partial w}{\partial x_1}, \qquad \sigma_{23} = \mu \frac{\partial w}{\partial x_2}, \tag{2.1}$$

where μ, μ_1 are the shear moduli of the matrix and inclusion, respectively. The corresponding elastic strains will be denoted by e_{13} and e_{23}.

Contributed by the Applied Mechanics Division for publication in the JOURNAL OF APPLIED MECHANICS.
Discussion on this paper should be addressed to the Editorial Department, ASME, United Engineering Center, 345 East 47th Street, New York, N.Y. 10017, and will be accepted until two months after final publication of the paper itself in the JOURNAL OF APPLIED MECHANICS. Manuscript received by ASME Applied Mechanics Division, March, 1984; final revision, August, 1984.

Copyright © 1985 by ASME
Downloaded 02 May 2010 to 171.66.16.54. Redistribution subject to ASME license or copyright; see http://www.asme.org/terms/Terms_Use.cfm

If X_3 is the body-force, the only nonvanishing equation of equilibrium can be written as

$$\sigma_{13,1} + \sigma_{23,2} + X_3 = 0. \tag{2.2}$$

Here, and in sequel, a suffix preceded by comma indicates differentiation with respect to the corresponding coordinate. Using (2.1) and (2.2) we obtain

$$\mu \nabla^2 w + X_3 = 0. \tag{2.3}$$

Following Eshelby [1], we replace the inhomogeneity (Ω), by the same material as the matrix but with a suitable eigenstrain β_{i3} ($i = 1, 2$) such that

$$X_3 = -\mu \beta_{i3,i}, \quad (\mathbf{x} \subset \Omega) \tag{2.4}$$

where the summation convention over the repeated indices is assumed. From (2.3) and (2.4) we have, writing $\beta_{i3} = \beta_i$ for brevity,

$$\nabla^2 w = \beta_{i,i}. \tag{2.5}$$

In other words, the eigenstrain may be viewed as a body force in the inclusion. The debonded arc is denoted by Γ which is a part of the elliptic boundary

$$\Gamma: \frac{x_1^2}{a^2} + \frac{x_2^2}{b^2} = 0, \qquad -l < x_2 < l. \tag{2.6}$$

Next consider Green's function

$$G(\mathbf{x},\mathbf{x}') = \log|\mathbf{x} - \mathbf{x}'|, \tag{2.7}$$

which is a solution of the equation

$$\nabla^2 G(\mathbf{x},\mathbf{x}') = 2\pi\, \delta(\mathbf{x} - \mathbf{x}'), \tag{2.8}$$

where $\delta(x)$ is the Dirac delta function. From (2.5) and (2.8) we obtain

$$\begin{aligned} 2\pi w(x) = & \int_V \{ w(\mathbf{x}') \nabla^2 G(\mathbf{x},\mathbf{x}') \\ & - G(\mathbf{x},\mathbf{x}') \nabla^2 w(\mathbf{x}') \} dV(\mathbf{x}') \\ & + \int_V \beta_{i,i}(\mathbf{x}') G(\mathbf{x},\mathbf{x}') dV(\mathbf{x}'); \\ & (\mathbf{x} \subset V) \end{aligned} \tag{2.9}$$

for any region V. Applying Green's Theorem to the first integral and ensuring continuity of normal derivative of w across Γ, we have

$$\begin{aligned} w(x) = & \frac{1}{2\pi} \fint_\Gamma \gamma(\mathbf{x}') G_{,j}(\mathbf{x},\mathbf{x}') n_j(\mathbf{x}') d\Gamma(\mathbf{x}') \\ & + \frac{1}{2\pi} \int_\Omega \beta_{i,i}(\mathbf{x}') G(\mathbf{x},\mathbf{x}') d\Omega(\mathbf{x}'), \end{aligned} \tag{2.10}$$

where $n_j(\mathbf{x}')$ is the unit normal at $\mathbf{x}'$ on the debonded elliptical arc Γ drawn outward from Ω, and

$$\gamma(\mathbf{x}') \equiv \Delta \mathbf{w}(\mathbf{x}') \tag{2.11}$$

is the displacement of the outer face of the debonded arc relative to the inner face. The symbol $\fint$ stands for Cauchy principal value.

Let the stress field applied remote from the inclusion be given by

$$\begin{aligned} \sigma^0_{i3}(\mathbf{x}) &\equiv \mu e^0_{i3}(\mathbf{x}) \\ &= \mu \sum_{p,q} a^{(i)}_{pq} x_1^p x_2^q. \end{aligned} \tag{2.12}$$

The problem therefore reduces to that of determining the eigenstrains β_i in the inclusion and the displacement $\gamma(\mathbf{x}')$ across the debonded arc.

3 Equivalence Relation and Boundary Condition

The equivalence relation for the elliptic inhomogeneity in terms of an equivalent inclusion with the eigenstrain, according to [1–4], is

$$\mu\{ e^0_{i3} + e_{i3}(w) - \beta_i(\mathbf{x}) \} = \mu_1 \{ e^0_{i3} + e_{i3}(w) \}, \tag{3.1}$$

where μ_1 is the shear modulus of the inclusion.

Substitution of (2.10) into (3.1) gives the relation

$$\begin{aligned} \kappa\, \beta_i(\mathbf{x}) = & e^0_{i3}(\mathbf{x}) \\ & + \frac{1}{2\pi} \fint_\Gamma \gamma(\mathbf{x}') G_{,ij}(\mathbf{x},\mathbf{x}') n_j(\mathbf{x}') d\Gamma(\mathbf{x}') \\ & + \frac{1}{2\pi} \int_\Omega \beta_{j,j}(\mathbf{x}') G_{,i}(\mathbf{x},\mathbf{x}') d\Omega(\mathbf{x}'), \quad (\mathbf{x} \subset \Omega) \end{aligned} \tag{3.2}$$

where

$$\kappa = \mu/(\mu - \mu_1) = 1/(1 - \mu_1/\mu). \tag{3.3}$$

In (3.2), the following notation has been used:

$$G_{,ij}(\mathbf{x},\mathbf{x}') \equiv \partial^2 G/\partial x_i \partial x'_j, \tag{3.3}_1$$

$$G_{,i}(\mathbf{x},\mathbf{x}') \equiv \partial G/\partial x_i. \tag{3.3}_2$$

Next, we write the boundary condition that the stress across the debonded arc Γ must vanish, i.e., $n_i \{ e^0_{i3} + e_{i3}(w) \} = 0$ on Γ.

From (2.10) it follows that

$$\begin{aligned} & \frac{n_i(\mathbf{x})}{2\pi} \fint_\Gamma \gamma(\mathbf{x}') G_{,ij}(\mathbf{x},\mathbf{x}') n_j(\mathbf{x}') d\Gamma(\mathbf{x}') \\ & \quad = -e^0_{i3}(\mathbf{x}) n_i(\mathbf{x}) \\ & \qquad - \frac{n_i(\mathbf{x})}{2\pi} \int_\Omega \beta_{j,j}(\mathbf{x}') G_{,i}(\mathbf{x},\mathbf{x}') d\Omega(\mathbf{x}'); \quad (\mathbf{x} \subset \Gamma) \end{aligned} \tag{3.4}$$

The notation introduced previously in $(3.3)_1$ and $(3.3)_2$ applies here too. Obviously, each interchange in the derivatives with respect to x_i and x'_i leads to a change of sign.

4 Solution to (3.2) and (3.4)

It has been shown in [1, 8] that when the inhomogeneity (inclusion) is in perfect contact with the matrix, an applied stress of a polynomial form in the coordinates x_1, x_2 will lead to an eigenstrain $\beta_i(\mathbf{x})$ which is also of a polynomial type. Moreover, the $\beta_i(\mathbf{x})$ polynomial will be of the same degree as the applied stress. In the present case however, debonding will give an additional term in $\beta_i(\mathbf{x})$ which will exhibit the well-known singular behavior near the tips of the debonded arc Γ. Accordingly, we may write $\beta_i(\mathbf{x})$ as a sum of two terms

$$\beta_i(\mathbf{x}) = \beta^I_i(\mathbf{x}) + \beta^{II}_i(\mathbf{x}), \tag{4.1}$$

such that $\beta^I_i(\mathbf{x})$ is a polynomial in x_1 and x_2 that satisfies (3.2) without the singular integral term over Γ as in all previous works, and $\beta^{II}_i(x)$ is the singular part of the eigenstrain that will balance the remaining terms in (3.2) arising from itself and from the integral over Γ. In other words, the component β^I_i will satisfy

$$\begin{aligned} \kappa\, \beta^I_i(\mathbf{x}) = & e^0_{i3}(\mathbf{x}) \\ & + \frac{1}{2\pi} \int_\Omega \beta^I_{j,j}(\mathbf{x}') G_{,i}(\mathbf{x},\mathbf{x}') d\Omega(\mathbf{x}'), \quad (\mathbf{x} \subset \Omega) \end{aligned} \tag{4.2}$$

Integrating by parts the integral over the domain of the inclusion Ω we obtain the well-known form reported in [2, 9]

$$\begin{aligned} \kappa\, \beta^I_i(\mathbf{x}) = & e^0_{i3}(\mathbf{x}) \\ & - \frac{1}{2\pi} \int_\Omega \beta^I_j(\mathbf{x}') G_{,ij}(\mathbf{x},\mathbf{x}') d\Omega(\mathbf{x}'), \quad (\mathbf{x} \subset \Omega) \end{aligned} \tag{4.3}$$

For the applied stress field (2.12), we assume the expected polynomial form for β^I_i to be

$$\beta^I_i(\mathbf{x}) = \sum_{p,q} b^{(i)}_{pq} x_1^p x_2^q. \tag{4.4}$$

The integral in (4.3) again leads to a polynomial, as is shown in Appendix A, so that we may write it as

Downloaded 02 May 2010 to 171.66.16.54. Redistribution subject to ASME license or copyright; see http://www.asme.org/terms/Terms_Use.cfm

$$\left\{-\frac{1}{2\pi}\int_\Omega \beta_j^I(\mathbf{x}')G_{,ij}(\mathbf{x},\mathbf{x}')d\Omega(\mathbf{x}')\right\} = \sum_{p,q} c_{pq}^{(i)} x_1^p x_2^q, \tag{4.5}$$

where the coefficients $c_{pq}^{(i)}$ are known in terms of $b_{pq}^{(i)}$ and of certain integrals over the elliptic region Ω. In consequence of (2.12) and (4.5), (4.3) reduces to an identity in x_1 and x_2 which is satisfied if

$$\kappa\, b_{pq}^{(i)} = a_{pq}^{(i)} + c_{pq}^{(i)},\ (p,q=0,1,2,\ldots;\quad i=1,2) \tag{4.6}$$

The identities (4.6) can be solved exactly for $b_{pq}^{(i)}$ for any given polynomial applied stress field (2.12). Thus the eigenstrain component $\beta_i^I(\mathbf{x})$ is completely determined.

$\beta_i^{II}(x)$ Component of Eigenstrain. Next, we consider the singular part of the eigenstrain, which must satisfy the relation (follows from (3.2))

$$\kappa\,\beta_i^{II}(\mathbf{x}) = \frac{1}{2\pi}\oint_\Gamma \gamma(\mathbf{x}')G_{,ij}(\mathbf{x},\mathbf{x}')n_j(\mathbf{x}')d\Gamma(\mathbf{x}') + \frac{1}{2\pi}\int_\Omega \beta_{j,j}^{II}(\mathbf{x}')G_{,i}(\mathbf{x},\mathbf{x}')d\Omega(\mathbf{x}'),\ (\mathbf{x}\subset\Omega). \tag{4.7}$$

The boundary condition (3.4) also simplifies by virtue of (4.2) to give

$$\frac{n_i(\mathbf{x})}{2\pi}\oint_\Gamma \gamma(\mathbf{x}')G_{,ij}(\mathbf{x},\mathbf{x}')n_j(\mathbf{x}')d\,\Gamma(\mathbf{x}') + \frac{n_i(\mathbf{x})}{2\pi}\int_\Omega \beta_{j,j}^{II}\mathbf{x}')G_{,i}(\mathbf{x},\mathbf{x}')d\Omega(\mathbf{x}') = -\kappa\{\Sigma b_{pq}^{(i)}x_1^p x_2^q\}n_i(\mathbf{x}),\qquad (\mathbf{x}\subset\Gamma) \tag{4.8}$$

We recall that summation convention is assumed over the repeated indices. We have to solve the integral equations (4.7) and (4.8) in $\gamma(\mathbf{x})$ and $\beta_i^{II}(\mathbf{x})$.

As $\beta_i^{II}(\mathbf{x})$ is a singular solution arising from the debonding, we assume that it is given by a distribution of dislocations: $B(\mathbf{x})$

$$\beta_i^{II}(\mathbf{x}) = \frac{1}{2\pi}\oint_\Gamma B(\mathbf{x}')G_{,ij}(\mathbf{x},\mathbf{x}')n_j(\mathbf{x}')d\,\Gamma(\mathbf{x}') \tag{4.9}$$

In (4.7) and (4.8) we meet an integral of the form

$$I_i = \frac{1}{2\pi}\int_\Omega \beta_{j,j}^{II}(\mathbf{x}')G_{,i}(\mathbf{x},\mathbf{x}')d\Omega(\mathbf{x}'). \tag{4.10}$$

By virtue of (4.9) it reduces to the following form after interchanging the order of integration (assuming such an operation to be valid):

$$I_i = \frac{1}{(2\pi)^2}\int_\Omega G_{,i}(\mathbf{x},\mathbf{x}')d\Omega(\mathbf{x}')\oint_\Gamma B(\mathbf{x}'')n_k(\mathbf{x}'')\{G_{,jk}(\mathbf{x}',\mathbf{x}'')\}_{,j}d\,\Gamma(\mathbf{x}'') \tag{4.11}$$
$$= \frac{1}{(2\pi)^2}\oint_\Gamma B(\mathbf{x}'')n_k(\mathbf{x}'')d\Gamma(\mathbf{x}'')\int_\Omega G_{,i}(\mathbf{x},\mathbf{x}')\{G_{,jk}(\mathbf{x}',\mathbf{x}'')\}_{,j}d\Omega(\mathbf{x}').$$

The following notation has been used in (4.11)

$$G_{,i}(\mathbf{x},\mathbf{x}') = \frac{\partial}{\partial x_i}G(\mathbf{x},\mathbf{x}'), \tag{4.11}_1$$

and

$$\{G_{,jk}(\mathbf{x}',\mathbf{x}'')\}_{,j} = \frac{\partial}{\partial x_j'}\frac{\partial}{\partial x_j'}\frac{\partial}{\partial x_k''}G(\mathbf{x}',\mathbf{x}'') = \frac{\partial}{\partial x_k''}\nabla'^2 G(\mathbf{x}',\mathbf{x}''). \tag{4.11}_2$$

Thus together with (2.8), equation (4.11) becomes

$$I_i = \frac{1}{(2\pi)^2}\int_\Gamma B(\mathbf{x}'')n_k(\mathbf{x}'')d\Gamma(\mathbf{x}'')\times \frac{\partial}{\partial x_k''}\frac{\partial}{\partial x_i}\int_\Omega G(\mathbf{x},\mathbf{x}')2\pi\delta(\mathbf{x}'-\mathbf{x}'')d\Omega(\mathbf{x}') \tag{4.12}$$
$$= \frac{1}{2\pi}\oint_\Gamma B(\mathbf{x}'')n_k(\mathbf{x}'')G_{,ik}(\mathbf{x},\mathbf{x}'')d\Gamma(\mathbf{x}'')$$

Then (4.7) readily gives the relation

$$(\kappa-1)B(\mathbf{x}) = \gamma(\mathbf{x}). \tag{4.13}$$

Finally, substitution from (4.13) into the relation (4.8) gives the equation for determining $B(\mathbf{x})$

$$\frac{n_i(\mathbf{x})}{2\pi}\oint_\Gamma B(\mathbf{x}')n_j(\mathbf{x}')G_{,ij}(\mathbf{x},\mathbf{x}')d\Gamma(\mathbf{x}') = -(\Sigma b_{pq}^{(i)}x_1^p x_2^q)n_i(\mathbf{x}),\qquad (\mathbf{x}\subset\Gamma) \tag{4.14}$$

Using (2.7), equation (4.14) reduces to an integral equation of the type

$$\oint_{-l}^{l}\frac{B(x_2')F(x_2,x_2')}{(x_2'-x_2)^2}dx_2' = P(x_2),\qquad -l<x_2<l \tag{4.15}$$

Here,

$$F(x_2,x_2') = \frac{1}{2\pi}\frac{d\,\Gamma(\mathbf{x}')}{dx_2'}T(\mathbf{x})n_i(\mathbf{x})n_j(\mathbf{x})(x_2'-x_2)^2G_{,ij}(\mathbf{x},\mathbf{x}'),$$
$$P(x_2) = -T(\mathbf{x})n_i(\mathbf{x})\sum_{p,q}b_{pq}^{(i)}x_1^p x_2^q, \tag{4.16}$$
$$B(\mathbf{x}') = B(x_2') = \sqrt{l^2-x_2'^2}\sum_n B_n x_2'^n,$$

and $T(\mathbf{x})$, $n_i(x)$, and $d\Gamma(\mathbf{x}')/dx_2'$ are defined later (6.2) and (6.3). The singular integral equation (4.15) can be solved exactly up to any desired degree of accuracy using well-known procedures ([10, 11]). Finally, from (4.9), the eigenstrain $\beta_i^{II}(\mathbf{x})$ can be determined to complete the solution of the main problem.

5 A Specific Example

To illustrate the preceding approach, let us take a specific example and assume that the applied strain field (2.12) is given explicitly in the following form:

$$e_{i3}^0(\mathbf{x}) = a_{00}^{(i)} + a_{10}^{(i)}x_1 + a_{01}^{(i)}x_2,\quad (i=1,2) \tag{5.1}$$

For consistency it is essential that $a_{01}^{(1)} = a_{10}^{(2)}$. Let the eigenstrain $\beta_i^I(x)$ be expressible as

$$\beta_i^I(\mathbf{x}) = b_{00}^{(i)} + b_{10}^{(i)}x_1 + b_{01}^{(i)}x_2. \tag{5.2}$$

Then from (4.5) and Appendix A, we obtain

$$\begin{aligned}
c_{00}^{(i)} &= b_{00}^{(i)}I_i,\qquad (i=1,2,\text{ no summation over } i)\\
c_{10}^{(1)} &= b_{10}^{(1)}(3I_1-2I_3)+(b^2/a^2)b_{00}^{(2)}(I_2-2I_4)\\
c_{01}^{(1)} &= b_{10}^{(2)}(I_2-2I_4)+b_{01}^{(1)}(I_1-2I_4)\\
c_{10}^{(2)} &= c_{01}^{(1)}\\
c_{01}^{(2)} &= (a^2/b^2)b_{01}^{(1)}(I_1-2I_4)+b_{01}^{(2)}(3I_2-2I_5)
\end{aligned} \tag{5.3}$$

The integrals $I_1, I_2, \ldots I_5$ are calculated in Appendix A.

Substituting from (5.3) into (4.6) and solving for the coefficients $b_{pq}^{(i)}$ we obtain

$$\begin{aligned}
b_{00}^{(1)} &= a_{00}^{(1)}/(\kappa-I_1)\\
b_{00}^{(2)} &= a_{00}^{(2)}/(\kappa-I_2)\\
b_{10}^{(1)} &= (E_4a_{10}^{(1)}+E_2a_{01}^{(2)})/(E_1E_4-E_2E_3)\\
b_{01}^{(2)} &= (E_1a_{01}^{(2)}+E_3a_{10}^{(1)})/(E_1E_4-E_2E_3)\\
b_{01}^{(1)} &= (F_4a_{01}^{(1)}+F_2a_{10}^{(2)})/(F_1F_4-F_2F_3)\\
b_{10}^{(2)} &= (F_1a_{10}^{(2)}+F_3a_{01}^{(1)})/(F_1F_4-F_2F_3)
\end{aligned} \tag{5.4}$$

Downloaded 02 May 2010 to 171.66.16.54. Redistribution subject to ASME license or copyright; see http://www.asme.org/terms/Terms_Use.cfm

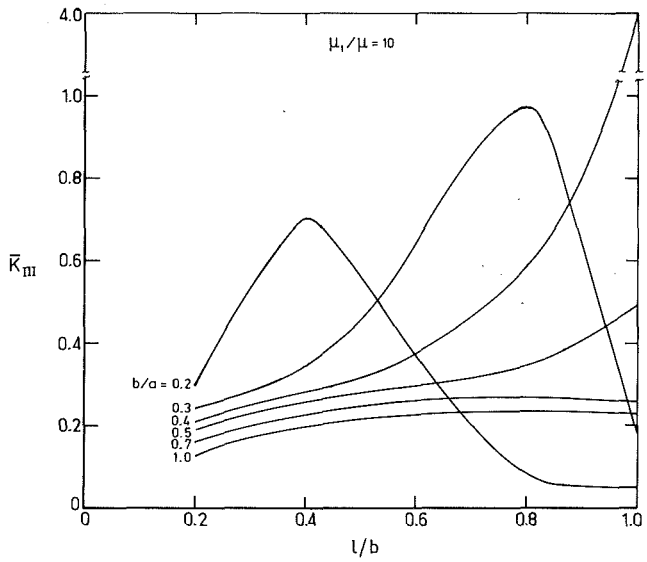


Fig. 2 Stress intensity factor $\bar{K}_{III}$ for the uniform applied strain defined by equation (6.10) (note that $\bar{K}^{+}_{III} = \bar{K}^{-}_{III}$)

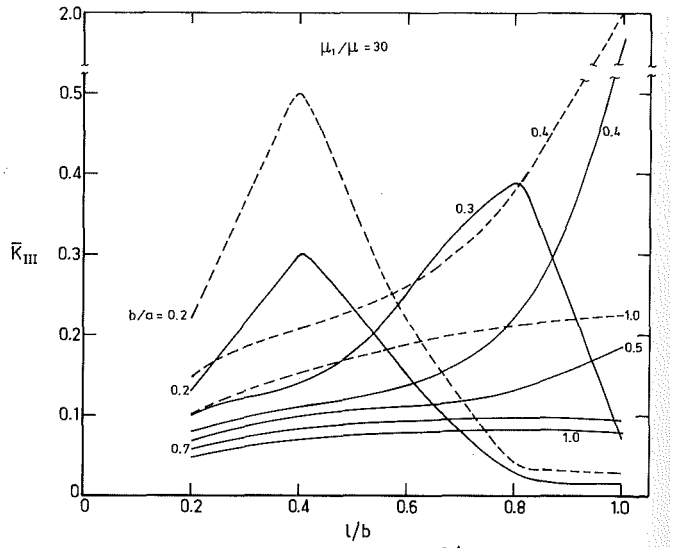


Fig. 3 Comparison of stress intensity factors $\bar{K}^{\pm}_{III}$ at debond tip $x_2 = \pm l$; solid lines correspond to uniform applied strain (6.10) and broken lines to the polynomial-type strain (6.12)

where the integrals E_1, E_2, E_3, E_4 and F_1, F_2, F_3, F_4 are defined in Appendix B. Thus $\beta_i^I(\mathbf{x})$ is completely determined.

Finally, the function $B(\mathbf{x}) \equiv B(x_2)$ in (4.9) is assumed in the form

$$B(x_2) = (l^2 - x_2^2)^{1/2}(B_0 + B_1 x_2 + B_2 x_2^2 + \ldots\ldots) \tag{5.5}$$

and the resulting integral equation (4.14) (or, (4.15)) is solved for the first few expansion coefficients. The result is

$$\begin{aligned} B_0 &= [3(b_{00}^{(1)} + a\, b_{10}^{(1)}) + (l^2/4b^2)\{-a^2 b_{00}^{(1)}/2b^2 \\ &\quad - a\, b_{10}^{(1)}(1 + a^2/2b^2) + 2a\, b_{01}^{(2)}\}]/D \\ B_1 &= -\{b_{00}^{(2)} + b^2 b_{01}^{(1)}/a + a\, b_{10}^{(2)}\} \\ &\quad /\{a(b^2/a^2 + l^2/8b^2)\} \\ B_2 &= [(-a\, b_{10}^{(1)}/2 + a\, b_{01}^{(2)}) + (a^2 l^2/16b^4)(b_{00}^{(1)} \\ &\quad + 2\, a\, b_{10}^{(1)} - 2a\, b_{01}^{(2)})]/b^2 D, \end{aligned} \tag{5.6}$$

where

$$D = (-3/2) + (a^2 l^2/4b^4). \tag{5.7}$$

Higher-order terms of $B(\mathbf{x})$ can also be determined in the same manner. Thus $\beta_i^{II}(\mathbf{x})$ is also found up to any desired order of accuracy.

6 Stress Intensity Factor and Relative Displacement of Crack Faces

The singular part of the solution in (2.10) is obtained by combining the first integral over Γ with the β^{II} part of the second integral over Ω. In this manner, we obtain the corresponding stress across the debonded arc Γ,

$$\begin{aligned} \sigma_{n3}(\mathbf{x}) &= \mu \frac{\partial w}{\partial n} \\ &= \mu n_i(\mathbf{x})\left[\frac{1}{2\pi}\oint_\Gamma \gamma(\mathbf{x}')G_{,ij}(\mathbf{x},\mathbf{x}')n_j(\mathbf{x}')d\Gamma(\mathbf{x}')\right. \\ &\quad \left. + \frac{1}{2}\int_\Omega \beta^{II}_{k,k}(\mathbf{x}')G_{,i}(\mathbf{x},\mathbf{x}')d\Omega(\mathbf{x}')\right] \\ &= \frac{\mu\, \kappa n_i(\mathbf{x})}{2\pi}\oint_\Gamma B(\mathbf{x}')G_{,ij}(\mathbf{x},\mathbf{x}')n_j(\mathbf{x}')d\Gamma(\mathbf{x}'). \end{aligned} \tag{6.1}$$

We have retained only the singular parts and also made use of (4.9)–(4.12) and (4.13). Using (2.7) and (5.5), and noticing that on Γ,

$$\begin{aligned} n_1(\mathbf{x}) &= (x_1/a^2 T(\mathbf{x})) \\ n_2(\mathbf{x}) &= (x_2/b^2 T(\mathbf{x})) \\ T(\mathbf{x}) &= (x_1^2/a^4 + x_2^2/b^4)^{1/2}, \end{aligned} \tag{6.2}$$

and

$$d\Gamma(\mathbf{x}') = T(\mathbf{x}')\,(a^2/x_1')\,d\,x_2', \tag{6.3}$$

the equation (6.1) may be rewritten as

$$\sigma_{n3}(\mathbf{x}) = \frac{\kappa\,\mu}{2\pi T(\mathbf{x})}\int_{-l}^{l}\frac{(l^2 - x_2'^2)^{1/2}F(x_2,x_2')dx_2'}{(x_2' - x_2)^2}. \tag{6.4}$$

$F(x_2, x_2')$ is a known function which can be expanded in a power series

$$F(x_2,x_2') = \sum_{p,q}\alpha_{pq}(x_2')^q(x_2)^p, \tag{6.5}$$

where the coefficients of expansion α_{pq} are defined in Appendix B. The integral in (6.4) can now be evaluated term-by-term. The singular term of the stress is found to be

$$\begin{aligned} \sigma_{n3}(x_2) &= \frac{\kappa\,\mu\, x_2}{2(x_2^2 - l^2)^{1/2}}\{\alpha_{00} + (\alpha_{01} + \alpha_{10})x_2 \\ &\quad + (\alpha_{02} + \alpha_{11} + \alpha_{20})x_2^2 + \ldots\} \\ &\quad /\left\{1 + \frac{l^2}{b^2}\left(\frac{a^2}{b^2} - 1\right)\right\}^{1/2} \\ &\quad (|x_2| > l). \end{aligned} \tag{6.6}$$

Thus, near the tips of the debonded arc,

$$\sigma_{n3}\Big|_{x_2 \to \pm(l+0)} = K^{\pm}_{III}/(2\pi d)^{1/2}, \tag{6.7}$$

where d is the distance along the tangential directions from either of the tips, and $K^{\pm}_{III}$—the usual "stress intensity factor" in antiplane strain mode at the debond tips $x_2 = \pm l$—is given by

$$\begin{aligned} K^{\pm}_{III}\Big|_{x_2 = \pm l} &= (1/2)\kappa\,\mu(\pi l)^{1/2}(1 + a^2 l^2/b^4)^{1/4} \\ &\quad \left\{1 + \frac{l^2}{b^2}\left(\frac{a^2}{b^2} - 1\right)\right\}^{-1/2} \times \\ &\quad \times \{a\alpha_{00} \pm al(\alpha_{01} + \alpha_{10}) \\ &\quad + al^2(\alpha_{02} + \alpha_{11} + \alpha_{20}) + \ldots\} \end{aligned} \tag{6.8}$$

Downloaded 02 May 2010 to 171.66.16.54. Redistribution subject to ASME license or copyright; see http://www.asme.org/terms/Terms_Use.cfm

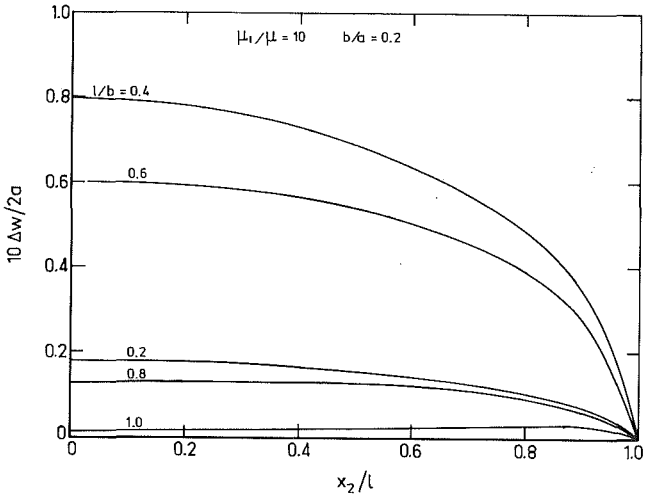


Fig. 4 Relative displacement of the debonded faces under the uniform applied strain (6.10)

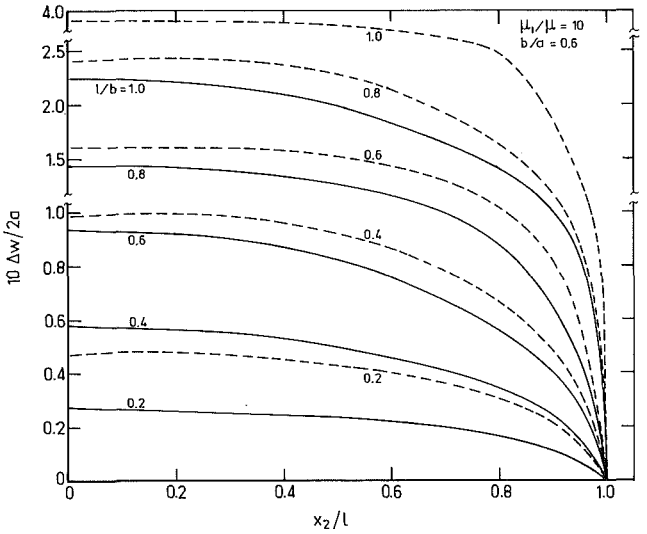


Fig. 5 Comparison of relative displacements of the debonded faces in the region $x_2 > 0$; solid lines correspond to uniform applied strain (6.10) and broken lines to the polynomial-type strain (6.12)

We define the nondimensional stress intensity factor to be

$$\bar{K}_{III} = K_{III}/(\mu b^{1/2}). \tag{6.9}$$

The values of $\bar{K}_{III}$ for different combinations of the shear moduli ratio (μ_1/μ), aspect ratio of the elliptical inclusion (b/a), and size of the debonding (l/b) are shown in Fig. 2 and Fig. 3. Two cases of loading were considered:

Case (*i*)

$$e^0_{13}(\mathbf{x}) = 1, \quad e^0_{23}(\mathbf{x}) = 0, \tag{6.10}$$

so that from (5.1),

$$\begin{aligned} a^{(1)}_{00} &= 1 \\ a^{(1)}_{01} &= a^{(1)}_{10} = 0 \\ a^{(2)}_{00} &= a^{(2)}_{01} = a^{(2)}_{10} = 0. \end{aligned} \tag{6.11}$$

In this case, the results will be symmetric about the $0x_1$-axis, and hence the results for $x_2 < 0$ will be the same as those for $x_2 > 0$;

Case (*ii*)

$$e^0_{13}(\mathbf{x}) = 1 + x_1 + x_2, \quad e^0_{23}(\mathbf{x}) = x_1, \tag{6.12}$$

which is a polynomial-type applied strain. From (5.1) it follows that

$$\begin{aligned} a^{(1)}_{00} &= a^{(1)}_{10} = a^{(1)}_{01} = 1 \\ a^{(2)}_{00} &= a^{(2)}_{01} = 0, \quad a^{(2)}_{10} = 1. \end{aligned} \tag{6.13}$$

Here the results for $x_2 < 0$ will be different from those for $x_2 > 0$. For the purposes of comparison, the results for $x_2 \to l + 0$ arising from this case are shown by broken lines in Fig. 3.

The values of the relative displacement (4.13) of the two faces of the debonded arc are shown (for the region $x_2 \geq 0$) in Fig. 4 and Fig. 5 for the preceding two cases.

It should be noted that the higher terms in the polynomial loading generally enhance the stress intensity factors, as well as the crack-opening displacements.

7 Conclusion

Eshelby's equivalent inclusion technique is again found to be convenient for the analysis of more complex situations such as a partially debonded inhomogeneity. The stress intensity factors and the relative displacement of the crack faces are easily determined and found to be significantly affected by the higher terms of the polynomials representing the applied stress or strain field. This technique is being applied to plane-strain fields and to three-dimensional bodies. These results will be reported in future communications.

Acknowledgments

The visit of K. Viswanathan to the University of Newcastle is funded by a grant (F8215322) to B. L. Karihaloo from the Australian Research Grants Scheme.

References

1 Eshelby, J. D., "The Determination of the Elastic Field of an Ellipsoidal Inclusion, and Related Problems," *Proceedings of the Royal Society*, London, Series *A*, Vol. 241, 1957, pp. 376–396.

2 Moschovidis, Z. A., and Mura, T., "Two Ellipsoidal Inhomogeneities by the Equivalent Inclusion Method," ASME JOURNAL OF APPLIED MECHANICS, Vol. 42, 1975, pp. 847–852.

3 Taya, M., and Chou, T. W., "On Two Kinds of Ellipsoidal Inhomogeneities in an Infinite Elastic Body: An Application to a Hybrid Composite," *Int. J. Solids and Structures*, Vol. 17, 1981, pp. 553–563.

4 Taya, M., and Mura, T., "On Stiffness and Strength of an Aligned Short-Fiber Reinforced Composite Containing Fiber-End Cracks Under Uniaxial Applied Stress," ASME JOURNAL OF APPLIED MECHANICS, Vol. 48, 1981, pp. 361–367.

5 Taya, M., and Patterson, W. G., "Growth of a Debonded Void at a Rigid Secondary Particle in a Viscous Metal," *Journal of Materials Science*, Vol. 17, 1982, pp. 115–120.

6 Sendeckyj, G. P., "Debonding of Rigid Curvilinear Inclusions in Longitudinal Shear Deformations," *Engineering Fracture Mechanics*, Vol. 6, 1974, pp. 33–45.

7 Viola, E., and Piva, A., "Fracture Behavior by Two Cracks Around an Elliptic Rigid Inclusion," *Engineering Fracture Mechanics*, Vol. 15, 1981, pp. 303–325.

8 Eshelby, J. D., "Elastic Inclusions and Inhomogeneities," in: *Progress in Solid Mechanics*, Sneddon and Hill, eds., Vol. 2, North-Holland, Amsterdam, 1961, pp. 89–140.

9 Mura, T., "The Continuum Theory of Dislocations," in: *Advances in Materials Research*, Vol. 3, Herman, H., ed., Wiley-Interscience, New York, 1968.

10 Karihaloo, B. L., "Numerical Integration of a Singular Integral Equation," *Proc. 1983 Int. Conf. on Computational Techniques and Applications*, Sydney, Australia, Noye, J., and Fletcher, C., eds., North-Holland, Amsterdam, 1984, pp. 297–307.

11 Ioakimidis, N. I., "A New Singular Integral Equation for the Classical Crack Problem in Plane and Antiplane Elasticity," *International J. of Fracture*, Vol. 2, 1983, pp. 115–122.

12 Ferrers, N. M., "On the Potentials of Ellipsoids, Ellipsoidal Shells, Elliptic Laminae, and Elliptic Rings of Variable Densities," *Quarterly Journal of Pure and Applied Mathematics*, Vol. XIV, 1877, pp. 1–22.

13 Dyson, F. W., "The Potentials of Ellipsoids of Variable Densities," *Quarterly Journal of Pure and Applied Mathematics*, Vol. XXV, 1891, pp. 259–288.

APPENDIX *A*

Here we consider the evaluation of the integral in (4.5) when β^j_i is represented by the polynomial (4.4). As reported in

Downloaded 02 May 2010 to 171.66.16.54. Redistribution subject to ASME license or copyright; see http://www.asme.org/terms/Terms_Use.cfm

[7, 8], such an integral is related to certain potentials that can be evaluated following the analysis suggested in the works of Ferrers [12] and Dyson [13]. In the course of this analysis it was found that the integrals arising from individual terms of the polynomials (4.4) could also be evaluated by a more direct and mechanical approach. In essence, it is a generalization of the approach taken by Eshelby himself [1] for the simple case of a constant eigenstrain. We start with a general term arising from the substitution of (4.4) into (4.5):

$$I_{mn}^{(i,j)} = -\frac{1}{2\pi}\int_\Omega (x_1')^m (x_2')^n G_{,ij}(\mathbf{x},\mathbf{x}')\,d\Omega(\mathbf{x}')$$

$$= \frac{1}{2\pi}\frac{\partial}{\partial x_j}\int_\Omega \frac{(x_1')^m (x_2')^n (x_i'-x_i)}{R^2(\mathbf{x},\mathbf{x}')}\,dx_1'dx_2'; \qquad (A1)$$

where

$$R(\mathbf{x},\mathbf{x}') = |\mathbf{x}-\mathbf{x}'|.$$

Following [1], we shift the origin of coordinates to (x_1, x_2) so that

$$x_1' = x_1 + Rl_1, \qquad x_2' = x_2 + Rl_2, \qquad (A2)$$

where

$$(l_1, l_2) = (\cos\phi, \sin\phi) \qquad (A3)$$

are the direction cosines in the local cylindrical coordinates at (x_1, x_2). Thus (A1) gives

$$I_{mn}^{(i,j)} = \frac{1}{2\pi}\frac{\partial}{\partial x_j}\int_0^{2\pi} d\phi \int_0^{R_\phi} (x_1+Rl_1)^m (x_2+Rl_2)^n l_i\,dR \qquad (A4)$$

where

$$R_\phi = -\frac{g}{f} + \frac{(g^2+fe)^{1/2}}{f}$$
$$= R^{odd} + R^{even} \text{ (say)}. \qquad (A5)$$

In (A5),

$$g = \frac{l_1x_1}{a^2} + \frac{l_2x_2}{b^2}, \quad f = l_1^2/a^2 + l_2^2/b^2$$
$$e = (1 - x_1^2/a^2 - x_2^2/b^2). \qquad (A6)$$

Expanding the binomial factors in (A4), we get

$$I_{mn}^{(i,j)} = \frac{1}{2\pi}\frac{\partial}{\partial x_j}\sum_{r=0}^{m}\sum_{s=0}^{n}\binom{m}{r}\binom{n}{s}x_1^{m-r}x_2^{n-s}$$
$$\int_0^{2\pi} l_1^r l_2^s l_i\,d\phi \int_0^{R_\phi} R^{r+s}\,dR$$
$$= \frac{1}{2\pi}\frac{\partial}{\partial x_j}\sum_{r=0}^{m}\sum_{s=0}^{n}\binom{m}{r}\binom{n}{s}\frac{x_1^{m-r}x_2^{n-s}}{(r+s+1)}$$
$$\int_0^{2\pi} l_1^r l_2^s l_i R_\phi^{r+s+1}\,d\phi \qquad (A7)$$

It is now necessary to evaluate

$$P_{rs}^{(i)} = \int_0^{2\pi} l_1^r l_2^s l_i R_\phi^{r+s+1}\,d\phi. \qquad (A8)$$

Substitution from (A5) into (A8) gives

$$P_{rs}^{(i)} = \int_0^{2\pi} l_1^r l_2^s l_i (R^{odd}+R^{even})^{r+s+1}\,d\phi$$
$$= \sum_{M=0}^{r+s+1}\binom{r+s+1}{M}\int_0^{2\pi} l_1^r l_2^s l_i$$
$$(R^{odd})^{M_1}(R^{even})^{M}\,d\phi \qquad (A9)$$
$$\le \sum_{M=0}^{\frac{r+s+1}{2}}\binom{r+s+1}{2M}\int_0^{2\pi} l_1^r l_2^s l_i$$
$$(R^{odd})^{M_2}(R^{even})^{2M}\,d\phi$$

where $M_1 = r+s+1-M$ and $M_2 = r+s+1-2M$. The last step follows from the preceding one because the integrals with odd values of M vanish. From (A5) and (A6)

$$R^{odd} = -(l_1x_1/a^2 + l_2x_2/b^2)/(l_1^2/a^2 + l_2^2/b^2),$$
$$(R^{even})^2 = \frac{g^2+fe}{f^2} \qquad (A10)$$
$$= \frac{(l_1x_1/a^2 + l_2x_2/b^2)^2}{(l_1^2/a^2+l_2^2/b^2)^2} + \frac{(1-x_1^2/a^2-x_2^2/b^2)}{(l_1^2/a^2+l_2^2/b^2)}$$

are, respectively, explicit linear and second-order polynomials in x_1 and x_2. It is a trivial matter to substitute from (A10) into (A9) and to obtain an explicit expression for $P_{rs}^{(i)}$ as a polynomial of degree $(r+s+1)$. Finally, $I_{mn}^{(i,j)}$ in (A7) will therefore be a polynomial of degree $(m+n)$.

For the specific example chosen in (5.1) and (5.2) where β_i^I consists of only the constant term and the linear terms in x_1 and x_2, the foregoing analysis gives

$$\Sigma c_{pq}^{(j)} x_1^p x_2^q = \frac{\partial}{\partial x_j}\{b_{00}^{(i)}I_{00}^{(i)} + b_{10}^{(i)}I_{10}^{(i)} + b_{01}^{(i)}I_{01}^{(i)}\}, \qquad (A11)$$

where we have written for $I_{mn}^{(i,j)}$ defined in (A7), the notation

$$I_{mn}^{(i,j)} \equiv \frac{\partial}{\partial x_j}\{I_{mn}^{(i)}\}. \qquad (A12)$$

The results (5.3) for $c_{pq}^{(i)}$ follow from the identity (A11) with the following expressions derived for $I_{mn}^{(i)}$:

$$\begin{aligned}
I_{00}^{(1)} &= I_1x_1\\
I_{00}^{(2)} &= I_2x_2\\
I_{10}^{(1)} &= -\frac{a^2}{2}I_1 + x_1^2(3I_1/2 - I_3)\\
&\quad + x_2^2(a^2I_1/2b^2 - a^2I_4/b^2)\\
I_{10}^{(2)} &= x_1x_2(I_2 - 2I_4)\\
I_{01}^{(1)} &= x_1x_2(I_1 - 2I_4)\\
I_{01}^{(2)} &= -b^2I_2/2 + x_1^2(b^2I_2/2a^2 - b^2I_4/a^2)\\
&\quad + x_2^2(3I_2/2 - I_5),
\end{aligned} \qquad (A13)$$

where

$$I_1 = \frac{1}{2\pi}\int_0^{2\pi}\frac{(l_1^2/a^2)}{(l_1^2/a^2+l_2^2/b^2)}\,d\phi$$
$$I_2 = \frac{1}{2\pi}\int_0^{2\pi}\frac{(l_2^2/b^2)}{(l_1^2/a^2+l_2^2/b^2)}\,d\phi \qquad (A14)$$
$$\{I_3, I_4, I_5\} = \frac{1}{2\pi}\int_0^{2\pi}\{l_1^4/a^4, l_1^2l_2^2/a^2b^2, l_2^4/b^4\}$$
$$\frac{d\phi}{(l_1^2/a^2+l_2^2/b^2)^2},$$

Note that $l_1 = \cos\phi$, $l_2 = \sin\phi$.

The preceding integrals can be exactly evaluated:

$$I_1 = (b/a)/(1+b/a)$$
$$I_2 = 1/(1+b/a)$$

Downloaded 02 May 2010 to 171.66.16.54. Redistribution subject to ASME license or copyright; see http://www.asme.org/terms/Terms_Use.cfm

$$I_3 = (b^2/a^2)(1 + a/2b)/(1 + b/a)^2 \qquad (A15)$$
$$I_4 = (b/a)/2(1 + b/a)^2$$
$$I_5 = (1 + b/2a)/(1 + b/a)^2$$

APPENDIX B

The values of E_1, E_2, E_3, E_4 and F_1, F_2, F_3, F_4 are given by

$$E_1 = \kappa - 3I_1 + 2I_3,$$
$$E_2 = (b^2/a^2)(I_2 - 2I_4),$$
$$E_3 = (a^2/b^2)(I_1 - 2I_4), \qquad (B1)$$
$$E_4 = (\kappa - 3I_2 + 2I_5),$$

and

$$F_1 = (\kappa - I_1 + 2I_4),$$
$$F_2 = I_2 - 2I_4,$$
$$F_3 = I_1 - 2I_4, \qquad (B2)$$
$$F_4 = (\kappa - I_2 + 2I_4).$$

Here a and b denote the semimajor and semiminor axes of the ellipse, κ is defined in (3.3), and the values of I_1, I_2, I_3, I_4 are given by (A15).

Next, the coefficients α_{pq} appearing in (6.5) are found after simplifications of the generating expressions from (6.1)–(6.4) to be

$$\alpha_{pq} = \sum_{m \le q} B_m P_{pm'}, \qquad (m' = q - m) \qquad (B3)$$

where the coefficients B_m are defined in (5.6), and

$$P_{00} = -1/a, \qquad P_{01} = P_{10} = 0,$$
$$P_{11} = a/2b^4, \qquad P_{20} = 1/2ab^2 - a/4b^4, \qquad (B4)$$
$$P_{02} = -a/4b^4.$$

Downloaded 02 May 2010 to 171.66.16.54. Redistribution subject to ASME license or copyright; see http://www.asme.org/terms/Terms_Use.cfm

T. L. George
Senior Development Engineer,
Battelle, Pacific
Northwest Laboratory,
Richland, Wash. 99352

T. C. Kennedy
Associate Professor,
Department of Mechanical Engineering,
Oregon State University,
Corvallis, Ore.
Mem. ASME

K. L. Peddicord
Professor,
Department of Nuclear Engineering,
Texas A & M University,
College Station, Texas

An Elastic Stress-Strain Relation for Sphere Arrays Undergoing Initial Stage Sintering

An analytical model for predicting the elastic constants for isotropic random sphere arrays is described. The model is based on the Hertz contact theory and accounts for the restructuring (neck growth) associated with initial stage sintering. The stress-strain relation is incremental since the stiffness depends on the loads at sphere contacts. As part of the model development, relationships are given for the elastic constants of an isotropic aggregate consisting of orthotropic parts. Predicted elastic constants are presented as functions of the neck size and hydrostatic compression, and comparisons are made with experimental data for cohesionless sphere arrays and fully restructured arrays approaching a porous body.

1 Introduction

When high temperatures and/or large compressive stresses are applied to a sample of granular material, solid necks are formed at the particle contact points in a process known as initial stage sintering. The necks result from the transport of material to free surfaces near the contact either by diffusional processes or by viscous or plastic flow. The model described in this paper can be used to predict the elastic properties of a random sphere array as a function of the intersphere neck ratio (neck radius divided by sphere radius). As a special case, the model is applicable to cohesionless sphere arrays (neck ratio equal to zero). The model was developed for a random array of uniform spheres and extended to predict the properties of a two-size sphere array with the smaller spheres able to infiltrate the large sphere array. One particular application of the model is in the analysis of sphere pac nuclear fuel [1] during irradiation. Sphere pac fuel is an advanced fuel concept in which ceramic fuel microspheres rather than the traditional pellets are loaded into the cylindrical cladding. The model also has applications in the general area of the mechanics of granular material and for the analysis of sintering.

For the model development it is assumed that the aggregate of spherical particles is homogeneous and is elastically isotropic. Furthermore, only necks between spheres of the same diameter are considered, and the necks of large and small spheres are separately assumed to be uniform throughout the array. Portions of this problem have been treated previously. Brandt [2] obtained an expression for the bulk modulus of a random sphere array consisting of successively smaller spheres occupying the interstitial spaces left by the next larger size. Incremental anisotropic stress-strain relations have been obtained for various regular packings of uniform spheres [3–6]. Takahashi and Sato [7] and Hersey [8] give expressions of the elastic constants of an isotropic aggregate in terms of the constants of the anistropic parts comprising the aggregate. Yanagisawa [9] considered a random array to consist of units of various regular packed arrays. He applied the results of Takahashi and Sato [7] to estimate the elastic constants of the isotropic random array as an average of the constants obtained for the regular arrays. More recently, Digby [10] developed a model for the elastic constants of a random array where the spheres could be initially bonded together across small areas, obtaining analytical expressions for two elastic constants. All the previous models assume that all deformation is in accordance with the Hertz contact theory. When the necks joining adjacent spheres become large the Hertz theory is not longer valid and significant deformation can occur in the sphere interiors away from the contact points. Further, the models of Yanagisawa [9] and Digby [10] consider only single sphere size arrays, and Brandt's [2] model provides only one elastic constant.

In the present model, a random array of uniform spheres is assumned to consist of a single repeated unit cell at various orientations. Energy principles are used to obtain an incremental stress-strain relation for the orthotropic unit cell. The neck between spheres is treated as a stiffness in parallel with the Hertzian contact stiffness. Composite materials theory [11, 12] is applied to obtain elastic properties for an isotropic random array of uniform spheres. For the elastic properties of a binary array, an approach similar to Brandt's [2] is used to estimate the bulk modulus, and results from the

Contributed by the Applied Mechanics Division and presented at the Winter Annual Meeting, New Orleans, La., December 9-14, 1984 of THE AMERICAN SOCIETY OF MECHANICAL ENGINEERS.

Discussion on this paper should be addressed to the Editorial Department, ASME, United Engineering Center, 345, East 47th Street, New York, 10017, and will be accepted until two months after final publication of the paper itself in the JOURNAL OF APPLIED MECHANICS. Manuscript received by ASME Applied Mechanics Division, January 1983; final revision, February, 1984. Paper No. 84-WA/APM-49,

Copies will be available until August, 1985.

Copyright © 1985 by ASME
Downloaded 02 May 2010 to 171.66.16.54. Redistribution subject to ASME license or copyright; see http://www.asme.org/terms/Terms_Use.cfm

theory of composites are applied to obtain a second elastic constant.

2 Random Array Unit Cell

The model for the elastic properties of a random array of uniform spheres is based on the elastic response of the unit cell shown in Fig. 1. The cell consists of two four-sided pyramids sharing a common base (forming an octahedron) and each having its apex at the center of one of two spheres in contact. The angle β between the sphere center-to-center line and each of the sides of the octahedron fixes the relative dimensions of the cell (edge length, s, relative to sphere radius, R) and is determined by the array packing factor p (p = solid volume/total volume). It may be noted that a simple cubic array can actually be constructed of these unit cells (β = 45 deg) but other regular and random arrays cannot. The cell does, however, have the essential features of a sphere packing: contact point at a particular orientation, void space, and solid material. As opposed to unit cells consisting of groups of spheres, the octahedral unit cell easily allows consideration of material deformation away from the contact, which becomes important when large necks are established.

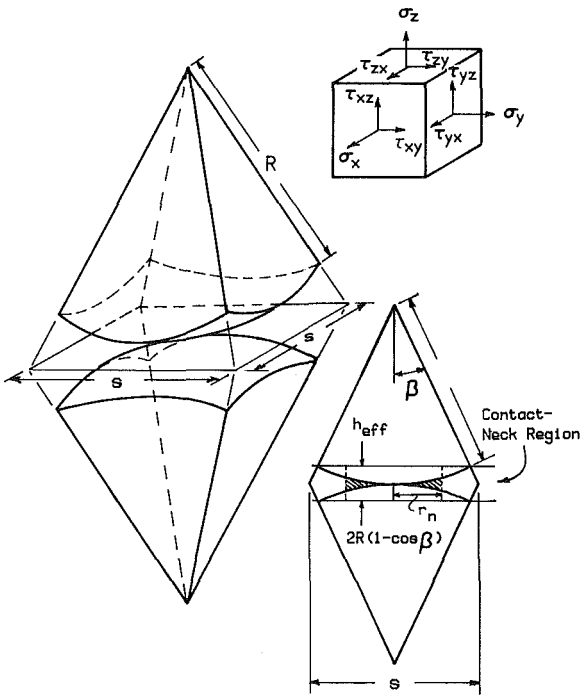


Fig. 1 Unit cell for uniform sphere array

The angle β is chosen so that the unit cell has the same packing factor as the sphere array to be modeled. To obtain β, let C be the average coordination number (number of contacts per sphere) of the array. If equal sphere surface areas (A_c) and volumes (V_c) are associated with each contact, then the packing factor and the coordination number C are related by

$$p = \frac{V_c}{V_u} = \frac{\pi}{C\tan^2\beta} \tag{1}$$

where V_u is one half the unit cell volume

$$\left(V_u = \frac{R}{3}s^2 = \frac{4R^3}{3}\tan^2\beta\right)$$

and

$$\frac{A_c}{R^2} = \frac{4\pi}{C} \tag{2}$$

A_c can be obtained in terms of the angle β through an integration in spherical coordinates giving

$$\frac{A_c}{R^2} = 2\int_0^{\beta}\int_{\omega}^{\pi-\omega}\sin\phi\, d\phi\, d\theta \tag{3}$$

where

$$\cot\omega = \tan\beta\cos\theta$$

Thus, for any packing factor, equations (1)–(3) can be combined to yield β and a coordination number. Equations (1)–(3) were solved numerically to give a unit cell packing factor versus coordination number curve. This is shown in Fig. 2 along with a results for regular packings and experimental data for random arrays. Most of the data falls above the unit cell curve except for the results of Bernal and Mason [14] who distinguish between close contacts (spheres actually in contact) and near contacts (spheres located within a radius of 1.05 R). The data from the other investigations includes both near and close contacts. With this consideration, the octahedral unit cell reasonably represents the packing factor-coordination number relation for both regular and random arrays.

3 Unit Cell Stress-Strain Relation

An incremental stress-strain relation or the orthotropic unit cell can be expressed as

$$\{\delta\epsilon\} = [D^u]\{\delta\sigma\} \tag{4}$$

where

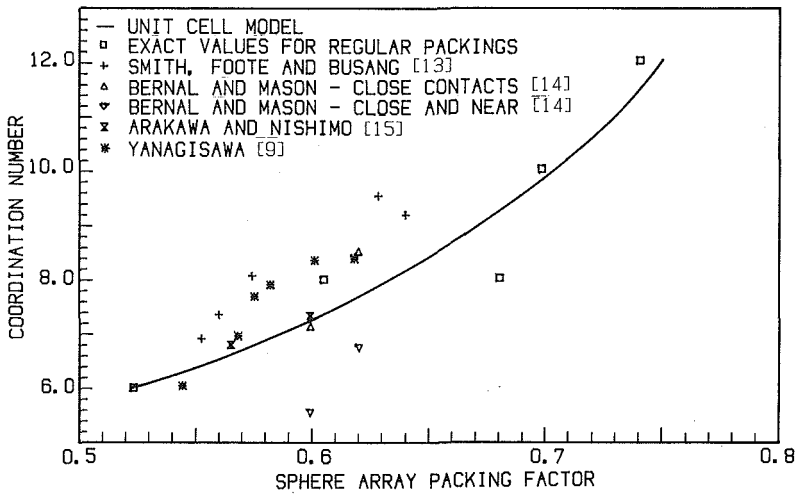


Fig. 2 Uniform sphere array coordination number versus packing factor

Downloaded 02 May 2010 to 171.66.16.54. Redistribution subject to ASME license or copyright; see http://www.asme.org/terms/Terms_Use.cfm

$$\{\delta\epsilon\}^T = [\delta\epsilon_x, \delta\epsilon_y, \delta\epsilon_z, \delta\gamma_{xy}, \delta\gamma_{xz}, \delta\gamma_{yz}]$$

$$\{\delta\sigma\}^T = [\delta\sigma_x, \delta\sigma_y, \delta\sigma_z, \delta\tau_{xy}, \delta\tau_{xz}, \delta\tau_{yz}]$$

and $[D^u]$ is the compliance matrix. An incremental stress-strain relation is used because the contact stiffness depends on the contact load through the Hertz contact theory.

The unit cell is assumed to be subjected to surface tractions, uniform over each surface, which are given by the stress state, $\{\sigma\}$, of the aggregate. The unit cell strain energy increment resulting from an incremental change in the stress state is

$$\delta H = V\{\sigma\}^T\{\delta\epsilon\} = V\{\sigma\}^T[D^u]\{\delta\sigma\} \tag{5}$$

where δH is the strain energy increment, V is the unit cell volume, and $\{\delta\epsilon\}$ is the strain increment resulting from application of $\{\delta\sigma\}$. In the following development, the strain energy increment is calculated and then equation (5) is used to define $[D^u]$.

To calculate δH, the unit cell is divided into two regions as indicated in Fig. 1: the contact-neck region between the two planes parallel to the contact plane and the solid portion that makes up the remainder of the unit cell. The stresses (and deformations) due to the contact are small at distances large compared to the contact radius. The strain energy associated with the contact and neck deformations are therefore assumed to be localized in the contact-neck region. The strain energy increment is equal to the sum of the strain energy increments in the contact-neck region, δH_{cn}, and the solid body region, δH_s; that is,

$$\delta H = \delta H_s + \delta H_{cn} \tag{6}$$

We now derive estimates for the two components of the strain energy.

The unit cell surface area associated with the contact-neck region is unsupported by solid material. The total surface forces are therefore supported by the solid body portions of the unit cell. The effective stress on the solid body portion of the unit cell can be obtained by simple force balances and is given by

$$\{\sigma'\} = \frac{A}{A_s}\{\sigma\} \tag{7}$$

where $\{\sigma'\}$ is the solid body effective stress, A is the area of one side of the unit cell, and A_s is that part of A associated with the solid body portion. From the geometry of the unit cell, $A/A_s = 1/\cos^2\beta$ so that

$$\{\sigma'\} = \frac{1}{\cos^2\beta}\{\sigma\} \tag{8}$$

Equation (5) applied to the solid body portion of the unit cell gives

$$\delta H_s = V_s\{\sigma'\}^T[D^u_m]\{\delta\sigma'\} = \frac{V_s}{\cos^4\beta}\{\sigma\}^T[D^u_m]\{\delta\sigma\} \tag{9}$$

where V_s is the volume of the solid body portion and $[D^u_m]$ is the standard compliance matrix for the assumed isotropic sphere material.

Using the principle of virtual work, the strain energy increment in the contact-neck region can be expressed in terms of the unit cell surface loads and displacements resulting from deformations in the contact-neck region. Thus,

$$\delta H_{cn} = \{F\}^T\{\Delta\} \tag{10}$$

where

$$\{F\}^T = [\sigma_x A_x, \sigma_y A_y, \sigma_z A_z, \tau_{xy} A_x, \tau_{xz} A_z, \tau_{yz} A_z]$$

$$\{\Delta\}^T = [\Delta_x, \Delta_y, \Delta_z, \Gamma_{xy}, \Gamma_{xz}, \Gamma_{yz}]$$

and Δ_x is the incremental displacement at the point of application of $\sigma_x A_x$, etc. The only deflections considered in the contact-neck region are deformations normal to the contact plane and shear deformations parallel to the contact plane so that we take $\Delta_x = \Delta_y = \Gamma_{xy} = 0$. The displacements are related to the forces through the stiffness equation

$$\{\delta F\} = [C^u_{cn}]\{\Delta\} \tag{11}$$

When there is no neck present, the stiffness matrix can be obtained from the Hertz contact theory. When large necks are present, the contact-neck region stiffness should be dominated by the stiffness of the cylindrical neck. The neck stiffness is approximated by the stiffness of a circular column with radius r_n and height h_{eff}. The contact-neck stiffness should vary, as a function of the neck ratio (neck radius/sphere radius), from the Hertz contact stiffness (when $r_n = 0$) to the circular column stiffness at large r_n. This functional dependence is achieved by assuming that the total contact-neck stiffness is the sum of the contact stiffness and the circular column stiffness, i.e., the neck and contact act as independent parallel springs. It is not clear what the effective column height is, but it should approach the height of the contact-neck region for large necks. For very small necks the column stiffness should be small compared to the contact stiffness. Both of these requirements are satisfied by letting h_{eff} equal the height of the contact-neck region. The contact-neck region stiffness matrix can be expressed as the sum of the contact and the neck stiffness matrices giving

$$[C^u_{cn}] = [C^u_c] + [C^u_n] \tag{12}$$

From the Hertz theory, the normal and transverse compliances give

$$\Delta_z = \frac{4Q}{3a}\delta F_z \tag{13}$$

$$\Gamma_{xz} = \frac{2-\nu}{4Ga}\Delta F_{xz}, \quad \Gamma_{yz} = \frac{2-\nu}{4Ga}\delta F_{yz} \tag{14}$$

where $Q = 3(1-\nu^2)/4E$, ν, G and E are the sphere material Poisson's ratio, shear modulus, and Young's modulus, respectively, and a is the contact radius. The contact radius is given by

$$a/R = (QL/R^2)^{1/3} \tag{15}$$

where L is the load normal to the contact plane.

The normal load depends on the particular orientation of the unit cell in the stress field. Since a stress-strain relation for the aggregate consisting of variously oriented unit cells is sought, an average value of L is used and is given by

$$L = -A_z\sigma h \tag{16}$$

where σ_h is the hydrostatic stress, $\sigma_h = 1/3(\sigma_x + \sigma_y + \sigma_z)$, and A_z is the projected area of the unit cell in the z direction. From equations (13) and (14), the diagonal contact stiffness matrix (zero off diagonal terms) can now be written as

$$Diag[C^u_c] = \left[M, M, \frac{3a}{4Q}, M, \frac{4Ga}{2-\nu}, \frac{4Ga}{2-\nu}\right] \tag{17}$$

The stiffness coefficients associated with the neglected displacements, Δ_x, Δ_y, and Γ_{xy}, are set to an arbitrarily large number M ($M >> E$). Similarly, the diagonal neck stiffness matrix can be written as

$$Diag[C^u_n] = \frac{\pi r_n^2}{h_{\text{eff}}}[M, M, E, M, G, G] \tag{18}$$

A contact-neck region compliance matrix is now defined by

$$[D^u_{cn}] = [C^u_{cn}]^{-1} \tag{19}$$

so that from equations (10) and (11)

$$\delta H_{cn} = \{\sigma\}^T[A][D^u_{cn}][A]\{\delta\sigma\} \tag{20}$$

where

$$Diag[A] = [A_x, A_y, A_z, A_x, A_z, A_z]$$

Downloaded 02 May 2010 to 171.66.16.54. Redistribution subject to ASME license or copyright; see http://www.asme.org/terms/Terms_Use.cfm

Then by combining equations (5), (6), (9), and (20) the unit cell compliance matrix is given by

$$V[D^u] = \frac{V_s}{\cos^4\beta}[D^u_m] + [A][D^u_{cn}][A] \tag{21}$$

For a typical random sphere array with a packing factor of 0.61, the first term in the foregoing expression for the compliance matrix can be neglected (contributes less than 10 percent) unless the hydrostatic stress is large ($-\sigma_h/E > 0.008$) or the neck ratio is greater than 0.04.

4 Elastic Constants for an Isotropic Made Up of Anisotropic Parts

Granular materials are generally assumed to behave isotropically on a scale larger than the grain size, although on a smaller scale the material is anisotropic. Takahashi and Sato [7] derived expressions for the elastic constants of an isotropic aggregate as functions of the elastic constants of its anisotropic composing parts. In their analysis they assumed that the complementary strain energy density of the aggregate was equal to the average complementary strain energy of the anisotropic part over all possible orientations. The elastic constants for the aggregate could then be obtained from the aggregate complementary strain energy density function. The strain energy of the aggregate using these constants is an upper bound for the actual strain energy (Voight model [16]). When the results of Takahashi and Sato [7] were applied to the unit cell elastic constants derived in the foregoing, the stiffness of random sphere arrays was considerably overpredicted compared to experimental results and previous theories.

Hershey [8] performed a similar analysis using the strain energy (Reuss model [17]) for the case of a unit cell that had cubic symmetry. Considerable work has been done to improve the bounds on the strain energy given by the Voight and Reuss models [18–21]. However, improved bounds can only be obtained if one has more information regarding the structure of the composite (or aggregate) than is required for the simple volume average of the strain energy [22].

In the present study, the approach used by Hershey is extended to the case of an orthotropic unit cell. Consider an anisotropic unit cell whose orientation with respect to a set of reference axes, X_I fixed to the aggregate, is given by the Euler angles ϕ_1, ϕ_2 and ϕ_3. A coordinate system, x_i, is fixed to the unit cell. Let t_{iI} be the transformation tensor from the x_i system to the X_I system. Consider also a stress field σ_{IJ} and differential stress field $\delta\sigma_{IJ}$ referenced to the X_I system. Assume that these stress fields are constant within and on any particular unit cell making up the aggregate. The differential strain energy resulting from the application of $\delta\sigma_{IJ}$ is given by

$$dh(\phi_1, \phi_2, \phi_3) = \sigma_{ij}d\epsilon_{ij} = \sigma_{ij}D_{ijkl}d\sigma_{kl} \tag{22}$$

where σ_{ij}, $d\sigma_{ij}$, and $d\epsilon_{ij}$ are the stress and strains referenced to unit cell coordinates and D_{ijkl} is the unit cell compliance tensor.

It is assumed that the strain energy density of the aggregate is equal to the average of the strain energy densities of the unit cells comprising the aggregate. Then, assuming a uniform distribution of unit cell orinetations, the aggregate strain energy density can be expressed as

$$dh^0 = \frac{1}{8\pi^2}\int_0^{2\pi}\int_0^{2\pi}\int_0^{\pi} dh\ \sin\phi_1 d\phi_1 d\phi_2 d\phi_3 = \sigma_{IJ}D^0_{IJKL}d\sigma_{IJ} \tag{23}$$

where D^0_{IJKL} is the compliance tensor for the isotropic aggregate. Substituting equation (22) and applying the coordinate transformation to the stress tensor gives

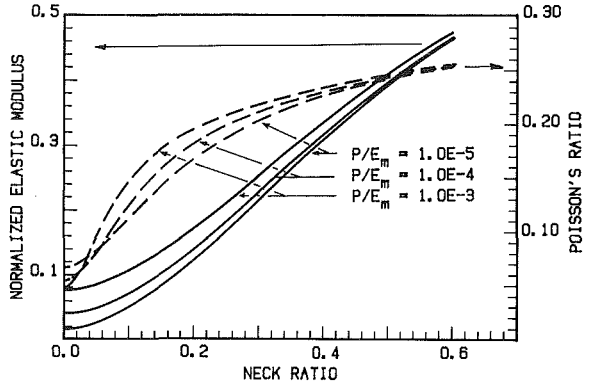


Fig. 3 Effective elastic constants for random array of uniform spheres

$$\sigma_{IJ}D^0_{IJKL}d\sigma_{KL} =$$

$$\frac{1}{8\pi^2}\int_0^{2\pi}\int_0^{2\pi}\int_0^{\pi}\sigma_{IJ}t_{iI}t_{jJ}t_Kt_{lL}D_{ijkl}d\sigma_{KL}\sin\phi_1 d\phi_1 d\phi_2 d\phi_3 \tag{24}$$

Since σ_{IJ} and $d\sigma_{IJ}$ are arbitrary and independent of ϕ_1, ϕ_2, and ϕ_3, equation (24) reduces to an expression for the aggregate compliance tensor

$$D^0_{IJKL} = \frac{1}{8\pi^2}\int_0^{2\pi}\int_0^{2\pi}\int_0^{\pi} t_{iI}t_{jJ}t_{kK}t_{lL}D_{ijkl}\sin\phi_1 d\phi_1 d\phi_2 d\phi_3 \tag{25}$$

For the special case of an orthotropic unit cell, integration of equation (25) gives

$$D_{11} = D_{22} = D_{33} = \frac{3}{15}(D^u_{11} + D^u_{22} + D^u_{33}) + \frac{2}{15}(D^u_{12} + D^u_{23} + D^u_{13}) + \frac{1}{15}(D^u_{44} + D^u_{55} + D^u_{66})$$

$$D_{12} = D_{13} = D_{23} = \frac{1}{15}(D^u_{11} + D^u_{22} + D^u_{33}) + \frac{4}{15}(D^u_{12} + D^u_{23} + D^u_{13}) - \frac{1}{30}(D^u_{44} + D^u_{55} + D^u_{66})$$

$$D_{44} = D_{55} = D_{66} = 2(D_{11} - D_{12})$$

$$\text{Others} = 0 \tag{26}$$

where D^u_{11}, D^u_{22}, etc., are the entries from the unit cell compliance matrix. Application of equation (26) to the unit cell compliance matrix provides reasonable estimates for the random array elastic properties as shown in the following section.

5 Elastic Constants for a Random Array of Uniform Spheres

The results of the preceding section were used to obtain the elastic properties for an array with a packing factor of 0.61 and sphere material Poisson's ratio of 0.3. Figure 3 shows the effective value of Poisson's ratio and Young's modulus (normalized by Young's modulus of the sphere material, E_m) as a function of the neck ratio at three different values of hydrostatic compression (normalized by E_m). At zero neck ratio, the effective Young's modulus is proportional to the 1/3 power of the confining pressure which is consistent with the Hertz contact theory. The pressure dependence decreases at larger neck ratios. For small neck ratios, Poisson's ratio is small (0.04 – 0.07) in agreement with analytic results for regular packed sphere arrays and experimental evidence for cohesionless granular material [23]. At large neck ratios, Poisson's ratio approaches the value of Poisson's ratio for the sphere material. This is in agreement with Paul's [24] model for Poisson's ratio of a composite material (see equation (46) of this paper) which reduces to $V_p = V_m$ where V_p, and V_m

Downloaded 02 May 2010 to 171.66.16.54. Redistribution subject to ASME license or copyright; see http://www.asme.org/terms/Terms_Use.cfm

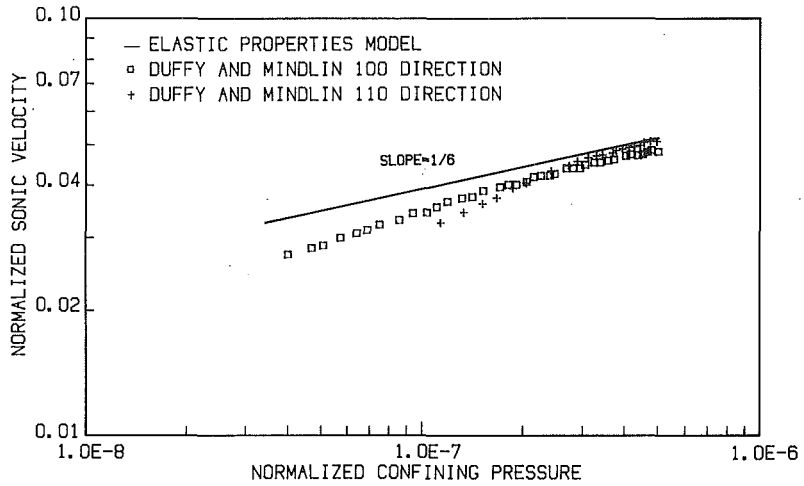


Fig. 4 Sonic velocity in face-centered cubic sphere array

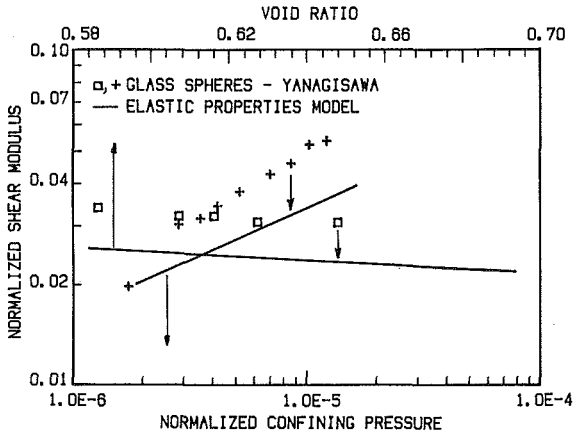


Fig. 5 Shear modulus in random array of uniform spheres

are the effective porous material and the matrix Poisson ratios, respectively. No experimental data has been found for the elastic constants as functions of the neck ratio, but some comparisons can be made with theory and data for cohesionless arrays. For the case of a random array of uniform spheres at a packing factor of 0.61, Brandt's [2] model for the bulk modulus reduces to

$$K/K_m = 0.3443\left(\frac{P/E_m}{(1-\nu^2)^2}\right)^{1/3} \tag{27}$$

where P is the hydrostatic compressive stress on the array. For the same case, the present model gives

$$(K/E_m)^{-1} = 3.211\left(\frac{P/E_m}{(1-\nu^2)^2}\right)^{-1/3} + (3-6\nu)/0.8 \tag{28}$$

Except for very large P ($P/E_m > 0.008$) the second term on the right-hand side can be neglected and the bulk modulus from equation (28) is 10 percent smaller than that predicted by Brandt's model. Experiments by Davis and Deresiewicz [25] indicate that for a two-dimensional random array, Brandt's model overpredicts the bulk modulus by about 20 percent. As can be observed in equation (27), Brandt's model predicts that the bulk modulus continually increases as the confining pressure increases. The second term on the right-hand side of equation (28), however, serves to limit the maximum bulk modulus predicted by the present model so that

$$K/E_m < \frac{0.8}{3-5\nu} < K_m/E_m = \frac{1}{3(1-2\nu)} \tag{29}$$

where K_m is the bulk modulus for the sphere material.

Duffy and Mindlin [3] measured the velocity of a compression wave in an array of steel spheres in a face-centered cubic arrangement. Wave speeds were measured in two directions through the array: parallel to an edge and parallel to a face diagonal of a unit cube. The wave speed (normalized by the sonic velocity in steel) predicted by the present model and the experimental data are shown in Fig 4. The model can predict only one velocity, independent of direction, but since the experimental wave speeds for the two directions are very close it is reasonable to expect nearly isotropic wave speed, and comparison with the present model is valid. The decrease in slope of the logarithmic wave speed as the confining pressure increased was attributed by Duffy and Mindlin to spheres that were not initially in contact but were brought into contact at higher compression. The agreement between the experimental data and the model is excellent at higher compression levels.

Yanigisawa [9] measured the effective shear modulus in random arrays of uniform glass beads and in packed sand. The experimental and model predicted values for the shear modulus of the glass sphere array (normalized by the shear modulus of crown glass) as functions of the packing factor and the applied compression are shown in Fig. 5. The model accurately predicts the packing factor dependence although the absolute magnitude is 20–30 percent larger than the experimental data. The slope of the experimental data versus the pressure is slightly larger than that predicted by the model, but this slope could decrease at higher pressure as it did for Duffy and Mindlin [3]. The underprediction of the shear modulus is consistent with the lower bound on strain energy approach used to derive the elastic constant. Yanagisawa used results from an upper bound approach and predicted shear moduli 60 percent larger than observed.

6 Elastic Constants for a Binary Sphere Array

The model for the elastic constants of a random array of uniform spheres has been extended to provide elastic constants for a two-size sphere array. The smaller spheres are assumed to be small enough to easily infiltrate a packed array of large spheres. Such infiltration is possible as long as the small-to-large sphere diameter ratio is less than 0.155. For the binary model, it is assumed that loading of the small sphere arrays in the interstitial spaces of the large sphere array can only occur through deformation of the large sphere array. The effective stress on the large spheres is therefore the same as that described in Section 3, but there is an additional reaction force on the large spheres due to the interaction with the small spheres. As the large sphere array is compressed, the small sphere arrays are subjected to some boundary displacement due to deformation in the contact-neck regions of the large shear array. The resulting stress in the small

Downloaded 02 May 2010 to 171.66.16.54. Redistribution subject to ASME license or copyright; see http://www.asme.org/terms/Terms_Use.cfm

sphere array acts to oppose the stress causing the contact-neck deformation in the large sphere array. This can be likened to pore pressure and effective stress used in soil mechanics. It is evident then that, under the foregoing assumption, the stresses in the small sphere array will not be the same as those of the aggregate or the large sphere array. A value for the aggregate bulk modulus is obtained using an approach similar to Brandt's except that deformation of the large sphere array contact-neck region and solid body regions are considered separately. The theory of composite materials is used to provide an estimate for the second elastic constant.

To obtain an estimate for the bulk modulus of a binary sphere array, consider a volume V_B of the aggregate under some hydrostatic compression P_B. The binary array bulk modulus K_B can be defined by

$$K_B = -V_B \frac{\delta P_B}{\delta V_B} \tag{30}$$

where δV_B is the change in volume V_B due to a change in compression. Momentarily neglecting the small spheres, a volume change of the large sphere array consists of two parts: a volume change due to deformation in the contact-neck region, and a volume change due to compression of the solid body region. The unit cell compliance matrix can be written as

$$[D_u] = [D_m^{u\prime}] + [D_{cn}^{u\prime}] \tag{31}$$

where $[D_m^{u\prime}]$ and $[D_{cn}^{u\prime}]$ are defined by comparison with equation (21). Since the relations used to obtain the aggregate compliance matix from the unit cell compliance matrix are linear, the aggregate compliance matix can be expressed as

$$[D] = [D_m] + [D_{cn}] \tag{32}$$

$[D_m]$ and $[D_{cn}]$ are obtained by applying equation (26) to $[D_m^{u\prime}]$ and $[D_{cn}^{u\prime}]$, individually. The bulk modulus for each of the two volume change components can be obtained from the respective compliance matrix giving

$$K_L^{cn} = \frac{1}{3(D_{cn11} + 2D_{cn12})}$$

$$K_L^{s} = \frac{1}{3(D_{m11} + 2D_{m12})} \tag{33}$$

K_L^{cn} and K_L^s are the bulk moduli corresponding to contact-neck deformation and solid body deformation, respectively. The total volume change of the large sphere array is

$$\delta V_L = \delta V_L^{cn} + \delta V_L^{s} \tag{34}$$

where δV_L^{cn} and δV_L^s are the volume changes due to contact-neck deformation and solid body deformation, respectively.

Now consider again the small sphere arrays in the interstitial spaces of the large sphere array. Contact-neck deformation of the large sphere array must result in a corresponding change in the volume of the small sphere array. Therefore, it is assumed that

$$\delta V_S = \delta V_L^{cn} \tag{35}$$

where δV_S is the change of all the small spheres in V_B. Further, it is assumed that the volume change of the binary array is equal to the volume change of the large sphere array giving

$$\delta V_B = \delta V_L \tag{36}$$

Let P_S be the hydrostatic compression developed in the small sphere arrays due to interaction with the large spheres. The various volume changes can be related to the compression changes by

$$\frac{\delta V_L^{s}}{V_B} K_L^{s} = -\delta P_B \tag{37}$$

$$\frac{\delta V_L^{cn}}{V_B} K_L^{cn} = -\delta P_B + \delta P_S \tag{38}$$

$$\frac{\delta V_S}{(1-p)\,V_B} K_S = -\delta P_S \tag{39}$$

where K_S is the small sphere array bulk modulus. It should be noted that K_L^{cn} is a function of $P_B - P_S$ and K_S is a function of P_S as these pressures are used to define the contact forces.

Equations (30), (34), and (36)–(38) can be combined to give

$$1/K_B = 1/K_L^{s} + \frac{1 - \delta P_S/\delta P_B}{K_L^{cn}} \tag{40}$$

and equations (35), (38), and (39) combine to yield

$$\delta P_S/\delta P_B = \left[1 + \frac{K_L^{cn}(1-p)}{K_S}\right]^{-1} \tag{41}$$

For infinitesimal changes in P_B, equation (41) becomes

$$dP_S/dP_B = \left[1 + \frac{(1-p)K_L^{cn}(P_B - P_S)}{K_S(P_S)}\right]^{-1} \tag{42}$$

where the functional dependence of K_L and K_S on P_B and P_S is indicated. The compression in the small sphere arrays can be computed from

$$P_S = \int_0^{P_B} (dP_S/dP_B)\, dP_B \tag{43}$$

Numerical solution to equations (42) and (43) has shown that dP_S/dP_B is nearly independent of P_B so that P_S can be assumed to be given by

$$P_S = R_{SB} P_B \tag{44}$$

where R_{SB} is the small-to-binary array compression ratio that depends only on the neck ratios of the large and small sphere arrays. The value of R_{SB} for particular neck ratios can be found by replacing dP_S/dP_B by R_{SB} in equation (42) and solving simultaneously with equation (44). The binary array bulk modulus can then be computed from equation (40) giving

$$1/K_B = 1/K_L^{s} + \frac{1 - R_{SB}}{K_L^{cn}} \tag{45}$$

Under the assumption that $K_L^{cn} = K_L - K_L^s$, where K_L is the effective bulk modulus of the large spheres alone, it can be shown that equation (45) matches the expression derived by Nur and Byerlee [26] for the effective bulk modulus of a granular material with fluid in the voids at pressure P_S.

A second elastic constant for the binary array is estimated using an expression derived by Paul [24] for Poisson's ratio of a two-material composite. The binary array effective Poisson's ratio is given by

$$\nu_B = \frac{\nu_L(1+\nu_S)(1-2\nu_S)pE_L + \nu_S(1+\nu_L)(1-2\nu_L)(1-p)E_S}{(1+\nu_S)(1-2\nu_s)pE_L + (1+\nu_L)(1-2\nu_L)(1-p)E_S} \tag{46}$$

where ν_S, ν_L, E_S, and E_L are the effective values of Poisson's ratio and Young's modulus for the small and large sphere arrays. These elastic constants are computed using the single size sphere array elastic properties model with effective compressions of P_S and $(P_B - P_S)$ for the small and large sphere arrays, respectively.

The effective values of Poisson's ratio and Young's modulus for a binary sphere array for three values of the normalized compression are shown in Fig 6. The array represented by these curves has a large sphere packing factor of 0.61 and the small spheres fill the remining void with a packing factor of 0.56. The sphere material Poisson's ratio is 0.3. The elastic constants are plotted as a function of the neck ratio between small spheres. The neck ratio between the large spheres was taken as one-half the small sphere neck ratio. The trends observed in the binary array elastic properties are similar to those of the single size sphere array (Fig. 3). When there are no necks present, the binary array Young's modulus

Downloaded 02 May 2010 to 171.66.16.54. Redistribution subject to ASME license or copyright; see http://www.asme.org/terms/Terms_Use.cfm

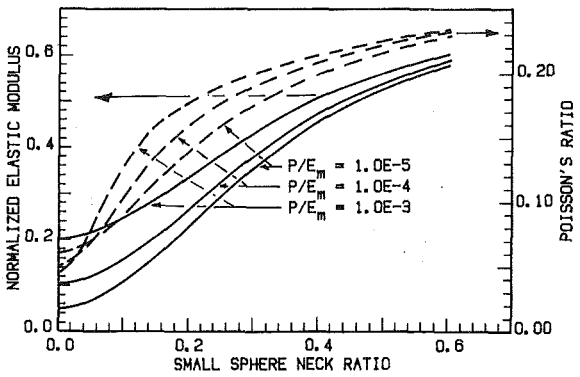


Fig. 6 Effective elastic constants for a binary sphere array

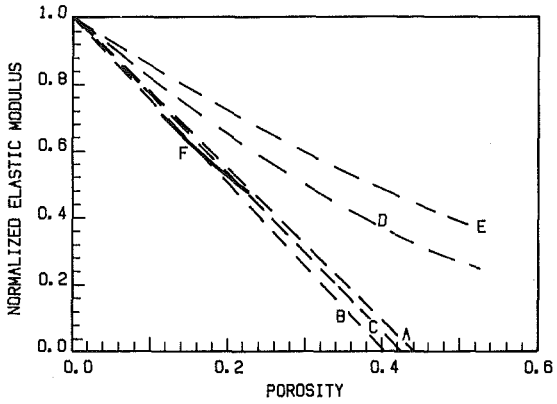


Fig. 7 Elastic modulus for porous media. (*a*) data for uranium carbide, (*b*) data for yttrium oxide, (c) Gatto's theory, (*d*) MacKenzie's theory, (*e*) Hashin's theory, and (*f*) present model

is more than a factor of two larger than that for the single size sphere array, and Poisson's ratio is nearly the same.

Acknowledgment

This work was sponsored by the Swiss Institute for Reactor Research, Wuerenligen, Switzerland.

References

1 Stratton, R. W., "Development of Advanced Fuels in Switzerland," *Adv. LMFBR Fuels Topical Meeting Proc.*, Tucson, Arizona, 1977, p. 74.

2 Brandt, H.,. "A Study of the Speed of Sound in Porous Granular Media," ASME JOURNAL OF APPLIED MECHANICS, Vol. 22, 1955, pp. 479–486.

3 Duffy, J., and Mindlin, R. D., "Stress-Strain Relations and Vibrations of a Granular Medium," ASME JOURNAL OF APPLIED MECHANICS, Vol. 24, 1975, pp. 585–593.

4 Deresiewicz, H., "Stress-Strain Relations for a Simple Model of a Granular Medium," ASME JOURNAL OF APPLIED MECHANICS, Vol. 25, 1958, pp. 402–406.

5 Duffy, J., "A Differential Stress-Strain Relation for the Hexagonal Close-Packed Array of Elastic Spheres," ASME JOURNAL OF APPLIED MECHANICS, Vol. 24, 1957, pp. 88–94.

6 Makhlouf, H. M., and Stewart, J. J., "Elastic Constants of Cubical-Tetradhedral and Tetragonal-Sphenoidal Arrays of Uniform Spheres," *Proc. Int. Symp. on Wave Propagation and Dynamic Properties of Earth Materials*, Univ. of New Mexico, 1967, pp. 825–837.

7 Takahashi, T., and Sato, Y., "On the Theory of Elastic Waves in Granular Substance," *Bull. Earthquake Res. Inst. (Tokyo Univ.)*, 1949, pp. 1–16.

8 Hershey, A. V., "The Elasticity of an Isotropic Aggregate of Anisotropic Cubic Crystals," ASME JOURNAL OF APPLIED MECHANICS, Vol. 21, p. 236, 1954.

9 Yanagisawa, E., "Relation Between the Shear Modulus and Void Ratio in Granular Media." *Technology Reports*, Tohoku Univ., 1978, pp. 211–220.

10 Digby, P. J., "The Effective Modulii of Porous Granular Rocks," ASME JOURNAL OF APPLIED MECHANICS, Vol. 48, 1981, pp. 803–808.

11 Christensen, R. M., *Mechanics of Composite Materials*, Wiley, New York, 1979.

12 Garg, S. K., Svalbonas, V., and Gurtman, G. A., *Analysis of Structural Composite Materials*, Marcel Dekker, New York, 1973.

13 Smith, W. O., et al., "Packing of Homogeneous Spheres," *Phys. Rev.*, Vol. 34, 1929, pp. 1271–1274.

14 Bernal, J. D., and Mason, J., "Coordination of Randomly Packed Spheres," *Nature*, Vol. 188, 1960, pp. 910–911.

15 Arakaw, M., and Nishino, M., *Zairyo*, Vol. 22, 1973, p. 658.

16 Voight, W., *Lehrbuck der Kristellphysik*, Teubner, Berlin, 1910.

17 Reuss, A., "Calculation of Flow Limits of Mixed Crystals on the Basis of the Plasticity of Single Crystals," *Z. Angew. Math. Mech.*, Vol. 9, 1929, p. 49.

18 Hashin, Z., and Shtrikman, S., "On Some Variational Principles in Anisotropic and Nonhomogeneous Elasticity," *J. Mech. Phys. Solids*, Vol. 10, 1962, pp. 343–352.

19 Hashin, Z., and Shtrikman, S., "A Variational Approach to the Theory of the Elastic Behavior of Polycrystals," *J. Mech. Phys. Solids*, Vol. 10, 1962, pp. 343–352.

20 Hashin, Z., and Shtrikman, S., "A Variational Approach to the Theory of Elastic Behavior of Multiphase Materials," *J. Mech. Phys. Solids*, Vol. 11, 1963, pp. 127–140.

21 Hashin, Z., "Theory of Mechanical Behavior of Heterogeneous Media," *Appl. Mech. Rev.*, Vol. 17, 1964. pp. 1–9.

22 Wu, C.-T. D., and McCullough, R. L., "Constitutive Relationships for Heterogeneous Materials," *Developments in Composite Materials-1*, Holister, G. S., ed., Applied Science, London, 1977, pp. 119–188.

23 Lade, P. V., and Duncan, J. M., "Elastoplastic Stress-Strain Theory for Cohesionless Soil," *Journal of Geotechnical Eng. Div. of ASCE*, Oct. 1975, pp. 1037–1053.

24 Paul. B., "Prediction of Elastic Constants for Multiphase Materials," *Trans. Metallurgical Soc. of AIME*, Vol. 218, pp. 36–41.

25 Davis, R. A., and Deresiewicz, H., "A Discrete Probablistic Model for Mechanical Response of a Granular Medium," *Acta Mechanics*, Vol. 27, 1977, pp. 69–89.

26 Nur, A., and Byerlee, J. D., "An Exact Effective Stress Law for Elastic Deformation of Rock and Fluids," *J. Geophys. Res*, Vol. 76, 1971, pp. 6414–6419.

27 Marlowe, M. D., and Wilder, D. R., "Elasticity and Internal Friction of Polycrystalline Yttrium Oxide," *J. Amer. Cer. Soc.*, Vol. 48, 1965, pp. 227–233.

28 Gatto, F., "Influence of Small Cavities on Velocity of Sound in Metals," *Alluminio*, Vol. 19, pp. 19–26.

29 George, T. L., "A Model for the Mechanical Behavior of Irradiated Mixed Carbide Sphere Pac Fuel," Ph.D. Thesis, Oregon State University, Corvallis, Oregon, 1982.

Downloaded 02 May 2010 to 171.66.16.54. Redistribution subject to ASME license or copyright; see http://www.asme.org/terms/Terms_Use.cfm

M. Fichman

D. Pnueli
Mem. ASME

Faculty of Mechanical Engineering,
Technion-Israel Institute of Technology,
Haifa, Israel

Sufficient Conditions for Small Particles to Hold Together Because of Adhesion Forces

An elastic-plastic collision between two small particles or between a small one and a larger one is considered. Adhesion forces are included. It is found that the elastic limit of the particles material is quite frequently reached, sometimes even without initial velocity at all. Conditions for the particles not to have enough energy to overcome the adhesion forces are formulated, and used to calculate conditions for the particles to stick together.

Introduction

The problem of whether two small particles that come into contact do stick together is of major importance in several engineering fields. An example of such a field is the filtration of particles from hot gas in a gas turbine, just after combustion and before the gas enters the turbine. The filter may be moving sand, chosen for its ability to withstand high temperaures. The hot dirty sand is then cleaned and cooled by clean air, which becomes hot and particle-laden. A nice thermodynamic possibility is to use this hot air for combustion. This idea works only if the returned particles stick together, increase in size, and eventually drop out of the gas.

A small variation of this problem is that of a small particle sticking to a collector, which is a basic problem in all filtration theories. Inspection of the literature on filtration reveals that very little has been done to solve this problem and that investigators assume the answer rather than tackle the problem. The popular assumption in filtration theories is that particles that come into contact stick together.

This investigation develops conditions for particles to stick to one another because of adhesion forces. The capture mechanism includes plastic work which dissipates the particle kinetic energy. The results are considered somewhat pessimistic (if capture is desired) because viscous dissipation was neglected.

After this paper was submitted for publication a similar treatment of the adhesion of particles undergoing an elastic-plastic impact with a surface appeared in print [8]. The model used here is more general than that in reference [8], which neglects yield stresses at the circumference of the contact area. Still, in principle the model used in this paper is similar to that used in [8]. The motivations for the investigations, however, seem to be quite different. Rogers and Reed [8] are presumably interested in surface coating by particles (though they remark, quite correctly, that their results can be extended to the collision between small particles) this investigation emphasizes the collision between small particles, though it suggests an application for filtration, where a collector in many cases is a "flat surface" from the point of view of the small particle.

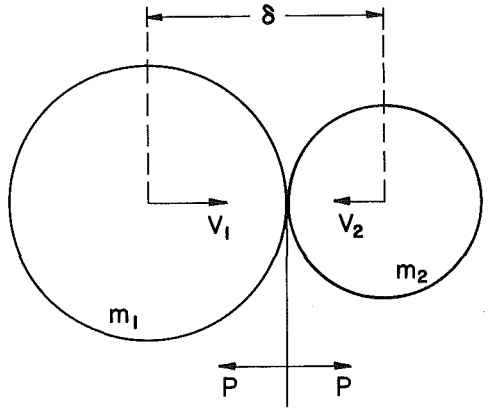


Fig. 1 Elastic collision between two spheres

The numerical results of [8] deal with materials and velocities typical to surface coating, while here a zero speed attachment between particles is emphasized, which might by itself be of some interest.

Finally it is noted that [8] uses support for its experimental results by those of [9], which also considers surface coating.

Analysis

(a) Elastic and Plastic Considerations for Colliding Spheres When Adhesion Forces are Present. Consider the two colliding spheres in Fig. 1. The total compression force acting between the spheres is P, and their equations of motion are

$$m_1 \frac{dV_1}{dt} = -P \qquad m_2 \frac{dV_2}{dt} = -P \tag{1}$$

The approach distance between the spheres centers, after contact has been made, is δ, hence

Contributed by the Applied Mechanics Divison for publication in the JOURNAL OF APPLIED MECHANICS.

Discussion on this paper should be addressed to the Editorial Department, ASME, United Engineering Center, 345 East 47th Street, New York, N.Y. 10077, and will be accepted until two months after final publication of the paper itself in the JOURNAL OF APPLIED MECHANICS. Manuscript received by ASME Applied Mechanics Division, July, 1983; final revision, June, 1984.

Copyright © 1985 by ASME
Downloaded 02 May 2010 to 171.66.16.54. Redistribution subject to ASME license or copyright; see http://www.asme.org/terms/Terms_Use.cfm

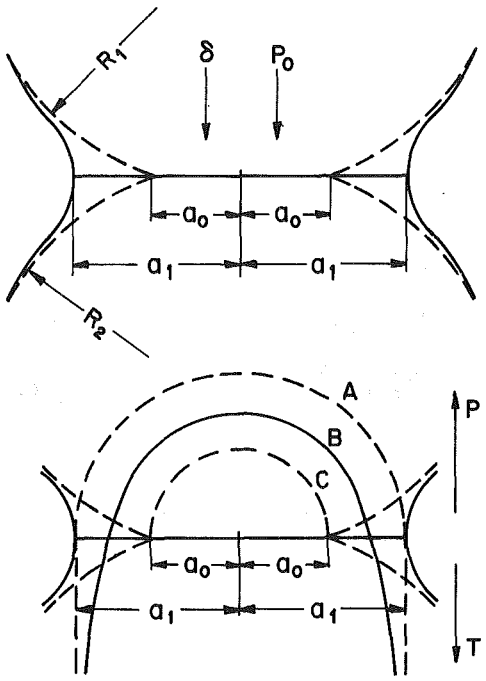


Fig. 2 Contact circles between two spheres. a_1: in presence of surface forces; A: projected circle; a_0: in absence of surface forces; C: projected circle; and B: schematic pressure distribution

$$\frac{d\delta}{dt} = \dot{\delta} = V_1 + V_2 \tag{2}$$

Equations (1) and (2) yield

$$M\frac{d^2\delta}{dt^2} = M\ddot{\delta} = -P(\delta) \tag{3}$$

where

$$M = m_1 m_2/(m_1 + m_2)$$

Equation (3) can also be put as

$$\tfrac{1}{2}Md(\dot{\delta}^2) = -P(\delta)\,d\delta \tag{4}$$

with the solution

$$\tfrac{1}{2}M(\dot{\delta}^2 - V^2) = -\int_0^{\delta} P(\delta)\,d\delta \tag{5}$$

where $V = V_1 + V_2$, the relative approach velocity before contact. The right-hand side of equation (5) is the deformation work, which increases as $\dot{\delta}$ decreases.

Consider a special case, where V is just enough to cause the elastic limit of the smaller sphere to be reached when $\dot{\delta} = 0$. Denote the corresponding V and δ by V_{el}, δ_{el} respectively, and then

$$\tfrac{1}{2}MV_{el}^2 = \int_0^{\delta_{el}} P(\delta)\,d\delta \tag{6}$$

Let the radius of the circular contact area between the two spheres, in the absence of adhesion forces be a_0, Fig. 2. The stress distribution for this case p_0 is given by the Hertz theory, and requires a total force of P_0. In the presence of adhesion forces the radius of the contact area is a_1, and the stress distribution is p_{10}, curve B in Fig. 2. The relations between a_1 and p_{10} are given by the Johnson, Kendal, and Roberts theory (JKR theory) [1], for statically pressed spheres. To apply the JKR theory to colliding particles we assume that the stress-strain relations for the static theory still apply during the dynamic collision.

From the JKR theory

$$P_0 = \frac{3}{2}K\delta a_1 \tag{7}$$

where

$$K = 4/[3\pi(k_1 + K_2)], \quad k_i = \frac{1-\nu_i}{\pi E_i} \qquad i = 1,2$$

and

$$a_1^3 = \frac{R}{K}\left(P_0 + 3\gamma\pi R + \sqrt{6\gamma\pi R P_0 + (3\gamma\pi R)^2}\right) \tag{8}$$

where $R = R_1R_2/(R_1 + R_2)$, R_1 and R_2 are the radii of the spheres, and γ is the surface free energy.
Equations (7) and (8) yield

$$\delta = \frac{2}{3R}a_1^2 \pm \frac{2}{3}\sqrt{\frac{6\gamma\pi}{K}}\,a_1^{1/2} \tag{9}$$

and substitution into equation (7)

$$P_0 = \frac{K}{R}a_1^3 \pm \sqrt{6\gamma\pi K}\,a_1^{3/2} \tag{10}$$

At constant a_1 an increase in the surface free energy makes the required force P_0 smaller, and therefore the minus sign is selected in equation (10).

From equation (9)

$$d\delta = \left(\frac{4}{3R}a_1 - \frac{1}{3}\sqrt{\frac{6\gamma\pi}{K}}\,a_1^{-1/2}\right)da, \tag{11}$$

which together with equations (10) and (6) yield

$$\epsilon_{KIN} = \tfrac{1}{2}MV_{El}^2 = \frac{4K}{15R^2}a_{1_{el}}^5 - \frac{0}{21R}a_{1_{el}}^{1/2} + \gamma\pi a_{1_{el}}^2 \tag{12}$$

Equation (12) connects $a_{1_{el}}$ with V_{el}.

p_{10} is the stress in the presence of adhesive forces and a compressive force P_0 (which alone would result in a contact radius a_0) Let P_1 be a compressive force that alone would result in a contact radius a_1, with a stress distribution p_1, according to Hertz theory. Define p' by

$$p_{10} = p_1 - p' \tag{13}$$

where p_1 is the stress according to Hertz theory for the contact radius a_1 hence given by [2]:

$$p_1 = \frac{3P_1}{2\pi a^2}\sqrt{1 - r^2/a_1^2} \tag{14}$$

By using JKR theory [3]:

$$p' = \frac{P'}{2\pi a_1^2} \cdot \frac{1}{\sqrt{1 - \dfrac{r^2}{a_1^2}}} \tag{15}$$

The maximum of p_{10} is in the center of the contact area when $a_1 = a_{1_{el}}$:

$$(p_{10})_{\max} = (3P_1 - P')/2\ a_{el}^2 \tag{16}$$

The total load $\mathbf{P}'$ is calculated as in equation (13)

$$P' = P_1 - P_0 = \sqrt{6\gamma\pi K}\,a_1^{3/2} \tag{17}$$

From Hertz theory

$$P_1 = a_1^3\frac{K}{R} \tag{18}$$

and equations (16)–(18) yield

$$\pi a_{1_{el}}^2 p_* = a_{1_{el}}^3\frac{K}{R} + \tfrac{1}{2}P_0 \tag{19}$$

where $P_* = (P_{10})_{\max}$ when the elastic limit of the material is reached. Equations (17) and (19) now yield

$$a_{1_{el}}^{3/2} \cdot \frac{3K}{2R} - a_{1_{el}}^{1/2}\,\pi p_* - \tfrac{1}{2}\sqrt{6\gamma\pi K} = 0 \tag{20}$$

Equation (20) is algebraic, of the third order in $a_{1_{el}}^{1/2}$. If there are three real roots $a_{1_{el}}$ is selected to be greater than that for the case of no adhesion ($\gamma = 0$).

Once $a_{1_{el}}$ is known, V_{el} can be obtained from equation (12).

Numerical Example. As an illustration of the calculation, some typical values are chosen: γ = 800 erg/cm^2 [4], p_* =

Downloaded 02 May 2010 to 171.66.16.54. Redistribution subject to ASME license or copyright; see http://www.asme.org/terms/Terms_Use.cfm

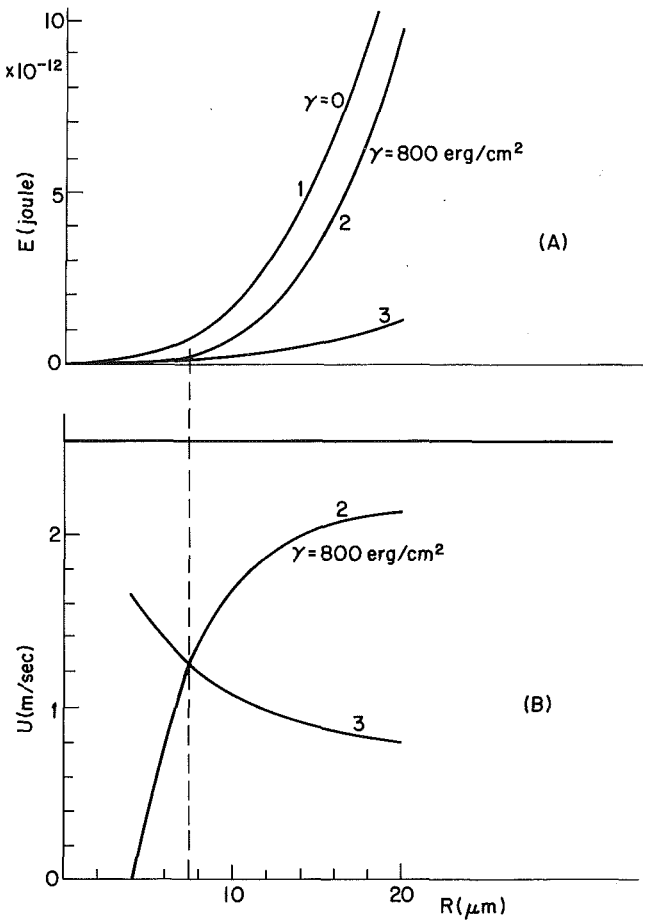


Fig. 3 (A) Critical kinetic energy; and (B) critical velocity. Curves 1 and 2: γ = surface energy; curve 3: minimal plastic work.

10^6 gf/cm^2 [5], $E = 0.8 \times 10^7$ N/m^2, $K = 3/2\pi(k_1 + k_2) = 3/4\pi k = 0.75 \times 10^9$ N/m^2, $\rho = 1$ gr/cm^3. Velocities V_{el} are calculated as functions of particle size, and shown in Fig 3. As seen in Fig. 3, the elastic limit is reached for certain particle sizes, even with no initial velocity at all, but just because of adhesion. Indeed, adhesion forces play a dominant role in the collision mechanics of particles.

Once the elastic limit has been reached, any excess kinetic energy is converted into heat by plastic work. Thus if a particle with just V_{el} stickes to another then that same particle will stick for all $V < V_{el}$. Thus all kinetic energies of

$$\epsilon_{KIN} \leqq \epsilon_{el} = \tfrac{1}{2}\, MV_{el}^2, \tag{21}$$

represent the situation of particles sticking together.

Curve 3 in Fig. 3 gives the total plastic energy which must be dissipated to ensure capture, as a function of the particle size.

(b) Conditions for Capture of Particles. In the absence of any dissipative mechanism mechanical energy is conserved and the particles cannot stick to each other. Dahneke [6, 7] takes into account several possible mechanisms for dissipation: plastic deformation, internal friction, radiation of surface waves. In considering plastic deformations we note that very small velocities, and sometimes even no velocity at all, suffice to reach the elastic limit at the center of the contact area. Moreover, according to the JKR theory the theoretical distribution of surface stress reaches infinity at the circumference of the contact circle, i.e., the elastic limit is always reached there. The plastic dissipation there is important, and when the original kinetic energy of the particles is less than this plastic work the particles stick together.

Let the plastic work in the center of the contact circle be ϵ_{p1_1} and that the circumference of the circle be ϵ_{p1_2}. The condition for particle capture becomes

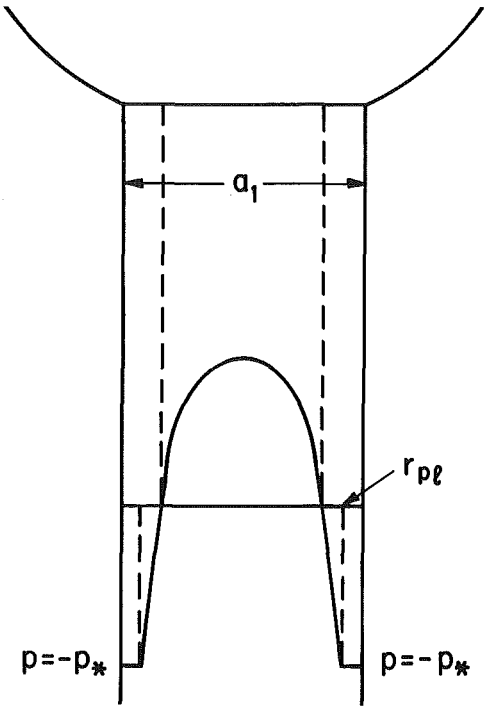


Fig. 4 Stress distribution at contact area

$$\epsilon_{KIN} \leqq \epsilon_{p1_2} + H(\epsilon_{KIN} - \epsilon_{el}) + \epsilon_{p1_1} \tag{22}$$

where the Heavyside function H is zero for negative argument and equals one for positive $(\epsilon_{kin} - \epsilon_{el})$. To obtain ϵ_{p1_2} consider Fig. 4 where the stress distribution over the contact circle is schematically shown, with the center not reaching the elastic limit. Plastic stress is reached in the region $r_{p1} \leqq r \leqq a_1$, and a_1 is taken from the JKR theory. The plastic work there is

$$d\epsilon_{p1_2} = d\delta \int_{r_{p1}}^{a_1} p_* 2\pi r dr \tag{23}$$

$$\epsilon_{p1_2} = \int_0^{\delta_{\max} d\delta} \int_{r_{p1}}^{a_1} p_* 2\pi r dr \tag{24}$$

During plastic deformation p_* is constant, hence,

$$\int_{r_{p1}}^{a} p_* 2\pi r dr = \pi p_* (a_1^2 - r_{p1}^2) \tag{25}$$

and r_{p1} is obtained from the condition for $r = r_{p1}$

$$p_{10} = -p_*.$$

This condition, together with equations (13)–(15) and (17) yield

$$-p_* = \frac{3P_1\sqrt{a_1^2 - r_{p1}^2}}{2\pi a_1^3} - \frac{P_1 - P_0}{2\pi a_1 \sqrt{a_1^2 - r_{p1}^2}} \tag{26}$$

Equations (10) and (18) yield

$$P_1 - P_0 = \sqrt{6\gamma\pi K}\; a_1^{3/2} \tag{27}$$

and with

$$x = \sqrt{a_1^2 - r_{p1}^2} \tag{28}$$

Equations (26)–(28) yield

$$x^2 \cdot \frac{3K}{R} + 2\pi p_* \cdot x - \sqrt{6\gamma\pi K a_1} = 0 \tag{29}$$

with

Downloaded 02 May 2010 to 171.66.16.54. Redistribution subject to ASME license or copyright; see http://www.asme.org/terms/Terms_Use.cfm

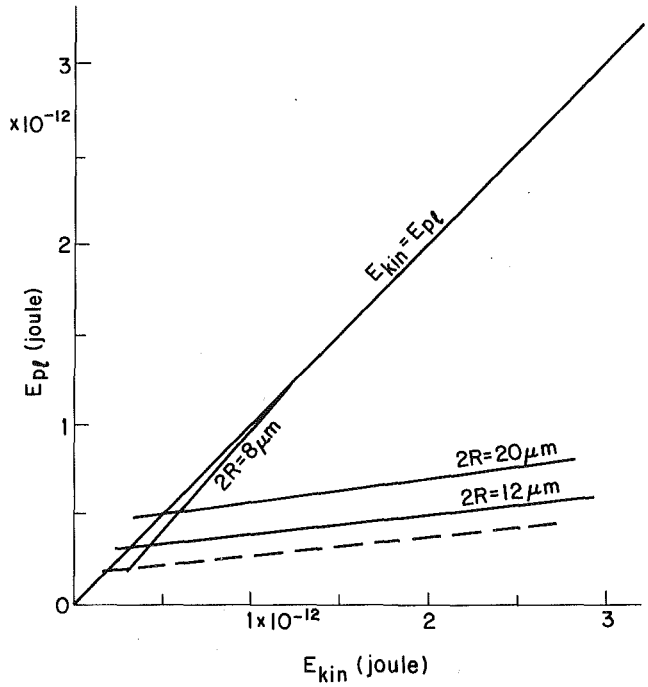


Fig. 5 Plastic work versus kinetic energy

$$A = \frac{\pi R}{3K} p_*, \quad B = \frac{R}{3K}\sqrt{6\gamma\pi K a_1} \tag{30}$$

Equation (29) is solved

$$x = -A + \sqrt{A^2 + B a_1^{1/2}} \tag{31}$$

where the sign is chosen to make $x = 0$ for $\gamma = 0$, $B = 0$.

Equations (31),(25), (11), and (24) yield:

$$\epsilon_{p1_2} = \pi p_* \int_0^{\delta_{\max}} (2A^2 + B a_1^{1/2} - 2A\sqrt{A^2 + B a_1^{1/2}}) \left(\frac{4}{3R} a_1 - \frac{1}{3}\sqrt{\frac{6\gamma\pi}{K}} a^{-1/2} \right)$$

$$= \pi p_* \left[\frac{4}{3}\frac{A^2}{R} a_{1\max}^2 - \frac{4}{3} A^2 \sqrt{\frac{6\gamma\pi}{K}} a_{1\max}^{1/2} + \frac{8}{15R} B \cdot a_{1\max}^{5/2} - \right.$$

$$\left. - \frac{B}{3}\sqrt{\frac{6\gamma\pi}{K}} a_{1_{\max}} - \frac{8}{3}\frac{A}{R} I_1 + \frac{2}{3} A \sqrt{\frac{6\gamma\pi}{K}} I_2 \right] \tag{32}$$

where

$$I_1 = \frac{2A^9}{B^4}\left[\frac{2}{9}\left(1 + \frac{B}{A^2}\sqrt{a_{1_{\max}}}\right)^{9/2} - \frac{6}{7}\left(1 + \frac{B}{A^2}\sqrt{a_{1\max}}\right)^{7/2} + \right.$$

$$\left. + \frac{6}{5}\left(1 + \frac{B}{A^2}\sqrt{a_{1\max}}\right)^{5/2} - \frac{2}{3}\left(1 + \frac{B}{A^2}\sqrt{a_{1_{\max}}}\right)^{3/2} + \frac{32}{315} \right]$$

$$I_2 = \frac{4A^3}{3B}\left[\left(1 - \frac{B}{A^2}\sqrt{a_{1_{\max}}}\right)^{3/2} - 1 \right]$$

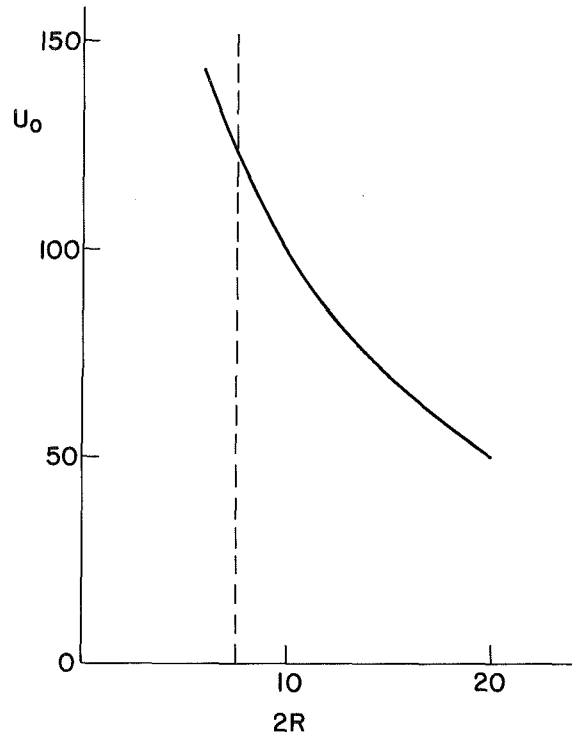


Fig. 6 Critical velocity versus particle size

Thus ϵ_{p1_2}, equation (32), can now be used in equation (22), the condition for the capture of the particle.

Results, Related to Numerical Example

The calculations of the numerical example is repeated for various particle radii, and the results are shown in Fig. 5. There is a linear relation between the energies, as can also be obtained from equations (12) and (32) by expansion in powers of δa_1.

Figure 6 shows the collision velocity U_0 necessary to satisfy

$$\epsilon_{KIN} = \epsilon_{p1}(R) = \epsilon_0(R) \tag{33}$$

For R to the left of this curves the particles stick together, while for R to the right of the curve they do not.

Line 3 in Fig. 3 gives the energy ϵ_{p1} dependence on the particle radius. Where lines 2 and 3 meet

$$\epsilon_{KIN} = \epsilon_{p1} = \epsilon_0$$

For smaller particles the critical kinetic energy increases and ϵ_0 increases. Below R_0 the particles always stick, whatever their kinetic energy might be.

References

1 Johnson, K. A., Kendall, K., and Roberts, A. D., "Surface Energy and the Contact of Elastic Solids," *Proc. Roy. Soc.*, Series A, Vol. 324, 1971, pp. 301-313.

2 Timoshenko, S. P., and Goodier, J. N., *Theory of Elasticity*, McGraw-Hill, New York, 1970.

3 Johnson, K. L., "A Note on the Adhesion of Elastic Solids," *Brit. J. Appl. Phys.*, Vol. 9, 1958, pp. 199-200.

4 Zimon, A. D., *Adhesion of Dust and Powder*, Consultants Bureau, New York, 1982.

5 Bitter, J. G. A., "A Study of Erosion Phenomena, Part I," *Wear*, Vol. 6, 1963, pp. 5-21.

6 Dahneke, B., "The Capture of Aerosol Particles by Surfaces," *J. Colloid Interface Sci.*, Vol. 37, 1971, pp. 342-353.

7 Dahneke, B., "The Influence of Flattening on the Adhesion of Particles," *J. Colloid Interface Sci.*, Vol. 40, 1972, pp. 1-13.

8 Rogers, L. N., and Reed, J., "The Adhesion of Particles Undergoing an Elastic-Plastic Impact With a Surface," *J. Phys.*, Series D., Inst. Phys., London, Vol. 17, 1984, pp. 677-689.

9 Brenner, S. S., Wriedt, H. A., and Oriani, R. A., "Impact Adhesion of Iron at Elevated Temperatures," *Wear*, Vol. 68, 1981, pp. 169-190.

Downloaded 02 May 2010 to 171.66.16.54. Redistribution subject to ASME license or copyright; see http://www.asme.org/terms/Terms_Use.cfm

C. Ruiz
Department of Engineering Science,
Oxford University,
Parks Rd.,
Oxford, England OX1 3PJ

D. Post
Mem. ASME

R. Czarnek
Department of Engineering Science
and Mechanics,
Virginia Polytechnic Institute
and State University,
Blacksburg, Va. 24061

Moiré Interferometric Study of Dovetail Joints

High sensitivity Moiré interferometry has been applied to the study of dovetail joints as found in turbomachinery. Without physical measurements, the true contact conditions cannot be known. The benefits to be gained when coupled with a finite element stress analysis are discussed. It is concluded that Moiré interferometry is of great potential in the study of fixed mechanical joints.

Introduction

Fixed mechanical joints, in which two parts are keyed-in together, present a challenging problem because of the difficulty of modeling mathematically the true contact conditions. Away from the contact surface, the state of stress can be determined by conventional methods, e.g., photoelasticity or finite elements, but the stresses and relative displacements around that surface, known to seriously affect the fretting and fatigue crack initiation, require special attention.

A recent investigation [1, 2] into the fatigue strength of dovetail joints, of the type normally used to fix blades to disks in turbomachinery, has revealed a clear relationship between the fatigue life and a fretting damage parameter k, defined as

$$k = \sigma\tau\delta \tag{1}$$

where σ is the stress acting on a plane normal to the contact surface, τ is the shear stress between the two surfaces in contact, and δ is the relative slip. A finite element program has been written [3] to calculate k for any given coefficient of friction, assumed to be constant. The program looks for contact – when contact stresses are compressive – and separation between the two mating surfaces. When there is contact, it looks for nodes that stick – where the shear stress is less than the friction coefficient times the compressive contact stress – or slip, in which case the shear stres is limited by that product. Verification of the results is only indirect, by comparison to the overall stress field obtained by photoelasticity and to fatigue test data, interpreted both in terms of life and of the fretting damage characterized by measuring the surface roughness at various times during the test.

The main limitation of the finite element analysis is the need to assume a value of the coefficient of friction, which remains fixed throughout the iterative procedure followed to calculate stresses and displacements and constant over the whole contact surface. Since friction strongly affects the behavior of the joint, it is necessary to repeat the analysis for several values or to deduce the correct value from the fatigue test [2]. Furthermore, the program is only an idealized model, whose accuracy depends on the importance of factors such as surface irregularities, machining imperfections, eccentricity of loading, etc., requiring experimental guidance and validation. Besides this function, experimental work also helps to ascertain the nonlinear load-displacement of the joint upon load cycling, of particular importance for the study of vibration damping. The most valuable information to be obtained from an experiment would be the amount of relative slip and separation at the contact surface since this can be incorporated into the numerical analysis, resolving the uncertainties described in the foregoing.

A method used to measure the relative displacement between two surfaces is traditional Moiré [4] in which two bar-and-space gratings form fringes by mechanical obstruction of the light. The displacement u corresponding to a fringe of order N is given by

$$u = \frac{N}{f} \tag{2}$$

where f is the frequency (lines/mm) of the fixed reference grating. Since the grating frequency is normally limited to about 40 lines/mm, the sensitivity of the traditional method is 25 μm, of the same order as the maximum displacement to be measured in the dovetail joint. The traditional method is thus too coarse for this particular application. Recently, Post [5] has extended the Moire method into the high-sensitivity domain, combining a technique for the production and replication of high frequency gratings with interferometric fringe multiplication, to achieve sensitivities of 0.417 μm/fringe or better. This level, corresponding to a traditional Moiré grating of 2400 lines/mm, is adequate for the investigation reported here.

Contributed by the Applied Mechanics Division for publication in the JOURNAL OF APPLIED MECHANICS.

Discussion on this paper should be addressed to the Editorial Department, ASME, United Engineering Center, 345 East 47th Street, New York, N.Y. 10017, and will be accepted until two months after final publication of the paper itself in the JOURNAL OF APPLIED MECHANICS. Manuscript received by ASME Applied Mechanics Division, January, 1984.

Copyright © 1985 by ASME
Downloaded 02 May 2010 to 171.66.16.54. Redistribution subject to ASME license or copyright; see http://www.asme.org/terms/Terms_Use.cfm

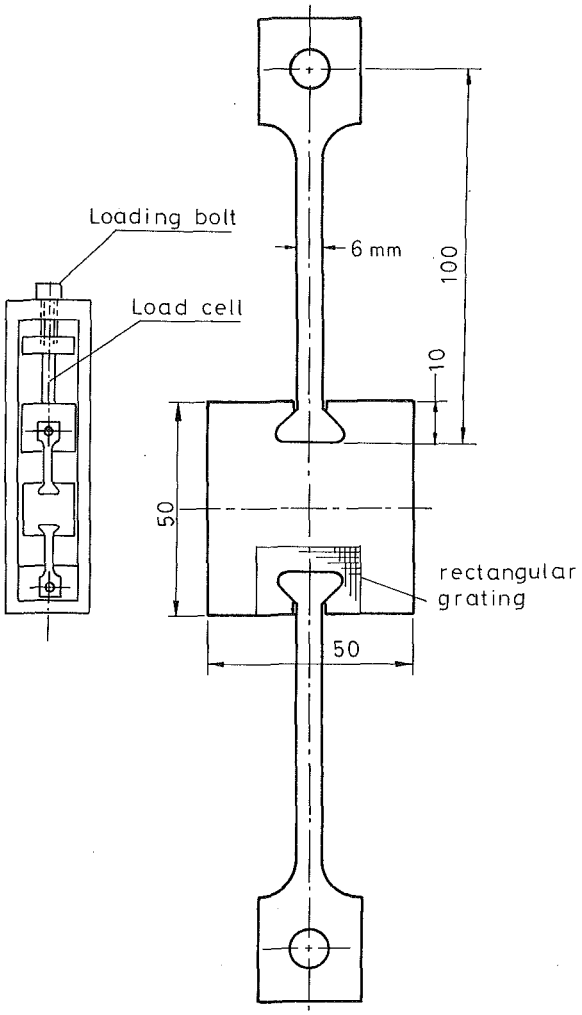


Fig. 1 General arrangement of test piece

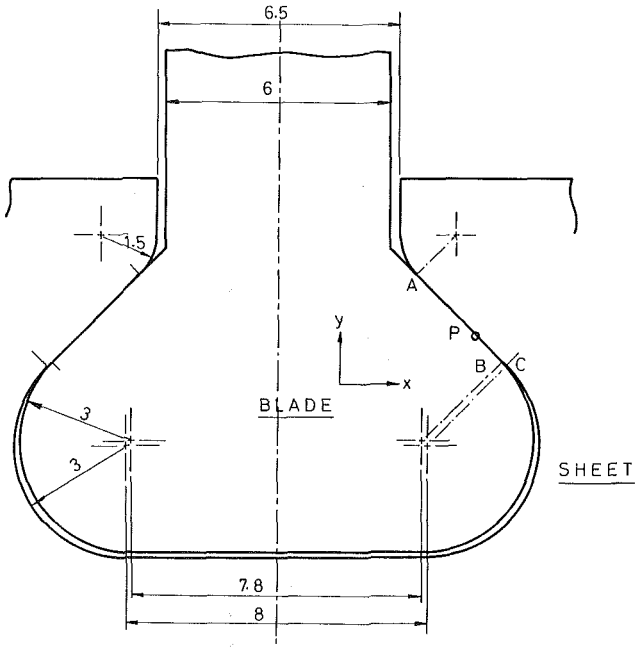


Fig. 2 Theoretical profile of dovetail joint

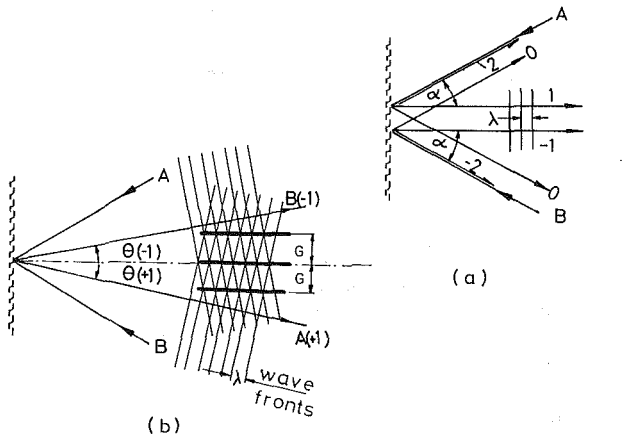


Fig. 3 Principle of the experiment: (*a*) incident beams and diffracted beams of orders 0, 1, 2, −1 and −2, (*b*) interference between diffracted beams of orders 1 and −1 for a small change in grating frequency; angles $\theta(\pm 1)$ are greatly exaggerated

Description of the Experiment

Test Piece. Figure 1 shows a general arrangement of the test piece and loading rig. The test piece consisted of a 3 mm-thick sheet with two blades of the same thickness dovetailed into it. Both faces were ground. The material used was bright carbon steel with a tensile strength of 600 MPa. The dovetail was finished by form grinding, to the profile shown in Fig. 2, leaving all edges sharp. The test piece was assembled and held flat in the frame and loaded through 3/8 in. (9.5 mm) diameter pins.

After assembly, the test piece was thoroughly degreased and loaded repeatedly between 1 kN and 4.5 kN. It was then preloaded to 1.33 kN. The grating was then replicated onto it following the technique described in reference [5], over the whole of the dovetail. To facilitate the interpretation of the fringe pattern, as will be discussed later, two "bridges" consisting of thin flexible plastic arches were fixed between blade and sheet – as shown in Fig. 5. Like the grating itself, the bridges were too flexible to make any significant contribution to the stiffness of the joint.

Principle of Operation. Consider a diffraction grating of frequency F fixed to the surface of a deformable solid and illuminated by a collimated beam of coherent light of wavelength λ. If the incident angle is ϕ, the direction of the diffracted beam of order m is given by

$$\sin \theta_m = m\lambda F + \sin \phi \tag{3}$$

For a beam A (Fig. 3(*a*)), $\phi = -\alpha$ and choosing the angle of incidence and the grating frequency so as to satisfy the equation

$$\lambda F = \sin \alpha \tag{4}$$

the direction of the diffracted beams of orders 0, 1, and 2 are as shown in the figure. A beam B, for which $\phi = \alpha$ gives the diffracted beams of orders 0, −1, and −2 also shown in Fig. 3(*a*), so that along the normal to the grating, the two diffracted beams of orders +1 and −1 produced by the incident beams A and B, respectively, are perfectly matched in direction of emergence. Interference of these two coherent-beams results in a field of uniform intensity and no gradient of interference fringes is seen.

If the grating frequency is decreased, for example by applying a uniform strain ϵ, the diffracted beams $A(+1)$ and $B(-1)$ are no longer directed along the normal to the grating. From equations (3) and (4),

$$\sin \theta(+1) = \lambda F' - \sin\alpha = \lambda F(1-\epsilon) - \sin\alpha = -\lambda F\epsilon \tag{5}$$

for A, and

$$\sin \theta(-1) = -\lambda F' + \sin\alpha = -\lambda F(1-\epsilon) + \sin\alpha = \lambda F\epsilon \tag{6}$$

for B. The two diffracted beams now produce interference fringes, as shown in Fig. 3(*b*) with a pitch

Downloaded 02 May 2010 to 171.66.16.54. Redistribution subject to ASME license or copyright; see http://www.asme.org/terms/Terms_Use.cfm

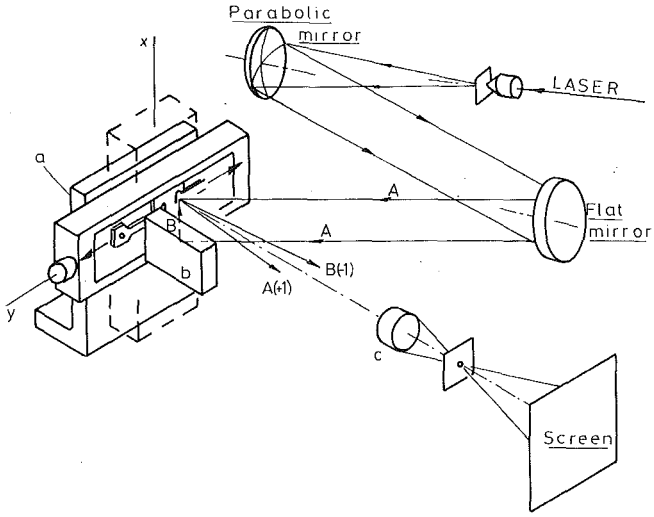


Fig. 4 Optical arrangement showing loading rig in rotatable mount (*a*), flat mirror (*b*), and photographic lens (*c*)

$$G = \left(\frac{\lambda}{2}\right)\frac{1}{\lambda F\epsilon} = \frac{1}{2F\epsilon} \tag{7}$$

The relative displacement u between a pair of points, a distance G apart, on two adjacent fringes of orders N and $N+1$, will then be

$$u = \epsilon G = \frac{1}{2F} \tag{8}$$

and, in general, the inplane displacement in a direction normal to the grating line is

$$u = \frac{N}{2F} \tag{9}$$

In this investigation, $F = 1200$ lines/mm and, for the argon laser light, $\lambda = 514.5$ nm and $\alpha = 38.12$ deg.

Comparing equations (9) and (2), the scheme shows twice the sensitivity of traditional Moire´ (assuming equal frequencies of the specimen gratings), or a fringe multiplication factor of 2. Reference [5] shows that mutual interference on input beams A and B generates a virtual reference grating of frequency $f = 2F$, thus completing the analogy between Moire´ interferometry and traditional Moire´. In this work, the virtual reference grating frequency was 2400 *l*/mm and, by equation (9) or (2), sensitivity corresponds to 1/2400 mm displacement per fringe order, or 0.417 μm/fringe.

Optical Arrangement. The optical arrangement is shown in Fig. 4. A beam of collimated light from an argon laser illuminates the test piece (beam A) and, after reflection on a flat mirror forms the second incident beam B. A decolimating and photographic lens projects an image of the interference pattern produced by the two diffracted beams $A(+1)$ and $B(-1)$ on a ground glass screen or a photographic film. The use of a rectangular grating permits measurement of displacements in the x and y directions by rotating the tests piece in its loading rig by 90 deg. In the experiment, the angle of incidence was first adjusted with the test piece horizontal, i.e., for the grating lines in the x direction, to obtain a uniform intensity field at the preload level of 1.33 kN. Interference fringes appeared upon 90 deg rotation of the test piece, indicating a difference in grating frequency for the lines in the x and in the y directions. A difference of only 1 line/mm on the nominal frequency of 2400 lines/mm, from equation (7), has the same effect as 417 μ strain over the whole of the measurement area. Quite clearly, this does not affect the relative displacements but it has to be taken into consideration where it is desired to analyze the results in terms of absolute strains.

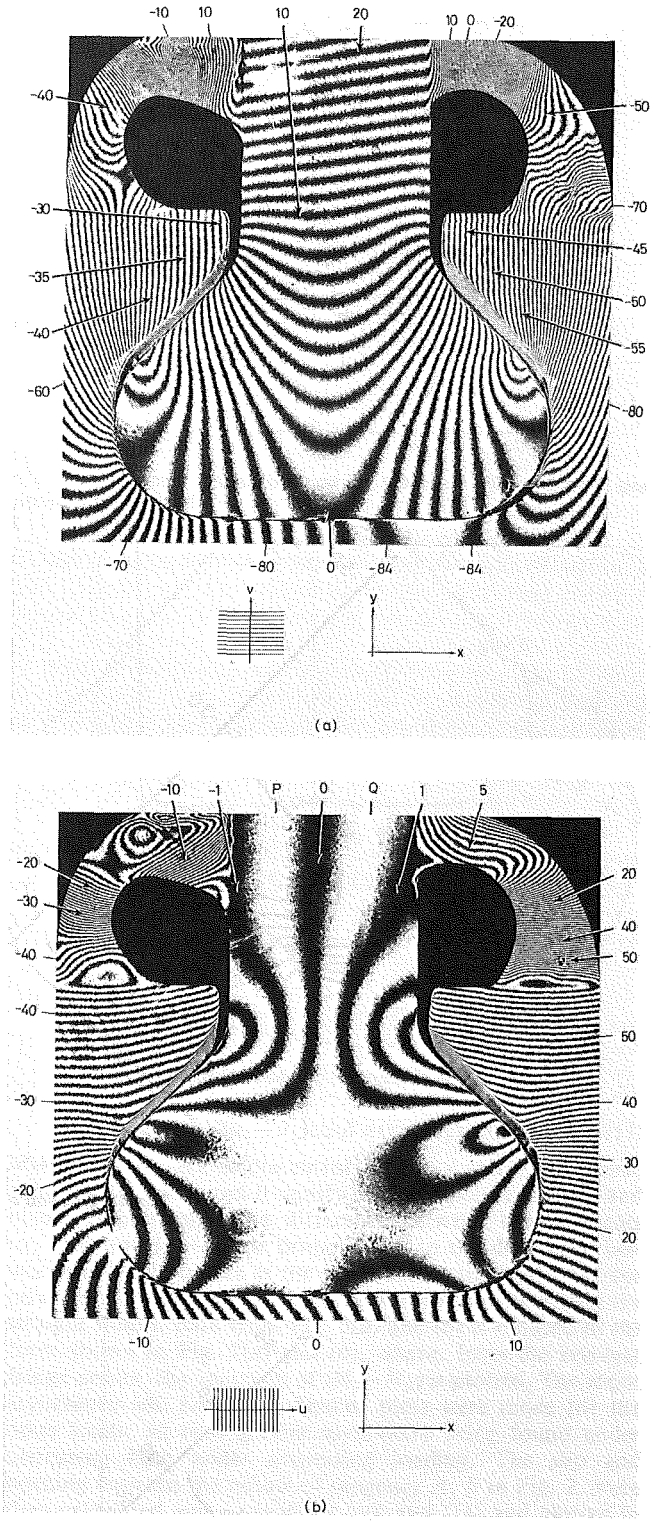
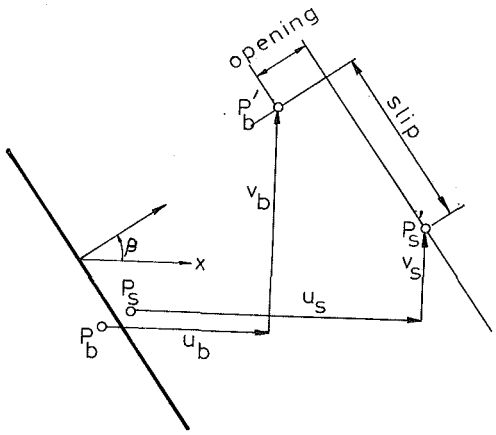


Fig. 5 Typical fringe patterns at 4.50 kN load: (*a*) displacements in *y*-direction and (*b*) displacements in *x*-direction

Test Procedure. After adjusting the mirrors for zero-fringes at 1.33 kN preload with the test piece horizontal, the load was increased to 4.50 kN and then decreased back to 1.33 kN. The fringe patterns were photographed at 2.23 kN and 3.32 kN (increasing and decreasing loads) and at 4.50 kN, with the test piece horizontal and vertical, to provide measurements of the displacements in the y and x directions, respectively. A typical set of photographs, obtained at the maximum load, is reproduced in Fig. 5.

Downloaded 02 May 2010 to 171.66.16.54. Redistribution subject to ASME license or copyright; see http://www.asme.org/terms/Terms_Use.cfm



Analysis of Photographic Data. The main objective is to determine relative tangential displacements (slip) and relative normal displacements (opening or closure) for adjacent points on the two sides of the joint boundary. Accordingly, relative fringe orders in the blade and sheet are required. The soft bridges provide the continuity necessary for relative fringe counting between the two members. The high density of fringes in the bridges (Fig. 5) indicates substantial relative motion between the blade and sheet.

Extraneous disturbances of the fringe patterns are seen along the 45 deg flanks of the joint. In this zone, the deformation of the grating did not follow the deformation of the specimen. True fidelity requires that the grating should crack along the joint boundary, which would allow the grating elements on the two sides to displace independently with the blade and sheet elements. The grating, which was a film of epoxy resin about 0.02 mm thick, did not crack, but instead delaminated near the joint boundary. Fringe orders in this disturbed zone were obtained by extrapolation, following the

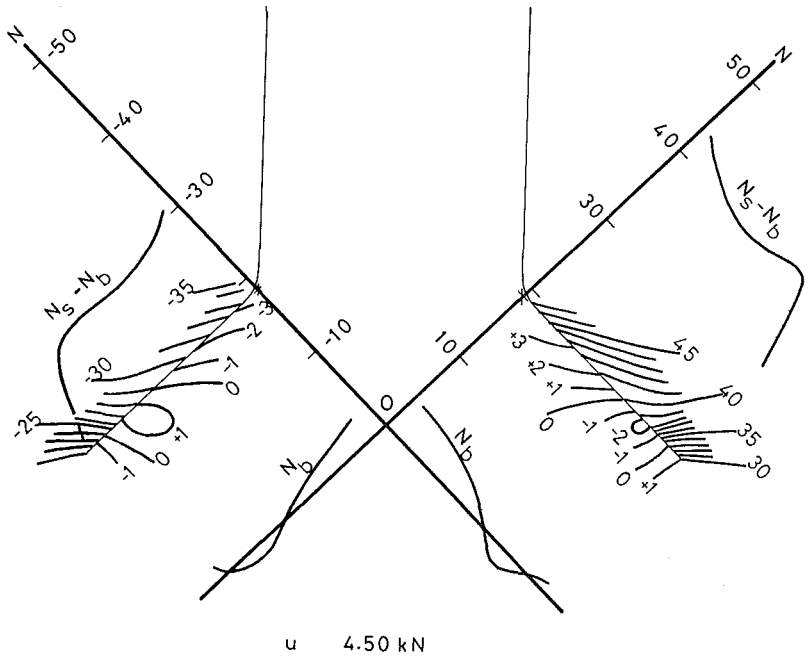


Fig. 6 Slip and opening along dovetail

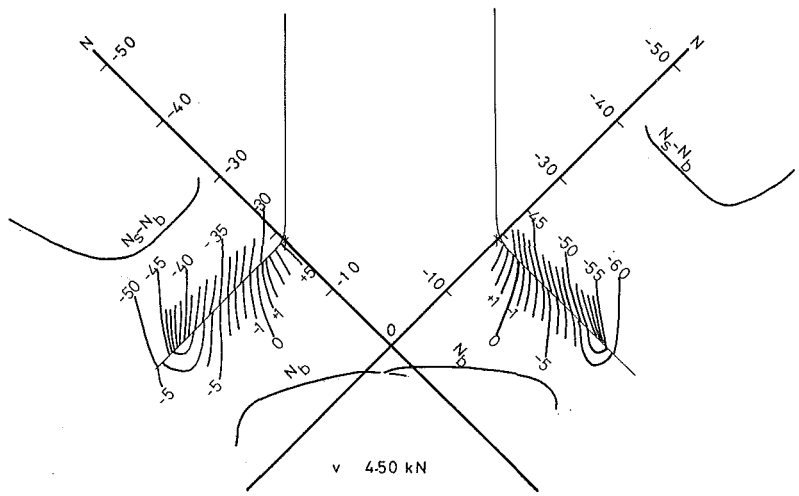


Fig. 7 Fringe order and fringe order difference along dovetail flanks: (*a*) displacements in *y*-direction and (*b*) displacements in *x*-direction

Downloaded 02 May 2010 to 171.66.16.54. Redistribution subject to ASME license or copyright; see http://www.asme.org/terms/Terms_Use.cfm

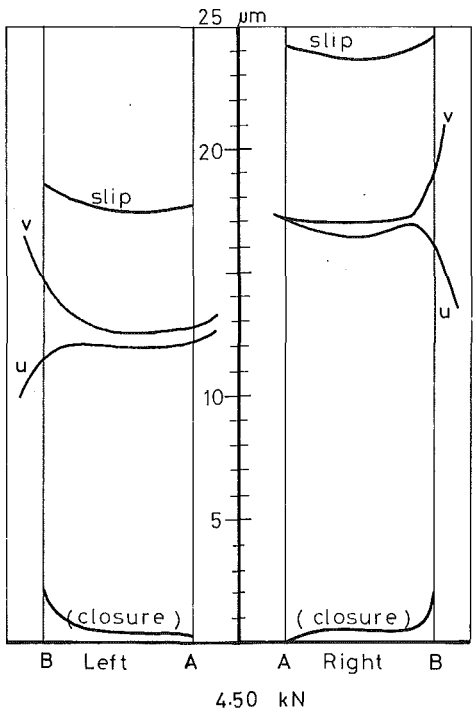


Fig. 8 Slip and opening (closure) along straight section of dovetail flanks at the maximum load

trends of fringes seen at lower load levels before the delamination had spread to the present 0.2 to 0.4 mm wide zone. Although it is not considered that extrapolation has introduced a significant error, any further work should be undertaken using a brittle, ultrathin, highly adherent grating.

Fringe orders are assigned by counting fringes from a chosen datum. Referring, for example to Fig. 5(*a*), the central fringe at the bottom of the blade is taken as the datum. Since the blade extends under tension, fringe orders along the central section will be positive and increasing away from 0. On the blade stem the separation between fringes is almost uniform and equal to 0.50 mm (on the actual test piece). This corresponds to a tensile strain, from equation (7), equal to 830 μ strain. The nominal stress increment between 4.50 kN load and the preload level of 1.33 kN is 176 MPa, which would produce a tensile strain of 838 μ strain for a Young's modulus of 210 GPa, in agreement with the experimental result. Orders are assigned to the fringes along the two bridges, counting in clockwise and anticlockwise directions around the dovetail, in the sheet, and in the two "ears" of the blade, checking that both counts are reconciled. Use of the two bridges therefore ensures that no error is made in counting and that there is no ambiguity in the fringe ordering. This is particularly important since, as is apparent from the pattern, the deformation is not perfectly symmetrical.

The slight mismatch between the grating frequencies in the x and in the y directions means that the pattern of Fig. 5(*b*) cannot be directly interpreted in terms of strain. Here, the two bridges become even more useful. Choosing as a datum the fringe shown in the blade and observing that the dovetail ears open up under load so that u is positive to the right and negative to the left of the datum, fringe orders are assigned as before. The original mismatch was equivalent to a fictitious tensile strain over the whole field, which when added to the Poisson's contraction gives fringes of order 1/2 and $-1/2$ at P and Q on the blade stem.

Considering a pair of adjacent points P_b and P_s as blade and sheet, respectively, Fig. 6, the slip of P_b with respect to P_s, measured along the flank of the dovetail, is,

$$\text{Slip} = (u_s - u_b)\sin\beta - (v_s - v_b)\cos\beta \qquad (10)$$

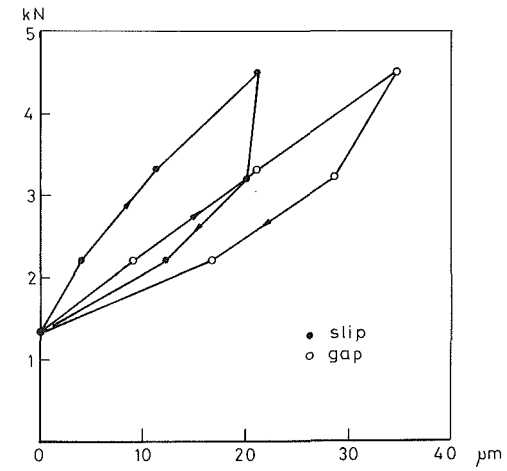


Fig. 9 Hysteresis loops obtained for the mean slip and back gap opening versus load

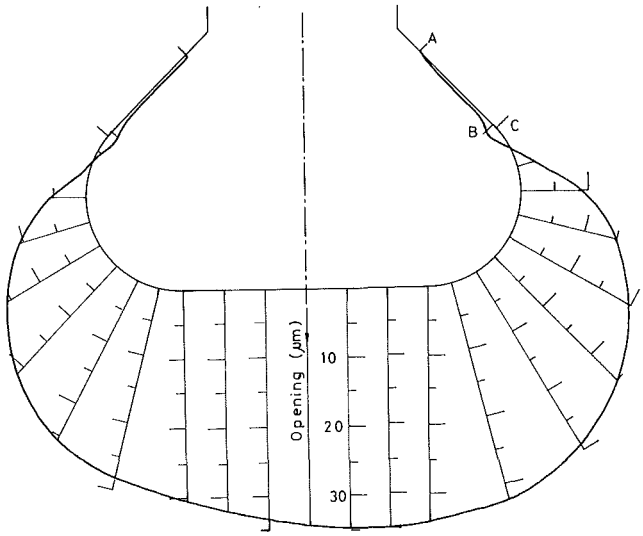


Fig. 10 Dovetail opening (closure) at maximum load

$$\text{Opening} = (u_s - u_b)\cos\beta + (v_s - v_b)\sin\beta \qquad (11)$$

where u and v are displacements in the x and y directions, respectively, and s and b signify adjacent points in sheet and blade, respectively. The difference between displacements $(u_s - u_b)$ and $(v_s - v_b)$ is proportional to the difference between the fringe orders at the sheet and at the blade, for the point considered, in accordance with equation (9). Along the straight flanks, data from Fig. 5(*a*) and (*b*) is reduced in the form shown in Fig. 7(*a*) and (*b*), where, from the relevant fringe orders, the variation of $(N_s - N_b)$ is plotted. The slight asymmetry will be noted. Similar plots were made for the other loads, an even greater asymmetry being found under increasing than under decreasing loading. The slip and opening between the points of tangency A, B in Fig. 2, were then calculated using equations (10) and (11) and plotted in Fig. 8. These, and similar results obtained for the other load levels analyzed, are summarized in Table 1. The mean of the slip on the left and right-hand sides is compared to the opening of the back gap, calculated in the same manner, in Fig. 9. Finally, Fig. 10 shows the opening (closure) of the joint at the maximum load.

Discussion

The asymmetry already observed in the photographs is made even more patent by Table 1, where the results for the right and left-hand flank are compared. It is noticeable that the slip along the contacting faces is more strongly affected by

Downloaded 02 May 2010 to 171.66.16.54. Redistribution subject to ASME license or copyright; see http://www.asme.org/terms/Terms_Use.cfm

Table 1 Average slip and closure along straight flanks in dovetail

Load (kN)	(μm) Slip		(μm) Closure	
	left	right	left	right
1.33 (Preload)	–	–	–	–
2.23 (Increasing)	0	8.2	0	0.2
3.32 (Increasing)	2.3	20.1	0.2	0.4
4.50 (Maximum)	18.0	24.1	0.6	0.6
3.32 (Decreasing)	17.0	23.2	0.5	0.6
2.23 (Decreasing)	12.9	11.3	0.4	0.4
1.33	–	–	–	–

friction than the opening of the joint which, as shown in Fig. 10, is almost symmetrical. Likewise, the hysteresis loop for the slip is wider than for the back gap, Fig. 9. This figure shows the average of slip on the two flanks, but analysis of Table 1 also indicates that the hysteresis for slip on the left flank is considerably more pronounced than for the right flank. Indeed, the back gap opens linearly under increasing load and the nonlinearity under decreasing load is less than ± 10 percent of its maximum value. A sharp change in the friction coefficient between the stick and slip conditions together with minor errors in manufacture and differences between the two surfaces in contact are the most likely cause of this behavior.

In the theoretical shape of Fig. 2, contact occurs between points A and B. At the point of tangency B, the gap between blade and sheet is already 10μm, or an order of magnitude higher than the higher closure of Table 1. Contact is therefore limited to the straight flank, the contact pressure decreasing toward the throat as predicted by numerical analysis [2]. The peak closure at B, Fig. 8, does not necessarily imply that at that point the contact pressure also peaks, since a slight tapering or blending between the straight flank and the radius results in the effective separation between blade and sheet, creating a gap at B prior to load application. It will be observed that the closure is only about 0.3 μm except in the immediate proximity of B, falling to between 0.1 μm and zero at A. In theory, of course, there cannot be any penetration of P_b into P_s when this pair of points is already in contact. In practice, a penetration of the same order as the surface roughness, 0.1 μm, is still possible.

The error in the determination of the fringe order at any given point will be less than 0.25, since interpolation between full orders is always possible. The error in the difference $(N_b - N_s)$ will therefore never exceed 0.5, equivalent to a displacement of 0.2 μm, in either direction. It follows, from equations (10) and (11) that the maximum absolute error in slip or opening (closure) is

$$0.2[\sin\beta \pm \cos\beta] < 0.28\mu\text{m}$$

and is likely to be considerably less. A further source of error is misalignment of the grating. If the grating is inclined by $\Delta\beta$ with respect to the x axis in Fig. 6, the error in slip is, from equation (10)

$$\Delta \text{ slip} = [(u_s - u_b)\cos\beta + (v_s - v_b)\sin\beta]\Delta\beta = (\text{opening})(\Delta\beta)$$

and in opening, from equation (11),

$$\Delta \text{ opening} = [-(u_s - u_b)\sin\beta + (v_s - v_b)\cos\beta]\Delta\beta = -(\text{slip})(\Delta\beta)$$

Given the relative magnitudes of slip and opening, the error on slip is clearly negligible while the error in opening for $\Delta\beta$ = 0.01 radian could be 0.3 μm.

It follows from this discussion that Moiré interferometry besides offering a high sensitivity is capable of accurate measurements to about 0.3 μm, or better, for any value of the displacement, only limited by the separation power of the photographic system. Fringes as close as 0.05 mm on the specimen can easily be distinguished in Fig. 5. Large displacements can be measured with high accuracy too, since fringe orders can be very high.

From the fatigue tests [1, 2] it was concluded that the worst fretting damage took place near the bottom end of the flank, with a slightly less damaged zone near the throat. This is consistent with the fact that, in Fig. 7, the slip tends to increase toward those ends and is also in agreement with the numerical results [2, 3]. Besides supporting the indirect evidence provided by the fatigue tests and the numerical analysis, the experiment has revealed the complexity of the real situation. The existence of a wide hysteresis loop in the slip versus load diagram also supports the assumption behind the use of a fretting damage parameter that represents the energy lost to the surfaces in contact.

A complete strain analysis could be performed from the Moiré patterns but it is far more efficient to combine the experimental method with numerical analysis, as discussed in the Introdution. The experiment is used as a guide to the establishment of the contact conditions and to check the validity of the simplification that must be introduced in the mathematical model, in particular, the value of the equivalent friction coefficient.

Conclusion

The dovetail joint studied has been shown to behave in an asymmetrical manner particularly under increasing load, and to exhibit a pronounced nonlinearity. This behavior, ascribed to the effect of friction and in particular to the change-over from a stick to a slip contact condition, was not predicted by a finite element analysis. To provide a satisfactory methematical model, the latter requires experimental input that can best be obtained by means of the high-sensitivity Moiré technique used in this investigation. The contact conditions that have been measured are consistent with observations from fatigue tests.

Relative displacements between the two surfaces in contact – blade and sheet – of up to 25 μm slip and 40 μm opening, have been measured with an estimated error of 0.3 μm. The high-sensitivity Moiré interferometric technique used offers unique potential for the study of many types of mechanical joints, in which friction between the elements in contact plays an important role. It permits, when complemented by numerical analysis, the determination of the energy losses that account for the fretting damage and damping characteristics of the joint, providing at the same time guidance in the setting up of the mathematical model and in the direct validation of its results.

Acknowledgments

This investigation was completed when one of the authors (C. Ruiz) was at VPI & SU, Department of Engineering Science and Mechanics as Visiting Professor. The support of the Head of the Department, Prof. Frederick, is gratefully acknowledged as is the assistance provided by Mr. P. Webb from Oxford University in making the test pieces and by Miss J. Wood and Mr. D. Joh of VPI & SU in processing some of the data. Support by the National Science Foundation Solid Mechanics Program, directed by Dr. Clifford Astill, under Grant MEA-8109230, is gratefully acknowledged.

References

1 Boddington, P. H. B., and Ruiz, C., "A Biaxial Fatigue Test for Dovetail Joints," *Proc. ASME Intl. Conf. on Advances in Life Prediction Methods*, Albany, Apr. 1983, pp. 277–283.

2 Boddington, P. H. B., Chen, K. C., and Ruiz, C., "An Investigation of Fatigue and Fretting in a Dovetail Joint," submitted for publication, *Exp. Mechanics*.

3 Boddington, P. H. B., Chen, K. C., and Ruiz, C., "The Numerical Analysis of Dovetail Joints," submitted for publication *J. Computers and Structures*, Vol. 24, 1984, pp. 208–217.

4 Durelli, A. J., and Parks, V. J., *Moire Analysis of Strain*, Prentice-Hall, Englewood Cliffs, N.J., 1970.

5 Post, D., "Moire Interferometry at VPI & SU," *Exp. Mechanics*, Vol. 23, 1983, pp. 203–210.

Downloaded 02 May 2010 to 171.66.16.54. Redistribution subject to ASME license or copyright; see http://www.asme.org/terms/Terms_Use.cfm

A Simplified Approach to Elastic-Plastic Response to General Pulse Loads[1]

P. S. Symonds
Professor of Engineering.
Fellow ASME

J. M. Mosquera
Research Assistant.

Division of Engineering, and
Division of Applied Mathematics,
Brown University,
Providence, R.I. 02912

The paper describes a method for estimating permanent and maximum (elastic plus plastic) deflections of a structure subjected to a force pulse loading of arbitrary shape and duration. The concept of artificially separating the response into purely elastic and purely plastic (i.e., rigid-plastic) stages is adopted. Previous applications have been to very short pulses. When the approach is applied to long pulses of only moderately large force compared to limit load magnitudes the interaction between elastic and plastic effects is more critical. The inclusion of plastic rate sensitivity and the determination of the duration of the initial elastic stage require new approaches. Insight is provided by studying a mass-spring (elastic-perfectly plastic) system of one degree of freedom. The duration of the elastic stage is chosen to maximize a specially defined work function. Comparisons are shown for examples of rate-independent and rate-sensitive frames between deflections given by the simple technique of the paper, final deflections obtained in laboratory tests, and maximum and final displacements furnished by the finite element code ABAQUS.

1 Introduction

As a means of determining the deformations of a ductile structure subjected to a pulse loading severe enough to cause plastic deformation, more simply than by a full numerical treatment for elastic-plastic behavior, an approach has been proposed in which the elastic and plastic behaviors are artificially separated [1-4]. Thus, the response is assumed to be made up of an initial wholly elastic stage (ignoring plastic yield conditions) followed by a wholly plastic one, i.e., by a rigid-plastic response. There is finally a stage of elastic vibrations. The actual response, for example of the frame of Fig. 1 to a force pulse such as one of those shown in Fig. 2, is much more complex, with mixed elastic and plastic effects; the plastic deformation occurs in zones between regions of elastic material. Following the boundaries of these zones, which may disappear and reappear (for example at corner *B* of the example frame) adds to the cost of numerical solutions, say by finite element or finite difference programs.

Separation of elastic and plastic response is also achieved in a so-called rigid-plastic analysis by the artifice of suppressing elastic strain increments, so that deformation occurs only where the yield condition is satisfied (as if Young's modulus E $\rightarrow \infty$). Although this type of analysis has had many useful applications [5, 6], and may allow some relatively simple solutions, it has some basic drawbacks. The numerical treatment of the initial response may be difficult. More fundamental is the lack of a general criterion for validity [3]. Some early-time details of rigid-plastic solutions are dubious in any case [7]. When the peak force magnitudes of the pulse are not greatly above the limit load, and substantial plastic

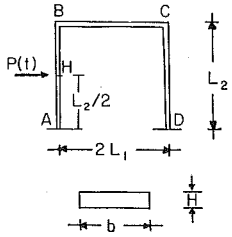


Fig. 1 Frame structure and loading used as example

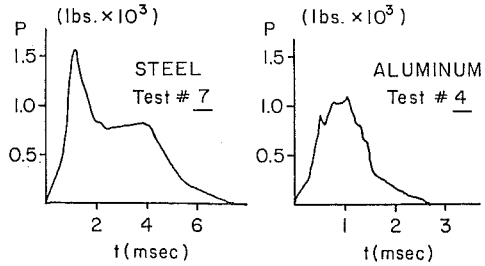


Fig. 2 Force pulses (obtained in tests): (*a*) on steel frame; (*b*) on aluminum alloy 6061-T6 frame

[1]This work was supported by the U.S. Office of Naval Research under Contract N00014-82-K-0063.

Contributed by the Applied Mechanics Division and presented at the Winter Annual Meeting, New Orleans, La., December 9-14, 1984 of THE AMERICAN SOCIETY OF MECHANICAL ENGINEERS.

Discussion on this paper should be addressed to the Editorial Department, ASME, United Engineering Center, 345 East 47th Street, New York, N.Y. 10017, and will be accepted until two months after final publication of the paper itself in the JOURNAL OF APPLIED MECHANICS. Manuscript received by ASME Applied Mechanics Division, February, 1984. Paper No. 84-WA/APM-52.

Copies will be available until August, 1985.

Copyright © 1985 by ASME
Downloaded 02 May 2010 to 171.66.16.54. Redistribution subject to ASME license or copyright; see http://www.asme.org/terms/Terms_Use.cfm

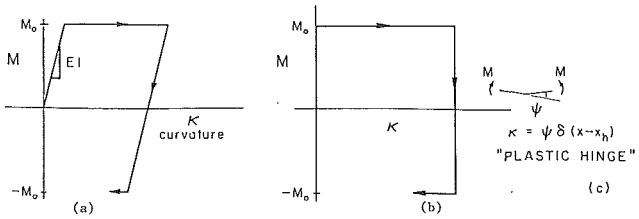


Fig. 3 Bending moment-curvature diagrams for (*a*) elastic-perfectly plastic behavior and (*b*) rigid-perfectly plastic behavior; (*c*) plastic hinge notation.

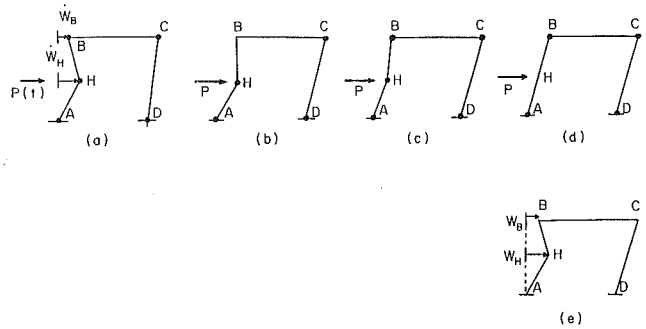


Fig. 4 (*a–d*) Illustrative sequence of velocity patterns ("phases") in rigid-plastic stage, leading to mode-form shape; (*e*) with velocities in constant ratio; (*f*) illustrates corresponding final deflections of rigid-plastic stage.

deformations occur because the pulse has long duration, a rigid-plastic solution may underestimate final displacements by an order of magnitude. However, the present method attempts to still take advantage of the relative simplicity of a rigid-plastic solution, while introducing elastic effects in such a way that realistic estimates of deflections (final and maximum, i.e., elastic plus plastic) are furnished, for arbitrary force pulse magnitudes, shapes, and durations. Thus, the approach – contrary to conventional "displacement method" finite element schemes – regards rigid-plastic response as primary and provides essential modifications for interactions with elastic response. The following section includes an outline of the rigid-plastic treatment adopted for the example frame, and the additional considerations required when the material is rate-sensitive.

Previous applications [1–4] of the simplified elastic-plastic ("SEP") technique took the load pulse idealized as "impulsive," i.e., delta function shape. Here the method is extended to arbitrary pulses such as illustrated in Fig. 2. Various decisions are required. In particular: (*a*) How should the energy and momentum of the elastic solution be transmitted to the frame modeled as rigid-plastic? (*b*) At what time t_1 should the elastic solution be stopped? (*c*) How should the maximum and final displacements be calculated? Guidance is obtained from an analysis of a mass-spring (single DOF) system; this is discussed in Section 3. Section 4 shows some details of two applications, including laboratory test results and predictions of an elastic-plastic numerical solution by finite elements, for comparison.

2 Elastic and Rigid-Plastic Treatments

The simplified elastic-plastic (SEP) method requires means of solving for the response of the structure first assuming elastic behavior and then assuming a rigid-plastic model. In the earlier applications where only delta-function load pulses were considered, elastic solutions were derived analytically, adopting finite component models with three or less degrees of freedom. This is still possible for finite arbitrarily shaped pulses, but many dynamic elastic codes are now available and will be more convenient. Linear (small deflection) capability will generally suffice. We used the program ABAQUS[2] for the present problems. This is a modular code with extensive nonlinear capability, but for the immediate purpose we set it to linear-elastic material behavior. The frame of Fig. 1 was modeled with 20 elements in each member (60 in all), the elements allowing for shear deformation and rotary inertia. (The same model set for elastic-perfectly plastic (or rate-dependent plastic) behavior was used also to obtain "exact" solutions, as will be cited later). For use in the simplified method a smaller number of elements and a less sophisticated code would undoubtedly be adequate.

For rigid-plastic analysis, general purpose finite-element type programs are not available with apparently one exception [8]. Our rigid-plastic solutions for the example frame are obtained for a discretized frame model having the smallest number of elements and degrees of freedom capable of representing both the "local" deformation (in the loaded column) and the "global" deformation (sidesway).

The meaning of "rigid-perfectly plastic" behavior in simple bending is illustrated in Fig. 3(*b*). Here M_0 is the fully plastic or limit moment. When it is maintained, the curvature κ can increase without limit, so that a finite rotation ψ can occur across a plastic hinge. The yield condition and flow laws are expressed as follows in terms of the plastic rotation rate $\dot{\psi}$ (Fig. 3(*c*)), bending moment M, and its time rate $\dot{M}$:

$$-M_0 \le M \le M_0 \qquad (1a,b)$$

$$(M-M_0)\dot{\psi} \ge 0; \qquad (M+M_0)\dot{\psi} \ge 0 \qquad (2a,b)$$

$$\dot{M}\dot{\psi} = 0 \qquad (3)$$

The flow rules, equations (2), in combination with the yield condition, equations (1), require that when $\dot{\psi} > 0$, $M = M_0$; while if $\dot{\psi} < 0$, $M = -M_0$. Equation (3) represents the unloading condition: plastic strain rates vanish ($\dot{\psi} = 0$) if the moment is not held constant ($\dot{M} \neq 0$). Here we are assuming the limit moment M_0 the same for positive and negative bending. In the example frame, M_0 is the same at all sections.

In the discrete model adopted, plastic hinges are allowed to occur at five cross sections ("nodes") A, H, B, C, D; H being the midpoint of column AB, where the force P acts. Thus the model consists of four rigid segments AH, HB, BC, and CD. Since the velocity varies linearly between nodes, the state of velocity of the frame can be expressed in terms of the velocities $\dot{w}_H$, $\dot{w}_B$ of points H and B. We will take it that the velocity vector $\dot{\mathbf{w}} = \{\dot{w}_H, \dot{w}_B\}$ and displacement vector $\mathbf{w} = \{w_H, w_B\}$ are adequate to define the velocity and displacement fields of the rigid-plastic stage. In the simplified approach we will be concerned with estimating maximum and final values of the displacement $\mathbf{w}$ with account taken of the initial elastic stage and of unloading in the final elastic stage.

This discrete model is a crude one, but it is considered adequate to describe the principal deformations. As already noted, the frame undergoes a type of hierarchical deformation process, in which a local "dishing" deformation of the column AB occurs first, transmitting momentum to the sidesway motion that follows. The displacements at H and B result from the interaction between the two modes of deformation. The major deformation is at the base A where the effects of the two modes reinforce, whereas at corner B they tend to cancel each other, the initial closing hinge being followed by an opening. The displacement magnitudes $\mathbf{w}^m$ (maximum) and $\mathbf{w}^f$ (final) are of interest, and the latter provide estimates of rotations at the five hinge sections.

The starting conditions of the rigid-plastic stage are the velocities at H and B, i.e., the vector $\dot{\mathbf{w}}^0 = \{\dot{w}_H^0, \dot{w}_B^0\}$. These are determined by the velocity field of the initial elastic stage in a manner discussed in the following section. Any pair of

[2] Kindly made available by Hibbitt, Karlsson and Sorensen, Inc., 35 South Angell Street, Providence, R.I. 02906.

Downloaded 02 May 2010 to 171.66.16.54. Redistribution subject to ASME license or copyright; see http://www.asme.org/terms/Terms_Use.cfm

velocities at H and B defines a "phase" of the rigid-plastic response, defined by a set of plastic hinges with particular signs of rotation rates at each hinge. For illustration, Fig. 4(a) shows a phase that might result from a force pulse that has a peak at an early time, the black circles designating the plastic hinges. The diagram shows the velocity field, and the types of rotation at each hinge are as indicated. The rigid-plastic stage consists of a succession of such phases, the details depending on the force pulse. The sequence shown in Fig. 4 for illustration is for the case of a force pulse with a large peak at an early time followed by relatively small values, where "large" means relative to the static collapse value. The structural resistance forces dominate after the peak in this case, causing the hinge at B first to disappear (b). In the following phase (c) this hinge has rotation rate of opposite sign. The final phase (d) with hinges at the four corners is a stable mode-form pattern. This sidesway mode is in fact the final phase for all pulse shapes.

The equations of dynamics for each phase can easily be derived from the free body diagrams of rigid segments AH, HB, BC, CD; these have linear acceleration fields, and after eliminating reaction forces a pair of equations for each phase is obtained. (Alternatively the derivation of accelerations can be done by applying Tamuzh's principle [10, 11], avoiding free body diagrams). We omit details but show the equations for the phase represented in Fig. 4(a) as an illustration:

$$\frac{1}{12}\bar{\rho}L_2\begin{bmatrix}4 & 1\\ 1 & 6+24\beta\end{bmatrix}\begin{bmatrix}\ddot{w}_H\\ \ddot{w}_B\end{bmatrix} = \begin{bmatrix}P(t)\\ 0\end{bmatrix} + \begin{bmatrix}-8\\ 2\end{bmatrix}\frac{M_0}{L_2} \tag{4}$$

where $\beta = L_1/L_2$ (see Fig. 1), $\bar{\rho}$ is mass per unit length $= \rho bH$ for a rectangular section of width b, depth H, and mass per unit volume ρ. This equation holds for a uniform frame of rigid-perfectly plastic material. It is valid so long as the flow conditions equations (2) and (3) are satisfied at all the hinges. In the example of Fig. 4, the accelerations have signs $\ddot{w}_H < 0$, $\ddot{w}_B > 0$. Hence one of the flow conditions associated with equation (4), namely $\dot{w}_H > \dot{w}_B$, will be violated if phase (a) in Fig. 4 is retained beyond the time when $\dot{w}_H = \dot{w}_B$. The next phase will be that of (b) or (c) in Fig. 4, depending on the bending moment at B, which in turn depends on the load. A computer program was written to integrate the equations in each phase. The flow conditions are examined at each time step, and the phase terminated at the time when any condition is about to be violated. The program selects the appropriate new phase so as to satisfy the yield condition and flow rules at all hinges, and carries out the integration in the new phase with the appropriate new flow conditions.

The foregoing illustrates the analysis of the rigid-plastic stage for the uniform frame of rate-independent material; a single value M_0 of limit moment applies to all the hinges. If the material is rate-sensitive the moments at the hinges will be different, since each depends on the local curvature rate. We adopt the familiar relations between uniaxial stress σ and plastic strain rate $\dot{\epsilon}$; and between bending moment M and plastic curvature rate $\dot{\kappa}$ [12, 13]:

$$\frac{\sigma}{\sigma_0} = 1 + \left(\frac{\dot{\epsilon}}{\dot{\epsilon}_0}\right)^{\frac{1}{n}}; \qquad \frac{M}{M_0} = 1 + \left(\frac{\dot{\kappa}}{\dot{\kappa}_0}\right)^{\frac{1}{n}} \tag{5a,b}$$

where σ_0, M_0 are quasistatic values with $M_0 = \sigma_0 bH^2/4$ for the rectangular section, n, $\dot{\epsilon}_0$ are material constants, and $\dot{\kappa}_0 = 2\dot{\epsilon}_0(1+1/2n)^n/H$. In our analysis of the strain-rate-sensitive frame we retain the idealization of plastic hinges localized at fixed cross sections; the length z_h of the hinge region is finite but assumed small compared to member lengths. Putting equation 5(b) in terms of rotation rate $\dot{\psi}$ across the hinge, the following relations are taken to replace equation (1)–(3):

$$\text{For}\quad \dot{\psi}=0: \qquad -M_0 \le M \le M_0 \tag{6a,b}$$

$$\text{For}\quad \dot{\psi}\neq 0: \qquad \frac{M}{M_0} = (\operatorname{sgn}\dot{\psi})\left[1+\left(\frac{\alpha|\dot{\psi}|}{\dot{\epsilon}_0}\right)^{\frac{1}{n}}\right] = \mu \tag{7}$$

The form of equation (7) is evidently obtainable from equation (5) by putting $\dot{\kappa} = \dot{\psi}/z_h$, so that $\alpha = H/2z_h(1 + 1/2n)^n$. However we obtained α directly from calculations of M and $\dot{\psi}$ by ABAQUS for an impulsively loaded cantilever beam [14], using values for the latter part of the response which consists essentially of a rigid-body rotation. α was found to increase as the rotation rate $\dot{\psi}$ decreases, but we take $\alpha = 0.15$ as a fair average. With values $n = 5$, $\dot{\epsilon}_0 = 40\ \text{sec}^{-1}$ for low carbon steel [12, 13], the moment increase factor μ (equation (7)) is insensitive to α. (For example, if $\mu = 2$, a change of α from 0.15 to 0.25 increases μ by about 5 percent).

The solution for the rigid-plastic stage for the frames of rate-sensitive material was carried out by the computer program described in the foregoing for the perfectly plastic case, with new equations of dynamics for each phase taking account of the different moment values at the plastic hinges and computing these by equation (7) from the local rotation rate. A forward (Runge-Kutta) integration was used. In the rate sensitive case, the value of $\dot{\psi}_j$ (for hinge j) calculated for each time step was used to determine the value of M_j/M_0 for use in the following time step. To illustrate, the equations replacing equations (4) for the phase shown in Fig. 4(a) are

$$\mathbf{G}\,\ddot{\mathbf{w}} = \mathbf{P} - \mathbf{A}\mathbf{M}(\dot{\psi}) \tag{8a}$$

$$\frac{M_j}{M_0} = \left[1+\left(\frac{\alpha|\dot{\psi}_j|}{\dot{\epsilon}_0}\right)^{\frac{1}{n}}\right]\operatorname{sgn}\dot{\psi}_j = \mu_j \tag{8b}$$

$$\dot{\psi} = \mathbf{A}^T\dot{\mathbf{w}} \tag{8c}$$

where

$$j = A, H, B, C, D$$

$$\mathbf{M} = \{M_A\ M_H\ M_B\ M_C\ M_D\}$$

$$\dot{\psi} = \{\dot{\psi}_A\ \dot{\psi}_H\ \dot{\psi}_B\ \dot{\psi}_C\ \dot{\psi}_D\}$$

$$\ddot{\mathbf{w}} = \{\ddot{w}_H\ \ddot{w}_B\}; \quad \dot{\mathbf{w}} = \{\dot{w}_H\ \dot{w}_B\}$$

$$\mathbf{A} = \frac{1}{L_2}\begin{bmatrix}2 & 4 & 2 & 0 & 0\\ 0 & -2 & -2 & 1 & 1\end{bmatrix}; \quad \mathbf{A}^T = \text{transpose of } \mathbf{A}$$

The mass matrix $\mathbf{G}$ and force matrix $\mathbf{P}$ are shown in equation (4); only the structure resistance terms are changed. More complete details on the calculations are given in a separate paper [15].

The rigid-plastic analysis for strain-rate-sensitive material outlined previously is more elaborate than used in [1–4] and by many other authors, e.g., Perrone [16]. The corrections for rate effects are more critical in cases of relatively small load magnitudes and long pulses. We mention also that a simpler process in which constant values of the moment factors μ_j were used during each phase, computed iteratively from average rotation rates $\bar{\dot{\psi}}_j$ in the phase, was sometimes unsuccessful because of difficulties of convergence, apparently due to the nonlinearity of equation (7). However, once a program is written for step-by-step integration, the cost of computation is minimal, and small steps may be used in a forward integration scheme, as indicated.

3 Problems in Simplified Technique

Here we consider the questions raised in the first section.

(a) When the elastic stage is stopped at time t_1 it has

Downloaded 02 May 2010 to 171.66.16.54. Redistribution subject to ASME license or copyright; see http://www.asme.org/terms/Terms_Use.cfm

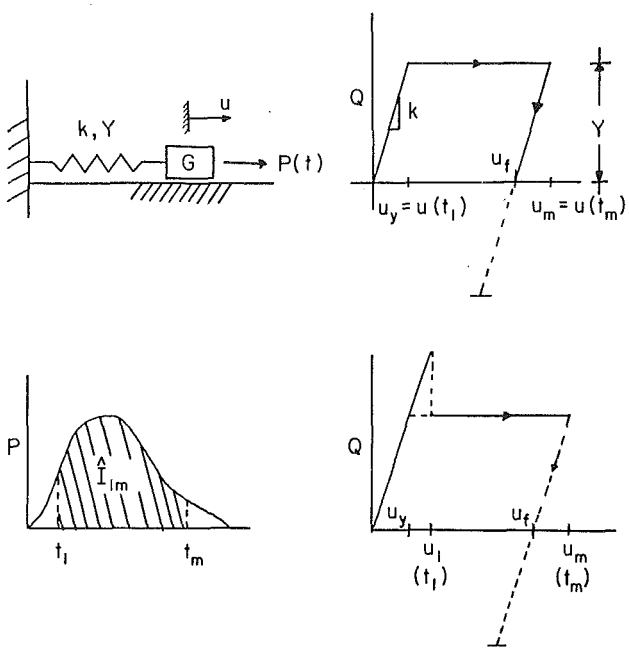


Fig. 5 *(a)* **Simple mass-spring system; *(b)* illustrates spring characteristic and also shows response to force pulse *(d)*; t_1 is time when displacement $u_y = Y/k$ is reached; t_m is time when velocity is reduced to zero; *(d)* illustrates response when duration t_1 of elastic stage is regarded as arbitrary.**

displacement and velocity fields different in shape from those of the succeeding rigid-plastic stage. Assuming the initial shape of the latter is known, how should the starting values $(\dot{w}_H^0,\ \dot{w}_B^0)$ be determined? We solve this problem by the same device used previously [1–4], namely by choosing these so as to minimize the function Δ_0 defined as

$$\Delta_0(\dot{w}_H^0,\ \dot{w}_B^0) = \frac{1}{2}\int \bar{\rho}(\dot{w}_1^e - \dot{w}_0^{rp})^2 ds \tag{9}$$

where $\dot{w}_1^e(s)$ is the velocity of the elastic solution at time t_1 and $\dot{w}_0^{rp}(s)$ is the initial velocity field of the rigid-plastic solution. The latter is expressible in terms of $\dot{w}_H^0$, $\dot{w}_B^0$, and Δ_0 is minimized in terms of them. The equations

$$\frac{\partial \Delta_0}{\partial \dot{w}_H^0} = 0; \qquad \frac{\partial \Delta_0}{\partial \dot{w}_B^0} = 0 \tag{10}$$

can be interpreted in terms of conservation of momentum [17]. This "$\Delta_0^{\min}$" device has proved useful in many contexts since it was suggested [17] for approximate rigid-plastic solutions; for example for transient elastic solutions [18].

(b) The time t_1 when the elastic stage terminates was found in previous applications [1–4] by invoking a "yield condition" involving weighted moments at the plastic hinge locations. An alternative approach, which seems preferable especially for long pulses, starts by treating t_1 as an arbitrary independent variable. For any choice of t_1 the SEP method can be carried through, and plastic deformations in the rigid-plastic stage computed. Intuitively one can surmise that too small values of these, or of plastic work, will be obtained if t_1 is chosen either too long or too short, i.e., that these quantities have maxima at some value of t_1. Evidently t_1 might be chosen so as to maximize an important displacement, or plastic work. This would be conservative, and could be taken as a good choice on that basis.

However, considerable insight is gained and a more satisfactory way to choose t_1 is suggested by study of a simple one degree-of-freedom mass-spring system (Fig. 5(*a*)), whose spring has an elastic-perfectly plastic characteristic, Fig. 5(*b*). Displacement u is measured from the unloaded rest position of the mass G. A typical load pulse sketched in Fig. 5 (*c*) shows the times t_1 and t_m when plastic deformation starts and stops, respectively. As indicated in Fig. 5(*b*), in the actual response t_1 is the time when the displacement $u(t_1) = u_y = Y/k$, where Y and k are the yield force and stiffness, respectively. At time t_m the velocity $\dot{u}(t_m) = 0$. The complete solution for the mass-spring system is easily written for an arbitrary pulse, the equation of motion being

$$G\ddot{u} + Q(u) = P(t) \tag{11}$$

The first stage $(0 \le t \le t_1)$ involves elastic response with $Q = ku$. At time t_1 we have

$$u(t_1) = u_1 = \frac{1}{\omega G}\int_0^{t_1} P(\tau)\sin\ \omega(t_1 - \tau)d\tau \tag{12a}$$

$$\dot{u}(t_1) = \dot{u}_1 = \frac{1}{G}\int_0^{t_1} P(\tau)\cos\ \omega(t_1 - \tau)d\tau \tag{12b}$$

where $\omega = \sqrt{k/G}$ is the natural frequency. For any given pulse, t_1 is obtained from equation (12*a*) by setting $u_1 = u_y = Y/k$. In the second stage $(t_1 \le t \le t_m)$ the response is plastic with $Q = Y$. (Since Y is assumed constant, this response of a system with elastic-plastic behavior can be regarded as a rigid-perfectly plastic response, disregarding the constant elastic displacement component $u_y = Y/k$). In terms of the initial velocity $\dot{u}_1$ given by equation (12*b*), the velocity in the second stage is given by

$$G\dot{u} = G\dot{u}_1 - Y(t - t_1) + \hat{I}_1(t) \tag{13}$$

where

$$\hat{I}_1(t) = \int_{t_1}^{t} P(\tau)d\tau$$

We suppose the maximum displacement is reached at time t_m when $\dot{u}(t_m) = 0$. t_m is obtained by solving

$$0 = G\dot{u}_1 - Y(t_m - t_1) + \hat{I}_{1m} \tag{14}$$

where

$$\hat{I}_{1m} = \hat{I}_1(t_m) = \int_{t_1}^{t_m} P(t)dt$$

Integrating equation (13) and putting $t = t_m$ the maximum displacement is obtained as

$$u_m = u_1 + \frac{G\dot{u}_1^2}{2Y} - \frac{\hat{I}_{1m}^2}{2GY} + \frac{1}{G}\int_{t_1}^{t_m} \hat{I}_1(t)dt \tag{15}$$

where $u_1 = u_y$.

However, instead of regarding t_1 as obtained by putting $u_1 = u_y$ and using equation (12*a*), we may regard t_1 as an independent variable. This is illustrated in Fig. 5(*d*). All the quantities on the right-hand side of equation (15) are then functions of t_1; note that t_m is related to t_1 through equation (14). To look for a maximum of u_m we compute its derivative. After some algebra we obtain the result

$$\frac{du_m}{dt_1} = \left(\dot{u}_1 + \frac{\hat{I}_{1m}}{G}\right)\left(1 - \frac{ku_1}{Y}\right) \tag{16}$$

This shows that u_m has a stationary maximum at t_1 such that $u_1 = u(t_1) = Y/k$. In other words, instead of calculating the correct value of t_1 by solving equation (12*a*) with $u_1 = u_y$, we can equally well find it by plotting $u_m(t_1)$ and locating the value at which u_m is maximum.

This result, which applies to force pulses of arbitrary shape on the single DOF mass-spring system, suggests that an analogous quantity may be defined for a general structure, such that its maximum may be used to single out the "best" value of t_1 to use in applying the SEP method. The quantity shown in the foregoing to be maximized by the correct t_1 is u_m

Downloaded 02 May 2010 to 171.66.16.54. Redistribution subject to ASME license or copyright; see http://www.asme.org/terms/Terms_Use.cfm

Table 1

Exper. S7 Steel Impulse $\hat{I}$ = 18.4 N-sec (4.14 lb-sec)

Displacements	Exper.	ABAQUS	SEP	RP
Max. w_H^m(mm)		8.4	7.1 = 1.3 + 5.8	
(in.)		0.33	0.29 = 0.05 + 0.23	
Max. w_B^m(mm)		11.2	9.1 = 1.5 + 7.6	
(in.)		0.44	0.36 = 0.06 + 0.30	
Final w_H^f(mm)	6.1	6.1	6.1 = 7.4 − 1.3	
(in.)	0.24	0.24	0.23 = 0.29 − 0.05	0.083
Final w_B^f(mm)	7.4	7.6	7.1 = 9.1 − 2.0	
(in.)	0.29	0.30	0.28 = 0.36 − 0.08	0.089
Plastic Work(m-N)		27.1	25.4	8.7
(in.-lb)		240	225	77

Exper. A4 Al 6061-T6 Impulse $\hat{I}$ = 5.4 N-sec (1.21 lb-sec)

Displacements	Exper.	ABAQUS	SEP	RP
Max. w_H^m(mm)		8.6	8.1 = 3.5 + 4.6	
(in.)		0.34	0.32 = 0.14 + 0.18	
Max. w_B^m(mm)		13.5	12.9 = 3.8 + 9.1	
(in.)		0.53	0.51 = 0.15 + 0.36	
Final w_H^f(mm)	3.8	4.6	4.8 = 8.1 − 3.3	
(in.)	0.15	0.18	0.19 = 0.32 − 0.13	0.011
Final w_B^f(mm)	4.3	4.6	4.9 = 13.0 − 8.1	
(in.)	0.17	0.18	0.19 = 0.51 − 0.32	0.015
Plastic Work(m-N)		23.5	25.7	1.2
(in.-lb)		208	227	10.5

Frame dimensions: span $2L_1$ = 146 mm (5.75 in.); height L_2 = 124 mm (4.88 in.); thickness H = 6.4 mm (0.25 in.), width b = 25.4 mm (1.00 in.)

Steel: yield stress σ_0 = 239 MN/m^2 (34.7 ksi), ϵ_0 = 40 sec^{-1}, n = 5; density ρ = 7800 kg/m^3 (0.73 × 10^{-3} lb sec^2 in.$^{-4}$)

Al 6061-T6: yield stress σ_0 = 308 MN/m^2 (44.7 ksi); rate-independent; density ρ = 2800 kg/m^3 (0.25 × 10^{-3} lb sec^2 in.$^{-4}$)

Note: both frames have fundamental period about 3.4 msec.

$= u_1 + u_{rp}$, where u_{rp} is the displacement during the second stage, equation (15). Hence the work quantity $Yu_m = Yu_1 + Yu_{rp}$ is maximized. We define the analogous work for the frame (or other) structure:

$$W_m(t_1) = W_1 + W_{rp} = \int M^p \kappa_1^e ds + W_{rp} \tag{17}$$

where W_{rp} is the plastic work of the rigid-plastic stage and W_1 is a work corresponding to the work Yu_1 of the mass-spring system; W_1 is computed as the work of moments M^p on curvatures κ_1^e where M^p are moments of the static limit load and κ_1^e are curvatures of the elastic solution computed at time t_1.

The function $W_m(t_1)$ defined in equation (17) is the one we have used in implementing the SEP method; the maximum of W_m identifies the "best" value of t_1. Plots of W_m for the two example pulses are shown in Fig. 6. In one of these the material is strongly strain-rate-sensitive. The quantities in W_m are as readily computed for this case as for the rate-independent one. The argument based on the mass-spring system of course pertains to a rate-independent material. We are also applying it empirically to the rate-sensitive case.

(*c*) The third question concerns displacements. The maximum displacements during the response are presumed to occur when plastic and elastic deflections add together, while the final static deflections should be obtainable by subtracting the deflections of an elastic vibration amplitude from the maximum values. The simplest scheme follows the mass-spring model as a guide. As shown in Fig. 5(*c*) for arbitrary t_1, the maximum displacement $u_m = u_1 + u_{rp}$, where u_{rp} is the displacement increment of the rigid-plastic stage from t_1 to t_m. The final elastic stage consists of a vibration of amplitude $u_y = Y/k$ about a mean displacement $u_f = u_m - u_y = u_{rp} + u_1 - u_y$, so that u_f is the final static displacement after the vibrations have been damped out. These forms can be immediately translated into analogous terms for the example frame, namely

$$\mathbf{w}^m = \mathbf{w}_1^e + \mathbf{w}^{rp}; \qquad \mathbf{w}^f = \mathbf{w}^m - \mathbf{w}^{er} = \mathbf{w}^{rp} + \mathbf{w}_1^e - \mathbf{w}^{er} \tag{18a,b}$$

where we use the vector notation $\mathbf{w} = \{w_H, w_B\}$, $\mathbf{w}_1^e$ are the displacements at time t_1 in the first stage elastic solution, $\mathbf{w}^{rp}$ are the displacement increments of the rigid-plastic second stage solution, and $\mathbf{w}^{er}$ denotes displacements corresponding to the amplitude of the final elastic vibration. These need no explanation except for $\mathbf{w}^{er}$. Before discussing this and showing comparisons, we note that a different procedure was used in [4, 9]: instead of $\mathbf{w}_1^e$, a vector $\mathbf{w}^{ep}$ was added to $\mathbf{w}^{rp}$, $\mathbf{w}^{ep}$ being the displacements corresponding to a deflection curve derived from elastic curvatures $M^f(s)/EI$, where $M^f(s)$ stands for the bending moment field of the final mode-form pattern, Fig. 4(*d*). We have already emphasized that the final phase of the rigid-plastic stage is always in this unchanging mode pattern, in a rigid-perfectly plastic analysis. The final displacements were taken in [4, 9] as $\mathbf{w}^{rp}$, assuming as an approximation that $\mathbf{w}_1^e$ and $\mathbf{w}^{er}$ are equal, as is true in the mass-spring model. The agreement obtained in [4, 9] was unsatisfactory in some respects. The forms of equations (18) are appealing because they are straightforward analogues of the equations for the one-DOF model. These and other procedures are discussed further in [15].

Returning to the estimation of the "elastic relaxation" amplitude $\mathbf{w}^{er}$ in equation (18*b*), we make the assumptions that only a fundamental vibration mode need be considered in

Downloaded 02 May 2010 to 171.66.16.54. Redistribution subject to ASME license or copyright; see http://www.asme.org/terms/Terms_Use.cfm

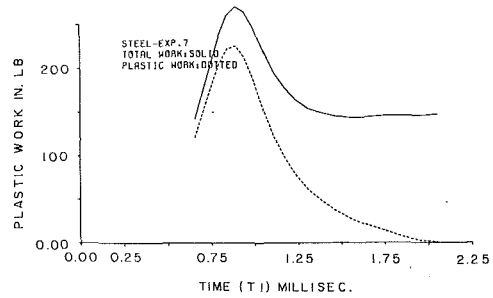


Fig. 6(*a*) Total work and plastic work as functions of t_1, equation (17)

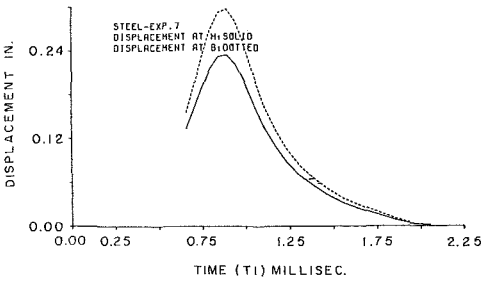


Fig. 6(*b*) Displacement at H and B as functions of t_1

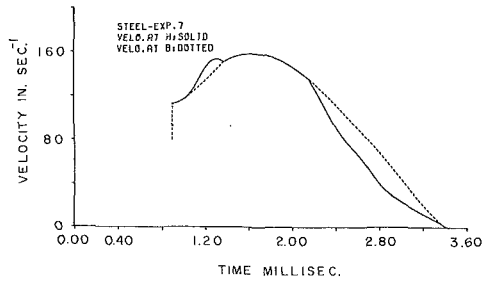


Fig. 6(*c*) Velocities in rigid-plastic stage (showing successive phases) with t_1 chosen so as to maximize total work

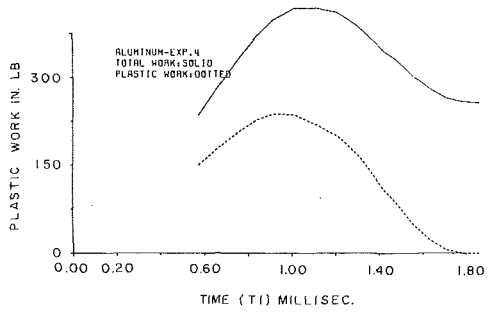


Fig. 6(*d*) Total work and plastic work as functions of t_1, equation (17)

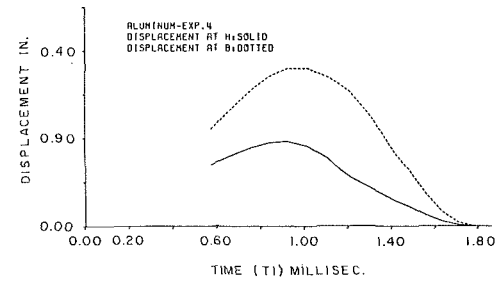


Fig. 6(*e*) Displacements at H and B as functions of t_1

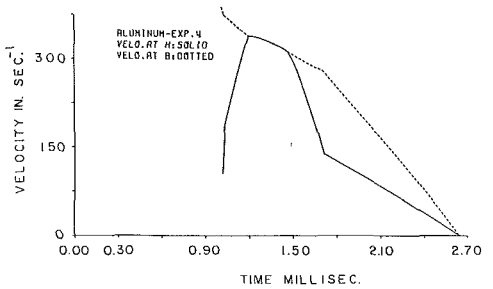


Fig. 6(*f*) Velocities in rigid-plastic stage (showing successive phases) with t_1 chosen so as to maximize total work

the final vibration, and that its amplitude can be determined by matching its strain energy to that present in the final phase of the rigid-plastic stage. As already noted, the final phase is that of simple sidesway, Fig. 4(*d*). The stress field is known; the bending moment in each member varies from positive M_0 to negative M_0. The associated elastic strain energy W_e^{rp} is taken equal to the strain energy of an elastic vibration in the fundamental mode. For simplicity we assume that the shape of the fundamental model is approximately the same as the deflected shape due to a force at corner B; if the deflection at B is δ, that at H is 0.42 δ. To find δ we set the two strain energies equal. Omitting details, we have

$$W_e^{rp} = \frac{M_0^2}{6EI}(2L_1 + 2L_2) = \frac{12EI}{L_2^3}\,\frac{1+3\dfrac{L_2}{L_1}}{4+3\dfrac{L_2}{L_1}} \tag{19}$$

For the proportions of the example frames we find

$$\mathbf{w}^{er} = 1.54(0.42,\ 1)\frac{M_0 L_2^2}{6EI} \tag{20}$$

This result (independent of the load pulse) is used in equation (18*b*) to give estimates of final permanent displacements.

4 Examples

To illustrate how displacement estimates furnished by the simplified approach compare with values from tests and numerical solutions we give details of two examples of force pulses applied to a steel and to an aluminum alloy 6061-T6 frame. These are representative of five tests on steel and seven tests on aluminum alloy frames; full details are reported separately [15]. In the tests the frame specimens were mounted at the end of a track and were impacted by a mass propelled along the track, measurements of the force applied to the frame during the impact being made by strain gages in the impacting hammer. The force-time curves of Fig. 2 are reproductions of measured pulses. Further test data for the two examples are listed in Table 1, which shows comparisons between the estimated final deflections (w_H^f, w_B^f) and those measured on the two test frames taken as examples.

The curves of Fig. 6 are included to illustrate some aspects of the procedure for the two example frames. Figures 6(*a*) and 6(*d*) show plots of the work function W_m whose maximum determines t_1; the plastic work is also shown, and in Figs. 6(*b*) and 6(*e*) it is shown that the plots of the two displacements have similar maxima. Finally Figs. 6(*c*) and 6(*f*) illustrate the rigid-plastic solution, having chosen t_1. The final mode-form phase, with $w_B = 2w_H$, is a major part of the response in Fig. 6(*f*) for the aluminum alloy frame, but is a less important part for the steel frame as shown in Fig. 6(*c*), due to the rate sensitivity of the latter.

Comparisons are also shown with computed deflections, both maximum and final, obtained from a complete numerical solution; these provide a check on the experiments as well as providing additional details of the response. As already mentioned, the finite element program ABAQUS was

Downloaded 02 May 2010 to 171.66.16.54. Redistribution subject to ASME license or copyright; see http://www.asme.org/terms/Terms_Use.cfm

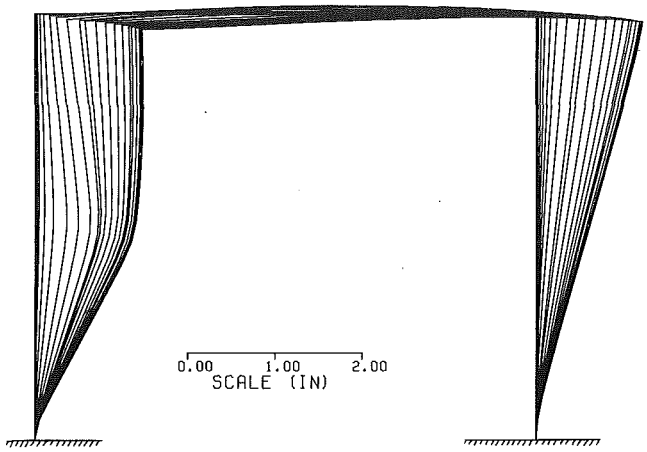


Fig. 7 Illustrative deflected shapes computed by ABAQUS at approximately equal time intervals. Data are for Experiment S7 (steel frame) with the forces of pulse Fig. 2(*a*) multiplied by $\sqrt{2}$.

used.[3] This has the advantage for these calculations of providing automatic control of the time step, based on the difference between a computed force residual and a stipulated value at each midtime step. For rate-sensitive behavior ABAQUS adopts the relation between stress and strain rate of equation (5*a*). For the steel frame we used values of the constants $\dot{\epsilon}_0$, n, σ_0 shown in Table 1; the aluminum alloy frames were taken as rate-independent on the basis of tensile tests at Instron machine rates. Since ABAQUS does not provide for structural damping, after plastic deformation has been completed an elastic vibration continues indefinitely. This is typically a nearly sinusoidal curve, and we have assumed that the final rest displacement is the mean of the extreme values. An example of computed frame configurations is shown in Fig. 7. To show more details with larger deflections, a larger load was used for these, namely the pulse of Fig. 2(*a*) with force multiplied by $\sqrt{2}$ but time scale unchanged.

The results shown in Table 1 represent typical agreements between the estimated displacements by the simplified technique, the measured final displacements of the test frames, and computed maximum and final displacements of the complete solution by finite elements. Also shown are deflections by a wholly rigid-plastic analysis. It is seen that the latter are much too small, in the two examples by factors of about 1/3 and 1/17. In contrast, the predictions of the SEP method here are in error by less than 20 percent. Since details for all the tests will be published separately [15], it will suffice here to summarize the results by stating that compared to both the test deflections (final values) and those computed by ABAQUS (final and maximum values), the agreement of the SEP predictions was to better than 20 percent in all the cases where the measured frame deflections exceeded about 3.0 mm (0.12 in.). In the several cases of small permanent deflections the SEP method was sometimes accurate but more often underestimated the displacement substantially. The largest deflection in any of the tests was about 11 mm. (0.44 in.), in test *A*6, and the errors in this case were less than 10 percent, whereas a wholly rigid-plastic treatment gave final deflections less than 1/4 those of the test and of the ABAQUS calculation. More tests and calculations are needed, but the present series is encouraging as far as the simplified elastic-plastic technique is concerned.

[3] All calculations were made on the Brown University, Division of Engineering VAX-11/780 computer, the acquisition of which was made possible by grants from the U.S. National Science Foundation (grant EN78/9378), the General Electric Foundation, and the Digital Equipment Corporation.

A brief note on costs may be of interest. We give these in terms of CPU time on the VAX-11/780, other computer costs (I/O counts etc.) being roughly in proportion. Running the "exact" elastic-plastic solution for the case shown in Fig. 7 took 1.02 hr. The simplified elastic-plastic technique required 13.5 min, of which 12.1 min was for the wholly elastic run, only 1.4 min being required for all the other calculations, including determining t_1 by maximizing W_m. The main expenses, of course, are not machine costs. One purpose of further research is to try to make the simplified technique more automatic. Many more applications are also needed to obtain information on its limitations and possible extensions.

Acknowledgment

The authors have benefited from many discussions with their colleague Professor H. Kolsky. The present work is part of a research project done in collaboration with Professor Kolsky.

References

1 Symonds, P. S., and Raphanel, J. L., "Large Deflections of Impulsively Loaded Plane Frames—Extensions of the Mode Approximation Technique," *Proc. Conf. on Mechanical Properties of Materials at High Rates of Strain*, Institute of Physics Conf. Ser. No. 47, Harding, J., ed., London and Bristol, 1979, pp. 277–287.

2 Symonds, P. S., "Finite Elastic and Plastic Deformations of Pulse Loaded Structures by an Extended Mode Technique," *Int. J. Mech. Sci.*, Vol. 22, 1980, pp. 597–605.

3 Symonds, P. S., "Elastic-Plastic Deflections due to Pulse Loading," in Proc. of the Second Specialty Conf. on *Dynamic Response of Structures: Experimentation, Observation, Prediction, and Control*, Hart, G., ed., New York, ASCE, 1980, pp. 887–901.

4 Raphanel, J. L., and Symonds, P. S., "The Estimation of Large Deflections of a Portal Frame under Asymmetric Pulse Loading," Report CEE 80/3, October 1982 of Brown University, Division of Engineering to U.S. National Science Foundation, ASME JOURNAL OF APPLIED MECHANICS, Vol. 51, 1984, pp. 494–500.

5 Jones, N., "A Literature Review of the Dynamic Plastic Response of Structures," *The Shock and Vibration Digest*, Vol. 7, No. 8, 1975, pp. 89–105.

6 Jones, N., "Recent Progress in the Dynamic Plastic Behavior of Structures," The Shock and Vibration Digest, Part I: Vol. 10, No. 9, Sept. 1978, pp. 21–33; Part II: Vol. 10, No. 10, Oct. 1978, pp. 13–19.

7 Symonds, P. S., and Fleming, W. T., Jr., "Parkes Revisited: On Rigid-Plastic and Elastic-Plastic Dynamic Structural Analysis," *Int. J. Impact Engineering*, Vol. 2, No. 1, 1984, pp. 1–36.

8 Lepik, U., and Just, M., "Automatic Calculation for Bending of Rigid-Plastic Beams under Dynamic Loading," *Computer Meth. Appl. Mech. and Eng.*, Vol. 38, 1983, pp. 19–28.

9 Symonds, P. S., and Raphanel, J. L., "Rigid-Plastic and Simplified Elastic-Plastic Solutions for Dynamically Side-Loaded Frames," in *Mechanics of Material Behavior*, (Drucker Anniversary Volume) Dvorak, G. J., and Shield, R. T., eds., Elsevier, Amsterdam, 1984, pp. 351–368.

10 Tamuzh, V. P., "On a Minimum Principle in the Dynamics of Rigid-Plastic Bodies," (in Russian) *Prik. Mat. Mekh.*, Vol. 26, 1962, pp. 715–722.

11 Martin, J. B., "Extremum Principles for a Class of Dynamic Rigid-Plastic Problems," *Int. J. Solids Structures*, Vol. 8, 1972, pp. 1185–1204.

12 Bodner, S. R., and Symonds, P. S., "Experimental and Theoretical Investigation of the Plastic Deformation of Cantilever Beams Subjected to Impulsive Loading," ASME JOURNAL OF APPLIED MECHANICS, Vol. 29, No. 4, 1962, pp. 719–727.

13 Aspden, R. J., and Campbell, J. D., "The Effect of Loading Rate on the Elasto-Plastic Flexure of Steel Beams," *Proceedings of the Royal Society*, Series *A*, Vol. 290, 1966, pp. 266–285.

14 Symonds, P. S., Mosquera, J. M., and Kolsky, H., "On Elastic-Plastic and Rigid-Plastic Dynamic Response With Strain Rate Sensitivity," Report NR-3 of Brown University, Division of Engineering to Office of Naval Research, Dec. 1983 (in preparation).

15 Mosquera, J. M., Kolsky, H., and Symonds, P. S., "Experiments, Finite Element Solutions, and a Simplified Elastic-Plastic Approach to Impact of Frames," Report NR-1 of Brown University, Division of Engineering to Office of Naval Research, Dec. 1983 (in preparation).

16 Perrone, N., "Response of Rate-Sensitive Frames to Impulsive Load," *J. Eng. Mech. Div., Proc. ASCE*, Vol. 97, No. EM1, 1971, pp. 49–62.

17 Martin, J. B., and Symonds, P. S., "Mode Approximations for Impulsively Loaded Rigid-Plastic Structures," *J. Eng. Mech. Div., Proc. ASCE*, Vol. 92, No. EM5, 1966, pp. 43–66.

18 Martin, J. B., and Lee, L. S. S., "Approximate Solutions for Impulsively Loaded Elastic-Plastic Beams," ASME JOURNAL OF APPLIED MECHANICS, Vol. 35, 1968, pp. 803–809.

Downloaded 02 May 2010 to 171.66.16.54. Redistribution subject to ASME license or copyright; see http://www.asme.org/terms/Terms_Use.cfm

Reliability of Axially Compressed Cylindrical Shells With General Nonsymmetric Imperfections

Isaac Elishakoff
Professor,
Department of Aeronautical Engineering,
Technion-Israel Institute of Technology,
Haifa, Israel

Johann Arbocz
Professor of Aircraft Structures,
Department of Aerospace Engineering,
Delft University of Technology,
Delft, The Netherlands

This paper deals with the effect of general, nonsymmetric random imperfections on the reliability of axially compressed cylindrical shells. Reliability is defined here as the probability of the structure not buckling below some fixed load. The paper is a sequel to an earlier study on cylindrical shells with axisymmetric imperfections. The problem is solved by the Monte Carlo Method. The initial imperfection functions are simulated via a numerical procedure, and the buckling load of each realization of the simulated initial imperfections is found by the Multimode Analysis. It is shown that the results of existing Initial Imperfection Data Banks can be directly incorporated in the reliability analysis. Experimental information and the data derived from it, rather than theoretical assumptions, is used for constructing the reliability-based design curves for shell structures.

Introduction

It is now generally recognized that initial geometric imperfections play a dominant role in reducing the buckling load of certain structures. As is well known, an axially compressed thin shell is highly imperfection sensitive in this context (see, for example, the surveys [1–3]).

This conclusion is mainly due to the work of a series of investigators [4–6], who arrived at it through recourse to specialized imperfections. However, despite the accepted theoretical explanation of the buckling behavior of these structures, the use of the concept of imperfection sensitivity in engineering practice is still in the ad-hoc stage and engineers prefer to rely on the "knockdown factor" [7] chosen so that its product with the classical buckling load yields a lower bound to available experimental data for the configuration in question. This apparent reluctance to take advantage of theoretical findings stems from the fact that most imperfection studies are conditional on detailed advance knowledge of the geometric imperfections of the particular structure, which is rarely possible. In an ideal case the imperfections can be measured experimentally and incorporated in the theoretical analysis to predict the buckling loads. This approach, however, while justified for single prototype-like structures, is impracticable as a general method of behavior prediction. Information on the type and magnitude of imperfections of a particular structure would be too specific and are not strictly valid for other realizations of the same structure even those obtained by the same manufacturing process.

In the light of these considerations and bearing in mind the scatter of the experimental results, it appears obvious that practical applications of the imperfection-sensitivity theories are conditional on their being combined with a statistical analysis of the imperfections and critical loads. The notion of randomness of the initial imperfections was given considerable attention in the literature, and a bibliography can be found in Amazigo's paper [8]. For the single-mode solutions the reader should consult Bolotin [9] (who pioneered the probabilistic approach to buckling) and Roorda [10].

Recently, Elishakoff [11–13] suggested to utilize the Monte Carlo Method for the solution of multimode problems involving random initial imperfection sensitivity. This method represents a logical remedy in view of the difficulties inherent in purely analytical approaches (based on unnecessary and often very restrictive assumptions on the properties of the initial imperfections and/or using heavily simplified solution procedures).

The first step of the Monte Carlo Method consists of simulating the random initial imperfection profiles via a special numerical procedure [14]; the second step comprises a numerical solution of the buckling problem for every realization of the initial imperfection profile; the third and last step involves a statistical analysis of the buckling loads (for a detailed description of the Monte Carlo Method see reference [15]). The reliability is determined as the fraction of an ensemble of shells of which the buckling loads exceed the specified load. In a recent paper the present writers [16] have applied the Monte Carlo Method to shells with random axisymmetric imperfections. In this paper, the same method will be applied to general nonsymmetric random imperfections.

To the best of our knowledge, there are three works that

Contributed by the Applied Mechanics Division for publication in the JOURNAL OF APPLIED MECHANICS.

Discussion on this paper should be addressed to the Editorial Department, ASME, United Engineering Center, 345 East 47th Street, New York, N. Y. 10017, and will be accepted until two months after final publication of the paper itself in the JOURNAL OF APPLIED MECHANICS. Manuscript received by ASME Applied Mechanics Division, April, 1982; final revision, November, 1983.

Copyright © 1985 by ASME
Downloaded 02 May 2010 to 171.66.16.54. Redistribution subject to ASME license or copyright; see http://www.asme.org/terms/Terms_Use.cfm

have been devoted to the analysis of cylindrical shells with general nonsymmetric random imperfections. Makaroff [17], at the Moscow Energetics Institute, carried out systematic analysis of initial imperfections. He used series of 30 cylindrical shells made of sheets of electrical grade pressboard. The initial imperfection was represented as a double Fourier series and the coefficients were treated as random variables. The analysis showed that the assumption of circumferential homogeneity of the initial imperfections was satisfactory (within the confidence limits used in the analysis), and the normality of their Fourier coefficients did not conflict with the experimental data. Makaroff also carried out a theoretical analysis of the buckling of stochastically imperfect shells, with the experimental data obtained earlier serving as the input for the description of the imperfections. He found a theoretical mean buckling load that exceeds its experimental counterpart by a factor of 1.35.

Fersht [18] generalized the method of truncated hierarchy, used earlier by Amazigo [19] for axisymmetric random imperfections, to include the nonsymmetric case. It turned out that for nonsymmetric imperfections a closed-form expression for the buckling load is unattainable and rather cumbersome numerical integrations have to be performed. Moreover, for the axisymmetric case, Fersht's numerical results do not agree with those of Amazigo [19].

Hansen [20] generalized his previous deterministic results of reference [21]. The main conclusion was that the imperfection parameters associated with the nonaxisymmetric modes appear only in three separate summations and the behavior of the system is governed by the values of these summations rather than by the individual imperfection amplitudes. It was assumed that the Fourier coefficients of the initial imperfections are jointly normal random variables with zero mean, that they are statistically independent and are identically distributed. Then the Monte Carlo Method was applied. For each sample problem the buckling load was found via the method of reference [21] and then the mean buckling loads were calculated. The role of the nonaxisymmetric imperfections turned out to be very important.

Probabilistic Properties and Simulation of the Initial Imperfections for a Finite Shell

Let us represent the initial imperfection functions as the following series

$$W_0(\xi,\theta)=\sum_{i=0}^{N_1}A_i\cos\, i\pi\xi+\sum_{k=1}^{N_2}\sum_{l=1}^{N_3}(C_{kl}\sin k\pi\xi\,\cos\, l\theta + D_{kl}\,\sin\, k\pi\xi\,\sin\, l\theta) \tag{1}$$

where

$$W_0(\xi,\theta)=\frac{w_0(\xi,\theta)}{t},\quad \xi=\frac{x}{L},\quad \theta=\frac{y}{R},\quad 0\le x\le L,\quad 0\le\theta\le 2\pi$$

$w_0(\xi,\theta)$ and $W_0(\xi,\theta)$ are dimensional and nondimensional initial imperfections; t, L, and R are the thickness, the length, and the radius of the shell, respectively; x is the axial and y is the circumferential coordinate. Notice that in equation (1) the first sum represents the axisymmetric part of the initial imperfection profile, whereas the second, double sum is associated with its nonsymmetric part. The axisymmetric part is expressed in the half-range cosine series, whereas the nonsymmetric part is represented by the half-range sine series, so that the series (1) sums up to the measured imperfection profile in the range $0\le x\le L$, $0\le\theta\le 2\pi$.

The mathematical expectation of $W_0(\xi,\theta)$ is given by

$$\langle W_0(\xi,\theta)\rangle=\sum_{i=0}^{N_1}\langle A_i\rangle\cos\, i\pi\xi+\sum_{k=1}^{N_2}\sum_{l=1}^{N_3}(\langle C_{kl}\rangle\sin\, k\pi\xi\,\cos\, l\theta + \langle D_{kl}\rangle\sin\, k\pi\xi\,\sin\, l\theta) \tag{2}$$

where $\langle\ \ldots\ \rangle$ denotes a mathematical expectation.

The autocovariance function becomes

$$\begin{aligned}C_{W_0}(\xi_1,\theta_1;\xi_2,\theta_2)&=\langle[W_0(\xi_1,\theta_1)-\langle W_0(\xi_1,\theta_1)\rangle][W_0(\xi_2,\theta_2)-\langle W_0(\xi_2,\theta_2)\rangle]\rangle\\&=\Big\langle\Big[\sum_{i=0}^{N_1}(A_i-\langle A_i\rangle)\cos\, i\pi\xi_1+\sum_{k=1}^{N_2}\sum_{l=1}^{N_3}(C_{kl}-\langle C_{kl}\rangle)\sin\, k\pi\xi_1\,\cos\, l\theta_1+\sum_{k=1}^{N_2}\sum_{l=1}^{N_3}(D_{kl}-\langle D_{kl}\rangle)\sin\, k\pi\xi_1\,\sin\, l\theta_1\Big]\\&\times\Big[\sum_{j=0}^{N_1}(A_j-\langle A_j\rangle)\cos\, j\pi\xi_2+\sum_{m=1}^{N_2}\sum_{n=1}^{N_3}(C_{mn}-\langle C_{mn}\rangle)\sin\, m\pi\xi_2\,\cos\, n\theta_2+\sum_{m=1}^{N_2}\sum_{n=1}^{N_3}(D_{mn}-\langle D_{mn}\rangle)\sin\, m\pi\xi_2\,\sin\, n\theta_2\Big]\Big\rangle\end{aligned} \tag{3}$$

For the sake of simplicity we rewrite equation (1) in an alternative way, replacing the double summation in equation (1) by a single summation

$$W_0(\xi,\theta)=\sum_{i=1}^{N_1}A_i\cos\, i\pi\xi+\sum_{r=1}^{N}(C_r\,\sin\, k_r\pi\xi\,\cos\, l_r\theta + D_r\,\sin\, k_r\pi\xi\,\sin\, l_r\theta) \tag{4}$$

where the quantities indexed with r are chosen so as to ensure the equivalence of the two series given by equations (1) and (4) and $N=N_2\times N_3$. The autocovariance function can be written as

$$\begin{aligned}C_{W_0}(\xi_1,\theta_1;\xi_2,\theta_2)&=\sum_{i=0}^{N_1}\sum_{j=0}^{N_1}K_{A_iA_j}\cos\, i\pi\xi_1\,\cos\, j\pi\xi_2+\sum_{i=0}^{N_1}\sum_{s=1}^{N}K_{A_iC_s}\cos\, i\pi\xi_1\,\sin\, k_s\pi\xi_2\,\cos\, l_s\theta_2+\sum_{i=0}^{N_1}\sum_{s=0}^{N}K_{A_iD_s}\cos\, i\pi\xi_1\,\sin\, k_s\pi\xi_2\,\sin\, l_s\theta_2\\&+\sum_{r=1}^{N}\sum_{j=0}^{N_1}K_{C_rA_j}\sin\, k_r\pi\xi_1\,\cos\, l_r\theta_1\,\cos\, j\pi\xi_2+\sum_{r=1}^{N}\sum_{j=0}^{N_1}K_{D_rA_j}\sin\, k_r\pi\xi_1\,\sin\, l_r\theta_1\,\cos\, j\pi\xi_2\\&+\sum_{r=1}^{N}\sum_{s=1}^{N}K_{C_rC_s}\sin\, k_r\pi\xi_1\,\cos\, l_r\theta_1\,\sin\, k_s\pi\xi_2\,\cos\, l_s\theta_2+\sum_{r=1}^{N}\sum_{s=1}^{N}K_{C_rD_s}\sin\, k_r\pi\xi_1\,\cos\, l_r\theta_1\,\sin\, k_s\pi\xi_2\,\sin\, l_s\theta_2\end{aligned} \tag{5}$$

Downloaded 02 May 2010 to 171.66.16.54. Redistribution subject to ASME license or copyright; see http://www.asme.org/terms/Terms_Use.cfm

$$+\sum_{r=1}^{N}\sum_{s=1}^{N} K_{D_rC_s} \sin k_r\pi\xi_1 \sin l_r\theta_1 \sin k_s\pi\xi_2 \cos l_s\theta_2$$

$$+\sum_{r=1}^{N}\sum_{s=1}^{N} K_{D_rD_s} \sin k_r\pi\xi_1 \sin l_r\theta_1 \sin k_s\pi\xi_2 \sin l_s\theta_2$$

where the variance-covariance matrices $K_{A_iA_j}$, . . . , etc. are defined as follows:

$$\begin{aligned}
K_{A_iA_j} &= \langle (A_i - \langle A_i \rangle)(A_j - \langle A_j \rangle) \rangle \\
K_{A_iC_s} &= \langle (A_i - \langle A_i \rangle)(C_s - \langle C_s \rangle) \rangle \\
K_{A_iD_s} &= \langle (A_i - \langle A_i \rangle)(D_s - \langle D_s \rangle) \rangle \\
K_{C_rC_s} &= \langle (C_r - \langle C_r \rangle)(C_s - \langle C_s \rangle) \rangle \\
K_{C_rD_s} &= \langle (C_r - \langle C_r \rangle)(D_s - \langle D_s \rangle) \rangle \\
K_{D_rD_s} &= \langle (D_r - \langle D_r \rangle)(D_s - \langle D_s \rangle) \rangle
\end{aligned} \tag{6}$$

If the autocovariance function $C_{W_0}(\xi_1, \theta_1; \xi_2, \theta_2)$ is known, then these quantities can be obtained as follows:

$$K_{A_iA_j} = \frac{1}{\pi^2}\int_0^{2\pi}\int_0^1\int_0^{2\pi}\int_0^1 C_{W_0}(\xi_1,\theta_1;\xi_2,\theta_2)$$

$$\times \cos i\pi\xi_1 \cos j\pi\xi_2 d\xi_1 d\theta_1 d\xi_2 d\theta_2$$

$$K_{A_iC_{mn}} = \frac{2}{\pi^2}\int_0^{2\pi}\int_0^1\int_0^{2\pi}\int_0^1 C_{W_0}(\xi_1,\theta_1;\xi_2,\theta_2)$$

$$\times \cos i\pi\xi_1 \sin m\pi\xi_2 \cos n\theta_2 \, d\xi_1 \, d\theta_1 \, d\xi_2 \, d\theta_2$$

$$K_{A_iD_{mn}} = \frac{2}{\pi^2}\int_0^{2\pi}\int_0^1\int_0^{2\pi}\int_0^1 C_{W_0}(\xi_1,\theta_1;\xi_2,\theta_2)$$

$$\times \cos i\pi\xi_1 \sin m\pi\xi_2 \sin n\theta_2 \, d\xi_1 \, d\theta_1 \, d\xi_2 \, d\theta_2$$

$$K_{A_jC_{kl}} = \frac{2}{\pi^2}\int_0^{2\pi}\int_0^1\int_0^{2\pi}\int_0^1 C_{W_0}(\xi_1,\theta_1;\xi_2,\theta_2)$$

$$\times \cos j\pi\xi_2 \sin k\pi\xi_1 \cos l\theta_1 \, d\xi_1 \, d\theta_1 \, d\xi_2 \, d\theta_2$$

$$K_{A_jC_{kl}} = \frac{2}{\pi^2}\int_0^{2\pi}\int_0^1\int_0^{2\pi}\int_0^1 C_{W_0}(\xi_1,\theta_1;\xi_2,\theta_2)$$

$$\times \cos j\pi\xi_2 \sin k\pi\xi_1 \sin l\theta_1 \, d\xi_1 \, d\theta_1 \, d\xi_2 \, d\theta_2$$

$$K_{C_{kl}C_{mn}} = \frac{4}{\pi^2}\int_0^{2\pi}\int_0^1\int_0^{2\pi}\int_0^1 C_{W_0}(\xi_1,\theta_1;\xi_2,\theta_2)$$

$$\times \sin k\pi\xi_1 \cos l\theta_1 \sin m\pi\xi_2 \cos n\theta_2 \, d\xi_1 \, d\theta_1 \, d\xi_2 \, d\theta_2$$

$$K_{D_{kl}C_{mn}} = \frac{4}{\pi^2}\int_0^{2\pi}\int_0^1\int_0^{2\pi}\int_0^1 C_{W_0}(\xi_1,\theta_1;\xi_2,\theta_2)$$

$$\times \sin k\pi\xi_1 \sin l\theta_1 \sin m\pi\xi_2 \cos n\theta_2 \, d\xi_1 \, d\theta_1 \, d\xi_2 \, d\theta_2$$

$$K_{D_{kl}D_{mn}} = \frac{4}{\pi^2}\int_0^{2\pi}\int_0^1\int_0^{2\pi}\int_0^1 C_{W_0}(\xi_1,\theta_1;\xi_2,\theta_2)$$

$$\sin k\pi\xi_1 \sin l\theta_1 \sin m\pi\xi_2 \sin n\theta_2 \, d\xi_1 \, d\theta_1 \, d\xi_2 \, d\theta_2 \tag{7}$$

Notice that if $W_0(\xi,\theta)$ is constant and

$$K_{A_iC_s} = K_{A_iD_s} = K_{C_rA_j} = K_{D_rA_j} = K_{C_rD_s} = K_{D_rC_s} = 0 \tag{8}$$

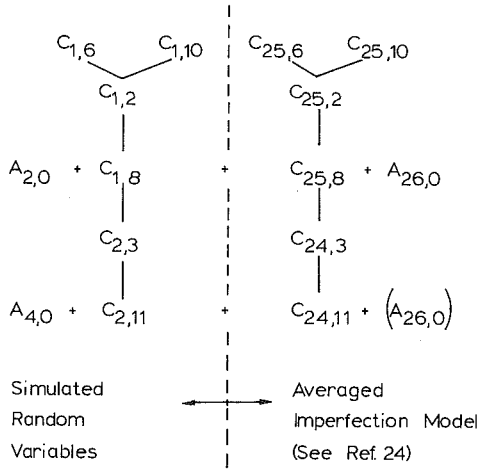


Fig. 1 Modified 15 modes imperfection model used for Monte Carlo method

for any combination of indices, and moreover

$$\begin{aligned}
K_{C_rC_s} &= K_{D_rD_s} \\
K_{C_rC_s} &= K_{C_rC_r}\delta_{l_rl_s}
\end{aligned} \tag{9}$$

where $\delta_{l_rl_s}$ is a Kronecker delta, then the initial imperfection is a weakly homogeneous function in the circumferential direction. Under the conditions (8) and (9) the autocovariance function takes the form

$$C_{W_0}(\xi_1,\theta_1;\xi_2,\theta_2) = \sum_{i=0}^{N_1}\sum_{j=0}^{N_1} K_{A_iA_j} \cos i\pi\xi_1 \cos j\pi\xi_2$$

$$+\sum_{r=1}^{N}\sum_{s=1}^{N} K_{C_rC_s} \sin k_r\pi\xi_1 \sin k_s\pi\xi_2 \cos l_r(\theta_2 - \theta_1) \tag{10}$$

i.e., it depends on $\theta_2 - \theta_1$ rather than on θ_1 and θ_2 separately. It can be shown that equations (8) and (9) represent not only the sufficient conditions but also the necessary ones. One could argue, that for the closed, nominally circular, seamless cylindrical shell the probabilistic properties would not be affected by a shift of the origin of the coordinate axes in the circumferential direction. Interestingly, in Makaroff's experiments [17] this weak homogeneity was preserved even for the series of shells with pronounced seams. Due to the frequent use of this property we will first show how to simulate the initial imperfections possessing weak homogeneity in the circumferential direction.

To simulate the large number of initial imperfection profiles needed for the Monte Carlo Method, first the mean values and the variance-covariance matrices of the measured initial imperfections must be determined. This involves the evaluation of the following ensemble averages for a sample of experimentally measured initial imperfections:

$$\tilde{A}_i^{(e)} = \frac{1}{M}\sum_{m=1}^{M} A_i^{(m)}; \quad \tilde{C}_r^{(e)} = \frac{1}{M}\sum_{m=1}^{M} C_r^{(m)}$$

$$K_{A_iA_j}^{(e)} = \frac{1}{M-1}\sum_{m=1}^{M}[A_i^{(m)} - \tilde{A}_i^{(e)}][A_j^{(m)} - \tilde{A}_j^{(e)}]$$

$$K_{C_rC_s}^{(e)} = \frac{1}{M-1}\sum_{m=1}^{M}[C_r^{(m)} - \tilde{C}_r^{(e)}][C_s^{(m)} - \tilde{C}_s^{(e)}] \tag{11}$$

where M is the number of sample shells, and m is the serial number of the shells. The variance-covariance matrices are positive-semidefinite and can be uniquely decomposed in the form

$$[K_{A_iA_j}^{(e)}] = [G][G]^T, [K_{C_rC_s}^{(e)}] = [G'][G']^T \tag{12}$$

Downloaded 02 May 2010 to 171.66.16.54. Redistribution subject to ASME license or copyright; see http://www.asme.org/terms/Terms_Use.cfm

where T means transpose and $[G]$, $[G']$ are lower-triangular matrices found by the Cholesky decomposition algorithm. Now we form the random vectors $\{B\}$ and $\{B'\}$, the elements of which are normally distributed, statistically independent with zero means and unit variance. Then the vectors of the Fourier coefficients of the initial imperfections are simulated as follows:

$$\{A\} = [G]\{B\} + \{\tilde{A}^{(e)}\}, \quad \{C\} = [G']\{B'\} + \{\tilde{C}^{(e)}\} \quad (13)$$

Having the desired large number of realizations of the vectors $\{B\}$ and $\{B'\}$ one obtains the same number of realizations of $\{A\}$ and $\{C\}$. The mean feature of this simulation technique [14] is that it is applicable for homogeneous, as well as nonhomogeneous random functions with given mean and autocovariance functions.

Equation (13) represents the simulated vectors $\{A\}$ and $\{C\}$ for the random imperfections, weakly homogeneous in the circumferential direction. For the imperfections which form a general nonhomogeneous random field, the refined simulation procedure, developed in reference [22] has to be utilized. The essence of this refinement is the replacement of the multiple summations in equations (2) and (4) by a single "string" and the dealing with the resultant mixed series (for details see reference [22]).

Multimode Deterministic Analysis for Each Realization of Random Initial Imperfections

The buckling load for each created shell is then calculated by the so-called Multimode analysis [23], which allows the incorporation of imperfection shapes in the form of the double Fourier series given in equation (1). By definition, the value of the loading parameter λ corresponding to the limit point of the prebuckling states is the theoretical buckling load. The number of modes of deformation included in the analysis is limited by practical considerations, like the available core size and the time required for obtaining the solution. Thus, since the shell buckling load will be determined by solving the governing equations for a particular set of modes, an attempt of optimizing the selection of these modes must be made. That is, it is necessary to locate those modes that dominate the prebuckling and buckling behavior of the shell. Previous investigations by Arbocz and Babcock [23, 24] have shown that to yield a noticeable decrease from the buckling load of the perfect shell, the initial imperfection harmonics used must include at least one mode with a significant initial amplitude and an associated eigenvalue that is close to the buckling load of the perfect shell. Furthermore, if the modes are so selected that the nonlinear coupling conditions are satisfied then the resulting buckling load of the shell generally will be lower than the buckling loads obtained with each mode considered separately.

Based on these considerations and the results published in reference [24] the imperfection model shown in Fig. 1 was selected for the Monte Carlo simulation. In this model $A_{2,0}$ stands for a half-wave cosine axisymmetric Fourier coefficient, with two half-waves in the axial direction and no waves in the circumferential direction. On the other hand $C_{1,10}$ stands for an asymmetric Fourier coefficient with a single half-wave in the axial direction and 10 full waves in the circumferential direction.

As pointed out in reference [24] the chosen imperfection model requires imperfection amplitudes at wave numbers that were not measured. This is due to the fact that in the early experimental work the mesh-spacing used was not sufficiently close to resolve all the harmonic amplitudes of interest. Therefore the Donnell-Imbert [25] imperfection model was fitted over the wave numbers actually measured and then the amplitudes of the harmonics of interest were obtained by extrapolation. It should be stressed here that the averaged (in

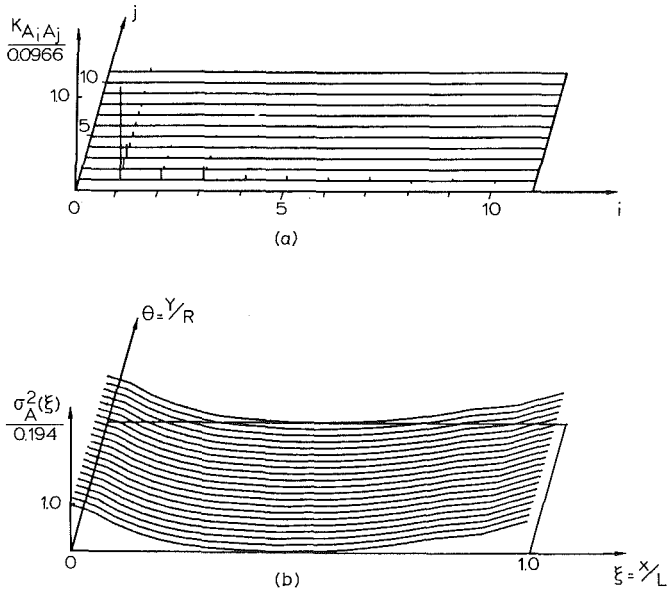


Fig. 2 (*a*) Elements of cross-correlation matrix $K_{A_iA_j}$ for simulated group of 500 *B*-shells, and (*b*) corresponding part of variance

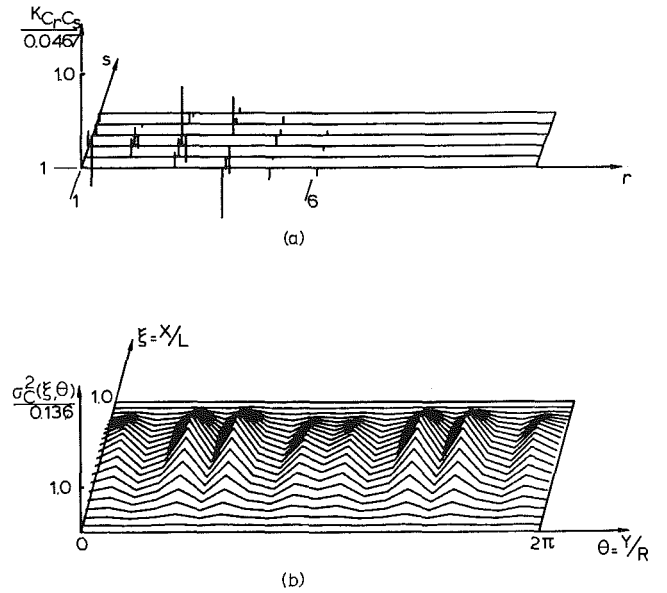


Fig. 3 (*a*) Elements of cross-correlation matrix $K_{C_rC_s}$ for simulated group of 500 *B*-shells, and (*b*) corresponding part of variance

the axial direction short wavelength) modes of the imperfection model shown in Fig. 1 must be included in the analysis in order to satisfy the nonlinear coupling conditions. Their initial amplitudes are actually insignificant.

For the purpose of the Monte Carlo Method the MIUTAM code [24] was incorporated into a new program, which then one by one automatically starts the calculations for the simulated imperfections and at the end lists all the buckling loads obtained.

Numerical Results and Discussion

The procedure described in the previous sections was applied to the group of shells, referred in reference [26] as *B*-shells. These shells were originally cut from thickwalled seamless brass tubing; the pieces were mounted on a mandrel and the outer surface was machined to the desired dimen-

Downloaded 02 May 2010 to 171.66.16.54. Redistribution subject to ASME license or copyright; see http://www.asme.org/terms/Terms_Use.cfm

Table 1 Fourier coefficients of *B*-shells

Coefficients \ Shell	*B*-1	*B*-2	*B*-3	*B*-4	Mean values
$A_{2,0}$	−0.0108	−0.0272	−0.0899	−0.0176	−0.0364
$A_{4,0}$	0.0226	−0.0078	−0.0255	−0.0096	−0.0050
$C_{1,2}$	0.417	0.393	0.741	0.223	0.4435
$C_{1,6}$	−0.078	−0.143	0.017	0.078	−0.0315
$C_{1,8}$	−0.264	−0.009	0.112	0.102	−0.0148
$C_{1,10}$	0.037	0.044	−0.246	−0.009	−0.0435
$C_{2,3}$	−0.101	0.034	−0.065	−0.002	−0.0335
$C_{2,11}$	0.010	−0.009	−0.028	0.014	−0.0033
$D_{1,2}$	0.024	−0.203	0.147	0.029	−0.0008
$D_{1,6}$	−0.390	0.058	0.128	−0.248	−0.1130
$D_{1,8}$	−0.029	0.087	0.185	−0.050	0.0483
$D_{1,10}$	−0.013	0.039	−0.031	−0.051	−0.0140
$D_{2,3}$	−0.070	−0.047	0.040	−0.015	−0.0230
$D_{2,11}$	0.013	−0.018	−0.004	0.002	−0.0018

For the group of *B*-shells:
$R = 101.6$ mm, $t = 0.2050$ mm, $L = 196.85$ mm,
$E = 1.065 \times 10^5$ N/mm^2, $\nu = 0.3$.
Note: Here $w_0^{(m)}$ is positive outward.

Table 2 Variance-covariance matrices $K_{C_rC_s}$ and $K_{D_rD_s}$

$K_{C_rC_s} =$

1,2	1,6	1,8	1,10	2,3	2,11	
0.46861^{-1}	-0.87197^{-3}	0.61544^{-2}	-0.24776^{-1}	-0.59778^{-2}	-0.37388^{-2}	1,2
-0.87197^{-3}	0.96697^{-2}	0.99562^{-2}	-0.65293^{-2}	-0.83271^{-3}	0.20500^{-3}	1,6
0.61544^{-2}	0.99562^{-2}	0.30567^{-1}	-0.13717^{-1}	0.56447^{-2}	-0.14967^{-2}	1,8
-0.24776^{-1}	-0.65293^{-2}	-0.13717^{-1}	0.18684^{-1}	0.26231^{-2}	0.20676^{-2}	1,10
-0.59778^{-2}	-0.83271^{-3}	0.56447^{-2}	0.26231^{-2}	0.37104^{-2}	0.21989^{-4}	2,3
-0.37388^{-2}	0.20500^{-3}	-0.14967^{-2}	0.20676^{-2}	0.21989^{-4}	0.36852^{-3}	2,11

$K_{D_rD_s} =$

1,2	1,6	1,8	1,10	2,3	2,11	
0.21394^{-1}	-0.33159^{-2}	0.24798^{-2}	-0.47927^{-2}	0.43517^{-2}	0.11773^{-2}	1,2
-0.33159^{-2}	0.60673^{-1}	0.24746^{-1}	0.32506^{-2}	0.76675^{-2}	-0.26069^{-2}	1,6
0.24798^{-2}	0.24746^{-1}	0.11956^{-1}	0.11053^{-2}	0.35032^{-2}	-0.80206^{-3}	1,8
-0.47927^{-2}	0.32506^{-2}	0.11053^{-2}	0.14992^{-2}	-0.88147^{-3}	-0.32594^{-3}	1,10
0.43517^{-2}	0.76675^{-2}	0.35032^{-2}	-0.88147^{-3}	0.22434^{-2}	-0.12750^{-3}	2,3
0.11773^{-2}	-0.26069^{-2}	-0.80206^{-3}	-0.32594^{-3}	-0.12750^{-3}	0.16719^{-3}	2,11

sions. The geometric and material properties of the *B*-shells are summarized in Table 1.

As is seen from Fig. 1, the simulation procedure was applied only to the eight lower order modes, namely $A_{2,0}$, $A_{4,0}$, $C_{1,2}$, $C_{1,6}$, $C_{1,8}$, $C_{1,10}$, $C_{2,3}$, and $C_{2,11}$. The remaining seven higher-order modes, namely $A_{26,0}$, $C_{24,3}$, $C_{24,11}$, $C_{25,2}$, and $C_{25,10}$ were obtained by extrapolation from the corresponding Donnell-Imbert imperfection model [24, 25].

Figure 2 shows the elements of the variance-covariance matrices $K_{A_iA_j}$ and the corresponding part of the variance, denoted by $\sigma^2{}_A(\xi)$

$$\sigma^2{}_A(\xi) = \sum_{i=0}^{N_1} \sum_{j=0} K_{A_iA_j}\, \delta_{ij} \cos\pi i\xi \cos\pi j\xi \tag{15}$$

For fixed ξ, this part of the variance is constant, since equation (15) is associated with the axisymmetric part of the imperfections.

Figures 3 and 4 show the elements of the variance-covariance matrices $K_{C_rC_s}$ and $K_{D_rD_s}$, respectively, and the associated parts of the variance, denoted by $\sigma^2{}_C(\xi,\theta)$ and $\sigma^2{}_D(\xi,\theta)$:

$$\sigma^2{}_C(\xi,\theta) = \sum_{r=1}^{N} \sum_{s=1}^{N} K_{C_rC_s} \times \sin k_r\pi\xi \sin k_s\pi\xi \cos l_r\theta \cos l_s\theta \tag{16}$$

$$\sigma^2{}_D(\xi,\theta) = \sum_{r=1}^{N} \sum_{s=1}^{N} K_{D_rD_s} \times \sin k_r\pi\xi \sin k_s\pi\xi \sin l_r\theta \sin l_s\theta \tag{17}$$

Figure 5 portrays the probabilistic characteristics of the 500 simulated shells. Figure 5(*a*) shows the mean imperfection function, whereas Fig. 5(*b*) displays the variance. As is seen from Fig. 5 neither the mean function nor the variance are constant in the circumferential direction, implying that the random imperfections do not constitute a circumferentially homogeneous field. This conclusion can also be deduced from Table 2, which lists the values of $K_{C_rC_s}$ and $K_{D_rD_s}$. An examination of this table reveals that the corresponding elements of these matrices not only do not coincide, but a

Downloaded 02 May 2010 to 171.66.16.54. Redistribution subject to ASME license or copyright; see http://www.asme.org/terms/Terms_Use.cfm

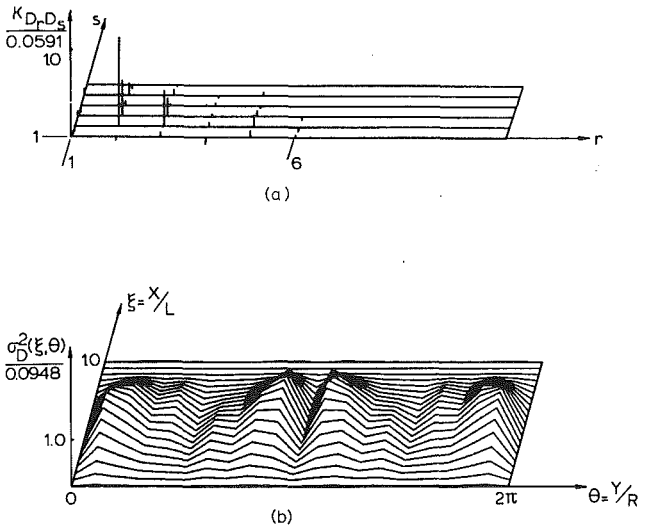


Fig. 4 (*a*) Elements of cross-correlation matrix $K_{D_r D_s}$ for simulated group of 500 *B*-shells, and (*b*) corresponding part of variance

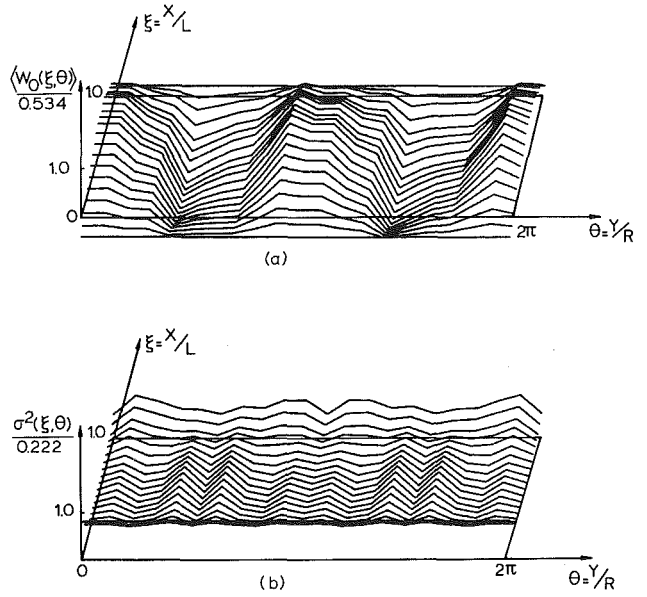


Fig. 5 Probabilistic characteristics of the simulated group of 500 *B*-shells. (*a*) mean function, and (*b*) variance.

ratio between them may well exceed 10. Thus the homogeneity assumption adopted in reference [8] turns out to be unjustifiable even for seamless shells.

To calculate the reliability functions shown in Fig. 6 the following dimensions corresponding to shell *B*-1 [26] were used: length of 196.85 mm, radius of 101.60 mm, and thickness of 0.205 mm. In addition, for the buckling load calculations of shells with axisymmetric imperfections the one-sided transfer-function shown in Fig. 7 was chosen. This was done due to the fact [27], that for a finite length shell the buckling load is sensitive only to those axisymmetric imperfections that point inward at the mid-plane of the shell (at $x = L/2$).

In Fig. 6, curve 1 represents the reliability function for the case of purely axisymmetric imperfections (with an estimated mean buckling load of 0.935), whereas curve 2 shows the reliability function for the 15-modes nonsymmetric imperfection mode (with an estimated mean buckling load of 0.739). As can be seen, the reliability estimate depends strongly on the number of terms taken into account, i.e., it is

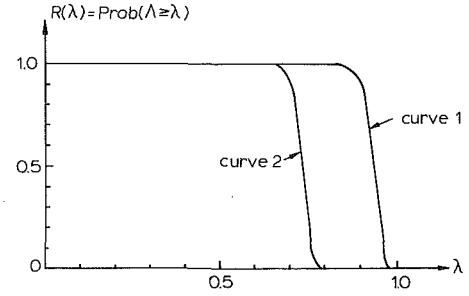


Fig. 6 Reliability functions for simulated group of 500 *B*-shells

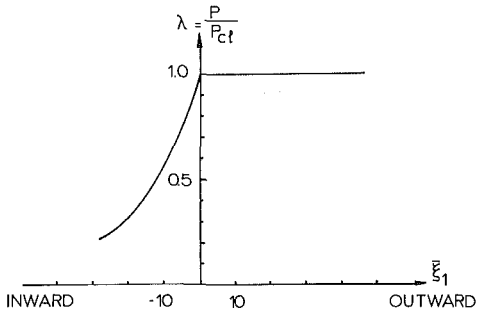


Fig. 7 One-sided transfer function used for axisymmetric imperfections only [27]

sensitive to the adequacy of the underlying deterministic model. As a check on the correctness of the simulated results the 15-modes imperfection model shown in Fig. 1 was used to calculate the collapse loads of the original four *B*-shells involved, using the experimentally measured initial imperfections in place of the simulated random variables. These computations yielded for the shells *B*-1, *B*-2, *B*-3, and *B*-4, respectively, the following collapse loads 0.751, 0.746, 0.740, and 0.781 with a mean of 0.756. Closeness to the simulated results is remarkable. It should also be mentioned here that the theoretical collapse load of $\rho_s = 0.66$, reported in reference [24] for the shell *B*-1, was entirely based on the Donnell-Imbert [25] imperfection model. Considering the results shown in Fig. 6 further, one sees that the inclusion of some asymmetric imperfection components has reduced the estimate of the mean buckling load considerably, though it is still higher than the experimental mean buckling load for the group of B-shells of 0.592 [26]. However, as work currently in progress has shown, further refinements in the nonsymmetric random imperfection model will lead to lower simulated buckling loads.

Conclusions

One can summarize the results obtained so far as follows:

1 It has been demonstrated that the Monte Carlo Method can be used successfully to obtain reliability functions for shells with axisymmetric as well as asymmetric imperfections.

2 It has been found that for finite shells, nonstationary statistic must be used (thus ergodicity is strictly speaking not applicable).

3 Using the simulation procedure developed by Elishakoff [11, 22] the measured initial imperfections have been used directly to generate input for the Monte Carlo Method.

It is hoped that these preliminary results will encourage many investigators all over the world to compile extensive

Downloaded 02 May 2010 to 171.66.16.54. Redistribution subject to ASME license or copyright; see http://www.asme.org/terms/Terms_Use.cfm

experimental information on initial imperfections classified according to the manufacturing procedures. The existence of these Initial Imperfection Data Banks will make it possible to associate statistical measures with the different methods of fabrication. As outlined in this paper, the variance-covariance matrices and the mean vectors can be used effectively to generate input for the Monte Carlo Method, which in turn yields the reliability functions associated with the different manufacturing processes. It is felt that by this means the imperfection sensitivity concept can be finally introduced routinely into the design procedures since the Monte Carlo Method described in this paper seems to offer the means of combining the Lower Bound Design Philosophy with the notion of Goodness Classes. Thus shells manufactured by a process, which produces inherently a less damaging initial imperfection distribution, will not be penalized because of the low experimental results obtained with shells produced by another process, which generates a more damaging characteristic initial imperfection distribution.

Acknowledgment

This work has been supported by the Delft University of Technology during I. Elishakoff's sabbatical stay at the Department of Aerospace Engineering in 1979/1980 and by the Dutch Foundation of the Technical Sciences (STW) during a visit in the summer of 1983. These aids and the warm and kind hospitality are gratefully acknowledged. Thanks are also due to the Technion Research Promotion Fund for partial support of this study.

References

1 Hutchinson, J. W., and Koiter, W. T., "Postbuckling Theory," ASME *Applied Mechanics Review*, Dec. 1970, pp. 1353–1366.

2 Tvergaard, V., "Buckling Behaviour of Plate and Shell Structure," in *Theoretical and Applied Mechanics*, Koiter, W. T., ed., North-Holland, 1976, pp. 233–247.

3 Budiansky, B., and Hutchinson, J. W., "Buckling: Progress and Challenge," in *Trends in Solid Mechanics 1979*, Proceedings of the Symposium Dedicated to the 65th Birthday of W. T. Koiter, Besseling, J. F., and Van der Heijden, A. M. A., eds., Sijthoff and Nordhoff, Alphen aan den Rijn, 1979, pp. 93–116.

4 Donnell, L. H., and Wan, C. C., "Effect of Imperfections on the Buckling of Thin Cylinders and Columns Under Axial Compression," ASME JOURNAL OF APPLIED MECHANICS, Vol. 17, 1950, pp. 73–83.

5 Koiter, W. T., "The Effect of Axisymmetric Imperfections on the Buckling of Cylindrical Shells Under Axial Compression," *Proceedings of the Royal Netherlands Academy of Sciences*, Amsterdam, Series B., Vol. 66, No. 5, 1963, pp. 265–279.

6 Budiansky, B., and Hutchinson, J. W., "Dynamic Buckling of Imperfection Sensitive Structures," in *Proceedings of the Eleventh Congress on Theoretical and Applied Mechanics*, Gortler, M., ed., Springer-Verlag, Berlin, 1964, pp. 636–651.

7 NASA, "Buckling of Thin-Walled Circular Cylinders," NASA SP 8007, Aug. 1968.

8 Amazigo, J. C., "Buckling of Stochastically Imperfect Structures," in *Buckling of Structures*, Budiansky, B., ed., IUTAM Symposium, Cambridge, Mass., 1974, Springer-Verlag, Berlin, 1976, pp. 172–182.

9 Bolotin, V. V., *Statistical Methods in Structural Mechanics*, Holden-Day, San Francisco, 1969.

10 Roorda, J., *Buckling of Elastic Structures*, University of Waterloo Press, 1980.

11 Elishakoff, I., "Impact Buckling of Thin Bar Via Monte Carlo Method," ASME JOURNAL OF APPLIED MECHANICS, Vol. 45, 1978, pp. 586–590.

12 Elishakoff, I., "Buckling of a Stochastically Imperfect Finite Column on a Nonlinear Elastic Foundation—A Reliability Study," ASME JOURNAL OF APPLIED MECHANICS, Vol. 46, 1979, pp. 411–416.

13 Elishakoff, I., "Hoff's Problem in a Probabilistic Setting," ASME JOURNAL OF APPLIED MECHANICS, Vol. 47, 1980, pp. 403–408.

14 Elishakoff, I., "Simulation of Space-Random Fields for Solution of Stochastic Boundary-Value Problems," *Journal of the Acoustical Society of America*, Vol. 65, No. 2, 1979, pp. 399–403.

15 Elishakoff, I., *Probabilistic Methods in the Theory of Structures*, Wiley-Interscience, New York, 1983, pp. 433–468.

16 Elishakoff, I., and Arbocz, J., "Reliability of Axially Compressed Cylindrical Shells With Random Axisymmetric Imperfections," *International Journal of Solids and Structures*, Vol. 18, 1982, pp. 563–585.

17 Makaroff, B. P., "Statistical Analysis of Deformation of Imperfect Cylindrical Shells," in *Strength Calculations* (in Russian), Vol. 15, 1971, Moscow "Mashinostroenie" Publishing House, pp. 240–256.

18 Fersht, R., "Buckling of Cylindrical Shells With Random Imperfections," in *Thin Shell Structures, Theory, Experiment and Design*, Fung, Y. C., and Sechler, E. E., eds., Prentice-Hall, Englewood Cliffs, N.J., 1974, pp. 325–341.

19 Amazigo, J. C., "Buckling Under Axial Compression of Long Cylindrical Shells with Random Axisymmetric Imperfections," *Quarterly of Applied Mathematics*, Vol. 26, 1969, pp. 537–566.

20 Hansen, J., "General Random Imperfections in the Buckling of Axially Loaded Cylindrical Shells," *AIAA Journal*, Vol. 15, 1977, pp. 1250–1256.

21 Hansen, J., "Influence of General Imperfections in Axially Loaded Cylindrical Shells," *International Journal of Solids and Structures*, Vol. 11, 1975, pp. 1223–1233.

22 Elishakoff, I., "Simulation of an Initial Imperfection Data Bank, Part 1: Isotropic Shells With General Imperfections," TAE Report 500, Department of Aeronautical Engineering, Technion-Israel Institute of Technology, Haifa, Israel, July, 1982.

23 Arbocz, J., and Babcock, C. D., Jr., "A Multi-Mode Analysis for Calculating Buckling Loads of Imperfect Cylindrical Shells," GALCIT Report SM-74-4, California Institute of Technology, Pasadena, Calif., June 1974.

24 Arbocz, J., and Babcock, C. D., "Prediction of Buckling Loads Based on Experimentally Measured Initial Imperfections" in *Buckling of Structures*, Budiansky, B., ed., IUTAM Symposium, Cambridge, Mass., 1974, Springer-Verlag, Berlin, 1976, pp. 291–311.

25 Imbert, K., "The Effect of Imperfections on the Buckling of Cylindrical Shells," Aeronautical Engineer Thesis, California Institute of Technology, Pasadena, Calif., June 1971.

26 Arbocz, J., and Abramovich, H., "The Initial Imperfection Data Bank at the Delft University of Technology—Part I," Report LR-290, Department of Aerospace Engineering, Delft University of Technology, Delft, The Netherlands, Dec., 1979.

27 Babcock, C. D., Jr., and Sechler, E. E., "The Effect of Initial Imperfections on the Buckling Stress of Cylindrical Shells," NASA TN D-1510, Dec. 1962, pp. 135–142.

Downloaded 02 May 2010 to 171.66.16.54. Redistribution subject to ASME license or copyright; see http://www.asme.org/terms/Terms_Use.cfm

Postbuckling Analysis for the Bending of a Long Beam With a Thin, Open, Circular Cross Section

R. C. Benson
Associate Professor,
Department of Mechanical Engineering,
University of Rochester,
Rochester, N.Y. 14627
Mem. ASME

A longitudinal bending moment applied to a thin, open section beam induces limit point buckling, due to a second-order effect that flattens the leaves of the cross section. It is shown here, for the case of a circular cross section, that the leaves themselves may exhibit multiple equilibrium configurations. Thus, the postbuckling behavior of the beam is not uniquely defined, and perturbations may shift the system to an unexpected loading path. In this paper, the various equilibrium configurations are examined and judged for stability. A "perfect" bifurcating geometry is identified, and a form of imperfection sensitivity is observed.

Introduction

Thin, open section beams in bending have long been known to exhibit limit point buckling [1]. More recently there have been observations of bifurcation-type instabilities in conjunction with the limit point behavior. For example, Benson [2] found bifurcating moment-curvature graphs for certain types of open section beams, and Fabian [3] found that thin tubes bifurcate when a mode of cylindrical flattening gives way to a mode of axial wrinkling. An interesting feature of reference [2] is that the bifurcating behavior is not associated with a fundamentally different form of deformation. Rather, the deformation throughout remains within the kinematical restrictions of longitudinal bending and cross-sectional flattening.

It is the purpose of this paper to develop further an understanding of multiple-path postbuckling in an open section beam. Using an open circular section for the model, it is shown that the familiar loading path, with the buckling limit point, is also accompanied by a nonintersecting equilibrium path. Together, these two curves create the possibility that, for specified beam curvature, there is either a single stable solution or two stable solutions separated by an unstable solution. For one critical cross-sectional geometry the equilibrium curves touch, creating the "perfect" bifurcating geometry reported in reference [2]. In relation, the other geometries exhibit behavior familiar from the study of imperfection sensitivity [4].

Governing Equations

Considered here is the equilibrium, in pure bending, of a long beam with a thin, symmetrical, open, cross section. The kinematical assumptions and definitions of symbols are the same as in reference [2] to which the reader is directed. A representative geometry is shown in Fig. 1. Equilibrium of the beam is governed by the following nondimensional equations drawn from reference [2]:

$$\frac{dx}{ds} = \cos\phi(s), \qquad x(0) = 0, \tag{1}$$

$$\frac{dy}{ds} = \sin\phi(s), \qquad y(0) = 0, \tag{2}$$

$$\frac{dV}{ds} = \rho(s) = -12\kappa^2[y(s) - \bar{y}], \quad V(0) = 0, \quad V(1) = 0, \tag{3}$$

$$\frac{dM_s}{ds} = -V(s)\cos\phi(s), \qquad M_s(1) = 0, \tag{4}$$

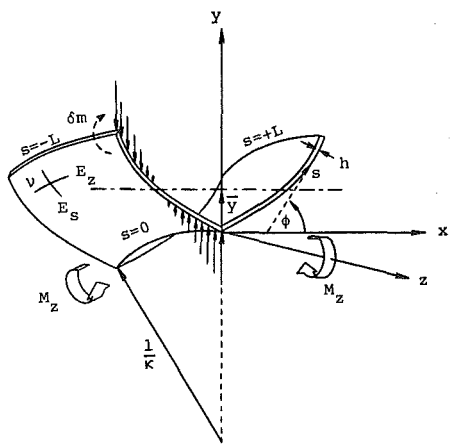


Fig. 1 Geometry

Contributed by the Applied Mechanics Division and presented at the Winter Annual Meeting, New Orleans, La., December 9-14, 1984 of THE AMERICAN SOCIETY OF MECHANICAL ENGINEERS.

Discussion on this paper should be addressed to the Editorial Department, ASME, United Engineering Center, 345 East 47th Street, New York, N.Y. 10017, and will be accepted until two months after final publication of the paper itself in the JOURNAL OF APPLIED MECHANICS. Manuscript received by the ASME Applied Mechanics Division, November, 1983; final revision, May 1984. Paper No. 84-WA/APM-46.

Copies will be available until August, 1985.

Copyright © 1985 by ASME
Downloaded 02 May 2010 to 171.66.16.54. Redistribution subject to ASME license or copyright; see http://www.asme.org/terms/Terms_Use.cfm

$$\frac{d\phi}{ds} = \frac{d\phi_0}{ds} + M_s(s), \qquad \phi(0) = \phi_0(0), \tag{5}$$

$$\bar{y} = \int_0^1 y(s)ds, \tag{6}$$

$$M_s(0) = \int_0^1 x(s)\rho(s)ds, \tag{7}$$

$$I = 2\int_0^1 [\,y(s) - \bar{y}]^2 ds + (\epsilon/6)\int_0^1 [\cos\phi(s)]^2 ds, \tag{8}$$

$$M_z = 12I\kappa. \tag{9}$$

In equation (9), ϵ is the square of the ratio of the leaf thickness, h, to the leaf length, L.

To restore dimensionally to the geometric variables that describe the cross section, the following replacements should be made for the arc length, horizontal coordinate, vertical coordinate, neutral axis, and area moment of inertia.

$$s \to \frac{s}{L}, \quad x \to \frac{x}{L}, \quad y \to \frac{y}{L}, \quad \bar{y} \to \frac{\bar{y}}{L}, \quad I \to \frac{I}{hL^3}. \tag{10}$$

The cross-sectional leaf profile is defined in general by the slope angle functions $\phi_0(s)$, before deformation, and $\phi(s)$, after deformation. For the distributed load, shear force, and bending moment acting in the cross section, the dimensional replacements are

$$\rho \to \frac{\rho L^3}{D}, \quad V \to \frac{VL^2}{D}, \quad M_s \to \frac{M_s L}{D}, \tag{11}$$

where $D = E_s h^3/[12(1-\nu^2)]$. The longitudinal variables of bending moment and curvature are dimensionalized by taking

$$M_z \to \frac{M_z h}{DL\gamma}, \quad \kappa \to \frac{\kappa L^2 \gamma}{h}, \tag{12}$$

where $\gamma = [(1-\nu^2)E_z/E_s]^{1/2}$.

To integrate equations (1)–(5) one must specify ϕ_0, and κ and iteratively adjust the values of the neutral axis, $\bar{y}$, and the centerline cross moment, $M_s(0)$, to satisfy the boundary conditions $V(1) = 0$ and $M_s(1) = 0$ at the free edge of the leaf. All of this may be done without knowledge of I and M_z which are uncoupled from equations (1)–(7) and may be calculated afterward. The resultants $\bar{y}$ and $M_s(0)$ also serve as identifying parameters to distinguish among the several solutions that can exist for the same $\phi_0(s)$, and κ (and sometimes even for the same I and M_z).

In what follows, an analysis is made for the case of a very thin beam with a circular cross section:

$$\epsilon = 0, \qquad \phi_0(s) = \psi s. \tag{13}$$

Here ψ denotes the sweep angle (used in radians in all equations but discussed in degrees) of one of the leaves. Solutions were obtained numerically.

Multiple Solutions

Three cross sections are to be studied in detail: $\psi = 130$ deg $\psi = 155$ deg, and $\psi = 180$ deg. Results are graphed for the longitudinal bending moment M_z, the centerline cross moment $M_s(0)$, and the neutral axis $\bar{y}$ in Fig. 2, 3, and 4, respectively. An examination of these results begins with the $\psi = 155$ deg curves of Fig. 2. It is seen that for $\kappa < 2$, M_z rises in the expected "soft" elastic response (i.e., increasingly diminished from the linear elastic response). Near $\kappa = 2$, the curve peaks at $M_z \approx 2.41$ and makes a sharp turn downward to follow the "collapse-inward" path. Crossing this first path is a secondary equilibrium branch, which only exists for $\kappa > 2$. The lower half of the secondary branch is labeled the "collapse-outward" path, and the upper half is labeled the "center-geometry." The motivation for these path names is based on the type of postbuckling deformation that occurs in the leaves.

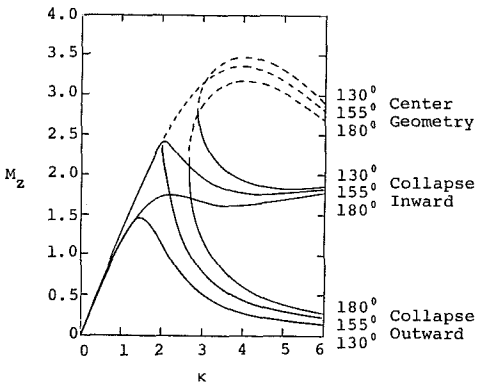


Fig. 2 Longitudinal moment

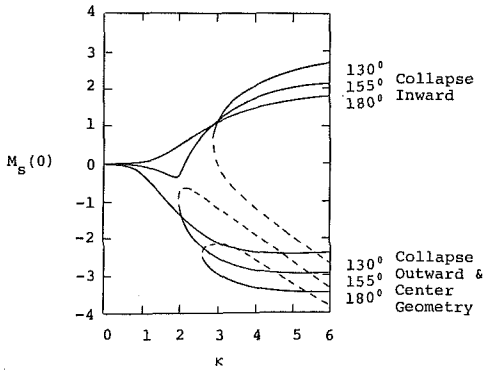


Fig. 3 Centerline cross moment

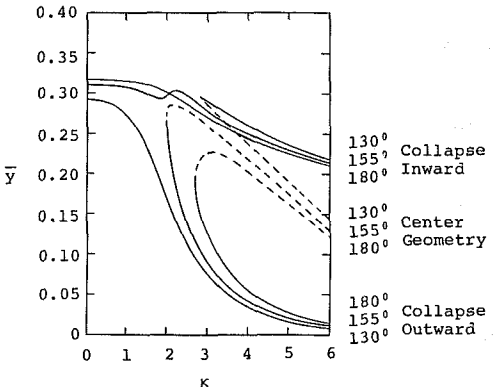


Fig. 4 Neutral axis

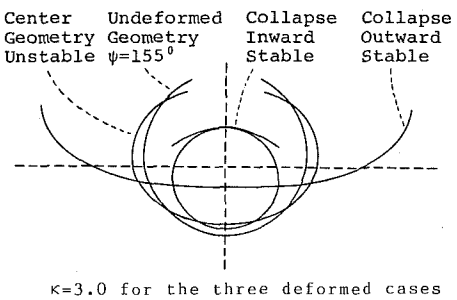


Fig. 5 Example cross-sectional deformations

For illustration see Fig. 5. On a common neutral axis and centerline, the three possible deformed geometries that can exist for $\psi = 155$ deg and $\kappa = 3$ are shown. For comparison, the undeformed geometry is also shown. The collapse-inward

Downloaded 02 May 2010 to 171.66.16.54. Redistribution subject to ASME license or copyright; see http://www.asme.org/terms/Terms_Use.cfm

drawing of Fig. 5 corresponds to the postbuckling behavior attributed to the $\psi = 155$ deg circular section of reference [2]. The leaves reach equilibrium by rolling in on each other.[1] The collapse-outward drawing shows the leaves opening out from each other. This matches the postbuckling behavior attributed to the $\psi = 155$ deg circular section of reference [2]. The center-geometry, which to the author's knowledge is newly presented here, is an unstable equilbrium that separates the stable collapse-inward and collapse-outward configurations. The center-geometry also shows the least change from the undeformed configurations. In Figs. 2–4 and 6, the loci of unstable equilibria are drawn with dashed, rather than solid, lines.

Continued study of Figs. 2–4 reveals that the $\psi = 155$ deg beam experiences a near-bifurcation at $\kappa = 2$. As κ is diminished from a greater value, all three postbuckled configurations approach each other in every mechanical detail and then coalesce to form the single, stable, loading for $\kappa < 2$. With the reader's indulgence the $\psi = 155$ deg geometry will henceforth be referred to as the "bifurcating" case, despite the fact that Figs. 2–4 reveal a slight favoritism for the collapse-inward branch[2].

Attention is next focused on the open circular geometries of $\psi = 130$ deg and $\psi = 180$ deg, which are both 25 deg removed from the bifurcating geometry. The continuous deformation path for $\psi = 130$ deg distinctly favors the collapse-outward postbuckling geometry. The secondary branch, which combines the collapse-inward and center-geometry equilibria, is considerably far removed. The $\psi = 130$ deg beam could be made to hold a collapse-inward equilibrium, but that would require the temporary intervention of an external load on the leaves to roll them inward. The $\psi = 180$ deg results are similarly interpreted, only this time the continuous deformation path favors the collapse-inward geometry, and the collapse-outward geometry joins the center-geometry on the secondary branch. The two branches do not meet at a bifurcation point.

There is other interesting information to be gleaned from Figs. 3 and 4. As κ increases past the point where three equilibria appear, $\kappa \equiv \kappa_3$, the centerline cross moment, $M_s(0)$, becomes, respectively, positive, negative, and negative for the collapse-inward, collapse-outward, and center-geometry cases. The author can further report that, for the two stable geometries, the cross moment, $M_s(s)$, tends monotonically to zero over the leaf profile, $0 \le s \le 1$. The unstable center-geometry, however, exhibits a cross moment that is negative at the centerline, rises to a peak positive value, and then diminishes to zero at the free edge. Physically interpreted, the two stable configurations are everywhere rolled out or rolled in from the undeformed cross section. The center-geometry lies flatter across the middle portion of the cross section and more inwardly curled near the leaf edges. Figure 5 reflects this behavior.

Figure 4 exhibits a convenient result. In the postbuckled regime, the unstable center-geometry always has a neutral axis, $\bar{y}$, which falls between a lesser and greater $\bar{y}$ associated with the two stable geometries. It is known from the study of single degree-of-freedom systems that two stable equilibria are necessarily separated by an unstable equilibrium. There is no such rule for multiple degree-of-freedom systems or continuum models as there is not, in general, a sensible way to determine if one geometry is "between" others. Thus it comes as a pleasant surprise that this continuum problem yields a scalar quantity that may be used to order the equilibria.

[1] The depicted geometry is self-penetrating and thus physically inadmissible. The true geometry would have the leaves sliding over each other. This complicated configuration was not calculated as it would not aid in the principal task of demonstrating the existence of multiple equilibrium configurations.

[2] True bifurcation was found numerically to be bracketed by $\psi = 154.5$ deg and $\psi = 155.0$ deg.

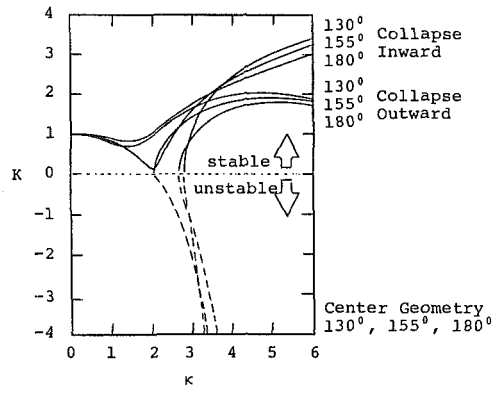


Fig. 6 Perturbation stiffness

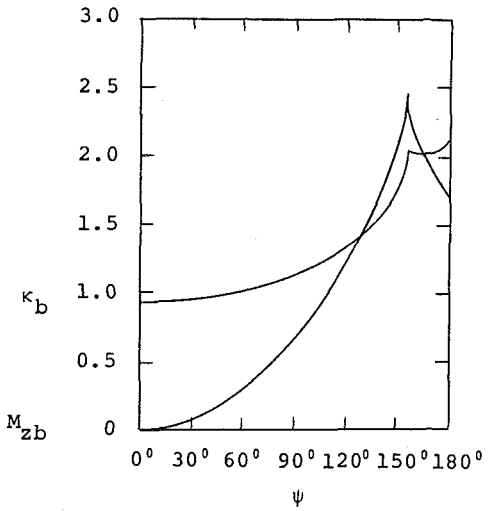


Fig. 7 Buckling moment and curvature

Note in Figs. 4 and 5 that, over the range of deformation, the greatest $\bar{y}$ occurs for $\kappa = 0$. Although it is not depicted, the same may be said for the area moment of inertia, I. The curvature value at which three solutions appear, κ_3, is seen in Fig. 2 to be greater than or equal to the curvature at which the bending moment peaks, κ_b. The two are equal for the bifurcating geometry.

Stability

Throughout this paper the terms "buckling" and "instability" are used to describe different phenomena. "Buckling" refers to the limit point collapse usually associated with this problem. When a bending moment is increased past the local maximum M_{zb}, the beam jumps to a distant configuration, $\kappa >> \kappa_b$. As is well understood, if curvature, rather than bending moment is specified, then the beam can follow the downward sloping portion of Fig. 2. However, for $\kappa > \kappa_3 \ge \kappa_b$ there can be three distinct solutions, and it is reasonable to ask if the equilibria are "stable" with respect to small perturbations in the cross section. An unstable geometry will jump dynamically to a stable configuration at the same κ but with different resultants $M_s(0)$, $\bar{y}$, I, and M_z. Put briefly, buckling is a horizontal jump in Fig. 2; instability is a vertical jump in Fig. 2.

A perturbation loading, artificially applied to the cross section, could be represented in a power series as follows:

$$\delta M_s(s) \equiv \delta m + \delta m' s + \delta m'' s^2 + \ldots, \qquad (14)$$

where δm, $\delta m'$, etc. are constant coefficients. Complete generality of form is not required, however, as it proves sufficient to consider only the leading term

Downloaded 02 May 2010 to 171.66.16.54. Redistribution subject to ASME license or copyright; see http://www.asme.org/terms/Terms_Use.cfm

$$\delta M_s(s) = \delta m, \qquad \delta m' = \delta m'' = \ldots = 0, \tag{15}$$

to observe the earliest occurrence of instability, i.e., at $\kappa = \kappa_3$. With all other parameters held fixed, δm was applied to the leaf edges (see Fig. 1), and the perturbed cross-sectional geometry was calculated. For the collapse-inward and collapse-outward geometries it was found that the leaves were everywhere rotated, $\delta\phi(s)$, in the same sense as δm, and that the rotation increased or decreased monotonically from $\delta\phi(0) = 0$ to $\delta\phi(1) = 0$, Conversely, the center-geometry was montonically rotated in the opposite sense of δm. Given this monotonicity, a "perturbation stiffness" was defined,

$$K \equiv \lim_{\delta m \to 0} \left[\frac{\delta\phi(1)}{\delta m} \right]^{-1}, \tag{16}$$

as a resultant measure of the entire cross-sectional change induced by δm.

The perturbation stiffness was calculated numerically for the same geometries as were considered in the last section. Results are presented in Fig. 6, using the format of Figs. 2–4. It will be seen that, in all cases, the secondary equilibrium branch crosses the $K = 0$ line with vertical slope at $\kappa = \kappa_3$. The collapse-inward and collapse-outward geometries occupy the zone $K > 0$, and the center geometry occupies the zone $K < 0$. Using the "kinetic approach" to stability [5], one concludes that, with $K < 0$, the center-geometry departs the equilibrium configuration exponentially when perturbed by δm. Hence it is unstable. With $K > 0$, the collapse-inward and collapse-outward geometries (and of course the solutions for $\kappa < \kappa_3$) experience bounded vibrations and thus are stable under perturbations by δm.

Some retrospective stability observations can be made now. As would be expected, the $\psi = 155$ deg primary loading path (i.e., the union of the prebuckled path and the center-geometry path) changes from stable to unstable at the bifurcation point. The center-geometry is always possessed of a greater area moment of inertia, I, than the corresponding collapse-inward and collapse-outward geometries (see Fig. 2). Thus the two stable geometries are always at a lower state of strain energy, stored in longitudinal bending, than is the unstable center-geometry. A perturbation with sign $\delta m > 0$ or $\delta m < 0$ sends the center-geometry to the collapse-inward or collapse-outward configuratation, respectively.

Buckling Moment and Curvature

Figure 7 shows a graph of the buckling moment and curvature, M_{zb} and κ_b, as a function of the sweep angle ψ. Both curves rise to a cusp at the bifurcation value, $\psi = 155$ deg. The following approximation reproduces the values of M_{zb} to within plus or minus 1 percent of those found by numerical integration:

$$M_{zb} \approx \begin{cases} 0.281\,(\psi)^2, & 0 \le \psi \le 2.269 (130 \text{ deg}) \\ 2.412 - 1.662(2.705 - \psi)^{2/3}, & 2.269 \le \psi \le 2.705 (155 \text{ deg}) \\ 2.412 - 1.303(\psi - 2.705)^{3/4}, & 2.705 \le \psi \le 3.142 (180 \text{ deg}) \end{cases} \tag{17}$$

The approximation in the range $0 \le \psi \le 130$ deg is consistent with the square-of-the-angle formulas found in reference [2].

The power law drop-off in the neighborhood of $\psi = 155$ deg is reminiscent of Thompson and Hunt's study of imperfection sensitivity [7]. With this as a guide, the $\psi = 155$ deg case may be regarded as the "perfect" bifurcating geometry and $\psi - 155$ deg as a measure of the imperfection. The sign of the imperfection biases the postbuckling behavior toward a collapse-inward ($\psi > 155$ deg) or a collapse-outward ($\psi < 155$ deg) mode. With a cusp maximum for M_{zb} at $\psi = 155$ deg, the circular section beam is judged to be "imperfection sensitive." The sensitivity is slightly greater on the $\psi < 155$ deg side (2/3 power law drop-off) as compared to the $\psi > 155$ deg side (3/4 power law drop-off).

Summary

The nonlinear bending of a thin, open, circular section beam has been studied. It has been shown that, as the longitudinal curvature of the beam is increased, it passes through the following stages:

1. $0 \le \kappa \le \kappa_b$. The beam bends in a "soft" elastic response. A single stable solution exists.

2. $\kappa = \kappa_b$. The bending moment M_z reaches a local maximum M_{zb}. The next equilibrium point, with the property $M_z > M_{zb}$, occurs for κ much greater than κ_b.

3. $\kappa_b \le \kappa \le \kappa_3$. The beam bends through the downward-sloping portion of the M_z-versus-κ graph. The solution is stable and unique.

4. $\kappa = \kappa_3$. A secondary branch of equilibria appears. This branch is disjoint from the primary branch, except for the case $\psi \ge 155$ deg. The the two curves touch at a bifurcation point, and $\kappa_b = \kappa_3$.

5. $\kappa_3 < \kappa$. There are three distinct equilibria: a stable collapse-outward geometry, a stable collapse-inward geometry, and an unstable center-geometry, which separates the other two. If $\psi < 155$ deg, then the continuous deformation path favors the collapse outward mode. If $\psi > 155$ deg, then the collapse-inward mode is favored.

Acknowledgment

The author gratefully acknowledges and thanks the sponsor of this research, the Xerox Corporation.

References

1 Axelrad, E. L., "Flexible Shells," *Proceedings of the XV International Congress of Theoretical and Applied Mechanics*, Rimrott, F. P. J., and Tabarrok, B., eds., North Holland, 1980, pp. 45–50.

2 Benson, R. C., "Nonlinear Bending and Collapse of Long, Thin, Open Section Beams and Corrugated Panels," ASME JOURNAL OF APPLIED MECHANICS, Vol. 51, 1984, pp. 141–145.

3 Fabian, O., "Collapse of Cylindrical Elastic Tubes Under Combined Bending Pressure and Axial Loads," *International Journal of Solids and Structures*, Vol. 13, 1977, pp. 1257–1270.

4 Hutchinson, J. W., and Koiter, W. T., "Postbuckling Theory," ASME *Applied Mechanics Reviews*, Vol. 13, pp. 1353–1366.

5 Simitses, G. J., *Elastic Stability of Structures*, Prentice-Hall, Englewood Cliffs, N.J., 1976.

6 Carnahan, B., Luther, H. A., and Wilkes, J. O., *Applied Numerical Methods*, Wiley, New York, 1969.

7 Thompson, J. M. T., and Hunt, G. W., *A General Theory of Elastic Stability*, Wiley, New York, 1973.

Downloaded 02 May 2010 to 171.66.16.54. Redistribution subject to ASME license or copyright; see http://www.asme.org/terms/Terms_Use.cfm

A. Scheurkogel
Scientific Collaborator,
Department of Mathematics,
Delft University of Technology,
Delft, The Netherlands

I. Elishakoff
Professor,
Department of Aeronautical Engineering,
Technion–Israel Institute of Technology,
Haifa 32000, Israel

On the Ergodicity Assumption in an Applied Mechanics Problem

A deformation of a thin uniform cylindrical shell is considered under random axisymmetric loading. Mathematically this is equivalent to the study of a quasi-linear differential equation with random inhomogeneous term and random coefficient. The approximate method of solution, based on the assumption of ergodicity of the shell slope, is first described. It is shown that sometimes this assumption is valid but when not, it may yield non-negligible errors. In particular, it is shown via the ***exact*** *solution that assumption of ergodicity of the shell slope is correct if the loading is ergodic in correlation. However, this assumption may yield an error of about 20 percent if the loading in ergodic in mean-square but not in correlation.*

Introduction

A variety of problems in structural mechanics are governed by random nonlinear differential equations, for which exact solutions are unavailable, and approximate solutions must be resorted to. In a number of papers the ergodicity assumption of the output was utilized for obtaining its probabilistic characteristics. In an earlier study [1] it was shown that this assumption may yield good or poor approximation, depending on the circumstances, but the example presented there was of nonmechanical character. The present study is concerned with an applied mechanics problem first studied by Bolotin [2] who used this assumption to derive the second moment of the solution for the case of a white-noise input, and further showed that the first few terms of a perturbation solution (for which he again, albeit implicitly, assumed ergodicity) were in agreement with the original result. Here, an *exact* solution is given for Bolotin's problem for particular loading conditions. It is found that:

(*a*) The assumption of ergodicity of the output may yield a large error even for a mean-square ergodic input;

(*b*) This assumption is correct if the input is ergodic in correlation; and

(*c*) For an input that is ergodic in correlation, various probabilistic characteristics of the output are obtainable in terms of appropriate characteristics of the input.

1 Formulation of the Problem

Consider the random differential equation

$$DY'''' - (Eh/2)M^2 Y'' + (Eh/R^2)Y = P(x), \quad -\infty < x < \infty \qquad (1)$$

where

$$M^2 = \lim_{l\to\infty} (1/l)\int_{-l/2}^{l/2} [Y'(x)]^2 dx, \qquad M > 0 \qquad (2)$$

and D is the stiffness

$$D = Eh^3/12(1-\nu^2) \qquad (3)$$

where E is the modulus of elasticity, h is the thickness, R is the radius, l is the length, and ν is Poisson's ratio. Equation (1) describes the deformation of a cylindrical shell under a load $P(x)$ (Fig. 1). The latter is supposed to be a wide-sense homogeneous random function with zero mean and specified autocorrelation function. For derivation of equation (1), see reference [2]. With the following notation

$$\alpha = Eh/4D, \quad \beta = (Eh/DR^2)^{1/2}, \quad Q(x) = P(x)/D \qquad (4)$$

Equation (1) can be written in the form

$$Y'''' - 2\alpha M^2 Y'' + \beta^2 Y = Q(x) \qquad (5)$$

Mathematically this a quasilinear differential equation with random inhomogeneous term (input) and, through M, with random coefficients.

We seek the mean square value $E(M^2)$, E denoting mathematical expectation.

2 Method of Solution According to Reference [2]

Since reference [2] is not readily available, we first reproduce here Bolotin's solution to the problem. While assuming that the first derivative of the output process is ergodic, he did not specify the mode of ergodicity nor did he define the function relative to which the input is ergodic; in other words, he considered mean-square ergodicity of $Y'(x)$ per se. In this case we have, from equation (2):

$$M^2 = \lim_{l\to\infty} (1/l)\int_{-l/2}^{l/2} [Y'(x)]^2 dx = E\{[Y'(x)]^2\} \qquad (6)$$

with probability one. Denoting the second moment of M by σ^2, it follows from this equation that

$$M^2 = E[M^2] = \sigma^2 = E\{[Y'(x)]^2\} \qquad (7)$$

Contributed by the Applied Mechanics Division for publication in the JOURNAL OF APPLIED MECHANICS.

Discussion on this paper should be addressed to the Editorial Department, ASME, United Engineering Center, 345 East 47th Street, New York, N.Y. 10017, and will be accepted until two months after final publication of the paper itself in the JOURNAL OF APPLIED MECHANICS. Manuscript received by ASME Applied Mechanics Division, October, 1983; final revision, May, 1984.

Copyright © 1985 by ASME
Downloaded 02 May 2010 to 171.66.16.54. Redistribution subject to ASME license or copyright; see http://www.asme.org/terms/Terms_Use.cfm

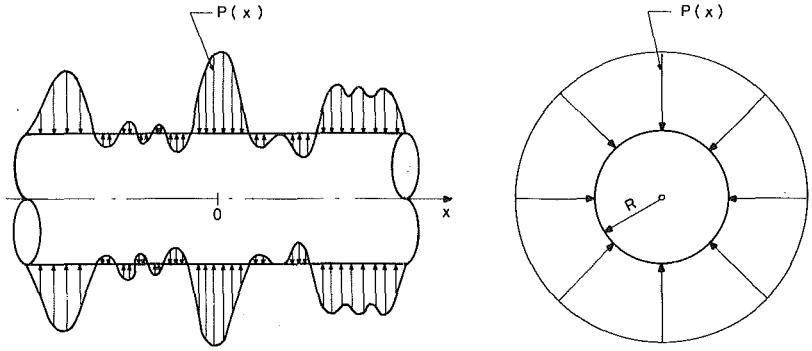


Fig. 1

again with probability one. This implies that the random variable M can be treated as a deterministic constant and may be replaced by σ in equation (5), which thus becomes

$$Y'''' - 2\alpha\sigma^2 Y'' + \beta^2 Y = Q(x) \tag{8}$$

With σ a given constant to be determined eventually from equation (7), we now have a differential equation with deterministic coefficients and random input. We apply directly some results for this class of equations (see, e.g., references [3, 4]). Consider the spectral density functions of Q and Y, representing the Fourier transforms of the corresponding autocorrelation functions K_{QQ} and K_{YY}, respectively:

$$S_{QQ}(\lambda) = \frac{1}{2\pi}\int_{-\infty}^{\infty} K_{QQ}(u)e^{-i\lambda u}du \tag{9}$$

$$S_{YY}(\lambda) = \frac{1}{2\pi}\int_{-\infty}^{\infty} K_{YY}(u)e^{-i\lambda u}du \tag{10}$$

The following relation is then valid [3, 4] between the spectral densities of the input and output of equation (8):

$$S_{YY}(\lambda) = \frac{S_{QQ}(\lambda)}{(\lambda^4 + 2\alpha\sigma^2\lambda^2 + \beta^2)^2} \tag{11}$$

The second moment of $Y'(x)$ is then

$$E\{[Y'(x)]^2\} = \int_{-\infty}^{\infty} \lambda^2 S_{YY}(\lambda)d\lambda \tag{12}$$

Finally, substituting equations (7) and (11) into equation (12), we have

$$\sigma^2 = \int_{-\infty}^{\infty} \frac{\lambda^2 S_{QQ}(\lambda)d\lambda}{(\lambda^4 + 2\alpha\sigma^2\lambda^2 + \beta^2)^2} \tag{13}$$

which is identical to equation (219) in reference [2].

As an illustrative application of Bolotin's approach, consider the following loading on the shell:

$$Q(x) = c\cos(\omega x - \Phi) \tag{14}$$

where c and ω are real constants and Φ is uniformly distributed on $(0,2\pi)$. $Q(x)$ is wide-sense homogeneous with

$$S_{QQ}(\lambda) = \frac{c^2}{4}\delta(\lambda - \omega) + \frac{c^2}{4}\delta(\lambda + \omega)$$

where $\delta(\bullet)$ denotes Dirac's delta function; equation (13) takes the form

$$\sigma^2 = \frac{c^2\omega^2}{2(\omega^4 + 2\alpha\sigma^2\omega^2 + \beta^2)^2}$$

The solution to equation (5), bounded at infinity, yields the shell slope:

$$Y'(x) = \frac{-\omega c\sin(\omega x - \Phi)}{\omega^4 + 2\alpha M^2\omega^2 + \beta^2} \tag{15}$$

Therefore

$$M^2 = \lim_{l\to\infty}(1/l)\int_{-l/2}^{l/2}[Y'(x)]^2dx = \frac{c^2\omega^2}{2(\omega^4 + 2\alpha M^2\omega^2 + \beta^2)^2}$$

which implies that M is a deterministic constant, coincident with σ. It is seen that in this case Bolotin's approach is valid, and σ^2 is readily found from the latter equation.

It should be borne in mind that the assumption of ergodicity of the output – in the present case, the shell slope – may turn out to be erroneous. An example is given in the following section with both the exact and approximate solutions found and compared.

3 Worked Example

Let the loading on the cylindrical shell be given as

$$Q(x) = a\sqrt{2}\sin\Theta\cos(\omega x - \Phi) + a\cos\Theta \tag{16}$$

where

$$a = \left[\frac{6(\omega^4 + \beta^2)^3}{\alpha\omega^4}\right]^{1/2} \tag{17}$$

Φ and Θ being independent random variables, the former uniformly distributed on $(0,2\pi)$ and the latter having the following probability density function:

$$P_\Theta(\theta) = \begin{cases} \frac{1}{2}\cos\theta, & |\theta| \le \frac{\pi}{2} \\ 0, & |\theta| > \frac{\pi}{2} \end{cases} \tag{18}$$

We first show that the random function $Q(x)$ is wide-sense homogeneous and mean-square ergodic. Its mathematical expectation is

$$E[Q(x)] = a\sqrt{2}E(\sin\Theta)E[\cos(\omega x - \Phi)] + a\,E(\cos\Theta) = a\,E(\cos\Theta) = \frac{\pi}{4}a \tag{19}$$

and is independent of x. To calculate the autocorrelation function we form the product

$$\begin{aligned} Q(x)Q(x+u) &= a^2\sin^2\Theta\{\cos(\omega u + 2\omega x - 2\Phi) + \cos\omega u\} \\ &+ a^2\sqrt{2}\sin\Theta\cos\Theta\{\cos(\omega x - \Phi) \\ &+ \cos(\omega u + \omega x - \Phi)\} + a^2\cos^2\Theta \end{aligned} \tag{20}$$

Taking the expectation and recalling the probabilistic properties of Θ and Φ, we find for the autocorrelation function

$$\begin{aligned} E[Q(x)Q(x+u)] &= a^2E(\sin^2\Theta)\cos\omega u + a^2E(\cos^2\Theta) \\ &= \frac{a^2}{3}\cos\omega u + \frac{2a^2}{3} \end{aligned} \tag{21}$$

Downloaded 02 May 2010 to 171.66.16.54. Redistribution subject to ASME license or copyright; see http://www.asme.org/terms/Terms_Use.cfm

depending on u alone. Equations (19) and (21) imply that $Q(x)$ is wide-sense homogeneous.

For the mean-square value of $Q(x)$, we have from equation (21)

$$E[Q^2(x)] = a^2 \tag{22}$$

On the other hand, from equation (20) it follows that

$$\lim_{l\to\infty} (1/l)\int_{-l/2}^{l/2} Q^2(x)\,dx = a^2 \tag{23}$$

with probability one. The last two equations imply that $Q(x)$ is mean-square ergodic. The question aries whether so is $Y'(x)$. We derive $E\{[Y'(x)]^2\}$ both approximately, utilizing the ergodicity assumption for $Y'(x)$, and exactly, without it.

4 Approximate Solution

We assume that $Y'(x)$ is mean-square ergodic, that is,

$$M^2 = \sigma^2 = E\{[Y'(x)]^2\} \tag{24}$$

with probability one. According to equation (21) the spectral density of $Q(x)$ is

$$S_{QQ}(\lambda) = \frac{a^2}{6}\delta(\lambda-\omega) + \frac{a^2}{6}\delta(\lambda+\omega) + \frac{2a^2}{3}\delta(\lambda) \tag{25}$$

Substitution of equation (25) in equation (13) yields

$$\sigma^2 = \frac{a^2\omega^2}{3(\omega^4 + 2\alpha\sigma^2\omega^2 + \beta^2)^2} \tag{26}$$

which, after substitution of the expression for a (equation (17)), can be simplified to

$$\sigma^3 + 3\gamma^2\sigma - 6\sqrt{3}\gamma^3 = 0 \tag{27}$$

where

$$\gamma = \left(\frac{\omega^4+\beta^2}{6\alpha\omega^2}\right)^{1/2} \tag{28}$$

It is readily verified that the only real root of equation (27) is

$$\sigma = \gamma\sqrt{3} \tag{29}$$

which is also obtainable without recourse to $S_{QQ}(\lambda)$. Indeed, the unique solution to equation (5), bounded at infinity, is

$$Y(x) = \frac{a\sqrt{2}\sin\Theta\cos(\omega x-\Phi)}{\omega^4+2\alpha\sigma^2\omega^2+\beta^2} + \frac{a}{\beta^2}\cos\Theta \tag{30}$$

Consequently, in view of equation (24), we find

$$\begin{aligned}\sigma^2 &= E\{[Y'(x)]^2\} \\ &= \frac{2a^2\omega^2}{(\omega^4+2\alpha\sigma^2\omega^2+\beta^2)^2}\int_{-\pi/2}^{\pi/2}\frac{1}{2}\sin^2\theta\cos\theta\,d\theta \\ &\quad \int_0^{2\pi}\sin^2(\omega x-\phi)\frac{1}{2\pi}\,d\phi\end{aligned} \tag{31}$$

which after evaluation of the integrals brings us back to equation (26).

5 Exact Solution

We first note that M is a random variable, hence a constant for every realization of the shell displacement $Y(x)$. The solution to equation (5), bounded at infinity, therefore reads

$$Y(x) = \frac{a\sqrt{2}\,\sin\Theta\,\cos(\omega x-\Phi)}{\omega^4+2\alpha M^2\omega^2+\beta^2} + \frac{a}{\beta^2}\cos\Theta \tag{32}$$

The value of M is obtained by substitution of equation (32) into equation (2):

$$M^2 = \frac{a^2\omega^2\sin^2\Theta}{(\omega^4+2\alpha M^2\omega^2+\beta^2)^2} \tag{33}$$

With the aid of equation (17) this equation can be rewritten as

$$M^3 + 3\gamma^2 M - 18\gamma^3|\sin\Theta| = 0 \tag{34}$$

where γ is again as per equation (28).

It is immediately seen that the shell slope $Y'(x)$ is wide-sense homogeneous, but not mean-square ergodic. This means that the solution, described in Section 4, is incorrect. Let us determine the magnitude of the error. To do this, we must find $E(M^2)$.

Using the substitution

$$9|\sin\Theta| = \sinh\Psi \tag{35}$$

equation (34) can be factorized to yield

$$\left(M - 2\gamma\sinh\frac{1}{3}\Psi\right)\left\{\left[M+\gamma\sinh\left(\frac{1}{3}\Psi\right)\right]^2 + 3\gamma^2\cosh^2\left(\frac{1}{3}\Psi\right)\right\} = 0 \tag{36}$$

It is immediately concluded that the only real root of this equation is

$$M = 2\gamma\sinh\left(\frac{1}{3}\Psi\right) \tag{37}$$

Referring again to equation (35), we have

$$\begin{aligned}E(M^2) &= 4\gamma^2\int_{-\pi/2}^{\pi/2}\sinh^2\left(\frac{1}{3}\psi\right)\frac{1}{2}\cos\theta\,d\theta \\ &= \frac{4}{9}\gamma^2\int_0^{\Psi_0}\sinh^2\left(\frac{1}{3}\psi\right)\cosh\psi\,d\psi\end{aligned} \tag{38}$$

where

$$\Psi_0 = ln(9+\sqrt{82}) \tag{39}$$

Evaluation of the integral in equation (38) yields

$$E(M^2) = \frac{\gamma^2}{9}\left[\frac{3}{5}\sinh\left(\frac{5}{3}\Psi_0\right) + 3\sinh\left(\frac{1}{3}\Psi_0\right)\right] - 2\gamma^2 \tag{40}$$

With

$$p = (9+\sqrt{82})^{1/3} \tag{41}$$

the exact value of $E(M^2)$ is expressed as

$$E(M^2) = \gamma^2\left(\frac{p^5-p^{-5}}{30} + \frac{p-p^{-1}}{6} - 2\right) = 2.51557\gamma^2 \tag{42}$$

Comparison of this result with the approximate value as per equation (29) shows that the percentage error induced by the ergodicity assumption relative to the exact value is as high as 19.26 percent. In other words, assumption of the mean-square ergodicity for the shell slope may lead to a considerable error, even if the loading is mean-square ergodic.

6 Discussion

The difference between the loading given by equation (14) and that given by equation (16) is that the random function (14) is ergodic in the correlation function, whereas (16) is ergodic in the mean-square only. This might serve as an indication that ergodicity of the loading in the autocorrelation function is a sufficient and necessary condition for mean-square ergodicity of the shell slope. It can be proved (see reference [5]) that ergodicity of the loading in the autocorrelation function is in this test case a *sufficient* condition, but *not* a necessary one. This can be illustrated by an example of the following loading on the shell:

$$Q(x) = c\,\cos(\omega x-\Phi) + p\Phi \tag{43}$$

with equation (14) extended to include an additional term $p\Phi$, p being a real constant. From

$$Q(x)\,Q(x+u) = \frac{c^2}{2}[\cos(2\omega x - 2\Phi + \omega u) + \cos\omega u]$$

Downloaded 02 May 2010 to 171.66.16.54. Redistribution subject to ASME license or copyright; see http://www.asme.org/terms/Terms_Use.cfm

$$+cp\Phi\cos(\omega x-\Phi)+cp\Phi\cos(\omega x-\Phi+\omega u)+p^2\Phi^2 \quad (44)$$

we have the autocorrelation function

$$K_{QQ} = E[Q(x)Q(x+u)] = \frac{c^2}{2}\cos\omega u - cp\sin\omega x - cp\sin(\omega x+\omega u)+p^2E(\Phi^2) \quad (45)$$

which depends on x; hence $Q(x)$ is not wide-sense homogeneous. The shell slope, however, coincides with expression (15). $Y'(x)$ is ergodic both in the mean and in the autocorrelation function. In this case Bolotin's approach turns out to be correct despite the nonergodicity (in the autocorrelation) of the applied loading.

The peculiarities demonstrated in this problem stem from the fact that equation (5) is a quasilinear random differential equation, with properties that differ widely from those of stable linear equations with constant coefficients. For the equation considered here, it might happen that despite ergodicity of the input in some sense (e.g., relative to a given function) the output would not even be wide-sense homogeneous. The other "nice" properties of the linear differential equation with constant coefficients (e.g., the zero mean output due to vanishing of the mean input, under homogeneous boundary conditions) are not in general inherited by its quasilinear counterparts.

Acknowledgment

This study has been supported in part by the Fund for the Promotion of Research at Technion–Israel Institute of Technology.

References

1 Scheurkogel, A. J., Elishakoff, I. and Kalker, J. J., "On the Error That can be Induced by an Ergodicity Assumption," ASME JOURNAL OF APPLIED MECHANICS, Vol. 48, 1981, pp. 654–656.

2 Bolotin, V. V., *Application of the Methods of the Theory of Probability and the Theory of Reliability to Analysis of Structures*, Section 1.14, Methods of Solution of Nonlinear Stochastic Boundary-Value Problems, State Publishing House for Buildings, Moscow 1971, pp. 101–105, Second Edition 1981, in Russian (English translation: FTD-MT-24-771-73, Foreign Technology Division, Wright-Patterson AFB, Ohio, 1974, pp. 129–136).

3 Soong, T. T., *Random Differential Equations in Science and Engineering*, Academic Press, New York, 1973.

4 Elishakoff, I., *Probabilistic Methods in the Theory of Structures*, Wiley-Interscience, New York, 1983.

5 Scheurkogel, A. J., "On a Sufficient Condition for the Mean-Square Ergodicity of the Shell Slope," in preparation.

Downloaded 02 May 2010 to 171.66.16.54. Redistribution subject to ASME license or copyright; see http://www.asme.org/terms/Terms_Use.cfm

Transverse Impact of a Hyperelastic Stretched String

M. F. Beatty
Department of Engineering Mechanics,
University of Kentucky,
Lexington, Ky. 40506
Mem. ASME

J. B. Haddow
Department of Mechanical Engineering,
University of Alberta,
Edmonton, Alberta, Canada T6G 2G8

Governing equations are derived for the plane motion of a stretched hyperelastic string subjected to a suddenly applied force at one end. These equations can be put in the form of a quasilinear system of first-order partial differential equations, which is totally hyperbolic for an admissible strain energy function. There are, in general, two wave speeds and two corresponding shock speeds. Special consideration is given to the jump relations across the shocks. Similarity solutions for a string moved at one end in loading or unloading are obtained for a general hyperelastic solid. The results are applicable to the familiar neo-Hookean or Mooney-Rivlin material, and the nature of the solution for another special hyperelastic material is discussed. These solutions are valid for a semi-infinite string, or until the first reflection occurs. It is shown that a special case of the similarity solution is valid for the normal impact of a stretched string by a constant speed, point application of load. Exact solution to the equations for the neo-Hookean model is derived in terms of elliptic integrals, and some numerical results are provided.

1 Introduction

The dynamic finite deformation of flexible strings by impact has been studied extensively. A detailed treatment along with numerous references may be found in [1], wherein various constitutive relations, including elastic-plastic and rate-sensitive elastic-plastic models, are studied. Of course, provided no unloading occurs, the elastic-plastic problem is very similar to the finite deformation, nonlinear elasticity problem, which is the central interest of this paper.

Solutions of the longitudinal impact problem, which involves only longitudinal waves, have been derived by Rakhmatulin [2], Karman and Duwez [3], Taylor [4], and others. More recently, the propagation of finite amplitude longitudinal disturbances in bars of rubberlike materials in finite strain have been studied by Nowinski [5]. Explicit solutions for the speed of propagation, the particle velocity, and shock conditions are obtained for a neo-Hookean material; and it is shown that shock waves may occur either for unloading in the extension case or for loading in the compression case, otherwise a continuous wave motion may be propagated. The dependence of the uniaxial disturbance on the form of the stress-strain relationship, the direction of loading or unloading, and the state of tension or compression is also described.

The transverse or oblique impact problem, with the assumption that the influence of lateral contractions of the small but finite diameter is negligible, involves both transverse and longitudinal waves and shocks, depending on the constitutive equation and the initial tension. We recall that a transverse wave is usually defined as a wave for which the particle velocity is normal to the direction of propagation; however, in the transverse impact problem considered here, the term transverse is used somewhat loosely because the particle velocity is normal to the direction of propagation only for the special case of normal impact. This is consistent with common usage in cable dynamics.

Practical applications of the transverse impact of aircraft arrestment cables, towing cables, and textile yarns prompted earlier studies of this problem by Ringleb [6], Smith, McCrackin, and Schiefer [7], and others. Li [8] solved the problem for strings characterized by a linear relation between the longitudinal tensile force and the corresponding finite engineering strain, assumptions that yield a constant longitudinal wave speed and sharp wave fronts which result in considerable simplification and admit exact characteristic analysis of various wave interaction effects. The transverse normal impact on a cable of rubberlike material under initial finite strain has been examined by Nowinski [9] for the loading phase in the case when the longitudinal wave speed exceeds the speed of the transverse wave front and no wave reflections occur. Some graphical results for the relation between the impact velocity and the initial stretch are provided for the neo-Hookean and Zahorski material models. Experiments reported by Riegel and Nowinski [10] appear to show reasonable agreement with the results in [9].

In this paper, we consider a general hyperelastic string subjected to initial tension and given a step function disturbance at one end. It is shown that different realistic constitutive relations result in different types of solution; and, for certain constitutive equations, the type of solution depends on the initial stretch. Solutions are obtained that involve centered simple waves and shocks, or shocks only. These are valid for a semi-infinite string or until the first

Contributed by the Applied Mechanics Division for publication in the JOURNAL OF APPLIED MECHANICS.

Discussion on this paper should be addressed to the Editorial Department, ASME, United Engineering Center, 345 East 47th Street, New York, N.Y. 10017, and will be accepted until two months after final publication of the paper itself in the JOURNAL OF APPLIED MECHANICS. Manuscript received by ASME Applied Mechanics Division, December, 1983.

Copyright © 1985 by ASME
Downloaded 02 May 2010 to 171.66.16.54. Redistribution subject to ASME license or copyright; see http://www.asme.org/terms/Terms_Use.cfm

reflection occurs. Reflected waves are not investigated here; this difficult analysis is reserved for later work. A special case of the aforementioned solutions is valid for the normal impact of a stretched string by a constant velocity, point application of load. An exact solution in terms of elliptic integrals is obtained for the neo-Hookean rubberlike solid, and some numerical results are provided for this case. Though only plane motion is considered, the method of reaching the governing equations is applicable to spatial motions as well.

2 Formulation of the Problem and the Governing Equations

We consider a semi-infinite uniform string occupying the region $[0, \infty)$ of the x axis of a rectangular cartesian coordinate system and subjected to an initial uniform stretch $\lambda_0 \geq 1$. Let $X \epsilon [0, \infty)$ be the x coordinate of the string in its straight and unstretched reference configuration in the x direction, and $x_0 \epsilon [0, \infty)$ the corresponding coordinate in the stretched initial state so that $x_0 = \lambda_0 X$. The place $\mathbf{x}$ at time t of the particle which was at $(x_0, 0, 0)$ in the stretched initial condition at $t = 0$ is given by $\mathbf{x} = \mathbf{x}(X, t)$. The cartesian coordinates of $\mathbf{x}$ may be described by the parametric equations

$$x = x(s,t), \quad y = y(s,t), \quad z = z(s,t),$$

in which $s = s(X, t)$ denotes the arc length in the deformed configuration at time t measured from the end $X = 0$. The stretch λ is given by $\lambda = ds/dX$.

Since the string is assumed to be perfectly flexible, the tensile force $\mathbf{P}$ is tangential to the string and can be expressed as $\mathbf{P} = A_0 T\mathbf{l}$, wherein

$$\mathbf{l} = \frac{d\mathbf{x}}{ds} = \frac{1}{\lambda}\frac{\partial \mathbf{x}}{\partial X} \tag{2.1}$$

is the unit vector tangential to the string, A_0 is the uniform cross-sectional area in the reference configuration and T denotes the engineering stress. The equation of motion is

$$\ddot{\mathbf{x}} = \frac{1}{\rho_0}(T\mathbf{l})' + \mathbf{F}, \tag{2.2}$$

where $\mathbf{F}(X, t)$ is the prescribed external force per unit mass and ρ_0 is the uniform density in the reference configuration. Also, a superposed dot and prime denote partial differentiation with respect to time t and X, respectively. It follows from (2.1) that

$$\dot{\mathbf{x}}' = \dot{\lambda}\mathbf{l}. \tag{2.3}$$

We will suppose that the string is uniform and that the stress is a monotone function of the stretch so that

$$T = T(\lambda(X,t)), \quad \frac{dT}{d\lambda} > 0, \quad T(1) = 0. \tag{2.4}$$

Equations (2.2), (2.3), and $(2.4)_1$ can be reduced to a system of quasilinear first-order partial differential equations in two independent variables, X and t. Condition $(2.4)_2$ guarantees that the system is hyperbolic. To accomplish the reduction, we introduce the tangential and normal components of the velocity of a point of the string. Henceforth, we consider only plane motion, but it is clear that the method may be easily extended to spatial motion.

Let $\mathbf{n}$ denote a unit vector normal to the string, as shown in Fig. 1. Then

$$\dot{\mathbf{x}} = \tau\mathbf{l} + \nu\mathbf{n}, \tag{2.5}$$

where $\tau(X, t)$ and $\nu(X, t)$ are the tangential and normal components, respectively, of the velocity $\dot{\mathbf{x}}$. It follows from elementary kinematics that

$$\dot{\mathbf{l}} = \dot{\theta}\mathbf{n}, \quad \mathbf{l}' = \theta'\mathbf{n}, \quad \dot{\mathbf{n}} = -\dot{\theta}\mathbf{l}, \quad \mathbf{n}' = -\theta'\mathbf{l}, \tag{2.6}$$

where $\theta(X, t)$ is the angle that $\mathbf{l}$ makes with an arbitrary fixed

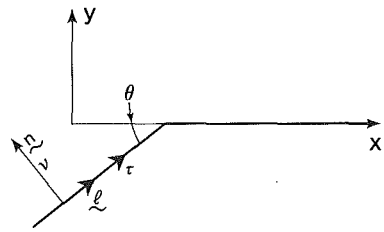


Fig. 1 Problem geometry

line in the plane, say, the string in its initial configuration. Differentiation of (2.5) and use of (2.6) gives

$$\dot{\mathbf{x}} = (\dot{\tau} - \nu\dot{\theta})\mathbf{l} + (\dot{\nu} + \tau\dot{\theta})\mathbf{n},$$

$$\dot{\mathbf{x}}' = (\tau' - \nu\theta')\mathbf{l} + (\nu' + \tau\theta')\mathbf{n}; \tag{2.7}$$

and (2.2), (2.3), and (2.4) yield

$$\dot{\mathbf{x}} = (c_L{}^2\lambda' + F_l)\mathbf{l} + (\lambda c_T{}^2\theta' + F_n)\mathbf{n}, \quad \dot{\mathbf{x}}' = \dot{\lambda}\mathbf{l} + \lambda\dot{\theta}\mathbf{n}, \tag{2.8}$$

where

$$c_T{}^2 = \frac{T}{\rho_0\lambda}, \quad c_L{}^2 = \frac{1}{\rho_0}\frac{dT}{d\lambda}. \tag{2.9}$$

Also, $F_l = \mathbf{F} \cdot \mathbf{l}$ and $F_n = \mathbf{F} \cdot \mathbf{n}$ are the tangential and normal components, respectively, of the external force $\mathbf{F}$. We observe that c_L and c_T have the dimensions of velocity and that they correspond to the longitudinal and transverse wave speeds, respectively. Equating (2.7) and (2.8) gives the governing equations of the problem:

$$\begin{aligned} &\dot{\tau} - \nu\dot{\theta} - c_L{}^2\lambda' - F_l = 0, \\ &\dot{\nu} + \tau\dot{\theta} - \lambda c_T{}^2\theta' - F_n = 0, \\ &\tau' - \nu\theta' - \dot{\lambda} = 0, \\ &\nu' + \tau\theta' - \lambda\dot{\theta} = 0. \end{aligned} \tag{2.10}$$

Equations (2.10) are a system of four first-order, quasilinear equations that are totally hyperbolic with four families of distinct characteristics with slopes $\pm c_L$, $\pm c_T$ in the (X, t) plane. Upon writing $\tau = V$ for the particle speed and putting $\nu = \theta = F_l = F_n = 0$ in (2.10), we find that this system reduces to Nowinski's Lagrangian equations for the propagation of longitudinal waves (cf. equations (2) and (3) in [5]).

3 Discontinuity Relations

With regard to the dependent variables τ, ν, θ, and λ in (2.10), discontinuities in their first or higher partial derivatives with respect to the independent variables X and t are known as weak discontinuities; these are propagated along characteristics in the (X, t) plane. Discontinuities in the dependent variables themselves are called strong discontinuities, or shocks; these discontinuities may or may not be propagated along characteristics. The discontinuity conditions appropriate to the string impact problem are easily obtained.

From now on, we will assume that the body force $\mathbf{F}$ vanishes, and that the string is uniform and incompressible so that ρ_0 is constant and continuous. Then, (2.2) may be written in the conservation form

$$\frac{\partial \dot{\mathbf{x}}}{\partial t} - \frac{1}{\rho_0}\frac{\partial (T\mathbf{l})}{\partial X} = \mathbf{0}.$$

It follows that if a shock is present, the discontinuity relation

$$\rho_0 V[\dot{\mathbf{x}}] = -[T\mathbf{l}] \tag{3.1}$$

must be satisfied across the shock front. The bold bracket terms $[Q]$ denote the jump in the quantity Q across the shock, and V denotes the Lagrangian shock speed [cf. 11]. Since (2.3) is also in conservation form, we have

$$[\dot{\mathbf{x}}] = -V[\lambda\mathbf{l}]. \tag{3.2}$$

Downloaded 02 May 2010 to 171.66.16.54. Redistribution subject to ASME license or copyright; see http://www.asme.org/terms/Terms_Use.cfm

Suppose that the string has a kink in it so that $\mathbf{I}$ is discontinuous, but T is continuous, which implies that λ is continuous. Then it follows from (3.1) and (3.2), in which we set $V = V_T$, that

$$\rho_0 V_T[\dot{\mathbf{x}}] = -T[\mathbf{I}], \quad [\dot{\mathbf{x}}] = -V_T\lambda[\mathbf{I}]. \tag{3.3}$$

These give

$$V_T = \left(\frac{T}{\rho_0\lambda}\right)^{1/2}. \tag{3.4}$$

Hence, V_T is identified as the Lagrangian speed of a transverse shock. This is the same as the characteristic, transverse wave speed in $(2.9)_1$. Consequently, a discontinuity in $\mathbf{I}$, hence θ, is a transverse shock that propagates with the Lagrangian speed V_T along a characteristic with slope $\pm c_T$.

Similarly, if λ is discontinuous and $\mathbf{I}$ is continuous, then with $V = V_L$ in (3.1) and (3.2), we have

$$\rho_0 V_L[\dot{\mathbf{x}}] = -[T]\mathbf{l}, \qquad [\dot{\mathbf{x}}] = -V_L[\lambda]\mathbf{l}. \tag{3.5}$$

Therefore, the Lagrangian speed of a longitudinal shock due to a discontinuity in λ is identified as

$$V_L = \left(\frac{[T]}{\rho_0[\lambda]}\right)^{1/2}. \tag{3.6}$$

Comparison of $(2.9)_2$ and (3.6) shows that, in general, a discontinuity in λ is not propagated along a characteristic.

4 Constitutive Equations

The relation $T = T(\lambda)$ for uniaxial tension of an incompressible, isotropic hyperelastic solid may be expressed in the form

$$T(\lambda) = 2\left(\frac{\partial W}{\partial I_1} + \frac{1}{\lambda}\frac{\partial W}{\partial I_2}\right)\left(\lambda - \frac{1}{\lambda^2}\right), \tag{4.1}$$

where $W = W(I_1, I_2)$ is the strain energy per unit volume and

$$I_1 = \lambda^2 + \frac{2}{\lambda}, \qquad I_2 = 2\lambda + \frac{1}{\lambda^2}$$

[cf. 12]. We will consider only strain energy functions for which the restriction $(2.4)_2$ is satisfied for all λ.

The simplest realistic constitutive equation for a hyperelastic material is that for the neo-Hookean solid, whose strain energy function is defined by

$$W = \frac{\mu}{2}(I_1 - 3), \tag{4.2}$$

where $\mu > 0$ is the constant shear modulus of the material in its undeformed configuration [12]. It follows from (4.1) and (4.2) that for the neo-Hookean solid

$$T = \mu\left(\lambda - \frac{1}{\lambda^2}\right), \tag{4.3}$$

and $(2.4)_{2,3}$ are satisfied. It is easily verified by (2.9) and (4.3) that $c_L > c_T$ for all finite λ. Indeed, it is seen that for all $\lambda \geq 1$,

$$0 \leq {c_T}^2 < \frac{\mu}{\rho_0} < {c_L}^2 \leq 3\frac{\mu}{\rho_0}.$$

The Mooney-Rivlin solid is described by the strain energy function

$$W = \frac{\mu}{2}\{\alpha(I_1 - 3) + (1-\alpha)(I_2 - 3)\}, \tag{4.4}$$

where $0 < \alpha \leq 1$ and $0 < \mu$, as before. When $\alpha = 1$, (4.3) reduces to (4.1) for the neo-Hookean solid. We find from (4.1) and (4.4) that

$$T = \mu\left[\alpha + \frac{(1-\alpha)}{\lambda}\right]\left(\lambda - \frac{1}{\lambda^2}\right); \tag{4.5}$$

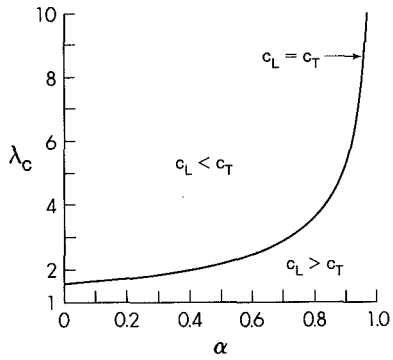


Fig. 2 Relation $(1-\alpha)(4-{\lambda_c}^3) + 3\alpha\lambda_c = 0$ for a Mooney-Rivlin material

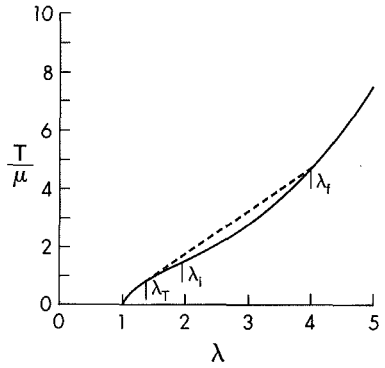


Fig. 3 Uniaxial engineering stress-stretch relation for $W = \mu/2\{\alpha(I_1 - 3) + (1-\alpha)(I_2 - 3) + \gamma(I_1 - 3)^2\}$

and it may be seen that $(2.4)_2$ holds for all λ. It follows from (2.9) and (4.5) that $c_L > c_T$ provided that $\lambda < \lambda_c$, where λ_c depends on α. Their relation

$$(1-\alpha)(4-{\lambda_c}^3) + 3\alpha\lambda_c = 0 \tag{4.6}$$

is shown graphically in Fig. 2. Thus, $c_L > c_T$ for all λ holds only for $\alpha = 1$, which gives the neo-Hookean model.

A strain energy function proposed by Ishihara et al. [13] as a realistic model for certain elastomers is given by

$$W = \frac{\mu}{2}\{\alpha(I_1 - 3) + (1-\alpha)(I_2 - 3) + \gamma(I_1 - 3)^2\}, \tag{4.7}$$

where α, γ, and μ are material constants for which $0 < \alpha \leq 1$, $0 < \gamma \ll 1$, and $\mu > 0$, as before. With a suitable choice of α and γ this strain energy function results in an S-shaped (T, λ) curve, quantitatively similar to those shown in [8, pp. 91, 121]. The T, λ curve for $\alpha = 0.5$ and $\gamma = 0.02$ is shown in Fig. 3. It is interesting to note that for a string of this material $c_L > c_T$ for all λ and a discontinuity with both $\mathbf{I}$ and T discontinuous is not possible.

The results that will be derived in the next section are not restricted to these special cases. Nevertheless, these realistic constitutive equations may be used to motivate some of the assumptions met along the way. We will return to these again in Section 6 where explicit exact solution of the transverse impact problem will be presented.

5 Similarity Solutions

Equations (2.10) are a system of hyperbolic first-order partial differential equations. The characteristic directions, $dX/dt = \pm c_L, \pm c_T$, of the four families of characteristics, and the relations along the characteristics, can be obtained by standard methods as described by Whitham [11]. Instead of using these relations, we adopt a procedure similar to that used by Davison [14] to study the problem of plane elastic

Downloaded 02 May 2010 to 171.66.16.54. Redistribution subject to ASME license or copyright; see http://www.asme.org/terms/Terms_Use.cfm

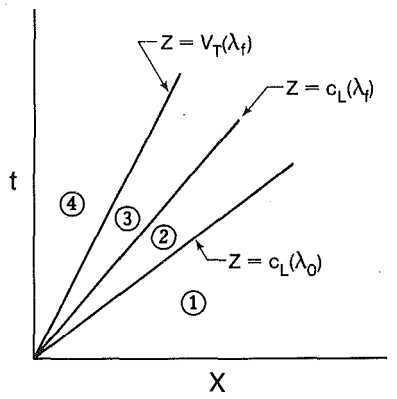


Fig. 4 Characteristics in the (X, t) plane for $d^2T/d\lambda^2 < 0$ and $c_L(\lambda) > c_T(\lambda)$, $\lambda < \lambda_f$, with $\lambda_f > \lambda_0$

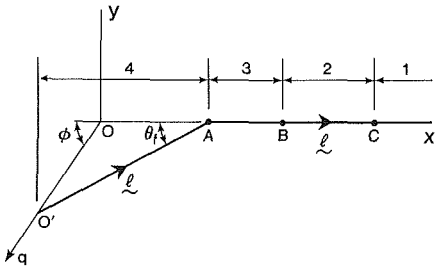


Fig. 5 Deformed configuration of the string

waves in a half space. We seek similarity solutions of (2.10) subject to the initial conditions

$$\lambda(X,0)=\lambda_0\geq 1, \quad \theta(X,0)=0, \quad \tau(X,0)=\nu(X,0)=0, \tag{5.1}$$

which specify that the string is initially at rest in a straight form with stretch λ_0, and the boundary conditions

$$\lambda(0,t)=\lambda_f, \quad \theta(0,t)=\theta_f \quad \text{for} \quad t>0, \tag{5.2}$$

which specify that the end $X = 0$ is moved impulsively. We assume that the remote end of the string remains undisturbed so that $\lambda(\infty,t) = \lambda_0$ and $\theta(\infty, t) = 0$ for all time t.

We seek a solution in which the body force vanishes and the dependent variables are functions of $Z = X/t$, so that the solution consists of centered simple waves and/or shocks propagating in the x direction. In this case, the system (2.10) is reduced to the following system of ordinary differential equations:

$$\begin{aligned} &Z\tau_z - Z\nu\theta_z + c_L{}^2\lambda_z = 0\\ &Z\nu_z + (Z\tau + \lambda c_T{}^2)\theta_z = 0,\\ &\tau_z - \nu\theta_z + Z\lambda_z = 0,\\ &\nu_z + (\tau + Z\lambda)\theta_z = 0, \end{aligned} \tag{5.3}$$

where the subscript z denotes differentiation with respect to Z. A nontrivial solution to equations (5.3) exists if and only if $Z = \pm c_L$ or $Z = \pm c_T$. Since the propagation is in the x direction, we need only consider $Z = c_L$, $Z = c_T$.

First, we consider the impact loading case for which $\lambda_f > \lambda_0$ and require that the constitutive relation be such that

$$\frac{d^2T}{d\lambda^2}(\lambda)<0 \quad \text{and} \quad c_L(\lambda)>c_T(\lambda) \quad \text{for all} \quad \lambda<\lambda_f. \tag{5.4}$$

It follows from the first of conditions (5.4) that $c_L(\lambda_f) < c_L(\lambda_0)$; consequently, no shock involving a discontinuity of λ(or T) is initiated at $X = 0$, $t = 0$. The solution obtained consists of the solutions in four regions of the (X, t) plane. These four regions are bounded by characteristics as shown in Fig. 4. Region 1 is the undisturbed region of uniform state ahead of the wave front, which propagates with speed $c_L(\lambda_0)$; region 2 represents a centered simple wave; region 3 is a region of uniform state, separated from region 4, also of uniform state, by the transverse shock $Z = c_T(\lambda_f) = V_T(\lambda_f)$. The solution satisfying (5.3), the discontinuity relation (3.3), and the initial and boundary data (5.1) and (5.2) is as follows:

Region 1: $\dfrac{X}{t}\geq c_L(\lambda_0)$:

$$\lambda=\lambda_0, \quad \theta=\tau=\nu=0. \tag{5.5}$$

Region 2: $c_L(\lambda_0)\geq \dfrac{X}{t}\geq c_L(\lambda_f)$;

$$\frac{X}{t}=c_L(\lambda), \quad \theta=\nu=0, \quad \tau=-\int_{\lambda_0}^{\lambda} c_L(\eta)d\eta. \tag{5.6}$$

Region 3: $c_L(\lambda_f)\geq \dfrac{X}{t}>c_T(\lambda_f)$;

$$\lambda=\lambda_f, \quad \theta=\nu=0, \quad \tau=-\int_{\lambda_0}^{\lambda_f} c_L(\lambda)d\lambda. \tag{5.7}$$

Region 4: $c_T(\lambda_f)>\dfrac{X}{t}\geq 0$;

$$\lambda=\lambda_f, \quad \theta=\theta_f,$$

$$\tau=U(\lambda_f)\cos\theta_f-\lambda_f c_T(\lambda_f), \quad \nu=-U(\lambda_f)\sin\theta_f, \tag{5.8}$$

wherein, for future convenience, we define the function

$$v(\lambda)\equiv\lambda c_T(\lambda)-\int_{\lambda_0}^{\lambda}c_L(\eta)\,d\eta. \tag{5.9}$$

The last two equations in the set (5.8) derive from $(3.3)_2$ and $(5.7)_4$.

A typical deformed configuration of the string at time t is shown in Fig. 5, wherein the four segments of the deformed string $O'ABC$ correspond to the four regions of the foregoing solution. The absolute Eulerian speeds v_A, v_B, and v_C of the points A, B, and C are given by

$$\begin{aligned} v_A &= U(\lambda_f)=\lambda_f c_T(\lambda_f)-\int_{\lambda_0}^{\lambda_f} c_L(\lambda)d\lambda,\\ v_B &= \lambda_f c_L(\lambda_f)-\int_{\lambda_0}^{\lambda_f} c_L(\lambda)d\lambda,\\ v_C &= \lambda_0 c_L(\lambda_0). \end{aligned} \tag{5.10}$$

These denote the speeds of the discontinuity of θ, the junction point of regions 2 and 3, and of the longitudinal wave-front, respectively.

Let q denote the constant impact speed at which O' is moved at an angle ϕ with the x axis as shown in Fig. 5. Then

$$\tau_0=-q\cos(\phi-\theta_f), \quad \nu_0=-q\sin(\phi-\theta_f), \tag{5.11}$$

where τ_0 and ν_0 are the tangential and normal velocity components given by (5.8). It follows from (5.8) and (5.11) that

$$\begin{aligned} &q\cos\phi+U(\lambda_f)\\ &\quad=\lambda_f c_T(\lambda_f)\cos\theta_f, \quad q\sin\phi=\lambda_f c_T(\lambda_f)\sin\theta_f. \end{aligned} \tag{5.12}$$

Elimination of θ_f from (5.12) gives q as a function of the impact angle ϕ and stretch λ_f; we find

$$\begin{aligned} &q^2+2qU(\lambda_f)\cos\phi\\ &\quad-\int_{\lambda_0}^{\lambda_f}c_L(\lambda)d\lambda[U(\lambda_f)+\lambda_f c_T(\lambda_f)]=0 \end{aligned} \tag{5.13}$$

for an assigned initial stretch λ_0. When $\phi = \pi/2$, we have

$$q^2=\int_{\lambda_0}^{\lambda_f}c_L(\lambda)d\lambda\{\lambda_f c_T(\lambda_f)+U(\lambda_f)\}, \tag{5.14}$$

which is the relation for the impact speed in a normal impact of the string. And when $\phi = 0$, $(5.12)_1$ yields the longitudinal impact speed

$$q=\int_{\lambda_0}^{\lambda_f}c_L(\lambda)d\lambda. \tag{5.15}$$

This well-known result has been used by Karman and Duwez

Downloaded 02 May 2010 to 171.66.16.54. Redistribution subject to ASME license or copyright; see http://www.asme.org/terms/Terms_Use.cfm

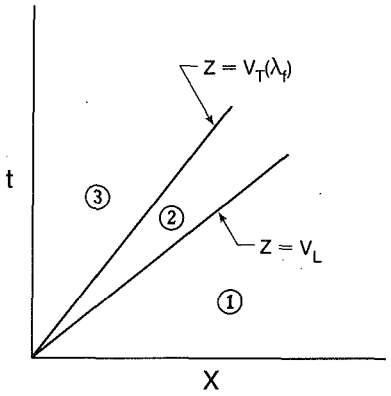


Fig. 6 Characteristics in the (X, t) plane for $d^2T/d\lambda^2 < 0$ and $c_L(\lambda) > c_T(\lambda)$, $\lambda < \lambda_f$, with $1 \le \lambda_f < \lambda_0$

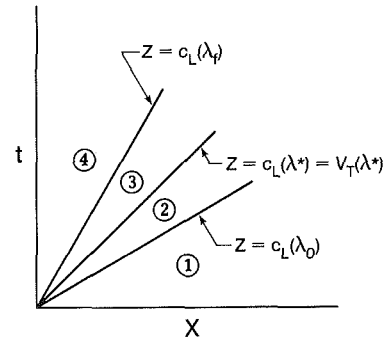


Fig. 7 Characteristics in the (X, t) plane for $d^2T/d\lambda^2 < 0$ and $c_L(\lambda_f) < c_T(\lambda_f)$

[3] in their study of plastic deformation of solids, and by Nowinski [5] in an investigation of the propagation of finite longitudinal disturbances in rubber bars in which $\lambda_0 = 1$.

It thus appears that a realistic formulation of the problem consists of the prescription of λ_0 and the constant values of q and ϕ. Then λ_f is found from (5.13), and θ_f is obtained from $(5.12)_2$. Other solutions for the same initial and boundary conditions (5.1) and (5.2) are outlined in the following.

Let us consider the previous problem in the unloading case for which $1 \le \lambda_f < \lambda_0$. Since $c_L(\lambda_0) < c_L(\lambda_f)$, a longitudinal shock is initiated at $X = 0$, $t = 0$. Moreover, because $V_T(\lambda_f) = c_T(\lambda_f) < c_L(\lambda_f)$ follows from (5.4), the solution is given by three uniform state regions in the (X, t) plane, as shown in Fig. 6. The solution obtained from the jump conditions (3.5) and (3.6) is as follows:

Region 1: $\dfrac{X}{t} > V_L;$

$$\lambda = \lambda_0, \quad \theta = \tau = \nu = 0. \tag{5.16}$$

Region 2: $V_L > \dfrac{X}{t} > c_T(\lambda_f);$

$$\lambda = \lambda_f, \quad \theta = \nu = 0, \quad \tau = -V_L \lambda_f. \tag{5.17}$$

Region 3: $\dfrac{X}{t} < c_T(\lambda_f);$

$$\lambda = \lambda_f, \quad \theta = \theta_f$$

$$\tau = \{\lambda_f c_T(\lambda_f) - V_L \lambda_f\}\cos\theta_f - \lambda_f c_T(\lambda_f),$$

$$\nu = -\{\lambda_f c_T(\lambda_f) - V_L \lambda_f\}\sin\theta_f, \tag{5.18}$$

where

$$V_L = \frac{T(\lambda_f) - T(\lambda_0)}{\rho_0(\lambda_f - \lambda_0)}. \tag{5.19}$$

The remaining details are similar to the previous case.

We reconsider the impact loading case $\lambda_f > \lambda_0$, but now we suppose that $V_T(\lambda_f) = c_T(\lambda_f) > c_L(\lambda_f)$ in addition to (5.4). Let λ^* denote the value of λ for which $dT/d\lambda = T/\lambda$ so that $c_T(\lambda^*) = c_L(\lambda^*)$. We recall, for example, that for the Mooney-Rivlin material $\lambda^* = \lambda_c$ in (4.6). In order that $c_T(\lambda_f) > c_L(\lambda_f)$, it is necessary that $\lambda_f > \lambda^*$. For $\lambda_0 > \lambda^*$, the solution that derives from $(3.3)_2$ consists of four regions in the (X,t) plane, as indicated in Fig. 7. Recalling (5.9), we find

Region 1: $\dfrac{X}{t} \ge c_L(\lambda_0);$

$$\lambda = \lambda_0, \quad \theta = \tau = \nu = 0. \tag{5.20}$$

Region 2: $c_L(\lambda_0) \ge \dfrac{X}{t} > c_T(\lambda^*) = V_T(\lambda^*),$

$$\frac{X}{t} = c_L(\lambda), \quad \theta = \nu = 0, \quad \tau = -\int_{\lambda_0}^{\lambda} c_L(\eta)\,d\eta. \tag{5.21}$$

Region 3: $c_T(\lambda^*) > \dfrac{X}{t} \ge c_L(\lambda_f);$

$$\frac{X}{t} = c_L(\lambda), \quad \theta = \theta_f,$$

$$\tau = U(\lambda^*)\cos\theta_f - \{\lambda^* c_T(\lambda^*) + \int_{\lambda^*}^{\lambda} c_L(\eta)\,d\eta\},$$

$$\nu = -U(\lambda^*)\sin\theta_f. \tag{5.22}$$

Region 4: $\dfrac{X}{t} \le c_L(\lambda_f);$

$$\lambda = \lambda_f, \quad \theta = \theta_f,$$

$$\tau = U(\lambda^*)\cos\theta_f - \{\lambda^* c_T(\lambda^*) + \int_{\lambda^*}^{\lambda_f} c_L(\lambda)\,d\lambda\},$$

$$\nu = -U(\lambda^*)\sin\theta_f. \tag{5.23}$$

Let p denote the constant impact speed at which O' is moved at an angle ϕ with the x axis, as described earlier in Fig. 5. Then, it can be shown that p may be written as the following function of the impact angle ϕ and the stretch λ_f:

$$p^2 + 2pU(\lambda^*)\cos\phi - \int_{\lambda_0}^{\lambda_f} c_L(\lambda)\,d\lambda[U(\lambda^*) + \lambda^* c_T(\lambda^*) + \int_{\lambda^*}^{\lambda_f} c_L(\lambda)\,d\lambda] = 0, \tag{5.24}$$

in which λ^* and λ_0 are assigned quantities. Of course, for the longitudinal impact problem, we still have $p = q$ in (5.15).

If the same problem is considered with $\lambda^* \le \lambda_0 < \lambda_f$, the solution in the (X, t) plane consists of three regions separated by the characteristics $Z = c_L(\lambda_0) = V_T(\lambda_0)$ and $Z = c_L(\lambda_f)$. We omit these details.

Finally, we sketch solutions for an S-shaped T, λ curve of the form shown in Fig. 3. When the strain energy function (4.5) with $\alpha = 0.5$ and $\lambda = 0.02$ is considered, $c_L(\lambda) > c_T(\lambda)$ for all λ. Of course, we now discard the restriction (5.4).

First, we assume that $\lambda_f > \lambda_i$ and $\lambda_f > \lambda_0 > \lambda_T$, where λ_i is the value of λ corresponding to the inflexion point and λ_T is the tangent point indicated in Fig. 3. It is shown in Fig. 8 that the solution in the (X, t) plane consists of uniform state regions separated by the shocks $Z = V_L$ and $Z = c_T(\lambda_f) = V_T(\lambda_f)$, where

$$V_L = \left[\frac{T(\lambda_f) - T(\lambda_0)}{\rho_0(\lambda_f - \lambda_0)}\right]^{1/2}. \tag{5.25}$$

Details of the solution are readily obtained from the discontinuity relations across the shocks.

If $\lambda_f > \lambda_i$ and $\lambda_f > \lambda_T > \lambda_0$, the solution consists of four regions in the (X, t) plane, as shown in Fig. 9. Regions 1, 3, and 4 are uniform state regions, and

$$V_L = \left[\frac{T(\lambda_f) - T(\lambda_T)}{\rho_0(\lambda_f - \lambda_T)}\right]^{1/2}. \tag{5.26}$$

Downloaded 02 May 2010 to 171.66.16.54. Redistribution subject to ASME license or copyright; see http://www.asme.org/terms/Terms_Use.cfm

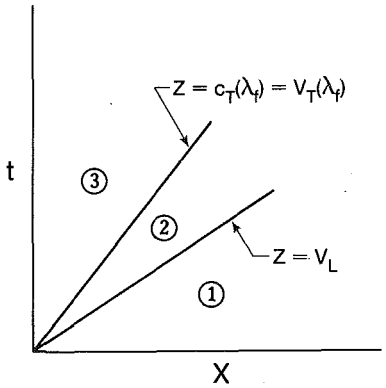


Fig. 8 Characteristics in the (X, t) plane for an S shaped T, λ curve and $\lambda_f > \lambda_i$, $\lambda_f > \lambda_0 > \lambda_T$

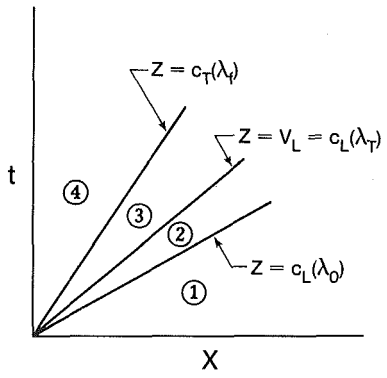


Fig. 9 Characteristics in the (X, t) plane for an S shaped T, λ curve and $\lambda_f > \lambda_i$, $\lambda_f > \lambda_T > \lambda_0$

It is interesting that $Z = V_L = c_L(\lambda_T)$ is both a characteristic and a longitudinal shock.

6 Numerical Results for a Neo-Hookean Material

Numerical results are now presented for a neo-Hookean string for the loading case $\lambda_f > \lambda_0$ due to a transverse impact. To obtain numerical results for the solution indicated in Fig. 4, the integral

$$I \equiv \int_{\lambda_0}^{\lambda} c_L(\eta)\, d\eta \tag{6.1}$$

must be evaluated. The neo-Hookean, rubberlike solid described in (4.2) and (4.3) is the simplest example for which an explicit solution may be obtained. In this case, the conditions (5.4) are satisfied for all $\lambda_f > \lambda_0$. Use of $(2.9)_2$ and (4.3) in (6.1) gives

$$\frac{I}{c_0} = \int_{\lambda_0}^{\lambda} \frac{1}{\eta}\left[\frac{\eta^3+2}{3\eta}\right]^{1/2} d\eta, \tag{6.2}$$

where $c_0 = [3\mu/\rho_0]^{1/2}$ is identified as the longitudinal wave speed for infinitesimal amplitude waves propagating on the undeformed state of the material.

The integral (6.2) can be evaluated in terms of elliptic integrals. First, we note that integration by parts gives

$$\frac{I}{c_0} = {}_{\lambda_0}^{\lambda}\left[\frac{\eta^3+2}{3\eta}\right]^{1/2} + \int_{\lambda_0}^{\lambda} \frac{d\eta}{\eta\left[\eta\dfrac{(\eta^3+2)}{3}\right]^{1/2}}. \tag{6.3}$$

A lengthy calculation shows that the transformation

$$\phi(\lambda) = \cos^{-1}\left[\frac{(1-\sqrt{3})\lambda + 2^{1/3}}{(1+\sqrt{3})\lambda + 2^{1/3}}\right]$$

$$= 2\tan^{-1}\left\{3^{1/4}\left[\frac{\lambda}{\lambda+2^{1/3}}\right]^{1/2}\right\} \tag{6.4}$$

converts the last term in (6.3) to a sum of elliptic integrals and an elementary trigonometric integral. The result is an exact expression

$$\frac{I}{c_0} = H(\lambda,\phi;k) - H(\lambda_0,\phi_0;k) \tag{6.5}$$

where $\phi_0 \equiv \phi(\lambda_0)$ is defined by (6.4), and

$$H(\lambda,\phi;k) = \left[\frac{\lambda^3+2}{3\lambda}\right]^{1/2} - 2^{1/3}3^{3/4}\left[\left(\frac{\sqrt{3}-3}{6}\right)F(\phi;k) + E(\phi;k) + \frac{\sin\phi(1-k^2\sin^2\phi)^{1/2}}{1-\cos\phi}\right]. \tag{6.6}$$

No significant simplification results from the use of (6.4) in the last term. The functions $F(\phi;k)$ and $E(\phi;k)$ in (6.6) are the usual tabulated elliptic integrals of the first and second kind, respectively, with modulus

$$k = \left[\frac{2+\sqrt{3}}{4}\right]^{1/2}. \tag{6.7}$$

It follows from (6.4) that for $\lambda\epsilon[1, \infty)$, $\phi(\lambda)\ \epsilon[1.438, 1.842) = [82.40 \text{ deg}, 105.54 \text{ deg})$; consequently, it may be helpful to note that for $\pi \geq \phi \geq \pi/2$, $F(\phi;k) = 2F(\pi/2;k) - F(\pi-\phi;k)$ and $E(\phi;k) = 2E(\pi/2;k) - E(\pi-\phi;k)$.

Finally, use of (4.3) for the neo-Hookean material in (2.9) yields

$$\frac{c_T(\lambda)}{c_0} = \frac{1}{\lambda}\left[\frac{\lambda^3-1}{3\lambda}\right]^{1/2}. \tag{6.8}$$

Upon using (6.5) and (6.8) in (5.5) to (5.8), we obtain an exact solution to the transverse impact loading problem. A similar procedure may be applied to derive in terms of elliptic integrals the exact solution for the Mooney-Rivlin model, but we will omit this more complicated result. An alternative procedure is to evaluate the integral (6.1) numerically which would be necessary for more complicated strain energy functions.

In the normal impact of a hyperelastic string under a given initial stretch λ_0, the impact speed q and the maximum stretch λ_f following the impact are related by (5.12), and the kink angle θ_f may be obtained from (5.10). The relations between q/c_0 and θ_f, and between q/c_0 and λ_f are shown graphically in Fig. 10 for the neo-Hookean material with stretch $\lambda_0 = 1.1$ and 2. It is evident from these results that for a given value of

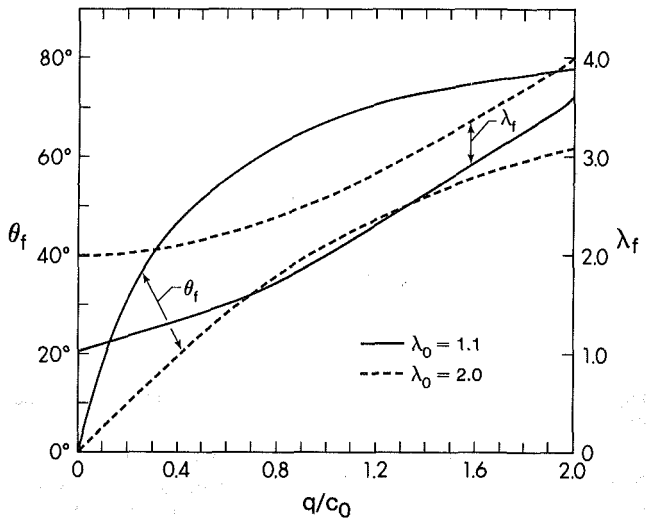


Fig. 10 Relations between q/c_0 and θ_f and between q_0/c_0 and λ_f for normal impact of a neo-Hookean string

Downloaded 02 May 2010 to 171.66.16.54. Redistribution subject to ASME license or copyright; see http://www.asme.org/terms/Terms_Use.cfm

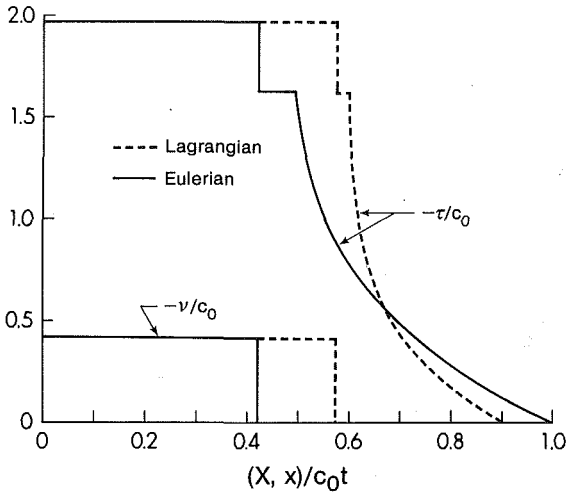


Fig. 11 Variation of velocity components with the Eulerian coordinate x and the Lagrangian coordinate X for normal impact of a neo-Hookean string with $q/c_0 = 2.01$, $\lambda_0 = 1.1$

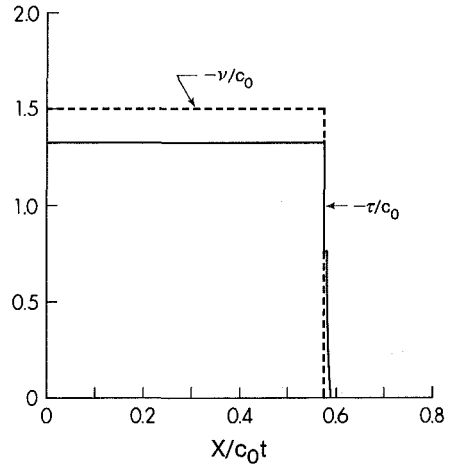


Fig. 12 Variation of velocity components with the Lagrangian coordinate X for normal impact of a neo-Hookean string with $q/c_0 = 2.01$ and $\lambda_0 = 4.0$

q/c_0, the value of θ_f increases as λ_0 decreases. Also, it is easily shown that $\theta_f \to \pi/2$ as $q_0/c_0 \to \infty$. The variation of the velocity components τ and v with the Eulerian coordinate x and the Lagrangian coordinate X is shown in Fig. 11 for $\lambda_0 = 1.1$ and $q/c_0 = 2.01$ corresponding to $\lambda_f = 3.6$.

It is interesting to note that for a given value of q_0/c_0, regions 2 and 3 shrink as λ_0 is increased. This is indicated in Fig. 12, which shows that for $q/c_0 = 2.01$ and $\lambda_0 = 4$, the wave front and the discontinuity of θ almost coincide. Numerical results for normal impact of strings with more complicated strain energy density functions show qualitatively similar relations between q_0/c_0 and λ_f and q/c_0 and θ_f. It is seen also that for a given value of λ_0 the kink angle θ_f increases as q_0/c_0 increases.

Acknowledgment

M. F. Beatty acknowledges support of this research by a grant from the National Science Foundation; and he thanks Dr. Tim Wright for his thoughtful comments concerning an earlier draft of some related work on this topic.

References

1 Cristescu, N., *Dynamic Plasticity*, North Holland, Netherlands, 1967.

2 Rakhmatulin, K. A., "Propagation of a Wave of Unloading," *Prik. Math. Mech.*, Vol. 9, 1945, pp. 91–100.

3 vonKarman, T., and Duwez, P., "The Propagation of Plastic Deformation in Solids," *J. Appl. Phys.*, Vol. 21, 1950, pp. 987–994.

4 Taylor, G. I., "The Plastic Wave in a Wire Extended by an Impact Load," *The Scientific Papers of G. I. Taylor*, Vol. I, Cambridge, U.P., 1958, pp. 567–579.

5 Nowinski, J. L., "On the Propagation of Finite Disturbances in Bars of Rubberlike Materials," ASME *Journal of Engineering for Industry*, Vol. 87, 1965, pp. 523–529.

6 Ringleb, F. O., "Motion and Stress of an Elastic Cable Due to Impact," ASME JOURNAL OF APPLIED MECHANICS, Vol. 24, 1957, pp. 417–425.

7 Smith, J. C., McCrackin, F. L., and Schiefer, H. F., "Stress-Strain Relationships in Yarns Subjected to Rapid Impact Loading, Part IV," *Text. Res. J.*, Vol. 28, 1958, pp. 288–302.

8 Li, W. H.,"Elastic Flexible Cable in Plane Motion Under Tension," ASME JOURNAL OF APPLIED MECHANICS, Vol. 26, 1959, pp. 587–593.

9 Nowinski, J. L., "Transverse Perpendicular Impact on a Cable of a Highly Elastic Material," *AIAA J.*, Vol. 5, 1967, pp. 332–333.

10 Riegel, C., and Nowinski, J., "An Experimental Investigation of Wave Propagation in a Rubber String Impacted by a Projectile," *Int. J. Nonlin. Mech.*, Vol. 11, 1976, pp. 229–237.

11 Whitham, G. B., *Linear and Nonlinear Waves*, Wiley-Interscience, New York, 1974.

12 Treloar, L. R. G., *The Physics of Rubber Elasticity*, 2nd Ed., Oxford U.P., 1967.

13 Inshihara, N., Hashisune, N., and Tatibana, M., "Statistical Theory of Rubber-Like Elasticity, IV," *J. Chem. Phys.*, Vol. 19, 1951, pp. 1508–1520.

14 Davison, L., "Propagation of Plane Waves of Finite Amplitude in Elastic Solids," *J. Mech. Phys. Solids*, Vol. 14, 1966, pp. 249–270.

Downloaded 02 May 2010 to 171.66.16.54. Redistribution subject to ASME license or copyright; see http://www.asme.org/terms/Terms_Use.cfm

A. Lakhtakia
V. K. Varadan
Mem. ASME
V. V. Varadan

Wave Propagation Laboratory,
Department of Engineering Science
and Mechanics,
The Pennsylvania State University,
University Park, Pa. 16802

The Acoustic Response of a Periodically Rough Elastic Plate (Ice) in Contact With Water

The plane wave scattering matrix theory is applied to formulate a T-*matrix which characterizes the acoustic response of an infinite solid plate bounded by semi-infinite vacuum and fluid half spaces on either side. Individual* T-*matrices for the periodically rough vacuum/solid and solid/fluid interfaces are used in this derivation. Using the computed results, the anomalies in the scattering response of the rough solid plate are explained in terms of the Rayleigh, the Scholte, and the Lamb waves.*

1 Introduction

The scattering of a wave by a rough interface between two media has several important applications in acoustic, electromagnetic, as well as in elastic scattering theories. Although wave scattering by plane interfaces is quite well understood, the reflection and transmission characteristics of rough surfaces is a topic of current research. For rough surfaces, in addition to specular scattering, reflection and transmission also occur at many different angles owing to nonplanar nature of the surfaces. The analysis for random rough surfaces is still in its infancy because the fields scattered by them are diffuse; however, scattering by periodically rough surfaces is being tackled with increasing success since scattering takes place in discrete, well-defined directions, specular as well as otherwise. The reader is referred to a good review of the recent results in this area presented by Wirgin [1].

Two types of theoretical procedures have been recently used for analyzing periodic surfaces. The first of these involves the solution of an integral equation, but calculations tend to be tedious [2–4]. Preferrable on account of its computational tractability is the T-matrix method, variously known as the null field method and the extended boundary condition method. This matrix approach was pioneered by Waterman [5] who constructed T-matrices to characterize the acoustic and electromagnetic responses of these surfaces to plane wave excitation. Recently, his approach has been extended to scattering by rough interfaces between elastic media as well [6, 7]. Furthermore, the restrictions on the degree of roughness placed by the Rayleigh hypothesis [8], in the application of the T-matrix approach for periodic surfaces, have been shown [9] to be removable by a judicious choice of the surface field representation. Deeply corrugated surfaces can be examined now by this method, at least for the scalar scattering problems.

Since the T-matrix method is particularly suitable for evaluating the spectral composition of the scattered energy, we have been investigating its use in solving for the response of layered media separated by periodially rough interfaces. Our motivation is because of our interest in the scattering of acoustic waves by an infinite ice plate having periodically rough surfaces. This is a problem of significant relevance in floating ice studies. The problem is also of interest in the ultrasonic NDE of flawed rough plates.

In this communication we present a procedure for formulating a T-matrix for the complete vacuum(air)-solid(ice)-fluid(water) system, given the individual T-matrices for the vacuum-solid and the solid-fluid interfaces, each interface being periodically rough. In using this approach we can consider several different types of excitation. This becomes possible by using a plane wave spectral (PWS) representation of the field of interest, a technique that has been extensively used, for example, by Kearns [10] in studying electromagnetic antenna-body interactions. Since the T-matrix approach itself involves PWS field representations, extension of this method to different excitations is theoretically trivial, albeit computationally quite formidable. In our preliminary studies we have, therefore, confined ourselves to plane wave excitation.

In the following section we will briefly develop an appropriate nomenclature for the T-matrices of each of the two interfaces involved, but for computational details on these two T-matrices we refer the readers to references [6, and 7]. Then, we derive a T-matrix for the complete vacuum-solid-fluid system in Section 3. Finally, in the last section we present some of computed results and discuss the resulting spectra.

2 Preliminaries

A homogeneous, isotropic, perfectly elastic plate having an infinite area of a finite thickness is interposed between two half spaces of which one is vacuum and the other an ideal fluid, as shown in Fig. 1. The solid-fluid interface S_1 is defined by

$$x_2 = h_1(x_1), -\infty < x_1 < \infty$$

Contributed by the Applied Mechanics Division for publication in the JOURNAL OF APPLIED MECHANICS.

Discussion on this paper should be addressed to the Editorial Department, ASME, United Engineering Center, 346 East 47th Street, New York, N.Y. 10017, and will be accepted until two months after final publication of the paper itself in the JOURNAL OF APPLIED MECHANICS. Manuscript received by ASME Applied Mechanics Division, March 1984; final revision, May, 1984.

Copyright © 1985 by ASME
Downloaded 02 May 2010 to 171.66.16.54. Redistribution subject to ASME license or copyright; see http://www.asme.org/terms/Terms_Use.cfm

where h_1 is single-valued and has period L_1 in its argument, i.e.,

$$h_1(x_1) = h_1(x_1 + L_1).$$

The vacuum-solid interfaces S_2 is also a similar surface defined by

$$x_2' = h_2(x_1'), -\infty < x_1' < \infty, x_2' = x_2 - d,$$

where again, h_2 is a single valued function of x_1' and has a periodicity L_2 such that

$$h_2(x_1') = h_2(x_1' + L_2),$$

and d represents the average thickness of the solid plate. In general, $L_1 \neq L_2$; however, we will take $L_1 = L_2 = L$ for simplicity although that is in no way a limitation on the formulation of the problem [10, 11]. We will further assume that the problem is independent of the x_3 variable; hence it is only two-dimensional.

Wave propagation in an elastic solid is characterized by two types of wave motion; longitudinal and the shear waves. In particular, in the elastic plate four types of these waves can exist: one pair of longitudinal (P) and shear ($SV-$) waves moving toward S_2 in the $-x_2$ direction, and another pair of P and SV-waves moving away from S_2 in the $+ x_2$ direction. Although SH-waves can also exist they can be analyzed by scalar methods, and the interested reader is referred to reference [5]. On the other hand, inside the fluid half space only longitudinal modes can exist and we designate them as F-waves. Of these, one set of F-waves is incident on the surface S_1 from the $-x_2$ direction, while the second set of F-waves moves away from S_1 in the $+ x_2$ direction. Since the vacuum cannot support any elastic wave motion, there are six sets of waves to be accounted for.

In general, mode conversion between the various modes occurs at the boundaries, hence it is necessary to consider P, SV, and F-waves simultaneously. We will use a combination of vector and tensor notation for our formulas. Latin subscripts are to be assigned the values 1, 2, and 3 while Greek subscripts have the values 1 and 2 assigned to them. For repeated subscripts the summation convention holds.

2a T-Matrix for the Solid/Fluid Interface. Since a complete formulation of a T-matrix to characterize the response of the surface S_1 is given in reference [6], we only present final results in brief here for the sake of completeness.

Consider, therefore, the definitions associated with the PWS expansion of the fields on either side of the solid-fluid interface S_1:

$$\mathbf{k}_n^{f\pm} = k^f[\sin\theta_n^f \hat{x}_1 \pm \cos\theta_n^f \hat{x}_2] \equiv [k_{n,1}^{f\pm}, k_{n,2}^{f\pm}] \quad (1a)$$

$$\mathbf{k}^{p\pm} = k^p[\sin\theta_n^p \hat{x}_1 \pm \cos\theta_n^p \hat{x}_2] \equiv [k_{n,1}^{p\pm}, k_{n,2}^{p\pm}] \quad (1b)$$

$$\mathbf{k}_n^{s\pm} = k^s[\sin\theta_n^s \hat{x}_1 \pm \cos\theta_n^s \hat{x}_2] \equiv [k_{n,1}^{s\pm}, k_{n,2}^{s\pm}] \quad (1c)$$

with $k^f = \omega/c_f$ being the wave number in the fluid; and k^p and $\omega/c_p = k^s = \omega/c_s$ being the longitudinal and the shear wave numbers, respectively, for the solid. Further, each of the $\cos\theta_n$'s in equations (1) is defined as

$$\cos\theta_n = \begin{cases} [1 - \sin^2\theta_n]^{1/2} \\ i[\sin^2\theta_{n-1}]^{1/2} \end{cases} ; \sin^2\theta_n = \begin{cases} \leq 1 \\ > 1 \end{cases} \quad (2a)$$

where the superscripts on θ_n can be f,p,s in accordance with equations (1a–c) respectively. Finally, the $\sin\theta_n$'s are themselves defined as

$$\sin\theta_n^{f,p,s} = \sin\theta_0^{f,p,s} + 2\pi n/k^{f,p,s}L, \; n = 0, \pm 1, \pm, 2, \ldots \quad (2b)$$

with Snell's law constraining them by

$$k^p \sin\theta_n^p = k^s \sin\theta_n^s = k^f \sin\theta_n^f \quad (2c)$$

In this section θ_0^f is a reference angle to be decided by the angle the wave vector of the exciting field makes with the x_2-axis.

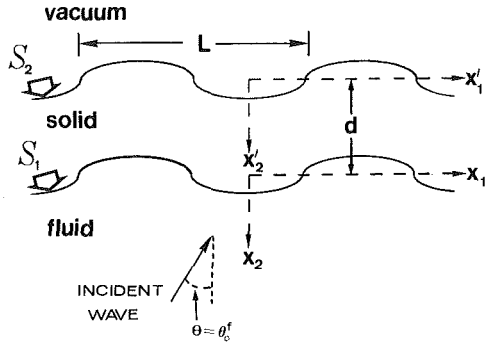


Fig. 1 Schematic of the problem. The periodically rough surfaces S_1 and S_2 are the interfaces of a solid plate with a fluid and vacuum, respectively.

On the fluid side of the interface two fluid modes exist as indicated in the previous section. These are

$$u_\gamma^f(\mathbf{x}) = a_n^\pm (k_{n,\gamma}^{f\pm}/k^f) \exp[i\mathbf{k}_n^{f\pm} \cdot \mathbf{x}] \quad (3a)$$

where the superscripts $\pm$ refer to the fact the particular mode propagates in the $\pm$ x_2 direction, and $a_n^\pm$ are the plane wave expansion coefficients. Likewise, the four solids modes are

$$u_\gamma^{p\pm}(\mathbf{x}) = b_n^\pm (k_{n,\gamma}^{p\pm}/k^p) \exp[i\,\mathbf{k}_n^{p\pm} \cdot \mathbf{x}] \quad (3b)$$

and

$$u_\gamma^{s\pm}(\mathbf{x}) = c_n^\pm (\epsilon_{\gamma\beta} k_{n,\beta}^{s\pm}/k^s) \exp[i\,\mathbf{k}_n^{s\pm} \cdot \mathbf{x}] \quad (3c)$$

where $\epsilon_{\gamma\beta}$ is an unit antisymmetric tensor; and, $b_n^\pm$ and $c_n^\pm$ are the coefficients of the plane wave expansion of the field existing on the solid side of S_1. It must be noted that whereas $\{a_n^-, b_n^+, c_n^+\}$ constitute a set of plane waves incident on S_1; $\{a_n^+, b_n^-, c_n^-\}$ denote the plane waves generated and consequently, they move away from S_1. Following reference [6] we relate coefficients as

$$[a_n^+] = [R_1][a_n^-] \quad (4a)$$

$$[b_n^-, c_n^-]^{Tr} = [T_1][a_n^-] \quad (4b)$$

$$[a_n^+] = [T_2][b_n^+, c_n^+]^{Tr} \quad (4c)$$

while,

$$[b_n^-, c_n^-]^{Tr} = [R_2][b_n^+, c_n^+]^{Tr}, \quad (4d)$$

the superscript Tr indicating a transpose, and R_1, R_2, T_1, and T_2 being the reflection and the transmission matrices obtained from a partitioning of the T-matrix given by equation (32) of reference [6]. The matrix R_1 has a 1×1 substructure, R_2 has a 2×2 substructure, whereas T_1 and T_2 have, respectively, 1×2 and 2×1 substructures.

2b T-Matrix for the Vacuum/Solid Interface. In reference [7] we have described a T-matrix procedure for obtaining the elastic scattering response of a traction-free periodic rough surface. Therefore, only the pertinent equations are presented here. The fields existing on the solid side of S_2 are given by

$$u_\gamma^{p\pm}(\mathbf{x}') = b_n'^{\pm} (k_{n,\gamma}^{p\pm}/k^p) \exp[i\,k_{\mathbf{n}}^{p\pm} \cdot \mathbf{x}'] \quad (5a)$$

and

$$u_\gamma^{s\pm}(\mathbf{x}') = c_n'^{\pm} (\epsilon_{\gamma\beta}\, k_{n,\beta}^{s\pm}/k^s) \exp[i\,\mathbf{k}_{\mathbf{n}}^{s\pm} \cdot \mathbf{x}'] \quad (5b)$$

where the primes refer to the coordinate system for surface S_2. The fields superscripted "+" are the scattered (reflected) fields while the "−" superscripted fields are incident on S_2. The coefficients $b_n'^{\pm}$ and $c_n'^{\pm}$ are related as

$$[b_n'^{+}, c_n'^{+}]^{Tr} = [T_3][b_n'^{-}, c_n'^{-}]^{Tr} \quad (6)$$

where T_3 is the reflection (T-)matrix of the S_2 and has a 2×2 substructure. It is obvious that there are no waves existing in the vacuum.

3 Joining Equations and the System T-Matrix

With the individual T-matrices available from both the

Downloaded 02 May 2010 to 171.66.16.54. Redistribution subject to ASME license or copyright; see http://www.asme.org/terms/Terms_Use.cfm

surfaces S_1 and S_2 we are now in a position to formulate a T-matrix for obtaining the response of the total vaccum-solid-fluid system. We have, however, first to relate the coefficients $b_n^{\pm}$ and $c_n^{\pm}$ with $b_n'^{\pm}$ and $c_n'^{\pm}$. This we do by means of the "joining" equations. Thus a wave generated at S_2 has only to propagate a distance $-d\hat{x}$ in the elastic plate to become incident on S_2. During this propagation from S_1 to S_2 all that happens is that its phase changes by an amount proportional to the thickness of the plate. Then,

$$\begin{bmatrix} b_n'^{-} \\ \cdots\cdots \\ c_n'^{-} \end{bmatrix} = \begin{bmatrix} F_p^- & \vdots & 0 \\ \cdots & \cdots & \cdots \\ 0 & \vdots & F_s^- \end{bmatrix} \begin{bmatrix} b_n^- \\ \cdots \\ c_n^- \end{bmatrix} \tag{7a}$$

where the matrices F_p^- and F_s^- are diagonal matrices with 1×1 substructure and

$$(F_p^-)_{nm} = e^{-id(\mathbf{k}_n^{p-} \cdot \hat{x}_2)} \delta_{nm} \tag{7b}$$

$$(F_s^-)_{nm} = e^{-id(\mathbf{k}_n^{s-} \cdot \hat{x}_2)} \delta_{nm} \tag{7c}$$

Similarly,

$$\begin{bmatrix} b_n^+ \\ \cdots\cdots \\ c_n^+ \end{bmatrix} = \begin{bmatrix} F_p^+ & \vdots & 0 \\ \cdots & \cdots & \cdots \\ 0 & \vdots & F_s^+ \end{bmatrix} \begin{bmatrix} b_n'^{+} \\ \cdots\cdots \\ c_n'^{+} \end{bmatrix} \tag{7d}$$

where, again,

$$(F_p^+)_{nm} = e^{id(\mathbf{k}_n^{p+} \cdot \hat{x}_2)} \delta_{nm} \tag{7e}$$

$$(F_s^+)_{nm} = e^{id(\mathbf{k}_n^{s+} \cdot \hat{x}_2)} \delta_{nm} \tag{7f}$$

It is easy to recognize that $F_p^- \equiv F_p^+$ and $F_s^- \equiv F_s^+$, so that our joining equations are given as

$$[b_n'^{-}, c_n'^{-}]^{Tr} = [F][b_n^-, c_n^-]^{Tr} \tag{8a}$$

and

$$[b_n^+, c_n^+]^{Tr} = [F][b_n'^{+}, c_n'^{+}]^{Tr} \tag{8b}$$

with the definition of $[F]$ taken from equations (7).

Armed with equations (4), (6), and (8) we now examine the T-matrix of the complete scattering system. When an $[a_n^-]$ ensemble is incident on S_1, it generates $[a_n^+]$ on the fluid side while a $[b_n^-, c_n^-]^{Tr}$ ensemble is generated on the solid side of S_1. The ensemble $[b_n^-, c_n^-]$ hits S_2 and then is incident as $[F]$ $[T_3]$ $[F]$ $[b_n^-, c_n^-]^{Tr}$ on S_1 from its solid side. At this point it creates $[T_2]$ $[F]$ $[T_3]$ $[F]$ $[b_n^-, c_n^-]^{Tr}$ waves on the fluid side of S_1 while a $[R_2]$ $[F]$ $[T_3]$ $[F]$ $[b_n^-, c_n^-]^{Tr}$ ensemble is generated on the solid side of S_1. On doing our bookkeeping at this juncture on the reflected F waves we find it to be composed of $\{[R_1] + [T_2][A][T_1]\}[a_n^-]$ waves, where $[A] \equiv [F]$ $[T_3]$ $[F]$ characterizes one round-trip $S_1 \rightarrow S_2 \rightarrow S_1$. Continuing in this manner with $[R_2]$ $[A]$ $[T_1]$ $[a_n^-]$ we see the end of the next roundtrip, the total reflected ensemble on the fluid side is given by $\{R_1] + [T_2][A][T_1] + [T_2][A][R_2][A][T_1]\}[a_n^-]$. This process continues ad infinitum, and we obtain the total scattered field on the fluid side to be composed of

$$\left\{[R_1] + [T_2]\left\{\sum_{l=0}^{\infty} \{A][R_2]\}^l\right\}[A][T_1]\right\}[a_n^-]$$

Thus, if we represent the final scattered field ensemble on the fluid side as $[A_n^+]$, then

$$[A_n^+] = [T][a_n^-] \tag{9}$$

and

$$[T] = [R_1] + [T_2]\left\{\sum_{l=0}^{\infty} \{[A][R_2]\}^l\right\}[A][T_1] \tag{9a}$$

In equation (9a) it is easy to recognize that the arguments of the summation sign constitute a Neumann series. Then, by virtue of the properties of a convergent Neumann series, we can write

$$[T] = [R_1] + [T_2]\{[I] - [A][R_2]\}^{-1}[A][T_1] \tag{9b}$$

where $[I]$ is an identity matrix. The transition from equation (9a) to (9b) holds mathematically if the maximum eigenvalue λ of $[I] - [A][R_2]$ is such that $|\lambda| < 1$. However, the physics of the problem guarantees this convergence at and beyond some level of the size $2N + 1$ of the vector $[a_n^-]$ when $|n|$ has been restricted to $|n| \leq N$. When a wave is incident on S_2 it cannot transfer any energy into the vacuous half space, while when it hits S_1 from the solid side it "leaks" a part of its energy into the fluid half-space. The summation in equation (9a) reflects this energy radiation into the fluid. Therefore, we can conclude that equation (9b) constitutes a T-matrix for the vacuum-solid-fluid system.

In particular, we are interested in the scattering of a plane wave incident on S_1 from the fluid half-space, at an angle Θ with the x_2 axis. Then, $a_n^- = \delta_{n0}\forall n$ where $\delta_{nn'}$ is the Kronecker delta, $\theta_0^f = \Theta$, and θ_0^p and θ_0^s can be determined from equation (2c).

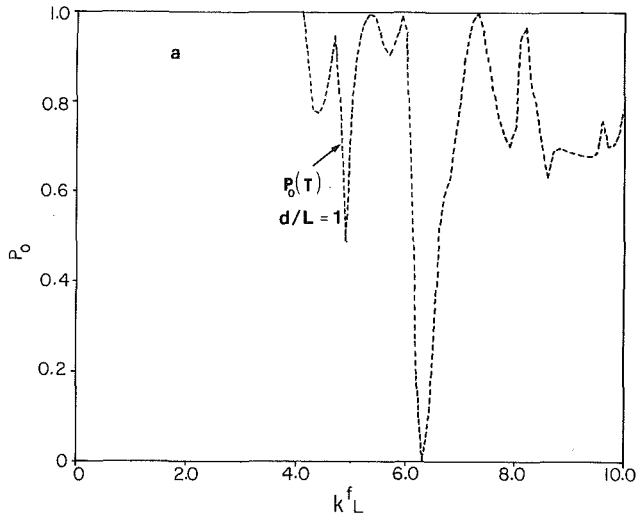


Fig. 2(*a*)

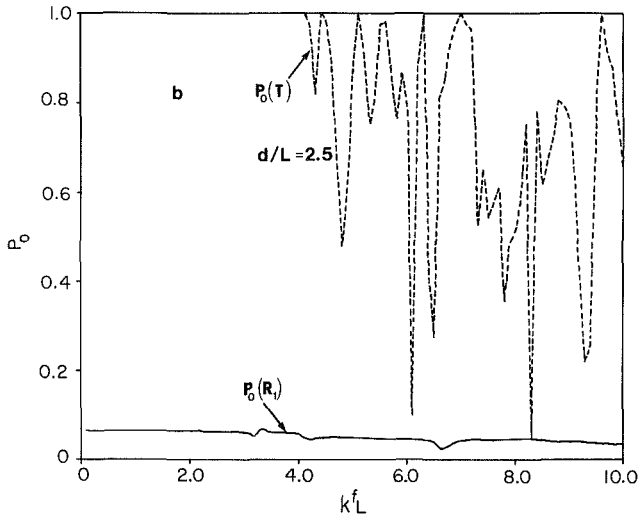


Fig. 2(*b*)

Fig. 2 Computed values of $P_0(T)$ as the normalized frequency $k^f L$ varies from 0.1 to 10. $h_1/L = h_2/L = 0.07$; $\Theta = \theta_0^f = 30$ deg. The plate thickness is (a) $d/L = 1.0$, and (b) $d/L = 2.5$. For comparison, $P_0(R_1)$ is plotted in Fig. 2(b). The wave speeds $c_f = 1493$ m s^{-1} $c_p = 1433$ m s^{-1}, and $c_s = 2743$ m s^{-1}, while the density of the solid (ice) is 0.917 times that of the fluid (water).

Downloaded 02 May 2010 to 171.66.16.54. Redistribution subject to ASME license or copyright; see http://www.asme.org/terms/Terms_Use.cfm

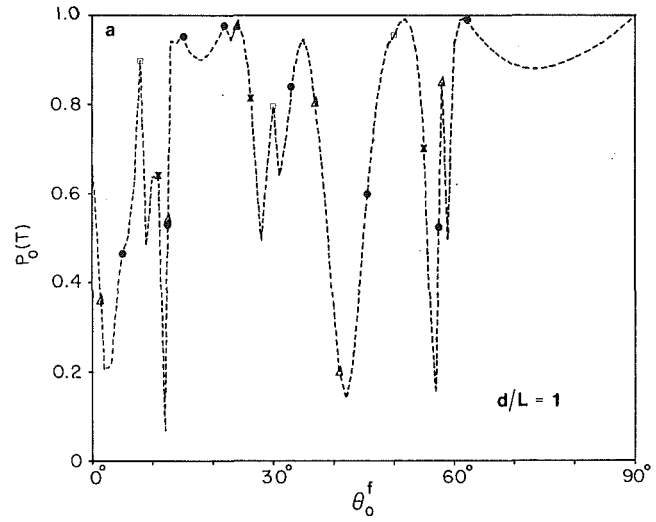


Fig. 3(a)

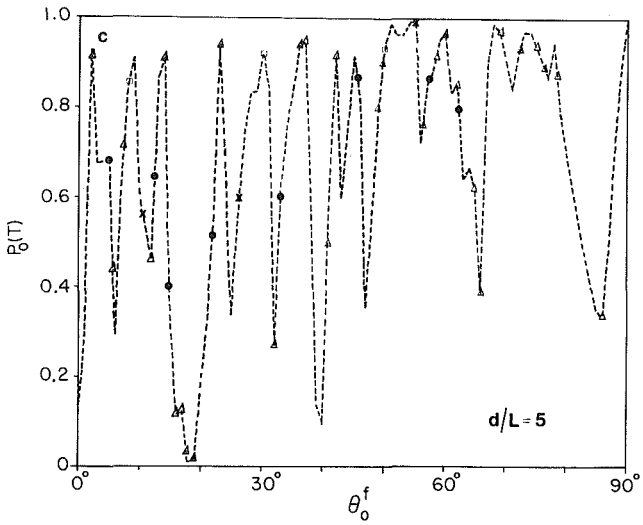


Fig. 3(c)

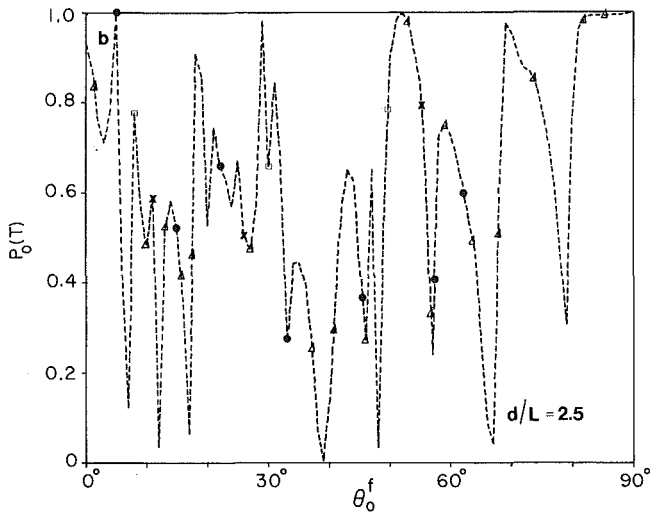


Fig. 3(b)

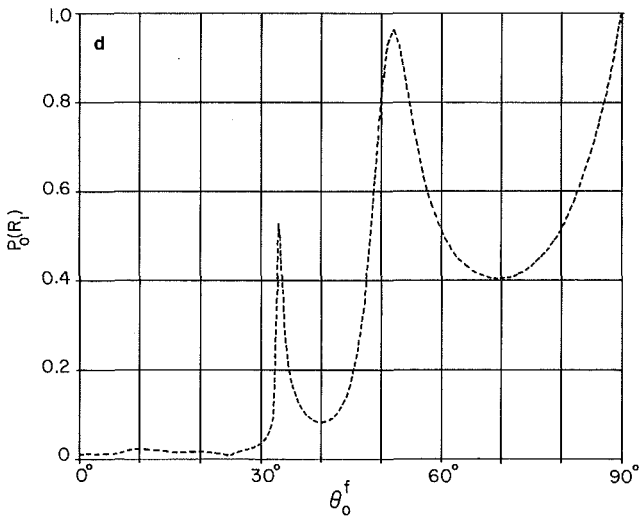


Fig. 3(d)

Fig. 3 Computed values of $P_0(T)$ as the angle of incidence $\Theta = \theta_0^f$ varies from 0 to 90 deg. $h_1/L = h_2/L = 0.07$; $k^fL = 10.0$. The plate thickness is (a) $d/L = 1.0$, (b) $d/L = 2.5$, and (c) $d/L = 5.0$. For comparison, $P_0(R_1)$ is plotted in Fig. 3(d). The dots represent the conversion of a wave of special order n from being propagating to evanescent, or vice versa. The boxes are the anomalies due the presence of a Rayleigh wave on S_2; the crosses, a Scholte wave on S_1. The presence of Lamb modes in the solid plate is denoted by triangles.

4 Numerical Results and Discussion

In deriving the T-matrix for the complete system we have, till now, made only two assumptions. First, the periodicity of both of the interfaces has been assumed to be the same, i.e., $L_1 = L_2$, but we have made no assumptions regarding the boundary profiles. This assumpiton is, however, not very serious since the matrices $F^{\pm}_{p,s}$ can be modified to incorporate the condition $L_1 \neq L_2$. Secondly, in presenting our numerical computations made on a DEC VAX 11/730 minicomputer, we have considered sinusoidal interfaces.

$$S_1: \quad x_2 = h_1 \cos(2\pi x_1/L)$$

$$S_2: \quad x_2 = h_2 \cos(2\pi x_1/L) - d$$

so that the point-to-point thickness of the solid plate is d. Furthermore, as stated earlier, we have considered a vacuum-ice-water system with the relevant velocities $c_f = 1493$ m s^{-1}, $c_p = 1433$ m s^{-1} and $c_s = 2743$ m s^{-1}, with the ratio of the fluid density to solid density equal to 1.0902 (ice floats on water!).

In Figs. 2(a) and (b), respectively, we have plotted the specularly returned power $P_0(T)$ as a function of the normalized frequency $k^fL = 0.1(0.1)10.0$ for a plate described by $h_1 = h_2 = 0.07L$ when the plate thickness $d/L = 1.0$ and 2.5. The angle of incidence $\Theta = \theta_0^f = 30$ deg, and the quantity $P_0(T)$ is defined as

$$P_0(T) = |A_0^+ / a_0^- |^2.$$

Furthermore, in Fig. 2(b), we also plot $P_0(R_1)$ for only the ice-water interface for purposes of comparison, where $P_0(R_1)$ is given by

$$P_0(R_1) = |a_0^+ / a_0^- |^2.$$

There is one noticeable feature in Figs. 2(a) and (b): $P_0(R_1)$ is almost always less than $P_0(T)$. We have observed this in other calculations made by us which are shown in Fig. 3. This is not surprising because whatever be the value of d, the interface S_2 completely reflects back all the power incident on it. However, were S_2 not there, then the waves generated by $[a_n^-]$ in the solid would continue to propagate in the $-x_2$ direction

Downloaded 02 May 2010 to 171.66.16.54. Redistribution subject to ASME license or copyright; see http://www.asme.org/terms/Terms_Use.cfm

indefinitely and would never be reflected back so that they could hit S_1 again.

Another important characteristic of $P_0(T)$ is the presence of several extremas in the Figs. 2(*a*) and (*b*). To investigate these "anomalies," we concentrated our attention on $k^f L = 10.0$ for the same layer parameters while the angle of incidence was varied as $\Theta = \theta_0^f = 0$ deg (1 deg) 90 deg. The resulting plots of $P_0(T)$ for $d/L = 1.0, 2.5$, and 5.0 are shown in Figs. 3(*a*)–(*c*), while in Fig. 3(*d*) $P_0(R_1)$ is shown for comparison.

5 Interpretation of the Reflection Spectrum

In so far as the extremas of $P_0(R_1)$ are concerned, they have been adequately dealt with in reference [6]. We are, however, more interested in the anomalies of $P_0(T)$. From a review of Brekhovskikh's work [12] we have been able to identify, at least, four *reasons* for these extremas of $P_0(T)$. These extremas are due to the characteristic spectra of each of the two periodic interfaces involved as well as the vibration (Lamb) modes of the elastic plate. We now discuss them in some detail.

1. The first reason involves a *F*, *P*, or *SV*-wave which changes from being evanescent to propagating or vice versa. Thus, a *F*-wave of spectral order "*n*" changes from being evanescent to propagating at

$$\theta_0^f = \sin^{-1}\{1 - 2\pi n/k^f L\} \tag{10a}$$

while it changes from being propagating to evanescent at

$$\theta_0^f = -\sin^{-1}\{1 + 2\pi n/k^f L\} \tag{10b}$$

provided, of course, $|\theta_0^f| \le \pi/2$. Analogous equations for the changes for the *P* and the *SV*- waves can be derived from the equations (2). We have marked the locations of these changes in Figs. 3(*a*)–(*c*) by the symbol "•."

2. Next, anomalous behavior may also occur when the quantity $|k^f \sin\theta_n^f|$ equals k_R, the wave number of a surface Rayleigh wave on S_2. This k_R is given by [13]

$$\frac{k_R}{k^s} = \frac{1+\nu}{0.862 + 1.14\nu}, \tag{11a}$$

$$\nu = (k^{s^2} - 2k^{p^2})/2(k^{s^2} - k^{p^2}) \tag{11b}$$

for $0 \le \nu \le 0.5$. Such an anomaly would occur at

$$\theta_0^f = \sin^{-1}\left\{\frac{2\pi m}{k^f L} \mp \frac{k_R}{k^f}\right\} \tag{11c}$$

and has been identified in Figs. 3(*a*)–(*c*) by the "□" sign. It must be mentioned that this type of anomaly has nothing to do with the plate, since it is dependent on the spectral characteristics of a periodically rough traction-free surface [3] only.

3. The third reason for this anomalous behavior is due to the occurence of a Scholte wave on S_1 at a given angle of incidence θ_0^f. This wave propagates on the surface S_1 and the angle θ_0^f is a solution of [12]

$$4m\, k_{n,2}^f\, (k^f \sin\theta_n^f)^2\, [k_{n,2}^p\, k_{n,2}^s + p^2] + k_{n,2}^p\, k^{s^4} = 0 \tag{12a}$$

where

$$\sin\theta_n^f = \sin\theta_0^f + 2\pi n/k^f L, \tag{12b}$$

$$p = \frac{k^{s^2} - 2(k_{n,2}^s)^2}{2\, k_{n,1}^s}, \tag{12c}$$

and m is the ratio of the fluid density to the solid density. The solutions of (12*a*) where $k_{n,2}^{f,p,s}$ are positive imaginary quantities have been identified in Figs. 3(*a*)–(*c*) by the "x" sign. Again, this anomalous behavior is entirely governed by the scattering characteristics of the solid/fluid interface S_1, although Ewing et al. [14] have observed that these roots also arise in the frequency equation for a planar floating ice sheet.

4. Finally, the last explanation we found is the occurrence of a Lamb wave [8]. The solution for these Lamb waves is directly dependent on the mean thickness d of the plate and can be obtained by solving [12]

$$\tan[k_{n,2}^p d/2] \cot[k_{n,2}^s d/2] = -q^2/k_{n,2}^p k_{n,2}^s \tag{13a}$$

for the symmetric Lamb waves, and

$$\tan[k_{n,2}^p d/2] \cot[k_{n,2}^s d/2] = -k_{n,2}^p\, k_{n,2}^s/q^2 \tag{13b}$$

for the antisymmetric Lamb waves, where

$$q = [(k_{n,1}^f)^2 - (k^s)^2/2]/k_{n,1}^f \tag{13c}$$

These solutions have been identified by the "Δ" symbol in Figs. 3(*a*)–(*c*). It is to be noted that these equations have been obtained for a free elastic plate of constant thickness d, and these roots are very close to the real parts of the roots obtained for planar floating ice sheets [14].

In spite of all of these four reasons we were able to identify, several of the anomalities are still unexplained. It must, however, be noted, that the last three of the reasons identified have been for *plane* interfaces [2, 3, 6, 7], and certainly a great deal of work has to be done in order to competely explain all of the anomalies occurring in $P_0(T)$ for periodically rough interfaces.

References

1 Wirgin, A., "Scattering of Sound From Hard and Soft Eggcrate Surfaces," *J. Acoust. Soc. Am.*, Vol. 75, 1984, pp. 340–345.

2 Fokkema, J. T., and Van den Berg, P. M., "Elastodynamic Diffraction by a Periodic Rough Surface (Stress-Free Boundary)," *J. Acoust. Soc. Am.*, Vol. 62, 1977, pp. 1095–1101.

3 Jungman, A., Adler, L., Achenbach, J. D., and Roberts, R., "Reflection from a Boundary With Periodic Roughness: Theory and Experiment," *J. Acoust. Soc. Am.*, Vol. 74, 1983, pp. 1025–1032.

4 Holford, R. L., "Scattering of Sound Waves at a Periodic, Pressure-Release Surface: An Exact Solution," *J. Acoust. Soc. Am.*, Vol. 70, 1981, pp. 1116–1128.

5 Waterman, P. C., "Scattering of Periodic Surfaces," *J. Acoust. Soc., Am.*, Vol. 57, 1975, pp. 791–802.

6 Chuang, S. L., and Johnson, R. K., "Acoustic Wave Scattering From a Fluid/Solid Periodic Rough Surface," *J. Acoust. Soc. Am.*, Vol. 71, 1982, pp. 1368–1376.

7 Lakhtakia, A., Varadan, V. K., Varadan, V. V., and Wall, D. J. N., "The *T*-Matrix Approach for Scattering by a Traction-Free Periodic Rough Surface," *J. Acoust. Soc. Am.*, 1984, in press.

8 Millar, R. F., "The Rayleigh Hypothesis and a Related Least-Squares Solution to Scattering Problems for Periodic Surfaces and Other Scatterers," *Radio Science*, Vol. 8, 1973, pp. 785–796.

9 Lakhtakia, A., Varadan, V. K., and Varadan, V. V., "On The Acoustic Response of a Deeply Corrugated Periodic Surface—A Hybrid *T*-Matrix Approach," *J. Acoust. Soc. Am.*, submitted, 1984.

10 Kearns, D. M., "Plane-Wave Scattering Matrix Theory of Antennas and Antenna-Antenna Interactions," National Bureau of Standards Technical Report No. NBSIR 78-890, Boulder, Colo., 1978.

11 Booker, H. G., and Clemmow, P. C., "The Concept of an Angular Spectrum of Plane Waves and its Relation That of Polar Diagram and Aperture Distribution," *Proc. IEE (England)*, Vol. 97, 1950, pp. 11–17.

12 Brekhovskikh, L. M., *Waves in Layered Media*, 2nd Ed., Academic Press, New York, 1980, Chapter 2.

13 Achenbach, J. D., *Wave Propagation in Elastic Solids*, North-Holland, Amsterdam, 1973, Chapter 5.

14 Ewing, W. M., Jardetsky, W. S., and Press, F., *Elastic Waves in Layered Media*, McGraw-Hill, New York, 1957, pp. 295–299.

Downloaded 02 May 2010 to 171.66.16.54. Redistribution subject to ASME license or copyright; see http://www.asme.org/terms/Terms_Use.cfm

Free Vibrations of Noncircular Cylindrical Shells Having Circumferentially Varying Thickness

K. Suzuki
Associate Professor,
Faculty of Engineering,
Yamagata University,
Yonezawa, Japan

A. W. Leissa
Professor,
Department of Engineeirng Mechanics,
Ohio State University,
Columbus, Ohio 43210
Fellow ASME

An exact method using power series expansions is presented for solving free vibration problems for noncircular cylindrical shells having circumferential thickness variation. The method is used to obtain the first known results for this class of problems. Frequencies and mode shapes are presented for a set of elliptical cylindrical shells having second degree thickness variation in each quadrant.

1 Introduction

Although the number of published references dealing with the free vibrations of closed, circular cylindrical shells is of the order of 1000 (cf., reference [1]), relatively little has been written about noncircular cylindrical shells. In reference [1] one finds 10 references which appeared before 1971 that treat such problems. Since that time a similar number of pertinent references have appeared [2-11]. The configurations studied were typically elliptical or oval cylindrical shells having uniform thickness. Rosen and Singer [12] approached the problem by treating the deviations from circularity as geometric imperfections, in the manner often used in shell buckling analysis. They showed that imperfections in-circularity of the order of the shell thickness or less may cause significant changes in the vibration frequencies.

Experimental studies with fluid filled shells have shown that axisymmetric acoustic modes of the fluid can excite asymmetric shell modes [13, 14]. It was hypothesized that the asymmetric response was due to noncircularity of the shells. However, it is also possible that the phenomenon may be due to circumferential variation in the thickness and/or material properties. This conjecture encouraged additional studies by Yousri and Fahy [15] and by Tonin and Bies [16]. The former [15] attempted to solve the coupled elastoacoustic problem involving both the shell and the internal fluid, including circumferential asymmetry in three shell parameters—noncircularity, thickness, and modulus of elasticity. However, incorrect shell equations were used; these accounted for variation of the three parameters in some terms of the equations, but not in others. The latter [16] studied circular cyindrical shells having circumferential thickness variation. The shell configuration was defined by two circular boundaries having centers that are not coincident. This gives rise to vibration modes that are either symmetric or antisymmetric with respect to the diametral symmetry plane. Theoretical results were obtained by the Ritz method and compared with experiment. The results purport to show that, even for shells with large thickness variation (e.g., $h_{max}/h_{min}=4.21$); the symmetric and antisymmetric mode frequencies are nearly identical.

The purpose of the present work is to present a correct and accurate method for analyzing the free vibrations of cylindrical shells having circumferentially varying curvature and thickness, a class of problems for which no previous solutions apparently have been publishsed. Approximate solutions to such problems could be obtained by, for example, the Ritz or finite element methods, with considerable time spent on digital computers finding the roots of large eigenvalue determinants. The present method demonstrates an exact method for dealing with a shell having both ends supported by shear diaphragms (also called "freely supported ends"), a set of edge conditions that have received enormous attention by researchers for the case of circular cylindrical curvature and uniform thickness (see, for example, the large number of such publications summarized in reference [1]).

2 Analysis

2.1 Lagrangian Formulation of the Equations of Motion and Boundary Conditions. Let us consider the free vibrations of a noncircular thin cylindrical shell of which the centerline of the cross section is a smoth curve and the thickness varies along the centerline. This centerline, which is the intersection of the middle surface of the shell with the plane x = constant, is shown in Fig. 1. Let the length of the shell be $l=\mu r_0$ where r_0 is a representative radius, and let the curvature at any point along the centerline be $1/\rho$. Take the coordinate axis x' along the generator of the middle surface, the arc length s measured along the centerline of the cross section (the centerline and the generator being orthogonal) and the z axis in the direction normal to the middle surface (positive inward). Let the thickness of the shell be $h=h_0H(s)$,

Contributed by the Applied Mechanics Division and presented at the Winter Annual Meeting, New Orleans, La., December 9-14, 1984 of THE AMERICAN SOCIETY OF MECHANICAL ENGINEERS.

Discussion on this paper should be addressed to the Editorial Department, ASME, United Engineering Center, 345 East 47th Street, New York, N.Y. 10017, and will be accepted until two months after final publication of the paper itself in the JOURNAL OF APPLIED MECHANICS. Manuscript received by ASME Applied Mechanics Division, November, 1983; final revision, May, 1984. Paper No .84-WA/APM-50.

Copies will be available until August, 1985.

Copyright © 1985 by ASME
Downloaded 02 May 2010 to 171.66.16.54. Redistribution subject to ASME license or copyright; see http://www.asme.org/terms/Terms_Use.cfm

where h_0 is the thickness at $s=0$ and $H(s)$ is a function of s. Employing a nondimensional coordinate $x=x'/r_0$, the displacements in the x', s and z directions $(\bar{u},\bar{v},\bar{w})$ are written as follows:

$$\bar{u}=u(s,x)\sin\omega t, \qquad \bar{v}=v(s,x)\sin\omega t, \qquad \bar{w}=w(s,x)\sin\omega t \tag{1}$$

where ω and t denote the circular frequency and the time. Let us consider the following transformation of variable:

$$\frac{d\theta}{ds}=\frac{1}{\rho}=\frac{G}{r_0}\Phi(\theta) \tag{2}$$

where θ is a variable that shows an angle between the tangent at the origin of s and the one at any point on the centerline, G is a constant determined by the shape of the curve and $\Phi(\theta)$ is a function of θ. As an example, consider an ellipse, for which the equation is denoted by the rectangular coordinates (ξ_1,ξ_2) as $\xi_1=a\cos\eta$, $\xi_2=b\sin\eta$, in which $2a$, $2b$, and η are the major and the minor axes and a parameter, respectively. Setting the representative radius r_0 and the ellipticity of the curve μ_0 as

$$r_0=\sqrt{(a^2+b^2)/2}, \qquad \mu_0=(a^2-b^2)/(a^2+b^2) \tag{3}$$

one obtains

$$\tan\theta=\sqrt{(1+\mu_0)/(1-\mu_0)}\tan\eta, \quad \frac{1}{G}=1-\mu_0^2,$$
$$\Phi(\theta)=(1+\mu_0\cos 2\theta)^{3/2} \tag{4}$$

One can denote $\Phi(\theta)$ by a simple expression for a number of other curves as well (cf. [17]). By modifying the Lagrangian for a vibratory period of a noncircular thin cylindrical shell with uniform thickness, which was given previously [11], the corresponding expression for a noncircular thin cylindrical shell with varying thickness may be determined as follows:

$$\begin{aligned}L=-\frac{D_0}{2r_0^2G}\int_{\theta_1}^{\theta_2}\int_0^{\mu}\Big[&-\alpha_0^4H(u^2+v^2+w^2)+\beta_0H\Big[\Big\{\frac{\partial u}{\partial x}\\&+G\Phi\Big(\frac{\partial v}{\partial\theta}-w\Big)\Big\}^2-2(1-\nu)\Big\{G\Phi\frac{\partial u}{\partial x}\Big(\frac{\partial v}{\partial\theta}-w\Big)\\&-\frac{1}{4}\Big(\frac{\partial v}{\partial x}+G\Phi\frac{\partial u}{\partial\theta}\Big)^2\Big\}\Big]+\\&+H^3\Big[\frac{\partial^2 w}{\partial x^2}+G^2\Phi\frac{\partial}{\partial\theta}\Big\{\Phi\Big(\frac{\partial w}{\partial\theta}+\nu\Big)\Big\}\Big]^2\\&-2(1-\nu)G^2H^3\Big[\Phi\frac{\partial^2 w}{\partial x^2}\frac{\partial}{\partial\theta}\Big\{\Phi\Big(\frac{\partial w}{\partial\theta}+v\Big)\Big\}\\&-\Phi^2\Big(\frac{\partial^2 w}{\partial x\partial\theta}+\frac{\partial v}{\partial x}\Big)^2\Big]+G\Phi H^3\Big[2\Big\{\frac{\partial u}{\partial x}\frac{\partial^2 w}{\partial x^2}\\&-G^3\Phi^2\Big(\frac{\partial v}{\partial\theta}-w\Big)\frac{\partial}{\partial\theta}\Big(\Phi\Big(\frac{\partial w}{\partial\theta}+v\Big)\Big)\Big\}\\&-(1-\nu)G\Phi\Big(\frac{\partial v}{\partial x}+\frac{\partial^2 w}{\partial x\partial\theta}\Big)\Big(\frac{\partial v}{\partial x}+G\Phi\frac{\partial u}{\partial\theta}\Big)\Big]\\&+G^2\Phi^2H^3\Big[G^2\Phi^2\Big(\frac{\partial v}{\partial\theta}-w\Big)^2\\&+\frac{1-\nu}{2}\Big(\frac{\partial v}{\partial x}+G\Phi\frac{\partial u}{\partial\theta}\Big)^2\Big]\Big]\Big(\frac{1}{\Phi}\Big)dxd\theta\end{aligned} \tag{5}$$

where

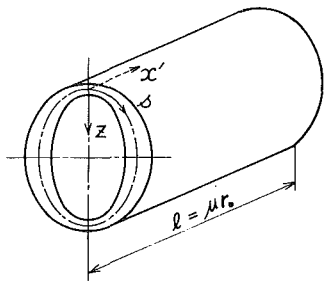


Fig. 1 Coordinates

$$D_0=\frac{Eh_0^3}{12(1-\nu^2)}, \qquad \alpha_0^4=\frac{\rho h_0\omega^2 r_0^4}{D_0}, \qquad \beta_0=\frac{12r_0^2}{h_0^2} \tag{6}$$

and where ν, E, and ρ denote Poisson's ratio, Young's modulus, and the mass density, respectively. Taking the first variation of L to obtain the stationary condition of the Lagrangian, $\delta L=0$, one obtains

$$\begin{aligned}\delta L=&-\frac{D_0}{r_0^2G}\int_{\theta_1}^{\theta_2}\int_0^{\mu}[E_1\delta u+E_2\delta v+E_3\delta w]dxd\theta\\&+\int_{\theta_1}^{\theta_2}\Big[T_1\delta u+T_2\delta v+T_3\delta w+M_1\delta\Big(\frac{\partial w}{\partial x}\Big)\Big]_{x=0}^{x=\mu}d\theta\\&+\int_0^{\mu}\Big[T_4\delta u+T_5\delta v+T_6\delta w+M_2\Big(\frac{\partial w}{\partial\theta}\Big)\Big]_{\theta=\theta_1}^{\theta=\theta_2}dx\\&+[T_7\cdot\delta w]_{x=0\ \ \theta=\theta_1}^{x=\mu\ \ \theta=\theta_2}\end{aligned} \tag{7}$$

where

$$\left.\begin{aligned}E_1&=-\alpha_0^4H(u/\Phi)-\frac{\partial T_1}{\partial x}-\frac{\partial T_4}{\partial\theta},\\E_2&=-\alpha_0^4H(v/\Phi)+\frac{\partial\Phi}{\partial\theta}(M_2/\Phi)-\frac{\partial T_2}{\partial x}-\frac{\partial T_5}{\partial\theta},\\E_3&-\alpha_0^4H(w/\Phi)+M_2-T_5-\frac{\partial T_6}{\partial\theta}+\frac{\partial^2 M_1}{\partial x^2}.\end{aligned}\right\} \tag{8}$$

$$\begin{aligned}T_1&=GH^3\frac{\partial^2 w}{\partial x^2}+\beta_0H\Big\{\frac{1}{\Phi}\frac{\partial u}{\partial x}+\nu G\Big(\frac{\partial v}{\partial\theta}-w\Big)\Big\},\\T_2&=\frac{(1-\nu)}{2}\Big[\beta_0H\Big(\frac{\partial v}{\partial x}+G\Phi\frac{\partial u}{\partial\theta}\Big)+3G^2\Phi^2H^3\Big(\frac{\partial v}{\partial x}\\&\quad+\frac{\partial^2 w}{\partial x\partial\theta}\Big)\Big]\Big/\Phi,\\T_3&=-\Big[H^3\Big[\frac{\partial^3 w}{\partial x^3}+G\Phi\frac{\partial^2 u}{\partial x^2}+\nu G^2\Phi\frac{\partial}{\partial\theta}\Big\{\Phi\Big(\frac{\partial^2 w}{\partial x\partial\theta}+\frac{\partial v}{\partial x}\Big)\Big\}\Big]\\&\quad+\frac{(1-\nu)}{2}G^2\Phi\frac{\partial}{\partial\theta}\Big\{\Phi H^3\Big(4\frac{\partial^2 w}{\partial x\partial\theta}+3\frac{\partial v}{\partial x}-G\Phi\frac{\partial u}{\partial\theta}\Big)\Big\}\Big]\Big/\Phi,\\T_4&=\frac{(1-\nu)}{2}\Big[\beta_0GH\Big(\frac{\partial v}{\partial x}+G\Phi\frac{\partial u}{\partial\theta}\Big)+G^3H^3\Phi^2\Big(G\Phi\frac{\partial u}{\partial\theta}\\&\quad-\frac{\partial^2 w}{\partial x\partial\theta}\Big)\Big],\\T_5&=\beta_0GH\Big\{\nu\frac{\partial u}{\partial x}+G\Phi\Big(\frac{\partial v}{\partial\theta}-w\Big)\Big\}+\nu G^2\Phi H^3\frac{\partial^2 w}{\partial x^2},\end{aligned} \tag{9}$$

Downloaded 02 May 2010 to 171.66.16.54. Redistribution subject to ASME license or copyright; see http://www.asme.org/terms/Terms_Use.cfm

$$T_6 = -G^2\Phi\Big[\frac{\partial}{\partial\theta}\Big[H^3\Big[\nu\frac{\partial^2 w}{\partial x^2}+G^2\Phi\frac{\partial}{\partial\theta}\Big\{\Phi\Big(\frac{\partial w}{\partial\theta}+v\Big)\Big\}\Big]$$

$$-G^2\Phi^2H^3\Big(\frac{\partial v}{\partial\theta}-w\Big)\Big]+\frac{(1-\nu)}{2}H^3\Big\{4\frac{\partial^3 w}{\partial x^2\partial\theta}$$

$$+3\frac{\partial^2 v}{\partial x^2}-G\Phi\frac{\partial^2 u}{\partial x\partial\theta}\Big],$$

$$T_7=\frac{(1-\nu)}{2}G^2\Phi H^3\Big(3\frac{\partial v}{\partial x}+4\frac{\partial^2 w}{\partial x\partial\theta}-G\Phi\frac{\partial u}{\partial\theta}\Big),$$

$$M_1=H^3\Big[\frac{\partial^2 w}{\partial x^2}+\nu G^2\Phi\frac{\partial}{\partial\theta}\Big\{\Phi\Big(\frac{\partial w}{\partial\theta}+v\Big)\Big\}+G\Phi H^3\frac{\partial u}{\partial x}\Big]\Big/\Phi,$$

$$M_2=G^2\Phi H^3\Big[\nu\frac{\partial^2 w}{\partial x^2}+G^2\Phi\frac{\partial}{\partial\theta}\Big\{\Phi\Big(\frac{\partial w}{\partial\theta}+v\Big)\Big\}\Big]$$

$$-G^4\Phi^3H^3\Big(\frac{\partial v}{\partial\theta}-w\Big)$$

The quantities $(T_1\ldots T_7)\times(D_0/r_0^2G)$ and $(M_1,M_2)\times(D_0/r_0^2G)$ are proportional to the forces and the moments, respectively [11]. Euler's equations (equations of motion) are

$$E_1=0,\qquad E_2=0,\qquad E_3=0 \tag{10}$$

The boundary conditions at $x=0$ and $x=\mu$ are

$$T_1u=T_2v=T_3w=M_1\frac{\partial w}{\partial x}=0 \tag{11}$$

For boundaries at $\theta=\theta_1$ and $\theta=\theta_2$ they are

$$T_4u=T_5v=T_6w=M_2\frac{\partial w}{\partial\theta}=0 \tag{12}$$

An additional condition to be satisfied at corners is

$$T_7\cdot w=0 \tag{13}$$

Setting $H=1$, one finds that equations (10)–(13) correspond with those for a noncircular thin cylindrical shell with uniform thickness [11].

2.2 Solutions of the Equations of Motion for Freely Supported Ends. Consider a noncircular cylindrical shell having its ends supported by shear diaphragms (or freely supported). That is, the conditions to be imposed at the ends are

$$v=w=T_1=M_1=0 \tag{14}$$

which satisfy equations (11). Equations (14) are exactly satisfied at $x=0$ and μ by choosing

$$u=u_m(\theta)\cos\frac{m\pi x}{\mu},\qquad v=v_m(\theta)\sin\frac{m\pi x}{\mu},$$

$$w=w_m(\theta)\sin\frac{m\pi x}{\mu} \tag{15}$$

where m is an integer. Substituting the displacements (15) into the equations of motion (10) yields the following set of ordinary differential equations:

$$(\beta_0k^2-\alpha_0^4)H(u_m/\Phi)+kGH(\nu\beta_0+k^2H^2)w_m$$

$$-\frac{kG\beta_0}{2}\Big\{2\nu H\frac{dv_m}{d\theta}+(1-\nu)\frac{d(Hv_m)}{d\theta}\Big\}$$

$$-\frac{(1-\nu)}{2}\beta_0G^2\frac{d}{d\theta}\Big(H\Phi\frac{du_m}{d\theta}\Big)+\frac{(1-\nu)}{2}G^3\frac{d}{d\theta}\Big\{H^3\Phi^2\Big(k\frac{dw_m}{d\theta}$$

$$-G\Phi\frac{du_m}{d\theta}\Big)\Big\}=0,$$

$$\Big\{\frac{(1-\nu)}{2}\beta_0k^2-\alpha_0^4\Big\}Hv_m+\frac{kG\beta_0\Phi}{2}\Big\{2\nu\frac{d}{d\theta}(Hu_m)$$

$$+(1-\nu)H\frac{du_m}{d\theta}\Big\}-\beta_0G^2\Phi\frac{d}{d\theta}\Big\{H\Phi\Big(\frac{dv_m}{d\theta}-w_m\Big)\Big\}$$

$$+G^4\Phi^2H^3\Big[\Big(\frac{d\Phi}{d\theta}\Big)^2\Big(\frac{dw_m}{d\theta}+v_m\Big)+\Phi\frac{d\Phi}{d\theta}\Big(\frac{d^2w_m}{d\theta^2}+w_m\Big)\Big]$$

$$+\frac{k^2G^2\Phi^2}{2}\Big[3(1-\nu)H^3\Big(v_m+\frac{dw_m}{d\theta}\Big)$$

$$+2\nu\frac{d}{d\theta}(H^3w_m)\Big]=0,$$

$$kG\Phi H(\nu\beta_0+k^2H^2)u_m+(k^4H^2-\alpha_0^4)Hw_m$$

$$-\beta_0G^2\Phi^2H\Big(\frac{dv_m}{d\theta}-w_m\Big)$$

$$+G^4\Big(\Phi^2+\Phi\frac{d\Phi}{d\theta}\frac{d}{d\theta}+\Phi^2\frac{d^2}{d\theta^2}\Big)H^3\times\Big[\Phi\frac{d}{d\theta}\Big\{\Phi\Big(\frac{dw_m}{d\theta}$$

$$+v_m\Big)\Big\}-\Phi^2\Big(\frac{dv_m}{d\theta}-w_m\Big)\Big]$$

$$-\frac{1}{2}kG^2\Phi\frac{d}{d\theta}\Big[\Phi\Big[2\nu k\frac{d}{d\theta}(H^3w_m)+(1-\nu)H^3\Big(4k\frac{dw_m}{d\theta}$$

$$+3k\quad v_m-G\Phi\frac{du_m}{d\theta}\Big)\Big]\Big]$$

$$-\nu k^2G^2H^3\Phi\frac{d}{d\theta}\Big\{\Phi\Big(\frac{dw_m}{d\theta}+v_m\Big)\Big\}=0 \tag{16}$$

where

$$k=\frac{m\pi}{\mu} \tag{17}$$

Although equations (16) are complicated and have variable coefficients, exact solutions may be obtained by expressing the ellipticity functions (Φ) and the thickness functions ($H,H^3\ldots$) as infinite power series in θ, and assuming solutions for u_m, v_m, and w_m which are also infinite power series in θ. The solution procedure will be demonstrated here for shells having cross sections with one or more axes of symmetry.

Let $\theta=0$ correspond to a symmetry axis. Then the variable coefficients of equations (16) may be expanded as

$$\{\Phi^2,H,H^3,H\Phi^2,H^3\Phi^2,H^3\Phi^4\}=\sum_{n=0}^{\infty}\{\Phi_0\zeta_n,R_n^{(1)},R_n^{(2)},$$

$$\Phi_0R_n^{(3)},\Phi_0R_n^{(4)},\Phi_0^2R_n^{(5)}\}\theta^{2n},$$

$$H^3\Big(\Phi\frac{d\Phi}{d\theta}\Big)^2=\Phi_0^2\sum_{n=1}^{\infty}R_n^{(6)}\theta^{2n}, \tag{18}$$

$$\Big\{H\Phi\frac{d\Phi}{d\theta},H^3\Phi\frac{d\Phi}{d\theta},H^3\Phi^3\frac{d\Phi}{d\theta}\Big\}=\sum_{n=0}^{\infty}\{\Phi_0R_n^{(7)},$$

$$\Phi_0R_n^{(8)},\Phi^2R_n^{(9)}\}\theta^{2n+1}$$

$$R_n^{(2)}=\sum_{q=0}^{n}R_{n-q}^{(1)}\Big\{\sum_{p=0}^{q}R_{q-p}^{(1)}R_p^{(1)}\Big\},$$

$$\{R_n^{(3)},R_n^{(4)},R_n^{(5)}\}=\sum_{p=0}^{n}\{R_{n-p}^{(1)}\zeta_p,R_{n-p}^{(2)}\zeta_p,R_{n-p}^{(4)}\zeta_p\}, \tag{19}$$

Downloaded 02 May 2010 to 171.66.16.54. Redistribution subject to ASME license or copyright; see http://www.asme.org/terms/Terms_Use.cfm

$$R_n^{(6)} = \sum_{q=1}^{n} R_{n-q}^{(2)} \left\{ \sum_{p=1}^{q} p(q+1-p)\,\zeta_p \zeta_{q+1-p} \right\},$$

$$\{R_n^{(7)}, R_n^{(8)}, R_n^{(9)}\} = \sum_{p=1}^{n+1} \{P\zeta_p R_{n+1-p}^{(1)}, P\zeta_p R_{n+1-p}^{(2)}, P\zeta_p R_{n+1-p}^{(4)}\}$$

One can denote Φ^2 as equation (18) for the curves for which the curvatures are expressed as even functions of θ.

Equation (16) has two solutions: one in which u_m/Φ and w_m are even functions of θ and v_m is an odd function of θ, and another in which u_m/Φ and w_m are odd functions of θ and v_m is an even function of θ. They are considered separately.

In the case that u_m/Φ is an even function of θ, one takes:

$$u_m/\Phi = \sum_{n=0}^{\infty} A_n \theta^{2n}, \quad v_m = \sum_{n=0}^{\infty} B_n \theta^{2n+1}, \quad w_m = \sum_{n=0}^{\infty} C_n \theta^{2n} \tag{20}$$

In the case that u_m/Φ is an odd function of θ, one takes:

$$u_m/\Phi = \sum_{n=0}^{\infty} A_n \theta^{2n+1}, v_m = \sum_{n=0}^{\infty} B_n \theta^{2n}, w_m = \sum_{n=0}^{\infty} C_n \theta^{2n+1} \tag{21}$$

Substituting equations (20) and (21), in turn, into equations (16), one obtains sets of equations relating the coefficients A_{n+1}, B_{n+1}, and C_{n+2} ($n \geq 0$) to A_0, B_0, C_0, and C_1. Hence, four independent solutions arise from each set. In this way, eight independent solutions for the complete problem are obtained. The general solutions to equations (16) are expressed by combining linearly these eight independent solutions. However, when the cross section is symmetric about $\theta = 0$, the vibrations are divided into a symmetric vibration and an antisymmetric one about the axis of symmetry passing through the axis $\theta = 0$. Then the displacements given by equation (20) are the solutions for the symmetric modes of vibration, and those from equation (21) are for the antisymmetric modes.

3 Numerical Calculations

To demonstrate the method of solution, numerical calculations are made for elliptical cylindrical shells of variable thickness. For this type of curvature, $\Phi(\theta)$ was given previously in equation (4). Then

$\Phi_0 = (1+\mu_0)^3, \zeta_0 = 1,$

$$\zeta_n = \frac{3\mu_0^3(-1)^n 2^{2n}}{(1+\mu_0)^3(2n)!} \left[\frac{1+3^{2n-1}}{4} + \frac{2^{2n-1}}{\mu_0} + \frac{1}{\mu_0^2} \right] \tag{22}$$

To be specific, the following shell parameters are used: $\mu_0 = 0.2$ ($\sim a/b = 1.22$), $\beta_0 = 10^4$ ($\sim r_0/h = 28.9$), and $\nu = 0.3$. The cross section is symmetric with respect to $\theta = 0$, π, and $H(\theta)$ in equation (18) is taken as

$$H(\theta) = 1 + \epsilon\theta^2 \tag{23}$$

where ϵ is an arbitrary constant. In the calculations, three cases where $\epsilon = 0, \pm 0.2$ were considered. These yield ratios of thickness at $\theta = \pi/2$ to that at $\theta = 0$ which are 1.493, 1 and 0.507. When $H(\theta)$ is expressed by equation (23), the expansion coefficients of H in equation (18) are $R_0^{(1)} = 1$, $R_1^{(1)} = \epsilon$, $R_n^{(1)} = 0$ ($n \geq 2$). The axes of symmetry are the ξ_1 axis passing through the points $\theta = 0$, π and the ξ_2 axis passing through the points $\theta = \pm\pi/2$. Vibrations are divided into four symmetry classes ($S-S, S-A, A-S, A-A$), depending on whether they are symmetric (S) or antisymmetric (A) with respect to the ξ_1 and ξ_2 axes, respectively. These symmetry classes are obtained by utilizing the symmetric (even) functions (20) or the antisymmetric (odd) functions (21), and by enforcing the conditions at $\theta = \pi/2$ that either

$$T_4 = v = T_6 = \frac{\partial w}{\partial \theta} = 0 \qquad \text{(symmetric)} \tag{24}$$

or

$$u = T_5 = w = M_2 = 0 \qquad \text{(antisymmetric)} \tag{25}$$

The displacement functions u_m, v_m, and w_m were calculated by retaining 100 terms for each of the coefficients A_n, B_n, and C_n in equations (20) and (21). Each of the independent solutions corresponding to each symmetry class was obtained by setting one of A_0, B_0, C_0, and C_1 equal to unity and the others equal to zero. The rate of convergence of the solutions is almost as rapid as for the case of uniform thickness [11], and varies with parameters such as β_0, α_0^4/β_0, k and μ_0. In general, the convergence becomes better as β_0 or μ_0 becomes smaller and as k becomes larger. For the same values of β_0 and k, the convergence becomes better as α_0^4/β_0 becomes smaller.

Table 1 shows the convergence of the solutions arising from equation (20). In the table are shown the significant figures of accuracy of the functions obtained from ($A_0 = 1$, $B_0 = C_0 = C_1 = 0$) in the case where $\beta_0 = 10^4$, $\mu_0 = 0.2$, and $\epsilon = 0.2$. The nondimensional frequency parameter α_0^4/β_0 is related to the frequency by

$$\frac{\alpha_0^4}{\beta_0} = \frac{w^2 r_0^2 \rho(1-\nu^2)}{E} \tag{26}$$

which is the parameter typically used to express results for circular cylindrical shells of constant thickness (cf. [1]). The numbers 12(90), 9(75), . . .in Table 1 show that 90 terms are necessary to obtain a function with accuracies of 12 digits, and 75 terms are necessary to obtain a function with 9 digits, respectively. The symbols T_{4m}, T_{5m}, T_{6m}, and M_{2m} show the functions obtained by substituting u, v, and w into T_4, T_5, T_6, and M_2, and by omitting $\sin(m\pi x/\mu)$ or $\cos(m\pi x)/\mu$. Almost all the functions converge with accuracies of 12 digits by 100 terms. For the solutions obtained from ($B_0 = 1$,

Table 1 Convergence of solutions from equation (20) ($\beta_0 = 10^4$, $\mu_0 = 0.2$, $\epsilon = 0.2$)

Parameters		Functions							
		u_m/Φ	v_m	w_m	$dw_m/d\theta$	$T_{4m}/\frac{G}{2}(1-\nu)$	$T_{5m}/G\Phi$	$-T_{6m}/G^2\Phi$	$M_{2m}/G^2\Phi H^3$
$\beta_0 = 10^4$	$k = 3.0$	12(90)	12(93)	12(93)	12(99)	12(85)	12(92)	12(98)	12(89)
	$\alpha_0^4/\beta_0 = 0.4$	9(75)	9(65)	9(75)	9(86)	9(63)	9(73)	9(85)	9(69)
	$k = 3.0$	12(77)	12(79)	12(84)	12(91)	12(82)	12(82)	12(94)	12(79)
	$\alpha_0^4/\beta_0 = 0.1$	9(64)	9(62)	9(67)	9(70)	9(57)	9(63)	9(74)	9(61)
	$k = 1.0$	12(95)	12(85)	12(95)	12(99)	12(84)	12(95)	11(100)	12(99)
	$\alpha_0^4/\beta_0 = 0.4$	9(76)	9(65)	9(72)	9(81)	9(68)	9(76)	9(77)	9(77)
	$k = 1.0$	12(85)	12(79)	12(89)	12(91)	12(87)	12(87)	12(91)	12(89)
	$\alpha_0^4/\beta_0 = 0.1$	9(65)	9(64)	9(72)	9(70)	9(65)	9(67)	9(69)	9(76)

Downloaded 02 May 2010 to 171.66.16.54. Redistribution subject to ASME license or copyright; see http://www.asme.org/terms/Terms_Use.cfm

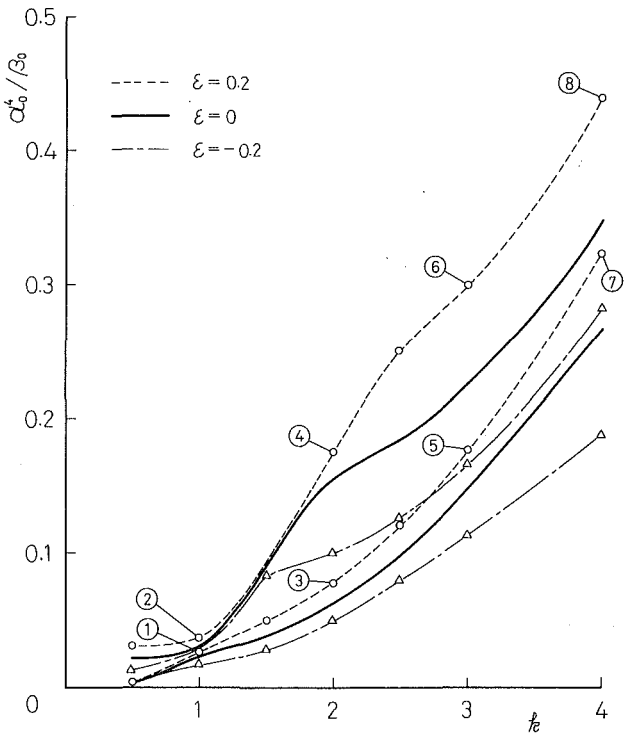


Fig. 2 Frequency curves, $(S-S)$ modes ($\beta_0 = 10^4$, $\mu_0 = 0.2$)

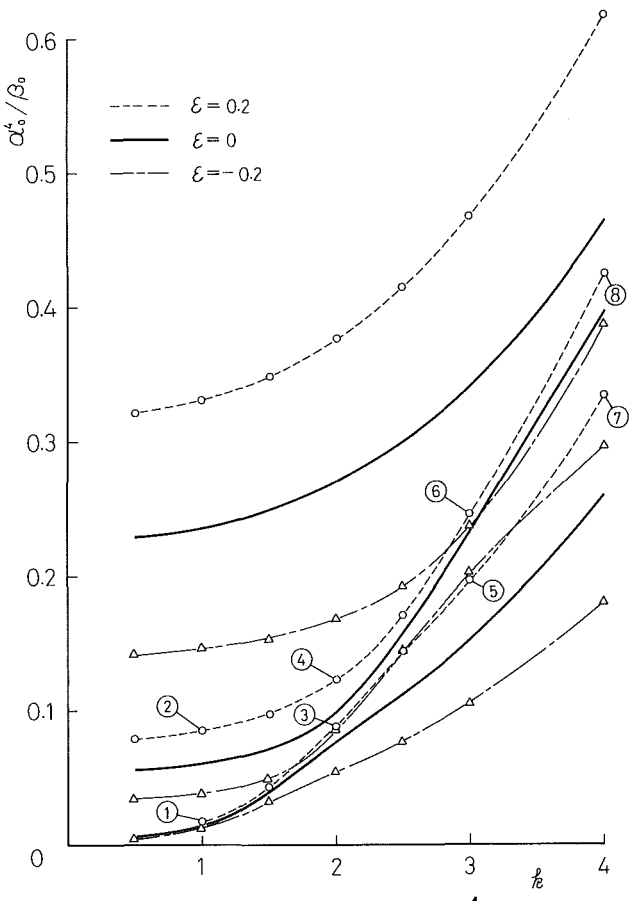


Fig. 3 Frequency curves, $(S-A)$ modes ($\beta_0 = 10^4$, $\mu_0 = 0.2$)

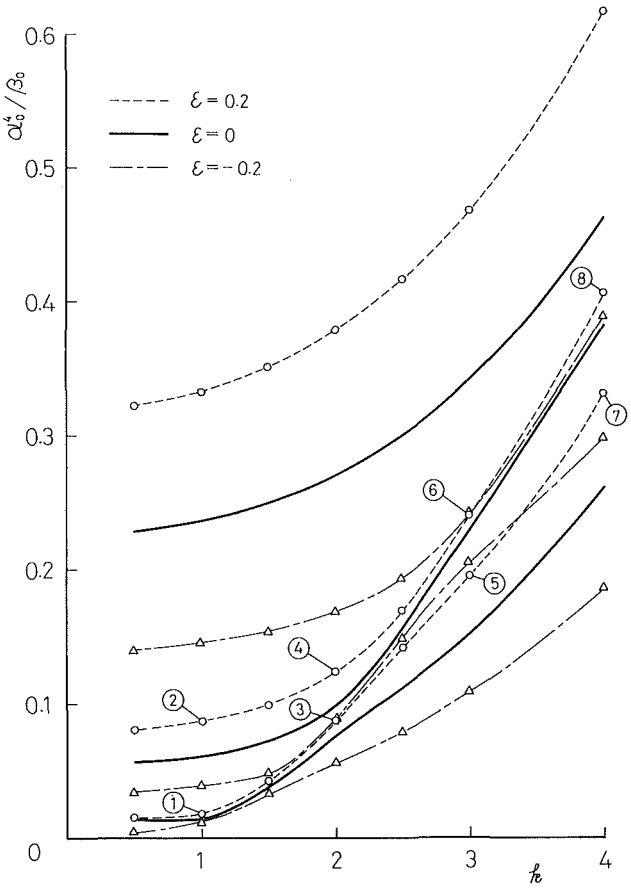


Fig. 4 Frequency curves, $(A-S)$ modes ($\beta_0 = 10^4$, $\mu_0 = 0.2$)

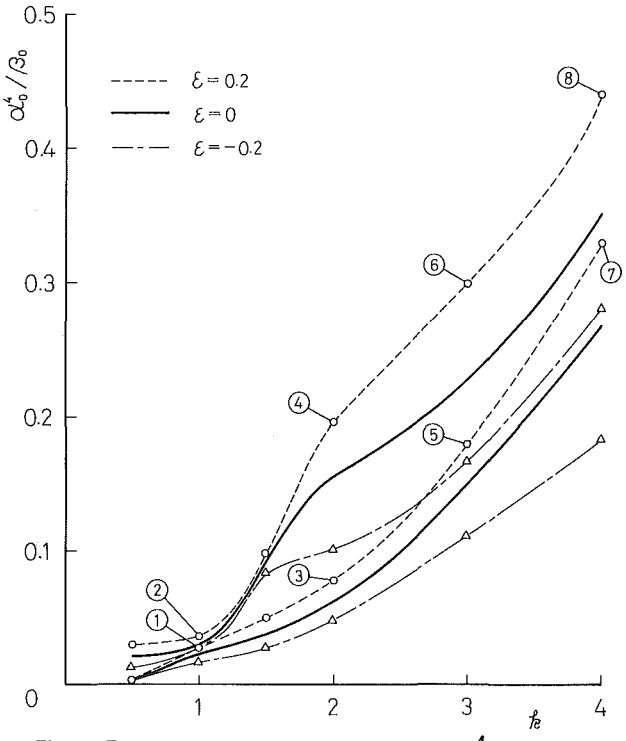


Fig. 5 Frequency curves, $(A-A)$ modes ($\beta_0 = 10^4$, $\mu_0 = 0.2$)

$C_0 = C_1 = A_0 = 0$), ($C_0 = 1$, $C_1 = A_0 = B_0 = 0$), ($C_1 = 1$, $A = {}_0 = B_0 = C_0 = 0$), the same statement can be made. The convergence of the solutions of equation (21) is similar.

The general solutions to equation (16) for symmetric vibration about ξ_1 axis, for example, are expressed by combining linearly four independent solutions from equation (20) as follows:

$$\{u_m, v_m, w_m\} = \sum_{i=1}^{4} \{\lambda_i u_{mi}, \lambda_i v_{mi}, \lambda_i w_{mi}\} \tag{27}$$

where $\lambda_1 \sim \lambda_4$ are arbitrary constants. Consequently, con-

Downloaded 02 May 2010 to 171.66.16.54. Redistribution subject to ASME license or copyright; see http://www.asme.org/terms/Terms_Use.cfm

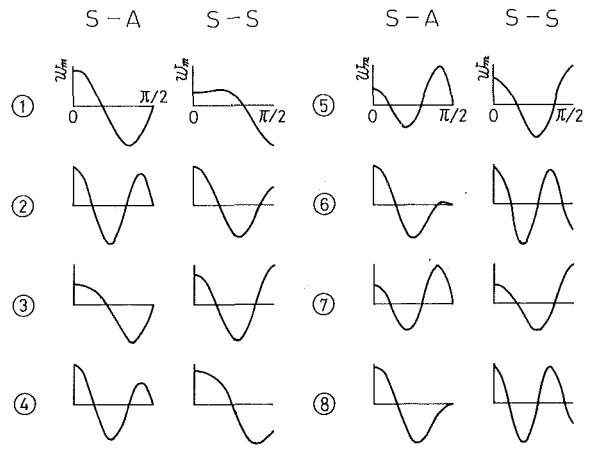


Fig. 6 Mode shapes corresponding to numbered points in Figs. 2 and 3

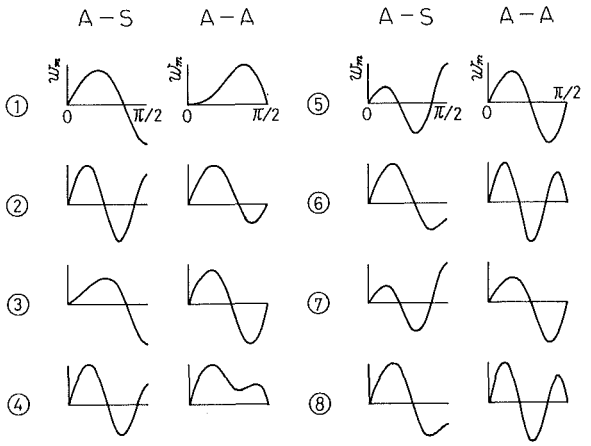


Fig. 7 Mode shapes corresponding to numbered points in Figs. 4 and 5

sidering the symmetry conditions of equations (24) and (25), one obtains the frequency equations for $(S-S)$ and $(S-A)$ modes in the form of a fourth order determinant. One can obtain similarly the frequency equations for $(A-S)$ and $(A-A)$ modes using the solutions to equation (21). The roots of these finite (and relatively small) order frequency determinants are exact values of the frequency parameter α_0^4/β_0. In the calculations for the results shown hereafter, β_0 and k were first chosen, and then a search was conducted for the values of α_0^4/β_0 which satisfy the frequency equations.

Figures 2–5 show the relation between α_0^4/β_0 and k for the four symmetry classes of vibration in the case where $\beta_0 = 10^4$ and $\mu_0 = 0.2$. The curves are for the first, second, and third modes of vibration in the order from below, in which the curves are illustrated by joining the points for the values of α_0^4/β_0 at $k = 0.5, 1.0, 1.5, \ldots, 4.0$. The numbers $1 \sim 8$ on the curves for $\epsilon = 0.2$ denote the points at which the mode shapes were also calculated. (The mode shapes will be shown later in Figs. 6 and 7.) With the curves for $\epsilon = 0$ (uniform thickness) as a reference, the curves for $\epsilon = 0.2$ are above the curves for $\epsilon = 0$ and the curves for $\epsilon = -0.2$ are below. The difference between the curves for $\epsilon = 0$ and the curves for $\epsilon = \pm 0.2$ becomes large as k (and hence r_0/l) becomes large or the vibration mode becomes higher. And as seen from the figures, the $(S-S)$ curves are very similar to the $(A-A)$ ones, and the $(S-A)$ curves are also similar to the $(A-S)$ ones. This is partly because the ellipticity of shells with $\mu_0 = 0.2$ is not large. The results of this paper in the case where $\epsilon = 0$ agree with those of reference [11] except the results for the $(A-A)$ modes. It is believed that the numerical results for the $(A-A)$ modes of reference [11] are in error.

Figures 6 and 7 show the mode shapes in the case where $\beta_0 = 10^4$, $\mu_0 = 0.2$ and $\epsilon = 0.2$. They are the displacements w_m for $0 \le \theta \le \pi/2$, in which the maximum amplitude is taken to be unity. Mode numbering corresponds to the numbered points of the frequency curves found in Figs. 2–5. As seen from the figures, the mode shapes vary with k or α_0^4/β_0 even for the same mode of vibration. Comparing mode shapes of the elliptical cylindrical shells of uniform thickness found in reference [11] with those of Figs. 6 and 7 of the present work, one finds that the mode shapes vary in almost the same manner.

4 Conclusions

In this paper, an exact method for analyzing free vibrations of a noncircular thin cylindrical shell of which the thickness varies in the circumferential direction has been demonstrated. The method is a general one applicable to various noncircular thin cylindrical shells with varying thickness, although limited to shells having freely supported ends. Although it is used here only on free vibration problems, the exact method of solution developed here could also be applied to problems involving stress and displacement analysis of statically loaded shells, or to classical, bifurcation shell buckling studies. As numerical examples, natural frequencies and mode shapes were found for elliptical cylindrical shells for which the thicknesses vary parabolically in the circumferential direction. From these results it is clear that the mode shapes of the elliptical cylindrical shells with varying thickness do not differ much from those with uniform thickness, but the frequency curves change very much when the thickness varies.

References

1 Leissa, A. W., "Vibration of Shells," NASA SP-288, U.S. Government Printing Office, 1973.

2 Sewall, J. L., and Pusey, C. G., "Vibration Study of Clamped-Free Elliptical Cylindrical Shells," *AIAA Journal*, Vol. 9, 1971, pp. 1004–1011.

3 Sewall, J. L., Thompson, W. M., and Pusey, C. G., "An Experimental and Analytical Vibration Study of Elliptical Cylindrical Shells," NASA TN D-6089, 1971.

4 Culberson, L. D., and Boyd, D. E., "Free Vibrations of Freely Supported Oval Cylinders," *AIAA Journal*, Vol. 9, 1971, pp. 1474–1480.

5 Bergman, R. M., "Investigations of the Free Vibrations of Non-Circular Cylindrical Shells," *Journal of Mathematics and Mechanics*, Vol. 37, No. 2, 1973, pp. 1068–1077.

6 Elsbernd, G. F., and Leissa, A. W., "The Vibrations of Noncircular Cylindrical Shells With Initial Stress," *Journal of Sound and Vibration*, Vol. 29, No. 3, 1973, pp. 309–329

7 Chen, Y. N., and Kempner, J., "Modal Method for Free Vibration of Oval Cylindrical Shells With Simply Supported or Clamped Ends," ASME JOURNAL OF APPLIED MECHANICS, Vol. 45, 1978, pp. 142–148.

8 Koumisis, V. K., "Vibration of Cylindrical Shells and Panels of Oval Cross Section," Ph.D. Thesis, Poly. Inst., New York, 1980, 285 pp.

9 Soldatos, K. P., and Tzivanidis, G. J., "Buckling and Vibration of Cross-Ply Laminated Noncircular Cylindrical Shells," *Journal of Sound and Vibration*, Vol. 82, No. 3, 1982, pp. 425–434.

10 Shirakawa, K., and Morita, M., "Vibration and Buckling of Cylinders With Elliptical Cross Section," *Journal of Sound and Vibration*, Vol. 84, No. 1, 1982, pp. 121–131.

11 Suzuki, K., Tamura, S., Kosawada, T., and Takahashi, S., "Vibrations of Noncircular Cylindrical Shells," *Bulletin of JSME*, Vol. 26, No. 215, 1983, pp. 818–826.

12 Rosen, A., and Singer, J., "Influence of Asymmetric Imperfections on the Vibrations of Axially Compressed Cylindrical Shells," *Israel Journal of Technology*, Vol. 14, 1976, pp. 23–36.

13 Bentley, P. G., and Firth, D., "Acoustically Excited Vibrations in a Liquid-Filled Cylindrical Tank," *Journal of Sound and Vibration*, Vol. 19, No. 2, 1971, pp. 179–191.

14 Firth, D., "The Vibration of a Distorted Circular Cylinder Containing Liquid," Trans. of the 3rd International Conference on Structural Mechanics in Reactor Technology, Paper F2/10, 1975.

15 Yousri, S. N., and Fahy, F. J., "Distorted Cylindrical Shell Response to Internal Acoustic Excitation Below the Cut-Off Frequency," *Journal of Sound and Vibration*, Vol. 52, No. 3, 1977, pp. 441–452.

16 Tonin, R. F., and Bies, D. A., "Free Vibration of Circular Cylinders of Variable Thickness," *Journal of Sound and Vibration*, Vol. 62, No. 2, 1979, pp. 165–180,

17 Suzuki, K., Takahashi, S., and Ishiyama, H., "In-plane Vibrations of Curved Bars," *Bulletin of JSME*, Vol. 21, No. 154, 1978, pp. 618–627.

Downloaded 02 May 2010 to 171.66.16.54. Redistribution subject to ASME license or copyright; see http://www.asme.org/terms/Terms_Use.cfm

Effects of Geometric Imperfections on Frequency-Load Interaction of Biaxially Compressed Antisymmetric Angle Ply Rectangular Plates

David Hui
Assistant Professor,
Department of Engineering Mechanics,
The Ohio State University,
Columbus, Ohio 43210
Mem. ASME

The present paper deals with the influence of small geometric imperfections on the vibration frequencies of rectangular, simply supported, angle ply, thin composite plates subjected to inplane uniaxial or biaxial compressive preload. Depending on the amount of preload, the frequencies of laminated plates with different imperfection shapes may be significantly higher than those for perfect plates, especially in a certain range of fiber angles. Interaction curves between frequency and applied preload are plotted for various fiber angles and imperfection amplitudes for both the uniaxial and equal biaxial loading cases.

1 Introduction

Vibration of fiber-reinforced plates and shells has been a subject of significant current interest since it is an important design consideration in many light-weight, high-strength, engineering structural configurations. Based on the pioneering work on the effects of bending-stretching coupling of composite plates by Ambartsumyan [1] and Reissner and Stavsky [2], the vibration frequencies of antisymmetric angle and cross-ply perfect plates with no preload were studied by Whitney and Leissa [3] and subsequently by Jones [4]. Excellent reviews on the current state of the art were written by Chia [5], Leissa [6], and Bert [7].

However, it should be emphasized that none of the foregoing analyses for laminated plates and shells involves the study of the effects of small, usually unavoidable, geometric imperfections (that is, deviation from flatness). Geometric imperfections have been found to be very significant, in some cases, in affecting the linear small-amplitude vibration frequencies of isotropic, homogeneous thin-walled structures such as simply supported rectangular preloaded flat plates [8], externally pressurized shallow spherical shells [9], unstiffened cylindrical shells [10, 11], cylindrical panels [12], and stiffened cylindrical shells [13], even in the absence of inplane compressive preload. Of particular concern is whether the fiber orientation and bending-stretching coupling for laminated plates will significantly affect the sensitivity of the vibration frequencies due to the presence of small geometric imperfections (already found to be significant for homogeneous isotropic flat plates). The effects of a static previbration deformation due to inplane compressive preload will be examined.

If Koiter's work in 1945 on the effects of geometric imperfections on buckling of thin-walled structures is considered a major breakthrough in applied mechanics [14], then the work on establishing the influence of geometric imperfections on vibration of similar structures should also be considered a major breakthrough in the field. Among the existing publications on the possible effects of imperfections on vibrations of plates and shells [8–13], not one of them deals with laminated thin-walled structures. This paper is the first in the open literature to point out that if these laminated structures were actually tested in the laboratory, it is possible that significant increases in the fundamental frequencies may occur due to the presence of unavoidable small geometric imperfections and inplane compressible preload. Further studies on the large-amplitude vibrations of laminated plates will be presented in a separate paper [15].

The present analysis is based on a solution of the nonlinear von Kármán-type governing differential equations within the context of Koiter's special theory of elastic stability [16]. The geometric imperfection is assumed to take the shape of a sinusoidal wave in both of the inplane directions. The static previbration nonlinear compatibility equation is satisfied exactly. Further, the nonlinear previbration static equilibrium equation is satisfied approximately using a Galerkin procedure. Using a perturbation technique, the dynamic equilibrium and compatibility differential equations are

Contributed by the Applied Mechanics Division and presented at the Winter Annual Meeting, New Orleans, La., December 9–14, 1984 of THE AMERICAN SOCIETY OF MECHANICAL ENGINEERS.

Discussion on this paper should be addressed to the Editorial Department, ASME, United Engineering Center, 345 East 47th Street, New York, N.Y. 10017, and will be accepted until two months after final publication of the paper itself in the JOURNAL OF APPLIED MECHANICS. Manuscript received by ASME Applied Mechanics Division, September, 1983; final revision, May, 1984. Paper No. 84-WA/APM-44.

Copies will be available until August, 1985.

Copyright © 1985 by ASME
Downloaded 02 May 2010 to 171.66.16.54. Redistribution subject to ASME license or copyright; see http://www.asme.org/terms/Terms_Use.cfm

linearized with respect to the perturbed dynamic state. The linearized compatibility equation is solved exactly (exact relative to the assumed vibration mode shape) and the dynamic equilibrium equation is then satisfied approximately using a Galerkin procedure. An explicit expression for the vibration frequency is obtained as a function of the biaxial preload, the imperfection amplitude, the vibration wave number, and the imperfection wave numbers.

Example problems are chosen from typical graphite-epoxy angle ply rectangular plates [4, 5, 17] where the optimum fiber angle, taking into account the effects of bending-stretching coupling and imperfection sensitivity, are investigated. Frequency versus uniaxial or equal biaxial load interaction curves are presented for various fiber angles and imperfection amplitudes. It is found that the amplitudes of imperfections on the order of a fraction of the total laminated plate thickness may significantly raise the vibration frequencies, especially in plate configurations corresponding to a certain range of fiber orientations and large uniaxial or biaxial compressive preload.

2 Governing Differential Equations

The von Kármán-type nonlinear equilibrium and compatibility equations for a thin laminated plate (written in terms of a normal displacement W and a stress function F) are, respectively [18, 19],

$$L_{D^*}(W)+L_{B^*}(F)+\rho W,_{\bar{t}\bar{t}}=F,_{YY}(W+W_0),_{XX}+F,_{XX}(W+W_0),_{YY}-2F,_{XY}(W+W_0),_{XY}$$

$$L_{A^*}(F)=L_{B^*}(W)+[(W+W_0),_{XY}]^2-(W_{0,XY})^2-(W+W_0),_{XX}(W+W_0),_{YY}+W_{0,XX}W_{0,YY} \quad (1,2)$$

In the foregoing, $\bar{t}$ is time, ρ is the mass of the plate per unit area, X and Y are the in-plane coordinates, and W_0 is the initial geometric imperfection. The strains and moments are related to the membrane stress resultants and curvatures by ($N_x=F,_{YY}$, $N_y=F,_{XX}$ and $N_{xy}=-F,_{XY}$)

$$[\epsilon_x,\epsilon_y,\gamma_{xy},M_x,M_y,M_{xy}]^T=\begin{bmatrix}[A^*_{ij}] & [B^*_{ij}]\\ -[B^*_{ij}]^T & [D^*_{ij}]\end{bmatrix}\cdot[N_x,N_y,N_{xy},-W,_{XX},-W,_{YY},-2W,_{XY}]^T \quad (3)$$

Introducing the nondimensionalization scheme,

$$(w,w_0)=(W/h,W_0/h),\qquad f=F/(Eh^3),$$
$$(x,y)=(1/b)(X,Y)$$
$$(a^*_{ij},b^*_{ij},d^*_{ij})=(EhA^*_{ij},B^*_{ij}/h,D^*_{ij}/(Eh^3)] \quad (4)$$

where E is an arbitrary Young's modulus, h is the total laminated plate thickness, and b is the width of the plate ($Y=0$ to b). The nonlinear dynamic equilibrium and compatibility equations can be written in nondimensional form,

$$L_{d^*}(w)+L_{b^*}(f)+[\rho b^4/(Eh^3)]w,_{\bar{t}\bar{t}}=f,_{yy}(w+w_0),_{xx}+f,_{xx}(w+w_0),_{yy}-2f,_{xy}(w+w_0),_{xy} \quad (5)$$

$$L_{a^*}(f)=L_{b^*}(w)+[(w+w_0),_{xy}]^2-(w_{0,xy})^2-(w+w_0),_{xx}(w+w_0),_{yy}+w_{0,xx}w_{0,yy} \quad (6)$$

In the special case of angle ply composite plates, the nondimensional linear differential operators are:

$$\begin{aligned}L_{a^*}(\ ) &= a^*_{22}(\ ),_{xxxx}+(2a^*_{12}+a^*_{66})(\ ),_{xxyy}+a^*_{11}(\ ),_{yyyy}\\ L_{b^*}(\ ) &= (2b^*_{26}-b^*_{61})(\ ),_{xxxy}+(2b^*_{16}-b^*_{62})(\ ),_{xyyy}\\ L_{d^*}(\ ) &= d^*_{11}(\ ),_{xxxx}+(2)(d^*_{12}+2d^*_{66})(\ ),_{xxyy}+d^*_{22}(\ ),_{yyyy}\end{aligned} \quad (7)$$

The rectangular angle ply plate is assumed to be simply supported along all four edges ($w=0$ and $M_y=0$ at $y=0$ and $y=1$ and $w=0$, $M_x=0$ at $x=0$ and $x=a/b$ where a is the length of the plate). Further, there is no inplane shear stress along all the edges ($f,_{xy}=0$ on all four edges) and the inplane displacement perpendicular to each edge is constant.

3 Previbration State

The previbration static deformation w_p is assumed to be of the same shape as the initial geometric imperfection ($J=jb/a$ and j and k are positive integers)

$$[w_p(x,y),w_0(x,y)]=(c_w,\mu)\sin(J\pi x)\sin(k\pi y) \quad (8)$$

Substituting $w=w_p(x,y)$ and $w_0(x,y)$ into the nonlinear compatibility equation, the previbration stress function $f_p(x,y)$ which satisfies this nonlinear differential equation exactly is:

$$f_p(x,y)=f^*(x,y)-(\bar{\sigma}_x)(y^2/2)-(\bar{\sigma}_y)(x^2/2) \quad (9)$$

where

$$(\bar{\sigma}_x,\bar{\sigma}_y)=(-N_x,-N_y)(b^2/(Eh^3))$$

and

$$f^*(x,y)=c_f\cos(J\pi x)\cos(k\pi y)+[(c_w+\mu)^2-\mu^2][A_1\cos(2J\pi x)+A_2\cos(2k\pi y)] \quad (10)$$

Further, the constants c_f, A_1, and A_2 are found to be:

$$\begin{aligned}c_f &= (-c_w)C_{b^*}(J,k)/C_{a^*}(J,k)\\ A_1 &= [1/(32a^*_{22})](k/J)^2,\qquad A_2=[1/(32a^*_{11})](J/k)^2\end{aligned} \quad (11)$$

$$\begin{aligned}C_{a^*}(P,Q) &= a^*_{22}P^4+(2a^*_{12}+a^*_{66})(P^2Q^2)+a^*_{11}Q^4\\ C_{b^*}(P,Q) &= (2b^*_{26}-b^*_{61})(P^3Q)+(2b^*_{16}-b^*_{62})(PQ^3)\end{aligned} \quad (12)$$

Substituting $w_p(x,y)$, $w_0(x,y)$, and $f_p(x,y)$ into the nonlinear previbration static equilibrium equation and applying the Galerkin procedure (multiplying both sides by $\sin(J\pi x)\sin(k\pi y)$ and integrating from $x=0$ to a/b and $y=0$ to 1), one obtains a cubic equation in $c_w+\mu$ of the form,

$$(c_w+\mu)^3(2J^2k^2)(A_1+A_2)+(c_w+\mu)\{(-\mu^2)(2J^2k^2)(A_1+A_2)-[(\bar{\sigma}_xJ^2+\bar{\sigma}_yk^2)/\pi^2]+C^*\}-(\mu)C^*=0 \quad (13)$$

where

$$C^*=C_{d^*}(J,k)+C_{b^*}(J,k)^2/C_{a^*}(J,k)] \quad (14)$$

$$C_{d^*}(P,Q)=d^*_{11}P^4+(2)(d^*_{12}+2d^*_{66})(P^2Q^2)+d^*_{22}Q^4 \quad (15)$$

As a check, it can be seen that $\bar{\sigma}_x=\bar{\sigma}_y=0$ implies $c_w=0$. Finally, the applied preloads $\bar{\sigma}_x$ and $\bar{\sigma}_y$ should not be so large as to cause excessive plate deformations. Neglecting the cubic terms in equation (13) (as was done in references [10] and [13]) will result in considerable errors in the previbration deformation for $|\mu|>0.1$.

4 Vibrations of Biaxially Compressed Imperfect Angle Ply Plates

Using a perturbation method, the perturbed dynamic state $w_B(x,y,t)$ and $f_B(x,y,t)$ is added to the previbration state of static equilibrium and the governing differential equations are linearized with respect to $w_B(x,y,t)$ and $f_B(x,y,t)$. Doing so, the dynamic equilibrium and compatibility equations become:

$$L_{d^*}(w_B)+L_{b^*}(f_B)+[\rho b^4/(Eh^3)]w_{B,\bar{t}\bar{t}}+(\bar{\sigma}_xw_{B,xx}+\bar{\sigma}_yw_{B,yy})=f^*,_{yy}w_{B,xx}+f^*,_{xx}w_{B,yy}-2f^*,_{xy}w_{B,xy}+(w_p+w_0),_{xx}f_{B,yy}+(w_p+w_0),_{yy}f_{B,xx}-2(w_p+w_0),_{xy}f_{B,xy} \quad (16)$$

$$L_{a^*}(f_B)=L_{b^*}(w_B)+(2)(w_p+w_0),_{xy}w_{B,xy}-(w_p+w_0),_{xx}w_{B,yy}-(w_p+w_0),_{yy}w_{B,xx} \quad (17)$$

The associated simply supported boundary conditions are $w_B=0$, $w_{B,xx}=0$, and $f_{B,xy}=0$ at $x=0$ and a/b. In anticipation that the two edges $y=0$ and $y=1$ have arbitrary, but uniform, boundary conditions acting along them (e.g.,

Downloaded 02 May 2010 to 171.66.16.54. Redistribution subject to ASME license or copyright; see http://www.asme.org/terms/Terms_Use.cfm

clamped, simply supported, or free), including the case when they are reinforced by stringers that may provide torsional restraint on the plate (the actual nonclassical boundary condition may lie somewhere between the simple support and clamped boundary conditions so that a discretized numerical solution is necessary [17]). It is desirable to reduce the dynamic equilibrium and compatibility equations to ordinary differential equations in the y direction.

The vibration mode is assumed to be of the form,

$$w_B(x,y,t) = \sin(M\pi x) w_B(y) \exp(i\omega \bar{t}) \tag{18}$$

where ω is the vibration frequency, $M = mb/a$, and m is the number of half sin-waves from $x=0$ to $x=a/b$. Substituting $w_B(x,y,t)$, $w_p(x,y)$, and $w_0(x,y)$ into the foregoing linearized compatibility equation, one obtains three coupled ordinary differential equations in the form,

$$\begin{aligned} &a_{22}^*(M\pi)^4 f_1(y) + (2a_{12}^* + a_{66}^*)(-M^2\pi^2) f_1(y)_{,yy} \\ &\quad + a_{11}^* f_1(y)_{,yyyy} = (2b_{26}^* - b_{61}^*)(-M^3\pi^3) w_B(y)_{,y} \\ &\quad + (2b_{16}^* - b_{62}^*)(M\pi) w_B(y)_{,yyy} \end{aligned} \tag{19}$$

$$\begin{aligned} &a_{22}^*(J-M)^4\pi^4 f_2(y) + (2a_{12}^* + a_{66}^*)(-\pi^2) \\ &\quad (J-M)^2 f_2(y)_{,yy} + a_{11}^* f_2(y)_{,yyyy} \\ &= (1/2)(c_w+\mu)[(2MJK\pi^3) w_B(y)_{,y} \cos(k\pi y) \\ &\quad + (J^2\pi^2) w_B(y)_{,yy} \sin(k\pi y) \\ &\quad - (M^2k^2\pi^4) w_B(y) \sin(k\pi y) \end{aligned} \tag{20}$$

$$\begin{aligned} &a_{22}^*(J+M)^4\pi^4 f_3(y) + (2a_{12}^* + a_{66}^*)(-\pi^2) \\ &\quad (J+M)^2 f_3(y)_{,yy} + a_{11}^* f_3(y)_{,yyyy} \\ &= (1/2)(c_w+\mu)[(2MJk\pi^3) w_B(y)_{,y} \cos(k\pi y) \\ &\quad - (J^2\pi^2) w_B(y)_{,yy} \sin(k\pi y) \\ &\quad + (M^2k^2\pi^4) w_B(y) \sin(k\pi y) \end{aligned} \tag{21}$$

where the stress function $f_B(x,y,t)$ is:

$$\begin{aligned} f_B(x,y,t) = \{&f_1(y)\cos(M\pi x) + f_2(y)\cos[\\ &(J-M)\pi x] + f_3(y)\cos[(J+M)\pi x]\} \exp(i\omega \bar{t}) \end{aligned} \tag{22}$$

Substituting $w_B(x,y,t)$, $f_B(x,y,t)$, $w_p(x,y)$, $w_0(x,y)$, and $f^*(x,y)$ into the linearized dynamic equilibrium equation and applying the Galerkin procedure (multiply both sides by $\sin(M\pi x)$ and integrating from $x=0$ to $x=a/b$), one obtains an ordinary differential equation involving $f_1(y)$, $f_2(y)$, $f_3(y)$, and $w_B(y)$ in the form:

$$\begin{aligned} &(1/2)\{[d_{11}^* M^4\pi^4 - \pi^4\Omega^2 - (M\pi)^2\bar{\sigma}_x] w_B(y) \\ &\quad + [\bar{\sigma}_y - 2(d_{12}^* + 2d_{66}^*)(M\pi)^2] w_B(y)_{,yy} \\ &\quad + d_{22}^* w_B(y)_{,yyyy} + (2b_{26}^* - b_{61}^*)(M\pi)^3 f_1(y)_{,y} \\ &\quad + (2b_{16}^* - b_{62}^*)(-M\pi) f_1(y)_{,yyy} \\ &\quad + 2(I_0)[(2b_{26}^* - b_{61}^*)(J-M)^3\pi^3 f_2(y)_{,y} \\ &\quad + (2b_{16}^* - b_{62}^*)(-\pi)(J-M) f_2(y)_{,yyy}\} \\ &= [(c_w+\mu)^2 - \mu^2]\{(2M^2k^2\pi^4 A_2) w_B(y)\cos(2k\pi y) \\ &\quad - (4J^2\pi^2 A_1)(I_1) w_B(y)_{,yy}\} \\ &\quad + (M^2k^2\pi^4 c_f)(I_2) w_B(y)\cos(k\pi y) \\ &\quad - (J^2\pi^2 c_f)(I_2) w_B(y)_{,yy}\cos(k\pi y) \\ &\quad - (2JkM\pi^3 c_f)(I_3) w_B(y)_{,y}\sin(k\pi y) \\ &\quad + (c_w+\mu)\sin(k\pi y)\{-I_3 J^2\pi^2 f_1(y)_{,yy} \\ &\quad + k^2M^2(I_3\pi^4) f_1(y) + (-J^2\pi^2 I_4) f_2(y)_{,yy} \\ &\quad + \pi^4 k^2 (J-M)^2 I_4 f_2(y) + (-J^2\pi^2 I_5) f_3(y)_{,yy} \\ &\quad + \pi^4 k^2 (J+M)^2 I_5 f_3(y)\} \\ &\quad + (c_w+\mu)\cos(k\pi y)\{(2JkM\pi^3) I_2 f_1(y)_{,y} \\ &\quad + (2Jk)(J-M)\pi^3 I_6 f_2(y)_{,y} \\ &\quad + (2Jk)(J+M)\pi^3 I_7 f_3(y)_{,y}\} \end{aligned} \tag{23}$$

In the preceding expression, $\pi^4\Omega^2 = \omega^2\rho b^4/(Eh^3)$ and $E = E_2$ where E_2 is Young's modulus in the plane of the plate, perpendicular to the fiber direction, and the definite integrals I_0, $I_1, \ldots, I_7$ are defined in the Appendix. Equations (19)–(21) and (23) constitute four coupled ordinary differential equations in four unknowns variables $f_1(y)$, $f_2(y)$, $f_3(y)$, and $w_B(y)$. The appropriate (possibly nonclassical) boundary conditions at $y=0$ and $y=1$ can be formulated in a manner similar to the one presented in reference [17]. The differential equations and boundary conditions may then be solved exactly, which involves considerable work, or they may be discretized and solved numerically.

Since the objective of the present paper is to examine the effects of the geometric imperfections on the vibrations of axially compressed angle ply plates in a relatively straightforward manner, the boundary conditions at the edges $y=0$ and $y=1$ are taken to be simply supported so that $w_B = 0$, $w_{B,yy} = 0$ and $f_{B,xy} = 0$. Thus, one may assume:

$$w_B(y) = \xi \sin(n\pi y) \tag{24}$$

where n is the number of half sine-waves from $y=0$ to $y=1$ and ξ is the amplitude of vibration mode normalized with respect to the laminated plate thickness. Substituting $w_B(y)$ into equations (16)–(18), one obtains:

$$\begin{aligned} f_1(y) &= \xi c_1 \cos(n\pi y) \\ f_2(y) &= \xi(c_w+\mu)\{c_2\cos[(k-n)\pi y] + c_3\cos[(k+n)\pi y]\} \\ f_3(y) &= \xi(c_w+\mu)\{c_4\cos[(k-n)\pi y] + c_5\cos[(k+n)\pi y]\} \end{aligned} \tag{25}$$

where ($c_2 = 0$ if $Jn = kM$),

$$\begin{aligned} c_1 &= -C_b^*(M,n)/C_a^*(M,n) \\ c_2 &= (-1)(Jn-kM)^2/[4C_a^*(J-M,k-n), \\ c_3 &= (Jn+kM)^2/[4C_a^*(J-M,k+n)] \\ c_4 &= (Jn+kM)^2/[4C_a^*(J+M,k-n)], \\ c_5 &= (-1)(Jn-kM)^2/[4C_a^*(J+M,k+n)] \end{aligned} \tag{26}$$

It may be verified that the preceding analysis is valid for the two special cases when $n = k/2$ and $n = k$.

Finally, substituting $f_1(y)$, $f_2(y)$, $f_3(y)$, and $w_B(y)$ into the linearized dynamic equilibrium equation (23) and again applying the Galerkin procedure (multiplying both sides by $\sin(n\pi y)$ and then integrating from $y=0$ to $y=1$), one obtains an explicit expression involving the frequency squared and the applied inplane biaxial loads $\bar{\sigma}_x$ and $\bar{\sigma}_y$ in the form:

$$\begin{aligned} \Omega^2 + [(M^2\bar{\sigma}_x + n^2\bar{\sigma}_y)/\pi^2] &= C_d^*(M,n) \\ &+ [C_b^*(M,n)^2/C_a^*(M,n)] \\ &- (4I_0H_0c_2)(c_w+\mu)C_b^*(J-M,k-n) \\ &- [(c_w+\mu)^2 - \mu^2][(8M^2k^2)(A_2H_1) \\ &+ (8J^2n^2)(A_1I_1)] - (4c_fI_2H_2)(M^2k^2 + J^2n^2) \\ &+ (8JkMn)(c_fI_3H_3) \\ &- (4c_1)(c_w+\mu)(J^2n^2 + k^2M^2)(H_3I_3) \\ &+ (8JkMn)(c_w+\mu)(I_2H_2c_1) \\ &- (4)(c_w+\mu)^2\{[J^2(k-n)^2 + k^2(J-M)^2](c_2I_4H_4) \\ &+ [J^2(k+n)^2 + k^2(J-M)^2](c_3I_4H_5) + [J^2(k-n)^2 \\ &+ k^2(J+M)^2](c_4I_5H_4) + [J^2(k+n)^2 \\ &+ k^2(J+M)^2](c_5I_5H_5)\} \\ &+ (8Jk)(c_w+\mu)\{(J-M)[c_2(k-n)(I_6H_6) \\ &+ c_3(k+n)(I_6H_7)] + (J+M)[c_4(k-n)(I_7H_6) \\ &+ c_5(k+n)(I_7H_7)]\} \end{aligned} \tag{27}$$

The definite integrals H_0, $H_1, \ldots, H_7$ are defined in the Appendix. As a check on the analysis, when both the frequency Ω and the imperfection amplitude μ are set equal to zero, the foregoing equation agrees with the buckling load

Downloaded 02 May 2010 to 171.66.16.54. Redistribution subject to ASME license or copyright; see http://www.asme.org/terms/Terms_Use.cfm

expression obtained by Harris [20]. The buckling load for a perfect ($\mu = 0$) rectangular angle ply plate is ($n = 1$ if $\bar{\sigma}_y = 0$),

$$\bar{\sigma}_x + \bar{\sigma}_y = (\pi^2)\{C_d^*(M,n) + [C_b^*(M,n)^2/C_a^*(M,n)]\} \quad (28)$$

5 Results and Discussion

Due to the large number of parameters involved, it is not practical to present a complete study on the effects of parameter variations. Thus, example problems are selected from typical graphite-epoxy angle ply laminated rectangular plates [4, 5, 17] with (E is chosen to be E_2)

$$E_1/E_2 = 40, \quad G_{12}/E_2 = 0.5, \quad \nu_{12} = 0.25, \quad \nu_{21} = \nu_{12}(E_2/E_1) \quad (29)$$

where E_1 and E_2 are inplane Young's moduli parallel and perpendicular to the filament direction, respectively, ν_{12} and ν_{21} are Poisson's ratios, and G_{12} is the shear modulus. The aspect ratio a/b is chosen to be unity and simple support boundary conditions at the four edges are enforced. Furthermore, to investigate the effects of bending-stretching coupling, laminated plates with even number of equal-thickness layers N being $N = 2$ and $N =$ infinite are considered. The angle ply plates are subjected to the possibility of two inplane compressive stresses and the initial geometric imperfections are taken to be sine waves in both the inplane x and y directions ($J = k = 1$; $J = k = 2$; $J = 1, K = 2$; $J = 2, k = 1$ for no preload and $J = k = 1$ for preload).

In the present example problem of square angle-ply plates with uniaxial preload in the x direction, the optimum value of the wave number n in the y direction that renders the frequency a minimum (that is, the fundamental mode) is found to be 1. For equal biaxial preload (that is, hydrostatic inplane compression), the optimum value of axial wave number m is found to be 1 for $\theta \leq 45$ deg while the optimum value of n in the y direction is 1 for $\theta \geq 45$ deg (θ is the fiber angle measured from the axial x direction). The optimum wave numbers are found to be $m = n = 1$ in both the uniaxial and equal biaxial preload cases provided the preload is sufficiently small or zero.

Figure 1(a) shows a graph of normalized fundamental frequency $\omega/\omega(\theta = \mu = 0)$ versus normalized uniaxial preload $\bar{\sigma}_x/\bar{\sigma}_{x_c}(\theta = \mu = 0)$. The fundamental frequency and the classical buckling load at $\theta = 0$ and $\mu = 0$ are, respectively,

$$\pi^2\Omega(\theta = \mu = 0) = [\rho b^4/(Eh^3)]^{1/2}\omega(\theta = \mu = 0) = 18.805$$

$$\bar{\sigma}_{x_c}(\theta = \mu = 0) = 35.8307 \quad (30)$$

Geometric imperfection amplitudes of 0, ± 0.5, and ± 1.0 are used for fiber angles of 0 deg and 90 deg. It can be seen that imperfections may significantly raise the frequencies due to initial curvature effects. For sufficiently small values of the uniaxial preload $\bar{\sigma}_x$, the 0 deg and 90 deg curves coincide for a fixed value of the imperfection amplitude. However, for larger amount of uniaxial preload, there is a significant decrease in the fundamental frequencies for the 90 deg curves due to the influence of vibrational modes with higher axial wave numbers. These higher modes do not correspond to lower fundamental frequencies for the 0 deg curves because the laminated plate for the 0 deg fiber angle is much stiffer against bending in the axial x direction than those for the 90 deg fiber angle. For design purposes, taking into account the possibility of the presence of geometric imperfections in the order of the laminated plate thickness, it can be seen that the 0 deg configuration is stiffer than the 90 deg orientation both in terms of vibration with uniaxial preload and buckling (note that buckling occurs when $\Omega = 0$). Clearly, the number of layers N will not affect either the 0 deg or 90 deg configurations.

Figure 1(b) shows a graph of normalized frequency versus normalized uniaxial preload for $\theta = 15$ deg with various values of imperfection amplitude and for the number of layers N being 2 and infinite ($N = 4$ curve is shown only for $\mu = 0$). Again, the presence of geometric imperfections may result in a significant increase in the vibration frequencies. The optimum value of the axial wave number m is found to be 1 for all these curves. A larger rate of increase of the frequency (μ is fixed) due to uniaxial preload is found for $N = 2$ (where the effects of bending-stretching coupling is most pronounced) than for $N =$ infinity (which corresponds to the orthotropic plate).

Figure 1(c) is a plot of normalized frequency versus normalized uniaxial preload for $\theta = 75$ deg with values of imperfection amplitude being 0, ± 0.5, and ± 1.0 for $N = 2$ and infinity. For a fixed value of the imperfection amplitude and for a sufficiently small amount of uniaxial preload, these curves for the 75 deg configuration coincide with those for the 15 deg orientation presented in Fig. 1(b). However, for larger uniaxial preload, the presence of higher modes with larger values of m is found to significantly reduce the vibration frequencies. The optimum axial wave numbers m are shown in the figure.

Similarly, Fig. 1(d) shows curves for $\theta = 45$ deg. Although the degrading effects of bending-stretching coupling ($N = 2$) in the vibration frequency for sufficiently small amount of uniaxial preload is quite pronounced, these curves rise quite rapidly for larger amount of uniaxial preload. Judging from all the preceding figures, it may be observed that the buckling loads ($\omega = 0$) are not reduced due to the presence of initial geometric imperfections ($J = k = 1$).

Summarizing Figs. 1(a)–(d), it may be said that for any given inplane uniaxial preload, an increase in imperfection amplitude causes increase in the fundamental frequency. This is due to two factors: (a) the slight initial curvature due to imperfection increases the stiffness, and (b) uniaxial preload causes additional curvature.

Figures 2(a)–(c) present results for the case of equal biaxial stress ($\bar{\sigma}_x = \bar{\sigma}_y$) showing the effects of preload on the fundamental frequency for various values of imperfection amplitude μ being 0, ± 0.5, and ± 1.0. The previously used values of $\omega(\theta = \mu = 0)$ and $\bar{\sigma}_{x_c}(\theta = \mu = 0)$ are again used as normalizing factors. Figure 2(a) shows curves for the case of 0 deg and 90 deg orientations. Unlike the case of 0 deg orientation for the uniaxial preload as shown in Fig. 1(a), none of the curves for lowest wave numbers (m = n = 1) is applicable for very large equal biaxial preload (that is, all the curves eventually drop) due to the dominance of vibration modes with higher wave numbers. The optimum wave number m is always 1 and the optimum value of n is shown in the figure for the 0 deg orientation. Due to symmetry consideration for square plates in equal biaxial loading, the curves for the 90 deg orientation are identical to that for the 0 deg configuration (for a fixed value of the imperfection amplitude) provided that the optimum values for m and n are interchanged. The number of layers do not affect the 0 deg nor the 90 deg configurations.

Figure 2(b) gives data in the cases of 15 deg and 75 deg configurations. Due to symmetry, unlike the uniaxial preload case ($\bar{\sigma}_y = 0$) of Figs. 1(b) and (c), the 15 deg and 75 deg curves coincide even for large values of the equal biaxial preload. Again, small imperfections are shown to have a pronounced effect on raising the vibration frequencies. In general, care should be taken not to apply excessively large inplane compressive preload (say twice the buckling load) in order to avoid numerical inaccuracies in the previbration deformations.

For brevity, the plot for $\theta = 45$ deg will not be presented. For $\theta = 45$ deg, the optimum wave numbers are found to be $m = n = 1$ for $a/b = 1$ in all these curves. Again, the presence of small imperfections may significantly raise the vibration frequencies. It should be noted that these curves are identical to that presented in Fig. 1(d) for uniaxial preload ($\bar{\sigma}_y = 0$) except that the compressive preload axis is shrunk by a factor

Downloaded 02 May 2010 to 171.66.16.54. Redistribution subject to ASME license or copyright; see http://www.asme.org/terms/Terms_Use.cfm

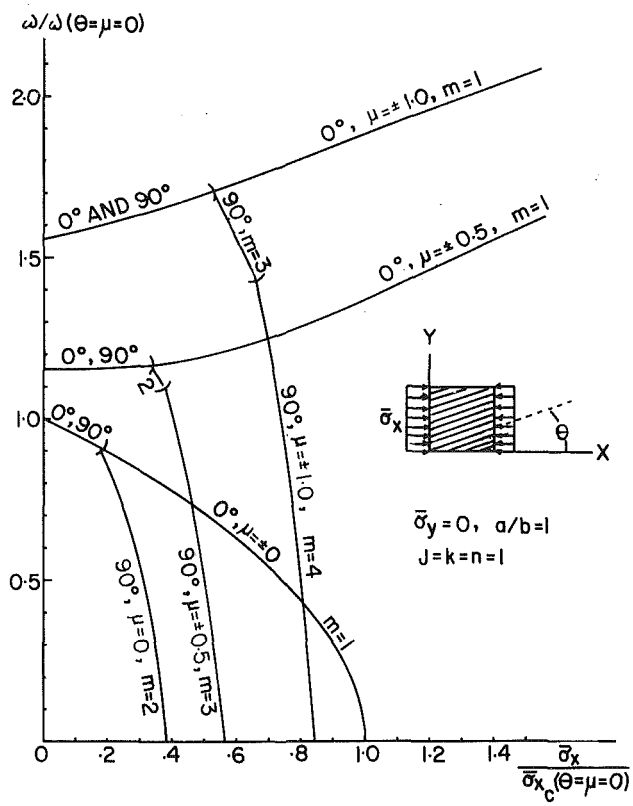


Fig. 1(*a*) Normalized fundamental frequency versus normalized uniaxial preload for imperfect angle ply plates ($\theta = 0$ deg and 90 deg, $J = k = 1$)

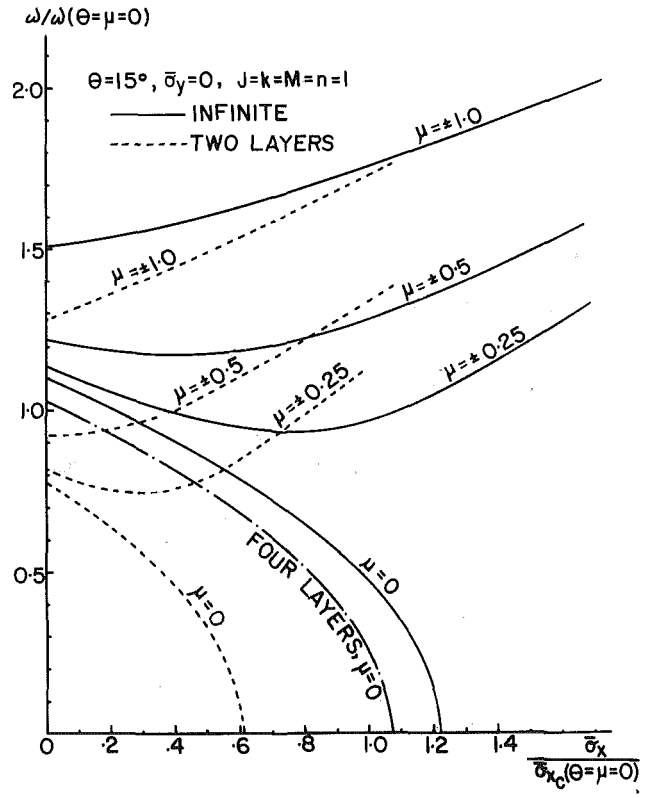


Fig. 1(*b*) Normalized fundamental frequency versus normalized uniaxial preload for imperfect angle ply plates ($\theta = 15$ deg, $J = k = 1$)

of 2. Thus, the frequency increase due to imperfections becomes more important for a given value of preload in the equal biaxial case.

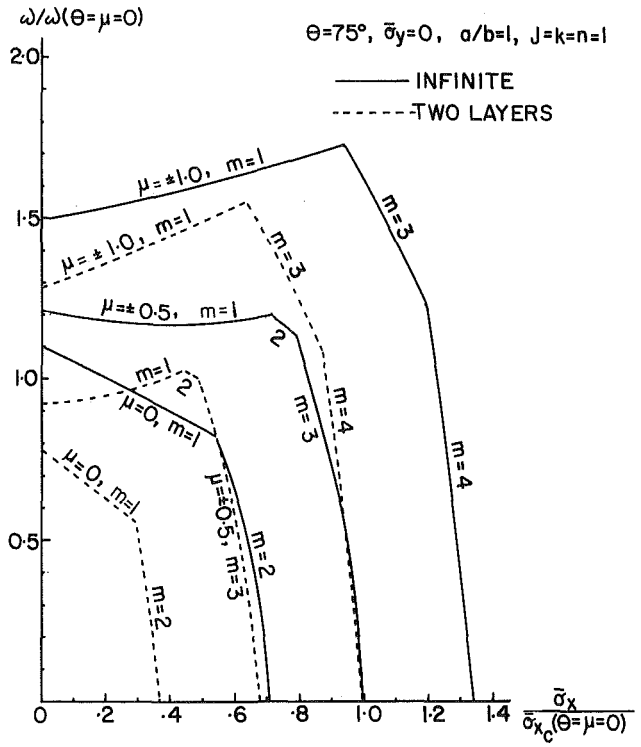


Fig. 1(*c*) Normalized fundamental frequency versus normalized uniaxial preload for imperfect angle ply plates ($\theta = 75$ deg, $J = k = 1$)

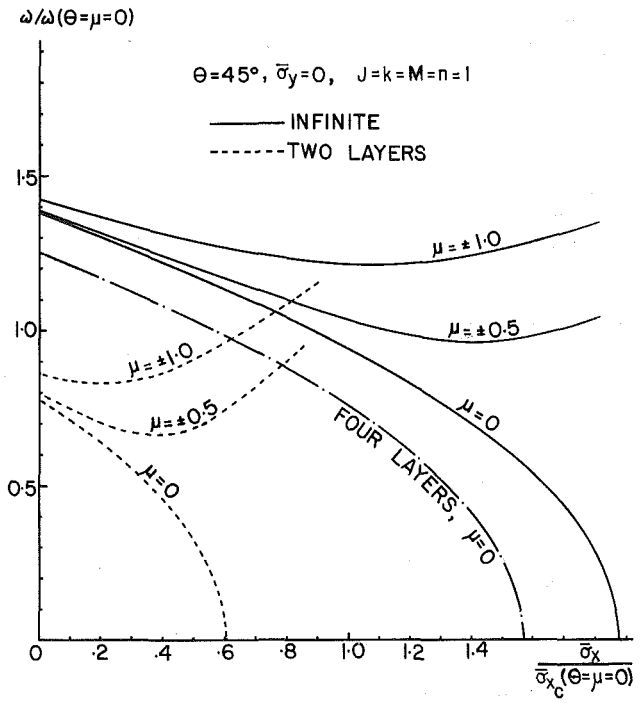


Fig. 1(*d*) Normalized fundamental frequency versus normalized uniaxial preload for imperfect angle ply plates ($\theta = 45$ deg, $J = k = 1$)

Fig. 1

Figure (3*a*) depicts normalized frequency versus fiber angle θ for simply supported square angle ply laminated plates with various values of imperfection amplitudes and imperfection wave numbers ($\mu = 0$, ± 0.5, and ± 1.0 for $J = k = 1$ and $\mu = 0$ and ± 1.0 for $J = k = 2$) and number of layers ($N = 2$ and $N =$ infinity), in the important special case of no inplane

Downloaded 02 May 2010 to 171.66.16.54. Redistribution subject to ASME license or copyright; see http://www.asme.org/terms/Terms_Use.cfm

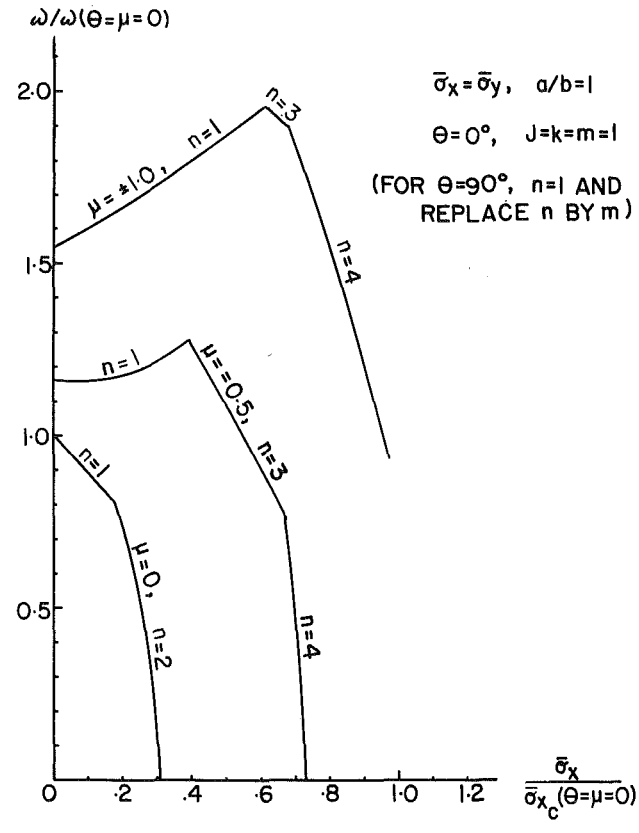


Fig. 2(a) Normalized fundamental frequency versus normalized equal biaxial preload for imperfect angle ply plates ($\theta = 0$ deg and 90 deg, $J = k = 1$)

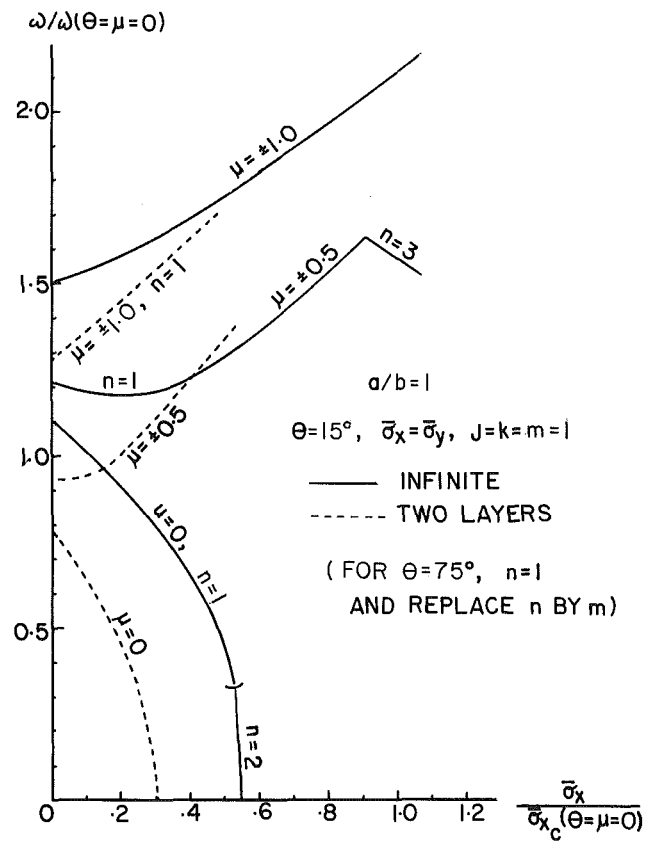


Fig. 2(b) Normalized fundamental frequency versus normalized equal biaxial preload for imperfect angle ply plates ($\theta = 15$ deg and 75 deg, $J = k = 1$)

Fig. 2

preload. Due to symmetry, the curves for the θ and 90 deg-θ configurations coincide. For orthotropic plates (N = infinity) with imperfection wave numbers $J = k = 1$, it can be seen that the effects of geometric imperfection on raising the fundamental frequencies are more pronounced for fiber orientations approximately parallel to the edges ($\theta \approx 0$ deg and 90 deg) than for the diagonal orientations ($\theta \approx 45$ deg). The same conclusion is also applicable to two-layer plates with $J = k = 1$. On the other hand, the effects of imperfections of the type $J = k = 2$ on raising the fundamental frequencies are more pronounced for fiber orientations θ between 15 deg and 30 deg than for the remaining range of θ, both in the case of N = infinity and $N = 2$. The reduction of the frequencies due to the bending-stretching coupling effects can be seen by comparing the N = infinity and $N = 2$ curves.

Finally, the normalized frequency versus fiber angle θ for the other two types of geometric imperfections ($\theta = 0, \pm 1.0$ for $J = 1$, $k = 2$ and $J = 2$, $k = 1$) are presented in Fig. 3(*b*). For a given number of layers, the effects of geometric imperfections of the type $J = 1$, $k = 2$ in raising the fundamental frequencies are more pronounced in the 0 deg $\leq \theta \leq$ 25 deg range than in the 25 deg $< \theta \leq 45$ deg range. On the other hand, the increases in fundamental frequencies due to the $J = 2$, $k = 1$ type of geometric imperfections are more pronounced in the 20 deg $< \theta <$ 35 deg than in the 0 deg $\leq \theta \leq$ 25 deg and 35 deg $\leq \theta \leq 45$ deg ranges. Due to symmetry, the curves for the θ configuration with $J = 1$, $k = 2$ are identical to those for the 90 deg-θ configuration with $J = 2$, $k = 1$. As a check, all the curves in Figs. 3(*a*) and (*b*) have zero slope at $\theta = 0$ deg and $\theta = 45$ deg. These curves agree with the plotted values in Figs. 1(*a*)-(*d*) and 2(*a*)-(*c*) in the special case of no preload ($J = k = 1$).

6 Concluding Remarks

The effects of geometric imperfections on vibrations of simply supported angle-ply plates in the cases of uniaxial or equal biaxial preload are analyzed. It is found that significant increases in the fundamental frequencies typically occur for geometric imperfection amplitudes of the order of the laminated plate thickness. In the case of uniaxial preload, the increase of frequency due to the geometric imperfection of the type $J = k = 1$ is much more pronounced for smaller fiber angles (e.g., $\theta = 0$ deg and $\theta = 15$ deg) than for larger angles (e.g., $\theta = 75$ deg and 90 deg) due to the fact that the vibration modes with larger axial wave numbers m correspond to higher (i.e., nonfundamental) frequencies for small fiber angles. For equal biaxial preload, the similar effects of geometric imperfections ($J = k = 1$) in raising the fundamental frequencies are again detected. The vibration modes with larger wave numbers may correspond to the lowest (i.e., fundamental) frequencies for both large and small fiber angles, but not at or near the $\theta = 45$ deg configurations. The influence of various types of geometric imperfections ($J = k = 1$, $J = k = 2$, $J = 1, k = 2$, and $J = 2, k = 1$) on the fundamental frequencies for all fiber angles with no preload have been examined. Extensions of this work to laminated cylindrical panels and laminated cylindrical shells are in progress.

Acknowledgment

This research was supported by the Ohio State research seed grant awarded to the author through the Office of Research and Graduate Studies.

Downloaded 02 May 2010 to 171.66.16.54. Redistribution subject to ASME license or copyright; see http://www.asme.org/terms/Terms_Use.cfm

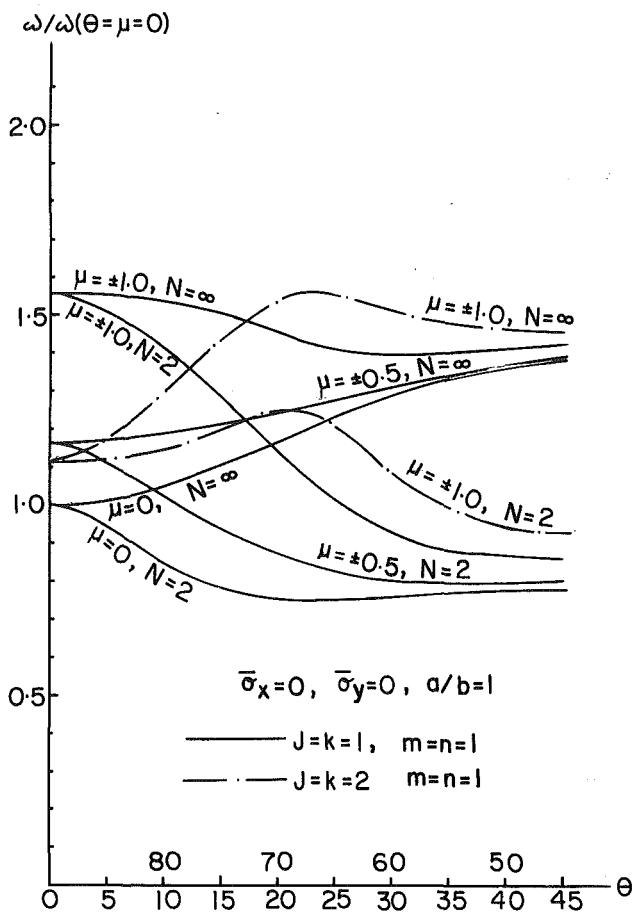


Fig. 3(a) Normalized fundamental frequency versus fiber angle with imperfection wave numbers $J = k = 1$ and $J = k = 2$ (no preload)

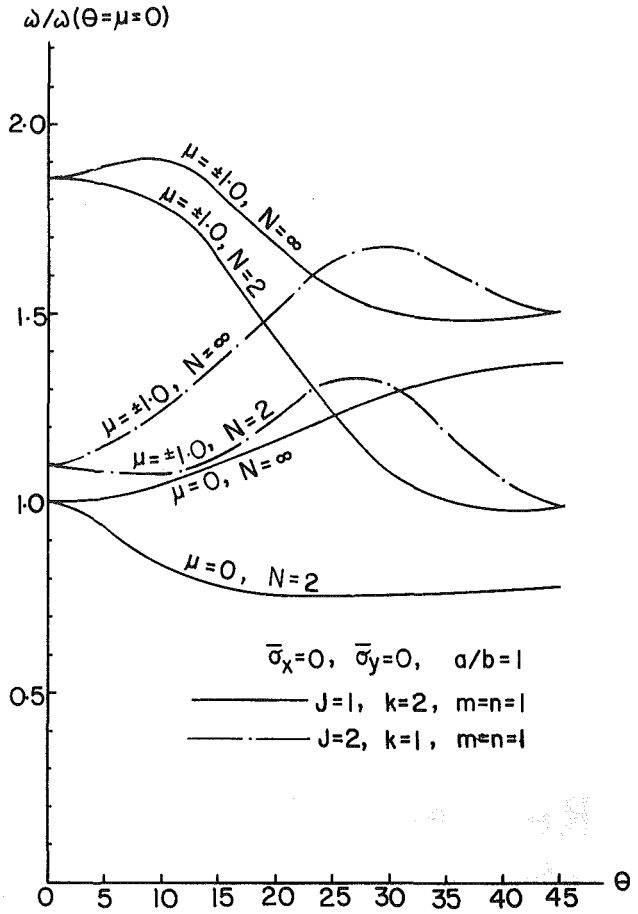


Fig. 3(b) Normalized fundamental frequency versus fiber angle with imperection wave numbers $J = 1, k = 2$ and $J = 2, k = 1$ (no preload)

Fig. 3

References

1 Ambartsumyan, S. A., "Calculation of Laminated Anisotropic Shells," *Izvestiia Akademiia Nauk Armenskoi SSR, Ser. Fiz. Mat. Est. Tekh. Nauk.*, Vol. 6, No. 3, 1953, p. 15.

2 Reissner, E., and Stavsky, Y., "Bending and Stretching of Certain Types of Heterogeneous Aeolotropic Elastic Plates," ASME JOURNAL OF APPLIED MECHANICS, Vol. 28, 1961, pp. 402–408.

3 Whitney, J. M., and Leissa, A. W., "Analysis of Heterogeneous Anisotropic Plates," ASME JOURNAL OF APPLIED MECHANICS, Vol. 36, 1969, pp. 261–266.

4 Jones, R. M., *Mechanics of Composite Materials*, Scripta, 1975.

5 Chia, C. Y., *Nonlinear Analysis of Plates*, McGraw-Hill, New York, 1980, 430 pp.

6 Leissa, A. W., "Advances in Vibration, Buckling and Postbuckling Studies on Composite Plates," *Composite Structures, Proc. of 1st Int. Conf. Sept. 1981*, Marshall, I. H., ed., Applied Science, 1981, pp. 312–334.

7 Bert, C. W., "Research on Dynamics of Composite and Sandwich Plates, 1979–1981," *The Shock and Vibration Digest*, Vol. 14, No. 10, Oct. 1982, pp. 17–34.

8 Hui, D., and Leissa, A. W., "Effects of Geometric Imperfections on Vibrations of Biaxially Compressed Rectangular Flat Plates," ASME JOURNAL OF APPLIED MECHANICS, Vol. 50, No. 4, 1983, pp. 750–756.

9 Hui, D., and Leissa, A. W., "Effects of Uni-Directional Geometric Imperfections on Vibrations of Pressurized Shallow Spherical Shells," *International Journal of Nonlinear Mechanics*, Vol. 18, No. 4, 1983, pp. 279–285.

10 Rosen, A., and Singer, J., "Influence of Asymmetric Imperfections on the Vibrations of Axially Compressed Cylindrical Shells," *Israel J. of Technology*, Vol. 14, 1976, pp. 23–26; also Technion Aeronautical Engineering, TAE Report No. 212, Mar. 1975.

11 Watawala, L., and Nash, W. A., "Influence of Initial Geometric Imperfections on Vibrations of Thin Circular Cylindrical Shells," *Computers and Structures*, Vol. 16, Nos. 1–4, 1983, pp. 125–230.

12 Hui, D., "Effects of Geometric Imperfections and In-Plane Constraints on Nonlinear Vibrations of Simply Supported Cylindrical Panels," ASME JOURNAL OF APPLIED MECHANICS, Vol. 51, No. 2, 1984, pp. 383–390.

13 Singer, J., and Prucz, J., "Influence of Initial Geometrical Imperfections on Vibrations of Axially Compressed Stiffened Cylindrical Shells," *J. of Sound and Vibration*, Vol. 80, No. 1, 1982, pp. 117–143; also Technion Aeronautical Engineering TAE Report No. 369, Feb. 1980, 113 pp.

14 Budiansky, B., and Hutchinson, J. W., "Buckling: Progress and Challenge," *Proceedings of Symposium on Trends in Solid Mechanics*, 1979, Delft University Press, The Netherlands.

15 Hui, D., "Soft-Spring Nonlinear Vibrations of Antisymmetrically Laminated Rectangular Plates," submitted to *Proc. of 5th ASCE-EM Specialty Conference*, University of Wyoming, Aug. 1–3, 1984, pp. 372–375.

16 Koiter, W. T., "The Effect of Axisymmetric Imperfection on the Buckling of Cylindrical Shells Under Axial Compression," *Koninklijke Nederlandse Academie Wetenschappen*, Proc. Series *B.*, Vol. 66, 1963, pp. 265–279.

17 Hui, D., and Hansen, J. S., "Effect of Stringer Torsional Rigidity on Buckling of Integrally Stiffened Angle Ply Plates," *Fibre Science and Technology Journal*, Vol. 16, Jan. 1982, pp. 39–43.

18 Stavsky, Y., and Hoff, N. J., "Mechanics of Composite Structures," *Composite Engineering Laminates*, Dietz, A.G.H., ed MIT Press, Cambridge, Mass., and London, England, 1969, pp. 5–59.

19 Tennyson, R. C., Muggeridge, D. B., Chan, K. H., and Khot, N. S., "Buckling of Fiber-Reinforced Circular Cylinders under Axial Compression," AFFDL-TR-72-102, Aug. 1972, 114 pp.

20 Harris, G. Z., "The Buckling and Post-Buckling Behavior of Composite Plates Under Biaxial Loading," *Int. J. of Mechanical Sciences*, Vol. 17, 1975, pp. 187–202.

APPENDIX

Definite Integrals

The functions $I(\ )$ and $H(\ )$ are defined to be,

$$I(\ ) = (b/a)\int_0^{a/b} (\ )dx, \qquad H(\ ) = \int_0^1 (\ )dy \quad (A1\text{–}A2)$$

Downloaded 02 May 2010 to 171.66.16.54. Redistribution subject to ASME license or copyright; see http://www.asme.org/terms/Terms_Use.cfm

and the definite integrals $I_0, I_1, I_2, \ldots, I_7$ are,

$$I_0 = I[\sin(M\pi x)\sin[(J-M)\pi x]] = 1/2 \quad \text{if} \quad 2M=J; \quad 0 \quad \text{otherwise}$$

$$I_1 = I[\sin^2(M\pi x)\cos(2J\pi x)] = -1/4 \quad \text{if} \quad M=J; \quad 0 \quad \text{otherwise}$$

$$I_2 = I[\sin^2(M\pi x)\cos(J\pi x)] = -1/4 \quad \text{if} \quad 2M=J; \quad 0 \quad \text{otherwise}$$

$$I_3 = I[\sin(M\pi x)\cos(M\pi x)\sin(J\pi x)] = 1/4 \quad \text{if} \quad 2M=J; \quad 0 \quad \text{otherwise}$$

$$I_4 = I[\sin(M\pi x)\sin(J\pi x)\cos[(J-M)\pi x]] = 1/2 \quad \text{if} \quad M=J; \quad 0 \quad \text{otherwise}$$

$$I_5 = I[\sin(M\pi x)\sin(J\pi x)\cos[(J+M)\pi x]] = -1/4$$

$$I_6 = I[\sin(M\pi x)\cos(J\pi x)\sin[(J-M)\pi x]] = -1/4 \quad \text{if} \quad 2M=J; \quad 0 \quad \text{otherwise}$$

$$I_7 = I[\sin(M\pi x)\cos(J\pi x)\sin[(J+M)\pi x]] = 1/4 \qquad (A3\text{–}A10)$$

The definite integrals H_i is defined to be I_i (where $i=0, 1, 2, \ldots 7$) by replacing J and M by k and n, respectively. For example,

$$H_0 = H[\sin(n\pi y)\sin[(k-n)\pi y]] = 1/2 \quad \text{if} \quad 2n=k; \quad 0 \quad \text{otherwise}$$

$$H_1 = H[\sin^2(n\pi y)\cos(2k\pi y)] = -1/4 \quad \text{if} \quad n=k; \quad 0 \quad \text{otherwise} \qquad (A11\text{–}A12)$$

It can be easily verified that $H_0=I_0, H_1=I_1, H_2=I_2, H_3=I_3, H_4=I_4, H_5=I_5, H_6=I_6$ and $H_7=I_7$ provided the foregoing substitutions are carried out.

Downloaded 02 May 2010 to 171.66.16.54. Redistribution subject to ASME license or copyright; see http://www.asme.org/terms/Terms_Use.cfm

M. Countryman
Department of Mathematics and Statistics,
Louisiana Tech University,
Ruston, La. 71272

R. Kannan
Department of Mathematics,
University of Texas at Arlington,
Arlington, Texas 76019

Nonlinear Forced Vibrations of Beams

An iterative procedure for computing periodic solutions of nonlinear vibrating beams is presented. The nonlinear partial differential equation is replaced by a coupled system of equations. The contraction mapping principle is then applied to generate a method of successive approximations. The coupled equations are then approximated by discrete equations that are solved by matrix-theoretic techniques and numerical quadrature procedures. Some numerical examples are provided to illustrate the method.

Introduction

We consider an iterative procedure for the numerical solution of nonlinear hyperbolic problems arising in the forced vibration of beams. Although the procedure is applicable to the general class of problems, for the sake of simplicity we restrict ourselves to the model problem

$$u_{tt}+u_{xxxx}+\beta u_t=\epsilon g(u)+f(x,t)$$
$$u(0,t)=u(\pi,t)=u_{xx}(0,t)=u_{xx}(\pi,t)=0 \tag{1}$$
$$u(x,t)=u(x,t+2\pi)$$

where β is a positive constant and $f(x,t)$ is 2π-periodic in t. We discuss here the problem of approximating periodic solutions of the same period as $f(x,t)$, but the procedure can be modified to also find periodic solutions of other periods.

The existence of periodic solutions to the preceding problem has been established in [3]. For other results on the existence of periodic solutions one is referred to [6, 9]. The numerical method discussed in this paper utilizes the ideas in the existence method of [3]. However the general problem of numerically solving nonlinear forced vibrations of beams has been studied quite extensively in the recent years in [1, 5, 7] and among the various techniques studied, two principal ones are Galerkin's method and the method of harmonic balance. We propose a method that utilizes the ideas of both but is iterative in nature. It must be noted here that the harmonic balance solution may not be close enough to a solution to the original problem.

In this paper we follow the general ideas of the iterative procedure discussed in [2, 8] and present an approximation procedure together with some numerical examples. The nonlinear partial differential equation is approximated by using a combination of finite differences and quadrature methods to generate a coupled system of discrete equations. For a discussion of the convergence and stability of the numerical method one is referred to [4]. It must be noted that the "$g(u)$" term in (1) implies nonuniqueness of solutions in general and thus a local convergence must be required. The harmonic balance method could thus be used to provide an initial point for the iterative process.

An Iterative Procedure

For the sake of simplicity we assume that $g(u)$ is odd and we look for odd periodic solutions of problem (1). Thus we can assume that a solution has a Fourier series expansion

$$u(x,t)=\sum_{l=1}^{\infty}\sum_{k=0}^{\infty}(a_{kl}\sin kt\sin lx+b_{kl}\cos kt\sin lx)$$

Let P be the operator defined by

$$Pu(x,t)=\frac{1}{2\pi}\int_0^{2\pi}u(x,s)\,ds.$$

It is easy to see that P is a projection operator mapping $u(x,t)$ onto

$$v(x)=\sum_{l=1}^{\infty}b_{0l}\sin lx.$$

Further, if we write $u(x,t)$ as

$$u(x,t)=v(x)+w(x,t)$$

then $Pw(x,t)=0$ and $(I-P)u=w$. Setting $N(u)=\epsilon g(u)+f(x,t)$, problem (1) can be expressed as

$$v_{tt}+w_{tt}+v_{xxxx}+w_{xxxx}+\beta v_t+\beta w_t=N(v+w).$$

This equation can now be rewritten as a coupled system of equations

$$w_{tt}+w_{xxxx}+\beta w_t=(I-P)[N(v+w)], \tag{2}$$
$$v_{xxxx}=PN(v+w). \tag{3}$$

Associated with the coupled system of equations we have the boundary conditions

$$w(0,t)=w(\pi,t)=w_{xx}(0,t)=w_{xx}(\pi,t)=0$$
$$w(x,t)=w(x,t+2\pi) \tag{4}$$
$$Pw(x,t)=0$$

and

$$v(0)=v(\pi)=v_{xx}(0)=v_{xx}(\pi)=0, \tag{5}$$

respectively.

Contributed by the Applied Mechanics Division for publication in the JOURNAL OF APPLIED MECHANICS.

Discussion on this paper should be addressed to the Editorial Department, ASME, United Engineering Center, 345 East 47th Street, New York, N.Y. 10017, and will be accepted until two months after final publication of the paper itself in the JOURNAL OF APPLIED MECHANICS. Manuscript received by ASME Applied Mechanics Division, September, 1983; final revision, April, 1984.

Copyright © 1985 by ASME
Downloaded 02 May 2010 to 171.66.16.54. Redistribution subject to ASME license or copyright; see http://www.asme.org/terms/Terms_Use.cfm

We thus define the iterative process for equations (2) and (3) by

$$(w_{n+1})_{tt} + (w_{n+1})_{xxxx} + \beta(w_{n+1})_t = (I-P)[N(v_n + w_n)] \tag{6}$$

and

$$(v_{n+1})_{xxxx} = PN(v_n + w_{n+1}) \tag{7}$$

together with the corresponding boundary conditions. Thus knowing v_n and w_n one solves (6) for w_{n+1}. Substituting this value of w_{n+1} in (7) we obtain v_{n+1} by solving the corresponding linear problem and thus the sequences $\{v_{n+1}\}$ and $\{w_{n+1}\}$ are generated.

The theoretical considerations in establishing the convergence of the sequences $\{v_{n+1}\}$ and $\{w_{n+1}\}$ to v and w, respectively, such that v and w satisfy (2)–(5) may be briefly outlined as follows. Equations (2) and (3) may be considered as finding the fixed point of the coupled operators (T_1, T_2) given by

$$\begin{pmatrix} T_1 \\ T_2 \end{pmatrix} : \begin{pmatrix} v \\ w \end{pmatrix} \rightarrow \begin{pmatrix} PN(v+w) \\ H(I-P)N(v+w) \end{pmatrix}$$

where Hf is the solution of the linear problem

$$w_{tt} + w_{xxxx} + \beta w_t = f(x,t)$$

together with the boundary conditions. Equations (6) and (7) may then be seen to be modified Picard iterates of (T_1, T_2). To ensure a unique fixed point (locally) we must prove that (T_1, T_2) is a contraction mapping. We utilize that g is locally Lipschitz and obtain inequalities involving f, ϵ, and β in order that (T_1, T_2) be a contraction mapping and map a ball in the (v,w) space into itself. Details of these inequalities may be seen in [4].

Remark. It must be remarked here that the equation $Pw(x,t) = 0$ in (4) is redundant because the kernel of the differential operator $w_{tt} + w_{xxxx} + \beta w_t$ is trivial. However, we have chosen to write all three conditions in (4) so that the applicability of the method is still valid when $Pw = 0$ is not a redundant equation as would be the case if we were studying

$$u_{tt} - u_{xx} + \epsilon u^3 = f(x,t)$$
$$u(0,t) = u(\pi,t) = 0$$
$$u(x,t) = u(x,t+2\pi)$$

In this case P would be the projection into the kernel of $u_{tt} - u_{xx}$ together with the boundary condition.

Discrete Equations

Due to the boundary conditions on x and the periodicity hypothesis on t, it suffices to solve the problem on the rectangle $[0,\pi] \times [0,2\pi]$.

We choose the x-axis to be horizontal; the t-axis, vertical. The interval $[0,\pi]$ is divided so that $x_0 = 0$, $x_1 = \Delta x$, $x_2 = 2\Delta x$, . . . , $x_N = N\Delta x$, and $x_{N+1} = \pi$; therefore, $\Delta x = \pi/(N+1)$. The inverval $[0,2\pi]$ is divided so that $t_1 = 0$, $t_2 = \Delta t$, . . . , $t_M = (M-1)\Delta t$, and $t_{M+1} = 2\pi$; therefore $\Delta t = 2\pi/M$. Since solution values are known for $x = 0$ and $x = \pi$ and since the solution values for $t = 0$ are the same as those for $t = 2\pi$ due to periodicity, we are primarily concerned with finding solution values at the points $(x_i, t_j) = (i\Delta x, (j-1)\Delta t)$ where $1 \le i \le N$ and $1 \le j \le M$. We see that there are N vertical grid lines while there are M horizontal grid lines. Finally, we choose $\Delta t = \Delta x$ for simplicity, in which case $M = 2(N+1)$.

To begin our discussions of the discrete equations themselves, we generate a discrete representation of the projection operators. If

$$Pw(x,t) = \frac{1}{2\pi}\int_0^{2\pi} w(x,s)ds$$

is approximated by the trapezoidal rule and Δs is chosen to be equal to Δt, we obtain

$$Pw(x_i,t_j) = \frac{1}{2\pi}\int_0^{2\pi} w(x_i,s)\,ds \cong \frac{\Delta t}{2\pi}\left[\frac{1}{2}w(x_i,t_1) + w(x_i,t_2) + \ldots + w(x_i,t_N) + \frac{1}{2}w(x_i,t_{N+1})\right].$$

Since $t_1 = 0$ and $t_{N+1} = 2\pi$, $\frac{1}{2}w(x_i,t_1) + \frac{1}{2}w(x_i,t_{N+1}) = w(x_i,t_1)$ by periodicity. Therefore,

$$Pw(x_i,t_j) = \frac{\Delta t}{2\pi}\sum_{k=1}^{M} w(x_i,t_k), \qquad i = 1,2,\ldots,N,$$

or

$$Pw(x_i,t_j) = \frac{\Delta t}{2\pi}\sum_{k=1}^{M} w_{ik}, \qquad i = 1,2,\ldots,N,$$

where we have used the notation $w(x_i,t_k) = w_{ik}$. The discrete approximation to the projection operator may now be defined by P_{ij} where

$$P_{ij}w_{ij} \equiv \frac{\Delta t}{2\pi}\sum_{k=1}^{M} w_{ik}$$

for $i = 1,2,\ldots,N$ and $j = 1,2,\ldots,M$. Note that for fixed x_i, the value of $P_{ij}w_{ij}$ does not depend on t_j. This is to be expected considering the way in which P is defined.

To approximate the differential equation in (6), the standard second-order, centered finite differences are used for w_{tt}, w_{xxxx}, and w_t. The choice of the second-order difference for w_t not only gives an approximation to the differential equation that is second-order overall, it is also important from the standpoint of numerical stability. However, the details of the stability analysis will appear elsewhere.

Since we have chosen $\Delta t = \Delta x$, the differential equation in (6) may be written as

$$\frac{w_{i,j+1} - 2w_{ij} + w_{i,j-1}}{(\Delta x)^2} + \frac{w_{i+2,j} - 4w_{i+1,j} + 6w_{ij} - 4w_{i-1,j} + w_{i-2,j}}{(\Delta x)^4} + \beta\frac{w_{i,j+1} - w_{i,j-1}}{2\Delta x} = (I_{ij} - P_{ij})h_{ij} \tag{8}$$

where I_{ij} is the discrete identity operator and $h_{ij} = N(v_n(x_i) + w_n(x_i,t_j))$ for $1 \le i \le N$ and $1 \le j \le M$.

We note that $w(0,t_j) = w(\pi,t_j) = 0$ for each j, so we set $w_{0,j} = w_{N+1,j} = 0$ whenever these terms appear in (8). Also, the periodicity of w with respect to t allows us to write $w_{i,M+1} = w(x_i,t_{M+1}) = w(x_i,t_1) = w_{i,1}$ and $w_{i,0} = w(x_i,t_0) = w(x_i,t_M) = w_{i,M}$ in (8). Finally, two additional questions concerning the difference approximation to the differential equation must be considered: (*a*) the method of incorporating the information given by $w_{xx}(0,t) = w_{xx}(\pi,t) = 0$ into the difference equations, and (*b*) how to evaluate $w_{i-2,j}$ if $x = \Delta x$ and how to evaluate $w_{i+2,j}$ if $x = \pi - \Delta x$. It will be seen that the answers to (*a*) and (*b*) are related.

First we consider the case $x = 0$. The equation $w_{xx}(0,t) = 0$ may be approximated by

$$\frac{w(\Delta x,t) - 2w(0,t) + w(-\Delta x,t)}{(\Delta x)^2} = 0$$

or since $w(0,t) = 0$, by $w(-\Delta x,t) = -w(\Delta x,t)$. Similarly, the approximation to $w_{xx}(\pi,t) = 0$ yields $w(\pi+\Delta x,t) = -w(\pi-\Delta x,t)$. Since $w_{i-2,j} = w(-\Delta x,t_j)$ when $x = \Delta x$ and $w_{i+2,j} = w(\pi+\Delta x,t_j)$ when $x = \pi - \Delta x$, we may write w_{i-}

Downloaded 02 May 2010 to 171.66.16.54. Redistribution subject to ASME license or copyright; see http://www.asme.org/terms/Terms_Use.cfm

$_{2,j} = -w_{1j}$ for $x = \Delta x$ and $w_{i+2,j} = -w_{N,j}$ for $x = \pi - \Delta x$. We note that the same conclusions may be reached a priori by virtue of the fact that the boundary conditions imply that $w(x,t)$ is odd in x about 0 and π.

By using (8) with the modifications listed previously, we obtain a difference equation at each of the MN grid points (x_i,t_j). The discrete projection condition $P_{ij}w_{ij} = 0$ also yields a set of MN equations. Since we have $2MN$ equations and only MN grid points, the system is clearly singular. If, however, we use only the projection equations for the first N grid points (x_i,t_1), $1 \le i \le N$) and only the difference equations for the remaining grid points $((x_i,t_j)$, $1 \le i \le N$, $1 < j \le M)$, we have a nonsingular set of linear equations. These equations may be solved by using standard matrix algebra techniques.

It must be noted that the remarks at the end of the preceding section should be recalled. The equations $P_{ij}w_{ij} = 0$ may be treated as redundant for this example but make sense for the general problem where the finite difference equation alone may form a singular system.

Having obtained the discrete analog of (2) and (4), we now proceed to develop the representation for (3) and (5). Since $v_n + w_{n+1}$ is known, we may write $N(v_n(x) + w_{n+1}(x,t)) = \hat{h}(x,t)$. Thus, equation (3) may be written as

$$v_{xxxx} = P\hat{h}$$
$$v(0) = v(\pi) = v_{xx}(0) = v_{xx}(\pi) = 0. \tag{9}$$

The solution of (9) may be obtained by the use of the Green's function for the operator

$$\left\{ \frac{d^4}{dx^4}, v(0) = v(\pi) = v''(0) = v''(\pi) = 0 \right\}.$$

That is,

$$v(x) = \int_0^\pi [G(x,s)P\hat{h}(s,t)]ds$$

where

$$G(x,s) = \begin{cases} \dfrac{1}{6\pi}x(x-\pi)(x-2\pi)s + \dfrac{1}{6\pi}(x-\pi)s^3, \\ \qquad 0 \le s \le x \le \pi \\ \dfrac{1}{6\pi}x(x-\pi)(x+\pi)(s-\pi) + \dfrac{1}{6\pi}x(s-\pi)^3, \\ \qquad 0 \le x \le s \le \pi. \end{cases}$$

(Recall that $P\hat{h}(s,t)$ is a function of s only.) Thus the solution of (9) may be accomplished by some numerical integration technique such as the trapezoidal rule. The value of v at x_i may be approximated by

$$v(x_i) = \int_0^\pi [G(x_i,s)P\hat{h}(\Delta s,t)]ds$$

$$\cong \Delta s\Big[\frac{1}{2}G(x_i,0)P\hat{h}(0,t) + G(x_i,\Delta s)P\hat{h}(\Delta,t) + G(x_i,2\Delta s)P\hat{h}(2\Delta s,t) + \ldots + G(x_i,k\Delta s)P\hat{h}(k\Delta s,t) + \frac{1}{2}G(x_i,\pi)P\hat{h}(\pi,t)\Big],$$

Now $G(x_i,0) = G(x_i,\pi) = 0$ for all x_i, so if the notation $s_j = j\Delta s$ is introduced we may write

$$v(x_i) \cong \Delta s \sum_{j=1}^{k} G(x_i,s_j)P\hat{h}(s_j,t).$$

In practice, however, the function $\hat{h}(s_j,t)$ is defined only at the grid points (x_i,t_j). Therefore, we replace P by P_{ij} and, to eliminate interpolation, we set $\Delta s = \Delta x$ (and thus $s_j = x_j$). We now have the relation that we have sought:

$$v(x_i) \cong \Delta x \sum_{j=1}^{N} G(x_i,x_j)P_{jk}\hat{h}_{jk} \tag{10}$$

where

$$G(x_i,x_j) = \begin{cases} \dfrac{1}{6\pi}x_i(x_i-\pi)(x_i-2\pi)x_j + \dfrac{1}{6\pi}(x_i-\pi)x_j^3, \\ \qquad 0 \le j \le i \le N \\ \dfrac{1}{6\pi}x_i(x_i-\pi)(x_i+\pi)(x_j-\pi) + \dfrac{1}{6\pi}x_i(x_j-\pi)^3, \\ \qquad 0 \le i \le j \le N \end{cases}$$

and $\hat{h}_{jk} = \hat{h}(x_j,t_k)$.

Finally note that $v(x_i)$ is constant for all points (x_i,t_k), $k = 1,2,\ldots,M$. This means that we need do the numerical integration calculation only for the points (x_i,t_1), $1 \le i \le N$.

In summary, the computational procedure may be described in the following way. At each point (x_i,t_1), $i = 1,2,\ldots,N$, a linear equation in the variable w is generated from the condition $P_{ij}w_{ij} = 0$, while at each point (x_i,t_j), $i = 1,2,\ldots N$, $j = 2,\ldots,M$, a linear equation in w is generated from (8). Taken together, these equations are solved by matrix algebra techniques (elimination) to obtain approximate values for w_{ij}, $i = 1,2,\ldots,N$, $j = 1,2,\ldots,M$. Next, at each point (x_i,t_1), $i = 1,2,\ldots,N$, the value of $v(x_i)$ is approximated from (10). Since $v(x)$ is constant with respect to t, values of $v(x_i)$ at points (x_i,t_j), $j = 2, 3, \ldots, M$ are assigned to be the same as the value of $v(x_i)$ at (x_i,t_1). Hence, given a set of starting values for w and v over the entire grid, the successive approximations to w and v may be computed as just described.

Numerical Examples

We now present three sample problems which have been solved numerically using the techniques described. The problems were run with a grid where $N = 8$ and $M = 18$. Thus, the total number of grid points is 144 and $\Delta x = \pi/9 \cong 0.349$. In the first and third examples, the exact solution $u(x,t)$ is known. This allows the computed solution to be checked against the actual solution. For convenience in testing the algorithm, a starting point of 0.7 $u(x,t)$ was used for the iterative scheme in Example 1 and Example 3. The second example is one in which the actual solution is not known. The harmonic balance solution $u(x,t) = \sin x + \sin x \sin t - 0.15 \sin x \cos t$ was used for the starting point for the iterations in Example 2.

Additional comments concerning the examples may be found in the concluding section.

Example 1.

$$u_{tt} + u_{xxxx} + 2u_t + 0.001u^3 = 0.001 \sin x + 0.000563 \sin x \sin t + 2 \sin x \cos t - 0.00000113 \sin x \cos 2t - 0.000188 \sin x \sin 3t - 0.000000376 \sin 3x - 0.000188 \sin 3x \sin t$$

The solution to this problem is known to be $u(x,t) = 0.001 \sin x + \sin x \sin t$. Therefore, $v(x) = 0.001 \sin x$ and $w(x,t) = \sin x \sin t$. The comparison of the computed results for Example 1 to the actual solution values is given in Table 1. Residual values are also included.

Downloaded 02 May 2010 to 171.66.16.54. Redistribution subject to ASME license or copyright; see http://www.asme.org/terms/Terms_Use.cfm

Table 1

Example	Number of iterations	Maximum V error	Mean V relative error	Maximum W error	Mean W relative error
1	2	0.000000[a]	0.000075	0.020797	0.018134
Maximum V residual		Mean V residual	Maximum W residual		Mean W residual
0.000000[b]		0.000000[a]	0.029242		0.001192

[a] The first nonzero digit appears in the eighth decimal place.
[b] The first nonzero digit appears in the seventh decimal place.

Table 2

Example	Number of iterations	Maximum V residual	Mean V residual	Maximum W residual	Mean W residual
2	6	0.041987	0.031423	0.031312	0.001249

Table 3

Example	Number of iterations	Maximum V error	Mean V relative error	Maximum W error	Mean W relative error
3	7	0.000055	0.054951	0.028872	0.023549
Maximum V residual		Mean V residual	Maximum W residual		Mean W residual
0.000029		0.000017	0.028904		0.001182

Example 2.

$$u_{tt} + u_{xxxx} + 2u_t + 0.1u^3 = \sin x + 0.3 \sin x \sin t + 2 \sin x \cos t$$

Since the solution to this problem is not known exactly, no comparison between computed and exact solution values can be made. Therefore, we list only the residual values and the iteration count in Table 2.

Example 3.

$$\begin{aligned} u_{tt} + u_{xxxx} + 2u_t + 0.3\,u^3 &= 0.00168 \sin x - 1.663 \sin x \sin t \\ &+ 3.125 \sin x \cos t \\ &+ 0.000675 \sin x \sin 2t + 0.113 \sin x \sin 3t \\ &- 0.113 \sin x \cos 3t \\ &- 0.000226 \sin 3x - 0.113 \sin 3x \sin t \\ &- 0.113 \sin 3x \cos t \\ &- 0.000225 \sin 3x \sin 2t - 0.0375 \sin 3x \sin 3t \\ &+ 0.0375 \sin 3x \cos 3t \end{aligned}$$

As in Example 1, the exact solution to this problem is known. Since $u(x,t) = 0.001 \sin x + \sin x \sin t + \sin x \cos t$, we have $v(x) = 0.001 \sin x$ and $w(x,t) = \sin x \sin t + \sin x \cos t$. Residual values and the comparison of the computed and exact solutions for Example 3 are given in Table 3.

Concluding Remarks

The three examples mentioned in the foregoing illustrate the difference between the harmonic balance approach and the iterative process discussed here. While in the first example the harmonic balance solution "$a \sin x \sin t + b \sin x \cos t$" yields a very good approximation by itself, the second example is a situation when the harmonic balance solution can be used as a good starting point. The third example illustrates a case when even though the harmonics $\sin x \sin t$ and $\sin x \cos t$ still dominate the solution, other harmonics of the forcing function such as $\sin x \sin 3t$ have coefficients that are significant. Finding them individually would involve solving a large system of nonlinear equations whereas we have used a sequence of linear problems which are more easily solved. These examples also illustrate the related problem of finding a good starting point for the iterative process. One candidate is the harmonic balance solution itself, but this problem needs further investigation.

References

1 Bennett, J. A., and Eisley, J. G., "A Multiple Degree-of-Freedom Approach to Nonlinear Beam Vibrations," *AIAA J.*, Vol. 8, 1970, pp. 734–739.

2 Cesari, L., "Alternative Method, Finite Elements, and Analysis in the Large," *Proceedings From the Uppsala 1977 International Conference on Differential Equations*, 1977, pp. 11–25.

3 Cesari, L., and Kannan, R., "Solutions of Hyperbolic Equations at Resonance," *J. Nonlinear Anal.*, Vol. 6, 1982, pp. 751–807.

4 Countryman, W. M., "Computations of Periodic Solutions of Forced Nonlinear Hyperbolic Problems," Ph.D. Dissertation, The University of Texas at Arlington, Arlington, Texas, 1982.

5 Eisley, J. G., and Bennett, J. A., "Stability of Large Amplitude Forced Motion of a Simply Supported Beam," *Int. J. Nonlinear Mechanics*, Vol. 5, 1970, pp. 645–657.

6 Hall, W. S., "On the Existence of Periodic Solutions for the Equations $D_{tt}u + (-1)^p D_x^{2p} u = \epsilon f(\cdot, \cdot, u)$," *J. Diff. Eqs.*, Vol. 7, 1970, pp. 509–526.

7 Lou, C. L., and Sikarskie, D. L., "Nonlinear Vibration of Beams Using a Form-Function Approximation," ASME JOURNAL OF APPLIED MECHANICS, Vol. 42, 1975, pp. 209–214.

8 Morel, K. J., "Numerical Methods for Nonlinear Boundary Value Problems at Resonance," Ph.D. Dissertation, The University of Texas at Arlington, Arlington, Texas, 1980.

9 Petzeltová, H., "Periodic Solutions of the Equation $u_{tt} + u_{xxxx} = f(\ ,\ , u, u_t)$," *Czech. Math. J.*, Vol. 23, No. 98, 1973, pp. 269–285.

Downloaded 02 May 2010 to 171.66.16.54. Redistribution subject to ASME license or copyright; see http://www.asme.org/terms/Terms_Use.cfm

P. Chan
Assoc. Mem. ASME

T. Han[2]
Assoc. Mem. ASME
Research Scientists,
Jaycor,
San Diego, Calif. 92101

W. L. Chow
Professor,
Department of Mechanical
and Industrial Engineering,
University of Illinois
at Urbana-Champaign,
Urbana, Ill. 61801
Mem. ASME

Gravitational Flow Discharge From a Horizontal Duct[1]

The problem of a potential flow discharge through a two-dimensional horizontal duct under the influence of gravitation is examined by the method of hodograph transformation. The stream function is considered and established in the hodograph plane, and the solution in the physical plane is established through additional integrations. The unknown boundary functions of the free jet must be determined as part of the solution. The initial pressure level and the discharge characteristics between the total head and the flow rate, have been established. Results are compared with those obtained previously by other method.

Introduction

The flow discharge from a conduit into the atmosphere is important in its practical applications. When the conduit is fairly short, the usual practice to estimate its discharge is based on the inviscid flow treatment with a subsequent correction of the viscous effects if it were necessary. This inviscid consideration is invariably based on the approximation of a uniform flow with atmospheric pressure prevailing at the exit section of the conduit. When the gravitational influence must be taken into account, no simple and effective method is available to deal with these problems. It should be noted that under the influence of both gravity and viscosity, a practical problem is usually of a three-dimensional nature even with the conduit of a simple geometry. The correct way to treat these problems must rely on the three-dimensional computation of the Navier-Stokes equation. The development of such methods at present is at its infancy even without the complications of a constant pressure-free surface.

Inasmuch as a treatment of gravitational discharge from an inviscid flow study is meritable, the present problem of an incompressible two-dimensional flow discharge from a constant area horizontal duct (see Fig. 1(*a*)) is considered on this basis. The basic difficulty of solving problems of this nature is that the unknown constant pressure-free jet boundary is no longer a constant velocity surface since the velocity varies with the jet elevation according to Bernoulli's Principle. Early studies for treating problems influenced by gravity through conformal mapping by Mark [2], Gurevich [3], or by asymptotic expansions, e.g., by Clarke [4], Keller [5], were not effective. Direct numerical calculations in the physical plane were carried out by Southwell [6], McNown [7], and by Varoglu [8], and Chan and Larock [9] through finite element methods. Recent studies by the authors [10–15] through computations in conjunction with the hodograph transformations were quite effective in dealing with inviscid flows influenced by gravitation. It is the intention of the present study to show the special features of the present

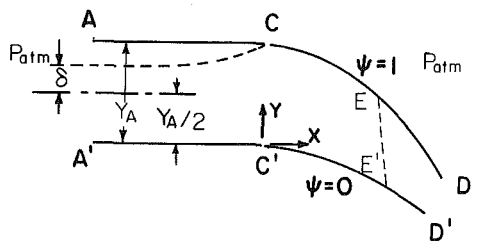


Fig. 1(*a*) The flow field in the physical plane

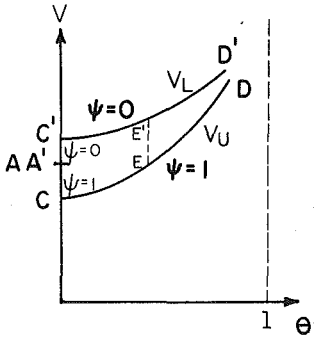


Fig. 1(*b*) The hodograph

Fig. 1 A jet discharging from a horizontal duct

[1] This work is partly based on a Ph.D Thesis by the first author [1].

[2] Present address: Senior Research Engineer, Fluid Mechanics Department, General Motors Research Laboratories, Warren, Mich. 48090.

Contributed by the Applied Mechanics Division for presentation at the 1985 joint ASME/ASCE Applied Mechanics, Fluids Engineering, and Bioengineering Conference, Albuquerque, N. Mex., June 24-26, 1985 of THE AMERICAN SOCIETY OF MECHANICAL ENGINEERS.

Discussion on this paper should be addressed to the Editorial Department, ASME, United Engineering Center, 345 East 47th Street, New York, N.Y. 10017, and will be accepted until two months after final publication of the paper itself in the JOURNAL OF APPLIED MECHANICS. Manuscript received by ASME Applied Mechanics Division, October, 1983; final revision, July 1984. Paper No. 85-APM-4.

Copies will be available until February, 1986.

Copyright © 1985 by ASME
Downloaded 02 May 2010 to 171.66.16.54. Redistribution subject to ASME license or copyright; see http://www.asme.org/terms/Terms_Use.cfm

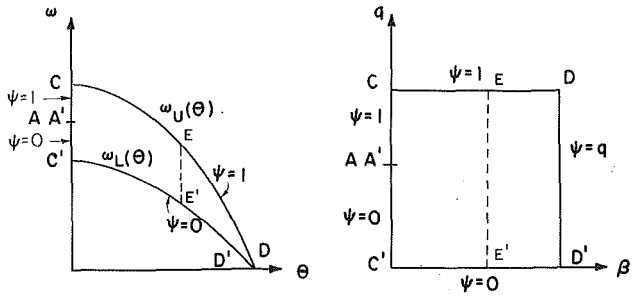


Fig. 2 Successive transformations of the hodograph (*a*) The $\omega-\theta$ plane and (*b*) the $q-\beta$ plane.

problem when it is treated from the scheme of hodograph transformation.

Theoretical Considerations

As shown in Fig. 1(*a*), an initally uniform horizontal flow of an incompressible fluid with a hydrostatic pressure distribution at a far upstream location AA' flows toward the exit CC' of the duct. The initial pressure level should be such that the lower streamline must accelerate along the wall due to a lower atmospheric pressure prevailing at the end of the duct. The top streamline must deaccelerate from the mass conservation principle. Thus, the initial pressure at the point A must be less than P_{atm}. The point of atmospheric pressure traces a curve inside the duct and its upstream asymptotic location with respect to the centerline, is labeled as δ in Fig. 1(*a*). With V_A and y_A as reference quantities for normalization of all velocities and lengths, the Bernoullis principle may be conveniently written as

$$Z=(C_{pA}+1)\frac{Fr_A^2}{2}+1=(C_p+V^2)\frac{Fr_A^2}{2}+y \tag{1}$$

with $Z=[H-P_{atm}/\gamma]/y_A$, where $C_p=p-p_{atm}/1/2\rho V_A^2$, $Fr_A=V_A/\sqrt{gy_A}$, and H is the total head which is constant everywhere. It should be mentioned that a dimensionless rate of discharge Q may be defined by

$$Q=\frac{q}{y_A\sqrt{g\ y_A}} \tag{2}$$

where q is the actual rate of discharge. When the flow completely fills the duct so that $q=V_Ay_A$, Q and Fr_A assume the same numerical value.

As the jet issues out from the conduit, it accelerates downwardly as a result of gravity. The jet becomes thinner and eventually reaches a state of infinite velocity. The corresponding hodograph is shown in Fig. 1(*b*) where the streamline angle θ has already been normalized by the asymptotic downstream flow direction $\sigma(\sigma=-\pi/2)$. It is obvious from equation (1) that for each value of Fr_A (or Q) within this regime, Cp_A must be determined from the detailed flow study before Z can be found.

The study of this problem has been performed by Garg [16] through computations in the potential-stream function plane. He had to truncate the downstream jet for keeping the region of consideration finite. Later Moayeri and Strelkoff [17] approached this problem by adopting conformal mapping and the Schwarz-Hilbert transformation. Their method required approximations to many improper integrals. As one will observe from the present approach of the problem that no approximations of any nature will be introduced to simplify the analysis. Thus, other than the possible error of numerical computation, the present approach is exact to the problem.

For a certain volumetric rate of flow Q (or Fr_A), it is obvious from equation (1) that

$$V_C=(1+Cp_A)^{1/2} \tag{3}$$

and

$$V_{C'}=\left(1+Cp_A+\frac{2}{Fr_A^2}\right)^{1/2} \tag{4}$$

The governing equation for the stream function ψ can be expressed as [18]

$$V^2\psi_{vv}+V\psi_v+\frac{\psi_{\theta\theta}}{\sigma^2}=0 \tag{5}$$

where subscripts V and θ indicate their partial derivatives. The dimensionless coordinates X-Y in the physical plane are also related through

$$dx = -\left[\frac{\cos\sigma\theta}{\sigma V^2}\psi_\theta+\frac{\sin\sigma\theta}{V}\psi_v\right]dV - \left[\frac{\sin\sigma\theta}{V}\psi_\theta-\sigma\cos(\sigma\theta)\psi_v\right]d\theta \tag{6}$$

$$dy = -\left\{\frac{\sin\sigma\theta}{\sigma V^2}\psi_\theta-\frac{\cos\sigma\theta}{V}\psi_v\right]dV + \left[\frac{\cos\sigma\theta}{V}\psi_\theta+\sigma\sin(\sigma\theta)\psi_V\right]d\theta. \tag{7}$$

It must be stressed that the hodograph boundaries V_L and V_U in Fig. 1(*b*) corresponding to the lower and upper free jet boundaries $C'D'$ and CD are not known. In fact, determination of V_U and V_L functions is part of the problem. This illustrats the unique feature of this approach in that the domain of concern is determined by the boundary functions V_U and V_L, while these functions must be in turn determined from the solution of the problem. Upon introducing the transformations of

$$q = \frac{\omega-\omega_L(\theta)}{\omega_u(\theta)-\omega_L(\theta)}$$
$$\beta = \theta \tag{8}$$

with

$$\omega=1/V, \tag{9}$$

the hodograph eventually becomes a square in the q-β plane as shown in Figs. 2(*a,b*). $\omega_U(\theta)$ and $\omega_L(\theta)$ are the corresponding unknown hodograph boundary functions of the two bounding streamlines CD and $C'D'$. Equations (5)–(7) now become

$$\psi_{qq}\left[\left(\frac{\omega_L+q(\omega_U-\omega_L)}{\omega_U-\omega_L}\right)^2+\frac{1}{\sigma^2}\left(\frac{\omega_L'+q(\omega_U'-\omega_L')}{\omega_U-\omega_L}\right)^2\right] + \psi_q\left[\frac{\omega_L+q(\omega_U-\omega_L)}{\omega_U-\omega_L}\right. + \frac{2}{\sigma^2}\frac{(\omega_U'-\omega_L')[\omega_L'+q(\omega_U'-\omega_L')]}{(\omega_U-\omega_L)^2}-\frac{1}{\sigma^2}\left.\frac{\omega_L''+q(\omega_U''-\omega_L'')}{\omega_U-\omega_L}\right] - \psi_{q\beta}\frac{2}{\sigma^2}\left[\frac{\omega_L'+q(\omega_U'-\omega_L')}{\omega_U-\omega_L}\right]+\psi_{\beta\beta}\frac{1}{\sigma^2}=0 \tag{10}$$

$$dX = (A\psi_q+B\psi_\beta)dq+(C\psi_q+D\psi_\beta)d\beta \tag{11}$$

$$dY = (E\psi_q+F\psi_\beta)dq+(G\psi_q+K\psi_\beta)d\beta \tag{12}$$

with

$$A = -\frac{\cos\sigma\beta[\omega_L'+q(\omega_U'-\omega_L')]}{\sigma}-\sin\sigma\beta[\omega_L+q(\omega_U-\omega_L)]$$

$$B = \frac{(\omega_U-\omega_L)\cos\sigma\beta}{\sigma}$$

$$C = -\frac{\cos\sigma\beta[\omega_L'+q(\omega_U'-\omega_L')]^2}{\sigma(\omega_U-\omega_L)}-\sigma\cos\sigma\beta\frac{[\omega_L+q(\omega_U-\omega_L)]^2}{\omega_U-\omega_L}$$

$$D = \frac{\cos\sigma\beta[\omega_L'+q(\omega_U'-\omega_L')]}{\sigma}-\sin\sigma\beta[\omega_L+q(\omega_U-\omega_L)] \tag{13}$$

Downloaded 02 May 2010 to 171.66.16.54. Redistribution subject to ASME license or copyright; see http://www.asme.org/terms/Terms_Use.cfm

$$E = -\frac{\sin\sigma\beta[\omega_L' + q(\omega_U' - \omega_L')]}{\sigma} + \cos\sigma\beta[\omega_L + q(\omega_U - \omega_L)]$$

$$F = \frac{\sin\sigma\beta(\omega_U - \omega_L)}{\sigma}$$

$$G = \frac{\sin\sigma\beta[\omega_L' + q(\omega_U' - \omega_L')]^2}{\sigma(\omega_U - \omega_L)} - \sigma\sin\sigma\beta\frac{[\omega_L + q(\omega_U - \omega_L)]^2}{\omega_U - \omega_L}$$

$$K = -\frac{\sin\sigma\beta[\omega_L' + q(\omega_U' - \omega_L')]}{\sigma} + \cos\sigma\beta[\omega_L + q(\omega_U - \omega_L)]$$

where ω_L', ω_L'', ω_U' and ω_U'' are, respectively, the first and second derivatives of ω_L and ω_U with respect to θ.

It should also be mentioned that for a selected Froude number Fr_A, there is only one compatible Cp_A value that yields a sensible solution within this regime. The solution to the problem thus includes the computation of the stream function ψ from equation (10), in conjunction with the determination of the free jet boundaries CD and $C'D'$ (ω_U and ω_L), and the determination of Cp_A compatible with the selected Froude number Fr_A.

Method of Calculation and Results

It has been mentioned that for a given Froude number Fr_A there is only one compatible far-upstream pressure coefficient C_{pA}. The only way to establish this correct C_{pA} value is through the trial and error procedure. For a pair of values of

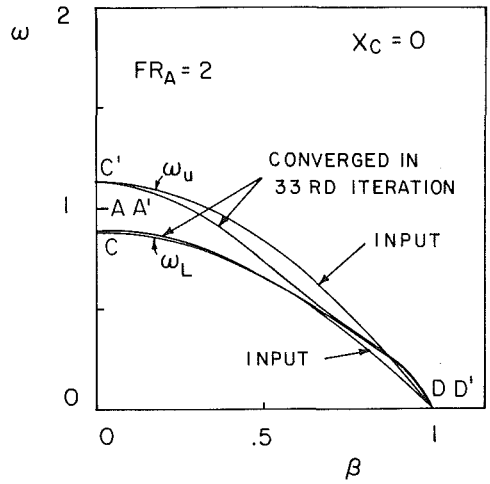


Fig. 3 A typical convergence pattern for the hodograph boundary functions

Fr_A and C_{pA}, the ω_U and ω_L functions are yet unknown, although their values at point c and c' can be determined. A sensible way to initiate computation is to approximate these functions initially by second degree polynomials. The stream function given by equation (10) can now be determined through the successive-line-overrelxation (*SLOR*) finite difference scheme in the q-β plane. It seems to be natural to sweep this plane in the β-direction with the tridiagonal matrix written for all grid points along a vertical line. A 41 × 41 mesh has been used for all calculations. The dimensionless stream function values are stabilized when the successive changes between iterations are all less than an arbitrarily small value (e.g. 10^{-4}) for all grid points in the q-β plane.

Once the stream function is stabilized, the geometric locations of the two free jet boundaries, CD and $C'D'$ can be traced from integrating equations (11) and (12) along the horizontal boundaries CD and $C'D'$ in the β-q plane in Fig. 2(*b*) with the respective initial conditions of $X_c = X_{C'} = 0$, $Y_{C'} = 0$, $Y_C = 1$. The required ψ_q is obtained from numerical differentiation of the established ψ function while both ψ_β and dq vanish along these boundaries. The established y coordinate along the jet boundaries would yield new V_U and V_L, and ω_U and ω_L functions from the Bernoulli's principle. The new V_U and V_L functions are clearly given from equation (1) by

$$V = \left[1 + C_{pA} + \frac{2}{Fr_A^2}(1 - y)\right]^{1/2} \tag{14}$$

since C_p vanishes along these jet boundaries. Calculations are repeated until the revised ω_U and ω_L functions are different only within a small margin (e.g., 10^{-3}) at every grid points from the functions upon which the calculations are based.

So far, these calculations are based on an arbitrarily chosen C_{pA} value. In general, for the incorrectly chosen C_{pA} value, a single difference between the relative x-locations of the two jet boundaries exists. For example, the x-coordinate of the point E on the upper boundary in Fig. 1(*a*) may be determined from the foregoing integration of equation (11) from the initial point C, or from C' and E' through additional integration across the hodograph from E' toward E. The two X_E values will be different if C_{pA} value is incorrectly chosen. In fact, this condition provides the criterion to determine the C_{pA} value compatible with the given Fr_A. Iteration of C_{pA} value is carried out until the disagreement in X_E values is within a small margin (e.g., 3×10^{-2}). It should be noted that points E and E' across the hodograph may be arbitrarily chosen for this C_{pA} iteration. The reason why one single difference in their relative locations betweeen the jet boundaries exists for incorrect C_{pA} value may be further discussed as follows:

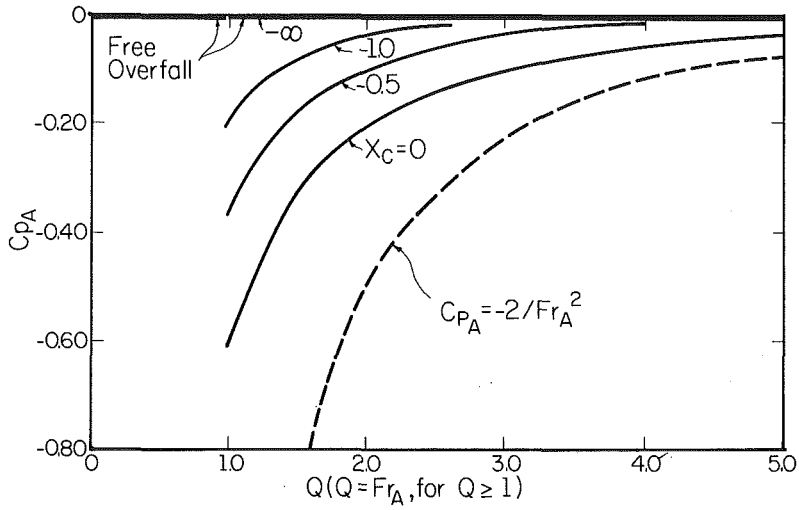


Fig. 4 Results of C_{pA} versus FR_A (or Q)

Downloaded 02 May 2010 to 171.66.16.54. Redistribution subject to ASME license or copyright; see http://www.asme.org/terms/Terms_Use.cfm

With ω_U and ω_L functions converged, it implies that the y locations of the upper and lower jet boundaries have been correctly established since they satisfy the Bernoulli's Principle. The jet boundaries are, however, established from integration with the streamline angle θ (or β) as the independent variable. Thus, at each value of θ, $\tan\theta = dy/dx$, and the correctly established y function would imply the dx is obtained correctly at each step of the integration. Thus, only one possible difference may exist in the integrated x-locations of the jet boundaries.

It is, of course, understood that for each new C_{pA} value, computations of ψ and determination of ω_U and ω_L functions must be repeated.

Results of Computations

Computations have been carried out for the range of Fr_A from unity to five for this flow regime. For any sensible solution, it is apparent from equations (3) and (4) that C_{pA} can never be smaller than negative unity, nor can it be smaller than $-2/Fr_A^2$. A typical illustration of the convergence of boundary functions, ω_U and ω_L, is shown in Fig. 3. With the allowable margin of x_E coordinate matching as 3×10^{-2}, convergence of C_{pA} is usually reached within 10–15 iterations. The final established C_{pA} results are shown in Fig. 4 (marked with $x_c = 0$). The corresponding jet boundaries are presented in Fig. 5 where results obtained by Garg are also shown for comparison purposes. A set of γ values, defined by:

$$\gamma = \frac{\delta}{y_A} = 0.5 + \frac{Fr_A^2 C_{pA}}{2} \tag{15}$$

which indicates the location of atmospheric pressure at the far-upstream section, has been obtained and is presented in Fig. 6. γ values obtained by Garg, Moayeri, and Strelkoff are also included in this figure. Since γ is very sensitive to C_{pA}, especially under large Fr_A conditions, the small differences between various results in Fig. 6 is really not significant.

It is obvious to see that these calculations can be extended to cover cases with different opening positions of the duct top wall, i.e., $X_c \neq 0$. This is equivalent to setting different constant of integration for equation (11) during tracing the top jet boundary streamline. The resulting C_{pA} values for

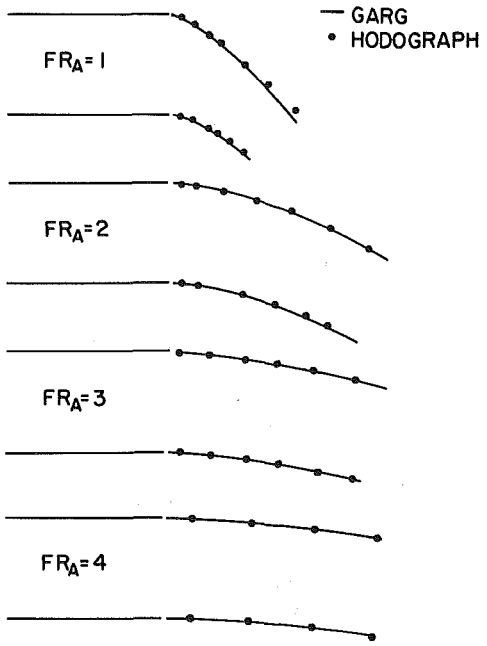


Fig. 5 Configuration of free jet boundaries

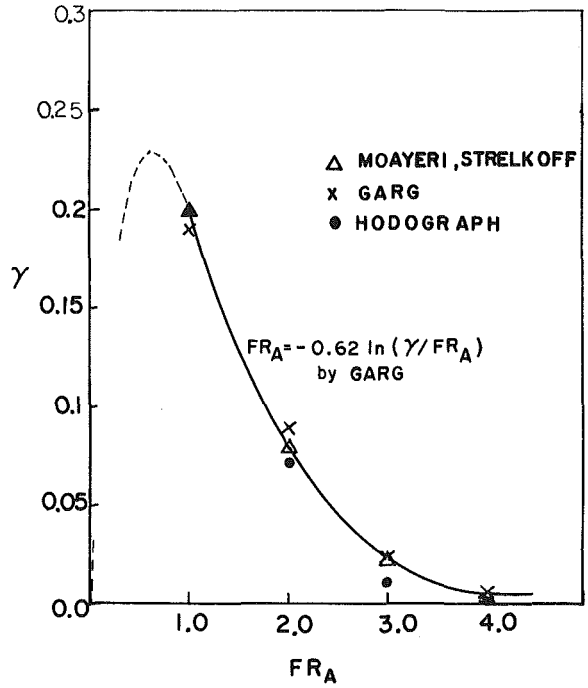


Fig. 6 Results of γ versus FR_A

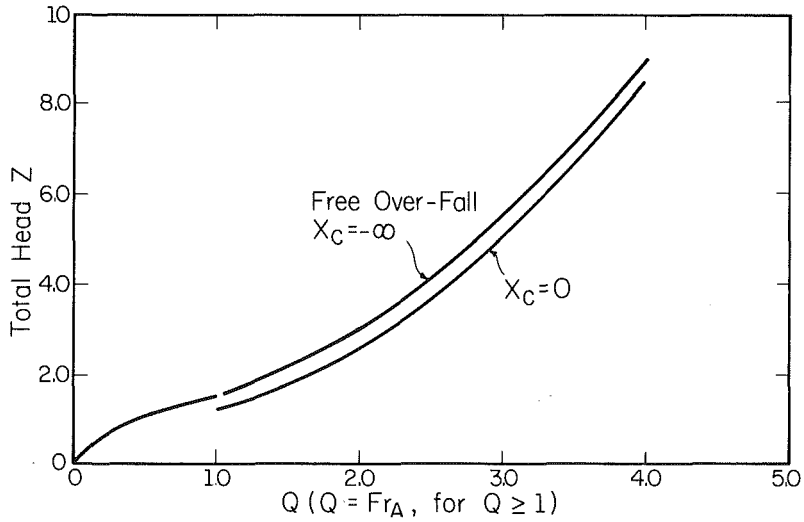


Fig. 7 The characteristic head-discharge curve of a horizontal duct

Downloaded 02 May 2010 to 171.66.16.54. Redistribution subject to ASME license or copyright; see http://www.asme.org/terms/Terms_Use.cfm

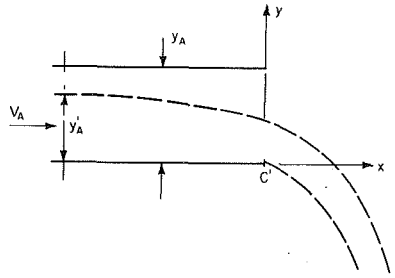


Fig. 8 Partially filled channel flow (free overfall)

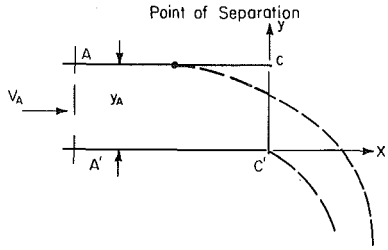


Fig. 9 Early-separation channel flow

different negative X_c positions have been obtained and are also presented in Fig. 4. When X_c approaches negative infinity, it becomes the case of a free overfall which has been studied previously [12, 19]. Vanishing C_{pA} value occurs under this situation. Although results can be obtained for positive X_c values, no attempt has been made to deal with these cases. It is believed that the viscous and surface tension effects are important under this condition.

The corresponding values of the total head Z obtained from numerical computations are presented in Fig. 7. Values of Z for a free overfall ($X_c = -\infty$) are also shown, which is given in equation (1) by

$$Z = 1 + \frac{Fr_A^2}{2} \tag{16}$$

whose values are also shown in Fig. 7 (marked by $X_c = -\infty$).

Discussion

Referring to Figs. 4 and 7 where the major characteristics of this gravitational duct discharge is presented, one naturally wonders what happens when the rate of discharge is small so that Q defined by equation (2) is less than unity. It may be observed that for sufficient small rate of flow so that the flow only partially fills the duct, as shown in Fig. 8 it becomes a free overfall with the approaching flow thickness y'_A. It is know from previous studies of inviscid flows over a free overfall [12, Appendix of 13, 19] that the approaching flow cannot be subcritical. With the approaching flow of unity Froude number, given by

$$Fr'_A = \frac{V_A}{\sqrt{qy'_A}} = 1 \tag{17}$$

it can be easily established that Q and Z are given by

$$Q = \frac{V_A y'_A}{y_A \sqrt{g y_A}} = \left(\frac{y'_A}{y_A}\right)^{3/2} \tag{18}$$

and

$$Z = \frac{3}{2}\frac{y'_A}{y_A} \tag{19}$$

for this regime. These characteristics have been plotted also in Fig. 7 for $Q \leq 1$. As the flow rate increases so that unity Q value is reached, the approaching flow Froude number is already unity. Thus, for the duct of $X_c = 0$, the flow must go through an "early separation" regime (see Fig. 9) where the flow separates from the top wall before the end the duct is reached. This regimes exists so that the discharge characteristic presented in Figs. 4 and 7 may change smoothly over from that of a free overfall to the "fully attached" results presented in this study. Although the criterion of such an inviscid flow sepration has not been established, it is certain that the point of separation is not a stagnation point (otherwise $C_{pA} = -1.0$ according to equation (1)). Thus, part of the results established in the present study in the vicinity of unity Fr_A value is to be replaced by the characteristics of the early separation flow regime. It is certainly an interesting topic of investigation to establish such characteristics so that the smooth transition between various flow regimes may be established.

Conclusion

From this series of investigations, it may be concluded that the technique of hodograph transformation is an effective scheme in dealing with potential flow problems even when the gravitational influence is predominant. It is usually recognized that the hodograph transformation is an indirect method. With the development of high speeed computers, the disadvantage of indirect method has been effectively suppressed if not completely eliminated.

References

1 Chan, P. C. T., "The Study of the Effect of Gravity on Nozzle Flows by Hodograph Transformations," Ph. D Thesis, Department of Mechanical and Industrial Engineering, University of Illinois, Urbana, Il. Oct. 1981.

2 Marchi, E., "Sue Fenomenidi Efflusso Piano da Luci a Bottente," *Ann. Mat. Pura ed Appl.*, Vol. 35, 1953, pp. 321-341.

3 Gurevich, M. I., and Pykhteev, G. N., "Approximate Solution of the Problem of Flow of a Heave Ideal Incompressible Fluid From Under a Sluice Gate," *PMTF (Akad. Nauk)*, Vol. 2, 1960, pp. 3-14.

4 Clarke, N. S., "On Two-Dimensional Inviscid Flow in a Waterfall," *J. of Fluid Mech.*, Vol. 22, Part 2, 1965, pp. 359-369.

5 Keller, J. B., and Geer, J., "Flows of Thin Streams with Free Boundaries," *J. of Fluid Mech.*, Vol. 59, Part 3, 1973, pp. 417-432.

6 Southwell, R. V., and Vaisey, G., "Relaxation Methods Applied to Engineering Problems: XII, Fludi Motion Characterized by Free Streamlines," *Philosophical Transactions of the Royal Society*, London, Series *A*., Vol. 240, 1946, pp. 117-161.

7 McNown, J. S., Hus, E. Y., and Yih, C. S., "Applications of the Relaxation Technique in Fluid Mechanics," *Transactions ASCE*, Vol. 120, 1955.

8 Varoglu, E., and Finn, W. D. L., "Variable Domain Finite Element Analysis of Free Surface Gravity Flow," *Computers and Fluids*, Vol. 6, 1977, pp. 103-114.

9 Chan, T. K., Larock, B. E., and Herrmann, L. R., "Free-Surface Ideal Fluid Flows by Finite Elements," *J. of the Hydraulics Division*, ASCE, Vol. 99, No. HY1, 1973, pp. 959; 974.

10 Liu, S. K., and Chow, W. L., "Numerical Solution for the Compressible Hodograph Equation," *AIAA J.*, Vol. 16, No. 2, 1978, pp. 188-189.

11 Chow, W. L., Han, T., and Wu, C., "Hydrodynamics Solution for Incompressible Flow as Influenced by Gravitational," *AIAA J.*, Vol. 16, No. 10, 1978, pp. 1097-1098.

12 Chow, W. L., and Han, T., "Inviscid Solution for the Problem of Free Overall," ASME JOURNAL OF APPLIED MECHANICS, Vol. 46, No. 1, 1979, pp. 1-5.

13 Han, T., "Applications of Hodograph Transformation to Hydrodynamic Problems Influenced by Gravitation," Ph.D. Thesis, 1979, Department of Mechanical and Industrial Engineering, University of Illinois at Urbana Champaign.

14 Han, T. Y., and Chow, W. L., "The Study of Sluice Gate and Sharp-Crested Weir Through Hodograph Transformation," ASME JOURNAL OF APPLIED MECHANICS, Vol. 48, June 1981, pp. 229-238.

15 Chow, W. L., and Chan, P. C., "The Effect of Gravity on Certain Curved Channel Potential Flows," ASME *Journal of Fluids Engineering*, Vol. 103, 1981, pp. 639-643.

16 Garg, S. P., "Distribution of Head at a Rectangular Conduit Outlet," *ASCE J. of the Hydraulics Division*, HY4, July 1966, pp. 11-31.

17 Moayeri, M. S., and Strelkoff, T. S., "Potential Flows at a Two-Dimensional Conduit Outlet," *ASCE J. of the Hydraulics Division*, Vol. 99, No. HY4, 1973, pp. 653-671.

18 Shapiro, A. H., *The Dynamics of Thermodynamics of Compressible Fluid Flow*, Vol. 1, The Ronald Press Co., New York, 1953, pp. 338-341.

19 Naghdi, P. M., and Rubin, M. B., "On Inviscid Flow in a Waterfall," *J. of Fluid Mech.*, Vol. 102, 1981, pp. 375-387.

Downloaded 02 May 2010 to 171.66.16.54. Redistribution subject to ASME license or copyright; see http://www.asme.org/terms/Terms_Use.cfm

C. S. Campbell[1]
Mem. ASME

C. E. Brennen
Mem. ASME

California Institute of Technology,
Pasadena, Calif. 91125

Chute Flows of Granular Material: Some Computer Simulations

A computer simulation has been developed to describe unidirectional flows of granular materials. Results are presented for a simulation of the two-dimensional flow of disks or cylinders down an inclined plane or chute. Velocity and solid fraction profiles were measured from the simulated systems and compared with theoretical analyses and are compared with the limited experimental results now available. The behavior is shown to be critically dependent on a third field quantity—the "granular temperature"—a measure of the kinetic energy contained in the random motions of the particles.

1 Introduction

In recent years there has been a significant increase of interest in the detailed mechanics of granular material and considerable progress has been made on understanding their behavior within the limiting flow regimes. The state of knowledge has been recently reviewed by Spencer [20], Mroz [13], and Savage [17]. Spencer and Mroz concentrated their review on flows with extremely low strain rates: the so-called "quasistatic" regime. Of greater relevance to the design of industrial chutes and hoppers are the high strain-rate flows in the "rapid flow" or "grain inertia" regime reviewed by Savage [17]. This latter regime encompasses any flow in which the particle interactions can be modeled as instantaneous collisions. All of these regimes are defined for flows in which the interstitial fluid plays a negligible role in determining the rheology.

Research on granular material flows has been severely hampered by the lack of reliable, nonintrusive instrumentation to measure precisely the velocity, solid fraction, and random particle motion within such flows. An alternative approach is to utilize the kind of computer simulations that have been quite successful in the analogous problems in molecular gas dynamics (e.g., [3, 23]).

The purpose of the present paper is to present results from computer simulations of the flow of dry granular material down inclined chutes or channels and to compare the results of these calculations with existing experimental measurements and theoretical models. The utility of such computer simulations is twofold. First, they provide insights and detailed results that can be used to suggest appropriate assumptions for the theoretical models and to validate existing models. At the present time this is best accomplished using simple shear, or Couette flows. Simulations of such flows by the present methods are reported in other papers (Campbell [4], Campbell and Brennen [5]) where the variation of velocity distributions (deviations from Maxwellian distributions at higher solid fractions), collision angle distributions, and other statistical information is provided.

A second objective of the computer simulations is to compare the results with experimental measurements to establish appropriate models of the mechanics of particle/particle and particle/wall interactions. Much of the existing measurements of the kind on shear flows come from experiments on granular material flow down inclined (or vertical) channels or "chutes" (see references of Section 5). Thus the objective of this paper is to briefly report on some comparisons between the results of computer simulation and the existing data for flows down inclined chutes. Further details can be found in Campbell [4].

Parenthetically one might add that a third use of computer simulations might be to explore the effects of additional forces such as those due to the interstitial fluid and electrostatic effects. For simplicity, such effects are not included at the present state of the development of the simulation. Discussion of interstitial fluid effects can be found in other recent works (Savage [17]).

Other computer models of granular material flows include the work Cundall [6], Davis and Deresiewicz [8], Cundall and Strack [7], Trollope and Berman [21], and Walton [22]. Most of these are directed toward the simulation of slower flows and smaller deformations. However, in his original work Cundall [6] did extend his methods to some higher speed but transient flows such as rockfalls and the emptying of a hopper. Also the versatility of Walton's [22] computer program is readily apparent from the excellent movies that the Lawrence Livermore Laboratory has produced. However, to our knowledge, none of the existing models have been used to produce continuous "steady" flows which could be used for basic rheological studies. The intent of the present model is to

[1] Presently, Assistant Professor of Mechanical Engineering, University of Southern California, Los Angeles, Calif. 90089-1453.

Contributed by the Applied Mechanics Division for publication in the JOURNAL OF APPLIED MECHANICS.

Dicussion on this paper should be addressed to the Editorial Department, ASME, United Engineering Center, 345 East 47th Street, New York, N.Y. 10017, and will be accepted until two months after final publication of the paper itself in the JOURNAL OF APPLIED MECHANICS. Manuscript received by ASME Applied Mechanics Division, April, 1983; final revision, May, 1983.

Copyright © 1985 by ASME
Downloaded 02 May 2010 to 171.66.16.54. Redistribution subject to ASME license or copyright; see http://www.asme.org/terms/Terms_Use.cfm

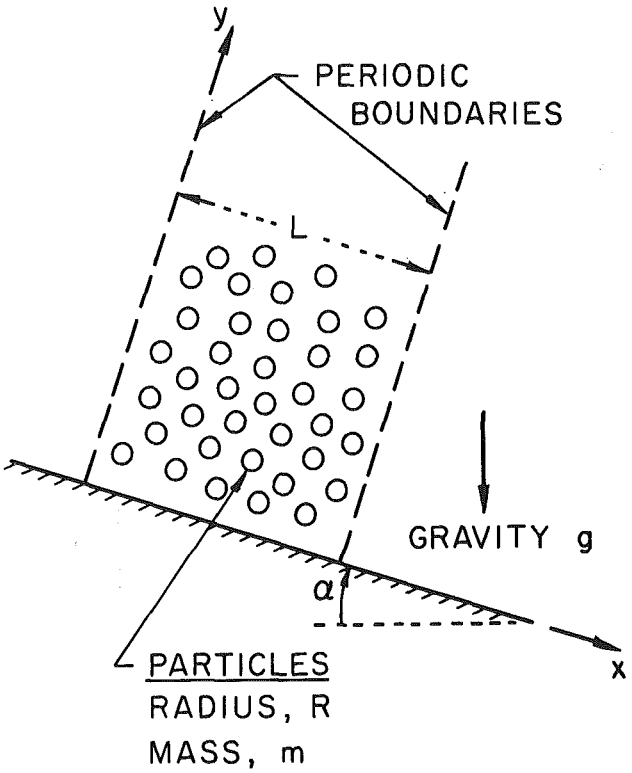


Fig. 1 Schematic of chute flow simulation

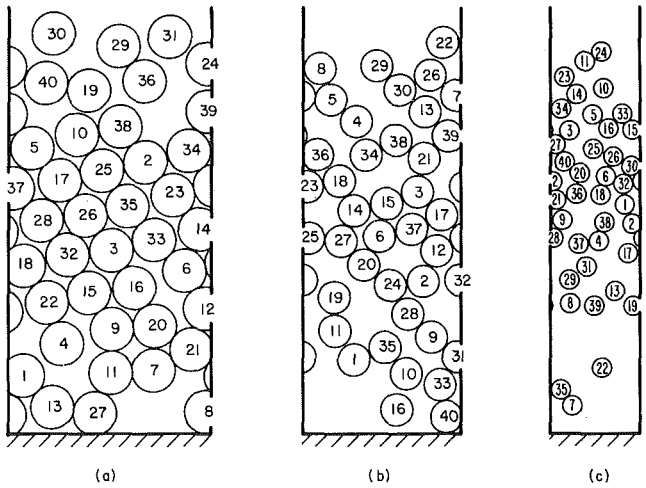


Fig. 2 Typical snapshots from the chute flow simulations for inclinations of (a) $\alpha = 20$ deg, (b) $\alpha = 30$ deg, and (c) $\alpha = 40$ deg

minimize the complexity of the geometry and the interactions so that steady flows of sufficiently long duration for rheological analysis would be produced. Thus the simulations are just two-dimensional and the particles are circular cylinders. Though extension of the simulation to the third dimension is possible, the necessary computer costs would be considerably greater.

2 Computer Simulation

The present method for the computer simulation of granular material flows has been documented elsewhere (Campbell [4], Campbell and Brennen [5]) and will only briefly be described in the present paper. Two-dimensional unidirectional flows of inelastic circular cylinders are followed mechanistically. Though both Couette flows and chute flows have been examined, the present paper is confined to discussion of the simulations of chute flow.

The simulation is initiated by placing a number of cylindrical particles in a control volume bounded by the chute bottom and two perpendicular "periodic" boundaries (see Fig. 1). A particle passing out of the control volume through one of the periodic boundaries immediately reenters the control volume through the other periodic boundary at the same relative height above the chute bottom and with the same instantaneous velocity. This greatly increases the computational efficiency of the simulation by restricting the number of particles to that originally placed in the control volume, but has the side effect of eliminating all gradients in the flow direction (x direction, Fig. 1). The number of particles originally placed in the control volume will also determine the eventual depth of the flow. The separation, L, between the periodic boundaries was adjusted until further doubling of this length (as well as the number of particles) had little effect on the results. For the flows described here values of L/R (R is the particle radius) of about 10 were found to be sufficient for this purpose (see Fig. 2).

All simulations were begun with a randomly perturbed square lattice array of particles in the control volume and randomly chosen instantaneous translation velocities (u, v, in the x, y directions of Fig. 1) and rotational velocity (ω). Consequently, it is convenient to refer to simulations by the dimensions of this initial array; for example, 10 × 4 is a simulation started with 10 rows of 4 particles.

The intent is to mechanistically follow the entire assemblage of particles, under the action of gravity (g), as it proceeds from collision to collision, until a final asymptotic state is reached in which the flow is steady in the sense of being invariant over long time scales. Details of the convergence toward such a state are described in Campbell [4] and will not be repeated here. The results presented here were run for as long as 200,000 collisions. Though the Couette flows described elsewhere required as little as 20,000 collisions for convergence of a typical 10 × 4 simulation, the present chute flows required considerably longer. Furthermore determination of convergence was clouded by the fact that most of the simulations exhibit the continuous fluctuations typical of small thermodynamic systems (Landau and Lifshitz [12]); this considerably increased the duration of "steady flow" necessary to perform meaningful evaluation of the flow properties.

In summary, it is believed that the simulations with chute inclinations of 30 deg are well converged. However, those at $\alpha = 20$ deg and $\alpha = 40$ deg may still have contained some small deceleration and acceleration, respectively, at the conclusion of the simulations.

Each individual particle/particle or particle wall collision is assumed to be instantaneous and the resulting departure velocities calculated by conventional means. The two closure conditions used were as follows. First the relative approach and departure velocity components parallel to the line of centers are related by a coefficient of restitution to represent the inelasticity of the collisions. Different coefficients (denoted respectively, by ϵ_p and ϵ_w) can be used for particle/particle and particle/wall collisions. Values of 0.6 and 0.8 were deemed appropriate as a result of experiments with typical polystyrene beeds and aluminum walls and most of the simulations used these values. Secondly, it is necessary to establish a frictional closure condition pertaining to the relative tangential velocities upon departure. Most of the simulations described in this paper employ a condition requiring zero relative tangential velocity of the contact points upon depature from a collision (Type A condition). In a real collision of finite duration, such closure condition would pertain provided the friction between the contact points was sufficient for relative tangential motion to cease at some time

Downloaded 02 May 2010 to 171.66.16.54. Redistribution subject to ASME license or copyright; see http://www.asme.org/terms/Terms_Use.cfm

prior to departure. This is a reasonable approximation for particle/particle collisions as the relative tangential velocities at impact are generally small. However, for particle/wall collisions, the relative tangential velocities may be large and the Type A collisions may result in too much momentum transfer into particle rotation. (This rough particle condition should not be confused with the artificial closure condition used for rough molecule models of gases). A few simulations were also performed using a more artificial closure condition for particle/wall collisions. This Type B condition involved setting the relative tangential velocity of the *center* of the particle to zero upon depature while leaving the rotational speed unchanged from its incident value. The motivation for this alternative is found in the results; the Type A condition yielded slip at the wall and an alternative was sought that would yield no-slip. Many other choices of wall boundary condition are possible. At the very least, these two rather arbitrary alternatives demonstrate the sensitivity of the solution to the choice of particle/wall closure condition (see Section 6).

3 Presentation of Results

All flow properties were obtained as functions of distance, y, from the chute bottom by dividing the control volume into strips and computing the particle-weighted mean of the property in each strip (Campbell [4]) over a substantial length of time (up to 20,000 collisions). The periodic boundary conditions assure that there will be no change of mean properties in the x direction. The mean velocity, $\langle u \rangle$, and mean solid fraction, ν, were obtained in this way. Data is also presented for the "translational temperature" defined as the kinetic energy (divided by $\nu\rho_p/2$) associated with the random motions of the particles. The latter is obtained by subtracting the kinetic energy of the mean shear flow from the total instantaneous kinetic energy. Specifically the nondimensional translational temperature is defined as $(\langle u^2 \rangle + \langle v^2 \rangle - \langle u \rangle^2 - \langle v \rangle^2)/gR$, and is denoted in the figures as $(\langle u'^2 \rangle + \langle v'^2 \rangle)/gR$. This quantity is of particular interest from a rheological point of view (Savage [17]) because it is presently believed that the ratio of the typical velocity difference due to shear, $2Rd\langle u \rangle/dy$, to the typical random translation velocity, $(\langle u'^2 \rangle + \langle v'^2 \rangle)^{1/2}$ plays a central role in determining the constitutive behavior of the flowing granular media (Savage [19], Jenkins and Savage [10], Savage and Jeffrey [18]). The results presented here are all nondimensionalized using the intrinsic scales for length, R, for velocity, $(gR)^{1/2}$, and for mass, m (mass of a particle). It should also be noted that the only nongeometric parameters inputed to the simulation are the coefficients of restitution, ϵ_p and ϵ_w, and the ratio, β, of the square of the radius of gyration of the particles to the square of their radius. All the present simulations were run with $\beta = 1/2$ the value appropriate to cylinders.

4 Results of the Chute Flow Simulations

Three typical instantaneous snapshots of the arrangement of particles in the control volume are presented in Fig. 2 for flows at $\alpha = 20$, 30, and 40 deg, respectively. Note in particular that as the angle and therefore the velocity and shear rate of the flow is increased, the bulk of the flow appears to ride on a lower solid fraction layer of highly agitated particles.

Typical velocity, solid fraction, and temperature profiles for simulations with the Type A wall condition are presented in Fig. 3. The velocity profile has the same shape one would expect with a liquid except for a slip velocity at the wall amounting to about 50 percent of the maximum velocity. The solid fraction profile attains its maximum value in the center

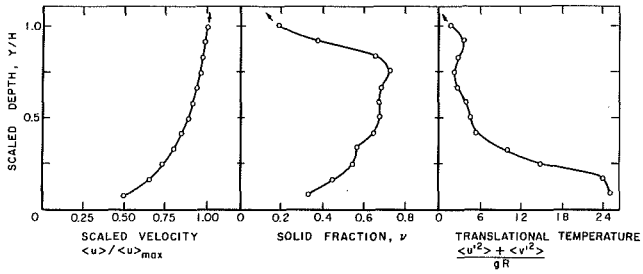


Fig. 3 Typical velocity, solid fraction, and translational temperature profiles for a 10 × 4 Type A simulation with $\alpha = 30$ deg, $\epsilon_p = 0.6$, $\epsilon_w = 0.8$

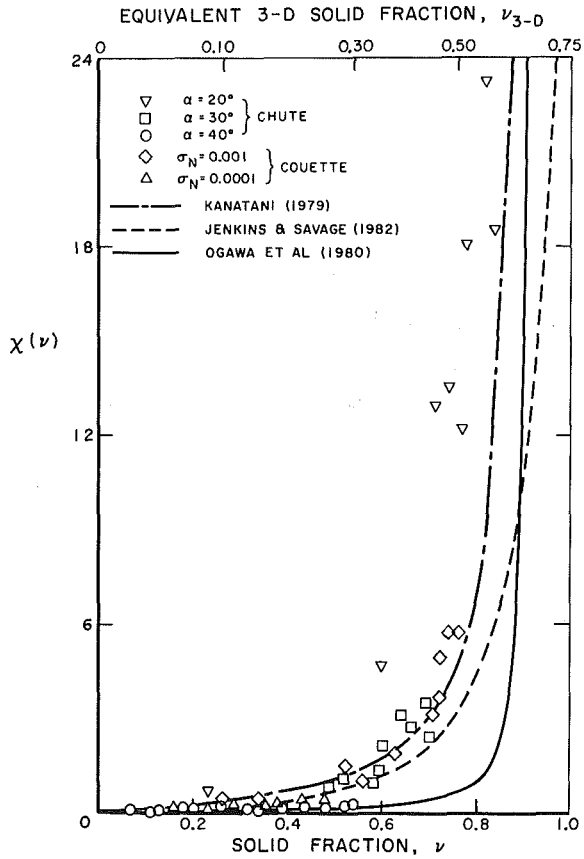


Fig. 4 Solid fraction dependence of the equation of state

of the flow and exhibits a region of reduced density next to the solid bottom and a "saltated" region of lower density on the upper surface.

The random kinetic energy of the particles, or temperature, is a by-product of the collisions between particles. Its magnitude depends on the magnitude of the relative velocity of the particles at collision, which will in turn be related to the local shear rate. (See Campbell [4], Campbell and Brennen [5].) Thus the largest temperature is found in the high shear zone next to the wall.

One might speculate that the low density region near the wall is a result of the high temperature in that region despite the overburden of the material. This suggests the existence of an "equation of state." Equations of state have been proposed by Jenkins and Savage [10], Ogawa et al. [15], and Kanatani [11]. All these have general form:

$$P = \chi(\nu)(\langle u'^2 \rangle + \langle v'^2 \rangle) \tag{1}$$

where $\chi(n)$ is a nonlinear function crudely similar in motivation to the high-density correction factor of the Van-

Downloaded 02 May 2010 to 171.66.16.54. Redistribution subject to ASME license or copyright; see http://www.asme.org/terms/Terms_Use.cfm

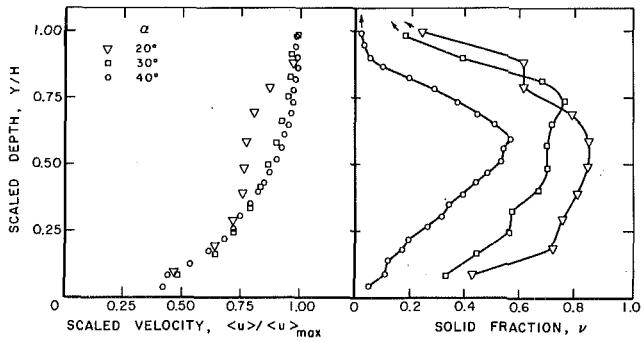


Fig. 5 Velocity and solid fraction profiles for different chute inclinations (α = 20, 30, and 40 deg) for Type *A* simulations (10 × 4) with ϵ_p = 0.6, and ϵ_w = 0.8

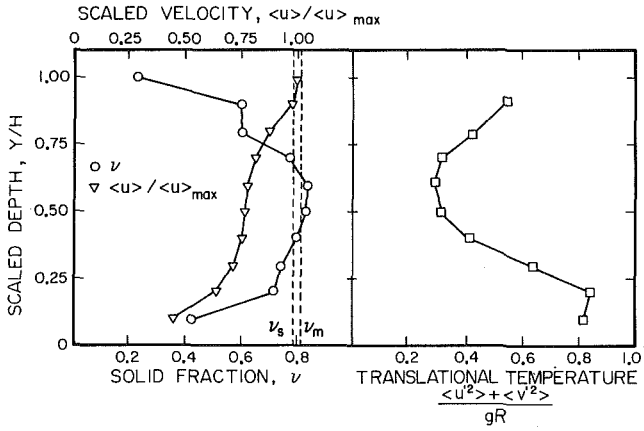


Fig. 6 Velocity, solid fraction, and translational temperature profiles for the α = 20 deg Type *A* simulation (10 × 4, ϵ_p = 0.6, ϵ_w = 0.8) showing plug flow region

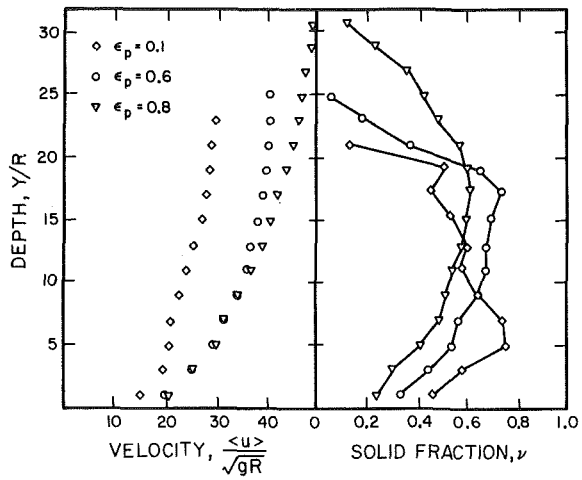


Fig. 7 Effect of particle/particle coefficient of restitution, ϵ_p on velocity and solid fraction profiles from Type *A* simulation (α = 30 deg, 10 × 4 simulation, ϵ_w = 0.8)

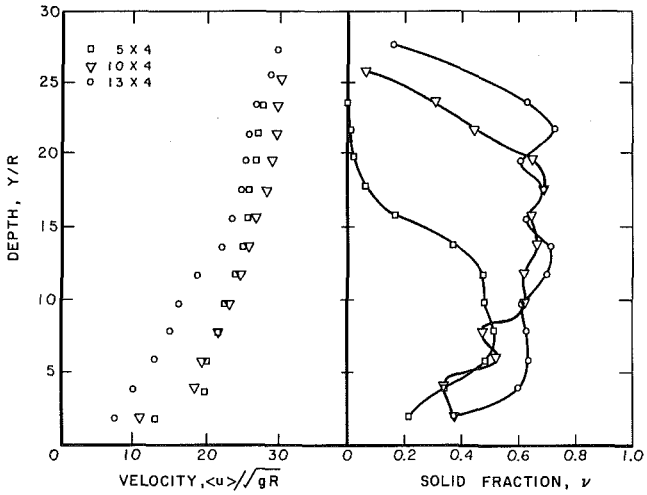


Fig. 8 Effect of flow depth on the velocity and solid fraction profiles of the α = 30 deg Type *A* simulation

der-Waal's equation of state. Values of $\chi(\nu)$, taken from the simulation by assuming p to the local static pressure due to the overburden are plotted in Fig. 4, and compared with the predictions of [10, 11, 14]. Some data from the simulations of Couette flows [4, 5] is also included in the figure. Note that the simulation yields values of χ that appear to asymptote to infinity near ν = 0.91, a value that corresponds to the maximum possible packing of disks. It also agrees qualitatively with the theories of Jenkins and Savage [10] and Kanatani [11] though the comparison is clouded by the fact that the asymptote in [10] occurs at ν = 1 whereas both Kanatani [11] and Ogawa [14] leave this asymptote unspecified; ν = 0.91 is used in plotting data from both these theories.

Velocity and solid fraction profiles for Type *A* simulations at chute inclination angles of 20, 30, and 40 deg are shown in Fig. 5. Note that the maximum solid fraction decreases as a function of inclination angle due to the generally higher temperatures generated by larger velocities.

Note also that the velocity profile for α = 20 deg deviates from that for α = 30 or 40 deg. This is due to the existence of a nonshearing plug in the center of the dense, slow moving flow, a phenomenon that did not occur at higher inclination angles. The data for α = 20 deg is repeated in Fig. 6 to further document this interesting example of the coexistence of a high-density unshearing plug and a lower-density shearing flow. Also indicated in Fig. 6 is the square packing solid fraction, ν_s, and the maximum solid fraction that permits the shearing of cylinders, ν_m (Campbell [4]). The solid fraction exceeds both these values in a central part of the flow and therefore the shear rate, $d\langle u\rangle/dy$ must be zero at least when $\nu > \nu_m$. However, the granular temperature of this plug is not zero. But in the absence of shear this temperature cannot be internally generated. Hence the temperature profile of Fig. 6 implies the conduction of fluctuating kinetic energy into the plug from the sheared regions both on top of and below the plug and the subsequent dissipation of this fluctuating kinetic energy by collisions within the matrix of the plug.

The typical data for different particle/particle coefficients of restitution, ϵ_p, is shown in Fig. 7. Lower values of ϵ_p tend to cause blunter, more plug-like velocity profiles with higher values of the solid fraction. The three simulations in Fig. 7 all have the same number of particles in identical control volumes (10 × 4 simulations). Consequently, the higher the value of ϵ_p, the more dilated and deeper the flow. Other simulations with different values of the particle/wall coefficient of restitution (ϵ_w) showed that this parameter had only a minor effect on the flow (Campbell [4]).

The effect of the flow depth is demonstrated in Fig. 8 using simulations with initial square lattice arrangements of 5 × 4, 10 × 4, and 13 × 4 particles and control volumes of the same width. The velocity variations across the depth tend to increase with increasing depth. Also the maximum solid fraction seems to approach a limiting value, which is first attained here in the 10 × 4 simulation; further increase in depth leads to an increase in the extent of this central region

Downloaded 02 May 2010 to 171.66.16.54. Redistribution subject to ASME license or copyright; see http://www.asme.org/terms/Terms_Use.cfm

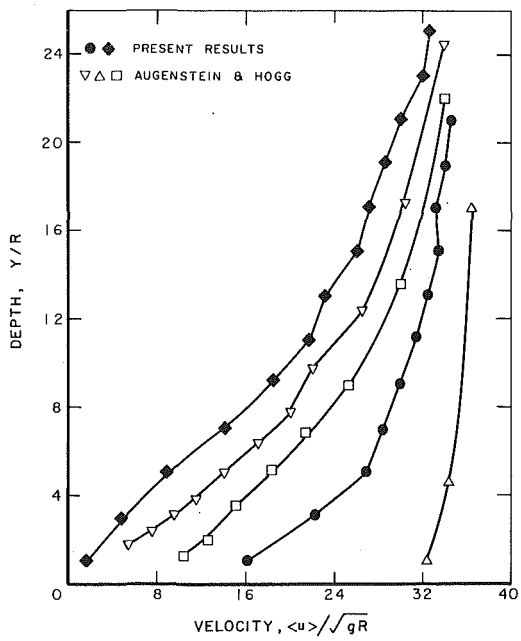


Fig. 9 Comparison of the velocity profiles from Type *A* (•) and Type *B* simulations (♦) with α = 40 deg, ϵ_p = 0.6, and ϵ_w = 0.8 (5 × 4 simulation) with profiles measured by Augenstein and Hogg [1]: Δ, 35 × 48 mesh sand on smooth stainless steel surface; □, 28 × 35 mesh sand on roughened with 65 × 100 mesh sand; and ▽, 35 × 48 mesh sand on surface roughened with 35 × 48 mesh sand

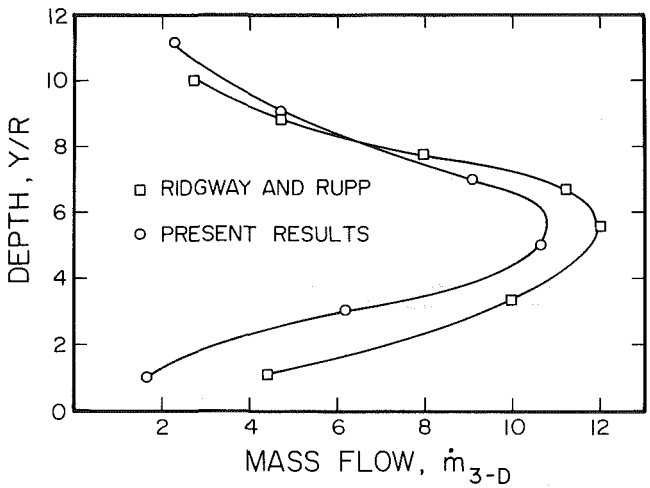


Fig. 10 Comparison of one of the mass flow rate ($\nu_{3D}\langle u\rangle/(gR)^{1/2}$) profiles of Ridgway and Rupp [15] with Type *A* simulation of the same flow (α = 40 deg, 4 × 4 simulation)

of roughly uniform solid fraction. Similar behavior was observed experimentally by Ridgway and Rupp [15].

The Type *A* wall condition, used for all of the preceding results, yielded substantial slip at the wall in accord with the experimental observations for smooth walls (see Section 5). Therefore a few simulations were subsequently performed with the rather artificial Type *B* wall condition since it had been found to yield no-slip (Campbell and Brennen [5]) and such simulations would allow comparison with the experimental results for roughened walls. The results of one such simulation (α = 30 deg, ϵ_p = 0.6, ϵ_w = 0.8) are presented in Fig. 11. The effect of the change in boundary condition is substantial. Not only does the velocity profile exhibit no slip, but the low solid fraction region next to the wall has disappeared. Also the behavior of the translational temperature close to the wall is rather peculiar; it is low in the first layer of particles due to the no-slip condition but high in the next layer of particles as the high rate of shear of the first layer generates increased translational temperature.

5 Comparison With Experiment

Although the experimental data is limited because of the lack of well-proven instrumentation capable of making local measurements of both solid fraction and velocity, it is valuable to compare the simulation results with the available data. Augenstein and Hogg [1], Bailard [2], Ishida and Shirai [9], Savage [16], and Ridgway and Rupp [15] have all attempted to measure the variation of flow properties with depth in chute flows at different inclination angles.

The form of the velocity profiles obtained from the present simulations are in qualitative agreement with those measured by Augenstein and Hogg [1] and Bailard [2] for both smooth and rough beds, but not with those measured by Savage [16] or Ishida and Shirai [9], who studied rough beds only. The latter measurements contain inflexion points in the profile several particle diameters from the wall, which are not present in the simulations or the other experimental data. The reason for this discrepancy is not clear at present, although Savage [17] suggests that they may represent at least two different types of flow.

A comparison between the velocity profiles of Augenstein and Hogg [1] and those from both Type *A* and Type *B* simulations of flows of similar depth is presented in Fig. 9. These α = 40 deg simulations used ϵ_p = 0.6, ϵ_w = 0.8, values that seemed roughly appropriate for the materials used in the experiments. Augenstein and Hogg performed experiments with various sizes of particles glued to the chute bottom. When the glued particles were the same size as those of the flow the velocity profile exhibited zero slip at the wall. On the other hand, for glued particles smaller than those of the flow a slip increased toward that measured for a smooth surface. Both the magnitude and shape of the simulation velocity profiles agree with the experiments. The Type *A* wall condition yields a profile that appears to correspond to a slightly roughened surface. On the other hand, the Type *B* wall condition yields a profile that corresponds to a fully rough surface. It is clear that the frictional boundary condition in the simulation could be modified so as to produce a family of profiles similar to those of Augenstein and Hogg. Experimental solid fraction profiles for the flow of various sands have been obtained by Bailard [2]. These agree qualitatively with the solid fraction profiles of the simulations. Specifically, Bailard's solid fraction profiles exhibit a layer of reduced ν near the chute bottom and a saltated layer of smaller ν on top of the flow.

Ridgway and Rupp [15] also present solid fraction profiles. However, their profiles are derived from mass flow rate profiles assuming uniform velocity, an assumption that can now be seen to be inappropriate. Consequently, we have reconstructed their mass flow-rate profiles for comparison with the simulation results. But it is also clear that the present two-dimensional flows of cylinders will exhibit higher solid fraction values than a flow of three-dimensional particles. One way of establishing an effective equivalent three-dimensional solid fraction (ν_{3D}) corresponding to a particular simulation value, ν, is to base it on similar interparticle spacing so that $\nu_{3D} = 4/3\ (\nu^3/\pi)^{1/2}$. One example of the corresponding effective three-dimensional mass flow-rate profile was calculated from a simulation of one of the 40 deg chute flows investigated by Ridgway and Rupp [15] and is presented in Fig. 10. The nondimensional mass flow rate, m_{3D} is defined as $\nu_{3D}\langle u\rangle/(gR)^{1/2}$. The agreement in Fig. 10 is as good as could be expected.

Downloaded 02 May 2010 to 171.66.16.54. Redistribution subject to ASME license or copyright; see http://www.asme.org/terms/Terms_Use.cfm

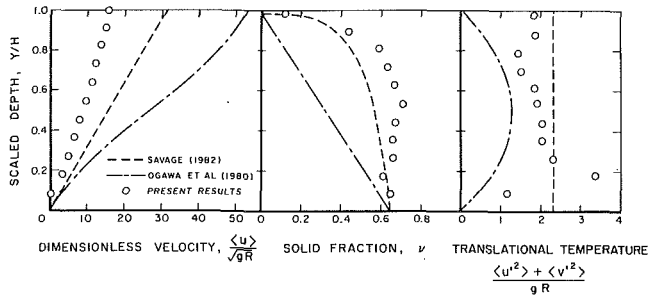


Fig. 11 Comparison of the profiles for a Type *B* simulation (α = 30 deg, ϵ_p = 0.6, ϵ_w = 0.8) with the theoretical results of Savage (1982) and Ogawa et al. (1980)

6 Comparison With Theoretical Profiles

Syntheses of granular material chute flows have been performed by Savage [19] and Ogawa et al. [14]. Both theories represent a significant advance because they attempt to account for temperature. The theory of Ogawa et al. [14] must be considered incomplete as they assumed a linear variation of the solid fraction profile. Both theories require a boundary condition on the mean velocity so a condition of no slip at the wall is applied. Consequently, we will compare their results with those of Type *B* simulation. However, since the theories are three-dimensional, it is necessary to adjust the solid fraction in the same manner as described for Fig. 10; the abscissas of Fig. 11 are therefore $\pi^{1/3}(3\nu_{3D}/4)^{1/3}$. Furthermore, to convert the translational temperature equipartition of energy is assumed so that the temperature abscissas of Fig. 11 are two-thirds the values of the theories. With these crude adjustments the resulting comparison of the simulation and the theoretical models can only be considered qualitative.

The most obvious discrepancy occurs in the velocities. The theories both yielded velocities more than twice the simulation velocities over the bulk of the flow. In this fundamental respect, the simulation results are much closer to the experimental values. The theories yield almost uniform shear rate whereas the shear rate declines with distance from the wall in the simulation. Despite the discrepancy in velocities, Savage's theory is remarkably successful in predicting both the solid fraction profile and the almost uniform temperature. The theory of Ogawa et al. is less successful in both respects.

Surprisingly, the low-density/high-shear rate zone that appears near the wall in the Type *A* simulations are absent from the Type *B* simulation, indicating that the behavior of the flow near solid boundaries is strongly influenced by the wall boundary condition. Heuristically, this effect may be attributed to the large rotational impulse that is applied to a particle on collision with a Type *A* wall. (The average rotation rate, $\langle\omega\rangle$, near the wall of a Type *A* flow is roughly one-half of the slip velocity. In a Type *B* flow, as a particle's rotation is unaffected by collisions with the wall, the average rotation rate $\langle\omega\rangle$ is about one-half of the local shear rate, $d\langle u\rangle/dy$, and consequently, much smaller than found in Type *A* flows.) On subsequent collisions with other particles, the rotational motion will be, in part, transferred to random linear motion causing a rise in the local temperature and a decrease in the local solid fraction. (It should be noted that the experiments of Ridgway and Rupp [15] showed similar behavior for angular sands that would resist rolling on collision with a flat surface.) The choice of appropriate wall boundary conditions for future simulations and theoretical anlayses of granular flow, must be made with great care.

Conclusions

The two-dimensional simulation of the flows of granular materials down inclined chutes described in this paper produce results that agree well with existing experimental data. Both the magnitudes and the profiles of the velocity and the solid fraction agree qualitatively with those of Augenstein and Hogg [1] and Ridgway and Rupp [15].

The simulations using the Type *A* or "smooth" wall boundary condition exhibit a velocity profile with substantial slip at the wall and a solid fraction profile with a layer of lower density next to the wall where the particles have the greatest random motion or temperature. Parenthetically it might also be remarked that the "fluidizing" effect of the low-density layer of highly agitated particles may provide an alternative explanation of certain landslide and avalanche behavior. Such a layer did not occur with a few simulations incorporating a different wall boundary condition (Type *B*) intended to simulate a rough wall by eliminating the slip. The differences generated by this change in the boundary condition emphasize the uncertainty in the detailed mechanics of the particle/wall interactions and the care that must be taken to treat this properly in any theoretical model.

The general consistency with experiment does confirm the validity of the simulations. Consequently, the model can be used to assess flow properties such as the granular temperature, which has been shown to be related to the solid fraction and pressure through an equation of state. It can also be used to provide statistical information on the particle/particle and particle/wall collisions, which is important in improving a basic understanding of granular media flows. (The comparison of the results of the two-dimensional model with actual three-dimensional flows is somewhat questionable. Certain quantities, like the solid fraction, ν, have different interpretations in two and three-dimensions. Also, Evan's [24] recent study showed that two-dimensional fluids do not possess the same transport properties as their three-dimensional counterparts.)

Several phenomena observed in the simulation emphasize the need for further understanding of the production and conduction of granular temperature. Particularly at higher inclination angles the chute flow appears to ride on a less dense layer of highly agitated particles. Artificial vibration of the wall would probably enhance this effect and generate faster flows. (In fact this is a common method of increasing the flow rate from hoppers.)

On the other end of the spectrum, the simulations of the slower flows at α = 20 deg demonstrate how an unshearable plug can develop in the center of the flow. Sufficient internal dissipation must occur within this plug so that the granular heat conducted in from the surrounding shearing flow does not result in a plug temperature sufficient to cause dilation to shearable solid fractions. These observations emphasize the need for the development of a production/dissipation equation for granular temperature similar to that used by Savage [19] and Ogawa et al. [14] as well as the coupling of the temperature to the density, via an equation of state.

Acknowledgments

Professor Rolf Sabersky provided encouragement and guidance throughout the conduct of this research. The authors are deeply appreciative of this and of the support provided by the National Science Foundation (Grant CME 79-15132). Additional support was provided by Union Carbide Corporation and Chevron Oil Field Research.

References

1 Augenstein, D. A., and Hogg, R., "An Experimental Study of the Flow of Dry Powders on Inclined Surfaces," *Powder Technology*, Vol. 19, 1978, p. 205.

2 Bailard, J., "An Experimental Study of Granular-Fluid Flow," Ph.D. thesis, University of California, San Diego, 1978.

3 Barker, J. A., and Henderson, D., "What is Liquid? Understanding the States of Matter," *Reviews Mod. Phys.*, Vol. 48, 1976, p. 587.

Downloaded 02 May 2010 to 171.66.16.54. Redistribution subject to ASME license or copyright; see http://www.asme.org/terms/Terms_Use.cfm

4 Campbell, C. S., "Shear Flows of Granular Materials," Ph.D. thesis and Report No. E-200.7, Division of Engineering and Applied Science, California Institute of Technology, Pasadena, 1982.

5 Campbell, C. S., and Brennen, C. E., "Computer Simulation of Shear Flows of Granular Materials," *Proc. 2nd U.S. Japan Seminar on New Models and Constitutive Relations in the Mechanics of Granular Materials*, Aug. 1982, Elsevier.

6 Cundall, P. A., "A Computer Model for Rock Mass Behavior Using Interactive Graphics for Input and Output of Geometrical Data," U.S. Army corps of Engineers (Missouri River Division) Tech. Rep. MRD-2074, 1974.

7 Cundall, P. A., and Strack, O. D. L., " A Discrete Numerical Model for Granular Assemblies," *Geotechnique*, Vol. 29, 1979, pp. 47-65.

8 Davis, R. A., and Deresiewicz, H., "A Discrete Probabilistic Model for the Mechanical Response of a Granular Medium," *Acta Mech.*, Vol. 26, 1977, pp. 69-89.

9 Ishida, M., and Shira, T., "Velocity Distributions in the Flow of Solid Particles in an Inclined Open Channel," *J. Chem. Eng. of Japan*, Vol. 12, 1979, pp. 46-50.

10 Jenkins, J. T., and Savage, S. B., "A Theory for the Rapid Flow of Identical, Smooth Nearly Elastic Spheres," *J. Fluid Mech.*, Vol. 130, 1983, pp. 187-202.

11 Kanatani, K., "A Micropolar Continuum Theory for the Flow of Granular Materials," *Int. J. Eng. Sci.*, Vol. 17, 1979, p. 419.

12 Landau, L., and Lifshitz, E. M., *Statistical Physics*, Pergamon Press, 1958.

13 Mroz, A., "On Hypoelasticity and Plasticity Approaches to Constitutive Modeling of Inelastic Behavior of Soils," *Int. J. Num. and Anal. Meth. in Geomech.*, Vol. 4, 1980, pp. 45-55.

14 Ogawa, S., Umemura, A., and Oshima, N., "On the Equations of Fully Fluidized Granular Materials," *Zamp*, Vol. 31, 1980, p. 483.

15 Ridgway, K., and Rupp, R., "Flow of Granular Materials Down Chutes," *Chem. Proc. Eng.*, Vol. 51, 1970, p. 82.

16 Savage, S. B., "Gravity Flow at Cohesionless Granular Materials in Chutes and Channels," *J. Fluid Mech.*, Vol. 92, 1979, pp. 53-96.

17 Savage, S. B., "The Mechanics of Rapid Granular Flows," in *Advances in Applied Mechanics*, Vol. 24, Hutchinson, J., and Wu, T. Y., eds., Academic Press, New York, 1984 (in press).

18 Savage, S. B., and Jeffrey, D. J., "The Stress Tensor in Granular Flows at High Shear Rates,"' *J. Fluid Mech.*, Vol. 110, 1981, pp. 255-272.

19 Savage, S. B., "Granular Flows at High Shear Rates," *Proc. of Advanced Seminar on Dispersed Multiphase Flow*, May 26-28, 1982, Mathematics Research Center, University of Wisconsin, Academic Press.

20 Spencer, A. J. M., "Deformation of an Ideal Granular Material," in *Mechanics of Solids, Rodney Hill 60th Anniversary Volume*, Hopkins, H. G., and Sewell, J. J., eds., Pergammon Press, 1981.

21 Trollope, D. H., and Burman, B. C., "Physical and Numerical Experiments With Granular Wedges," *Geotech*; Vol. 30, 1980, pp. 135-157.

22 Walton, O., "Particle Dynamics Modeling of Geological Materials," Univ. of California, Report UCRL-52915, 1981.

23 Wood, W. W., "Computer Studies on Fluid Systems of Hard-Core Particles," in: *Fundamental Problem of Statistical Mechanics Vol. 3*, Cohen, E. D. G., ed., North Holland, 1975.

24 Evans, "Rheological Properties of Simple Fluids by Computer Simulation," *Physical Review A.*, Vol. 23, 1981, pp. 1988-1997.

Downloaded 02 May 2010 to 171.66.16.54. Redistribution subject to ASME license or copyright; see http://www.asme.org/terms/Terms_Use.cfm

Clearing Maximum Height With Constrained Kinetic Energy

M. Hubbard
Department of Mechanical Engineering,
University of California,
Davis, Calif. 95616
Mem. ASME

J. C. Trinkle
Department of Systems Engineering,
University of Pennsylvania,
Philadelphia, Pa. 19104

This paper addresses the question: In order to clear a given height, defined as that which is passed over by all points in the moving body, what is the minimum initial kinetic energy required and what are the other conditions that specify the solution completely? An expression is derived for the height cleared above an original supporting ground plane. This transcendental expression is maximized numerically subject to certain equality and inequality constraints using nonlinear constrained optimization techniques. The optimal solution includes the height cleared and the required control variables. The parameter space of body descriptors in which the optimal solution is presented decomposes into two regions in which the solutions differ qualitatively.

Introduction

It is occasionally of interest to jump or to throw an object as high as possible with the height being defined as that which is cleared by all moving points in the object. This fundamental act forms the basis for many games, including several track and field events, has been practiced by almost all of us at one time or another in our lives, has some industrial applications, and has even inspired nursery rhymes. Yet, except for the particle ballistics problem so familiar to elementary physics students, there seems to have been little analytical study of the more general problem that includes the effects of the extended nature and geometrical shape of the moving body.

Conservation of energy in the case of a particle, of course, requires that the height cleared be a monotonic increasing function of initial kinetic energy. Intuitively, this carries over to the case of an extended (three-dimensional) rigid body and provides a conceptual framework for the problem formulation. One would also expect the height cleared by any connected set of rigid bodies to be a monotonic function of initial kinetic energy as long as the connections exhibit no dissipation or potential energy storage. With a given initial kinetic energy, what is the maximum height, which is possible for a body to clear (or equivalently, in order to clear a given height, what is the minimum initial kinetic energy required) and what are the other conditions that specify the solution completely?

In this paper a simple model for the extent of the body is assumed, but it is believed that similar techniques could be used for the solution with more complicated body shapes. An expression is derived for the height cleared, above an original supporting ground plane, in terms of the parameters that describe the body and its initial conditions. The maximization of this transcendental expression, subject to certain equality and inequality constraints on the variables, which arise naturally in the problem formulation, is necessarily accomplished numerically using nonlinear constrained optimization techniques. The parameter space of body descriptors in which the optimal solution (height cleared and the associated control variables that permit this) is presented, is shown to decompose into two regions in which the optimal solutions differ qualitatively.

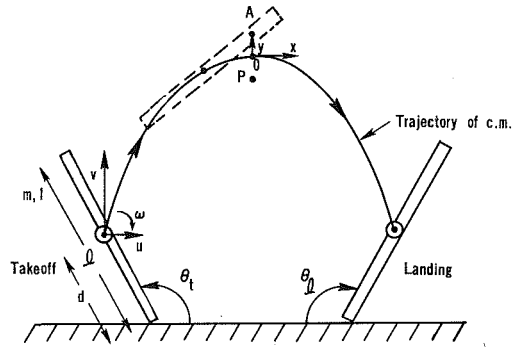


Fig. 1 Schematic diagram of model showing rod geometry, hypothetical center-of-mass trajectory, point *P* with maximum height cleared by all points in the rod, point *A* in rod above *P*, and point 0 at zenith of c.m. trajectory, the origin of *xy* frame

Model

Figure 1 shows a schematic diagram of the proposed motion. We consider the simplest possible model for the moving body, a thin rigid rod of length l, position of the center of mass along the rod d, mass m, and centroidal moment of inertia I. Further, the rod is assumed to move only

Contributed by the Applied Mechanics Division for presentation at the 1985 Joint ASME/ASCE Applied Mechanics, Fluids Engineering, and Bioengineering Conference, Albuquerque, N. Mex., June 24-26, 1985 of THE AMERICAN SOCIETY OF MECHANICAL ENGINEERS.

Discussion on this paper should be addressed to the Editorial Department, ASME, United Engineering Center, 345 East 47th Street, New York, N.Y. 10017, and will be accepted until two months after final publication of the paper itself in the JOURNAL OF APPLIED MECHANICS. Manuscript received by ASME Applied Mechanics Division, January, 1984; final revision, May 1984 Paper No. 85-APM-3.

Copies will be available until February, 1986.

Copyright © 1985 by ASME
Downloaded 02 May 2010 to 171.66.16.54. Redistribution subject to ASME license or copyright; see http://www.asme.org/terms/Terms_Use.cfm

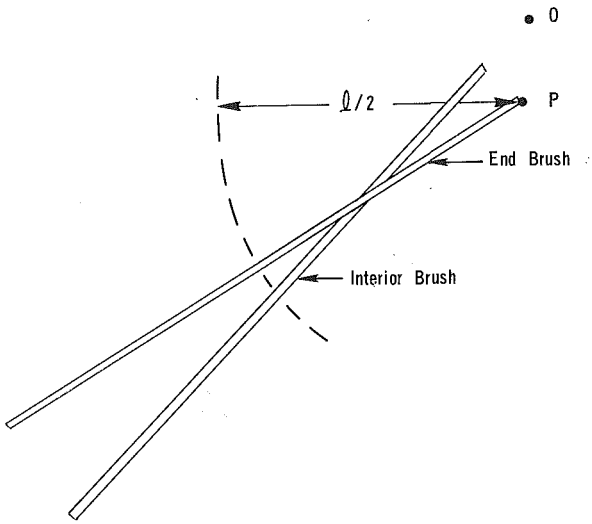


Fig. 2 Schematic of two possible rod positions at the first possible brush time, $-t_l$

under the influence of gravity in a vertical plane from an initial position which has at least one point of the rod in contact with the horizontal ground plane. Denote by P the fixed point (as yet unknown) with greatest height cleared by all points of the rod. This would be the position of the crossbar in an optimal high jump. Although the case with $d \neq l/2$ can be studied [1], in what follows we pick the simplest geometry, $d = l/2$.

Define an xy coordinate system with origin at 0, the (also unknown) zenith of the parabolic trajectory of the rod center of mass (c.m.) as shown in Fig. 1, and let $t = 0$ when the c.m. is at 0. Note that 0 must be either coincident with or above point P.

The final assumption concerns the symmetry of the optimal trajectory; the rod is taken to be horizontal when its center lies directly above P. This assumption is motivated from physical intuition and, based on a preliminary numerical study not reported here, is felt to be valid except possibly for extremely small initial kinetic energies. In this preliminary study the value of θ at $t = 0$ was allowed to vary freely together with the remaining variables to be discussed in the following and was always found to be zero.

Because of the choice of $t = 0$ when the c.m. is at $x = y = 0$, we may write particularly simple expressions for the velocities and positions of the c.m.

$$v_x = u = \text{constant} \qquad v_y = -gt \tag{1}$$

$$x = ut \qquad y = -\frac{gt^2}{2} \tag{2}$$

and the rod orientation

$$\theta = \omega t. \tag{3}$$

An Expression for the Height Cleared

From the definition of P, it is clear that the rod must touch (brush) P from above at least once during the motion (or else P would be able to be moved up, a contradiction). Consider now the point A on the rod (or rod extended) which lies directly above P and which varies throughout the rod during the motion. From kinematic considerations, we can write the vertical velocity of A as

$$\dot{h}_A = -gt + u \tan \omega t + u\omega t \sec^2 \omega t \tag{4}$$

the first term being the velocity of the rod c.m., the second the vertical component of the velocity of A relative to the c.m., and the last a term due to "convection." Integration of (4) gives an expression for the height h_{AP} of point A above P,

$$h_{AP}(t) = ut \tan \omega t - gt^2/2 + C. \tag{5}$$

Having chosen $t = 0$ when the rod c.m. is above P we denote by t_b the time of brush. We note that t_b may or may not be zero. When $t_b \neq 0$, then, by symmetry, brushes occur at both t_b and $-t_b$, but when $t_b = 0$ there is only one brush. Because of the symmetry assumed, various times introduced in the following enjoy a symmetry similar to that just described for t_b. For example, the take-off time t_t, while actually negative, has the same magnitude as the time of landing. To minimize unneccessary confusion resulting from signs of these quantities, the times (t_b, t_t, etc.) are taken in what follows to be positive whenever possible.

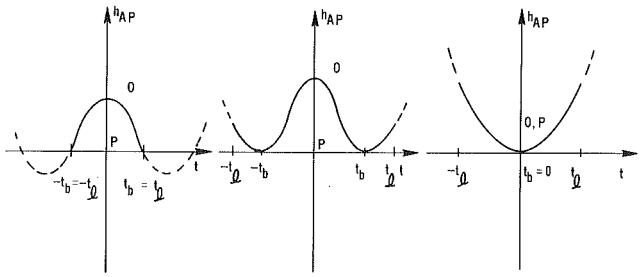


Fig. 3 h_{AP} versus t for (a) end brush ($t_b = t_l$), (b) noncentral interior brush ($2\tilde{\omega}\tilde{u} < 1$ and $t_b \neq 0$), and (c) central brush ($2\tilde{\omega}\tilde{u} \geq 1$ and $t_b = 0$)

Because $h_{AP}(t_b) = 0$, the constant C in (5) may then be evaluated with the result that the geometric height loss (i.e., the height of the rod c.m. above point P at its zenith) is given by

$$h_{AP}(0) = h_{0P} = \epsilon = C = gt_b^2/2 - ut_b \tan \omega t_b. \tag{6}$$

The label "geometric height loss" is somewhat of a misnomer since, by definition, P is as high as possible. Yet it focuses the idea that, as is shown in what follows, it is generally optimal for A and P not to coincide ($\epsilon \neq 0$). In addition, the label distinguishes between "geometric height loss" and the height that is lost because kinetic energy is associated with rotation and horizontal translation rather than only with vertical translation.

Now the height of point 0 is known from energy conservation and take-off conditions; at take-off $t = t_t$, $v_y = v$ so that

$$h_0 = \frac{l}{2} \sin \omega t_t + v^2/2g. \tag{7}$$

Further, the initial kinetic energy is divided into three parts

$$T = mu^2/2 + mv^2/2 + I\omega^2/2 \tag{8}$$

which provides an expression for the elimination of v in what follows.

Now the object must be to maximize the height h_P which, using (6), (7), and (8), is given by

$$\begin{aligned} h_P &= h_0 - \epsilon \\ &= \frac{l}{2} \sin \omega t_t + T/mg - u^2/2g \\ &\qquad - I\omega^2/2mg - [gt_b^2/2 - ut_b \tan \omega t_b]. \end{aligned} \tag{9}$$

Defining dimensionless variables (denoted by $\tilde{\ }$) $\tilde{T} = T/mgl$, $\tilde{I} = I/ml^2$, $\tilde{\epsilon} = \epsilon/l$, $\tilde{u} = u/\sqrt{lg}$, $\tilde{v} = v/\sqrt{lg}$, $\tilde{\omega} = \omega\sqrt{l/g}$, $\tilde{t}_t = t_t\sqrt{g/l}$, and $\tilde{t}_b = t_b\sqrt{g/l}$, we notice that (1) evaluated at t_t implies that $\tilde{v} = \tilde{t}_t$. The dimensionless height cleared $\tilde{h}_P = h_P/l$ can then be written as

$$\tilde{h}_P = \tilde{T} + (\sin \tilde{\omega}\tilde{t}_t - \tilde{u}^2 - \tilde{I}\tilde{\omega}^2 - \tilde{t}_b^2)/2 + \tilde{u}\tilde{t}_b \tan \tilde{\omega}\tilde{t}_b. \tag{10}$$

Downloaded 02 May 2010 to 171.66.16.54. Redistribution subject to ASME license or copyright; see http://www.asme.org/terms/Terms_Use.cfm

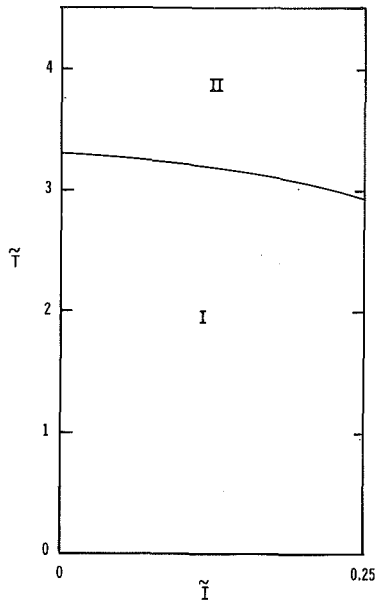


Fig. 4 $\tilde{T}$, $\tilde{I}$ solution space decomposes into two regions where interior brushes (*I*) and end brushes (*II*) are optimal, respectively

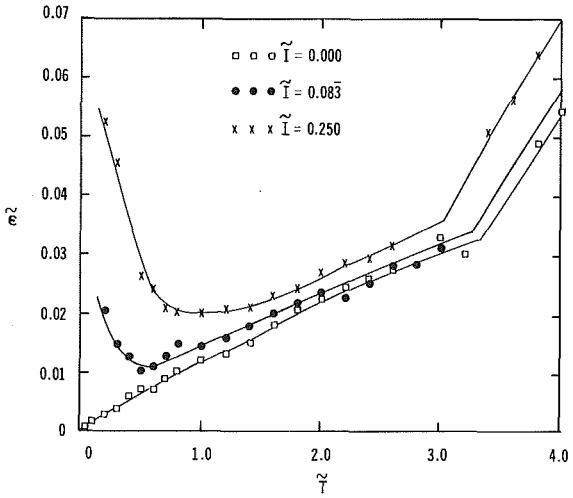


Fig. 5 Optimal $\tilde{\epsilon}$ versus $\tilde{T}$ with $\tilde{I}$ as parameter

In (10), the four independent variables $\tilde{\omega}$, $\tilde{u}$, $\tilde{t}_b$, and $\tilde{t}_l$ are to be chosen to maximize $\tilde{h}_P$, for given values of the parameters $\tilde{T}$, $\tilde{I}$ and subject to certain constraints. One of these constraints is the dimensionless form of (8) with v eliminated using (1),

$$2\tilde{T}=\tilde{I}\tilde{\omega}^2+\tilde{u}^2+\tilde{t}_l^2. \tag{11}$$

The remaining constraints on the independent variables arise from considerations that insure that a particular optimal solution $\tilde{\omega}$, $\tilde{u}$, $\tilde{t}_b$, $\tilde{t}_l$ results in a physically meaningful trajectory which passes *over* point P. The first of these is concerned with the fact that the brush time t_b in (6) is not completely arbitrary. We require that brush must occur at or after take-off (because this model treats only the airborne portion of the motion), which implies that the brush time must satisfy the inequality constraint

$$\tilde{t}_b \le \tilde{t}_l \tag{12}$$

Next we realize that brush can occur only at a time when the c.m. is on or within a circle of radius $l/2$ about point P. Defining the last (for $t_b>0$) possible brush time, t_l, to be that time when the c.m. is on the above circle, we have from geometry that

$$(y(t_l)+\epsilon)^2+x^2=l^2/4. \tag{13}$$

The two cases of a first possible brush and an interior brush, defined in what follows, are schematically illustrated in Fig. 2.

Using relations (2) and (6) to eliminate y and x, and nondimensionalizing (13) gives

$$(\tilde{t}_l^2/2-\tilde{\epsilon})^2+(\tilde{u}\tilde{t}_l)^2-1/4=0 \tag{14}$$

a quadratic in $\tilde{t}_l^2$. Thus, the dimensionless last possible brush time is given by

$$\tilde{t}_l=\left[2(\tilde{\epsilon}-\tilde{u}^2)+\sqrt{4\tilde{u}^4-8\tilde{u}^2\tilde{\epsilon}+1}\right]^{1/2} \tag{15}$$

where

$$\tilde{\epsilon}=\tilde{t}_b^2/2-\tilde{u}\tilde{t}_b\tan\tilde{\omega}\tilde{t}_b. \tag{16}$$

Therefore, the second inequality constraint that the actual brush time must satisfy is

$$\tilde{t}_b \le \tilde{t}_l, \tag{17}$$

where $\tilde{t}_l$ is related to the independent variables $\tilde{u}$, $\tilde{\omega}$, and $\tilde{t}_b$ by (15) and (16).

Whether or not constraint (17) is active turns out to be one of the most interesting features of the solution. In fact, the existence of a fourth constraint depends on the activity of (17). Obviously, $t_b<t_l$ corresponds to a brush in the interior of the rod, hereafter called an interior brush, while when $t_b = t_l$, brush occurs at the end of the rod. The position of the rod in these two cases, at time $-t_l$, is shown in Fig. 2. In the former case, point A approaches P from above, brushes P, and then departs from P from above, as illustrated schematically in Fig. 3(*b*). Here, clearly, $\dot{h}_{AP}(t_b)=0$. However, in an end brush on the way up, it is possible for point A (on the rod extended) to be below P until the first possible brush time $-t_l$, after which point A is above P. This implies that $\dot{h}_{AP}(t_b)\ge 0$ when $t_b<0$. This is illustrated in Fig. 3(*a*). When the positive brush time is considered, i.e., the brush on the way down, $t_b>0$ and $\dot{h}_{AP}(t_b)\le 0$. The preceding possibilities can be expressed in terms of dimensionless quantities as

$$\text{if}\quad \tilde{t}_l-\tilde{t}_b>0 \quad \text{then} \quad \dot{\tilde{h}}_{AP}(\tilde{t}_b)=-\tilde{t}_b+\tilde{u}\tan\tilde{\omega}\tilde{t}_b+\tilde{u}\tilde{\omega}\tilde{t}_b\sec^2\tilde{\omega}\tilde{t}_b=0, \tag{18a}$$

$$\text{or else}\quad \tilde{t}_l-\tilde{t}_b=0 \quad \text{and} \quad -\tilde{t}_b+\tilde{u}\tan\tilde{\omega}\tilde{t}_b+\tilde{u}\tilde{\omega}\tilde{t}_b\sec^2\tilde{\omega}\tilde{t}_b\le 0 \quad \text{for} \quad \tilde{t}_l>0,\ \tilde{t}_b>0. \tag{18b}$$

Interior brushes can be further decomposed into two subclasses: central and noncentral. Consider (18*a*), the dimensionless form of (4). Obviously, the tangent term eventually dominates making $\dot{\tilde{h}}_{AP}$ large and positive. Also, for all parameter combinations, $\tilde{h}_{AP}(0)=0$. For some parameter combinations, however, (when $\tilde{\omega}\tilde{u}\ge 1/2$), $\tilde{t}_b = 0$ is the *only* zero of (18*a*) and the $\tilde{h}_{AP}$ versus $\tilde{t}$ curve has only one minimum (at $\tilde{t}_b = 0$), as shown in Fig. 3(*c*). Large $\tilde{\omega}$ and $\tilde{u}$ represent energy that cannot be channeled into $\tilde{v}$ and hence result in a lower peak height for the c.m. Thus, from these considerations, it is seen that values for the parameters $\tilde{\omega}$, $\tilde{u}$ for which the product $2\tilde{\omega}\tilde{u}>1$ cannot be optimal. Indeed, in the numerical solutions discussed in what follows this was verified.

The optimization problem can now be summarized as follows: maximize $\tilde{h}_P$ ($\tilde{\omega}$, $\tilde{u}$, $\tilde{t}_b$, $\tilde{t}_l$) given by (10) for given $\tilde{T}$ and $\tilde{I}$ and subject to constraints (11), (12), and (17) augmented by (15), (16), and (18). Note that all constraints are in terms of the independent variables $\tilde{\omega}$, $\tilde{u}$, $\tilde{t}_b$, $\tilde{t}_l$ and restrict the possible

Downloaded 02 May 2010 to 171.66.16.54. Redistribution subject to ASME license or copyright; see http://www.asme.org/terms/Terms_Use.cfm

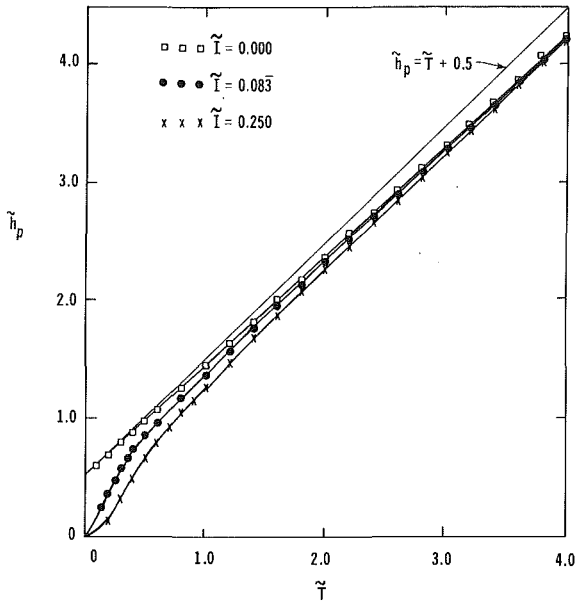


Fig. 6 Optimal $\tilde{h}_p$ versus $\tilde{T}$ with $\tilde{I}$ as parameter

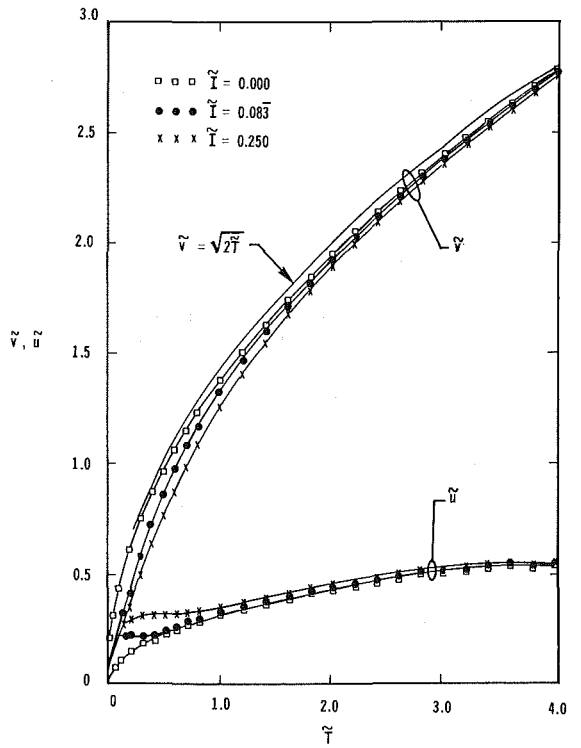


Fig. 7 Optimal $\tilde{v}$ and $\tilde{u}$ versus $\tilde{T}$ with $\tilde{I}$ as parameter

optimal solutions to a subset of the $\tilde{\omega}$, $\tilde{u}$, $\tilde{t}_b$, $\tilde{t}_t$ parameter four-space.

Numerical Solutions

Although the nonlinearity of the objective function (10) poses no problems, the rather complicated nature of the constraints motivates the use of numerical techniques to compute the solution. Over the last decade or two, dramatic advances have been made in the development of numerical methods and software for optimization [2, 3]. Even in the most complicated problem category, optimization with nonlinear inequality constraints (of which the present problem is an example), such methods have become much more efficient and reliable, to the point where reasonable results are possible using routines from software libraries [4].

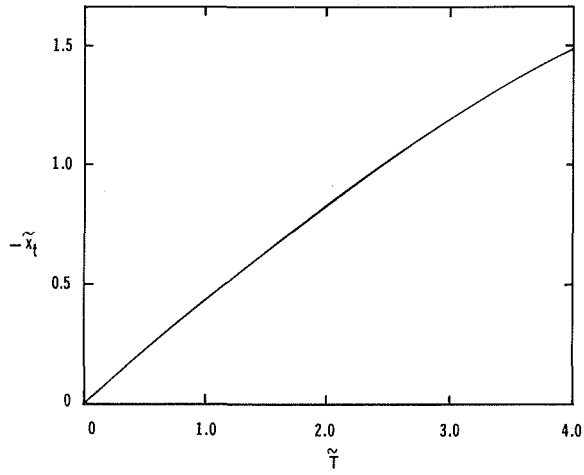


Fig. 8 Optimal $\tilde{x}_t$ versus $\tilde{T}$

The numerical solutions presented in the following were calculated using a computer program written by one of us (J.T.) based on sequential augmented Lagrangian method [3]. Since the computations are necessarily exceedingly detailed, a check was made using an entirely different computer program using the canned subroutine E04VBF from the Numerical Algorithms Group software library NAGLIB [4]. This subroutine is also based on a sequential augmented Lagrangian method and utilizes analytic expressions for the derivatives of the objective function.

For a time it was felt that an additional constraint on the curvature of the geometric height lost,

$$\ddot{\tilde{h}}_{AP}(\tilde{t}_b) \geq 0,$$

might be needed to insure that the object passed over rather than under P. This was not found necessary, however, since when the initial guess for the solution was a feasible one (resulting in a trajectory that passed over P and for which

$$\ddot{\tilde{h}}_{AP}(\tilde{t}_b) > 0)$$

the search never passed the hyperplane

$$\ddot{\tilde{h}}_{AP}(\tilde{t}_b) = 0$$

and the eventual optimal solution always satisfied this most fundamental constraint.

The conditional nature of constraint (18) was handled in the following way. The entire problem was solved twice, once assuming constraint (17) to be inactive and once assuming (17) to be active. In the former case (case *I*), equality constraint (18*a*) was used. In the latter case (case *II*), inequality constraint (18*b*) was applied. The final solution was then taken to be the one that yielded the maximum objective function. Optimal solutions were generated on a grid in the $\tilde{T}$, $\tilde{I}$ space over the range $0.0 < \tilde{T} < 4.0$ at 0.2 intervals and for three values of $\tilde{I}$; 0, 0.0833 = 1/12 (a homogeneous thin rod), 0.25 (a double point mass dumbbell with half the mass at either end). Note that while $\tilde{T}$ is theoretically unlimited, $\tilde{I}$, is restricted by geometry to lie in the range $0 < \tilde{I} < 0.25$. In Figs. 5–9, results are shown parameterized for only these values of I, the two limiting cases, and a nominal intermediate value.

As shown in Fig. 4, one of the features of the solution is that the $\tilde{T}$, $\tilde{I}$ space decomposes into two regions (*I* and *II*) where brush occurs in the interior and on the end of the bar, respectively. Interestingly, on the $\tilde{T}$, $\tilde{I}$ grid that was investigated, a central brush with $\tilde{\epsilon} = 0$ was *never* found to be optimal, In region *II*, the c.m. can reach its peak significantly

Downloaded 02 May 2010 to 171.66.16.54. Redistribution subject to ASME license or copyright; see http://www.asme.org/terms/Terms_Use.cfm

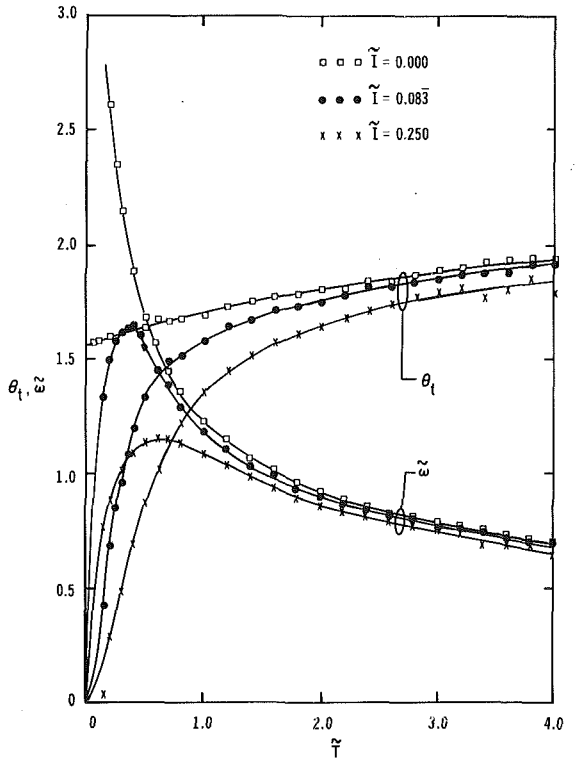


Fig. 9 Optimal θ_t and versus $\tilde{T}$ with $\tilde{I}$ as parameter

above the bar with relatively large geometric height loss, $\tilde{\epsilon} > 0.06$.

Figure 5 shows the geometric height loss $\tilde{\epsilon}$ versus $\tilde{T}$. The corners of the curves correspond to the boundary between regions *I* and *II* in Fig. 4. For a given energy $\tilde{T}$, the geometric height loss $\tilde{\epsilon}$ increases as $\tilde{I}$ increases, as would be expected since, for a given angular velocity, more energy must be stored in rotational motion. Yet an interesting fact is that even with $\tilde{I} \simeq 0$, corresponding to a rod with negligible mass except at the c.m. and essentially no rotational energy storage, the optimal solution is still driven by geometric factors. It predicts nonzero horizontal velocity $\tilde{u}$ (see Fig. 7) and less cleared height than would be predicted from a pure energy balance. For nonzero $\tilde{I}$, there is an energy at which the geometric height loss is a minimum, with $\tilde{\epsilon}$ rising steeply for very small $\tilde{T}$ and more gradually for large $\tilde{T}$. The geometric height loss can be larger than $\tilde{\epsilon} = 0.05$ when $\tilde{I} = 0.25$ and $\tilde{T} < 0.2$ or $\tilde{T} > 3.0$.

Shown in Fig. 6 is the optimal objective function, $\tilde{h}_P$, the maximum height clearable with given energy $\tilde{T}$ and geometry $\tilde{I}$. As is apparent, the percent deviation from the upper bound, $\tilde{h}_P = \tilde{T} + 0.5$ representing the maximum achievable c.m. height, is largest for small energies $\tilde{T}$ and larger $\tilde{I}$. For $\tilde{T} = 0.4$ and $\tilde{I} = 0.25$, the maximum height clearable is less than 50 percent of the height achievable by the c.m. if clearance were not required. For large energies ($\tilde{T}>4.0$), the optimal height cleared becomes insensitive to $\tilde{I}$ and the three $\tilde{I}$ curves coalesce. This happens significantly below the $\tilde{h}_P = \tilde{T} + 0.5$ boundary, however, since both the geometric height loss and the horizontal and rotational kinetic energies required are substantial. Cusps similar to those in Fig. 5 are not apparent in Fig. 6, however.

The four important control parameters, $\tilde{v}$, $\tilde{u}$, θ_t, $\tilde{\omega}$ (governing take-off conditions completely) are shown in Figs. 7 and 9. Figure 7 plots vertical and horizontal take-off velocities $\tilde{v}$ and $\tilde{u}$ versus $\tilde{T}$ and shows that for given $\tilde{T}$, $\tilde{v}$ decreases as $\tilde{I}$ increases and more rotational energy is demanded. Also shown is an upper bounding curve

$$\tilde{v} = \sqrt{2\tilde{T}}$$

(analogous to the one in Fig. 6) corresponding to the case where all initial kinetic energy is associated with vertical motion. As noted previously, $\tilde{v} = -\tilde{t}_f$, so the $\tilde{v}$ curves in Fig. 7 can also be viewed as plots of half the time of flight. At low energies, the three $\tilde{v}$ curves for different $\tilde{I}$ are rather widespread, but they converge at higher energies, and thus the time of flight and maximum c.m. height become insenstive to moment of inertia variations at high energies. They also approach the boundary

$$\tilde{v} = \sqrt{2\tilde{T}}.$$

Thus, the percentage of kinetic energy wasted in rotation and horizontal translation gradually decreases as $\tilde{T}$ increases. In the low energy case, the smaller times of flight require larger angular velocities (see Fig. 9) for clearance and thus larger rotational kinetic energies, especially for large $\tilde{I}$.

Also shown in Fig. 7 is the horizontal velocity $\tilde{u}$. As $\tilde{T}$ increases $\tilde{u}$ also becomes increasingly less sensitive to both $\tilde{I}$ and $\tilde{T}$, but at a given $\tilde{T}$, $\tilde{u}$ *increases* with increasing $\tilde{I}$. This can be understood by remembering the role of $\tilde{u}$ in the expression (18*a*) for $\tilde{h}_{AP}$. As the product $\tilde{u}\tilde{\omega}$ approaches 0.5, the $\tilde{h}_{AP}$ profile becomes flatter and more like Fig. 3(*c*), thus decreasing $\tilde{\epsilon}$. Thus, there is an incentive for the product $\tilde{u}\tilde{\omega}$ to remain reasonably near 0.5.

Note that, since $\tilde{v} = \tilde{t}_f$, the dimensionless initial x position of the center of mass, the only remaining take-off parameter not yet discussed, can be computed from $\tilde{x}_t = -\tilde{u}\tilde{v}$. Figure 8 shows $\tilde{x}_t$ versus $\tilde{T}$. As is clear from the figure, $-\tilde{x}_t$ gradually gets larger with increasing $\tilde{T}$ but is quite insensitive to $\tilde{I}$. Indeed, it was impossible to discern, within the accuracy of our numerical solutions, any regular variation of $\tilde{x}_t$ with $\tilde{I}$. Thus, only one curve is plotted.

Figure 9 portrays the rotational aspects ($\tilde{\omega}$ and θ_t) of the optimal trajectories. For small $\tilde{T}$ and especially for large $\tilde{I}$, the small take-off angles θ_t imply that a rather severe compensation (a sacrifice in initial c.m. height) must be made to decrease the required rotational kinetic energy. For large energies, however, the take-off angle becomes insensitive to both $\tilde{T}$ and $\tilde{I}$, remaining in the region slightly greater than vertical ($\pi/2$).

For low energies $\tilde{T}<1.0$ and nonzero moments of inertia $\tilde{I}$, the angular velocity $\tilde{\omega}$ reaches a maximum value. Below this point there is simply not enough kinetic energy available to allow large $\tilde{\omega}$, while for larger energies $\tilde{T}$ more time is available to achieve a horizontal attitude at the zenith and hence large angular velocities (and large rotational kinetic energies) are not needed. Thus, as $\tilde{T}$ increases beyond 1.0, $\tilde{\omega}$ decreases continuously and becomes, as do all other variables, less sensitive to $\tilde{I}$.

Summary and Conclusions

For the first time, an expression has been derived for the height cleared by an object in terms of the parameters that describe the object and its initial conditions and which accounts for the fact that any point in the object may limit the height cleared. Numerical nonlinear optimization techniques were used to maximize this transcendental expression subject to both equality and inequality constraints arising naturally in the problem formulation. Although a simple extent model for the object was used, similar techniques could be used for the solution in the case of more complicated body shapes.

Important aspects of the optimal solution are the following:

1. For given initial energy, the maximum height cleared by an object is less for larger moments of inertia and in the case of low energies can be less than half of the maximum achievable c.m. height for the same energy.
2. The $\tilde{T}$, $\tilde{I}$ space decomposes into two regions where the

Downloaded 02 May 2010 to 171.66.16.54. Redistribution subject to ASME license or copyright; see http://www.asme.org/terms/Terms_Use.cfm

brush characteristics differ qualitatively. Roughly speaking, for energy-inertia combinations satisfying $\tilde{T} + 1.5\ \tilde{I} > 3.3$, it is optimal to brush the highest point with the end of the rod, while when $\tilde{T} + 1.5\ \tilde{I} < 3.3$, a brush in the interior of the rod is optimal.

3. It is always optimal for brush to occur at times other than when the c.m. is at its zenith 0. Thus the highest point P cleared always lies below 0. This geometric height loss is a complicated function of the initial energy and can be more than 7 percent of the rod length when $\tilde{T} \geq 4$ and $\tilde{I} = 0.25$.

A specific application of the general theory presented in this paper is to a rather simple model of Fosbury-flop high jumping [5] where the jumper moves more or less in a plane perpendicular to the crossbar. In this case, the energies $\tilde{T}$ are usually considerably less than 1.0 and the moment of inertia $\tilde{I}$ is probably near 0.083.

References

1 Hubbard, M., and Trinkle, J. C., "Optimal Initial Conditions for the Eastern Roll High Jump," in: *Biomechanics: Principles and Applications*, Huiskes, R., Van Campen, D. and DeWijn, J., eds., Martinus Nijhoff, The Hague, 1982, pp. 169–174.

2 Gill, P. E., and Murray, W., eds., *Numerical Methods for Unconstrained Optimization*, Academic Press, New York, 1974.

3 Gill, P. E., Murray, W., and Wright, M. H., *Practical Optimization*, Academic Press, New York, 1981.

4 NAG Fortran Library Reference Manual (Mark 8), Numerical Algorithms Group Limited, Oxford, England, 1981.

5 Hubbard, M., and Trinkle, J. C., "Optimal Fosbury-Flop High Jumping," *Proceedings of the Ninth International Congress of Biomechanics*, Waterloo, Ontario, Canada, Aug. 1983, in press.

Downloaded 02 May 2010 to 171.66.16.54. Redistribution subject to ASME license or copyright; see http://www.asme.org/terms/Terms_Use.cfm

The Constitutive Theory for Fluid-Filled Porous Materials

N. Katsube
Assistant Professor,
Department of Engineering Mechanics,
The Ohio State University,
Columbus, Ohio 43210
Assoc. Mem. ASME

The static constitutive theory for fluid-filled porous materials, well established by Biot, is reinvestigated by modifying the recent developments of the micromechanical approach by Carroll. Introducing a new kinematical quantity that allows an equal treatment of fluid and solid, we show that the constitutive theory by Carroll is identical to that developed by Biot. This comparison provides a further insight into Biot's theory by clarifying the distinct deformation mechanisms that Biot did not express explicitly. Applying the same methods to the dynamic case, we investigate the fluid flow mechanism of a porous fluid material.

1 Introduction

Biot's three-dimensional theory for a fluid-filled porous material [1–4] has been well established. His theory is based on the classical theory of linear elasticity and Darcy's law. Rice and Cleary [5] reformulated Biot's theory and obtained some stress diffusion solutions. In recent years, constitutive relations for fluid-filled porous material have been investigated from viewpoints somewhat different from Biot. Nur and Byerlee [6] obtained the expression of the effective stress law based on isotropic linear elasticity. Motivated by their work, Carroll [7] introduced the notion of porosity change in the formulation and made clear the three distinct deformation mechanisms of fluid-filled porous material, i.e., solid deformation, relative pore geometry change, and the fluid compaction. In his work, however, attention was biased to the deformation of the porous solid skeleton, and the porous solid and the porous fluid were not treated on an equal basis.

In this work, we reformulate Carroll's work by introducing a new kinematical quantity, i.e., the volume change of porous fluid material, and treat the solid and the fluid equally. This reformation makes it possible to make a one-to-one correspondence between the recent development of constitutive relations and Biot's well-known constitutive equations and provides a further insight into the theory by Biot. We consider the anisotropic case and reduce it to the transversely isotropic case, where many geological applications exist, and also to the isotropic case as special cases. While the static deformation of a porous solid material with the effect of hydrostatic fluid pressure has been investigated, the flow mechanism of porous material has not been examined. As long as we assume that the fluid inside the pores is a Newtonian viscous fluid, we should not simply ignore the stress due to fluid viscosity. Applying the same methods of construction of constitutive theory to a porous fluid material, we consider the flow mechanism of a porous fluid material.

2 Preliminaries

As in [7], we will make use of the formulas

$$\bar{t}_{ij} = \frac{1}{V(R)} \int_R t_{ij} dv = \frac{1}{V(R)} \left[\int_{\partial R} t_i x_j da + \int_R \rho b_i x_j dv \right] \tag{1}$$

$$\bar{e}_{ij} = \frac{1}{V(R)} \int_R e_{ij} dv = \frac{1}{2V(R)} \int_{\partial R} (u_i n_j + u_j n_i) da \tag{2}$$

$$\bar{d}_{ij} = \frac{1}{V(R)} \int_R d_{ij} dv = \frac{1}{2V(R)} \int_{\partial R} (v_i n_j + v_j n_i) da \tag{3}$$

for the average stress components $\bar{t}_{ij}$, average infinitesimal strain components $\bar{e}_{ij}$, and average strain rate components $\bar{d}_{ij}$ in a body occupying a region R with boundary ∂R. $V(R)$ denotes the volume of the region R and ρ is the mass density. t_i, b_i, u_i, v_i, and n_i, respectively, are the components of the surface force, the body force, the infinitesimal displacement, the velocity, and the unit outward normal on ∂R. The average stress theorem (1), which applies in the case of equilibrium, shows that the average stress is determined by the loading and the geometry of the deformed body and is independent of the material response. The average strain theorem (2) and average strain rate theorem (3) allow us to define the strain and strain rate of a region (even a void space) in terms of surface displacements and velocities, respectively. Equations (1)–(3) follow directly from the definitions of surface force, strain, strain rate, the equation of equilibrium, and the divergence theorem.

We consider the response of a representative sample of an anisotropic fluid-filled porous material under the confining stress t_{ij}. This representative sample should be large enough to contain the detail of the microstructure (e.g., several pores or grains) and small enough so that the average response is representative of the local response of the porous material idealized as a continuum. We define the total average stress $\bar{t}_{ij}$, fluid average stress $\bar{t}^f_{ij}$, and solid average stress $\bar{t}^s_{ij}$ by applying equation (1) to the total region R, fluid region R_f, and solid region R_s of the representative volume element,

Contributed by the Applied Mechanics Division and presented at the Winter Annual Meeting, New Orleans, La., December 9–14, 1984 of THE AMERICAN SOCIETY OF MECHANICAL ENGINEERS.

Discussion on this paper should be addressed to the Editorial Department, ASME, United Engineering Center, 345 East 47th Street, New York, N.Y. 10017, and will be accepted until two months after final publication of the paper itself in the JOURNAL OF APPLIED MECHANICS. Manuscript received by ASME Applied Mechanics Division, February, 1984. Paper No. 84-WA/APM-48.

Copies will be available until August, 1985.

Copyright © 1985 by ASME
Downloaded 02 May 2010 to 171.66.16.54. Redistribution subject to ASME license or copyright; see http://www.asme.org/terms/Terms_Use.cfm

respectively. Introducing the volumetric porosity $\phi = V(R_f)/V(R)$ of this representative volume element, we obtain the following equations from the definition of volume average stress

$$t_{ij} = \phi t_{ij}^f + (1-\phi)t_{ij}^s = t_{ij}' + t_{ij}'' \tag{4}$$

$$t_{ij}' = -\phi P_f \delta_{ij} + (1-\phi)t_{ij}^s \tag{5}$$

$$t_{ij}'' = \phi(t_{ij}^f + P_f \delta_{ij}) \tag{6}$$

where the bar, to indicate the volume average values, is omitted for convenience, and P_f is the volume average hydrostatic fluid pressure. While equation (4) is derived from volume averages, it has the appropriate form to describe the manner in which the total force on a surface element with areal porosity ϕ in the porous material is shared by fluid and solid. In equation (4), the total stress t_{ij} is also expressed as a sum of the static total stress t_{ij}' caused by the solid deformation with the effect of fluid hydrostatic pressure P_f and the dynamic total stress t_{ij}'' caused by the fluid flow through porous material. We investigate the static deformation mechanism of porous material with the effect of hydrostatic fluid pressure and the dynamic fluid flow mechanism due to fluid viscosity separately. This separation is possible since these two constitutive relations are uncoupled within the infinitesimal assumption of solid deformation. First we limit our attention to the static deformation of porous material with the effect of fluid hydrostatic pressure inside the pores.

3 Static Deformation of Fluid-Saturated Porous Material

(a) Kinematics.

Hydrostatic Case. Let us investigate the hydrostatic kinematical variables by considering the control volume V of fluid-saturated porous material, fixed in space, which consists of the volume occupied by solid V_s and the volume occupied by fluid V_f. We also introduce the volumetric porosity ϕ.

$$V = V_s + V_f, \quad \phi = \frac{V_f}{V}, \quad 1-\phi = \frac{V_s}{V} \tag{7}$$

Let ΔV_s, ΔV_f, $\Delta V^{(1)}$, and $\Delta V^{(2)}$ denote the volume increase of the solid (solid matrix), the fluid (fluid without pores), the porous solid material, and the porous fluid material, respectively, inside the control volume. The increase of the solid volume inside the control volume may be separated into the volume expansion of the solid $\Delta \hat{V}_s$ and the volume increase due to the solid entering the control volume $\Delta \tilde{V}_s$. Similarly ΔV_f, $\Delta V^{(1)}$, and $\Delta V^{(2)}$ also may be separated into two parts, i.e., the increase due to volume expansion, denoted by $\hat{}$, and those due to quantities entering the control volume, denoted by $\tilde{}$.

$$\Delta V_s = \Delta \hat{V}_s + \Delta \tilde{V}_s, \quad \Delta V_f = \Delta \hat{V}_f + \Delta \tilde{V}_f \tag{8}$$

$$\Delta V^{(1)} = \Delta \hat{V}^{(1)} + \Delta \tilde{V}^{(1)}, \quad \Delta V^{(2)} = \Delta \hat{V}^{(2)} + \Delta \tilde{V}^{(2)}$$

$\Delta V^{(1)}$ and $\Delta V^{(2)}$ are zero because after the deformation both the volume of the porous solid material and that of the porous fluid material inside the control volume are the same with the control volume, which is fixed in space. We note that the solid volume entering the control volume $\Delta \tilde{V}_s$ is equal to $(1-\phi)\Delta \tilde{V}^{(1)}$ where $\Delta \tilde{V}^{(1)}$ is the volume of the porous solid material entering the control volume. Similarly the fluid volume entering the control volume, $\Delta \tilde{V}_f$, and the volume of the porous fluid material entering the control volume $\Delta \tilde{V}^{(2)}$ are related by equation $(10)_2$.

$$\Delta V^{(1)} = 0, \quad \Delta V^{(2)} = 0 \tag{9}$$

$$\Delta \tilde{V}_s = (1-\phi)\Delta \tilde{V}^{(1)}, \quad \Delta \tilde{V}_f = \phi \Delta \tilde{V}^{(2)} \tag{10}$$

Equations (7)–(10) lead to

$$\frac{\Delta \hat{V}^{(1)}}{V} = \frac{\Delta \hat{V}_s}{V_s} + \frac{\Delta \phi}{1-\phi}, \quad \frac{\Delta \hat{V}^{(2)}}{V} = \frac{\Delta \hat{V}_f}{V_f} - \frac{\Delta \phi}{\phi}. \tag{11}$$

The volume expansion of the porous solid material $\Delta \hat{V}^{(1)}$ can be separated into the volume expansion of the solid matrix $\Delta \hat{V}_s$ and the pore volume increase of the porous solid material, denoted by $\Delta V_p{}^{(1)}$. Similarly, the volume expansion of the porous fluid material $\Delta \hat{V}^{(2)}$ can be separated into the volume expansion of the fluid $\Delta \hat{V}_f$ and the pore volume increase of the porous fluid material, denoted by $\Delta V_p{}^{(2)}$.

$$\Delta \hat{V}^{(1)} = \Delta \hat{V}_s + \Delta \hat{V}_p{}^{(1)}, \quad \Delta \hat{V}^{(2)} = \Delta \hat{V}_f + \Delta \hat{V}_p{}^{(2)} \tag{12}$$

Equations (7) and (12) lead to

$$\frac{\Delta \hat{V}^{(1)}}{V} = (1-\phi)\frac{\Delta \hat{V}_s}{V_s} + \phi \frac{\Delta \hat{V}_p{}^{(1)}}{V_p{}^{(1)}},$$

$$\frac{\Delta \hat{V}^{(2)}}{V} = \phi \frac{\Delta \hat{V}_f}{V_f} + (1-\phi)\frac{\Delta \hat{V}_p{}^{(2)}}{V_p{}^{(2)}} \tag{13}$$

where, within the infinitesimal assumption, $V_p{}^{(1)}$ and $V_p{}^{(2)}$ in equation (13) are equal to V_f and V_s, respectively. Equation $(11)_1$ resolves the volumetric strain of the porous solid material $\Delta \hat{V}^{(1)}/V$ into a component due to solid volumetric strain and one due to change in porosity. Equation $(13)_1$ expresses the volumetric strain of the porous solid material as a weighted sum of the volumetric strain of the solid and the volumetric strain of the pore. Equations $(11)_2$ and $(13)_2$ are the fluid counterpart of equations $(11)_1$ and $(13)_2$, respectively. Equations (11) are most useful because they identify three distinct deformation mechanisms, i.e., the solid compaction, the fluid compaction, and the porosity change.

In the laboratory, it is not easy to measure the volumetric increase of porous fluid skeleton. Instead, we can measure the fluid volume increase from the porous solid skeleton after the deformation. For this purpose we introduce the fluid mass increase per unit volume of the porous solid skeleton Δm. Applying the same notion to the solid, we can also introduce the solid mass increase per unit volume of the porous fluid skeleton Δn.

$$\Delta m = \frac{\rho_f \phi (\Delta \hat{V}^{(1)} - \Delta \hat{V}^{(2)})}{V}$$

$$\Delta n = \frac{\rho_s (1-\phi)(\Delta \hat{V}^{(2)} - \Delta \hat{V}^{(1)})}{V} \tag{14}$$

where ρ_f and ρ_s are the fluid mass density and the solid mass density, respectively.

Nonhydrostatic Case. The outer boundary of the actual sample is composed of the solid boundary and the fluid boundary. We introduce a thin elastic membrane that covers the outer boundary of the sample but allows the fluid to go through so that we can apply the shear stress on the outer boundary. The average strains of the porous solid material, the solid matrix, and the pore space, denoted by $e_{ij}^{(1)}$, e_{ij}^s, and $e_{ij}^{p(1)}$, respectively, are defined through the formula (2). The superscript (1) indicates the association with the porous solid material as opposed to the porous fluid material where the superscript (2) is used. Use of equations (2) and (7) leads to

$$e_{ij}^{(1)} = (1-\phi)e_{ij}^s + \phi e_{ij}^{p(1)}, \quad e_{ij}^{(1)} = e_{ij}^s + e_{ij}^{*(1)},$$

$$e_{ij}^{*(1)} = \phi(e_{ij}^{p(1)} - e_{ij}^s). \tag{15}$$

Equations $(15)_{1,2}$, which are the three-dimensional counterpart of equation $(13)_1$ and $(11)_1$, express the strain of the porous solid material as a weighted sum of a solid strain e_{ij}^s and a pore strain $e_{ij}^{p(1)}$ and as a sum of a solid strain e_{ij}^s and a strain $e_{ij}^{*(1)}$ due to change in relative pore geometry (or differential straining of the pore space and the solid matrix). From the one-to-one correspondence between the study of the hydrostatic case and the preceeding formulation, we have

Downloaded 02 May 2010 to 171.66.16.54. Redistribution subject to ASME license or copyright; see http://www.asme.org/terms/Terms_Use.cfm

$$\frac{\Delta \hat{V}^{(1)}}{V} = e^{(1)}_{mm}, \quad \frac{\Delta \hat{V}_s}{V_s} = e^s_{mm},$$

$$\frac{\Delta \hat{V}^{(1)}_p}{V^{(1)}_p} = e^{p(1)}_{mm}, \quad \frac{\Delta\phi}{1-\phi} = e^{*(1)}_{mm}. \tag{16}$$

We shift our attention from the deformation of the porous solid material to the volumetric change of the porous fluid material. In the static case, there is no deviatoric strain in the fluid. Recalling the previous section, we introduce the identities (17) and obtain equations (18) and (19).

$$\frac{\Delta \hat{V}^{(2)}}{V} = e^{(2)}_{mm}, \quad \frac{\Delta \hat{V}_f}{V_f} = e^f_{mm}$$

$$\frac{\Delta \hat{V}^{(2)}_p}{V^{(2)}_p} = e^{p(2)}_{mm}, \quad -\frac{\Delta\phi}{\phi} = e^{*(2)}_{mm} \tag{17}$$

$$e^{(2)}_{mm} = \phi\, e^f_{mm} + (1-\phi)e^{p(2)}_{mm}, \quad e^{(2)}_{mm} = e^f_{mm} + e^{*(2)}_{mm},$$

$$e^{*(2)}_{mm} = (1-\phi)(e^{p(2)}_{mm} - e^f_{mm}) \tag{18}$$

$$\Delta\phi = (1-\phi)e^{*(1)}_{ii} = -\phi e^{*(2)}_{ii},$$

$$\Delta m = \rho_f \phi\ (e^{(1)}_{ii} - e^{(2)}_{ii})$$

$$\Delta n = \rho_s(1-\phi)(e^{(2)}_{ii} - e^{(1)}_{ii}) \tag{19}$$

(b) Constitutive Equations. We are interested in the response of the representative volume element to homogeneous tractions, i.e., to loading conditions of the type

$$t_i = t'_{ij} n_j \quad \text{on} \quad B_0, \qquad t_i = -P_f n_i \quad \text{on} \quad B_p \tag{20}$$

where t'_{ij} and P_f are constants. The linear response equations are given as follows.

$$t^s_{ij} = M^s_{ijkl} e^s_{kl}, \quad e^s_{ij} = C^s_{ijkl} t^s_{kl} \tag{21}$$

$$t'_{ij} + P_f \delta_{ij} = M^{*(1)}_{ijkl} e^{*(1)}_{kl},$$

$$e^{*(1)}_{ij} = C^{*(1)}_{ijkl}\,(t'_{kl} + P_f \delta_{kl}) \tag{22}$$

$$P_f = -K_f e^f_{kk} \tag{23}$$

In the linear range the relation between the average stress and average strain in either the solid matrix or the fluid are identical to either the local-solid constitutive relation and the local-fluid constitutive relation, respectively. This leads to the response equations (21) and (23) for solid and fluid, respectively. M^s_{ijkl} and C^s_{ijkl} denote tensors of solid elastic moduli and compliances, respectively, while K_f denotes the fluid bulk modulus. The derivation of the response equation (22) is shown in Carroll and Katsube [8] where $C^{*(1)}_{ijkl}$ is found to be related to the effective compliance tensor $C^{(1)}_{ijkl}$ (relating an overall strain to the confining stress without pore fluid pressure) and the solid compliance tensor C^s_{ijkl} as follows:

$$C^{*(1)}_{ijkl} = C^{(1)}_{ijkl} - \frac{1}{1-\phi} C^s_{ijkl}. \tag{24}$$

Within the context of anisotropic linear elasticity, it is proven that the overall strain component due to change in the relative pore geometry is determined by the Terzaghi effective stress. When $t'_{ij} = -P_f \delta_{ij}$, the stress state in the solid matrix is a uniform hydrostatic pressure P_f and the resulting pore space strain is equal to the uniform strain in the solid matrix. There is no change in the relative pore geometry (e.g., a spherical sample with spherical pores becomes an ellipsoidal sample with similar ellipsoidal pores.) It follows that, in the linear response range, the change in relative pore geometry is proportional to the Terzaghi effective stress. The preceding formulation is an extension of the isotropic case [7] to the anisotropic case. As in [7], we can obtain effective stress laws for different kinematical values, i.e., $e^{(1)}_{ij}$, $e^{p(1)}_{ij}$, $e^{(2)}_{mm}$ and Δm from equations (5), (15), (18), (19), and (21)–(23), and also consider the undrained response for the anisotropic case. The effective stress laws for $e^{(1)}_{ij}$ and $e^{p(1)}_{ij}$ are obtained in Carroll [9] and Carroll and Katsube [8]. To complete our investigation of effective stress laws, we record the effective stress laws for Δm and $e^{(2)}_{mm}$:

$$\Delta m = \rho_f \phi C^{p(1)}_{iikl}\ [[t'_{kl}]],$$

$$e^{(2)}_{kk} = -\frac{(1-\phi)}{\phi} C^{*(1)}_{mmkl}\{\{t'_{kl}\}\} \tag{25}$$

where

$$[[t'_{kl}]] = t'_{kl} + P_f\left\{\delta_{kl} + \frac{1}{3} M^{p(1)}_{klmm}\left(\frac{1}{K_f} - C^s_{jjnn}\right)\right\},$$

$$\{\{t'_{kl}\}\} = t'_{kl} + \left\{\delta_{kl} + M^{*(1)}_{klrr}\frac{\phi}{3K_f(1-\phi)}\right\} P_f \tag{26}$$

and

$$C^{p(1)}_{ijkl} = \frac{1}{\phi} C^{*(1)}_{ijkl} + \frac{1}{1-\phi} C^s_{ijkl}. \tag{27}$$

We note that, in the anisotropic case, the deviatoric confining stress contributes to expel the fluid out of the porous solid material. Focusing our attention on the deformation of the porous solid material, we may obtain the drained response by setting $P_f = 0$ in equations (22) and (26) and the effective stress laws for $e^{(1)}_{ij}$ and $e^{p(1)}_{ij}$. Also, by setting $\Delta m = 0$ in equation (25), we may obtain, for example, the undrained response for hydrostatic confining stress $t'_{kl} = -P\delta_{kl}$ for the total volumetric strain as follows:

$$P = -K_u e^{(1)}_{ii}$$

$$K_u = \frac{3 + \frac{1}{3} M^{p(1)}_{nnmm}\left(\frac{1}{K_f} - C^s_{iill}\right)}{\frac{1}{3}\, C^{(1)}_{iikk} M^{p(1)}_{nnmm}\left(\frac{1}{K_f} - C^s_{jjll}\right) + 3\, C^{(1)}_{iikl} M_{klrs} C^s_{rsmm}} \tag{28}$$

where K_u is the anisotropic undrained bulk modulus for hydrostatic confining stress.

(c) Alternative Constitutive Equations. From the viewpoint that the fluid and the solid should be treated equally, we choose $e^{(1)}_{ij}$ and $e^{(2)}_{mm}$ as independent variables. The constitutive equations (21)–(23) can be rewritten with the help of equations (5), (15), and (18) as

$$t^s_{ij} = M^s_{ijkl}\left[\frac{1}{2}\,(\delta_{km}\delta_{ln} + \delta_{kn}\delta_{lm}) - (1-\phi)C^a_{klrs}M^s_{rsmn}\right] e^{(1)}_{mn} + (1-\phi)K_f M^s_{ijkl} C^a_{klrr} e^{(2)}_{ss} \tag{29}$$

$$P_f = -\frac{(1-\phi)^2}{\phi} K_f M^s_{rskl} C^a_{klii} e^{(1)}_{rs} - K_f\left[1 - \frac{(1-\phi)^2}{\phi} C^a_{iinn} K_f\right] e^{(2)}_{mm} \tag{30}$$

where

$$M^a_{ijkl} = M^{*(1)}_{ijkl} + (1-\phi)M^s_{ijkl} + \frac{(1-\phi)^2}{\phi} K_f \delta_{ij}\delta_{kl}$$

$$C^a_{ijkl} M^a_{klrs} = \frac{1}{2}\,(\delta_{ir}\delta_{js} + \delta_{is}\delta_{jr}). \tag{31}$$

It is worth noting that once $e^{(1)}_{ij}$ and $e^{(2)}_{mm}$ are given, we can calculate not only t^s_{ij} and P_f but also all the other kinematical quantities such as e^s_{ij}, $e^{p(1)}_{ij}$, $e^{*(1)}_{ij}$, e^f_{mm}, and Δm.

For many practical problems, the fluid can be assumed to be incompressible. Setting $e^f_{mm} = 0$ and $K_f \to \infty$, and choosing $e^{(2)}_{mm}$ and $e^{(1)}_{ij}$ as independent variables, the constitutive relations for the incompressible fluid case is obtained from the previous formulations (5), (15), (18), (21), and (22) as

$$t^s_{ij} = M^s_{ijkl} C^b_{klmn}\left[M^{*(1)}_{mnrs}\right.$$

Downloaded 02 May 2010 to 171.66.16.54. Redistribution subject to ASME license or copyright; see http://www.asme.org/terms/Terms_Use.cfm

$$+\frac{(1-\phi)\delta_{mn}C^b_{ppqt}M^s_{qtrs}}{C^b_{uuvv}}\Big]e^{(1)}_{rs}$$

$$+\frac{\phi\ M^s_{ijkl}C^b_{klmn}}{(1-\phi)C^b_{uuvv}}e^{(2)}_{ss} \tag{32}$$

$$P_f=-\frac{M^s_{ijkl}C^b_{klmm}}{C^b_{uuvv}}e^{(1)}_{ij}-\frac{\phi}{(1-\phi)^2C^b_{uuvv}}e^{(2)}_{ss}, \tag{33}$$

where

$$M^b_{ijkl}=M^{*(1)}_{ijkl}+(1-\phi)M^s_{ijkl}$$

$$C^b_{ijkl}M^b_{klrs}=\frac{1}{2}(\delta_{ir}\delta_{js}+\delta_{is}\delta_{jr}). \tag{34}$$

The lengthy calculation shows that the relations (32) and (33) can be obtained by considering the limit case $K_f\to\infty$ in the coefficients of $e^{(1)}_{ij}$ and $e^{(2)}_{mm}$ in equations (29) and (30).

(d) **Transverse Isotropy.** Since the transversely isotropic case has applications in many geological materials, we reduce our results for the anisotropic case to the transversely isotropic. Denoting direction cosines of the axis of symmetry by h_i, the constitutive relation (21) reduces to

$$t^s_{ij}=\lambda^s e^s_{mm}\delta_{ij}+2\mu^s e^s_{ij}+2\alpha^s(e^s_{im}h_jh_m+e^s_{jm}h_ih_m)$$
$$+\beta^s(\delta_{ij}h_kh_le^s_{kl}+h_ih_je^s_{mm})+\gamma^s h_ih_jh_kh_le^s_{kl}$$
$$e^s_{ij}=\lambda^s_1 t^s_{mm}\delta_{ij}+2\mu^s_1 t^s_{ij}+2\alpha^s_1(t^s_{im}h_jh_m+t^s_{jm}h_ih_m)$$
$$+\beta^s_1(\delta_{ij}h_kh_lt^s_{kl}+h_ih_jt^s_{mm})+\gamma^s_1h_ih_jh_kh_lt^s_{kl} \tag{35}$$

where the compliances $(\mu^s_1,\lambda^s_1,\alpha^s_1,\beta^s_1,\gamma^s_1)$ are expressed in terms of the moduli $(\mu^s,\lambda^s,\alpha^s,\beta^s,\gamma^s)$ as follows:

$$\mu^s_1=\frac{1}{4\mu^s}\qquad \alpha^s_1=\frac{-\alpha^s}{4\mu^s(\mu^s+\alpha^s)}\qquad \beta^s_1=\frac{\lambda^sB^s-\beta^sA^s}{2\mu^s(D^sA^s-C^sB^s)}$$

$$\lambda^s_1=-\frac{\lambda^s(D^sA^s-C^sB^s)+C^s(\lambda^sB^s-\beta^sA^s)}{2\mu^sA^s(D^sA^s-C^sB^s)}$$

$$\gamma^s_1=\frac{(\mu^s+\alpha^s)(\beta^sB^s-\gamma^sA^s)-\alpha^s\{2C^sB^s-(4\alpha^s+2\beta^s+2\gamma^s)A^s\}}{2\mu^s(\mu^s+\alpha^s)(D^sA^s-C^sB^s)}$$

$$A^s=2\mu^s+3\lambda^s+\beta^s,\quad B^s=4\alpha^s+3\beta^s+\gamma^s$$
$$C^s=\lambda^s+\beta^s,\quad D^s=2\mu^s+4\alpha^s+\beta^s+\gamma^s$$
$$A^s_1=\frac{D^s}{A^sD^s-B^sC^s},\quad B^s_1=-\frac{B^s}{A^sD^s-B^sC^s}$$
$$C^s_1=-\frac{C^s}{A^sD^s-B^sC^s},\quad D^s_1=\frac{A^s}{A^sD^s-B^sC^s}. \tag{36}$$

The constitutive relations (22) reduce to equations similar to the foregoing with the moduli $(\mu^{*(1)},\lambda^{*(1)},\alpha^{*(1)},\beta^{*(1)},\gamma^{*(1)})$ and the compliances $(\mu^{*(1)}_1,\lambda^{*(1)}_1,\alpha^{*(1)}_1,\beta^{*(1)}_1,\gamma^{*(1)}_1)$. The relations (24) and (27) reduce to

$$\mu^{*(1)}_1=\mu^{(1)}_1-\frac{1}{1-\phi}\mu^s_1,\qquad \mu^{p(1)}_1=\frac{1}{\phi}\mu^{*(1)}_1+\frac{1}{1-\phi}\mu^s_1 \tag{37}$$

for $(\mu^{*(1)}_1,\alpha^{*(1)}_1,\beta^{*(1)}_1,\lambda^{*(1)}_1,\gamma^{*(1)}_1)$ and $(\mu^{p(1)}_1,\alpha^{p(1)}_1,\beta^{p(1)}_1,\lambda^{p(1)}_1,\gamma^{p(1)}_1)$, respectively.

The effective stress laws for the overall strain and pore strain are

$$t'_{ij}+P_f\Big[\Big(1-\frac{D^sA^{(1)}-B^sC^{(1)}}{A^sD^s-B^sC^s}\Big)\delta_{ij}$$
$$-\Big(\frac{D^sB^{(1)}-B^sD^{(1)}}{A^sD^s-B^sC^s}\Big)h_ih_j\Big]$$
$$=\lambda^{(1)}e^{(1)}_{mm}\delta_{ij}+2\mu^{(1)}e^{(1)}_{ij}$$
$$+2\alpha^{(1)}(e^{(1)}_{im}h_jh_m+e^{(1)}_{jm}h_ih_m)$$
$$+\beta^{(1)}(\delta_{ij}h_kh_le^{(1)}_{kl}+h_ih_je^{(1)}_{mm})$$
$$+\gamma^{(1)}h_ih_jh_kh_le^{(1)}_{kl}$$

$$t'_{ij}+P_f\Big[\Big(1-\frac{D^sA^p-B^sC^p}{A^sD^s-B^sC^s}\Big)\delta_{ij}-\Big(\frac{D^sB^p-B^sD^p}{A^sD^s-B^sC^s}\Big)h_ih_j\Big]$$
$$=\lambda^pe^{p(1)}_{mm}\delta_{ij}+2\mu^pe^{p(1)}_{ij}+2\alpha^p(e^{p(1)}_{im}h_jh_m+e^{(1)}_{jm}h_ih_m)$$
$$+\beta^p(\delta_{ij}h_kh_le^{p(1)}_{kl}+h_ih_je^{p(1)}_{mm})+\gamma^ph_ih_jh_kh_le^{p(1)}_{kl} \tag{38}$$

It is straightforward to reduce the alternative constitutive relations (29) and (30) as well as the undrained bulk modulus for hydrostatic confining stress (28) for the transversely isotropic case.

(e) **Isotropy.** When the transverse isotropy is purely structural and the solid matrix is isotropic, α^s_1, β^s_1, and γ^s_1 in equation (35) vanish. When both the pore structure and the solid matrix are isotropic, then $\alpha^{*(1)}_1$, $\beta^{*(1)}_1$, and $\gamma^{*(1)}_1$ in the consitutive equations similar to equation (35) vanish. In this case, introducing the bulk moduli k^s, $k^{(1)}$, $k^{*(1)}$, and $k^{p(1)}$, equations (24) and (27) reduce to

$$\frac{1}{\mu^{*(1)}}=\frac{1}{\mu^{(1)}}-\frac{1}{(1-\phi)\mu^s},\qquad \frac{1}{\mu^{p(1)}}=\frac{1}{\phi\mu^{*(1)}}+\frac{1}{(1-\phi)\mu^s} \tag{39}$$

$$\frac{1}{k^{*(1)}}=\frac{1}{k^{(1)}}-\frac{1}{(1-\phi)k^s},\qquad \frac{1}{k^{p(1)}}=\frac{1}{\phi k^{*(1)}}+\frac{1}{(1-\phi)k^s} \tag{39}$$

With these constitutive relations and equations (39), we recover the effective stress laws for isotropic porous material obtained by Carroll [7]. Also, from equation (28), we recover the undrained bulk modulus for the isotropic case [7]. The alternative constitutive equations (29) and (30) reduce to

$$\frac{1}{3}t^s_{mm}=-P_s=\frac{k^s\Big\{k^{*(1)}+\dfrac{(1-\phi)^2}{\phi}K_f\Big\}}{k^{*(1)}+(1-\phi)k^s+\dfrac{(1-\phi)^2}{\phi}K_f}e^{(1)}_{kk}$$
$$+\frac{(1-\phi)k^sK_f}{k^{*(1)}+(1-\phi)k^s+\dfrac{(1-\phi)^2}{\phi}K_f}e^{(2)}_{mm}$$

$$\tilde{t}^s_{ij}=\frac{2\mu^s\mu^{*(1)}}{\mu^{*(1)}+(1-\phi)\mu^s}\tilde{e}^{(1)}_{ij} \tag{40}$$

$$P_f=\frac{-(1-\phi)^2k^sK_f}{\phi k^{*(1)}+\phi(1-\phi)k^s+(1-\phi)^2K_f}e^{(1)}_{rr}$$
$$-\frac{K_f\{\phi k^{*(1)}+\phi(1-\phi)k^s\}}{\phi k^{*(1)}+\phi(1-\phi)k^s+(1-\phi)^2K_f}e^{(2)}_{rr}.$$

where $\tilde{}$ indicates the deviatoric part of the tensor.

When the fluid is incompressible, the alternative constitutive relations (32) and (33) reduce to

$$\frac{1}{3}t^s_{mm}=-P_s=k^se^{(1)}_{mm}+\frac{\phi k^s}{1-\phi}e^{(2)}_{mm}$$

$$\tilde{t}^s_{ij}=\frac{2\mu^s\mu^{*(1)}}{\mu^{*(1)}+(1-\phi)\mu^s}\tilde{e}^{(1)}_{ij} \tag{41}$$

$$P_f=-k^se^{(1)}_{kk}-\frac{\phi(k^{*(1)}+k^s(1-\phi))}{(1-\phi)^2}e^{(2)}_{mm}$$

(f) **Comparison With Biot's Formulation.** The constitutive relations reestablished in this paper are basically identical to those by Biot. The solid stress tensor (σ_{xx}, σ_{xy}, σ_{xz}, etc.) and the fluid stress σ in Biot's formulation corresponds to $(1-\phi)t^s_{ij}$ and $-\phi P_f$ in this formulation, respectively. The strain components of the solid (e_{xx}, e_{yy}, e_{zz}, $1/2\ e_{xy}$, $1/2e_{yz}$, $1/2e_{xz}$) and the fluid volumetric strain ϵ in Biot's theory likewise correspond to $e^{(1)}_{ij}$ and $e^{(2)}_{mm}$, respectively. Comparing the constitutive relations for the isotropic case (40) with those of Biot, we relate the material constants in Biot's theory, i.e., N, A, Q, and R to those in our formulation as follows:

Downloaded 02 May 2010 to 171.66.16.54. Redistribution subject to ASME license or copyright; see http://www.asme.org/terms/Terms_Use.cfm

$$\frac{2}{3}N+A=\frac{(1-\phi)k^s\{\phi k^{*(1)}+(1-\phi)^2K_f\}}{\phi k^{*(1)}+\phi(1-\phi)k^s+(1-\phi)^2K_f}$$

$$N=\mu^{(1)}=\frac{(1-\phi)\mu^s\mu^{*(1)}}{\mu^{*(1)}+(1-\phi)\mu^s} \tag{42}$$

$$Q=\frac{\phi(1-\phi)^2k^sK_f}{\phi k^{*(1)}+\phi(1-\phi)k^s+(1-\phi)^2K_f}$$

$$R=\frac{\phi K_f\{\phi k^{*(1)}+\phi(1-\phi)k^s\}}{\phi k^{*(1)}+\phi(1-\phi)k^s+(1-\phi)^2K_f}.$$

It is important to note that the introduction of the new kinematical quantity $e^{(2)}_{mm}$ in Carroll's constitutive theory has made this comparison possible. Biot [4] obtained equations equivalent to equation (42) by considering the jacketed and the unjacketed case. He expressed the material constants $2/3\ N+A$, Q, and R in terms of physically measurable constants γ, κ, and δ which correspond to $\phi(1/K_f-1/k^s)$, $1/k^{(1)}$, and $1/k^s$, respectively. While Biot did not have any kinematical quantity related to porosity change, he had the notion of strain for the pore space and used the fact that the porosity does not change in an unjacketed test in the hydrostatic case. By making clear the three distinct deformation mechanisms, i.e., the deformation of solid matrix, deformation due to relative pore geometry change, and fluid compaction throughout its formulation, Carroll's approach has provided a new insight into the notion that Biot did not express explicitly in his formulation.

4 Dynamic Fluid Flow of Fluid-Saturated Porous Material

(a) Kinematics. We recover the porous fluid material if we remove the solid matrix from the fluid-saturated porous material exactly in the same manner as we obtain the porous solid material on removal of the fluid from the fluid-saturated porous material. From the point of view that the solid and the fluid should be treated equally, we now consider the overall dynamic flow in fluid-saturated porous material. Applying the same methods employed previously for the porous solid material to the porous fluid material, we introduce the average strain rates of the porous fluid material, the fluid (without pores) and the pore space (of the porous fluid material), denoted by $d^{(2)}_{ij}$, d^f_{ij}, and $d^{p(2)}_{ij}$, respectively. Equations (3) and (7) give

$$d^{(2)}_{ij}=\phi d^f_{ij}+(1-\phi)d^{p(2)}_{ij},\quad d^{(2)}_{ij}=d^f_{ij}+d^{*(2)}_{ij},$$
$$d^{*(2)}_{ij}=(1-\phi)(d^{p(2)}_{ij}-d^f_{ij}). \tag{43}$$

Equations (43) are the dynamic counterpart of equations (18) and are connected by the relation (44):

$$d^{(2)}_{mm}=\dot{e}^{(2)}_{mm},\ d^f_{mm}=\dot{e}^f_{mm},\ d^{p(2)}_{mm}=\dot{e}^{p(2)}_{mm},$$
$$d^{*(2)}_{mm}=\dot{e}^{*(2)}_{mm}. \tag{44}$$

(b) Constitutive Equations. Throughout the pore walls of the actual sample we will find the pointwise shear stress distributions due to the fluid viscosity. This shear interaction between the fluid and the solid on the pore boundaries cannot be investigated by the methods employed here because the quantities averaged over the volumes cannot describe the effect of the pointwise shear stress distribution. Considering the superposition within the linear theory, this pointwise shear interaction on the pore walls can be considered separately from the volume average quantities.

In this section, we consider the response of the representative volume element to constant dynamic tractions on the outer boundary and zero tractions on the pore boundary, corresponding to the constant boundary conditions (20) for the static case. Then

$$\mathcal{P}^{(2)}: t_i=t''_{ij}n_j \quad \text{on} \quad B_0; \qquad t_1=0 \quad \text{on} \quad B_p \tag{45}$$

where t''_{ij} is a constant, and given by (6). The response equations are given as follows.

$$t^f_{ij}+P_f\delta_{ij}=\lambda_f d^f_{kk}\delta_{ij}+2\mu_f d^f_{ij} \tag{46}$$

$$t''_{ij}=M^{*(2)}_{ijkl}\,d^{*(2)}_{kl},\quad d^{*(2)}_{ij}=C^{*(2)}_{ijkl}\,t''_{kl} \tag{47}$$

with

$$C^{*(2)}_{ijkl}=C^{(2)}_{ijkl}-\frac{1}{\phi}C^f_{ijkl} \tag{48}$$

where

$$C^f_{ijkl}=\lambda_f\delta_{ij}\delta_{kl}+\mu_f(\delta_{ik}\delta_{jl}+\delta_{il}\delta_{kj}). \tag{49}$$

As previously discussed, within the linear theory, the volumetric average kinetical and kinematical quantities are related through the local response equations and therefore λ_f and μ_f in equation (46) are viscosities of fluid without pores. Equation (47) is the dynamic counterpart of equation (22). Using the effective viscosity tensor of the porous fluid material $C^{(2)}_{ijkl}$, equation (47) can be proven in the same manner that Carroll and Katsube [7] obtained equation (22). In lieu of equation (47), the relationships

$$t''_{ij}=M^{(2)}_{ijkl}d^{(2)}_{kl},\quad d^{(2)}_{ij}=C^{(2)}_{ijkl}t''_{kl} \tag{50}$$

may be used in addition to equation (46) as constitutive relations governing the flow.

5 Concluding Remarks

Constitutive relations for deformation of and flow through a porous media have been developed using a micromechanical approach along the lines developed by Carroll [7, 8]. Here additional kinematical quantities have been defined that permit a correspondence to the established theory of Biot [1–4]. Furthermore, the present theory accounts for viscosity effects in the fluid, which are present whenever flow occurs. The relative importance of viscosity compared to the resistance to fluid permeation (considered by Biot) depends on the particular boundary value problem under consideration. For example, this term will be of greater importance in close to impermeable boundaries. Such problems have been studied by Katsube [10] using a continuum theory of mixtures.

Acknowledgement

The author is thankful for valuable criticisms from Prof. M. M. Carroll during the preparation of this manuscript. Major support was provided by an Amelia Earhart Fellowship from Zonta International.

References

1 Biot, M. A., "General Theory of Three-Dimensional Consolidation," *Journal of Applied Physics*, Vol. 12, 1941, pp. 155–164.

2 Biot, M. A., "Theory of Elasticity and Consolidation for a Porous Anisotropic Solid," *Journal of Applied Physics*, Vol. 26, 1955, pp. 182–185.

3 Biot, M. A., "General Solutions of the Equations of Elasticity and Consolidation for a Porous Material," *Journal of Applied Physics*, Vol. 78, 1956, pp. 91–96.

4 Biot, M. A., and Willis, D. G., "The Elastic Coefficients of the Theory of Consolidation," ASME Journal of Applied Mechanics, Vol. 24, 1957, pp. 594–601.

5 Rice, J. R., and Cleary, M. P., "Some Basic Stress Diffusion Solutions for Fluid-Saturated Elastic Porous Media With Compressible Constituents," *Reviews of Geophysics and Space Physics*, Vol. 14, 1976, pp. 227–241.

6 Nur, A., and Byerlee, J. D., "An Exact Effective Stress Law for Elastic Deformation of Rock With Fluids," *Journal of Geophysical Research*, Vol. 76, 1971, pp. 6414–6419.

7 Carroll, M. M., "Mechanical Response of Fluid-Saturated Porous Materials," *Proceedings of 15th International Congress of Theoretical and Applied Mechanics*, Rimrott, F. P. J., and Tabarrok, B., eds., 1980, North-Holland, New York.

8 Carroll, M. M., and Katsube, N., "The Role of Terzaghi Effective Stress in Linearly Elastic Deformation," ASME *Journal of Energy Resources Technology*, Vol. 105, 1983, pp. 509–511.

9 Carroll, M. M., "An Effective Stress Law for Anisotropic Elastic Deformation," *Journal of Geophysical Research*, Vol. 84, 1979, pp. 7510–7512.

10 Katsube, N., "Mechanical Response of Fluid-Filled Poroelastic Solids," Ph.D. Dissertation, Univesity of California-Berkeley, 1982.

Downloaded 02 May 2010 to 171.66.16.54. Redistribution subject to ASME license or copyright; see http://www.asme.org/terms/Terms_Use.cfm

Asymptotic Approximation and Perturbation Stream Functions in Viscous Flow Calculations

B. S. Berger
Department of Mechanical Engineering,
University of Maryland,
College Park, Md. 20742
Mem. ASME

An asymptotic approximation technique is shown to substantially decrease the number of interations necessary for the accurate computation of steady solutions for viscous incompressible flows. A numerical study of flows exterior to a circular cylinder indicates that the technique reduces the required number of iterations by a factor of 10. The flux formulation of the vorticity stream function solution for the flow of a viscous incompressible fluid external to a circular cylinder requires the solution of the Poisson equation for the stream function. The use of the FACR (1), fast direct Poisson equation solver leads to serious errors in the computation of the stream function near the cylinder. However it is shown that these errors are eliminated through the introduction of a perturbation stream function.

Introduction

The first numerical solution to a viscous, incompressible flow external to a circular cylinder appeard in 1933, [1]. Study of the problem continues into the present. Bibliographies of the considerable body of work are given in [2–8, 11]. As shown in Table 2 of [2], steady and time-dependent methods have been used to solve the steady flow case. Both methods are discussed in [3] where it is shown that certain steady and time-dependent methods are equivalent.

A numerical study was made, [12], of viscous incompressible flows external to a circular cylinder. The computational algorithms used were a modification of the flux formulation of the vorticity-stream function solution given in [4–6]. It was found that, for steady flows, the convergence rate decreased rapidly as asymptotic values were approached, thus requiring many interations before sufficient accuracy was attained. In the following, an asymptotic expansion is used to approximate the asymptotic values of the stream function and drag coefficient. For the same accuracy, the number of iterations required by the asymptotic method is one-tenth of the number required by direct computation.

In the numerical study of [12], the Liebmann iteration solution of the Poisson equation used in [4–6] was replaced with the direct method, FACR (1), [13–15]. It was found that the stream function, ψ, computed from the vorticity, w, using the FACR (1) Poisson equation solver exhibited large relative errors in the boundary region of the cylinder. These errors seriously effect the accuracy of the computed values of vorticity on the surface of the cylinder. The origin of the errors was found to be the large variation of ψ as a function of the radial variable. This difficutly is resolved through the introduction of a perturbation stream function which vanishes on the surface of the cylinder and at infinity.

Contributed by the Applied Mechanics Division for publication in the JOURNAL OF APPLIED MECHANICS.
Discussion on this paper should be addressed to the Editorial Department, ASME, United Engineering Center, 345 East 47th Street New York, NY 10017, and will be accepted until two months after final publication of the paper itself in the JOURNAL OF APPLIED MECHANIC. Manuscript received by ASME Applied Mechanics Division, November, 1983 final revision. May 1984.

Asymptotic Expansion

Assuming a steady flow, let $f(T_i)$ represent any one of the spatially dependent flow quantities such as stream function, velocity, or vorticity evaluated at a specific spatial point or a quantity defined by a spatial integral such as the coefficients of drag, lift, or torque. The independent variable, T_i, may represent physical or scaled time for time-dependent methods or an interation index in the case of steady methods. For the cases studied it was found that there exists some T_m such that for $T_i > T_m$, $f(T_i)$ approached an asymptotic value monotonically. It follows that $f(T_i)$ may be approximated by a partial sum of an asymptotic series of the form

$$f(T) \sim \sum_{k=0}^{n} a_k T^{-k} \tag{1}$$

See [10] for a discussion of asymptotic expansions. From (1) it follows that a_0 is the asymptotic value of $f(T)$. The coefficients, a_k, in (1) were found by a pointwise fitting of a numerical solution. Figure 1 shows the coefficient of drag, C_D, for a circular cylinder in a uniform flow as a function of time for Re = 10. The solution for $0 < t < 9.9975$, indicated by a solid line in Fig. 1, was computed using the vorticity-stream function formulation over a 64 × 64 mesh with a time step of 0.0075. This solution was approximated by choosing a_K so that the sum of m terms of (1) equaled the computed values for m different values of T. Solving (1) for a_0, $n = 1$, gives the two term approximation

$$a_0(2) = (T_1 \cdot f(T_1) - T_2 \cdot f(T_2))/\Delta T_1 \tag{2}$$

where $\Delta T_1 \equiv T_1 - T_2$. Similarly for $n = 2$, the three term approximation is given by

$$a_0(3) = (T_1^2 \cdot f(T_1) - 2 \cdot T_2^2 f(T_2) + T_3^2 \cdot f(T_3))/(2 \cdot \Delta T_1^2) \tag{3}$$

Copyright © 1985 by ASME
Downloaded 02 May 2010 to 171.66.16.54. Redistribution subject to ASME license or copyright; see http://www.asme.org/terms/Terms_Use.cfm

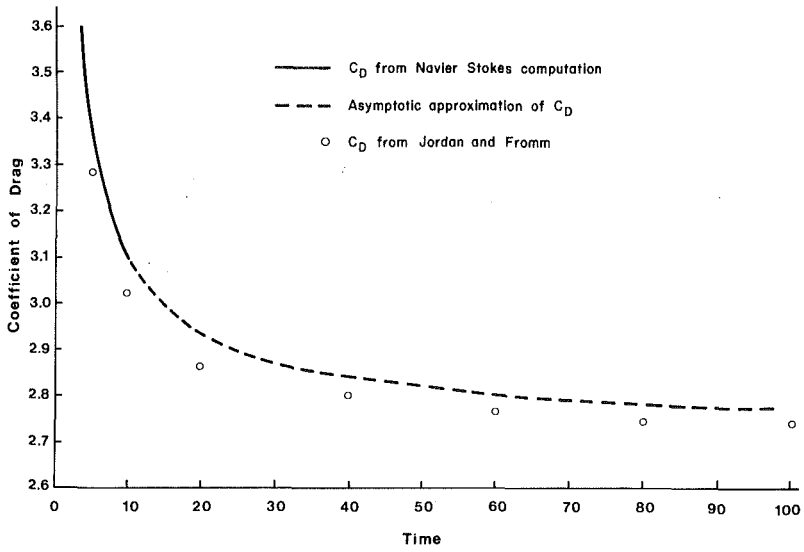


Fig. 1 Coefficient of drag C_D versus time

where $\Delta T_1 = T_1 - T_2 = T_2 - T_3$. The values of time given in the first column of Table 1 denote the upper limit, T_1, of the set of equally spaced time values, T_1, T_2, T_3 with $\Delta T_1 = 0.9975$. For $T = 9.9975$ then $T_1 = 9.9975$, $T_2 = 9.000$, and $T_3 = 8.0025$. The corresponding values of $a_0(2)$ and $a_0(3)$ in Table 1 were computed from (2) and (3). In [4] it was found that $C_D = 2.74$. This result which was attained at $T = 90$, required 11520 iterations with a time step, $\Delta T = 0.0078125$. From column three of Table 1 it is seen that $C_D = 2.737$ is given by (3) for $0 < T < 9$ which requires 1200 iterations with $\Delta T = 0.0075$.

The coefficients a_0, a_1, and a_2 were evaluated for the case $T = 9.9975$, $\Delta T_1 = 0.9975$. Substitution of these into (1) gave the dotted curve shown in Fig. 1. The points in Fig. 1, denoted by circles were scaled from Fig. 14 of [4]. Differences between the two solutions may be attributed to differing initial conditions used in starting the solution, differences in grid dimensions and scaling errors. However both solutions have the same asymptote.

The effect of varying ΔT_1 on a_0 (3) was studied for $T_1 = 9.9975$ with $\Delta T_1 = 0.9975$, 2.0025, and 2.985. The corresponding values of a_0 (3) were a_0 (3) = 2.739, 2.741, 2.757. It appears that a_0 (3) is not sensitive to changes in ΔT_1. However for small values of ΔT_1, equation (3) involves the difference of large and nearly equal numbers that may introduce large errors in a_0 (3).

The asymptotic approximation, (1), was applied to the computation of the steady state values of the stream function for the flow of an incompressible-viscous fluid between rotating cylinders. Since the stream function is known exactly for the two-dimensional laminar case it was possible to make a pointwise comparison over the spatial grid. As in the case of C_D for the flow around circular cylinder, the asymptotic approximation led to a substantial reduction in the number of iterations required to find the steady state values of the stream function.

The coefficients a_K in (1) may be calculated by methods over than collocation as follows. Let $x = 1/T$ in (1) to give a power series in x^K for $1/T_1 < x < 1/T_2$ where $T_1 > T_2$. Then $f(x)$ may be approximated in the interval by a series of orthogonal polynominals and a_0 found. Such computations, carried out for the case of flow between rotating cylinders, showed the method to be no more effective in determining a_0 than the simpler collocation technique.

To determine the effectiveness of approximations, the asymptotic series, (1) was replaced by expansions of the form

Table 1 Asymptotic values of C_D for various time intervals

Time	$a_o(2)$	$a_o(3)$
5.010	2.926	2.851
6.000	2.886	2.804
7.005	2.853	2.772
8.010	2.828	2.751
9.000	2.808	2.737
9.9975	2.794	2.739

Table 2 Exact, unmodified and modified values of the stream function

r	$\psi_{EX.}$	$\psi_{U.M.}$	$\psi_{MOD.}$
1.10316	.19237(-4)	.13433 (-1)	.20142 (-4)
1.21695	.82418(-4)	.26910 (-1)	.84233(-4)
1.34248	.19908(-3)	.40440(-1)	.20181 (-3)
1.48097	.38085(-3)	.54037 (-1)	.38447(-3)
7.12419	.42790(-1)	.31095	.42808(-1)
19.0153	.33118	.73250	.33121
50.7540	2.3970	2.9258	2.3970
135.468	17.125	17.741	17.125
485.418	220.00	220.14	220.00

$$f(T) = a_0 + b_0 \exp(-b_1 T) \tag{4}$$

and

$$f(T) = a_0 + (b_0 + b_1 T) \exp(-T) \tag{5}$$

where a_0 is the asymptotic value of $f(T)$. The constants appearing in (4) and (5) were evaluated through collocation of the values of C_D over various intervals of T. None of the asymptotic values found, a_0, were as accurate as those given by (2) or (3) for the series (1).

Perturbation Stream Functions

The vorticity-stream function method requires the computation of the stream function from vorticity, [4–6], though

Downloaded 02 May 2010 to 171.66.16.54. Redistribution subject to ASME license or copyright; see http://www.asme.org/terms/Terms_Use.cfm

$$\nabla^2\psi = -w \tag{6}$$

Consider the two-dimensional laminar flow between rotating cylinders as a convenient test case for the numerical study of errors in the computation of the stream function. For the case of a fixed inner cylinder of radius $r=1$ and a rotating outer cylinder, the stream function in polar coordinates is known to be

$$\psi = C_0(\ln(r) - r^2/2 + 0.5) \tag{7}$$

where C_0 is a constant. For exterior flows, discussed subsequently, a change of variable, $r=\exp(x)$ is advantageous, [4–6]. The assumption of a uniform 64 × 64 grid in Θ and x, with $\Delta\Theta = \Delta x$, places the outer boundary at $r=535.4916$ on which $\psi = 267.734$ for $C_0 = 0.0018674492$. Then $0 \le \psi \le 267.734$. The exact values of $-\psi$, denoted by ψ_{EX}, are given in Table 2 as a function of r.

Equation (6) was solved over a 64 × 64 grid using the FACR (1) Poisson equation solver, [13–15], given the exact values of w over the grid and exact boundary conditions on the inner and outer cylinders. The results of this unmodified computation of $-\psi$ are denoted by $\psi_{U.M.}$ and given in Table 2. It is seen that these solutions are seriously in error over the range $0 \le r \le 50.750$. Of particular significance are the large relative errors near the boundary of the inner cylinder. The vorticity on the surface of the inner cylinder is found by differencing ψ which implies that errors in ψ cause larger errors in surface vorticity. The large variation of ψ as a function of r appears to be the cause of the errors. An iterative solution to the vorticity-stream function formulation of the Helmholtz equations for the flow between two rotating cylinders in terms of $\psi_{U.M.}$ assuming the exact vorticity field and boundary conditions, initially, failed to converge in 200 iterations.

The difficulty was resolved through the introduction of a perturbation stream function, ψ_1, such that $\psi = \psi_1 + h$, $\psi_1 = 0$ on $r=1$, and ψ_1 vanishes or is small on the outer boundary. For the test case, it is seen that the term $C_0 r^2/2$ dominates in (7) as r increases. Then let

$$\psi = \psi_1 + C_0(1 - r^2)/2 \tag{8}$$

Since $\psi = 0$ on $r=1$ it follows from (8) that $\psi_1 = 0$ on $r=1$. Equations (7) and (8) imply that $\psi_1 = C_0$ in (r) so that ψ_1 is not large on the outer boundary. Substituting (8) into (6) gives:

$$\nabla^2\psi_1 = -w + 2\,C_0 \tag{9}$$

Solving (9) with FACR (1), for the test case, assuming the exact values of w, C_0, and boundary conditions, and substituting into (8) gives column four of Table 2, ψ_{MOD}. It is seen that these values are in very close agreement with ψ_{EX}. Iterative solutions for the flow between rotating cylinders based on ψ_{MOD} converged to the exact solution. In these computations, the exact solution for ψ was assumed to be known on the outer cylinder but not on the inner and initial estimates were made for the vorticity field. For the test case, the choice of h was predicated on a knowledge of the exact solution, which for the general case is not available. However, for exterior flows with boundary conditions given at infinity h may be readily found.

Consider the flow around a circular cylinder of a stream that is uniform at infinity. Then at infinity $\psi = r \cdot \sin\Theta$ with $U=1$. For the 64 × 64 grid, $0 \le \psi \le 535.4916 \sin\Theta$. From the foregoing, it is clear that ψ given by (6), utilizing FACR (1), will have large relative errors near the surface of the cylinder, $r=1$. Define a perturbation stream function such that

$$\psi = \psi_1 + (r - 1/r)\sin\Theta \tag{10}$$

Then $\psi_1 = 0$ on $r=1$ and $r=\infty$. Substituting into (6) gives

$$\nabla^2\psi_1 = -w \tag{11}$$

Comparisons with analytic solutions are not possible, however numerical tests carried out for the steady solution, $\mathrm{Re}=10$ and unsteady solutions for $\mathrm{Re}=400$ and 1000 show that convergence and accuracy are significantly improved if (10) and (11) are used rather than (6).

Conclusions

An asymptotic expansion technique has been shown to substantially decrease the number of iterations necessary for the computation of steady-state solutions for viscous incompressible flows. For the example given of flow exterior to a circular cylinder the technique reduced the required number of iterations for the determination of C_D by a factor of 10. The technique requires a minimal computational effort and may be readily incorporated into existing computer codes. There are very few references, [3, 11], in the literature of extrapolations to solutions of steady state flow problems. In [3] there is reference to a very approximate graphical method. An exponential extrapolation is alluded to in [11], where it was used to estimate a single value of C_D from published data for the purpose of checking a numerical solution. It appears that asymptotic expansion methods have not been employed in any systematic way to reduce computational effort in steady flow computations.

The use of perturbation stream functions in conjunction with the FACR (1) algorithm has been shown to be essential for exterior problems formulated in terms of vorticity and stream function. In [4] plots of solutions for a perturbation stream function are given. However, no mention is made regarding the form of the perturbation stream function nor whether it was used in the calculations. In [4] the Liemann iteration technique is employed to solve the Poisson equation.

Acknowledgments

The author wishes to express his appreciation to Dr Oscar Manley, D.O.E. and Professor Peter Grootenhuis of the Imperial College of Science and Technology, London for their encouragement. The study was supported by the Department of Energy under project number DE-A505-81ER 10809. A000.

References

1 Thom, A., "The Flow Past Ciorcular Cylinders at Low Speeds," *Proc. Roy. Soc.*, Series *A*, Vol. 141, 1933, pp. 651–666.

2 Fornberg, B., "A Numerical Study of Steady Viscous Flow Past A Circular Cylinder," *J. Fluid. Mech.*, Part 4, Vol. 98, *4*, 1980, pp. 819–855.

3 Roache, P. J., *Computational Fluid Dynamics*, Hermosa Publishers, Albuquerque N. W., 1976.

4 Jordan, S. K., "Numerical Solutions for Time-Dependent, Viscous, Incompressible Fluid Flow Past a circle, Dissertation," *DEpt. of Aero. and Astro.*, Stanford Univ., Dec., 1969.

5 Jordan, S. K., and Fromm, J. E., "Laminar Flow Past a Circle in a Shear Flow," *Physics of Fluids*, Vol. 15, No. 6, 1972, pp. 972–976.

6 Jordan, S. K., and Fromm, J. E., "Oscillatory Drag, Lift and Torque on a Cylinder in a Uniform Flow," *Physics of Fluids*, Vol. 15, No. 3, 1972, pp. 371–376.

7 Sarpkaya, T., "Vortex Induced Oscillations, a Selective Review," ASME JOURNAL OF APPLIED MECHANICS, Vol. 46, No. 2, June 1979, pp. 241–258.

8 McCroskey, W. J., "Some Current Research in Unsteady Fluid Dynamics," ASME *Journal of Fluids Engineering*, Vol. 99, No. 1, Mar. 1977, pp. 8–39.

9 Kirstein, A. F., "The Hyperbolic Character of Certain Experimental Results Which Tend Towards Limiting Values," N.B.S., Tech. Note 435, Nov. 1967.

10 Erdelyi, A., *Asymptotic Expansions*, Dover, New York, 1956.

11 Thoman, D., and Szewczyk, A. A., "Time Dependent Viscous Flow Over a Circular Cylinder," *Physics of Fluids Supplement*, Vol. II, 1969, pp. 76–87.

12 Berger, B. S., "Viscous, Incompressible, Time-Dependent Fluid Flow Around a Circular Cylinder," Tech. Report No. 83-11-17, Univ. of Md. and D.O.E., Nov. 17, 1983.

13 Temperton, C., "Direct Methods for the Solution of the Discrete Poisson Equation: Some Comparisons," *J. Comp. Phys.*, Vol. 31, 1979, pp. 1–20.

14 Temperton, C., "On the FACR (1) Algorithm for the Discrete Poisson Equation," *J. Comp. Phys.*, Vol. 34, 1980, pp. 314–329.

15 Hockney, R. W., "The Potential Calculation and Some Applications," *Methods of Computational Physics*, Academic Press, New York, Vol. 9, 1969, pp. 135–211.

Downloaded 02 May 2010 to 171.66.16.54. Redistribution subject to ASME license or copyright; see http://www.asme.org/terms/Terms_Use.cfm

Transient Buoyant Convection of a Contained Fluid Driven by the Changes in the Boundary Temperatures

J. M. Hyun
Department of Mechanical Engineering,
Clarkson College of Technology,
Potsdam, New York 13676
Mem. ASME

Finite-difference numerical solutions are obtained for transient buoyant convection at high Rayleigh numbers of a Boussinesq fluid in a closed cylinder. We consider the linear motions that occur due to a small change in the boundary temperature profiles linear in the vertical coordinate. Previous theoretical studies showed that the meridional circulation, driven by the sidewall boundary layer pumping, brings about the final state on a time scale $t_h = R_a^{1/4} N^{-1}$, where N is the Brunt-Väisälä frequency. By choosing t_h as the time scale of interest, the theory filters out the internal-gravity oscillations of time scale N^{-1}. New details on the radial and vertical structures of the flow and temperature fields are presented. The impact of the internal-gravity oscillations on the temperature field is shown to be minor. However, the evolution of the velocities is highly oscillatory in time due to the dominant presence of the internal-gravity oscillations. Numerically calculated contour maps of the temperature and stream function are constructed, which illustrate the effect of Ra on the flow patterns and on the temperature adjustment process.

1 Introduction

We are concerned with unsteady buoyant convective motions which occur during the transient adjustment process of a contained Boussinesq fluid to the change in the thermal boundary conditions. Consider a closed container [of aspect ratio, i.e., height/width, of (1)] enclosing a stably stratified fluid at rest. At the initial state the thermal stratification of the fluid system is characterized by the Brunt-Väisälä frequency N_i. At $t = 0$, the temperature of the container wall is impulsively altered by a small amount to a new temperature profile corresponding to the new Brunt-Väisälä frequency N_f [$= N_i + \Delta N$] and is maintained so thereafter. The resulting transient buoyant fluid motion was termed "heat-up by Veronis [1]. This is a useful theoretical model for the recent technological applications of such flows as the natural convection in a nuclear reactor during various types of power transients, transient convective heat transfer inside the fuel tank in a spacecraft, ect. More specific and relevant applications of this flow model were discussed by Jischke and Doty [2].

As was remarked by Jischke and Doty [2], the problem of transient buoyant flows of a contained fluid has received little attention. This is because of the complexity of the flows stemming from the inherent coupling between the buoyant boundary layers on the walls (for large Rayleigh number Ra) and the interior core. Here we restrict our interest to the flow regime of $Ra >> 1$; we will deal with stably stratified fluids only. The Prandtl number is assumed to be 0(1); and we will study laminar flows exclusively [2].

In a pioneering paper, Sakurai and Matsuda [3], based on physical scaling argument under the assumption of $\epsilon_N \equiv \Delta N/N_i << 1$, derived an analytical solution for the transient buoyant motion of a Boussinesq fluid in a vertically mounted cylinder. They considered the temperature profiles linear in the vertical coordinate z. It was clearly demonstrated that a meridional circulation, which is driven by a buoyant sidewall boundary layer pumping mechanism, redistributes the fluid, thereby bringing about the new equilibrium state of stratification N_f. The time scale for the temperature adjustment process in the interior was shown to be $t_h = Ra^{1/4} N^{-1}$. An extension of this linearized problem to more general temperature profiles at the walls was made by Jischke and Doty [2]. These theoretical solutions produce information vital to a proper understanding of the fundamental dynamical process in the transient buoyant flows. However, the quantitative correctness of these theoretical solutions has not been verified by other numerical or experimental investigations.

In the theory, the equations were scaled by using t_h. This choice of time scale removes from the theory processes occurring in time scales shorter than t_h. One of the serious consequences is that the interval-gravity oscillations, which

Contributed by the Applied Mechanics Division for publication in the JOURNAL OF APPLIED MECHANICS.
Discussion on this paper should be addressed to the Editorial Department, ASME, United Engineering Center, 345 East 47th Street, New York, N.Y. 10017, and will be accepted until two months after final publication of the paper itself in the JOURNAL OF APPLIED MECHANICS. Manuscript received by ASME Applied Mechanics Division, May, 1983; final revision, April, 1984.

Copyright © 1985 by ASME
Downloaded 02 May 2010 to 171.66.16.54. Redistribution subject to ASME license or copyright; see http://www.asme.org/terms/Terms_Use.cfm

occur in a time scale $0(N^{-1})$, are not included in the theoretical solutions. These internal-gravity oscillations, which are excited by the abrupt change of the boundary temperatures, are supported by the restoring force of the stable stratification. It is, therefore, important to inquire as to the impact of the internal-gravity oscillations on the flow field.

In this paper we present the results of finite-difference numerical solutions of the full Navier-Stokes equations describing transient buoyant convection of a Boussinesq fluid in a cylinder. The model problem to be considered is the same as that of Sakurai and Matsuda [3], i.e., the initial temperature distribution is linear in z and the wall temperature profile is changed to another linear function of z. This configuration was selected because, owing to its maximal geometrical simplicity, the calculations will illuminate the essential character of the flow central to transient buoyant convection generated by the changes in the boundary temperatures. Obviously, the additional advantage is that explicit, closed-form analytical solutions are available for this simple setup [2, 3], which enables direct comparisons with the numerical results.

This paper provides the detailed results on the radial and vertical structures of the transient flow and temperature fields over a range of Rayleigh number ($Ra = 10^6 \sim 10^8$). Computations were made for the linear flow regime ($\epsilon_N << 1$) to conduct specific comparisons with the theory. It is found that there exist significant discrepancies for the flow details between the numerical results and the theoretical solutions. The numerical solutions of the flow evolution are highly oscillatory in time, which is in contrast to the exponentially decaying flows predicted by the theory. This is due principally to the dominant presence of the high-frequency internal-gravity oscillations, which were filtered out in the theory. We note that the amplitudes of these oscillations in the flow field are substantially greater than the magnitudes of the monotonically decaying part of the flows. The spatial variations of the flow field are more complex than were described by the theoretical solutions. The temperature field exhibits comparatively better agreement with the theory. However, the scaled nondimensional temperature deviations from the initial profile show considerable variations in the vertical coordinate. Contour maps of the temperature and stream function are constructed to delineate the effect of Ra on the boundary layer structures and on the patterns of the meridional circulation in the interior.

2 Theoretical Development

In this section we briefly recount the theoretical analysis of [2] and [3].

Consider a cylinder of radius a and height h. The relevant fluid properties are kinematic viscosity ν, thermal diffusivity κ, and coefficient of volumetric expansion α. These properties are assumed to be constant.

The governing incompressible Navier-Stokes equations for a Boussinesq fluid are

$$\frac{\partial u}{\partial t} = -\frac{1}{r}\frac{\partial}{\partial r}(ru^2) - \frac{\partial}{\partial z}(uw) - \frac{1}{\rho_r}\frac{\partial p}{\partial r} + \nu\left(\nabla^2 u - \frac{u}{r^2}\right), \tag{1}$$

$$\frac{\partial w}{\partial t} = -\frac{1}{r}\frac{\partial}{\partial r}(ruw) - \frac{\partial}{\partial z}(w^2) - \frac{1}{\rho_r}\frac{\partial p}{\partial z} + \alpha g(T - T_r) + \nu\nabla^2 w, \tag{2}$$

$$\frac{\partial T}{\partial t} = -\frac{1}{r}\frac{\partial}{\partial r}(ruT) - \frac{\partial}{\partial z}(wT) + \kappa\nabla^2 T, \tag{3}$$

$$\frac{1}{r}\frac{\partial}{\partial r}(ru) + \frac{\partial w}{\partial z} = 0, \tag{4}$$

where

$$\nabla^2 = \frac{1}{r}\frac{\partial}{\partial r}r\frac{\partial}{\partial r} + \frac{\partial^2}{\partial z^2},$$

(u,w) are the velocity component in the radial (r) and vertical (z) direction, respectively, t is the time, p is the reduced pressure and T is the temperature.

The equation of state is

$$\rho = \rho_r[1 - \alpha(T - T_r)] \tag{5}$$

in which ρ is density and subscript r denotes the reference values.

At the initial state, the fluid system is at rest and the temperature distribution is given as T_i:

$$u = w = 0, \quad T = T_i \equiv T_0 + \Delta T_i z/h, \qquad \text{at} \quad t = 0, \tag{6}$$

where T_0 is the temperature at the bottom endwall $z = 0$. At $t = 0$, the temperature distribution at the container walls is impulsively changed (and maintained so thereafter) to a new profile T_f. The change is temperature is such that the stratification is increased, i.e., the temperature in the upper (lower) half of the cylinder wall is increased (decreased) linearly in z. Thus the boundary conditions are

$$\begin{aligned} u &= w = 0, \\ T &= T_f \equiv T_0 + \Delta T_i z/h + 2(\epsilon\Delta T_i)(z/h - 0.5), \\ &\quad \text{at} \quad r = a, \end{aligned} \tag{7}$$

and

$$\begin{aligned} u = w = 0, \quad T &= T_0 - \epsilon\Delta T_i, \qquad \text{at} \quad z = 0, \\ u = w = 0, \quad T &= T_0 + (1+\epsilon)\Delta T_i, \qquad \text{at} \quad z = h. \end{aligned} \tag{8}$$

In equations (7) and (8), ϵ indicates the order of nondimensional temperature change, and subscripts i and f refer to the initial and final state, respectively.

In the process of normalizing the equations, the following parameters emerge:

$$\begin{aligned} Ra &= \alpha g\Delta T h^3/\nu\kappa, \qquad \text{the Rayleigh number;} \\ Pr &= \nu/\kappa, \qquad \text{the Prandtl number;} \\ N &= (\alpha g\Delta T/h)^{1/2}, \qquad \text{the Brunt-Väisälä frequency;} \end{aligned}$$

where ΔT is the vertical temperature difference in the cylinder. The nondimensional change in Brunt-Vaisala frequency from N_i to $N_f \equiv N_i + \Delta N$, $\epsilon_N \equiv \Delta N/N_i$, is related to ϵ as, $\epsilon_N = 1 - (1-\epsilon)^{1/2}$. Thus, for linear flows, $\epsilon_N \cong 1/2\ \epsilon << 1$.

Jischke and Doty [2] argued that for $Ra >> 1$ the diffusive effects are confined to thin boundary layers at the container walls during the principal phase of the transient motion. Therefore, the flow field can be divided into the boundary layers and the essentially inviscid, adiabatic interior. An approximate solution for the interior motion is sought, which is matched to the boundary layer solutions. Recognizing that the buoyancy-driven meridional circulation redistributes the internal energy in the interior in the time scale $t_h = Ra^{1/4}N^{-1}$, they expanded the flow variables in powers of $\mathrm{Ra}^{-1/4}$. A systematic solution sequence is then established, which accounts for the interactive boundary-layer correction to the interior motion.

The lowest order, closed-form solutions in the interior for the linear temperature boundary conditions of equations (6), (7), and (8) are (see [2, 3])

$$\theta = 2(Z - 0.5)\{1 - \exp[-2^{1/2}(h/a)\tau]\}, \tag{9}$$

Downloaded 02 May 2010 to 171.66.16.54. Redistribution subject to ASME license or copyright; see http://www.asme.org/terms/Terms_Use.cfm

Table 1 Parameters for the numerical computations

Case no.	ϵ	Pr	Ra	N_i	t_h
$H1$	0.0005	5.69	2.53×10^6	0.22 s^{-1}	304 s
$H2$	0.0005	5.69	2.89×10^7	0.75 s^{-1}	166 s
$H3$	0.0005	7.10	2.42×10^8	1.58 s^{-1}	148 s

$$u = 2^{1/2}\epsilon Pr^{-1/2} Ra^{-1/4} hN_i R\exp(-\tau) \quad (10a)$$

$$w = 2^{3/2}\epsilon Pr^{-1/2} Ra^{-1/2}(h^2/a)N_i(0.5-Z)\exp(-\tau), \quad (10b)$$

in which we introduced the nondimensional quantities:

$$\theta \equiv (T-T_i)/\epsilon\Delta T_i; \quad \tau \equiv t/(2^{-1/2} Pr^{1/2} Ra^{1/4} N^{-1} a/h);$$

$$R \equiv r/a; \quad Z \equiv z/h.$$

Several comments on the foregoing theoretical solutions are in order. Equations (9) and (10) indicate that the interior will adjust over the time scale t_h, without oscillation, from the initial state to the final state. The temperature perturbation, expressed in equation (9), is independent of the horizontal coordinate. This is in line with the intrinsic property of a stratified fluid, i.e., the tendency to attain horizontal uniformity of density. We also note that the velocity fields, as expressed in (10), are not zero at the initial instant $t = 0$, which is in apparent contradiction to the initial state of rest. This is because the entire analysis is meaningful only after the quasisteady sidewall boundary layer has been formed over $O(N^{-1})$. Since $t_h >> N^{-1}$ for $Ra >> 1$, the initial instant for (10) is actually $O(N^{-1})$ after $t = 0$. It is important to recognize that the monotonically varying theoretical solutions of (9) and (10) were obtained after the internal-gravity oscillations of time scale $O(N^{-1})$ have been filtered out by choosing t_h as the time scale of interest. Equations (9) and (10) will, therefore, be a reasonably good approximation to the true transient flow only if the amplitudes of these high-frequency oscillations are small. As will be seen later, the amplitudes of these oscillations in the flow field are typically several times larger than the magnitudes of the theoretical solutions. These limitations point to a need to examine more comprehensive data of sufficient resolution to describe the flow details. We have decided to use the numerical model of Warn-Varnas et al. [4] to acquire such data.

3 The Numerical Model

The finite-difference numerical model of Warn-Varnas et al. [4] was amended to apply to the present problem. Equations (1)–(8) constitute the governing equations and the associated initial and boundary conditions. To satisfy numerical stability requirements, a thin solid cylinder of very small but finite radius ($r = r_i$) was inserted along the centeral axis of the cylinder. Symmetry conditions state that [4, 5]

$$u = \partial w/\partial r = \partial T/\partial r = 0 \quad \text{at} \quad r = r_i. \quad (11)$$

Equations (1)–(8) and (11) were finite-differenced on a staggered mesh. The grid was stretched in the r-direction to have adequate resolution of the thin sidewall boundary layer. The pressure was found from the Poisson equation by taking the divergence of (1) and (2), which was solved by an ADI iterative approach. For details on finite-differencing schemes and numerical techniques, the reader is referred to [4]. The reliability and accuracy of this numerical model have been verified previously for a variety of spin-up flow conditions by checking the model predictions against laser-Doppler velocimeter measurements in the laboratory. Such comparisons (see [4, 6]) exhibited excellent agreement between the numerical results and the laser measurements, validating the capability of this numerical model for the computations of transient, internal flows of a stratified fluid.

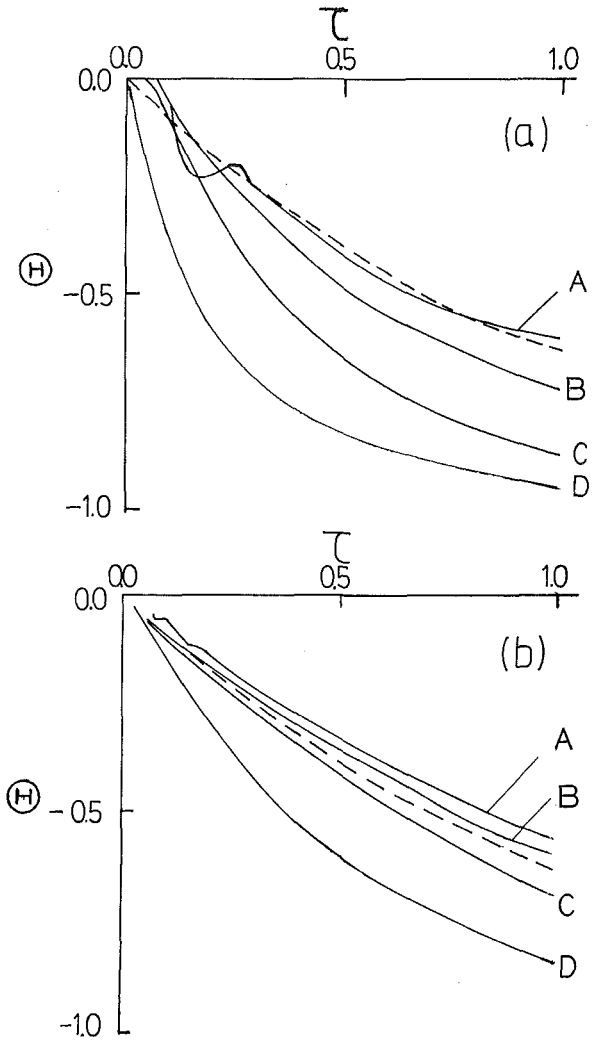


Fig. 1 Plots of scaled nondimensional temperature, Θ ≡ $(T-T_i)/[\epsilon\Delta T_i$ (0.5-Z)], versus scaled time $\tau \equiv t/t_h$ at the radial location R = 0.5. The theoretical solution, equation (9), is shown in broken line. (*a*) is for Case *H*1. Vertical locations for the curves are *A*: Z = 0.43, *B*: Z = 0.31, *C*: Z = 0.10, *D*: Z = 0.04. (*b*) is for Case *H*3. Vertical locations are *A*: Z = 0.45, *B*: Z = 0.25, *C*: Z = 0.12, *D*: Z = 0.05.

4 Results and Discussion

Computations were performed for three sets of experimental parameters. The dimensions of the cylinder were a = 5 cm and h = 5 cm. Table 1 lists the pertinent parameters for the three cases.

The radius of the small inner cylinder [see equation (11)] was set to be r_i = 0.01 cm; an increase of r_i to 0.1 cm produced no noticeable effect on the interior flow. We present the results obtained using a 30 × 36 grid. For a given set of parameters, the computer time to integrate the equations up to $\tau \sim 1$ was approximately 2 hrs on an IBM 4341 Computer.

Since the sidewall boundary conditions in the present problem are antisymmetric about the middepth plane $z = h/2$ [see equations (7) and (8)], the ensuing discussion will be restricted to the flow in the bottom half of the cylinder.

***(a)* The Temperature Field.** Figure 1 displays the numerical results of the temperature deviation from the initial state at different vertical locations at mid-radius R = 0.5. The ordinate denotes the scaled nondimensional temperature perturbation, Θ ≡ $(T-T_i)/\epsilon\Delta T_i(0.5-Z)$. Thus the theoretical solution for the interior [equation (1)], shown in dashed line in Fig. 1, collapses into a universal function of τ

Downloaded 02 May 2010 to 171.66.16.54. Redistribution subject to ASME license or copyright; see http://www.asme.org/terms/Terms_Use.cfm

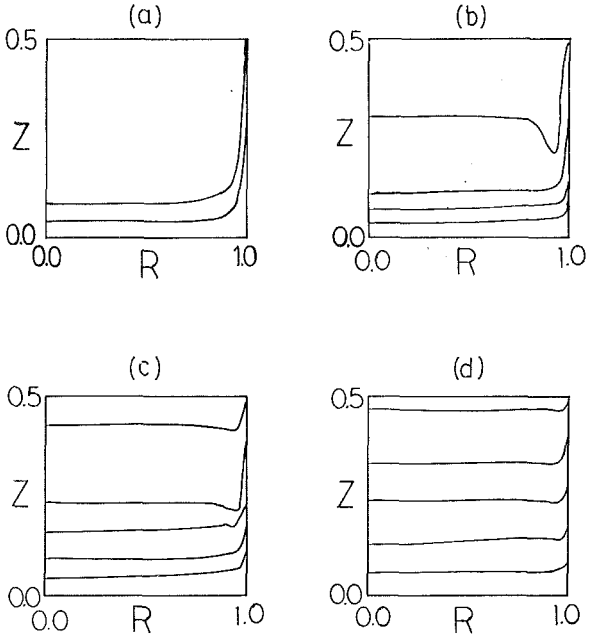


Fig. 2 Contour maps of temperature for Case *H*1. Times are (*a*) τ = 0.04, (*b*) τ = 0.16, (c) τ = 0.45, (*d*) τ = 0.94.

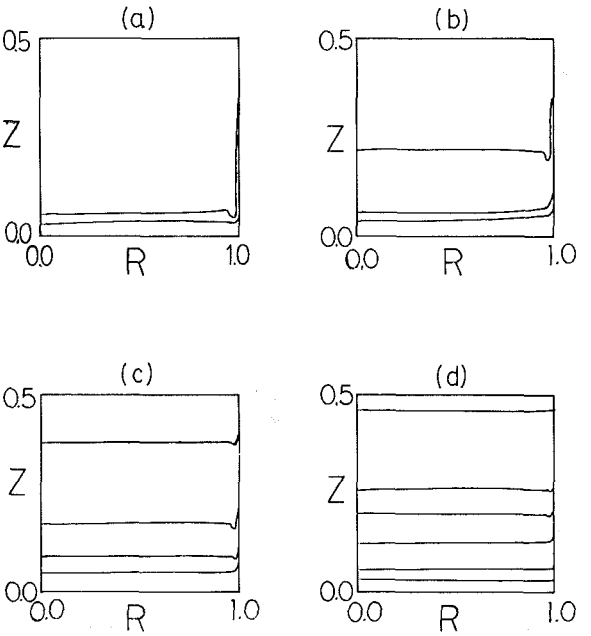


Fig. 3 Contour maps of temperature for Case *H*3. Times are (*a*) τ = 0.04, (*b*) τ = 0.17, (c) τ = 0.47, (*d*) τ = 0.95.

only. We observe in Fig. 1 that the temperature adjustment progresses faster as the vertical location moves close to the endwall. Obviously, the transient temperature adjustment process is substantially facilitated by the diffusive effects which are concentrated in the boundary layer regions [see curves *D*]. The effect of *Ra* on the temperature adjustment process can be analyzed by comparing Fig. 1(*a*), which is for Case *H*1 ($Ra = 2.53 \times 10^6$), and Fig. 1(*b*), which is for Case *H*3 ($Ra = 2.42 \times 10^8$). It is evident that the temperature adjustment associated with smaller *Ra* progresses appreciably faster than that of larger *Ra*, and this trend is more pronounced as the location moves close to the endwall. This is explained by noting that the relative importance of the diffusive effects increases as *Ra* decreases or as the location moves close to the endwall. The superposition of the internal-

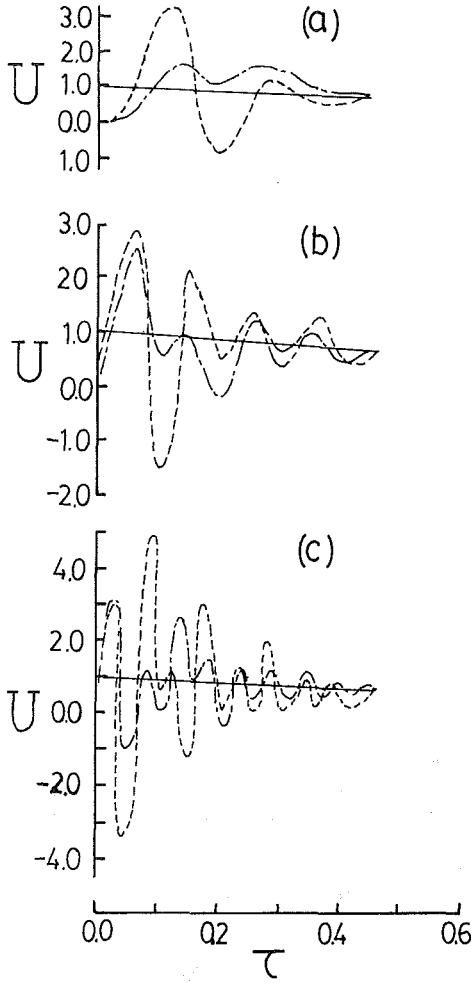


Fig. 4 Plots of scaled nondimensional radial velocity, $U = u/(2^{1/2}\epsilon Pr^{-1/2} Ra^{-1/4} h N_l R)$, versus scaled time τ at the radial location R = 0.5. The theoretical solution equation (10*a*), is shown in solid line.

(*a*) is for case *H*1. – – – Z = 0.31, ------ Z = 0.43;

(*b*) is for case *H*2. – – – Z = 0.34, ------ Z = 0.43;

(*c*) is for case *H*3. – – – Z = 0.35, ------ Z = 0.45.

gravity oscillations for early times is apparent in curve *A* of Fig. 1(*a*). However, the impact of the internal-gravity oscillations on the overall temperature field is quite minor. This is consistent with the fact that the temperature field reacts weakly to high-frequency changes in the flow field (see Küblbeck et al. [7]).

The contour maps of the nondimensional temperature deviation, $(T - T_i)/\epsilon\Delta T_i$, are presented in Fig. 2 (for Case *H*1) and Fig. 3 (for Case *H*3). These contour maps clearly demonstrate that the temperature field in the interior is substantially uniform in the horizontal direction. As time progresses, the temperature disturbances move vertically from the endwall to the middepth plane. The effect of *Ra* on the temperature field turns up principally in two areas. First, as was stated earlier, the temperature adjustment is faster for smaller *Ra*, due to the pronounced role of the diffusive effects. Secondly, the structure of the sidewall boundary layer is strongly affected by *Ra*. In the theoretical treatments of [2, 3], the thickness of the sidewall boundary layer is scaled with $Ra^{-1/4}h$. The results in Figs. 2 and 3 show qualitative consistency with this scaling.

(*b*) The Velocity Field. Figure 4 presents the numerical results of the radial velocity evolution at different vertical

Downloaded 02 May 2010 to 171.66.16.54. Redistribution subject to ASME license or copyright; see http://www.asme.org/terms/Terms_Use.cfm

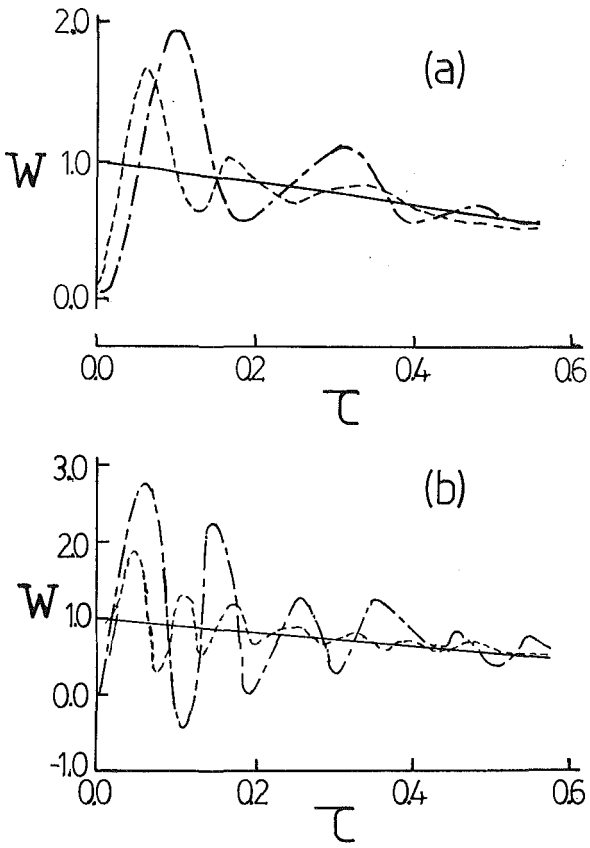


Fig. 5 Plots of scaled nondimensional vertical velocity, $W = w/[2^{3/2}\epsilon Pr^{-1/2}\,Ra^{-1/4}\,(h^2/a)\,N_i\,(0.5-Z)]$, versus scaled time τ at the vertical level $Z = 0.23$. The theoretical solution, equation (10b), is shown in solid line.

(a) is for case *H*1. – – – $R = 0.27$, ------ $R = 0.61$;

(b) is for case *H*2. – – – $R = 0.24$, ------ $R = 0.62$,

locations at midradius $R = 0.5$. The ordinate denotes the scaled nondimensional radial velocity, $U \equiv u/(2^{1/2}\epsilon Pr^{-1/2}\,Ra^{-1/4}hN_iR)$. Accordingly, the theoretical solution for the interior, equation (10*a*), falls onto a single curve $\exp(-\tau)$, which is shown in solid line in Fig. 4.

We first note that, unlike the evolution of the temperature field, the radial velocity field exhibits qualitative discrepancies between the numerical results and the theoretical solution. These discrepancies are mainly attributable to the dominant presence of the internal-gravity oscillations which were omitted in the theory (see Section 2). To ascertain that these high-frequency oscillations are indeed the internal-gravity oscillations, we proceed to calculate the frequencies obtainable from the dispersion relation for linearized, inviscid, internal-gravity modes about a state of rest with stratification N_i. This relation is (e.g., see [8])

$$\beta = N_i\left[\frac{(\alpha_n/m\pi A)^2}{1+(\alpha_n/m\pi A)^2}\right]^{1/2} \tag{12}$$

where α_n are the zeros of the first-order Bessel function, m is any integer, and $A = a/h$. The associated eigenfunctions of the problem are

$$u \sim m\,J_1(\alpha_n R)\cos[m\pi z/(h/2)] \tag{13}$$

$$w \sim (\alpha_n/a)J_0(\alpha_n R)\sin[m\pi z/(h/2)] \tag{14}$$

It is expected that, since the impulsive change causes a perturbation symmetrical about middepth and of the scale of the container, the dominant mode is given by $m = 2$, $n = 1$. The periods of the $m = 2$, $n = 1$ mode as calculated using (12) for the parameters of the three cases listed in Table 1 are (expressed in τ): 0.182 for *H*1, 0.096 for *H*2, and 0.051 for *H*3. The periods of oscillations detectable in Fig. 4 are 0.185 for *H*1, 0.098 for *H*2, and 0.052 for *H*3. This comparison of the periods establishes that the oscillations in the numerical results are due to the presence of the internal-gravity oscillations.

To check the possibility of numerical instability in the computational scheme, the numerical results were tested by employing two other grids (a 24 × 32 grid and a 24 × 24 grid) for case *H*2. The time step used was also varied, within the limit of the computational stability criteria [4]. The results of these calculations were in very close agreement with each other.

It is useful to mention the analogy between stratified fluid phenomena and rotating fluid phenomena (see Veronis [1] and Yih [9] for an extensive review). In particular, Veronis [1] described an explicit correspondence between heat-up of a stratified fluid and spin-up of a rotating fluid [4]. The physical counterpart of the internal-gravity oscillations in stratified fluids is the inertial oscillations in rotating fluids [1]. The periods of the $m = 2$, $n = 1$ mode for the inertial oscillations in spin-up were computed in numerical solutions [4], and they were shown to be in close agreement with the laboratory experiments ([4, 10]).

The numerical results of Fig. 4 reveal that the amplitudes of the radial velocities, which include the flows induced by the internal-gravity modes, are substantially greater than those of the theoretical solutions. Since the theory takes into account only the velocities arising from the meridional circulation, Fig. 4 suggests that the contributions from the motions with time scales shorter than t_h far outweigh those from the meridional circulation. This points to the inadequacy of the theoretical solution to describe the significant aspects of the true flow. We conclude that the theoretical curves are valid representations of the overall flow trend over the time span t_h when the internal-gravity oscillations are averaged out, apart from the anomalies for early times (see Section 2).

The vertical variations of the amplitudes of the radial velocities, as depicted in Fig. 4, do not seem to be described well by the eigenfunctions of the inviscid internal-gravity modes, equation (13). This is attributable to the influence of the diffusive effects, which is more pronounced for flows of small Ra and for flows in the region close to the endwall. The radial velocity curve for $Z = 0.31$ in Fig. 4(*a*) illustrates this point, i.e., the amplitude of the internal-gravity mode for $Ra = 2.53 \times 10^6$ at this location is seen to have been considerably damped by the diffusive effects.

Figure 5 displays the vertical velocity evolution at different radial locations at the vertical level $Z = 0.23$. The ordinate denotes the scaled nondimensional vertical velocity, $W = w/[2^{3/2}\epsilon Pr^{-1/2}Ra^{-1/4}(h^2/a)N_i(0.5-Z)]$. Then the theoretical solution, equation (10*b*), becomes a single curve $\exp(-\tau)$, which is plotted in solid line in Fig. 5. The dominant role of the internal-gravity modes in the oscillatory behavior of the vertical velocity is similar to that in the radial velocity field discussed earlier. The radial variation of W, as depicted by the two curves in Figs. 5(*a*) and 5(*b*), is in qualitative agreement with the eigenfunctions of the internal-gravity modes, equation (14).

Figure 6(*a*) shows the radial variation of the scaled radial velocity U, and Fig. 6(*b*) shows the vertical variation of the scaled vertical velocity W. These results are qualitatively consistent with the spatial variations given by the eigenfunctions of the internal-gravity modes, equations (13) and (14).

Figure 7 presents the contour maps of the stream function ψ in the bottom half of the cylinder. This illustrates the pattern of the internal circulation, which is in the clockwise sense. Near the sidewall, the sinking motion takes place in the thin

Downloaded 02 May 2010 to 171.66.16.54. Redistribution subject to ASME license or copyright; see http://www.asme.org/terms/Terms_Use.cfm

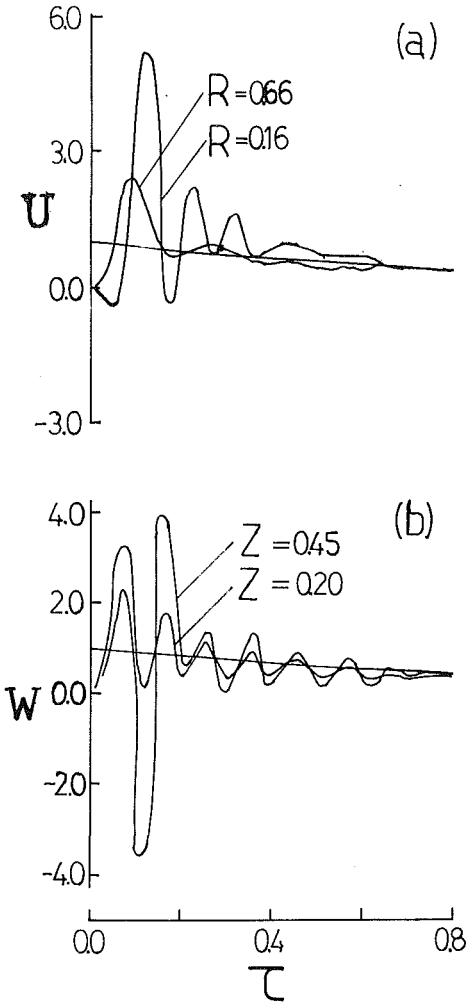


Fig. 6 *(a)* **Plots of scaled nondimensional radial velocity** U **versus scaled time** τ **for Case** $H2$ **at** $Z = 0.23$**. The theoretical curve is shown in dotted line. Radial locations are indicated in the figure.** *(b)* **Plots of scaled nondimensional vertical velocity** W **versus scaled time** τ **for Case** $H2$ **at** $R = 0.50$**. The theoretical curve is shown in dotted line. Vertical locations are indicated in the figure.**

boundary layer, as the fluid is being cooled by the boundary. This induces the pumping of the interior fluid into the sidewall boundary layer. The return circuit of the fluid into the interior is made in the region close to the endwall, thus completing the circulation. The effect of Ra on the flow pattern, especially on the boundary layer structures, is discernible by comparing Fig. 7(*a*) for $Ra = 2.53 \times 10^6$ and Fig. 7(*b*) for $Ra = 2.42 \times 10^8$. In the theory, the sidewall boundary layer thickness is scaled by $Ra^{-1/4}h$, and this is qualitatively validated by the results in Fig. 7. The endwall boundary layer is appreciably thicker than the sidewall boundary layer, but a definitive scaling of this layer thickness is difficult at this point.

5 Conclusions

Numerical solutions were obtained to examine the transient buoyant convection in a cylinder caused by a small change in the boundary temperature profile.

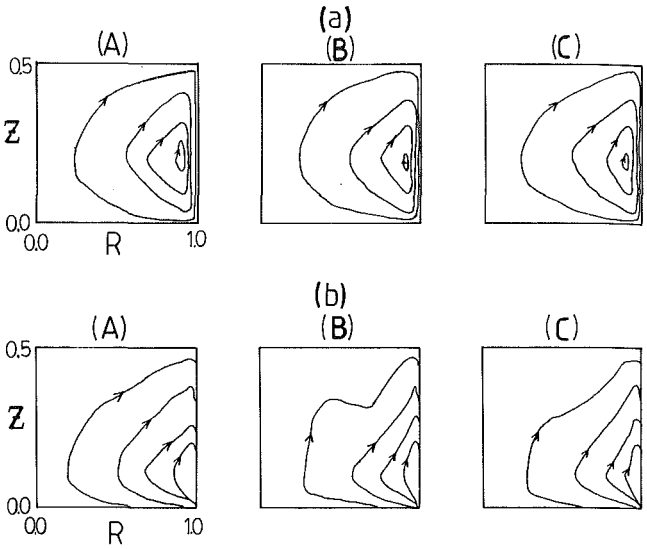


Fig. 7 Contour maps of streamfunction. *(a)* **is for Case** $H1$**. Times are** A**:** $\tau = 0.342$**,** B**:** $\tau = 0.356$**,** C**:** $\tau = 0.370$**.** *(b)* **is for Case** $H3$**. Times are** A**:** $\tau = 0.280$**,** B**:** $\tau = 0.287$ **and** C**:** $\tau = 0.295$**.**

The temperature field is substantially uniform in the horizontal direction. The impact of the internal-gravity oscillations on the temperature field is minor. The theoretical solution for the temperature evolution is qualitatively consistent with the numerical results.

The numerical solutions of the velocity field exhibit significant discrepancies from the theoretical solutions. The evolution of the velocity field is oscillatory in time, due to the dominant presence of the internal-gravity oscillations. The theory, which filters out high-frequency motions, only represents the qualitative overall flow trend over the time span t_h. The effect of Ra on the numerically computed temperature and velocity fields is examined in detail, which is in qualitative agreement with the theoretical predictions.

References

1 Veronis, G., "The Analogy Between Rotating and Stratified Fluids," *Annual Review of Fluid Mechanics*, Vol. 2, 1970, pp. 37-66.

2 Jischke, M. C., and Doty, R. T., "Linearized Buoyant Motion in a Closed Container," *J. Fluid Mech.*, Vol. 71, 1975, pp. 729-754.

3 Sakurai, T., and Matsuda, T., "A Temperature Adjustment Process in a Boussinesq Fluid via a Buoyancy-Induced Meridional Circulation," *J. Fluid Mech.*, Vol. 54, 1972, pp. 417-421.

4 Warn-Varnas, A., Fowlis, W. W., Piacsek, P., and Lee, S. M., "Numerical Solutions and Laser-Doppler Measurements of Spin-Up," *J. Fluid Mech.*, Vol. 85, 1978, pp. 609-639.

5 Barcilon, A., Lau, J., Piacsek, S., and Warn-Varnas, A., "Numerical Experiments on Stratified Spin-Up," *Geophysical Fluid Dynamics*, Vol. 7, 1975, pp. 29-42.

6 Hyun, J. M., Fowlis, W. W., and Warn-Varnas, A., "Numerical Solutions for the Spin-Up of a Stratified Fluid," *J. Fluid Mech.*, Vol. 117, 1982, pp. 71-90.

7 Kublbeck, K., Merker, G. P., and Straub, J., "Advanced Numerical Computation of Two-Dimensional Time-Dependent Free Convection in Cavities," *Int. J. Heat Mass Transfer*, Vol. 23, 1980, pp. 203-217.

8 Lee, S. M., "An Investigation of Stratified Spin-Up Using a Rotating Laser-Doppler Velocimeter," M.S. Thesis, Florida State University, Tallahassee, Florida, 1975.

9 Yih, C. S., *Stratified Flows*, Academic Press, New York, 1980.

10 Fowlis, W. W., and Martin, P. J., "A Rotating Laser Doppler Velocimeter and Some New Results on the Spin-Up Experiment," *Geophysical Fluid Dynamics*, Vol. 7, 1975, pp. 67-78.

Downloaded 02 May 2010 to 171.66.16.54. Redistribution subject to ASME license or copyright; see http://www.asme.org/terms/Terms_Use.cfm

A. Raman
Graduate Research Assistant.

V. S. Krishnan
Graduate Research Assistant.

R. P. Roy
Associate Professor.

Department of Mechanical and Aerospace Engineering, Arizona State University, Tempe, Ariz. 85287

Directional Sensitivity of Cylindrical Hot-Film Velocity Sensors

Directional sensitivities of alumina and quartz-coated cylindrical hot-film velocity sensors with l_s/d_s ratios near 20 were investigated in air and liquid Refrigerant-113 flows. The well-known effective cooling velocity relation $U_{eff}^2(\alpha) = U^2(0)[\cos^2\alpha + k^2\sin^2\alpha]$ represents the experimental data well. Values for the parameter k as well as heat transfer relations are presented.

1 Introduction

The measurement of turbulent shear stress and heat transport in fluid flow can be accomplished with the use of hot-wire or hot-film velocity sensors provided their directional sensitivities are accurately known. Cylindrical hot-film velocity sensors are preferable for measurements where ruggedness is of importance.

For hot-wire sensors, heat transfer characteristics are reasonably well understood – e.g., one has available the thorough work of Collis and Williams [1] for large l_s/d_s ratio wires (l_s and d_s indicate sensor length and diameter, respectively). Hinze [2], Webster [3], and Champagne, et al. [4] have suggested that the directional sensitivity for such wires can be expressed in terms of a parameter k in the relationship for the effective cooling velocity:

$$U_{\text{eff}}^2(\alpha) = U^2(0)[\cos^2\alpha + k^2\sin^2\alpha] \quad (1)$$

where α is the yaw angle. Experimental results indicate that k varies between zero and 0.3 and is a function of the l_s/d_s ratio, decreasing in value as the ratio increases.

Heat transfer characteristics of cylindrical hot-film sensors are far less well understood. Hill and Sleicher [5] reported on the evaluation of convective heat transfer from short (l_s/d_s ratio $\approx$ 20) quartz-coated cylindrical hot-film sensors to mercury. Friehe and Schwartz [6] presented directional sensitivity results for quartz-coated, hot-film sensors operating in air in the l_s/d_s range of 12 to 100, and suggested a new formula for the effective cooling velocity:

$$U_{\text{eff}}^2(\alpha) = U^2(0)[a + b\cos^{1/2}\alpha]^2 \quad (2)$$

where a and b depend on the l_s/d_s value. Andreas [7] reported a k-value of 0.20, based on equation (1) for the effective cooling velocity, for alumina-coated cylindrical hot-film sensors with $l_s/d_s \approx 20$ operating in air. He also reported a heat transfer relation for such sensors in the Reynolds number (Re_a; defined as $U_{\text{eff}}\, d_s/\nu_a$, where the subscript a denotes value at ambient fluid temperature) range of 1 to 18:

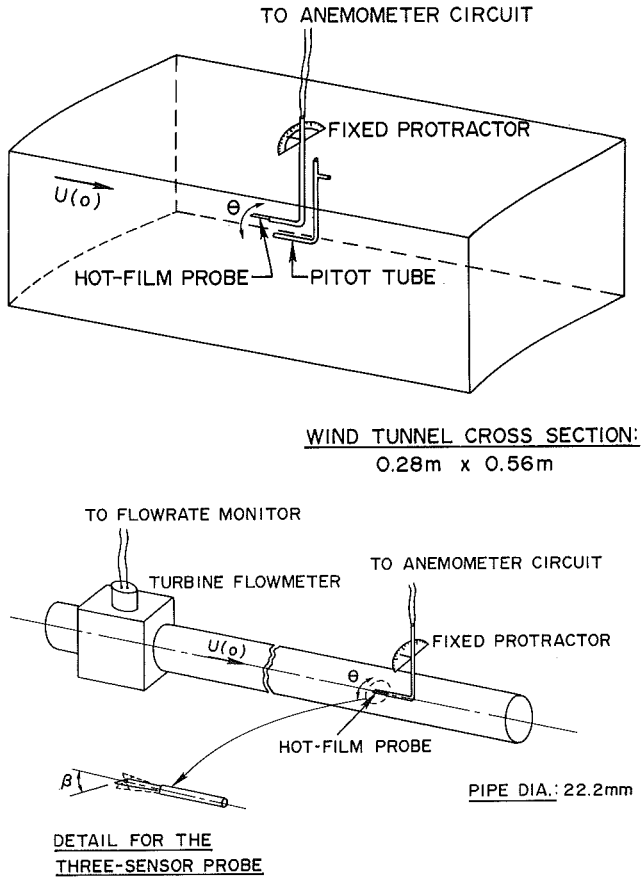


Fig. 1 Experimental arrangement; (a) in wind tunnel, and (b) in liquid Refrigerant-113 calibration section

Contributed by the Applied Mechanics Division for publication in the JOURNAL OF APPLIED MECHANICS.

Discussion on this paper should be addressed to the Editorial Department, ASME, United Engineering Center, 345 East 47th Street, New York, N.Y. 10017, and will be accepted until two months after final publication of the paper itself in the JOURNAL OF APPLIED MECHANICS. Manuscript received by ASME Applied Mechanics Division, March, 1984, final revision, June, 1984.

Copyright © 1985 by ASME
Downloaded 02 May 2010 to 171.66.16.54. Redistribution subject to ASME license or copyright; see http://www.asme.org/terms/Terms_Use.cfm

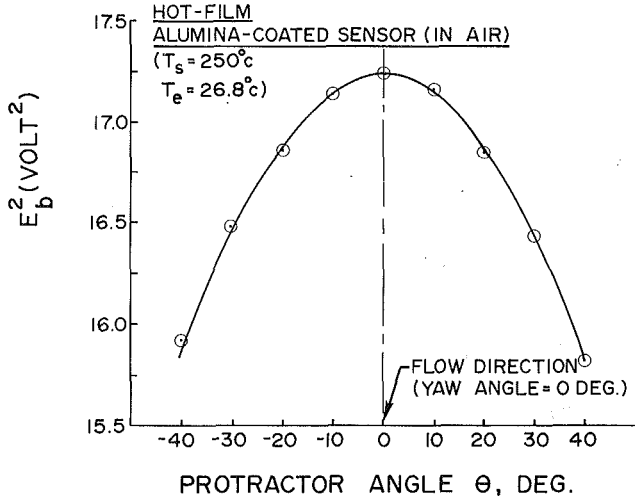


Fig. 2 Determination of flow direction in the wind tunnel

$$N - N_0 = -0.31 + 0.55\,Re_a^{0.46} \tag{3}$$

where N is the Nusselt number:

$$N = \frac{E_b^2 R_s}{\pi R_t^2 (T_s - T_a) l_s k_s} \tag{4}$$

In equation (4), R_s is the sensor operating resistance; R_t, the total resistance in the sensor leg of the anemometer bridge; T_s, the sensor temperature; T_a, the ambient fluid temperature; and k_s, the fluid thermal conductivity at the sensor temperature. In equation (3), the subscript 0 represents the zero-flow value.

In this paper, we report directional sensitivity measurements for alumina-coated cylindrical hot-film sensors ($l_s/d_s \approx 19$) in air, and quartz-coated, cylindrical hot-film sensors ($l_s/d_s \approx 18$) in both air and liquid Refrigerant-113. Both equations (1) and (2) were investigated, with equation (1) found to be a better representation for our data with both types of sensors (alumina-coated, quartz-coated). Finally, relations similar to (3) but with somewhat different coefficients and exponent were obtained for both sensor types in air.

2 Experiments

The following types of cylindrical hot-film sensors were tested:

Sensor type/Manuf. Model	l_s (mm)	d_s (μm)	Test fluid
Alumina-coated,/TSI 1212-20 single-sensor	1	53	air
Quartz-coated,/TSI 1212-20w single-sensor	1	55	air
Quartz-coated,/TSI 1295-20w three-sensor	1	55	Liquid Refrigerant-113

In the preceding table, the value of d_s includes the coating thickness.

The sensors were operated by a TSI 1050 constant-temperature anemometer at various sensor temperatures (and thus, overheat ratios). A four-channel data acquisition and analysis system (Data Precision 6000) was used to acquire and analyze the data.

Air Experiments. The air tests were conducted in the uniform axial velocity region of a low-speed wind tunnel. The experimental setup is shown schematically in Fig. 1(*a*). The velocity range available, as measured by a Pitot tube in conjunction with a "0-10 inches water" micromanometer (Meriam), was approximately 4 m/s to 7 m/s. Overall temperature variation of air was typically ± 0.2°C during the course of entire experiments.

As shown in Fig. 1(*a*), the anemometer probe stem could be rotated (θ, deg) to obtain various yaw angles (α, deg). The sensor was always horizontal. The zero yaw angle orientation of each sensor (which corresponds to the flow velocity being perpendicular to the sensor) was determined by a plot of $E_b^2(\theta)$ versus θ, where E_b denotes the anemometer bridge output voltage, the basis being that such a plot will be symmetrical with respect to $\alpha = 0$ deg, for positive and negative yaw angles [6]. Figure 2 shows a typical plot – in this particular case, the flow direction coincided with the $\theta = 0$ deg setting.

The yaw angle range for all sensors was restricted to -60 deg $\leq \alpha \leq 60$ deg in order to eliminate the possibility of flow disturbances due to the sensor supports at larger yaw angles.[1] The mean axial velocity variation in the wind tunnel for this range of sensor positions was negligible. The background turbulence level was less than 0.6 percent. The Reynolds number (Re; defined here as $U_{\text{eff}}\, d_s/\nu_f$, where the subscript f denotes property value at film temperature which is equal to $0.5(T_s + T_a)$) range was 4 to 12 for the alumina-coated sensors and 7 to 16 for the quartz-coated sensors.

Liquid Refrigerant-113 Experiments. These tests were conducted in the horizontal calibration section of a pressurized (upto 450 kPa) liquid Refrigerant-113[2] flow facility. The experimental setup is shown schematically in Fig. 1(*b*). The bulk velocity range available, limited at the low end by the turbine flow meter (Flow Technology FT-12) accuracy, was approximately 0.42 m/s to 2.5 m/s. The temperature variation of the liquid could be controlled to within ± 0.2°C during the course of entire experiments.

In case of the three-sensor probes, the upstream sensor, oriented horizontally in the calibration section, was used for yaw sensitivity measurements. The angle of inclination of this sensor to the probe stem (β; see Fig. 1(*b*)) was determined to within ± 0.4 deg by using an overhead projector for focusing the image of the probe on a wall [7].

The range of rotation with respect to the pipe centerline was typically ± 20 deg. The values of the axial velocity at the radial position in the pipe corresponding to the various angles of rotation, was separately determined by direct measurement of the velocity profile. The Reynolds number range for our experiments was 30–170. It was necessary to go into the Reynolds number domain where vortex shedding can potentially be problematic since we will be making turbulence measurements in liquid Refrigerant-113 at such conditions in the near future.

[1] As noted by earlier investigators [4, 6, 7], the accuracy of yaw angle measurement is crucial. It should also be noted that the range of yaw angles over which the experimental data span, may have a significant effect on the estimated value of the directional sensitivity parameter k, equation (1).

[2] Typical properties of Refrigerant-113 are [8]: at 49°C: density = 1507.7 (kg)/m^3; viscosity = 0.5 × 10^{-3} (kg)/m.s; thermal conductivity = 0.07 w/m.K.

Downloaded 02 May 2010 to 171.66.16.54. Redistribution subject to ASME license or copyright; see http://www.asme.org/terms/Terms_Use.cfm

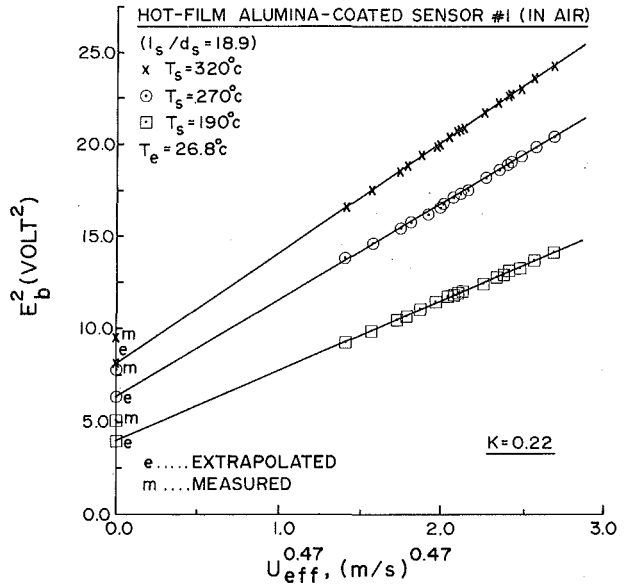


Fig. 3 Directional sensitivity of one hot-film alumina-coated sensor in air

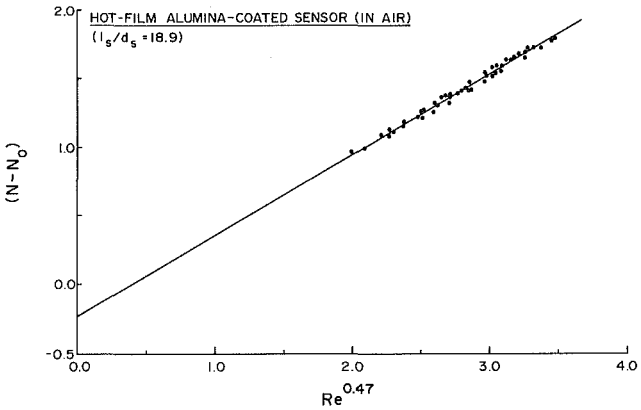


Fig. 4 Nusselt number plot for hot-film alumina-coated sensor in air

3 Results

Air Experiments. Figure 3 shows three plots of the square of the constant-temperature anemometer bridge voltage ($E_b{}^2$) versus $U_{\text{eff}}{}^{0.47}$ for one alumina-coated, hot-film sensor. The three plots correspond to three different sensor temperatures. The U_{eff} exponent of 0.47 was determined from calibration data for several such sensors. Equation (1) was used to calculate U_{eff}, with $k = 0.22$ found to be the best estimate (in the least square error sense) for this particular sensor.

We recommend:

Alumina-coated
hot-film sensor;
$l_s/d_s \approx 19$; $\quad k = 0.21 \pm 0.02$
in air;
Re range: 4–12

An interesting feature pertains to the measured bridge voltages at no-flow condition compared to the extrapolated bridge voltages at no-flow. The square of the measured bridge voltage was higher than the extrapolated value by typically ten to fifteen percent. This is in approximate agreement with Brun [9]. Andreas [7] pointed out that although hot-film sensors are expected to obey the standard heat transfer relation

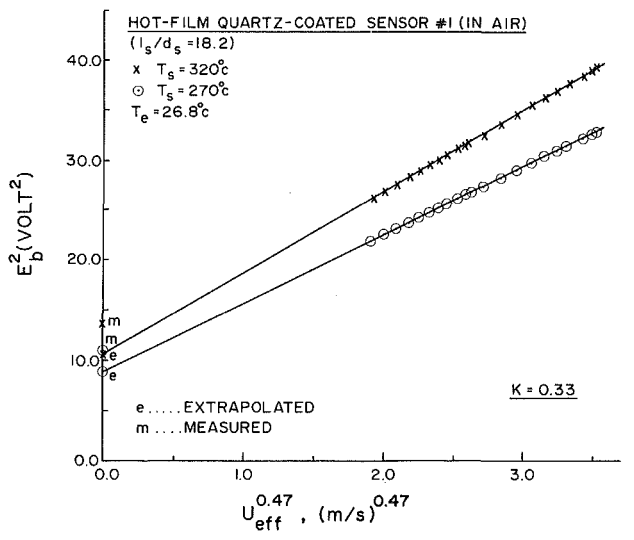


Fig. 5 Directional sensitivity of one hot-film quartz-coated sensor in air

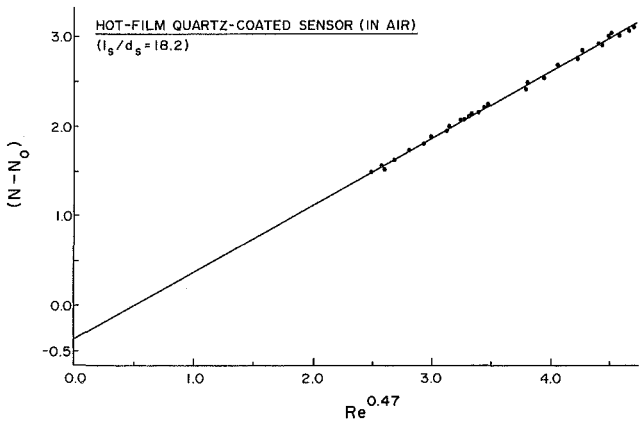


Fig. 6 Nusselt number plot for hot-film quartz-coated sensor in air

$$N = A + B\,Re^n \tag{5}$$

the relation does not hold as Re approaches zero. Under such circumstances, free convection replaces forced convection as the dominant mode of heat transfer, and consequently N does not equal N_0 although they are uniquely related.

Figure 4 is plot of the alumina-coated sensor data in the ($N - N_0$) versus $Re^{0.47}$ plane. The relation obtained is:

$$N - N_0 = -0.24 + 0.59\,Re^{0.47} \tag{6}$$

which is quite close to the one obtained by Andreas (equation (3)). We note that N_0 in the preceding equation represents the measured value at no-flow condition.

Figure 5 shows two plots of $E_b{}^2$ versus $U_{\text{eff}}{}^{0.47}$ for a quartz-coated, hot-film sensor. The plots correspond to two different sensor temperatures. The exponent of 0.47 is once again based on calibration data for several sensors. U_{eff} was calculated from equation (1), with $k = 0.33$ found to be the best estimate for this particular sensor. We recommend:

Quartz-coated
hot-film sensor;
$l_s/d_s \approx 18$; $\quad k = 0.30 \pm 0.04$
in air;
Re range: 7–16

The measured bridge voltages at no-flow condition were again somewhat higher than the extrapolated voltages at no-flow. Figure 6 is a plot of the sensor data in the ($N - N_0$) versus $Re^{0.47}$ plane. The relation obtained is:

Downloaded 02 May 2010 to 171.66.16.54. Redistribution subject to ASME license or copyright; see http://www.asme.org/terms/Terms_Use.cfm

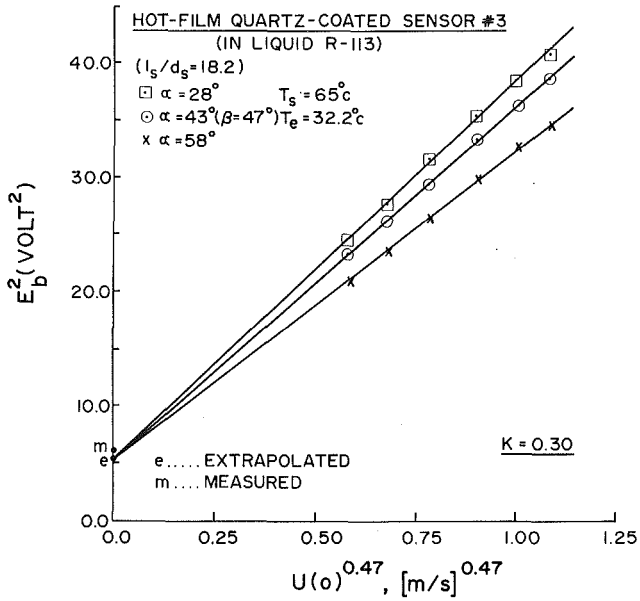


Fig. 7 Directional sensitivity of one hot-film quartz-coated sensor in liquid Refrigerant-113

$$N - N_0 = -0.37 + 0.75\,Re^{0.47} \tag{7}$$

Liquid Refrigerant-113 Experiments. Figure 7 shows three plots of E_b^2 versus $U(0)^{0.47}$ for one quartz-coated, hot-film sensor. The plots correspond to three different yaw angles. The $U(0)$ exponent of 0.47 provided the best fit for all calibration data. Based on equation (1), $k = 0.30$ was the best-estimate value for this sensor. It appears, on the basis of limited data on the sensors, that:

Quartz-coated
hot-film sensor;
$l_s/d_s' \approx 18$; $k = 0.30 \pm 0.04$
in liquid Refrigerant-113
Re range: 30–170

It should be noted that the extrapolated value of the no-flow condition bridge voltage is independent of the yaw angle in Fig. 7. This is in agreement with the finding of Friehe and Schwartz [6]. As with the other sensor type, the measured no-flow condition bridge voltage is somewhat higher than the extrapolated value.

4 Conclusions

In air, the directional sensitivity of alumina-coated, hot-film velocity sensors with l_s/d_s ratio close to 20 is well represented by the effective cooling velocity relation:

$$U_{\text{eff}}^2(\alpha) = U^2(0)[\cos^2\alpha + k^2\sin^2\alpha] \tag{8}$$

The value of k is (0.21 ± 0.02) in the Reynolds number range 4–12. The heat transfer relation is found to be:

$$N - N_0 = -0.24 + 0.59\,Re^{0.47} \tag{9}$$

In air, the directional sensitivity of quartz-coated hot-film velocity sensors with l_s/d_s ratio close to 20 is also well represented by effective cooling velocity relation given by equation (8). The value of k is (0.30 ± 0.04) in the Reynolds number range 7–16. The heat transfer relation is found to be:

$$N - N_0 = -0.37 + 0.75\,Re^{0.47} \tag{10}$$

In liquid Regrigerant-113, the directional sensitivity of quartz-coated hot-film velocity sensors with l_s/d_s ratio close to 20 is well represented by equation (8). The value of k is (0.30 ± 0.04) in the Reynolds number range 30-170. Further experiments are needed before a heat transfer relation can be suggested.

Acknowledgment

This work was partially supported by National Science Foundation under grant MEA 81-21995 to Arizona State University.

References

1 Collis, D. C., and Williams, M. J., "Two-Dimensional Convection From Heated Wires at Low Reynolds Numbers," *Journal of Fluid Mechanics*, Vol. 6, Part 3, 1959, pp. 357–384.

2 Hinze, J. O., *Turbulence*, 2nd Ed., McGraw-Hill, New York, 1975, pp. 123–127.

3 Webster, C. A. G., "A Note on the Sensitivity to Yaw of Hot-Wire Anemometer," *Journal of Fluid Mechanics*, Vol. 13, 1962, pp. 307–312.

4 Champagne, F. H., Sleicher, C. A., and Wehrmann, O. H., "Turbulence Measurements With Inclined Hot-Wires, Part 1," *Journal of Fluid Mechanics*, Vol. 28, 1967, pp. 153–175.

5 Hill, J. C., and Sleicher, C. A., "Convective Heat Transfer From Small Cylinder to Mercury," *International Journal of Heat and Mass Transfer*, Vol. 12, 1969, pp. 1595–1604.

6 Friehe, C. A., and Schwartz, W. H., "Deviations from the Cosine Law for Yawed Cylindrical Anemometer Sensors," ASME JOURNAL OF APPLIED MECHANICS, Vol. 35, 1968, pp. 655–662.

7 Andreas, E. L., "The Calibration of Cylindrical Hot-Film Velocity Sensors," ASME JOURNAL OF APPLIED MECHANICS, Vol. 46, 1979, pp. 15–20.

8 E. I. Dupont De Nemours and Co., Bulletins FST-11, -1, E-113, 1976–1979.

9 Brun, H. H., "Linearization and Hot Wire Anemometry," *Journal of Physics E: Scientific Instruments*, Vol. 4, 1971.

Downloaded 02 May 2010 to 171.66.16.54. Redistribution subject to ASME license or copyright; see http://www.asme.org/terms/Terms_Use.cfm

Boundary Layer Flow Over Long Cylinders With Suction

B. Bar-Haim
Graduate Instructor.

D. Weihs
Professor.

Department of Aeronautical Engineering,
Technion-Israel Institute of Technology,
Haifa, Israel

The full, axisymmetric boundary layer equations over a long circular cylinder have been repeatedly solved in the past by a variety of approximate Pohlhausen-type and series expansion methods. These methods are not suitable however, for axisymmetric solutions with wall suction boundary condition. In the present paper, the basic equations are solved by a simple approximate method, based on successive derivatives of the wall compatibility condition. A family of velocity profiles, which coincides with the asymptotic suction profile at infinity, is assumed, and the wall shear force is found by integrating an ordinary differential equation. The computed boundary layer properties for the impermeable (zero-suction) cylinder case are shown to be in good agreement with solutions of other, more sophisticated techniques. The case of an infinite cylinder with constant suction asymptotically approaches the well-known constant thickness boundary layer solution, in analogy with the case of constant suction on a flat plate. The present method is further explored to exhibit the drag reduction properties of wall suction. An optimal suction profile is found, as a function of free stream conditions and the cylinder fineness ratio. For example, in the case of a cylinder fineness ratio 5, and Re = 25 × 10^6, the flow can be laminarized with only 80 percent of the mass sucked off, relative to uniform suction.

1 Introduction

There has been a growing interest in recent years in the design of axially symmetric shapes of low drag for both aerial and underwater application. Such designs may enable the construction of faster, more quiet vehicles, with longer ranges of action than the present conventional bodies.

One way of reducing the drag is by shape manipulations so that the transition point of the boundary layer is transported to the stern of the body [1, 2]. However, although impressive theoretical drag reductions were achieved (for example, at $Re_v = 10^7$, a minimum drag coefficient of 0.0051 was achieved representing a reduction of 30 percent relative to previous designs [1]), these minimal drag bodies have highly complicated curved forms, which are difficult to manufacture, and are not suitable for tube launching. Other, more efficient means of reducing the drag such as active Boundary Layer Control (BLC) were proposed (for example: compliant surfaces [3] or body heating [4]) but no practical applications of these methods are known as yet.

One possibility of active BLC is distributed suction of the boundary layer. The capability of such suction to prevent transition to turbulence, and to a lesser degree to delay separation, was extensively demonstrated in the past for two-dimensional planforms [5].

As a preliminary examination of the applicability of distributed suction BLC to reduce the drag of underwater vehicles, the flow over a long circular cylinder is studied in this paper. The full axisymmetric boundary layer equations are solved by an approximate method to demonstrate the ability of this BLC method to substantially delay transition. As far as we know, this is the first approximate solution of these equations with a distributed suction boundary condition.

2 Analysis

The full axisymmetric boundary layer equations for incompressible flow (see Fig. 1 for the coordinate system) are:

$$uu_x + vu_y = UU_x + \nu\left(u_{yy} + \frac{r_y}{r}u_y\right) \tag{1a}$$

$$(ru)_x + (rv)_y = 0 \tag{1b}$$

where u, v are the longitudinal and radial velocity com-

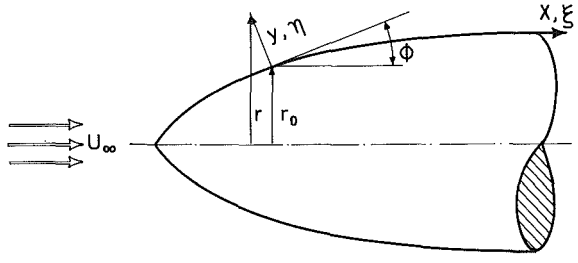


Fig. 1 Definition of system of coordinates fixed to body contour

Contributed by the Applied Mechanics Division for publication in the JOURNAL OF APPLIED MECHANICS.

Discussion on this paper should be addressed in the Editorial Department, ASME, United Engineering Center, 345 East 47th Street, New York, N.Y. 10017, and will be accepted until two months after final publication of the paper itself in the JOURNAL OF APPLIED MECHANICS. Manuscript received by ASME Applied Mechanics Division, November, 1983; final revision, May, 1984.

Copyright © 1985 by ASME
Downloaded 02 May 2010 to 171.66.16.54. Redistribution subject to ASME license or copyright; see http://www.asme.org/terms/Terms_Use.cfm

ponents, U is the external potential velocity, ν is the kinematic viscosity, and subscripts x, y indicate the derivatives in the x and y directions, respectively (see Fig. 1), with the following boundary conditions:

$$\begin{aligned} y=0: \quad & u = 0 \\ & u_x = 0 \\ & v \equiv v_0 \\ y\to\infty; \quad & u = U \end{aligned} \tag{2}$$

where v_0 is the normal velocity component at the permeable surface.

The last term in the momentum equation (1a) is the transverse curvature term. The transverse curvature effect, which is negligible for thin boundary layers, is retained here to enable solutions of flows over long axisymmetric cylindrical bodies where the boundary layer thickness is not small relative to the local body radius.

Following Ringleb's approach for two-dimensional flows [6], the first three y derivatives of the momentum equation (1a) are taken. For example, the first derivative is

$$u_y u_x + u u_{xy} + v_y u_y + v u_{yy} = \nu[u_{yyy} + (r_y/r)u_{yy} + (r_y/r)_y u_y] \tag{3}$$

and by assuming the wall condition $y = 0$, and introducing the suction velocity derivatives from the successive derivation of the continuity equation (1b), where $E = (r_y/r)$ at $y = 0$,

$$(v_y)_0 = -E v_0$$
$$\vdots$$

We define the following four compatibility conditions at the cylinder surface $y = 0$:

$$\begin{aligned} &(v_0 - \nu E)u_y = U U_x + \nu u_{yy} \\ &(v_0 - \nu E)u_{yy} - E(v_0 - \nu E)u_y = \nu u_{yyy} \\ &(v_0 - \nu E)u_{yyy} - 2E(v_0 - \nu E)u_{yy} + 2E^2(v_0 - \nu E)u_y \\ &+ u_y u_{xy} - G u_y^2 = \nu u_{yyyy} \\ &(v_0 - \nu E)u_{yyyy} - 3E(v_0 - \nu E)u_{yyy} + 6E^2(v_0 - \nu E)u_{yy} \\ &- 6E^3(v_0 - \nu E)u_y + 2u_y u_{xyy} - 4G u_y u_{yy} \\ &+ (3EG - 2K)u_y^2 + E u_y u_{xy} = \nu u_{yyyy} \end{aligned} \tag{5}$$

Here, $G = (r_x/r)$ at $y = 0$ and $K = (r_{xy}/r)$ at $y = 0$.

Except for a few exact solutions to special cases of the boundary layer equations, all the solutions of this set of partial differential equations are approximate. The approximation may be a numerical one (see reference [7] for example) or an analytical one [5]. While the numerical solutions are more versatile, they are prone to instabilities and other problems [8], and usually are significant consumers of computer time. On the other hand, the analytical approximations are easily applicable but only to relatively simple problems. We developed an approximate analytical method to solve equation (5). This method will be later shown to be simple, accurate and suitable to solutions of axial flow with suction on long thin cylinders.

Following Wuest's exact solution for the asymptotic suction flow over long thin cylinders [9]:

$$\frac{u}{U} = 1 - \left(\frac{r}{a}\right)^{\beta} \tag{6}$$

where

$$\beta \equiv \frac{v_0 a}{\nu} \quad ,$$

and a is the cylinder radius, we now define an approximate velocity profile of the form:

$$\frac{u}{U} = 1 - (1+\eta)^{(A(\xi) + B(\xi)\eta + C(\xi)\eta^2 + D(\xi)\eta^3)} \tag{7}$$

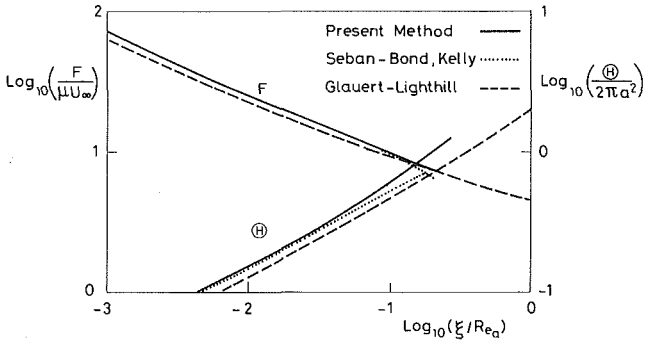


Fig. 2 Nondimensional friction force and nondimensional momentum defect area; present method results as compared with other solutions

where

$$\xi = \frac{x}{L} \quad , \qquad \eta = \frac{y}{L} \quad ,$$

L is a reference length (can be the cylinder length) and A, B, C, D are as yet unknown parameters. One can now compute the local properties A, B, C, and D from the compatibility conditions (5). Due to its resemblance to the exact solution (6), this velocity profile is expected to be particularly accurate for suction solutions.

The wall velocity derivatives are computed from equation (7):

$$\begin{aligned} u_y|_0 &= -\frac{U}{L}(A) \\ u_{yy}|_0 &= -\frac{U}{L^2}(A^2 + 2B - A) \\ u_{yyy}|_0 &= -\frac{U}{L^3}(A^3 - 3A^2 + 2A + 6AB - 3B + 6C) \\ u_{xy}|_0 &= -\frac{1}{L}(U_x A + U A_x) \end{aligned} \tag{8}$$

and inserted in the compatibility conditions (5). The first three equations (5) are solved for B, C, and D as functions of the coefficient A. Then, the last compatibility conditions defines an ordinary differential equation for the coefficient A, with the longitudinal coordinate ξ as independent variable, and with the body geometric and kinematic variables as parameters. This equation, when simplified for a semi-infinite circular cylinder (with the reference length L equal to the cylinder radius a), gives the final differential equation:

$$\begin{aligned} &(30A^2 - 3A - 18\beta A)\mathrm{Re}_a A = -144A^5 - 270A^4 - 220A^3 \\ &- 90A^2 + 12\mathrm{Re}_a \beta A^2 + \beta(360A^4 + 540A^3 + 330A^2) \\ &+ 90A) + \beta^2(-300A^3 - 315A^2 - 110A) \\ &+ \beta^3(90A^2 + 45A) + \beta^4(-6A) \end{aligned} \tag{9}$$

where

$$\mathrm{Re}_a = \frac{U a}{\nu} \quad .$$

3 Results

(*A*) Semi-Infinite Circular Cylinder With Impermeable Wall. The full axisymmetric boundary layer equations over a long circular cylinder were repeatedly solved in the past by a variety of approximate Pohlhausen-type and series expansion

Downloaded 02 May 2010 to 171.66.16.54. Redistribution subject to ASME license or copyright; see http://www.asme.org/terms/Terms_Use.cfm

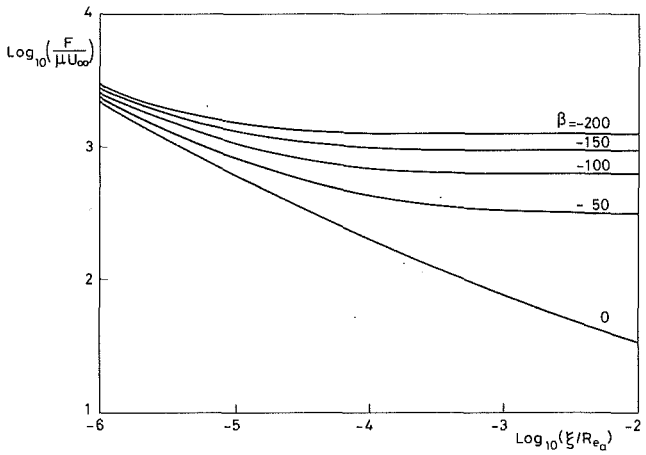


Fig. 3 Nondimensional friction force as function of the longitudinal coordinate, for various values of the suction parameter β

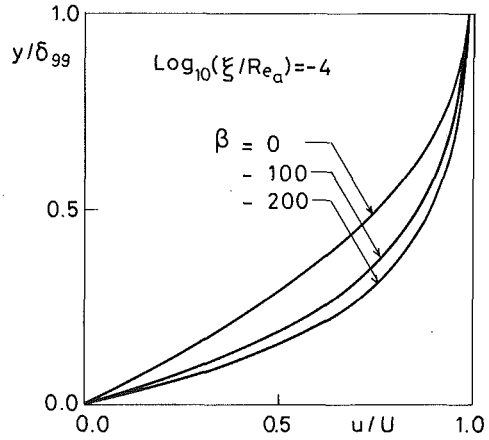


Fig. 4 Boundary layer velocity profiles for various values of the suction parameter. δ is the boundary layer thickness based on 99 percent recovery of the inviscid velocity

methods [10–12]. We now use these solutions as a check to test the accuracy of the proposed method.

In case of the cylinder with impermeable wall, equation (9) is reduced to:

$$\mathrm{Re}_a A = \frac{144A^4 + 270A^3 + 220A^2 + 90A}{3 - 30A} \tag{10}$$

which may be solved with $1/A \to 0$ for $\xi \to 0$ [12]. The nondimensional friction force per unit length $F(F/\mu U = -2\pi A)$ and the nondimensional momentum defect area $\theta(\theta/\pi a^2 = 2 \int_0^\infty (u/U)\,[1-u/U][1+y/a]d(y/a))$ are presented in Fig. 2 as function of the longitudinal coordinate ξ. It can be seen that the curve of the present solution for the friction force is identical to that of the exact series expansion due to Seban and Bond [10], up to $\xi = 0.178\ \mathrm{Re}_a$, where both solutions are no longer valid. This is due to the fact that far from the cylinder nose the coefficient A becomes positive, and the profile (7) ceases to fulfill the boundary condition (2) at $y -> \infty$. The point $\xi = 0.178\ \mathrm{Re}_a$ is equivalent to a cylinder length of over 17000 radii for $\mathrm{Re}_a = 10^5$, and thus the continuation of the solution beyond this point is of theoretical interest only.

The momentum area found here seems to be less accurate. This is in agreement with the fact that the compatibility conditions (5) are exact at the surface $y = 0$ while the velocity profile (7) is only approximate throughout the boundary layer [13].

Finally, the present solution method is shown to be accurate very far along the cylinder. In contrast, the Pohlhausen-type solution due to Glauert and Lighthill [12] suffers from an error of 12 percent in the friction force and 16 percent in the momentum area, relative to the Seban and Bond solution.

(*B*) Semi-Infinite Circular Cylinder With Constant Suction. The case of the semi-infinite circular cylinder with constant suction is analogous to the well-known Iglisch [14] flow over a flat plate. But although there are numerous solutions to the two-dimensional case [6, 7, 15], no solution is known to the axisymmetric case.

In this case of uniform suction, equation (8) reduces to:

$$(30A^2 - 3A - 18\beta A)\mathrm{Re}_a A = -144A^5 - 270A^4 - 220A^3 - 90A^2 + \beta(360A^4 + 540A^3 + 330A^2 + 90A) + \beta^2(-300A^3 - 315A^2 - 110A) + \beta^3(90A^2 + 45A) + \beta^4(-6A) \tag{11}$$

and equation (11) is solved by an integration from $\xi = 0$ $(1/A = 0)$ with constant β.

Figure 3 describes the nondimensional friction force as function of ξ, for various values of the suction parameter. The force asymptotically approaches the axisymmetric asymptotic suction solution due to Wuest [9]:

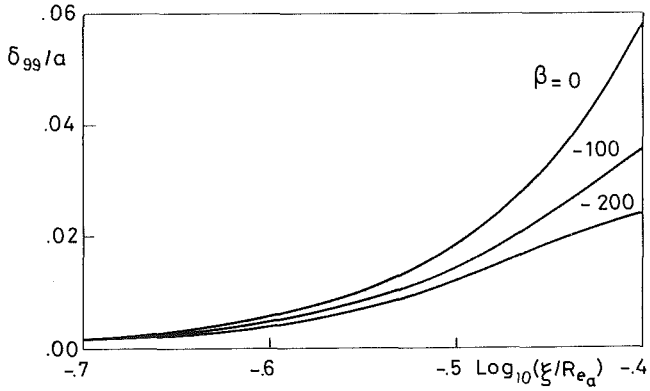


Fig. 5 Boundary layer thickness as function of the longitudinal coordinate, for various values of the suction parameter

$$\frac{F}{\mu U} = -2\,\pi\beta \tag{12}$$

a fact that can be checked by introducing the exact value $A = \beta$ in equation (11) which results in $dA/d\xi = 0$ at infinity. μ is the coefficient of viscosity.

Figure 4 describes the boundary layer velocity profiles for various suction parameters β. It can be observed that the increase in the suction velocity is accompanied by an increase in the local friction coefficient. Figure 5 describes the boundary layer thickess as function of ξ, for various β values. The boundary layer in the suction case is shown to be thinner than the equivalent zero suction layer. These two properties of suction (the velocity profile fullness and the decrease in thickness) are well-known stabilizing parameters [5]. This suggests the ability of distributed suction to prevent boundary layer transition and to a lesser degree to delay separation.

To evaluate qualitatively the influence of distributed suction on transition, the transition point location of the flow over a semi-infinite cylinder was calculated with the Michel-e^9 [16] criterion. The transition location as function of the suction parameter β, and Reynolds number based on cylinder radius Re_a is presented in Fig. 6. For moderate Reynolds numbers ($\mathrm{Re}_a \leq 10^6$), low suction velocities are sufficient to achieve a significant shift downstream in the transition location. For high Reynolds numbers ($\mathrm{Re}_a > 10^6$) the suction influence is insignificant, at least in the range of suction velocities examined.

For a given Reynolds number Re_a, an increase in the suction velocity causes a downstream displacement of the transition point. When the suction velocity is increased beyond a certain (Reynolds-number-dependent) value, the

Downloaded 02 May 2010 to 171.66.16.54. Redistribution subject to ASME license or copyright; see http://www.asme.org/terms/Terms_Use.cfm

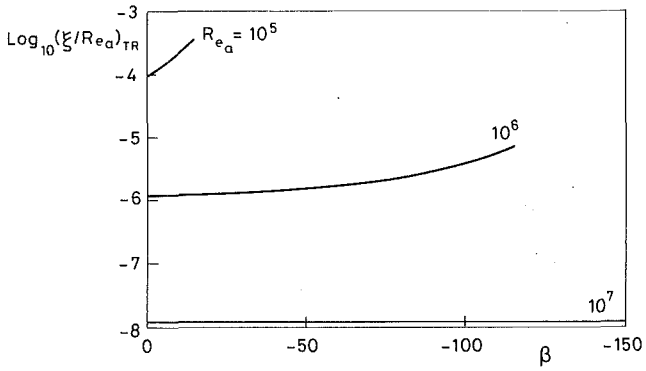


Fig. 6 Longitudinal transition location as function of the suction parameter, for various cylinder Reynolds numbers

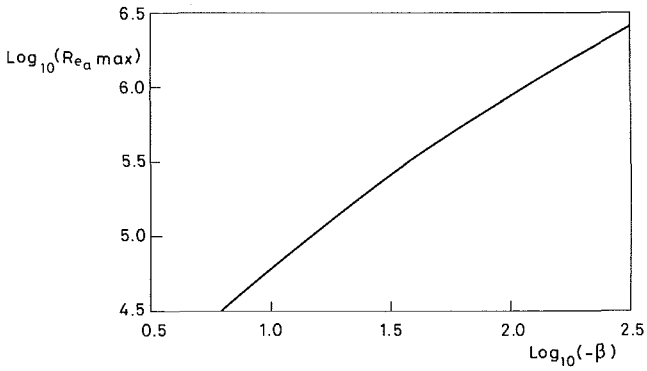


Fig. 7 Maximum Reynolds number along which there is no transition, as function of the suction parameter

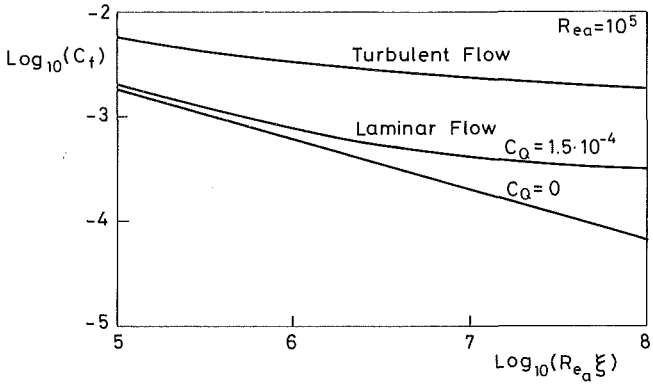


Fig. 8 Skin friction coefficients C_f for turbulent, laminar, and suction-controlled boundary layers, as function of the axial Reynolds number. $C_Q = -v_0/U$ is the suction volume coefficient [5]

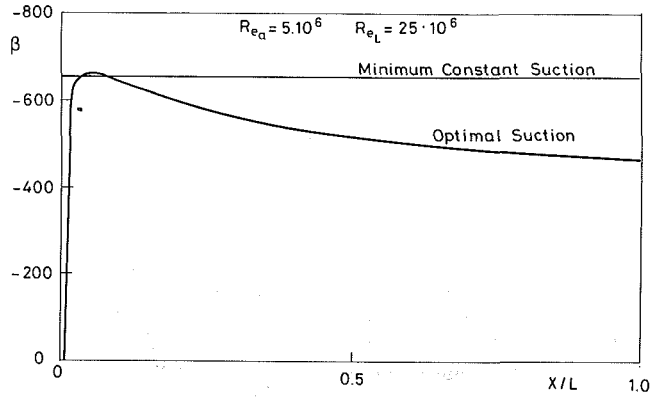


Fig. 9 Distribution of optimal suction required to delay the onset of instability. $Re_L = UL/\nu$ is the Reynolds number based on cylinder length L

transition pont is entirely eliminated. This is due to the fact that the boundary layer is then close to the asymptotic behavior while the transition criterion allows a certain increase of thickness with the longitudinal coordinate. Thus, for every suction parameter β, there is a maximum Reynolds number $Re_{a_{max}}$ along which there is no transition. $Re_{a_{max}}$ is presented in Fig. 7 as a function of β.

The validity of the Michel-e[9] transition criterion in our case is questionable. This semiempirical criterion was originally formulated for axisymmetric bodies with no suction and is not supposed to predict the transition location along a long thin cylinder with constant suction. Nonetheless, we believe that the trends of the delay in transition by the distributed suction can be demonstrated by this criterion, although the exact transition location is, most probably, not correctly predicted.

Finally the drag reduction capability of distributed suction is demonstrated in Fig. 8, where the skin friction coefficient C_f of the turbulent boundary layer is compared to the laminar skin friction and to that of the minimum suction velocity flow required to maintain the boundary layer laminar. A local friction coefficient reduction between 86–96 percent is achieved, depending on the longitudinal location along the cylinder.

(C) Semi-Infinite Circular Cylinder With Optimal Suction. To evaluate the stabilization capability of distributed suction, the optimal suction velocity distribution for a $Re_a = 5 \cdot 10^6$ cylinder was computed by means of equation (9), and is presented in Fig. 9. This optimal suction is defined as the distribution of minimum local suction velocity required to maintain the boundary layer stable, according to the Wieghardt stability criterion [7]:

$$(Re_{\delta_2})\text{crit} = \left(\frac{U\,\delta_2}{\nu}\right)_{\text{crit}} = e^{29.1\text{-}9H} \qquad (13)$$

where δ_2 is the momentum thickness, and H is the boundary layer shape factor. Here, a stability criterion is used instead of a transition criterion because the stability criterion is more sensitive to local changes in the boundary layer due to changes in the suction velocity. In the present case, the fluid volume withdrawn by suction is about 20 percent lower than the volume required when the minimum constant suction velocity is applied. This decrease in the suction volume (and correspondingly, in the energy required for suction) is expected to be more significant for longer cylinders of given radius.

4 Concluding Remarks

The preceding analyses of drag along a very long cylindrical body show that by withdrawing relatively small amounts of fluid from the boundary layer, the flow can be kept laminar at high Reynolds numbers, resulting in dramatic decreases in the drag.

This technique, which is well known for airfoils, has hitherto not been applied to fuselages, airships, and underwater bodies. However, the large savings possible makes this technically complicated method attractive as a drag-reducing technique.

References

1 Parsons, J. S., Goodson, R. E., and Goldschmied, F. R., "Shaping of Axisymmetric Bodies of Minimum Drag In Incompressible Flow," *J. Hydronautics*, Vol. 8, 1974, pp. 100–107.

2 Zedan, M. F., and Dalton, C., "Viscous Drag Computation for Axisymmetric Bodies at High Reynolds Numbers," *J. Hydronautics*, Vol. 13, 1979, pp. 52–60.

3 Bushnell, D. M., "Turbulent Drag Reduction for External Flows," AIAA Paper 83-0227, 1983.

Downloaded 02 May 2010 to 171.66.16.54. Redistribution subject to ASME license or copyright; see http://www.asme.org/terms/Terms_Use.cfm

4 Wazzan, A. R., Gazley, C., and Smith, A. M. O., "Tollmien-Schlichting Waves and Transition," *Prog. Aerospace Sci.*, Vol. 18, 1979, pp. 351–486.

5 Schlichting, H., *Boundary-Layer Theory*, McGraw-Hill, New York, 1968.

6 Ringleb, F. O., "Computation of the Laminar Boundary Layer With Suction," *J. Aeronautical Sci.*, Vol. 19, 1952, pp. 48–54.

7 Cebeci, T., and Bradshaw, P., *Momentum Transfer in Boundary Layers*, McGraw-Hill, New York, 1977.

8 Roache, P. J., *Computational Fluid Dynamics*, Hermosa Publishers, Albuquerque, N. Mex., 1972.

9 Wuest, W., "Asymptotische Absaugegrenzschichten an Langsangestromtem Zylindrischen Korper," *Ingr.-Arch.*, Vol. 23, 1955, pp. 198–208.

10 Seban, R. A., and Bond, R., "Skin Friction and Heat Transfer Characteristics of a Laminar Boundary Layer on a Cylinder in Axial Incompressible Flow," *J. Aeronautical Sci.*, Vol. 18, 1951, pp. 671–675.

11 Kelly, H. R., "A Note on the Laminar Boundary Layer on a Circular Cylinder in Axial Incompressible Flow," *J. Aeronautical Sci.*, Vol. 21, 1954, p. 634.

12 Glauert, M. B., and Lighthill, M. J., "The Axisymmetric Boundary Layer on a Long Thin Cylinder," *Proc. Royal Soc.*, London, Series A, Vol. 230, 1955, pp. 188–203.

13 Weihs, D., "On the Polynomial Approximation of Boundary-Layer Flow Profiles," *App. Sci. Res.*, Vol. 31, 1975, pp. 253–265.

14 Iglisch, R., "Exact Calculation of Laminar Boundary Layer in Longitudinal Flow Over a Flat Plate With Homogeneous Suction," NACA TM 1205, 1949.

15 Head, M. R., "An Approximate Method of Calculation the Laminar Boundary Layer in Two Dimensional Incompressible Flow," ARC R and M 3123, 1959.

16 White, F. M., *Viscous Fluid Flow*, McGraw-Hill, New York, 1974.

17 Wieghardt, K., "Zur Berechnung Ebener und Drehsymmetrischer Grenzschicten mit Kontinuierlicher Absaugung," *Ingr.-Arch.*, Vol. 22, 1954, pp. 368–377.

Downloaded 02 May 2010 to 171.66.16.54. Redistribution subject to ASME license or copyright; see http://www.asme.org/terms/Terms_Use.cfm

C. Katsis
Research Assistant.

T. R. Akylas
Assistant Professor.
Assoc. Mem. ASME

Department of Mechanical Engineering,
Massachusetts Institute of Technology,
Cambridge, Mass. 02139

Wind-Generated Surface Waves on a Viscous Fluid

The excitation of surface waves on a viscous fluid by shear flows is studied. Turbulent and laminar air flows over oil of low and high viscosity are considered. It is found that the dominant wave-generation mechanism depends crucially on the shear-flow profile: for a turbulent flow, long surface waves are generated at low wind speeds due to the work done by the stress components in phase with the surface slope, while Kelvin-Helmholtz instability is responsible for the excitation of short waves at higher wind speeds. On the other hand, for a laminar shear flow, direct resonance between surface waves and Tollmien-Schlichting waves in the shear flow is the dominant wave-generation mechanism.

Introduction

The problem of surface-wave generation by shear flows is of primary importance to the development of wave forecasting methods and to the understanding of boundary-layer interaction with flexible walls.

In the last three decades, extensive efforts have been made to gain an understanding of the generation mechanisms of surface waves by shear flows. In a series of pioneering papers, Miles [1–4] investigated various possibilities of energy transfer from an air shear flow to water; he pointed out [3] that surface waves can be generated by a shear flow due to static or dynamic instability; static instability, which does not depend on phase changes across the flow, is possible when the aerodynamic suction in phase with the surface displacement can overcome the surface restoring forces, while dynamic instability occurs due to the work done by the stress component in phase with the surface slope. Thus, static instability, as defined by Miles [3], is an extension of the classical Kelvin-Helmholtz instability of a vortex sheet.

As is well known, in an air-water system, the wind speed required for Kelvin-Helmholtz instability (about 660 cm/s) is much in excess of the observed minimum wind speed for water-wave generation. Accordingly, static instability is of minor importance to the initial growth of wind-driven water waves.

On the other hand, for an air shear flow over a rather viscous fluid, like oil, Miles [3] suggested that dynamic instability is inhibited by viscous effects and, thus, static instability should dominate. Miles's argument was based on an approximate variational formulation of the shear-flow stability problem, which took into account the forces in phase with the surface displacement only, and neglected the effect of the oil viscosity. Nevertheless, the theoretical predictions were in very good agreement with the experimental observations of Francis [5, 6], who found that the minimum wind speed for oil-wave excitation could be predicted by the simple Kelvin-Helmholtz instability model and was almost independent of the oil viscosity.

In the present study, the generation of surface waves on a viscous fluid by an air shear flow is investigated by solving the appropriate stability problem numerically; both turbulent and laminar mean air flows over oil of low and high viscosity are considered. Miles's approximate analysis [3] is assessed by calculating the aerodynamic suction in phase with the surface displacement and comparing it with the restoring forces of gravity and surface tension. It is found that the dominant wave-generation mechanism depends crucially on the shear-flow profile: for a turbulent shear flow, long surface waves are generated at low wind speeds due to dynamic instability, while Kelvin-Helmholtz instability is responsible for the excitation of short waves at higher wind speeds. As the fluid viscosity is increased, dynamic instability is suppressed and Kelvin-Helmholtz instability tends to dominate, in accordance with Miles's approximate analysis [3]. However, the numerical results indicate that, for highly viscous oil, Miles's criterion for static instability could be misleading, owing to the significant effect of viscosity on the short-wave growth rates. On the other hand, for a laminar air-flow, surface waves can be generated at quite low wind speeds, even for oil of very high viscosity, due to direct resonance [4, 7, 8] between surface waves and Tollmien-Schlichting waves in the shear flow.

Stability Analysis

Consider a steady parallel shear flow of two semi-infinite homogeneous incompressible fluids in contact. Let x be the streamwise coordinate and y the vertical coordinate, so that the undisturbed fluid interface is at $y = 0$. The fluid occupying the region $y > 0$ is taken to be air of density ρ_+ and kinematic viscosity ν_+, while the fluid in $y < 0$ is oil of density ρ_- and kinematic viscosity ν_-. The basic undisturbed flow consists of an air shear flow of the boundary-layer type,

Contributed by the Applied Mechanics Division for publication in the JOURNAL OF APPLIED MECHANICS.

Discussion on this paper should be addressed to the Editorial Department, ASME, United Engineering Center, 345 East 47th Street, New York, N.Y. 10017, and will be accepted until two months after final publication of the paper itself in the JOURNAL OF APPLIED MECHANICS. Manuscript received by ASME Applied Mechanics Division, February, 1984; final revision, June, 1984.

Copyright © 1985 by ASME
Downloaded 02 May 2010 to 171.66.16.54. Redistribution subject to ASME license or copyright; see http://www.asme.org/terms/Terms_Use.cfm

$(U_+(y), 0, 0)$ in $y > 0$ and an induced current in the oil $(U_-(y), 0, 0)$, $y < 0$.

The stability of the basic steady shear flow and the fluid interface to small-amplitude perturbations is examined by linearizing the governing equations of motion and assuming normal-mode disturbances:

$$\eta(x,t) = S\, e^{i\alpha(x-ct)}, \quad \psi_\pm(x,y,t) = \phi_\pm(y) e^{i\alpha(x-ct)} \quad (y \gtrless 0), \tag{1}$$

where $y = \eta(x, t)$ is the equation of the perturbed interface, and $\psi_\pm$ are the perturbation streamfunctions in $y \gtrless 0$.

Upon substitution of the assumed forms (1) in the linearized equations of motion, it is found that the amplitudes of the perturbation streamfunctions $\psi_\pm(y)$ satisfy the Orr-Sommerfeld equations:

$$(U_\pm - c)\left(\frac{d^2}{dy^2} - \alpha^2\right)\phi_\pm - U_\pm''\phi_\pm = \frac{\nu_\pm}{i\alpha}\left(\frac{d^2}{dy^2} - \alpha^2\right)^2 \phi_\pm \quad (y \gtrless 0), \tag{2}$$

subject to boundedness conditions at infinity:

$$\phi_\pm \to 0 \quad (y \to \pm\infty), \tag{3}$$

and the interface conditions:

$$S = \frac{\phi_+}{c - U_0} = \frac{\phi_-}{c - U_0} \quad (y = 0), \tag{4}$$

$$(U_0 - c)\frac{d\phi_+}{dy} - U_+'\phi_+ - (U_0 - c)\frac{d\phi_-}{dy} + U_-'\phi_- = 0 \quad (y = 0), \tag{5}$$

$$U_+''\phi_+ - (U_0 - c)\left(\frac{d^2\phi_+}{dy^2} + \alpha^2\phi_+\right) - \frac{\nu_-}{\nu_+}\frac{\rho_-}{\rho_+}\left[U_-''\phi_- - (U_0 - c)\left(\frac{d^2\phi_-}{dy^2} + \alpha^2\phi_-\right)\right] = 0 \quad (y = 0), \tag{6}$$

$$\alpha(U_0 - c)\left[(U_0 - c)\frac{d\phi_+}{dy} - U_+'\phi_+\right] + i\nu_+(U_0 - c)\left(\frac{d^3\phi_+}{dy^3} - 3\alpha^2\frac{d\phi_+}{dy}\right) + 2i\nu_+\alpha^2 U_+'\phi_+ - g\,\alpha\,\phi_+ - \frac{\rho_-}{\rho_+}\alpha(U_0 - c)\left[(U_0 - c)\frac{d\phi_-}{dy} - U_-'\phi_-\right] - i\nu_-\frac{\rho_-}{\rho_+}(U_0 - c)\left(\frac{d^3\phi_-}{dy^3} - 3\alpha^2\frac{d\phi_-}{dy}\right) - 2i\nu_-\frac{\rho_-}{\rho_+}\alpha^2 U_-'\phi_- + \frac{\rho_-}{\rho_+}g\,\alpha\,\phi_- + \frac{\alpha^3}{\rho_-}\phi_+ T = 0 \quad (y = 0), \tag{7}$$

where T is the interfacial tension, g is the gravitational acceleration, $U_0 = U_+(0) = U_-(0)$, and $U_\pm' = dU_\pm/dy$, $U_\pm'' = d^2U_\pm/dy^2$. The conditions (4) and (5) ensure that the continuity of normal and tangential velocities is satisfied at the interface, while (6) and (7) follow from the continuity of the tangential stresses and the balance of the normal stresses with the interfacial tension at $y = 0$; the detailed derivation of the equations (2)–(7) is given in [9] and will not be repeated here.

The equations (2) subject to the conditions (3)–(7) define an eigenvalue problem for c; for the temporal-stability problem, which is of interest here, the wave number α is taken to be real, so that the growth or decay of perturbations is decided by the sign of the imaginary part c_i of the generally complex phase speed $c = c_r + i\,c_i$. The numerical solution of the eigenvalue problem will be discussed in the following sections.

As already indicated, for wind-generated surface waves on a highly viscous fluid, like oil, Miles [3] suggested that the appropriate wave-generation mechanism is static, or Kelvin-Helmholtz, instability: independently of the fluid viscosity, instability should occur when the aerodynamic suction in phase with the interface displacement can dominate the restoring forces of gravity and interfacial tension. In the present formulation, the amplitude of the component of aerodynamic suction in phase with the interface displacement is

$$\rho_+\left[(U_0 - c_r)\frac{d\phi_{+r}}{dy} + c_i\frac{d\phi_{+i}}{dy} - U_+'\phi_{+r}\right] + \rho_+ g + \nu_+\rho_+\left[\alpha\frac{d\phi_{+i}}{dy} - \frac{1}{\alpha}\frac{d^3\phi_{+i}}{dy^3}\right] + 2\nu_+\rho_+\alpha\frac{d\phi_{+i}}{dy} \quad (y = 0), \tag{8}$$

and the restoring force due to gravity and interfacial tension is

$$-\rho_- g - T\alpha^2, \tag{9}$$

where S has been normalized to unity, and $\phi_\pm = \phi_{\pm r} + i\phi_{\pm i}$. Thus, according to Miles [3], wave growth should be initiated when the two expressions in (8) and (9) are of comparable magnitude.

Turbulent Shear Flow

The experiments of Francis [5, 6] involved a turbulent air flow over oil. Accordingly, in this section, the mean flow $U(y)$ is taken to be a linear-logarithmic profile, typical of turbulent boundary layers:

$$U_+(y) = \begin{cases} U_0 + \dfrac{U_{*+}^2}{\nu_+}y & (0 \le y \le \tilde{y}_+) \\ U_0 + \tilde{U}_+ + \dfrac{1}{\kappa}U_{*+}\left[\alpha - \tanh\left(\dfrac{\alpha}{2}\right)\right] & (y > \tilde{y}_+), \end{cases} \tag{10a}$$

$$U_-(y) = \begin{cases} U_0 + \dfrac{U_{*-}^2}{\nu_-}y & (\tilde{y}_- \le y \le 0) \\ U_0 + \tilde{U}_- - \dfrac{1}{\kappa}U_{*-}\left[\alpha - \tanh\left(\dfrac{\alpha}{2}\right)\right] & (y < \tilde{y}_-), \end{cases} \tag{10b}$$

with

$$y = \tilde{y}_\pm \pm \frac{1}{2\kappa}\frac{\nu_\pm}{U_{*\pm}}\sinh\alpha \quad (\alpha > 0, y \gtrless 0) \tag{10c}$$

and

$$\tilde{U}_\pm = \frac{U_{*\pm}^2}{\nu_\pm}\tilde{y}_\pm; \tag{10d}$$

$U_{*\pm}$ are the air and oil friction velocities, related through $U_{*-} = (\rho_+/\rho_-)^{1/2}U_{*+}$ by the continuity of shear stress at the interface, and $\kappa = 0.4$ is von Kármán's constant. Furthermore, in the subsequent analysis, it is assumed that the basic-flow profile (1) can be treated as quasilaminar: the effect of the turbulent Reynolds stresses on the waves is not taken into account.

The stability problem defined by the equations (2)–(7) was solved numerically for air ($\rho_+ = 0.0012$ g/cm^3, $\nu_+ = 0.15$ cm^2/s) over two kinds of oil of the same density, $\rho_- = 0.875$ g/cm^3, and interfacial tension, $T = 34$ dynes/cm, but quite different viscosities: $\nu_- = 2.5$ cm^2/s and $\nu_- = 28.75$ cm^2/s; these oil properties are in accordance with those used in the experiments of Francis [5, 6]. Also, the scales $\tilde{y}_\pm$ of the linear portions of the basic-flow profile in (10*a*) and (10*b*) were assigned the typical values: $\tilde{y}_\pm = 5\nu_\pm/U_{*\pm}$, the interface

Downloaded 02 May 2010 to 171.66.16.54. Redistribution subject to ASME license or copyright; see http://www.asme.org/terms/Terms_Use.cfm

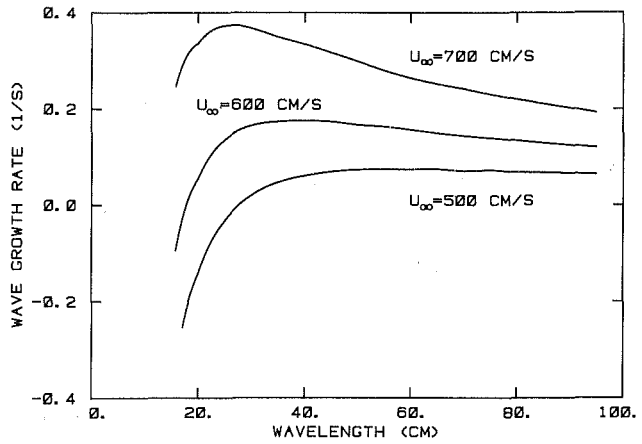


Fig. 1(*a*) Dynamic instability

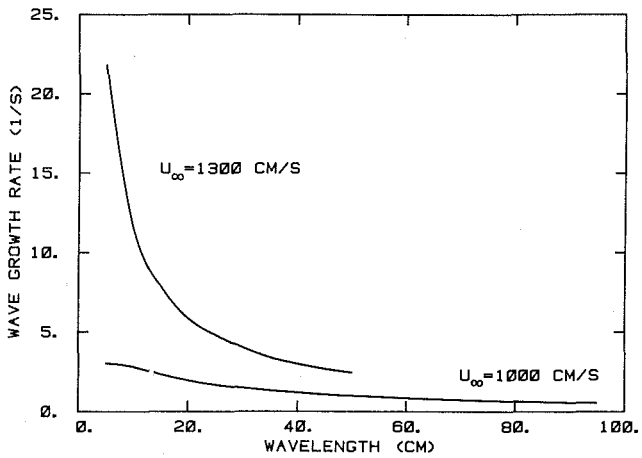


Fig. 1(*b*) Kelvin-Helmholtz instability

Fig. 1 Wave-growth rates for turbulent mean flow and oil of low viscosity

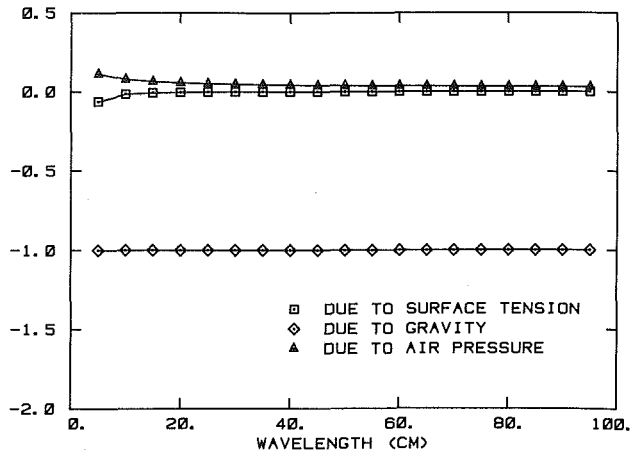


Fig. 2(*a*) U_∞ = 5 m/s

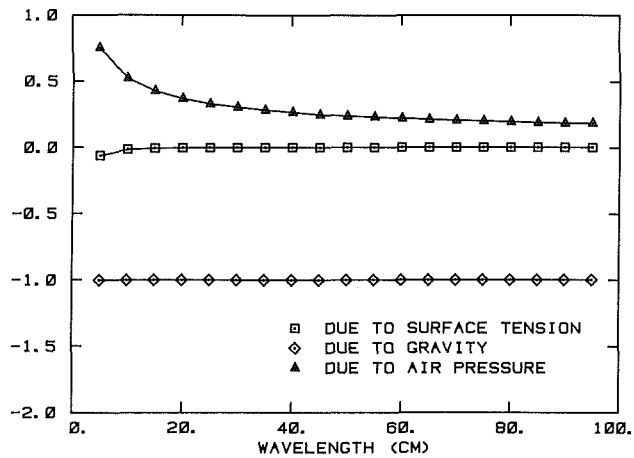


Fig. 2(*b*) U_∞ = 10 m/s

Fig. 2 Relative amplitudes of stresses in phase with the interface displacement for oil of low viscosity

velocity U_0 was taken to be 0.005 U_∞ for the oil of low viscosity and 0.002 U_∞ for the oil of high viscosity, and, finally, the free-stream wind speed U_∞ was related to the air friction velocity through $U_{*+} = 0.05\, U_\infty$.

The numerical solution of the eigenvalue problem (2)–(7) was carried out by a standard shooting method: for given α and a guess for c, the solutions of the Orr-Sommerfeld equations (2), which decay as $y \to \pm\infty$, were integrated numerically toward the interface $y = 0$, where the boundary conditions (4)–(7) were applied and an improved trial value of c was obtained through Newton iteration; the procedure was repeated until convergence to the eigenvalue was achieved within the desired accuracy. Particular care was given to the selection of the starting point of the numerical integration, so that the slow variation of $U_\pm(y)$ as $y \to \pm\infty$ did not influence the value of c; by numerical experiments, it was decided that it was adequate to start the numerical integration at a distance of $O(U_{*+}/\nu_+\alpha)$ from the interface. As a check of the numerical calculations, the adjoint eigenvalue problem was also solved and agreement with the eigenvalues of the original problem was obtained.

For the oil of low viscosity, the calculated growth rates are plotted in Figs. 1(*a*) and (*b*) as functions of wavelength, for various wind speeds. The minimum wind speed for surface-wave excitation is about 3 m/s, for waves about 1 m long. As the wind speed is increased, the maximum wave-growth rate increases and the wavelength of the most-unstable wave decreases; for wind speeds around 10 m/s, the most-unstable waves have wavelengths of a few cm. Figures 2(*a*) and (*b*) show the relative magnitudes of the aerodynamic suction and interfacial-tension force compared to the gravitational force (which is normalized to unity), for U_∞ = 5 m/s and U_∞ = 10 m/s, respectively. It is clear that for U_∞ = 5 m/s no static instability is involved since the aerodynamic suction is significantly smaller than the restoring gravity force. However, at U_∞ = 10 m/s and for short waves, static instability is certainly possible, for the aerodynamic suction is of the same order of magnitude as the sum of the restoring forces of gravity and interfacial tension; in addition, the wavelength of the wave with the maximum growth rate is about the same as the wavelength at which the aerodynamic suction attains its maximum value compared to gravity and interfacial tension.

Consider now the growth rates of surface waves on the oil of high viscosity. At U_∞ = 5 m/s, no amplified waves were found, implying that static instability is indeed suppressed by viscous effects, as conjectured by Miles [3]. However, it is clear (see Fig. 3) that the instability mechanism depends on viscosity: at U_∞ = 10 m/s, short waves (of wavelength less than about 35 cm) are damped, although, at the same wind speed, those waves are amplified on the oil of low viscosity due to static instability (see Fig. 1(*b*)). It is interesting to notice that the relative magnitude of the aerodynamic suction compared to the restoring forces of gravity and interfacial tension is, to an excellent approximation, independent of viscosity (see Figs. 2(*b*), 4); based on Miles's criterion for

Downloaded 02 May 2010 to 171.66.16.54. Redistribution subject to ASME license or copyright; see http://www.asme.org/terms/Terms_Use.cfm

static instability, therefore, without including the effect of viscosity on the wave-growth mechanism, one could be led to the erroneous conclusion that short waves are amplified on the oil of high viscosity at $U_\infty = 10$ m/s. In other words, there are two effects that determine the stability charcteristics of relatively short waves on a viscous fluid: first, the destabilizing effect of the aerodynamic suction, which can dominate the restoring forces of gravity and interfacial tension at high enough wind speed almost independently of the fluid viscosity; and, secondly, the damping effect of viscosity, which becomes more pronounced for short waves. Accordingly, at $U_\infty = 10$ m/s, the effect of the aerodynamic suction dominates the viscous damping for the oil of low viscosity (see Fig. 1(*b*)), while damping dominates the effect of the aerodynamic suction for the oil of high viscosity (see Fig. 3); at $U_\infty = 13$ m/s, the aerodynamic suction dominates in both kinds of oil, but the effect of damping is still apparent in the smaller growth rates obtained for the highly viscous oil (see Figs. 1(*b*), 3).

Some aspects of the theoretical predictions are in good agreement with the experimental results of Francis [5, 6]: the amplification of short waves (of about 2 cm wavelength and 1 cm/s phase speed) on the oil of low viscosity due to Kelvin-Helmholtz instability at $U_\infty = 10$ m/s, and the decrease of the wave-growth rates as the oil viscosity is increased are in accordance with the observations of Francis. On the other hand, Francis [6] estimates that the wind speed required for the excitation of short waves on the highly-viscous oil is only about 4 percent greater than that required for the excitation of the same waves on the less viscous oil. The theoretical results, however, indicate that an increase in wind speed of about 20 percent is required, primarily due to the effect of viscosity on the short-wave growth rates. Furthermore, Francis [5, 6] reports that, on both kinds of oil, as the wind speed is increased, the first observable waves are relatively short (of a few cm wavelength), while the analysis suggests that the onset of instability is realized for wave disturbances of substantially longer wavelength.

The cause of the discrepancy between the theoretical predictions and the experimental observation remains unclear. It may be argued that the long-wave instabilities at low wind speeds, predicted theoretically (Fig. 1(*a*)), involve very small growth rates and possibly could be stabilized by effects not included in the analysis, such as the action of turbulent Reynolds stresses, finite-amplitude effects, etc. In addition, the fact that the experiments of Francis [5, 6] were conducted in a shallow channel (15 cm oil depth) suggests that waves of wavelength comparable to the oil depth, or longer, could experience additional damping due to bottom friction. Further experiments are desirable to answer these questions.

Laminar Mean Flow

Lock [10] found a solution to the boundary-layer

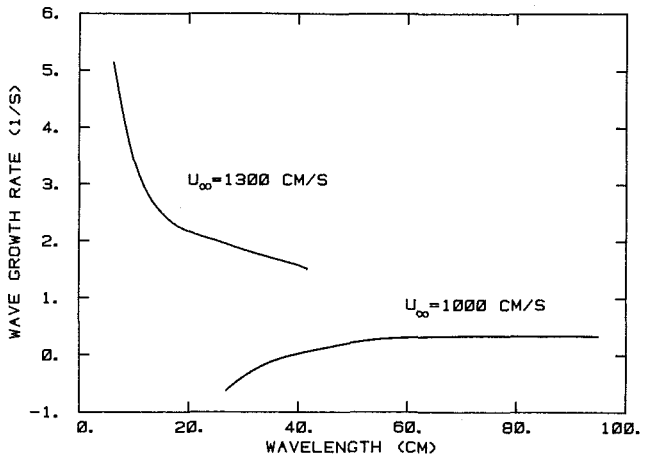


Fig. 3 Wave-growth rates for turbulent mean flow and oil of high viscosity

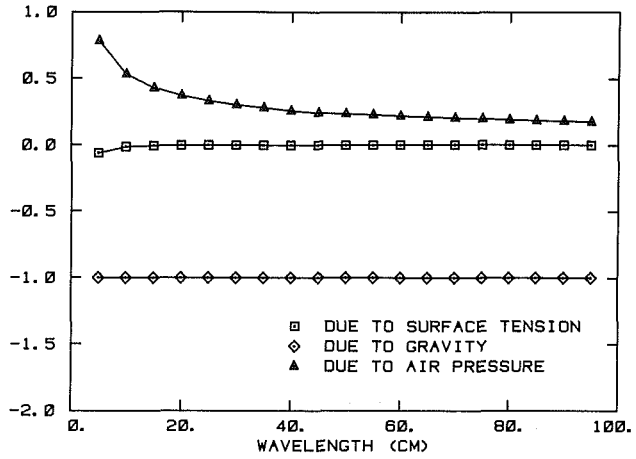


Fig. 4 Relative amplitudes of stresses in phase with the interface displacement for oil of high viscosity at $U_\infty = 10$ m/s

Table 1 Behavior of "air" and "oil" modes near direct resonance at $U_\infty = 3$ m/s and $R = 871.7$ for the oil of low viscosity

Wavelength (cm)	"Air mode"		"Oil" mode	
	c_r (cm/s)	αc_i (1/s)	c_r (cm/s)	αc_i (1/s)
33.65	87.33	−0.06	74.49	−0.095
36.24	85.49	−0.40	77.56	0.004
39.26	84.25	−0.85	80.23	0.209
42.83	83.90	−1.09	82.25	0.219
47.12	82.67	−1.15	85.47	0.056
52.35	80.07	−1.25	90.47	−0.035
58.90	77.29	−1.39	96.27	−0.044

Table 2 Behavior of "air" and "oil" modes near direct resonance at $U_\infty = 7$ m/s and $R = 2905.6$ for the oil of high viscosity

Wavelength (cm)	"Air mode"		"Oil" mode	
	c_r (cm/s)	αc_i (1/s)	c_r (cm/s)	αc_i (1/s)
84.14	148.8	−0.30	117.6	−0.16
96.17	144.1	−0.83	125.5	0.03
112.19	141.5	−1.22	132.2	0.13
134.63	137.2	−1.27	142.4	0.007
168.29	128.7	−1.26	160.6	−0.06

Downloaded 02 May 2010 to 171.66.16.54. Redistribution subject to ASME license or copyright; see http://www.asme.org/terms/Terms_Use.cfm

equations, describing the laminar flow induced by a uniform stream U_∞ coming into contact with an initially stationary viscous fluid. For air flowing over oil, the basic-flow profile consists of an air boundary layer, similar to the Blasius boundary layer, and a weak oil current; the width of the air boundary layer δ grows slowly in the streamwise direction: $\delta = (\nu_+ x/U_\infty)^{1/2}$, x being the distance from the point of initial contact of the two fluids. For the purposes of stability calculations, however, the basic flow will be treated as strictly parallel, so that the formulation of the stability equations, given earlier, applies.

Our main interest centers on the possibility of exciting oil waves by direct resonance between oil-wave disturbances and Tollmien-Schlichting waves in the air boundary layer; for earlier investigations [4, 7, 8], concerning water-wave generation by wind, have shown that direct resonance is the dominant wave-generation mechanism at low wind speeds.

The fact that the air-to-oil density ratio is small ($\rho_+ / \rho_- = 1.4 \times 10^{-3}$) suggests that one should be able to identify two kinds of wave modes in the coupled air-oil system: first, "air" modes, that are similar to Tollmien-Schlichting waves in the Blasius boundary layer and involve very little oil motion, and, secondly, "oil" modes, akin to free oil disturbances in the absence of a shear flow. Direct resonance is possible when the phase speed of an "air" mode of certain wavelength can match the phase speed of an "oil" mode of the same wavelength. For the turbulent mean flow considered in the previous section, the "air" modes are known to be highly damped [11] and direct resonance is not possible. The Blasius boundary layer, however, has a neutral-stability curve and, thus, the question arises as to whether direct resonance is of any importance.

Calculations were made for the same two types of oil considered before and the results can be summarized as follows. For the oil of low viscosity, as in water, direct resonance is possible even at very low wind speeds, $U_\infty \gtrsim 1.2$ m/s, the wavelength of the unstable waves increasing with the wind speed. A typical example of the behavior of the "air" and "oil" modes near direct-resonance conditions is given in Table 1, for $U_\infty = 3$ m/s and $R = U_\infty \delta/\nu_+ = 871.7$. Direct resonance occurs for waves of about 44 cm wavelength; far from resonance, the "oil" mode is damped, but, as the "oil"-mode phase speed approaches the "air"-mode phase speed, an interaction between the two modes takes place, giving rise to instability. The associated growth rates are substantially larger than those of the long-wave instabilities found at low wind speeds in the turbulent mean flow (Fig. 1(*a*)).

In the case of the highly viscous oil, direct resonance is still possible at higher wind speeds than for the low-viscosity oil. Table 2 gives an example of a resonance for $U_\infty = 7$ m/s, $R = 2906$; again, the "oil" mode is amplified only near direct-resonance conditions that is, for waves about 1.2 m long.

Conclusions

The stability analysis of turbulent and laminar air-oil systems discussed here gives a more complete picture of the generation mechanisms of surface waves on a viscous fluid by shear flows. For turbulent shear flow, and highly viscous fluid, the balance of aerodynamic suction with the restoring forces of gravity and interfacial tension is not sufficient to excite short surface waves, independently of viscosity. In addition, long-wave instabilities are possible at low wind speeds. Thus, the excellent agreement of Miles's approximate theory [3] with the experimental observations of Francis [5, 6] can be considered fortuitous. For laminar shear flow, even for highly viscous fluid, direct resonance between disturbances in the shear flow and the fluid provides an additional generation mechanism of long surface waves at low wind speeds.

There are still some open questions: first, on the theoretical side, the significance of three-dimensional and nonlinear effects, and the significance of the turbulent Reynolds stresses remain to be investigated. Secondly, additional experiments are required to check the theoretical predictions, concerning the variation with viscosity of the minimum wind speed required for wave excitation, and the role of direct resonance.

Acknowledgments

The authors are grateful to Professor J. H. Haritonidis for making available valuable computer time. This work is supported by the Office of Naval Research under contract NR 062-742.

References

1 Miles, J. W., "On the Generation of Surface Waves by Shear Flows, Part 1," *J. Fluid Mech.*, Vol. 3, 1957, pp. 185–204.

2 Miles, J. W., "On the Generation of Surface Waves by Shear Flows, Part 2," *J. Fluid Mech.*, Vol. 6, 1959, pp. 568–582.

3 Miles, J. W., "On the Generation of Surface Waves by Shear Flows, Part 3: Kelvin-Helmholtz Instability," *J. Fluid Mech.*, Vol. 6, 1959, pp. 583–598.

4 Miles, J. W., "On the Generation of Surface Waves by Shear Flows, Part 4," *J. Fluid Mech.*, Vol. 13, 1962, pp. 433–448.

5 Francis, J. R. D., "Wave Motions and the Aerodynamic Drag on a Free Oil Surface," *Phil. Mag.*, Vol. 45, 1954, pp. 695–702.

6 Francis, J. R. D., "Wave Motions on a Free Oil Surface," *Phil. Mag.*, Vol. 47, 1956, pp. 685–688.

7 Akylas, T. R., "A Nonlinear Theory for the Generation of Water Waves by Wind," *Stud. Appl. Math.*, Vol. 67, 1982, pp. 1–24.

8 Akylas, T. R., "A Note on the Generation of Surface Waves by Inviscid Shear Flows," *Wave Motion*, Vol. 6, 1984, pp. 141–148.

9 Valenzuela, G. R., "The Growth of Gravity-Capillary Waves in a Coupled Shear Flow," *J. Fluid Mech.*, Vol. 76, 1976, pp. 229–250.

10 Lock, R. C., "The Velocity Distribution in the Laminar Boundary Layer Between Parallel Streams," *Quart. J. Mech.*, Vol. 4, 1951, pp. 42–63.

11 Landahl, M. T., "A Wave-Guide Model for Turbulent Shear Flow," *J. Fluid Mech.*, Vol. 29, 1967, pp. 441–459.

Downloaded 02 May 2010 to 171.66.16.54. Redistribution subject to ASME license or copyright; see http://www.asme.org/terms/Terms_Use.cfm

N. Annapurna

A. S. Gupta

Mathematics Department,
Indian Institute of Technology,
Kharagpur, India 721302

B. S. Dandapat

Indian Statistical Institute,
Calcutta, India

Hydromagnetic Convective Diffusion Between Parallel Plates With Suction

This paper presents an analytical solution for the dispersion of a solute in an electrically conducting fluid flowing between parallel plates with a transverse magnetic field and uniform wall suction. For fixed values of the suction parameter P and Schmidt number Sc, the longitudinal diffusion coefficient K decreases rapidly with increase in the magnetic parameter M. Further, for fixed M and Sc, it is found that K increases with increasing P. The effect of variation of Sc on K is found to be very small.

1 Introduction

The dispersion of a soluble matter in an incompressible viscous fluid flowing in a circular pipe under laminar flow conditions was investigated by Taylor [1]. It is found that relative to a plane moving with the mean speed of the flow, the solute is dispersed with an apparent diffusion coefficient $R^2V^2/48D$, where R, V, and D are the radius of the pipe, the average velocity, and the molecular diffusion coefficient, respectively. Gupta and Chatterjee [2] extended Taylor's analysis to study the dispersion of a solute in the laminar flow of an electrically conducting fluid between two parallel plates in the presence of a uniform transverse magnetic field. In all these investigations, the walls of the pipe or the channel are assumed to be impermeable.

The purpose of the present paper is to use Taylor's conceptual model to obtain the longitudinal dispersion coefficient in the flow of an electrically conducting fluid in a parallel plate channel with permeable walls. It is assumed that there is uniform suction through the channel walls and a constant magnetic field acts transverse to the channel. The corresponding hydrodynamic problem was studied by Eroshenko and Zaichik [3] where there is fluid injection through the channel walls.

The results of the present investigation may have some relevance to problems involving dispersion and convection of a dye that is used in flow visualization techniques. Other aspects of the importance of dispersion of a solute in hydromagnetic flows were highlighted in the second Bat-Sheva Seminar held in Israel in March 1978 and well documented by Branover, Hunt, Proctor, and Pierson [4].

2 Solute Dispersion in a Permeable Channel

Consider the dispersion of a solute in the steady laminar flow of an incompressible viscous electrically conducting fluid between two porous parallel plates. The plates are subject to uniform suction and a constant magentic field acts transverse to the plates. The velocity distribution in this flow was found by Terrill and Shrestha [5] under the following assumptions:

(*a*) the induced magnetic field produced by the motion of the fluid is negligible. This assumption is, of course, justified for flows with small magnetic Reynolds numbers e.g., flows of mercury or liquid sodium under laboratory conditions (see Shercliff [6]).

(*b*) No external electric field is applied and the electric field produced by polarization of charges is negligible (this corresponds to the so-called short-circuit condition).

(*c*) Both the plates have equal permeability and are assumed to be electrically nonconducting.

Taking x-axis along the central axis of the channel (the plates being distant $2h$ apart) and y-axis normal to it, the velocity components (u, v) are assumed as

$$u=\left(\bar{u}_0-\frac{v_w x}{h}\right)f'(\lambda), v=v_w f(\lambda), \lambda=\frac{y}{h}. \tag{1}$$

Here v_w is the uniform suction velocity at the plates and $\bar{u}_0$ is the average axial velocity at $x=0$ given by

$$\bar{u}_0=\int_0^1 u(0,\lambda)d\lambda. \tag{2}$$

When a uniform magnetic field H_0 is applied parallel to y-axis, the expression for $f(\lambda)$ found in reference [5] for small values of the suction Reynolds number R is

$$f(\lambda)=\frac{1}{Q}(\sinh M\lambda-\lambda M\cosh M)+\frac{aR}{4}$$
$$\left[\frac{5M^2\cosh M}{Q}(\sinh M\lambda-\lambda\sinh M)\right.$$
$$\left.+M((6-\lambda^2)\sinh M\lambda-5\lambda\sinh M))+7\lambda(\cosh M\lambda-\cosh M)\right], \tag{3}$$

Contributed by the Applied Mechanics Division for publication in the JOURNAL OF APPLIED MECHANICS.

Discussion on this paper should be addressed to the Editorial Department, ASME, United Engineering Center, 345 East 47th Street, New York, N.Y. 10017, and will be accepted until two months after final publication of the paper itself in the JOURNAL OF APPLIED MECHANICS. Manuscript received by ASME Applied Mechanics Division, March, 1984.

Copyright © 1985 by ASME

Downloaded 02 May 2010 to 171.66.16.54. Redistribution subject to ASME license or copyright; see http://www.asme.org/terms/Terms_Use.cfm

where R, a, Q, and the Hartmann number M are given by

$$R = hv_w/\nu, \qquad a = \cosh M/Q^2,$$
$$Q = \sinh M - M\cosh M, \qquad M = \mu_e H_0 h(\sigma/\rho\nu)^{1/2} \tag{4}$$

Here μ_e, σ, ρ and ν denote the magnetic permeability, the electrical conductivity (assumed uniform), density, the kinematic viscosity, respectively.

The concentration c of the solute in the flow described in the foregoing satisfies the convective diffusion equation

$$\frac{\partial c}{\partial t} + u\frac{\partial c}{\partial x} + v\frac{\partial c}{\partial y} = D\frac{\partial^2 c}{\partial y^2}, \tag{5}$$

where the molecular diffusion coefficient D is assumed to be constant. It is further assumed that $\partial^2 c/\partial x^2 << \partial^2 c/\partial y^2$.

Substitution of (1) in (5) gives

$$\frac{\partial c}{\partial t_1} - \frac{Pe}{2}\frac{\partial c}{\partial X} - \frac{Pe}{2}[f'(\lambda) - 1]\frac{\partial c}{\partial X} + \frac{P}{2}f(\lambda)\frac{\partial c}{\partial \lambda} = \frac{\partial^2 c}{\partial \lambda^2}, \tag{6}$$

where

$$t_1 = \frac{tD}{h^2}, \quad X = \frac{Pe}{P}\ln\left(1 - \frac{v_w x}{h\bar{u}_0}\right), Pe = \frac{2h\bar{u}_0}{D}, \quad P = \frac{2hv_w}{D}. \tag{7}$$

Using the analogy with the problem of dispersion of a solute in a channel with impermeable walls (reference [1]), we construct an approximate solution of (6) by setting

$$\frac{\partial c}{\partial t_1} - \frac{Pe}{2}\frac{\partial c}{\partial X} = 0, \quad \frac{\partial c}{\partial X} = \frac{\partial \bar{c}}{\partial X} \tag{8}$$

in it, where $\bar{c}$ is the average concentration of the solute across a section of the channel of unit breadth and is given by $\bar{c} = \int_0^1 c d\lambda$. Equations (6) and (8) give

$$\frac{\partial^2 c}{\partial \lambda^2} - \frac{P}{2}f(\lambda)\frac{\partial c}{\partial \lambda} = -\frac{Pe}{2}[f'(\lambda) - 1]\frac{\partial \bar{c}}{\partial X}, \tag{9}$$

which represents the balance of convection of the solute in the longitudinal and transverse directions and of its transverse diffusion.

The boundary conditions for (9) are

$$\left(\frac{\partial c}{\partial \lambda}\right)_{\lambda=0} = 0; \quad \left(\frac{\partial c}{\partial \lambda}\right)_{\lambda=1} + \frac{P}{2}(c_m - c_w) = 0, \tag{10}$$

where $c_m (= \int_0^1 c f'(\lambda) d\lambda)$ is the average mass concentration and c_w is the concentration of the solute at the walls. The first condition in (10) follows from the symmetry of the concentration profile about the central axis of the channel. The second condition expresses the fact that the total flux of the transferred solute in the case of suction is equal to the sum of the convective and diffusional fluxes.

The solution of (9) satisfying (10) is

$$c(\lambda) = c(\lambda = 0) - \frac{Pe}{2} \cdot \frac{\partial \bar{c}}{\partial X} \cdot F(\lambda), \tag{11}$$

where

$$F(\lambda) = \int_0^\lambda \exp\left(\frac{P}{2}\int_0^\xi f(\zeta)d\zeta\right)\left(\int_0^\xi [f'(\eta) - 1] \exp\left(-\frac{P}{2}\int_0^\eta f(\theta)d\theta\right)d\eta\right)d\xi. \tag{12}$$

Integrating (6) with respect to λ from 0 to 1 and using the boundary conditions (10), we obtain

$$\frac{\partial \bar{c}}{\partial t_1} - \frac{Pe}{2}\frac{\partial \bar{c}}{\partial X} - \frac{Pe}{2}\frac{\partial}{\partial X}(c_m - \bar{c}) = 0. \tag{13}$$

This equation expresses the dispersion of the solute relative to a plane moving with the mean speed of the flow in the channel. Now if $c_m - \bar{c}$ is computed from (11) and inserted in (13), the result is

$$\frac{\partial \bar{c}}{\partial t_1} - \frac{Pe}{2}\frac{\partial \bar{c}}{\partial X} = \frac{D_c}{D}\frac{\partial^2 \bar{c}}{\partial X^2}, \tag{14}$$

where D_c is the longitudinal diffusion coefficient given by

$$\frac{D_c}{D} = \frac{Pe^2}{4}\int_0^1 [1 - f'(\lambda)]F(\lambda)d\lambda. \tag{15}$$

Substituting (12) in (15) and expanding in powers of the suction parameter P, the expression for D_c/D for small values of P is

$$\frac{4D_c}{D(Pe)^2} = \int_0^1 [f(\lambda) - \lambda]^2 d\lambda + \frac{P}{2}\int_0^1 [f(\lambda) - \lambda]\left(\int_0^\lambda [f(\xi) - \xi]f(\xi)d\xi\right)d\lambda + 0(P^2). \tag{16}$$

The second term on the right side of (16) represents the correction to the longitudinal diffusion coefficient due to suction at the walls.

Using (3) in (16) and remembering that P is small so that its squares and higher powers are negligible, we obtain after a lengthy calculation the expression for D_c as

$$\begin{aligned}\frac{4D_c}{D(Pe)^2} = \Bigg[& \frac{1}{Q^2}\left(1 + \frac{5aPM^2}{4Sc}\cosh M\right)\left(-\frac{3\sinh 2M}{4M} + \left(\frac{1}{6} + \frac{1}{M^2}\right)\cosh 2M - \left(\frac{1}{M^2} + \frac{2}{3}\right)\right) \\ & + \frac{aP}{4QSc}\left(\left(-\frac{31}{12} + \frac{25}{2M^2}\right)\sinh 2M + \left(-\frac{1}{M} + \frac{5M}{6} - \frac{10}{M^3}\right)\cosh 2M \right. \\ & \left. + \left(-\frac{4}{M} + \frac{10}{M^3} - \frac{11M}{3}\right)\right)\Bigg] \\ & + \frac{P}{2Q^3}\Bigg[\left(\left(\frac{1}{4M} + \frac{3}{2M^3}\right)\cosh 2M + \left(\frac{35}{12M^2} + \frac{M^2}{30} + \frac{1}{2}\right)\sinh 2M \right. \\ & \left. - \left(\frac{3}{2M} + \frac{3}{2M^3}\right)\right)\cosh M \\ & - \left(\left(\frac{17}{6M^2} + \frac{M^2}{30} - \frac{3}{2M^4} + \frac{1}{3}\right)\cosh 2M + \left(\frac{33}{16M^3} + \frac{1}{2M} + \frac{M}{30}\right)\sinh 2M \right. \\ & \left. + \left(\frac{29}{8M^2} + \frac{M^2}{30} + \frac{3}{2M^4} + \frac{1}{6}\right)\right)\sinh M\Bigg],\end{aligned} \tag{17}$$

where Sc is the Schmidt number ν/D. In deriving (17), we have made use of the fact that R as defined (4) is $P/2$ Sc (see equation (7)) and hence is very small for small P since Sc is quite large for liquids.

In the absence of suction, $P = 0$ and then (17) reduces to

$$D_c = \frac{h^2\bar{u}_0^2}{D\lambda_1^2}\left[\frac{5}{5} - \frac{\lambda_1^2}{2M^2} - \frac{5\lambda_1}{2M^2}\right], \tag{18}$$

where

$$\lambda_1 = M\coth M - 1. \tag{19}$$

This agrees with the result of Gupta and Chatterjee [2].

Downloaded 02 May 2010 to 171.66.16.54. Redistribution subject to ASME license or copyright; see http://www.asme.org/terms/Terms_Use.cfm

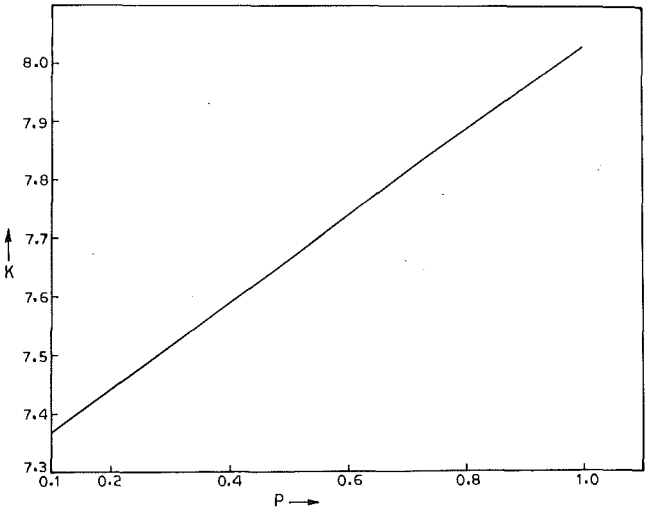


Fig. 1 Plot of K versus P for $Sc = 20$ and $M = 20$

Discussion

The variation of K $[=(4D_c/D.(Pe)^2) \times 10^4]$ is computed from (17) for several values of the parameters M, P, and Sc. Figure 1 shows that the longitudinal diffusion coefficient K increases with increasing P for $M=20$ and $Sc=20$. It is interesting to note that this behavior of K with respect to the suction parameter P is opposite to that in the case of injection through channel walls as found in reference [3].

The following table gives the values of K for several values of Sc with $M=25$ and $P=0.1$.

Table 1

Sc	K
20	4.849443
30	4.849581
100	4.849772
200	4.849816

It is worth noting that the variation of K with Sc is indeed very small although K slowly increases with Sc.

Figure 2 shows the variation of K with M for $Sc=30$ and $P=0.1$. It is important to mention that though the effect of the magnetic parameter M on the dispersion of the solute is indirect, i.e., through modification of the velocity profile, the influence of M on K is quite significant. In fact Fig. 2 reveals that K decreases very rapidly with increase in M. This is to be expected on physical grounds since the velocity profile becomes flatter with increase in the Hartmann number as compared with the nonmagnetic case $M=0$.

We might say a few words about the validity of Taylor's model in the present analysis. It is important to remember that this model is asymptotically valid for a large time after the injection of the solute (e.g., dye) in the flow. To be more specific, this model is valid if the time after the injection of the solute is such that the distance of diffusion across the channel during this time is comparable with the distance between the parallel plates and diffusion acts to average out the velocity of the different particles of the solute.

Finally a few comments are in order about the practical realizability of laminar flow conditions assumed in the present analysis. It is well known that both suction and a magnetic field generally stabilize a flow. Thus it is conceivable that it would be rather easy to maintain laminar conditions in the presence of these two effects when experiments are performed under laboratory conditions. To give a rough estimate

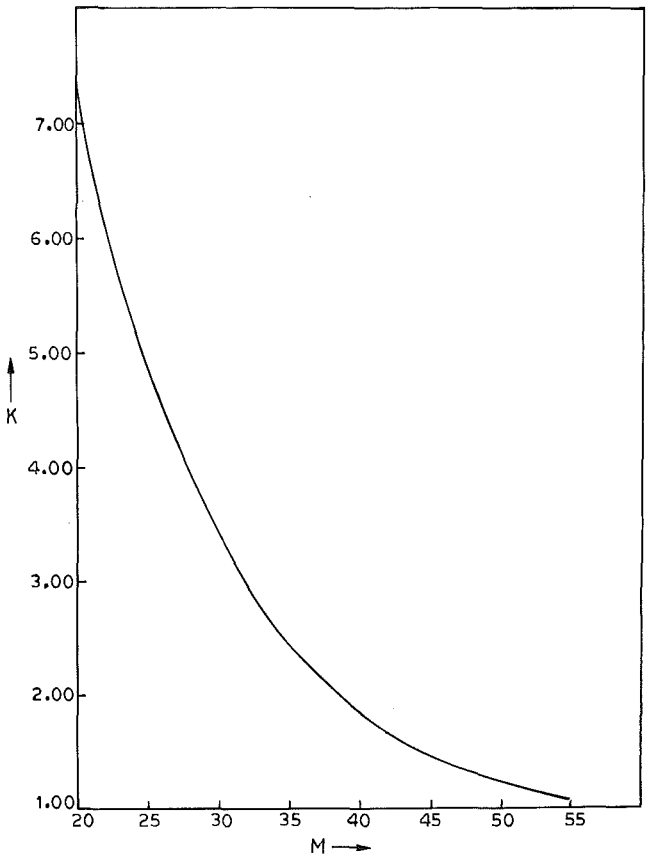


Fig. 2 Plot of K versus M for $Sc = 30$ and $P = 0.1$

of the range of Reynolds number for which laminar conditions prevail, we might mention the experiments of Murgatroyd (see Cowling [7]) who found that the Hartmann flow in a parallel plate channel with a uniform transverse magnetic field remains laminar provided the Reynolds number $Re(=V_0h/\nu$, V_0 being the velocity midway between the channel walls) does not exceed 225 M. Thus in our present problem, we may say with some confidence that laminar conditions will prevail at least for $Re \leq 225M$.

Acknowledgment

We thank Mr. S Bhattacharya for his kind help in checking the computations.

References

1 Taylor, G. I., "Dispersion of Soluble Matter in Solvent Flowing Slowly Through a Tube," *Proc. Roy. Soc.*, London, Series *A*, Vol. 219, 1953, pp. 186-203.

2 Gupta, A. S., and Chatterjee, A. S., "Dispersion of Soluble Matter in the Hydromagnetic Laminar Flow Between Two Parallel Plates," *Proc. Camb. Phil. Soc.*, Vol. 64, 1968, pp. 1209-1214.

3 Eroshenko, V. M., and Zaichik, L. I., "Longitudinal Diffusion of an Impurity in a Pipe With Permeable Walls," Translated from *Inzhenerno-Fizicheskii Zhurnal*, Vol. 38, 1980, pp. 314-317.

4 Branover, H., Hunt, J. C. R., Proctor, M. R. E., and Pierson, E. S., "Magneto hydrodynamic Flows and Turbulence : a Report on the Second, Bat-Sheva Seminar," *J. Fluid Mech.* Vol. 91, 1979, pp. 563-580.

5 Terrill, R. M., and Shrestha, G. M., "Laminar Flow Through Channels With Porous Walls and With an Applied Transverse Magnetic Field," *Appl. Sci. Res., B*, Vol. 11, 1964, pp. 134-144.

6 Shercliff, J. A., *A Textbook of Magnetohydrodynamics*, Pergamon Press, 1965, pp. 44-45.

7 Cowling, T. G., *Magnetohydrodynamic*, Interscience, 1957, pp. 62-63.

Downloaded 02 May 2010 to 171.66.16.54. Redistribution subject to ASME license or copyright; see http://www.asme.org/terms/Terms_Use.cfm

Elastic Stress Concentration Phenomena in an Axially Stressed Rectangular Plate With a Central Circular Hole and Other Related Problems

D. Shilkrut[1] and E. Ben-Gad[1]

Introduction

The important classical problem of stress concentration caused by a circular hole in a plane elastic body subjected to tensile loading has in the past been investigated mainly in the cases of an infinite plane or an infinitely long strip with various sizes of holes (see for example [1-7]). Analytical results have, however, been obtained in [8] for the stresses at the edge of a hole in a square plate subjected to tenison for hole diameters up to half of plate width. But in all the aforementioned works, no systematic results have been reported for the problem in question, viz. considering the influence of the proximity of loaded boundaries to the hole. Hence, we see that in reference books [9, 10] no data are given for the type of problem under discussion here, i.e., for rectangular bounded bodies. A number of works have been published giving approximate numerical solutions and also experimental results for the particular problem of a square plate with a hydrostatically pressurized central hole (see for example [11-13]).

We consider here the case of a finite rectangular plate with a large central circular hole under the loadings: uniaxial uniform tension, pure shear uniformly applied, and hydrostatic pressure at the hole. The approximate method used is based on Michell's general solution of the biharmonic equation in polar coordinates, with the boundary conditions being exactly satisfied at the hole and being satisfied in an integral sense of the external boundary. Quantitative and qualitative results for large holes (diameters up to 90 percent of plate width) were obtained. A new phenomenon that is discovered for axially loaded square and shorter plates is the existence of a region in compression in the neighborhood of the external unloaded boundary at the minimum section. The method proposed can also be used for investigating other cases of stress concentration phenomena for plane thermoelastic (anisotropic, as well as isotropic) bodies, and also for the bending of plates and for other similar problems.

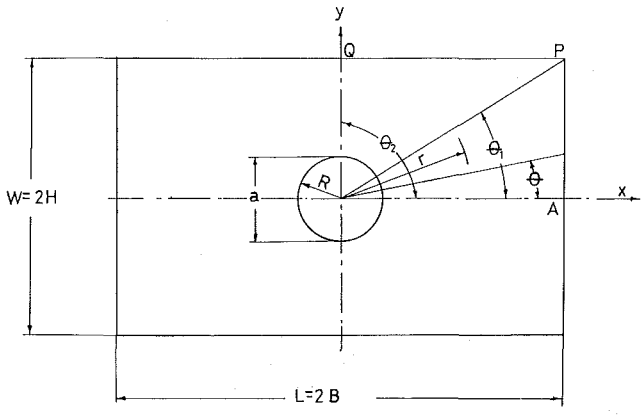


Fig. 1 The rectangular plate with central circular hole—dimensions and coordinate systems used

Method of Solution

The method of solution is best described by means of an example; we consider a rectangular plate with a central circular hole subjected to uniform tension (see Fig. 1). The basic equation is the biharmonic equation for the stress function Φ.

$$\Delta\Delta\Phi = 0 \tag{1}$$

The numerical solution to the problem is based on the well-known Michell solution of (1) in polar coordinates [14]. Each term in this solution exactly satisfies the biharmonic equation and hence the problem is reduced to determining the coefficients by satisfying approximately the appropriate boundary conditions. Due to symmetry it is sufficient to examine one quarter of the plate. The boundary conditions at the hole are:

$$\sigma_r|_{r=R} = \tau_{r\theta}|_{r=R} \equiv 0 \tag{2}$$

On the external contour C (broken line APQ in Fig. 1) we have:

$$\sigma_\nu|_c = f(\theta); \quad \tau_{xy}|_c \equiv 0 \tag{3}$$

[1]The Pearlstone Center for Aeronautical Engineering Sciences Department of Mechanical Engineering, Ben-Gurion University of the Negev, Beer Sheva, Israel.

Manuscript received by the ASME Applied Mechanics Division, May, 1984; final revision, July, 1984.

Copyright © 1985 by ASME
Downloaded 02 May 2010 to 171.66.16.54. Redistribution subject to ASME license or copyright; see http://www.asme.org/terms/Terms_Use.cfm

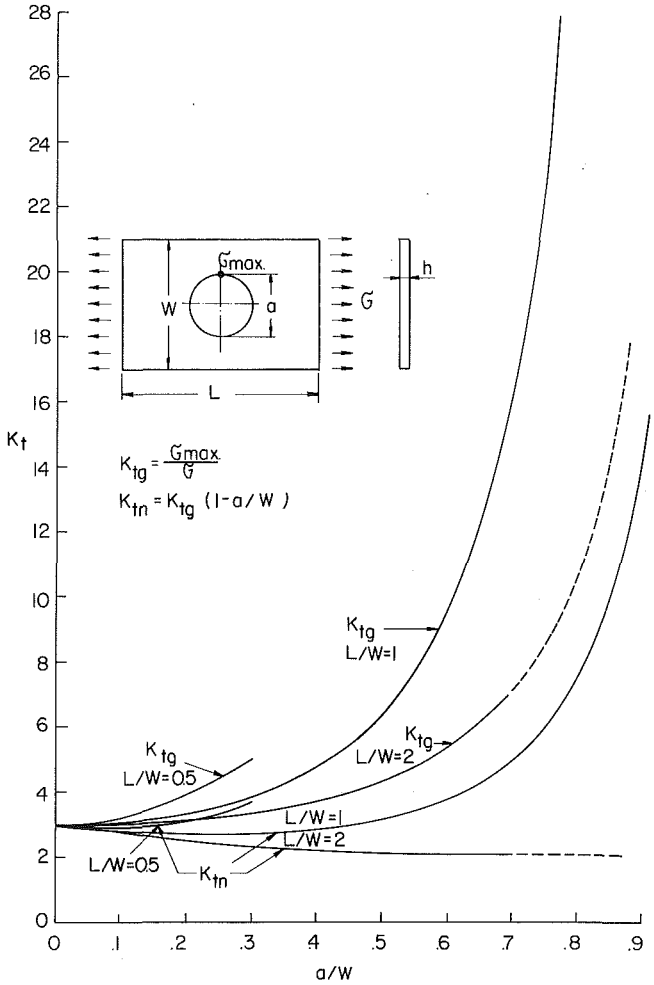


Fig. 2 Stress concentration factors K_{tg} and K_{tn} for tensile rectangular plate with central circular hole

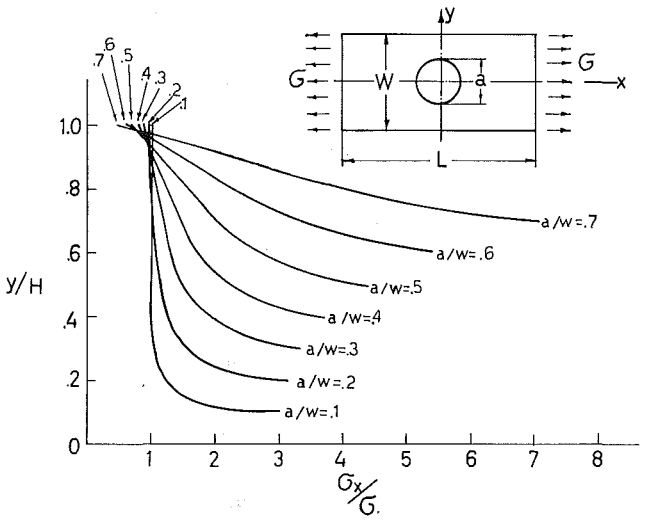


Fig. 3 Axial stress distribution in the minimal section of long tensile rectangular plate ($L/W = 2$) with central circular hole

where $\nu = x$ and $f(\theta) = \sigma$ (σ is the applied load) when $x = B$ (line AP); $\nu = y$ and $f(\theta) \equiv 0$ when $y = H$ (line PQ).

Using the standard relationship between Airy's stress function and stresses and taking into account the symmetry of the problem we obtain

$$\sigma_r = \frac{a_0}{r^2} + 2b_0 + \sum_{n=2}^{\infty} [n(1-n)a_n r^{n-2} + (n+2-n^2)b_n r^n - n(n+1)a_n' r^{-n-2} + (-n+2-n^2)b_n' r^{-n}]\cos n\theta \quad (4)$$

and similarly the expressions for σ_θ, $\tau_{r\theta}$, σ_x, σ_y, and τ_{xy} are obtained. Substitution of the expressions for σ_r and $\tau_{r\theta}$ in the boundary conditions (2) at the hole gives a system of algebraic equations for the unknown coefficients b_0, a_n and b_n; to determine the remaining unknown coefficients the boundary conditions on the external contour will be approximately satisfied in an integral form.

We clarify this approach by considering for example the first condition in (3). We require that the Fourier coefficients of the function $F(\theta) = \sigma_\nu|_c - f(\theta)$ be zero. Thus (for the first of conditions in (3)),

$$\int_0^{\theta_1} [\sigma_x|_{r=B/\cos\theta} - f(\theta)]\cos j\theta d\theta + \int_{\theta_1}^{\pi/2} \sigma_y|_{r=H/\sin\theta}\cos j\theta d\theta = 0; \quad j = 0,2,4 \quad (5)$$

However, the relationship $F(\theta) = 0$ must be satisfied for all parts of contour C. Naturally this approach is no longer the Fourier method. It may be considered as an integral collocation method which is a combination of two opposite approaches—the standard collocation method and the integral satisfaction of the boundary conditions. Using this approach we then obtain the following integral forms after substituting the exact boundary conditions (3). On the line AP:

$$\int_0^{\theta_1} [\sigma_x|_{AP} - \sigma]\cos j\theta d\theta = 0; \quad j = 0,2,4 \quad (6)$$

$$\int_0^{\theta_1} \tau_{xy}|_{AP} \sin j\theta d\theta = 0; \quad j = 2,4 \ldots \quad (7)$$

The division of contour C into two intervals was found to be sufficient for solving this problem. Each equation (6) and (7), and the analogous equations on line PQ, generates a linear algebraic equation for the unknown coefficients. The number of these equations is determined by the number of the terms taken in the expressions of the stresses.

Naturally, the preceding integral form for satisfying the boundary conditions is not the only approach possible. Instead of the weight-functions of simple trigonometric forms used in (6) and (7), others might have been used. A future paper will be devoted to this problem.

Results and Discussion

1. Axial Uniform Tension. Three proportions of plates with central circular holes subjected to uniform tension were examined: a long plate ($L/W = 2$), a square plate ($L/W = 1$), and a short plate ($L/W = 0.5$). The stress concentration factors for these plates are given in Fig. 2.

In the case of the long plate the stress concentrations obtained are very close to those for the infinite tensile strip [2]. The accuracy of the results is very good for $a/W \leq 0.7$ and decreases gradually for larger holes. To the best of our knowledge this is the first time that such a plate with so large a hole has been investigated numerically. The nominal stress concentration factor K_{tn} approaches the value 2 when a/W approaches 1, a result that coincides with [3–6] and others. These results and the stress distribution in the minimum section (Fig. 3) and in other sections [15], show that a plate of proportions $L/W = 2$ can be considered for all practical purposes as being of infinite length.

In the square plate K_{tn} reaches a minimum (2.7) when $a/W = 0.25$ (see Fig. 2) and it increases rapidly when the hole gets larger. This is caused by the superposition of two opposing influences. On the one hand, K_{tn} must decrease as the hole gets larger (as in the case of the infinite strip) because of the greater influence of the *unloaded* boundaries. On the other

Downloaded 02 May 2010 to 171.66.16.54. Redistribution subject to ASME license or copyright; see http://www.asme.org/terms/Terms_Use.cfm

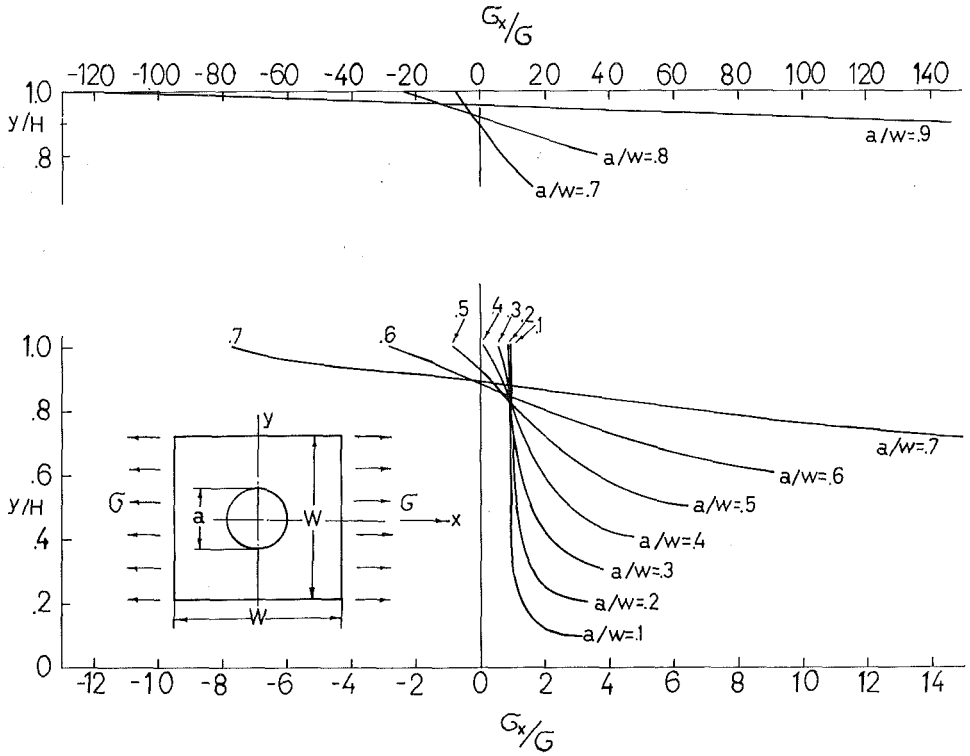


Fig. 4 Axial stress distribution in minimal section ($x = 0$) of square tensile plate with central circular hole. (Lower part of the figure corresponds to $a/w \leq 0.7$, upper part corresponds to $a/w \geq 0.7$.)

hand, K_{In} must increase because of the greater influence on the *loaded* boundaries when the hole becomes larger. For small holes the first influence predominates and for larger holes the second is the main factor. Comparison between the stress concentration factors of square plates and those of the long plate for corresponding holes shows that in the square plate the stress concentration factors increase faster as the holes get larger.

A new and very interesting phenomenon that shows up very clearly in the square plate under tension was discovered; a region of compressive stress exists at the minimal section ($x = 0$) in the neighborhood of $y = H$ when $a/W < 0.4$ (see Fig. 4). The accuracy of the results for the square plate is good for all hole sizes examined [15].

In the short plate ($L/W = 0.5$), stress concentration factors are the highest relative to those of longer plates for corresponding sizes of holes (see Fig. 2). Stress distributions in the minimum vertical section $x = 0$ of the short plate show (Fig. 5) that the tensile stress in the region of $y = H$ decreases as the hole gets larger. The stress in this region becomes compressive for holes larger than $a/W = 0.3$ [15]. This phenomenon is similar to the existence of compressive stress in the square plate. This may be explained by the influence of a large bending moment at the section $x = 0$ caused by the distribution of normal stress at the section $y = 0$. This distribution is nearly linear, varying, for example, in the square plate with hole size of $a/W = 0.9$ from about $\sigma_y/\sigma = -150$ at the edge of the hole, to about $\sigma_y/\sigma = +150$ at $x = B$ [15]. Modeling the cut out plate as a simple frame with hinges at the minimum sections clarifies that the compressive stresses in the unloaded minimum section always exist when the hole is sufficiently large.

2. Pure Shear. The results for pure shear loading acting on a square plate with central circular hole (Fig. 6) show higher stress concentration than those of a uniaxially stresses square plate for corresponding hole size. This is caused by the superposition of two perpendicular uniaxial loadings of opposite sense.

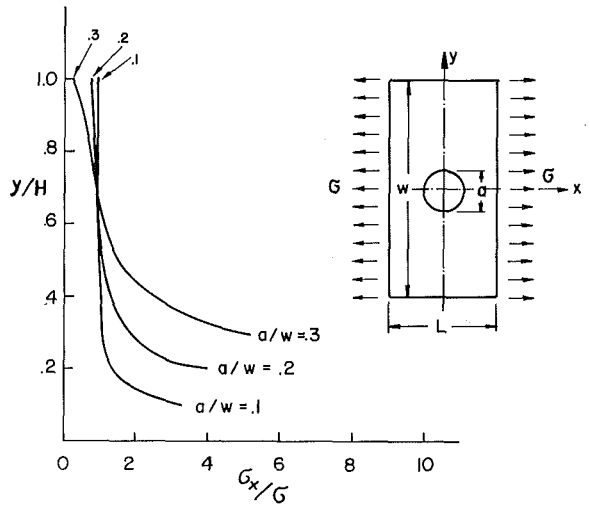


Fig 5 Axial stress distribution on minimal section ($x = 0$) of short tensile plate ($L/W = 0.5$) with central circular hole

3. Hydrostatic Pressure in the Hole. Stress distributions for the square plate with a central pressurized hole (Fig. 7) show that the maximum stress in the plate appears at point B on the hole for $a/W \leq 0.72$. For larger holes the maximum stress in the plate is at the external point A of the minimum section. These results are in good agreement with previous work [11-13], especially with [10-11]. It is interesting to note that the maximum stress at the hole when $a/W = 0.9$ appears at two points symmetric to the vertical plate axis ($\theta = \pi/8$ and $\theta = 3\pi/8$), with value of 9.8 P. The accuracy of the results for the square plate is very good.

In the rectangular plate ($L/W = 2$) with central pressurized

Downloaded 02 May 2010 to 171.66.16.54. Redistribution subject to ASME license or copyright; see http://www.asme.org/terms/Terms_Use.cfm

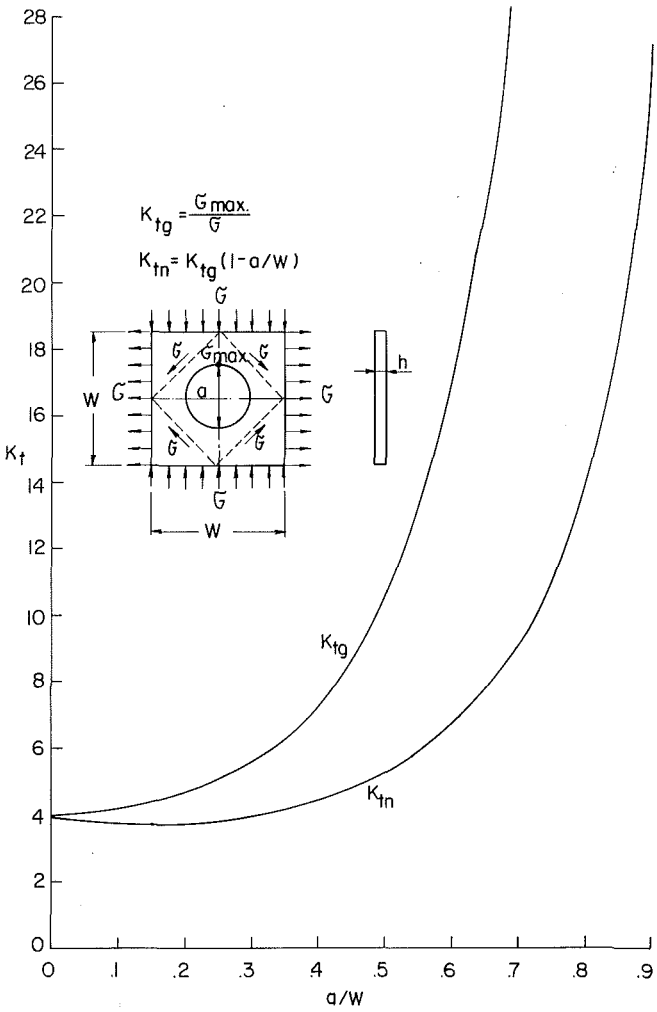


Fig. 6 Stress concentration factors K_{tg} and K_{tn} for square plate with central circular hole, under pure shear

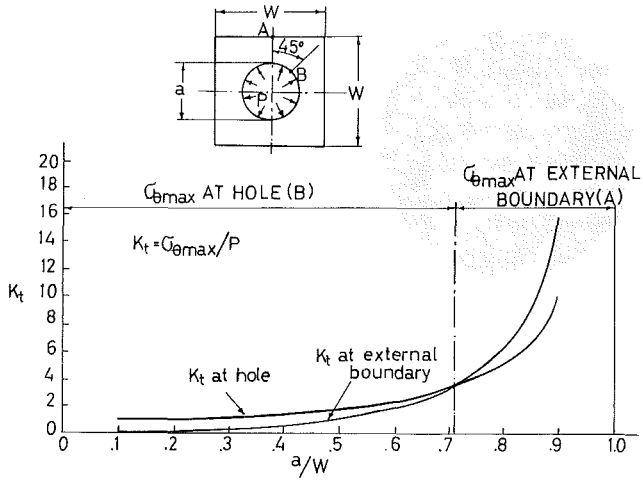


Fig. 7 Stress concentration factor K_t in square plate with pressurized central circular hole, at the hole and on the external boundaries

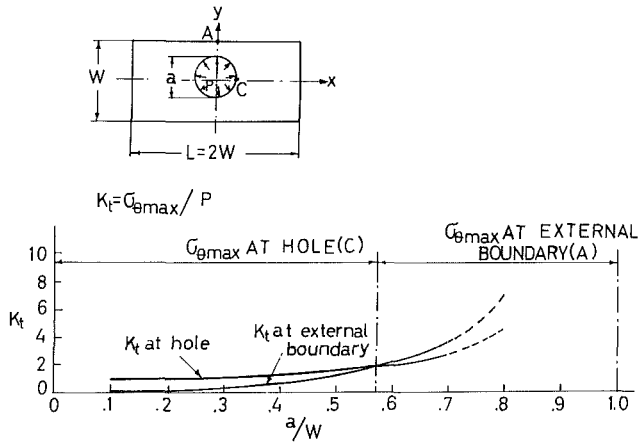


Fig. 8 Stress concentration factor K_t in a rectangular plate ($L/W = 2$) with pressurized central circular hole, at the hole and on the external boundaries

Table 1 Maximum stress at the hole and its location for large holes (for the rectangular plate with central pressurized hole)

a/W	σ_{max}/p	θ
0.5	1.71	0 deg
0.6	2.14	34 deg
0.7	2.92	45 deg
0.8	4.53	56 deg

hole the maximum stress in the plate occurs on the edge of the hole at point C (Fig. 8) for $a/W \leq 0.57$. For larger holes, the maximum stress occurs at point A on the external edge of the plate. The location of the maximum stress deviates from point C when $a/W > 0.5$ as is shown in Table 1. Results from [15] indicate that this tendency of the maximum stress at the hole to move along the edge of the hole continues for larger holes.

References

1 Kirsch, G., "Die Theorie der Elastizitat und die Bedurfuisse die Festigkeitslehrer," *Zeitscrift des Verlines Deutscher Ingenier*, Vol. 42, 1898, p. 797.

2 Howland, R. C. J., "On the Stresses in the Neighbourhood of a Circular Hole in a Strip Under Tension," *Philosophical Transactions of the Royal Society (London)*, Series A, Vol. 229, 1929–1930, pp. 49–86.

3 Koiter, W. T., "An Elementry Solution of Two-Stress Concentration Problems in the Neighbourhood of a Hole," *Qtly. of Appl. Math.*, Vol. 15, 1957, pp. 303–308.

4 Fuehring, H., "Stress Concentrations in Tensile Strips With Large Circular Holes—Discussion," *Experimental Mechanics*, Vol. 13, No. 6, 1973, pp. 255–256.

5 Van Riesen, P. E., and Spiering, R. M. E. J., "Investigation of Stress-Concentration Factors in Tensile Strips," *Experimental Mechanics*, Vol. 15, No. 3, 1975, pp. 111–113.

6 Flynn, P. D., "Stress Concentrations in Tensile Strips With Large Circular Holes," *Experimental Mechanics*, Vol. 15, No. 10, 1975, pp. 386–388.

7 Parks, V. J., and Mendoza, D. F., "Maximum Stress in Tensile Strips With Large Hole," *Experimental Mechanics*, Vol. 15, No. 10, 1975, pp. 389–391.

8 Hengst, H., "Beitrag zur Beurteilung des Spannungszustandes einer Gelochten Scheibe," *Ztschr. f. Angew. Math. und Mech.*, Vol. 18, 1938, pp. 44–48.

9 Peterson, R. E., *Stress Concentration Factors*, Wiley, New York, 1974.

10 Savin, G. N., *Stress Distribution Around Holes*, in Russian, Naukova Dumka, Kiev, 1968.

11 Sekiya, T., "An Approximate Solution in the Problem of Elastic Plates with an Aribtrary External Form and a Circular Hole," *Proc. of the 5th Japanese National Congress for Appl. Mech.*, 1955.

12 Davies, G. A. D., "Stresses in a Square Plate Having a Central Circular Hole," *Aeronautical Journal*, Vol. 69, No. 6, 1965, pp. 410–412.

13 Riley, W. F., Durelli, A. J., and Theocaris, P. S., "Further Stress Studies on a Square Plate With a Pressurized Central Circular Hole," *Proc. of the 4th Midwestern Conference on Solid Mechanics*, The University of Texas, 1959.

14 Timoshenko, S. P., and Goodier, J. N., *Theory of Elasticity*, 2nd Ed., McGraw-Hill, New York, 1951, p. 133.

15 Ben-Gad, E., "Solution of the Problem of Stress Concentration in Axially Loaded Rectangular Plate with Central Circular Hole, and Related Problems," M.Sc. Thesis, Department of Mechanical Engineering, Ben-Gurion University of the Negev, Beer Sheva, Israel, 1982.

Downloaded 02 May 2010 to 171.66.16.54. Redistribution subject to ASME license or copyright; see http://www.asme.org/terms/Terms_Use.cfm

Journal of Applied Mechanics

Brief Notes

A Brief Note is a short paper that presents a specific solution of technical interest in mechanics but which does not necessarily contain new general methods or results. A Brief Note should not exceed 1500 words *or equivalent* (a typical one-column figure or table is equivalent to 250 words; a one line equation to 30 words). Brief Notes will be subject to the usual review procedures prior to publication. After approval such Notes will be published as soon as possible. The Notes should be submitted to the Technical Editor of the JOURNAL OF APPLIED MECHANICS. Discussions on the Brief Notes should be addressed to the Editorial Department, ASME, United Engineering Center, 345 East 47th Street, New York, N. Y. 10017, or to the Technical Editor of the JOURNAL OF APPLIED MECHANICS. Discussions on Brief Notes appearing in this issue will be accepted until two months after publication. Readers who need more time to prepare a Discussion should request an extension of the deadline from the Editorial Department.

Rayleigh Revisited

D. A. Johnson[1]

Introduction

The Rayleigh quotient is such an universally used concept and tool that it needs no introduction and, in spite of more refined and accurate techniques, it has retained its appeal and usefulness, at least as a first rough estimate.

For a finite-dimensional undamped mechanical system described by the following matrix equation:

$$M\ddot{X}+KX=0 \tag{1}$$

where $X=[x_1 \ldots x_n]^T$ vector of generalized coordinates
M: Mass matrix (symmetrical positive definite) = $[m_{ij}]$
K: Stiffness matrix (symmetrical positive semi-definite) = $[k_{ij}]$
$\dot{(\ )}$ denotes a time-derivative

the Rayleigh quotient is defined as

$$R(U)=\frac{U^TKU}{U^TMU} \tag{2}$$

where $U=[u_1 \ldots u_n]^T$ is any nontrivial vector belonging to the same vector space as X.

We are interested in the rate of variation (curvature) of $R(U)$ around local extremal values.

The basic properties of the Rayleigh quotient $R(U)$ are [1]:

$$R(U_i)=\omega_i^2$$

where U is an eigenvector and ω_i is an eigenfrequency

$$\omega_1^2 \le R(U) \le \omega_n^2$$

for any U in the n-dimensional vector space (the eigenfrequencies are ordered such that $\omega_1 \le \omega_2 \le \ldots \le \omega_n$). If U is "close" (error of the order ϵ) to an eigenvector U_i, then $R(U)$ is even "closer" (error of the order ϵ^2) to ω_i^2.

This ensures that a good approximation to e.g., the fundamental mode shape will yield an excellent upper bound for ω_1^2 and frequent use is made of this property.

Curvature of Rayleigh Function Around Extremals

The Rayleigh function of an n-degree-of-freedom system is a surface in an $(n+1)$ dimensional space which exhibits constant extremals along directions provided by the eigenvectors of the system.

It is therefore a ruled surface and an analysis of its variation requires that some constraint on the variation of $X=(x_1 \ldots x_n)^T$ be introduced. R will then be a function of some reduced set of $(n-1)$ variables. A section of the surface by a hyperplane $x_i = A =$ constant yields a surface $R(x_1, \ldots, x_{i-1}, A, \ldots x_n)$ for which the extremals are isolated points. In particular, the hyperplane $x_1 = 1$ leads to a surface $R(1, x_2, \ldots x_n)$ corresponding to the linear variety obtained by translating the subspace $(0, x_2, \ldots x_n)$.

The resulting surface $R(1, x_2, \ldots x_n)$ corresponds to a reduced set of variables $x_2 \ldots x_n$ which is the classical choice considering a vector is defined by the *ratios* of its components. Other sets of variables could be chosen, based on any set of base vectors of the original vector space. The above choice is, of course, founded on the canonical base

$$V_i=[0,0, \ldots, v_{ii}=1,0, \ldots 0]^T$$

a trial vector being:

$$U=V_1+x_2V_2+ \ldots +x_nV_n$$

In [1], it is stated that "The slope of the [Rayleigh function] surface in the region surrounding the maximum value is extremely steep compared with that in the region around the minimum while slopes round the saddle points are intermediate between these. The authors are not aware of any general proof of this property, and it seems probably that it would be possible to design systems for which it would not hold."

What we propose to show in the sequel is that, in fact, this property does not depend on the *system*, but on the *choice of coordinates* describing the system and the *choice of variables* describing the variations of R.

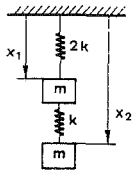
Let us first consider that the trial vector U is resolved into the eigenvectors U_j and that U is close to U_i:

$$U=U_i+\sum_{\substack{j=1\\ j\neq i}}^{n}\epsilon_jU_j \qquad \text{where} \quad \epsilon_j \ll 1 \tag{3}$$

and we suppose that U_j are normalized by $U_j^TMU_j = 1$.

In this case, the constraint is $\epsilon_i = 1$ and the reduced set of variables describing R is $\epsilon = [\epsilon_1 \ldots \epsilon_n]$ (ϵ_i excluded) around U_i. To within a second-order approximation, this

Copyright © 1985 by ASME
Downloaded 02 May 2010 to 171.66.16.54. Redistribution subject to ASME license or copyright; see http://www.asme.org/terms/Terms_Use.cfm



m = 1
k = 1 in homogeneous physical units

Equilibrium position $x_1 = x_2 = 0$

Fig. 1 First choice of coordinates

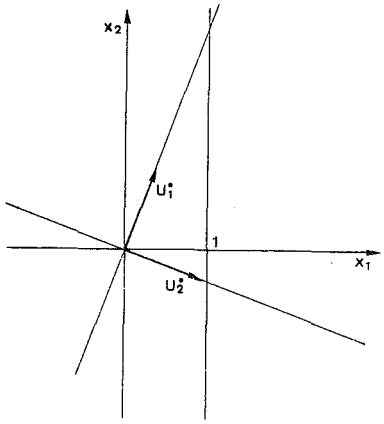


Fig. 2 Eigenvectors in configuration space

amounts to choosing a subspace of normalized vectors such that $U^TMU = 1$ (if $U_j^TMU_j = 1$ for all j): in fact $U \epsilon$ linear variety tangent to the hyperellipsoid $X^TMX = 1$ at $X = U_i$.

We have of course

$$\frac{\partial R}{\partial U}\Big|_{\epsilon=0} = 0 \tag{4}$$

and, from

$$R = \frac{U^TKU}{U^TMU} = \frac{N}{D}:$$

$$\frac{\partial^2 R}{\partial \epsilon_j{}^2}\Big|_{U=U_i} = U_j{}^T\left[\frac{\partial^2 R}{\partial U \partial U^T}\right]_{U_i} U_j = U_j{}^T H^i U_j \tag{5}$$

where H^i is the Hessian at $U = U_i$ and turns out to be

$$H^i = \frac{2(K - M\omega_i^2)}{U_i^TMU_i}$$

For normalized eigenvectors $H^i = 2(K - M\omega_i{}^2)$ and

$$\frac{\partial^2 R}{\partial \epsilon_j{}^2}\Big|_{U=U_i} = 2(\omega_j^2 - \omega_i^2) \tag{7}$$

If the variables in R are the ϵ_j, this result shows that the curvatures of the Rayleigh function around an extremal, in the directions determined by the remaining eigenvectors, depend only on the relative values of the eigenfrequencies and so, for this choice of variables, any shape of the Rayleigh function can be envisaged.

Admittedly, many systems have an eigenvalue sequence such that the curvatures will be weaker around U_1 than around U_n (supposing the eigenfrequencies have been ordered such that $\omega_1 \leq \omega_2 \leq \ldots \leq \omega_n$), but this is due basically to the choice of the coordinates defining the vector space. We shall return to this point later on.

Let us now consider a different choice of variables for expressing the trial vector U, namely the aforementioned "classical" choice:

$$U = (1, x_2, \ldots . x_n)^T \tag{8}$$

in which case, the U_i are no longer such that $U_i^TMU_i = 1$ (linear variety).

The curvatures around U_i are given by

$$\frac{\partial^2 R}{\partial x_j^2}\Big|_{U_i} = V_j{}^T\left[\frac{\partial^2 R}{\partial U \partial U^T}\right]_{U_i} V_j = V_j{}^T H^i V_j = \frac{2(k_{jj} - m_{jj}\omega_i^2)}{U_i^TMU_i} \tag{9}$$

It so happens that for many systems, the generalized coordinates are chosen in such a way (e.g., absolute displacements) that $U_i^TMU_i$ is larger for U_1 than for U_n. Indeed, the lowest frequency mode often corresponds to a shape such that the absolute displacements obey the following relation:

$$1 = x_1 \leq x_2 \leq x_3 \leq \ldots . \leq x_n \tag{10}$$

higher modes introducing non monotonic variations in the sequence, hence a reduction in $U_i^TMU_i$.

For comparable absolute values of the numerator $k_{jj} - m_{jj}\omega_i^2$, which will also often be the case for ω_1 and ω_n, this shows that, for the choice (8), the curvature will in fact often be greater for U_n than for U_1. However, if we had chosen the variables of the system to be $x_1 \ldots . x_{n-1}$, i.e.,

$$U = (x_1, x_2, \ldots . x_{n-1}, 1)^T \tag{11}$$

these conclusions would be reversed, as the following example will show. Moreover, a different choice of generalized coordinates could also lead to opposite conclusions, for choice (8). The example also shows up this particularity (this remark had been made earlier).

Example

The following simple example will hopefully clarify these different points. We consider a system consisting of two masses and two springs (Fig. 1). If we make the "natural" choice of generalized coordinates i.e., x_1 for the absolute displacement of the mass nearer the supporting frame and x_2 for that of the other mass, then the eigenmodes will be those of Fig. 2 with $\omega_1 = 0.77$, $\omega_2 = 1.85$ (U_i^* denotes a normalized eigenvector).

Let us now review the various possible choices outlined in the foregoing.

1. Choice ϵ_j Around U_1^*: $\dfrac{\partial^2 R}{\partial \epsilon_2^2} = \omega_2^2 - \omega_1^2$

   Around U_2^*: $\dfrac{\partial^2 R}{\partial \epsilon_1^2} = \omega_1^2 - \omega_2^2$

These curvatures are of course of equal norm, but the variable is different in each case.

2. Choice $U = (1\ x_2)^T$

A variation in the variable means we shall be following the line $x_1 = 1$ in Fig. 2.

The Rayleigh function is $R_1(x_2) = (3 - 2x_2 + x_2^2)/(1 + x_2^2)$ and its curvatures around extremals $R_1''(U_i)$:

$$R_1''(U_1) = 0.12$$
$$R_1''(U_2) = -4.12$$

If, however, we make the following choice:

3. Choice $U = (x_1\, 1)^T$: variations are along $x_2 = 1$ in Fig. 2.

The Rayleigh function is

$$R_2(x_1) = (3x_1^2 - 2x_1 + 1)/(x_1^2 + 1) = R_1\left(\frac{1}{x_1}\right) \tag{12}$$

and the curvatures are $R_2''(U_1) = 4.12$, $R_2''(U_2) = -0.12$ and are therefore reversed compared to choice 2.

4. Choice of generalized coordinates.

Downloaded 02 May 2010 to 171.66.16.54. Redistribution subject to ASME license or copyright; see http://www.asme.org/terms/Terms_Use.cfm

Finally, if we had reversed the coordinates, i.e., interchanged x_1 and x_2 (admittedly not a natural choice, but all systems are not so clearcut), then all the preceding results would be reversed, both for the ϵ_j and x_j variables.

Conclusions

We have attempted to clarify the observation made by many authors that the Rayleigh function is "flatter" around the fundamental eigenvector than around higher eigenmodes, the strongest variations being around the highest mode.

We have shown that the choice of coordinates defining the system and of variables defining the Rayleigh function are of utmost importance in qualfying the observation, which remains no more than the consequence of a fortunate coincidence of factors.

Summary

This note investigates the influence of the choice of coordinates and variables on the variations of the Rayleigh quotient of a general discrete mechanical system, and draws conclusions as to the "flatness" of the function around extremals.

References

1 Bishop, R. E. D., and Johnson, D. C., *The Mechanics of Vibration*, Cambridge University Press, Cambridge, England, 1960, pp. 144–154.

2 Lord Rayleigh, *Theory of Sound* (two volumes), 2nd ed., Dover, New York, 1945 reissue.

Wave Propagation in Semi-Infinite Elastic Bars With Randomly Varying Elastic Modulus

Dr. S. K. Roy Choudhuri[1]

1 Introduction

Elastic wave propagation in nonhomogeneous rods has attracted the attention of many researchers [3, 5]. But very few have studied the corresponding problems in a nonhomogeneous medium of randomly varying elastic properties. Problems of wave propagation in continuous media with random variation in material constants are receiving considerable attention in recent years. In geometrical optics, several problems on wave motion in random media have been solved [1, 2]. Two types of methods called "honest" and "dishonest" are utilized in such problems. In the honest method, the solution for displacement $u(x, \alpha, t)$ where x is the space coordinate, t the time, and α is a parameter ranging over a probability space S with probability density $p(\alpha)$ is determined for each value of α. After that its mean value and other statistics such as variance are computed. In the dishonest method randomness is considered before determining $u(x, \alpha, t)$ and some assumptions without sufficient reasons are made about the statistical properties of the random wave motion. In the honest method, the solution is expressed in the form of a series expansion in some parameter which is supposed to be small in view of slight random variations of the elastic properties of the medium. Keller [1] utilized perturbation method to solve the problem of propagation of light rays in a slightly nonhomogeneous random medium. It may be mentioned that very recently G. Singh and A. Singh [4] have studied a similar problem in viscoelasticity where viscoelastic properties are subject to slight random variations.

In this note the honest method is utilized to obtain a truncated series solution for the mean displacement distribution as well as the variance of the displacement distribution on a large sample of elastic bars each with a perfectly smooth exponential decay but in which the initial Young's modulus varies slightly and randomly from bar to bar. Three specific cases of continuous probability distributions of the random variable such as Gamma type etc. are considered.

2 Formulation of the Problem: Governing Equations

We consider one thin semi-infinite elastic bar (of the large sample under consideration) occupying the region $x \geq 0$. The end $x = 0$ is subjected to a time-dependent displacement input. The stress equation of motion is

$$\frac{\partial \sigma}{\partial x} = \rho \frac{\partial^2 u}{\partial t^2} \tag{1}$$

The stress σ is connected with the strain by

$$\sigma = E \frac{\partial u}{\partial x}. \tag{2}$$

Here ρ is the initial density taken as a constant and u is the displacement in the bar. The elastic property is characterized by E taken as a function of x, α. The parameter α ranges over a probability space S with probability density $p(\alpha)$. The equation (1) with (2) then reduces to

$$\frac{dE}{dx} \cdot \frac{\partial u}{\partial x} + E \frac{\partial^2 u}{\partial x^2} = \rho \frac{\partial^2 u}{\partial t^2} \tag{3}$$

3 Approximate Solution to Equation (3) in the Form of a Series

We assume spatial nonhomogeneity in the form $E = E_0 + \epsilon g(x, \alpha)$ where g is a bound function of x and α. Since the elastic property is of a random nature with only slight variations, the parameter ϵ is supposed to be small. We shall later set

$$g(x, \alpha) = e^{\beta x} \cdot f(\alpha) \tag{4}$$

where β is a positive constant supposed deterministic (because of nonrandom spatial variation in E) and f is some random function (because of random variation in E from bar to bar). Physically this corresponds to a large sample of elastic bars, each with a perfectly smooth exponential decay, but in which the initial Young's modulus $E(0) = E_0 + \epsilon f(\alpha)$ varies slightly and randomly from bar to bar. Introducing E into equation (3) and taking Laplace transform assuming initial condition

$$u(x,0) = \frac{\partial u(x,0)}{\partial t} = 0,$$

we obtain

$$\frac{\epsilon}{E_0} \frac{dg}{dx} \cdot \frac{d\bar{u}}{dx} + \left(1 + \frac{\epsilon}{E_0} g\right) \frac{d^2 \bar{u}}{dx^2} = \frac{s^2}{e^2} \bar{u} \tag{5}$$

where

$$c = \sqrt{\frac{E_0}{\rho}}$$

is the longitudinal wave speed in the homogeneous case and s is the Laplace transform parameter.

We assume the solution to (5) in the form

[1] Professor, Department of Mathematics, Burdwan University, Burdwan, West Bengal, India 713 104.

Manuscript received by ASME Applied Mechanics Division, December, 1981; final revision, August 1983.

Downloaded 02 May 2010 to 171.66.16.54. Redistribution subject to ASME license or copyright; see http://www.asme.org/terms/Terms_Use.cfm

Finally, if we had reversed the coordinates, i.e., interchanged x_1 and x_2 (admittedly not a natural choice, but all systems are not so clearcut), then all the preceding results would be reversed, both for the ϵ_j and x_j variables.

Conclusions

We have attempted to clarify the observation made by many authors that the Rayleigh function is "flatter" around the fundamental eigenvector than around higher eigenmodes, the strongest variations being around the highest mode.

We have shown that the choice of coordinates defining the system and of variables defining the Rayleigh function are of utmost importance in qualfying the observation, which remains no more than the consequence of a fortunate coincidence of factors.

Summary

This note investigates the influence of the choice of coordinates and variables on the variations of the Rayleigh quotient of a general discrete mechanical system, and draws conclusions as to the "flatness" of the function around extremals.

References

1 Bishop, R. E. D., and Johnson, D. C., *The Mechanics of Vibration*, Cambridge University Press, Cambridge, England, 1960, pp. 144–154.

2 Lord Rayleigh, *Theory of Sound* (two volumes), 2nd ed., Dover, New York, 1945 reissue.

Wave Propagation in Semi-Infinite Elastic Bars With Randomly Varying Elastic Modulus

Dr. S. K. Roy Choudhuri[1]

1 Introduction

Elastic wave propagation in nonhomogeneous rods has attracted the attention of many researchers [3, 5]. But very few have studied the corresponding problems in a nonhomogeneous medium of randomly varying elastic properties. Problems of wave propagation in continuous media with random variation in material constants are receiving considerable attention in recent years. In geometrical optics, several problems on wave motion in random media have been solved [1, 2]. Two types of methods called "honest" and "dishonest" are utilized in such problems. In the honest method, the solution for displacement $u(x, \alpha, t)$ where x is the space coordinate, t the time, and α is a parameter ranging over a probability space S with probability density $p(\alpha)$ is determined for each value of α. After that its mean value and other statistics such as variance are computed. In the dishonest method randomness is considered before determining $u(x, \alpha, t)$ and some assumptions without sufficient reasons are made about the statistical properties of the random wave motion. In the honest method, the solution is expressed in the form of a series expansion in some parameter which is supposed to be small in view of slight random variations of the elastic properties of the medium. Keller [1] utilized perturbation method to solve the problem of propagation of light rays in a slightly nonhomogeneous random medium. It may be mentioned that very recently G. Singh and A. Singh [4] have studied a similar problem in viscoelasticity where viscoelastic properties are subject to slight random variations.

In this note the honest method is utilized to obtain a truncated series solution for the mean displacement distribution as well as the variance of the displacement distribution on a large sample of elastic bars each with a perfectly smooth exponential decay but in which the initial Young's modulus varies slightly and randomly from bar to bar. Three specific cases of continuous probability distributions of the random variable such as Gamma type etc. are considered.

2 Formulation of the Problem: Governing Equations

We consider one thin semi-infinite elastic bar (of the large sample under consideration) occupying the region $x \geq 0$. The end $x = 0$ is subjected to a time-dependent displacement input. The stress equation of motion is

$$\frac{\partial \sigma}{\partial x} = \rho \frac{\partial^2 u}{\partial t^2} \tag{1}$$

The stress σ is connected with the strain by

$$\sigma = E \frac{\partial u}{\partial x}. \tag{2}$$

Here ρ is the initial density taken as a constant and u is the displacement in the bar. The elastic property is characterized by E taken as a function of x, α. The parameter α ranges over a probability space S with probability density $p(\alpha)$. The equation (1) with (2) then reduces to

$$\frac{dE}{dx} \cdot \frac{\partial u}{\partial x} + E \frac{\partial^2 u}{\partial x^2} = \rho \frac{\partial^2 u}{\partial t^2} \tag{3}$$

3 Approximate Solution to Equation (3) in the Form of a Series

We assume spatial nonhomogeneity in the form $E = E_0 + \epsilon g(x,\alpha)$ where g is a bound function of x and α. Since the elastic property is of a random nature with only slight variations, the parameter ϵ is supposed to be small. We shall later set

$$g(x,\alpha) = e^{\beta x} \cdot f(\alpha) \tag{4}$$

where β is a positive constant supposed deterministic (because of nonrandom spatial variation in E) and f is some random function (because of random variation in E from bar to bar). Physically this corresponds to a large sample of elastic bars, each with a perfectly smooth exponential decay, but in which the initial Young's modulus $E(0) = E_0 + \epsilon f(\alpha)$ varies slightly and randomly from bar to bar. Introducing E into equation (3) and taking Laplace transform assuming initial condition

$$u(x,0) = \frac{\partial u(x,0)}{\partial t} = 0,$$

we obtain

$$\frac{\epsilon}{E_0} \frac{dg}{dx} \cdot \frac{d\bar{u}}{dx} + \left(1 + \frac{\epsilon}{E_0} g\right) \frac{d^2 \bar{u}}{dx^2} = \frac{s^2}{e^2} \bar{u} \tag{5}$$

where

$$c = \sqrt{\frac{E_0}{\rho}}$$

is the longitudinal wave speed in the homogeneous case and s is the Laplace transform parameter.

We assume the solution to (5) in the form

[1] Professor, Department of Mathematics, Burdwan University, Burdwan, West Bengal, India 713 104.

Manuscript received by ASME Applied Mechanics Division, December, 1981; final revision, August 1983.

Copyright © 1985 by ASME
Downloaded 02 May 2010 to 171.66.16.54. Redistribution subject to ASME license or copyright; see http://www.asme.org/terms/Terms_Use.cfm

$$\bar{u}(x,\alpha,s)=\bar{u}_0(x,s)$$

$$+\frac{\epsilon}{E_0}\bar{u}_1(x,\alpha,s)+\left(\frac{\epsilon}{E_0}\right)^2\bar{u}_2(x,\alpha,s)+\ldots. \tag{6}$$

where ϵ/E_0 is small.

Inserting (6) into (5) and equating different powers of E we obtain,

$$\bar{u}_{0,xx}=\frac{s^2}{c^2}\bar{u}_0 \tag{7}$$

and

$$\frac{dg}{dx}\bar{u}_{n-1,x}+g\bar{u}_{n-1,xx}+\bar{u}_{n,xx}=\frac{s^2}{c^2}\bar{u}_n \tag{7a}$$

for $n\geq 1$.

Boundary Conditions. A time-dependent displacement input $u(0,t)=f_1(t)$ is applied at $x=0$. Of course f_1 is such that $f_1(0)=f_1^{(0)}=0$ to ensure $u=\dot{u}=0$ when $t=0$. The condition $\bar{u}(0,s)=\bar{f}_1(s)$ is satisfied if $\bar{u}_0(0,s)=\bar{f}_1(s)$ and $\bar{u}_n(0,\alpha,s)=0$ for $n\geq 1$. The solution to (7) bounded as $x\to\infty$ is then

$$\bar{u}_0(x,s)=\bar{f}_1(s)\cdot e^{sx/c} \tag{8}$$

Inverting the Laplace transform

$$u_0(x,t)=f_1\left(t-\frac{x}{c}\right)\qquad \text{for}\quad t>\frac{x}{c} \tag{9}$$

$$\text{for}\quad 0<t<\frac{x}{c}$$

This determines $u_0(x,t)$, which represents the solution for the homogeneous nonrandom case. When $\bar{u}_0$ is inserted into (7) we get

$$\bar{u}_{1,xx}-\frac{s^2}{c^2}\bar{u}_1=e^{xs/c}\frac{s}{c}\bar{f}_1(s)\left(\frac{dg}{dx}-g\cdot\frac{s}{c}\right) \tag{10}$$

The equation for $\bar{u}_2(x,\alpha,s)$ is given by (7*a*), which is

$$\bar{u}_{2,xx}-\frac{s^2}{c^2}\bar{u}_2=-\frac{dg}{dx}\bar{u}_{1,x}-g\bar{u}_{1,xx} \tag{10a}$$

The solutions to (10) and (10*a*) will satisfy

$$\bar{u}_{1,2}\to 0\qquad \text{as}\quad x\to\infty\qquad \text{and}\qquad \bar{u}_{1,2}(0,\alpha,s)=0.$$

The solution to (10) with g given by (4) and satisfying the conditions as stated in the foregoing is

$$\bar{u}_1(x,\alpha,s)=\frac{f(\alpha)}{2\beta c}e^{sx/c}(1-e^{\beta\cdot x})\frac{s\bar{f}_1(s)(s+\beta\cdot c)}{s+\beta\cdot c/2}$$

The solution to (10*a*) with $\bar{u}_1$ in the foregoing is given by

$$\bar{u}_2(x,\alpha,s)=e^{sx/c}f^2(\alpha)\cdot\mu(s)\Big[(s$$

$$+2\beta c)\cdot e^{2\beta x}/4\beta(s+\beta c)-$$

$$-se^{\beta x}/2\beta\left(s+\frac{\beta c}{2}\right)$$

$$-(s+2\beta c)/4\beta(s+\beta c)+s/2\beta\left(s+\frac{\beta_c}{2}\right)\Big]$$

where

$$\mu(s)=s\bar{f}_1(s)(s+\beta c)^2/2\beta e^2\left(s+\frac{\beta_e}{2}\right)$$

If f_1 is prescribed, then inverting, we can determine $u_1(x,\alpha,t)$, $u_2(x,\alpha,t)$. The solution for $\bar{u}_2$ is utilized in the next equation for the solution of $\bar{u}_3$ and so on. Thus by inverting we can determine $u_3,\ldots.$ for each value of α. Assuming the absolute and uniform convergence of the series, the solution for displacement is

$$u(x,\alpha,t)=u_0(x,t)+\frac{\epsilon}{E_0}u_1(x,\alpha,t)+$$

$$+\left(\frac{\epsilon}{E_0}\right)^2u_2(x,\alpha,t)+\ldots....$$

Now if the probability space S of the random variate α and its density function are specified, we can calculate the mean displacement distribution in the bars given by

$$<u>=u_0+\frac{\epsilon}{E_0}<u_1>+\left(\frac{\epsilon}{E_0}\right)^2<u_2>+\ldots....$$

where the mean of f is denoted by $<f>=\int f(\alpha)p(\alpha)d\alpha$ and Var $u=E(u-<u>)^2$ where E stands for the expectation. It is clear that the nth order perturbation field u_n will always be proportional to f^n because of equation (4). We can express $u_n(x,\alpha,t)=f^n(\alpha)\bar{u}_n(x,t)$ where $\bar{u}_n$ is deterministic. Then

$$<u>=\sum_{n=0}^{\infty}\left(\frac{\epsilon}{E_0}\right)^n<f^n>\bar{u}_n$$

$$\text{Var}u=\sum_{n=2}^{\infty}\left(\frac{\epsilon}{E_0}\right)^n[<f^n>-<f>^n]\sum_{j=0}^{n}\bar{u}_j\bar{u}_{n-j}$$

Considering second-order terms,

$$<u>\simeq u_0+\frac{\epsilon}{E_0}<f>\bar{u}_1+\left(\frac{\epsilon}{E_0}\right)^2<f^2>\bar{u}_2,$$

$$\text{Var}u\simeq\left(\frac{\epsilon}{E_0}\right)^2\text{Var}f(\alpha)(\bar{u}_1^2+2\bar{u}_0\bar{u}_2)+0(\epsilon^3)$$

4 Example

$\bar{f}_1=a_0(1-\cos\omega t)$ where a_0 is a constant, then

$$f_1(s)=a_0\left[\frac{1}{s}-\frac{s}{s^2+\omega^2}\right]$$

Then

$$u_0(x,t)=a_0\left[1-\cos\omega\left(t-\frac{x}{c}\right)\right]$$

$$=\bar{u}_0(x,t)\quad\text{for}\quad t>\frac{x}{c}$$

$$=0\quad\text{for}\quad 0<t<\frac{x}{c}.$$

$$u_1(x,\alpha,t)f(\alpha)\bar{u}_1(x,t)\quad\text{for}\quad t>\frac{x}{c}$$

$$=0\quad\text{for}\quad 0<t<\frac{x}{c}$$

where

$$\bar{u}_1(x,t)=\frac{(1-e^{-\beta\cdot x})a_0\omega^2}{2\beta c}\left[\sin\left\{\omega\left(t-\frac{x}{c}\right)\right\}/\omega+\right.$$

$$\left.+\frac{\beta c}{2}\left\{\frac{\beta c/2}{\frac{\beta^2c^2}{4}+\omega^2}\cdot\frac{\sin\omega\left(t-\frac{x}{c}\right)}{\omega}\right.\right.$$

Downloaded 02 May 2010 to 171.66.16.54. Redistribution subject to ASME license or copyright; see http://www.asme.org/terms/Terms_Use.cfm

$$- \frac{\cos\omega\left(t-\frac{x}{c}\right)}{\frac{\beta^2c^2}{4}+\omega^2} + \frac{e^{\frac{-\beta.c}{2}\left(t-\frac{x}{c}\right)}}{\frac{\beta^2c^2}{4}+\omega^2}\Bigg\}\Bigg],$$

$$u_2(x,\alpha,t) = f^2(\alpha)\bar{u}_2(x,t) \quad \text{for} \quad t > \frac{x}{c}$$

$$= 0 \quad \text{for} \quad 0 < t < \frac{x}{c}$$

where

$$\bar{u}_2(x,t) = \frac{(\bar{e}^{2\beta x}-1)}{4\beta}\chi\left(t-\frac{x}{c}\right) + \frac{(1-\bar{e}^{\beta x})}{2\beta}\psi\left(t-\frac{x}{c}\right),$$

$$\chi(t) = \frac{a_0\omega^2}{^2\beta c^2\left(\frac{\beta^2c^2}{4}+\omega^2\right)}\left[\frac{3}{4}\beta^2c^2\cdot e^{-\frac{\beta c}{2}t} + \left(\omega^2-\frac{\beta^2c^2}{2}\right)\cos\omega t + \frac{\beta c}{2}(2\beta^2e^2+5\omega^2)\cdot\frac{\sin(\omega t)}{\omega}\right],$$

$$\psi(t) = -\left\{\frac{\beta^2c^2/4}{\frac{\beta^2c^2}{4}+\omega^2}\left(1+\frac{\beta c}{2}t\right) + \frac{\beta^4c^4/8}{\left(\frac{\beta^2c^2}{4}+\omega^2\right)^2}\right\}\cdot e^{-\frac{\beta e}{2}t} + \left\{\frac{\frac{\beta^2c^2}{2}+\omega^2}{\frac{\beta^2c^2}{4}+\omega^2} + \frac{\beta^4c^4/8}{\left(\frac{\beta^2c^2}{4}+\omega^2\right)^2}\right\}\cos(\omega t) + \left\{\frac{\frac{\beta c}{2}\omega}{\frac{\beta^2c^2}{4}+\omega^2} + \frac{\beta c}{2}\omega\frac{\left(\frac{3}{4}\beta^2c^2+\omega^2\right)}{\left(\frac{\beta^2c^2}{4}+\omega^2\right)^2}\right\}\sin(\omega t)$$

Different Probability Distribution

(*i*) We compute the mean displacement distribution in the bars by taking the random function $f(\alpha)$ in the form

$$f(\alpha) = e^{-k\alpha}(k>0). \tag{11}$$

Here the probability distribution of the random variable α is specified by the density function of a gamma variate. In this case

$$p(\alpha) = \frac{\alpha^{l-1}\cdot e^{-\alpha}}{\Gamma(l)}$$

for $0<\alpha<\infty$ and is equal to zero elsewhere.
Here l is a positive constant.
Then

$$<f> = \frac{1}{(1+k)^l}, <f^2> = \frac{1}{(1+2k)^l}$$

Thus

$$<u> = a_0\left[1-\cos\left\{\omega\left(t-\frac{x}{c}\right)\right\}\right] + \frac{\epsilon}{E_0}\cdot\frac{1}{(1+k)^l}\bar{u}_1(x,t) + \left(\frac{\epsilon}{E_0}\right)^2\frac{1}{(1+2k)^l}\bar{u}_2(x,t) \quad \text{for} \quad t>\frac{x}{c}$$

$$= 0 \quad \text{for} \quad 0<t<\frac{x}{c} \tag{13}$$

Thus the effect of the continuous random medium with randomly varying Young's modulus represented by (4) and (11) on the wave propagation in the bars is to multiply the nonhomogeneous parts of the mean displacement distribution by the factors $(1+k)^{-l}$, $(1+2k)^{-l}$.

(*ii*) We take $f(\alpha) = k\alpha$, $k>0$ (a constant)

$$p(\alpha) = \frac{1}{2}(\alpha+1), -1<\alpha<1$$

$$= 0 \text{ elsewhere}$$

Then

$$<f> = \frac{k}{3}, <f^2> = \frac{k^2}{3}$$

The mean displacement is the same as that given by (13), whose nonhomogeneous parts are multiplied, respecitvely, by the factors $k/3$, $K^2/3$.

(*iii*) We take $f(\alpha) = k\alpha$ and $p(\alpha) = 1/2$, $-1<\alpha<1$,

$$= 0 \text{ elsewhere.}$$

In this case α has a uniform probability distribution over the interval $(-1, 1)$ and $<f> = 0$, $<f^2> = k^2/3$

$$<u> = a_0\left[1-\cos\left\{\omega\left(t-\frac{x}{c}\right)\right\}\right] + \left(\frac{\epsilon}{E_0}\right)^2\cdot\frac{k^2}{3}\cdot\bar{u}_2(x,t)$$

The mean displacement is the same as that given by (13), whose nonhomogeneous parts are multiplied, respectively, by the factors zero and $k^2/3$, respectively.

Computation of Variance. Retaining second-order terms

$$\mathrm{Var}u \simeq \left(\frac{\epsilon}{E_0}\right)^2\cdot\mathrm{Var}f\cdot(\bar{u}_1^2+2\bar{u}_0\bar{u}_2)$$

In case of constant probability distribution [Case (*iii*)],

$$\mathrm{Var}u \simeq \left(\frac{\epsilon}{E_0}\right)^2\cdot\frac{k^2}{3}(\bar{u}_1^2+2\bar{u}_0\bar{u}_2)$$

When $f(\alpha) = k\alpha$ where $p(\alpha) = 2(1-\alpha)$ for $0<\alpha<1$

$$= 0 \text{ elsewhere}$$

$$\mathrm{Var}u \simeq \left(\frac{\epsilon}{E_0}\right)^2\cdot\frac{k^2}{18}(\bar{u}_1^2+2\bar{u}_0\bar{u}_2)$$

Mean Stress Distribution. Mean stress distribution up to second-order terms is given by

$$<\sigma> \simeq E_0\left[\bar{u}_0' + \frac{\epsilon}{E_0}\left\{e^{-\beta x}\cdot\bar{u}_0' + \bar{u}_1'\right\}<f> + \left(\frac{\epsilon}{E_0}\right)^2\left\{e^{-\beta x}\bar{u}_1' + \bar{u}_2'\right\}<f^2>\right]$$

Remarks. If instead of displacement input, we specify the velocity or the stress at one end of the bars the mean wave motion in the bars can be determined in the same way together with their variances and other statistics. We note that the boundary conditions are supposed to be deterministic in nature whereas the physical properties are supposed to be random having only slightly random variations. It may be mentioned that it is possible to extend this problem in

Downloaded 02 May 2010 to 171.66.16.54. Redistribution subject to ASME license or copyright; see http://www.asme.org/terms/Terms_Use.cfm

presence of a thermal field by assuming the thermal field and all boundary conditions to be deterministic, whereas the elastic property only is subject to slight variations.

References

1 Keller, J. B., "Wave Propagation in Random Media," *Proc. Sym. in Appl. Math. Am. Math. Soc.*, Vol. 13, 1962, pp. 227–246.

2 Keller, J. B., "Stochastic Equations and Wave Propagation in Random Media," *Proc. Sym. in Appl. Math. Am. Math. Soc.*, Vol. 16, 1964, pp. 145–170.

3 Lindholm, U. S., and Doshi, K. D., "Wave Propagation in an Elastic Nonhomogeneous Bar of Finite Length," ASME JOURNAL OF APPLIED MECHANICS, Vol. 32, 1965, pp. 135–142.

4 Singh, G., and Singh, A., "Wave Propagation in a Linear Random Nonhomogeneous Viscoelastic Semi-infinite Bar," *Indian J. of Pure and Appl. Math.*, Vol. 11/8, 1980, pp. 1095–1104.

5 Vasudeva, R. Y., and Bhaskara, R. K., "Propagation of a Pulse in Nonhomogeneous Rod With Varying Cross Section," ASME JOURNAL OF APPLIED MECHANICS, Vol. 45, 1978, pp. 942–944.

Thermoelastic Stress Due To Surface Parallelepiped Inclusions[1]

S. Lee[2] and C. C. Hsu[2]

The thermoelastic stress generated by surface parallelepiped inclusions has been solved by the Mindlin method. The stress components near the free surface and inside the solid have been discussed. Numerical results using this method are compared with Chiu's results obtained by using the Fourier transform.

1 Introduction

Elastic inclusion problems have been studied for a long time. Many important mechanical properties such as toughness and ductility are controlled by inclusions. Eshelby [1, 2] has proposed a transformation strain method to solve the elastic stress field due to an inclusion in an infinite isotropic medium and suggested using the image field to match the finite boundary problems. The cuboidal inclusion inside an infinite solid has been solve by Chiu [3] using the Fourier transform method. The stress field due to a point force in a semi-infinite medium has been obtained by Mindlin [4] and used to obtain the thermoelastic stress due to spherical inclusion in the half space. Seo and Mura [6] used Mindlin's [4] solution as Green function to obtain the stress field due to ellipsoidal inclusions in a half space. Chiu [7] extended his method for the infinite medium to the half space and obtained an integral form of the stress field due to a cuboidal inclusion. In this paper, we present the analytic form of thermoelastic stress due to a parallelepiped inclusion close to a free surface obtained by the Mindlin method.

2 Formulation

Assume a parallelepiped thermoelastic inclusion with a uniform temperature T is embedded in an isotropic half space as shown in Fig. 1. The imaginary inclusion is obtained by

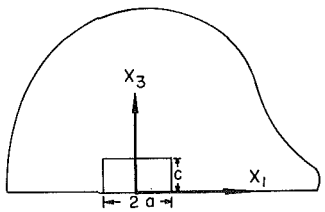


Fig. 1(a) Side view of half space with a parallelepiped inclusion

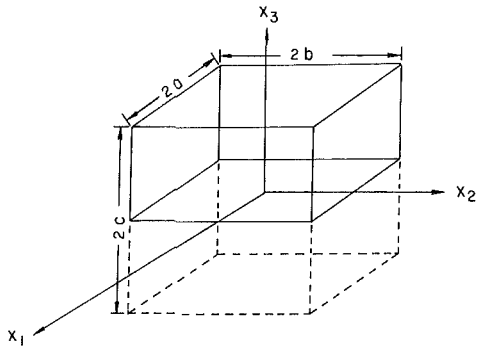


Fig. 1(b) Coordinate system with parallelepiped inclusion and its image

Fig. 1

mirror reflection on plane $x_3 = 0$ such that the plane $x_3 = 0$ is free from the surface traction. The displacement was derived by Mindlin and Cheng [5] and rewritten by Seo and Mura [6] as

$$4\pi u_i = \beta \int_V \left[-\left(\frac{1}{R_1}\right)_{,i} + (3-4\nu)(2\delta_{3i}-1)\left(\frac{1}{R_2}\right)_{,i} - 2x_3\left(\frac{1}{R_2}\right)_{,3i} \right] dv' \tag{1}$$

where

$$\beta = \alpha T(1+\nu)/(1-\nu) \tag{2}$$

$$R_1^2 = (x_1 - x_1')^2 + (x_2 - x_2')^2 + (x_3 - x_3')^2 \tag{3}$$

$$R_2^2 = (x_1 - x_1')^2 + (x_2 - x_2')^2 + (x_3 + x_3')^2 \tag{4}$$

and

$$\frac{\partial}{\partial x_i}\left(\frac{1}{R_1}\right) = \left(\frac{1}{R_1}\right)_{,i} \tag{5}$$

V is the volume of the elastic inclusion, α and ν are the linear thermal expansion coefficient and poisson ratio, respectively, δ_{3i} is kronecker delta.

It is conventional to define two potential functions as

$$\phi_A = \int_V \frac{1}{R_1}\, dv' \tag{6}$$

$$\phi_B = \int_V \frac{1}{R_2}\, dv' \tag{7}$$

Since R_2 is mirror symmetry of R_1 with plane $X_3 = 0$, potential ϕ_B is easily obtained if potential ϕ_A is given for point **r** outside of elastic inclusion.

In our study the shape of the inclusion is a parallelepiped and therefore the cartesian coordinate system is adopted. Define the function as

$$f(\bar{X}_{A1}, \bar{X}_{A2}, \bar{X}_{A3}) = f(x_1, x_2, x_3)\Big|_{x_1-a, x_2-b, x_3-c}^{x_1+a, x_2+b, x_3}$$

[1] This work was partially supported by the National Science Council, Republic of China.

[2] Associate Professor, Department of Materials Science, and Professor, Department of Physics, respectively, National Tsing Hua University, Hsinchu, Taiwan 300, Republic of China.

Manuscript received by ASME Applied Mechanics Division, March 1984; final revision, June, 1984.

Downloaded 02 May 2010 to 171.66.16.54. Redistribution subject to ASME license or copyright; see http://www.asme.org/terms/Terms_Use.cfm

presence of a thermal field by assuming the thermal field and all boundary conditions to be deterministic, whereas the elastic property only is subject to slight variations.

References

1 Keller, J. B., "Wave Propagation in Random Media," *Proc. Sym. in Appl. Math. Am. Math. Soc.*, Vol. 13, 1962, pp. 227–246.

2 Keller, J. B., "Stochastic Equations and Wave Propagation in Random Media," *Proc. Sym. in Appl. Math. Am. Math. Soc.*, Vol. 16, 1964, pp. 145–170.

3 Lindholm, U. S., and Doshi, K. D., "Wave Propagation in an Elastic Nonhomogeneous Bar of Finite Length," ASME JOURNAL OF APPLIED MECHANICS, Vol. 32, 1965, pp. 135–142.

4 Singh, G., and Singh, A., "Wave Propagation in a Linear Random Nonhomogeneous Viscoelastic Semi-infinite Bar," *Indian J. of Pure and Appl. Math.*, Vol. 11/8, 1980, pp. 1095–1104.

5 Vasudeva, R. Y., and Bhaskara, R. K., "Propagation of a Pulse in Nonhomogeneous Rod With Varying Cross Section," ASME JOURNAL OF APPLIED MECHANICS, Vol. 45, 1978, pp. 942–944.

Thermoelastic Stress Due To Surface Parallelepiped Inclusions[1]

S. Lee[2] and C. C. Hsu[2]

The thermoelastic stress generated by surface parallelepiped inclusions has been solved by the Mindlin method. The stress components near the free surface and inside the solid have been discussed. Numerical results using this method are compared with Chiu's results obtained by using the Fourier transform.

1 Introduction

Elastic inclusion problems have been studied for a long time. Many important mechanical properties such as toughness and ductility are controlled by inclusions. Eshelby [1, 2] has proposed a transformation strain method to solve the elastic stress field due to an inclusion in an infinite isotropic medium and suggested using the image field to match the finite boundary problems. The cuboidal inclusion inside an infinite solid has been solve by Chiu [3] using the Fourier transform method. The stress field due to a point force in a semi-infinite medium has been obtained by Mindlin [4] and used to obtain the thermoelastic stress due to spherical inclusion in the half space. Seo and Mura [6] used Mindlin's [4] solution as Green function to obtain the stress field due to ellipsoidal inclusions in a half space. Chiu [7] extended his method for the infinite medium to the half space and obtained an integral form of the stress field due to a cuboidal inclusion. In this paper, we present the analytic form of thermoelastic stress due to a parallelepiped inclusion close to a free surface obtained by the Mindlin method.

2 Formulation

Assume a parallelepiped thermoelastic inclusion with a uniform temperature T is embedded in an isotropic half space as shown in Fig. 1. The imaginary inclusion is obtained by

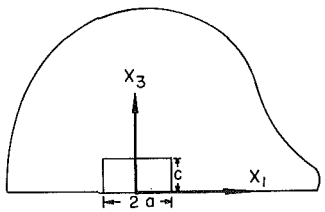


Fig. 1(a) Side view of half space with a parallelepiped inclusion

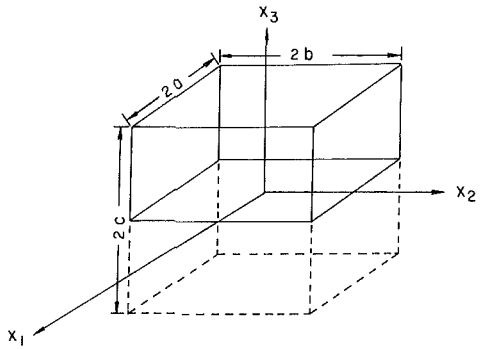


Fig. 1(b) Coordinate system with parallelepiped inclusion and its image

Fig. 1

mirror reflection on plane $x_3 = 0$ such that the plane $x_3 = 0$ is free from the surface traction. The displacement was derived by Mindlin and Cheng [5] and rewritten by Seo and Mura [6] as

$$4\pi u_i = \beta \int_V \left[-\left(\frac{1}{R_1}\right)_{,i} + (3-4\nu)(2\delta_{3i}-1)\left(\frac{1}{R_2}\right)_{,i} - 2x_3\left(\frac{1}{R_2}\right)_{,3i} \right] dv' \tag{1}$$

where

$$\beta = \alpha T(1+\nu)/(1-\nu) \tag{2}$$

$$R_1^2 = (x_1 - x_1')^2 + (x_2 - x_2')^2 + (x_3 - x_3')^2 \tag{3}$$

$$R_2^2 = (x_1 - x_1')^2 + (x_2 - x_2')^2 + (x_3 + x_3')^2 \tag{4}$$

and

$$\frac{\partial}{\partial x_i}\left(\frac{1}{R_1}\right) = \left(\frac{1}{R_1}\right)_{,i} \tag{5}$$

V is the volume of the elastic inclusion, α and ν are the linear thermal expansion coefficient and poisson ratio, respectively, δ_{3i} is kronecker delta.

It is conventional to define two potential functions as

$$\phi_A = \int_V \frac{1}{R_1}\, dv' \tag{6}$$

$$\phi_B = \int_V \frac{1}{R_2}\, dv' \tag{7}$$

Since R_2 is mirror symmetry of R_1 with plane $X_3 = 0$, potential ϕ_B is easily obtained if potential ϕ_A is given for point **r** outside of elastic inclusion.

In our study the shape of the inclusion is a parallelepiped and therefore the cartesian coordinate system is adopted. Define the function as

$$f(\bar{X}_{A1}, \bar{X}_{A2}, \bar{X}_{A3}) = f(x_1, x_2, x_3)\Big|_{x_1-a, x_2-b, x_3-c}^{x_1+a, x_2+b, x_3}$$

[1] This work was partially supported by the National Science Council, Republic of China.

[2] Associate Professor, Department of Materials Science, and Professor, Department of Physics, respectively, National Tsing Hua University, Hsinchu, Taiwan 300, Republic of China.

Manuscript received by ASME Applied Mechanics Division, March 1984; final revision, June, 1984.

Copyright © 1985 by ASME

Downloaded 02 May 2010 to 171.66.16.54. Redistribution subject to ASME license or copyright; see http://www.asme.org/terms/Terms_Use.cfm

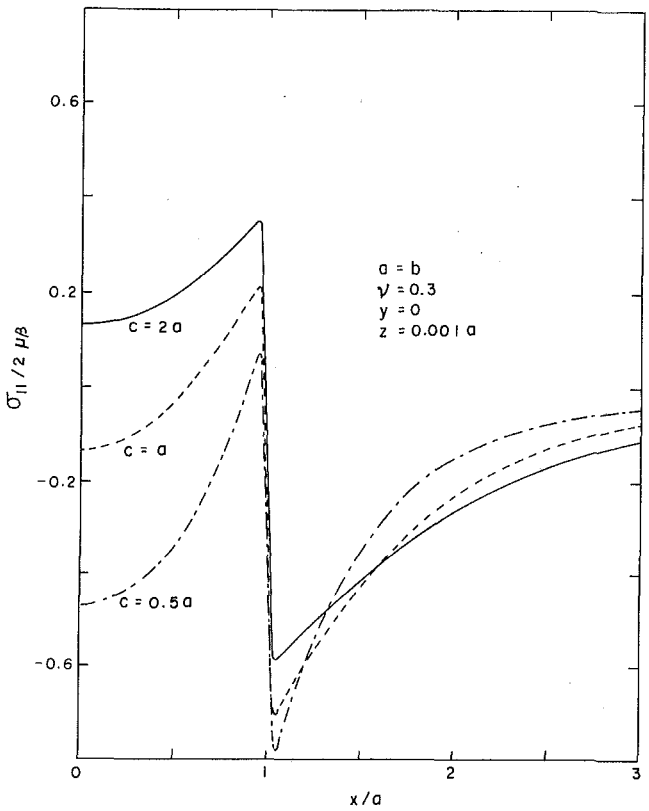


Fig. 2 Variation of the stress component σ_{11} near the free surface, where $a = b$, $\nu = 0.3$, $y = 0$, and $z = 0.001a$

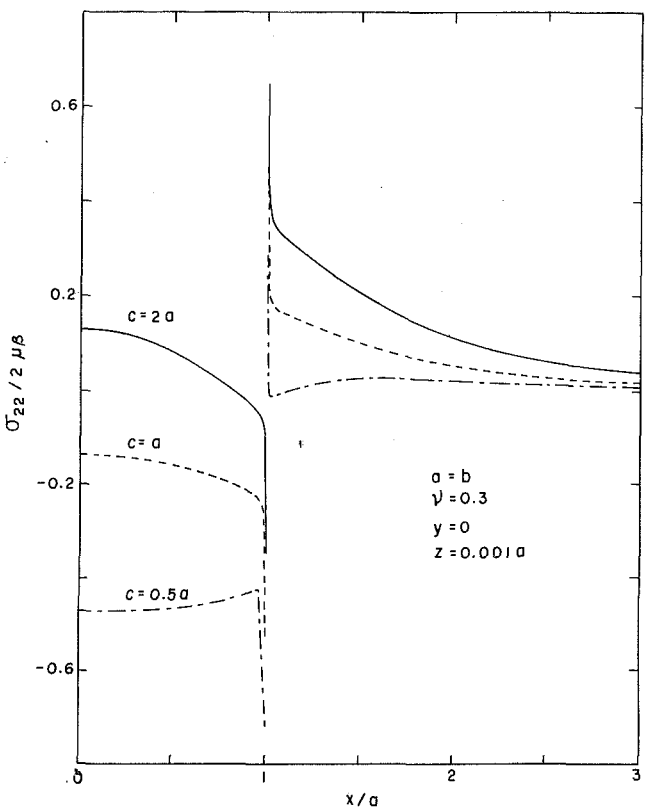


Fig. 3 Variation of the stress component σ_{22}. The statements are the same as Fig. 2.

$$=f(x_1+a,x_2+b,x_3)+f(x_1+a,x_2-b,x_3-c)$$
$$+f(x_1-a,x_2+b,x_3-c)$$
$$+f(x_1-a,x_2-b,x_3)-f(x_1-a,x_2-b,x_3-c)$$
$$-f(x_1-a,x_2+b,x_3)$$
$$-f(x_1+a,x_2-b,x_3)-f(x_1+a,x_2+b,x_3-c), \tag{8}$$

and

$$f(\bar{X}_{B1},\bar{X}_{B2},\bar{X}_{B3})=f(x_1,x_2,x_3)\Big|_{x_1-a,x_2-b,x_3}^{x_1+a,x_2+b,x_3+c}, \tag{9}$$

then the potential ϕ_A of equation (6) becomes

$$\phi_A=\frac{1}{2}S_{ijk}\left\{\bar{X}_{Ai}\bar{X}_{Aj}ln(\bar{\rho}_A+\bar{X}_{Ak})-\frac{1}{2}\bar{X}_{Ai}^2\tan^{-1}\frac{\bar{X}_{Aj}\bar{X}_{Ak}}{\bar{X}_{Ai}\bar{\rho}_A}\right\}, \tag{10}$$

where

$$\bar{\rho}_A=(\bar{X}_{A1}^2+\bar{X}_{A2}^2+\bar{X}_{A3}^2)^{1/2} \tag{11}$$

and S_{ijk} is equal to 1 if all indices are not repeated and zero if two or more of them are same.

The displacement from equation (1) is then written as

$$u_1=-\frac{\beta S_{1jk}}{4\pi}\left\{\bar{X}_{Aj}ln(\bar{\rho}_A+\bar{X}_{Ak})-\frac{1}{2}\bar{X}_{A1}\tan^{-1}\frac{\bar{X}_{Aj}}{\bar{X}_{A1}}\frac{\bar{X}_{Ak}}{\bar{\rho}_A}\right.$$
$$\left.+(3-4\nu)\left[\bar{X}_{Bj}ln(\bar{\rho}_B+\bar{X}_{Bk})-\frac{1}{2}\bar{X}_{B1}\tan^{-1}\frac{\bar{X}_{Bj}\bar{X}_{Bk}}{\bar{X}_{B1}\bar{\rho}_B}\right]\right\}$$
$$-\frac{\beta x_3}{2\pi}ln(\bar{\rho}_B+\bar{X}_{B2}) \tag{12}$$

$$u_3=-\frac{\beta S_{ij3}}{4\pi}\left\{\bar{X}_{Ai}ln(\bar{\rho}_A+\bar{X}_{Aj})-\frac{1}{2}\bar{X}_{A3}\tan^{-1}\frac{\bar{X}_{Ai}\bar{X}_{Aj}}{\bar{\rho}_A\bar{X}_{A3}}\right.$$

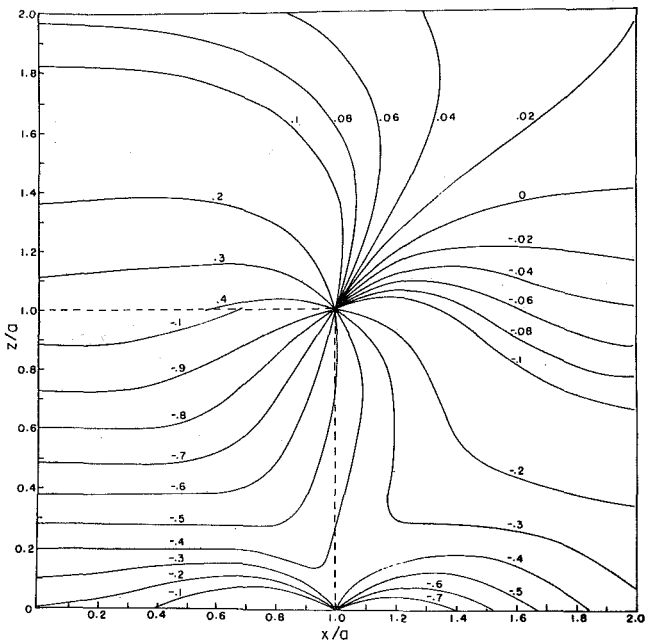


Fig. 4 σ_{11} contour, where $a = b = c$, $y = 0$. The dashed line is the interface of the inclusion and the solid.

$$\left.-(3-4\nu)\left[\bar{X}_{Bi}ln(\bar{\rho}_B+\bar{X}_{Bj})-\frac{1}{2}\bar{X}_{B3}\tan^{-1}\frac{\bar{X}_{Bi}\bar{X}_{Bj}}{\bar{X}_{B3}\bar{\rho}_B}\right]\right\}$$
$$+\frac{\beta x_3}{2\pi}\tan^{-1}\frac{\bar{X}_{B1}\bar{X}_{B2}}{\bar{X}_{B3}\bar{\rho}_B} \tag{13}$$

and the displacement component u_2 is obtained from u_1 if subscripts 1 and 2 exchange each other in equation (12).

Downloaded 02 May 2010 to 171.66.16.54. Redistribution subject to ASME license or copyright; see http://www.asme.org/terms/Terms_Use.cfm

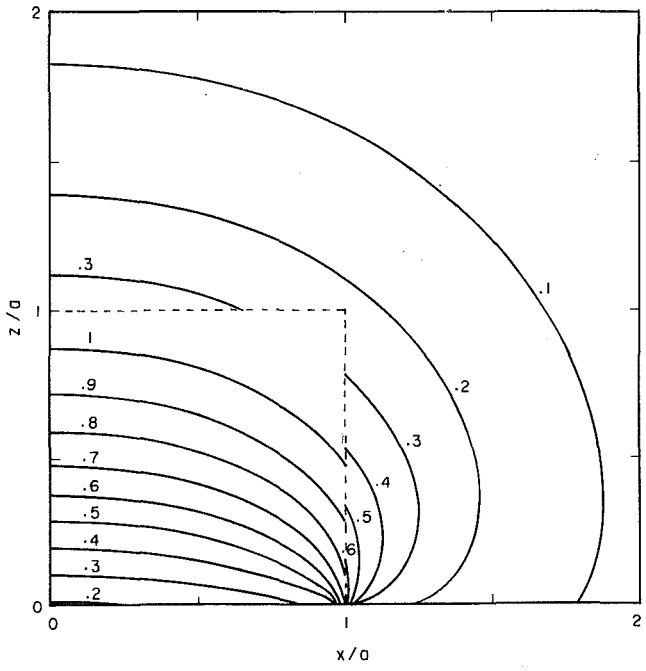


Fig. 5 σ_{22} contour. The statements are the same as Fig. 4.

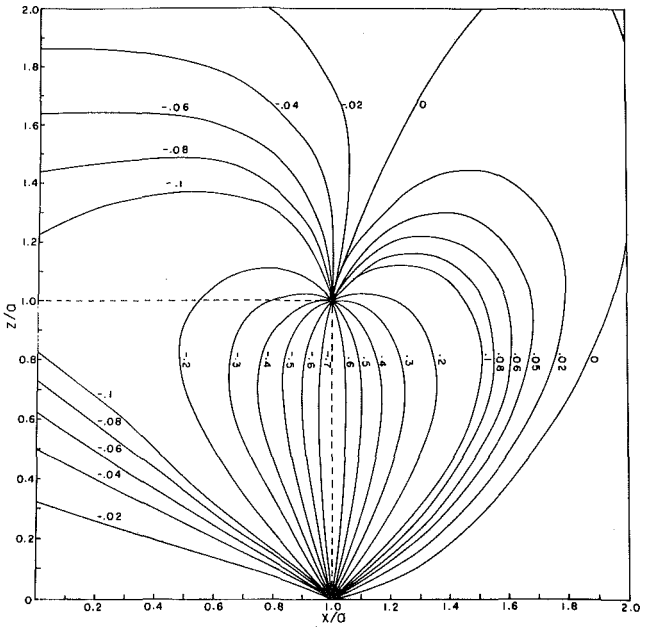


Fig. 6 σ_{33} contour. The statements are the same as Fig. 4.

The dilatation is

$$e=\beta\left[S(\mathbf{r})-\frac{1-2\nu}{\pi}\tan^{-1}\frac{\bar{X}_{B1}\bar{X}_{B2}}{\bar{X}_{B3}\bar{\rho}_B}\right] \tag{14}$$

the stress components are

$$\sigma_{11}=-2\mu\beta\, S(\mathbf{r})+\frac{\mu\beta}{2\pi}\left[\tan^{-1}\frac{\bar{X}_{A2}\bar{X}_{A3}}{\bar{X}_{A1}\bar{\rho}_A}+3\tan^{-1}\frac{\bar{X}_{B2}\bar{X}_{B3}}{\bar{X}_{B1}\bar{\rho}_B}\right.$$

$$\left.+4\nu\tan^{-1}\frac{\bar{X}_{B1}\bar{X}_{B3}}{\bar{X}_{B2}\bar{\rho}_B}-\frac{2x_3\bar{X}_{B1}}{\bar{\rho}_B(\bar{\rho}_B+\bar{X}_{B2})}\right], \tag{15}$$

$$\sigma_{33}=-2\mu\beta\, S(\mathbf{r})+\frac{\mu\beta}{2\pi}\left[\tan^{-1}\frac{\bar{X}_{A1}\bar{X}_{A2}}{\bar{X}_{A3}\bar{\rho}_A}-\tan^{-1}\frac{\bar{X}_{B1}\bar{X}_{B2}}{\bar{X}_{B3}\bar{\rho}_B}\right.$$

$$\left.-\frac{2x_3\bar{X}_{B1}\bar{X}_{B2}(\bar{\rho}_B^2+\bar{X}_{B3}^2)}{\bar{\rho}_B(\bar{\rho}_B^2-\bar{X}_{B1}^2)(\bar{\rho}_B^2-\bar{X}_{B2}^2)}\right], \tag{16}$$

$$\sigma_{12}=-\frac{\mu\beta}{2\pi}\left[ln(\bar{\rho}_A+\bar{X}_{A3})+(3-4\nu)ln(\bar{\rho}_B+\bar{X}_{B3})+\frac{2x_3}{\bar{\rho}_B}\right], \tag{17}$$

$$\sigma_{13}=-\frac{\mu\beta}{2\pi}\left[ln(\bar{\rho}_A+\bar{X}_{A2})+ln(\bar{\rho}_B+\bar{X}_{B2})+\frac{2x_3\bar{X}_{B3}}{(\bar{\rho}_B+\bar{X}_{B2})\bar{\rho}_B}\right] \tag{18}$$

where $S(\mathbf{r})$ is equal to 1 if $\mathbf{r}$ is inside the inclusion, otherwise it is zero, and the μ is shear modulus. The σ_{22} and σ_{23} could be obtained from equations (15) and (18), respectively, if subscripts 1 and 2 exchange each other.

3 Numerical Results and Discussions

In this section, we are interested in the surface inclusion, for which the distance of the inclusion from the free surface is zero as shown in Fig. 1.

In the following, β is assumed to be positive. The stress distribution σ_{11} along the x_1 direction near the free surface, $x_3 = a \times 10^{-3}$ for three values of c ($2a$, a, and $0.5a$), and $a = b$ are shown in Fig. 2. From this figure, it is seen that the magnitude of stress decreases with the parameter c. Due to force equilibrium, the stress inside the inclusion at the boundary $x_1 = a$ is equal to that outside the inclusion. The stress outside the inclusion is always compressive and approaches zero at infinity. The stress near the boundary (both in the inclusion and the matrix) is more compressive as the ratio c/a decreases, therefore crack nucleation and propagation become more difficult. For example, when phase transformation happens and the thermal expansion coefficient is positive, some material may absorb heat and increase in temperature, so that crack nucleation and propagation would be more difficult.

The stress distribution σ_{22} along the same line is shown in Fig. 3. The stress is positive (tension) at large values of c and changes sign (to compression) at low values of c, and it has a discontinuity ($2\mu\beta$) at the boundary $x_1 = a$. The stress outside the inclusion decreases as the distance increases and approaches zero at infinity, and the stress inside the inclusion decreases with the parameter c. The stress near the boundary decreases its magnitude in tension and increases its magnitude in compression as the ratio c/a decreases, thus it is more difficult to nucleate or propagate the crack.

If β is negative, the preceding conclusions would be changed into the opposite situations.

The normal stress σ_{33} and the shear stresses σ_{13} and σ_{23} are of course zero on the free surface. The shear stress components σ_{12}, σ_{23}, and σ_{13} in the solid are small compared to the normal stress components σ_{11}, σ_{22} and σ_{33}. It can be understood since the dilatation effect (thermal) generates normal strain only. Physically, the displacement and force inside and outside the inclusion are continuous at the boundary, and these are checked by both numerical and analytic results. The normal stress distributions on the plane $y = 0$ have been calculated and the results are as follows. σ_{11} and σ_{33} have large stress gradients at the corners $x_1 = a$, $x_3 = 0$, and $x_1 = a$, $x_3 = c$. There is a maximum value along the boundary $x_3 = c$ for σ_{11} and σ_{22} and along the boundary $x_1 = a$ for σ_{33}. It is obvious that all stress components decrease to zero at positions far away from the inclusion. The solution is valid for a parallelepiped inclusion that is close to the free surface or inside the solid. For the case of the inclusion inside the solid, the distance between the center of the inclusion and the free surface is $d + c/2$ and the variable x_3 in equations (8) and (9) are replaced by $x_3 - d$ and $x_3 + d$ respectively. The formulas for displacement, dilatation, and stress are unchanged. The stress components σ_{11} and σ_{33} along the centroid are calculated and the results are the same as that of Chiu's [7].

Downloaded 02 May 2010 to 171.66.16.54. Redistribution subject to ASME license or copyright; see http://www.asme.org/terms/Terms_Use.cfm

Acknowledgment

The authors would like to thank Professor J. C. M. Li for valuable discussions. They also thank Mr. F. T. Lin for checking some numerical results.

References

1 Eshelby, J. D., *Progress in Solid Mechanics*, North Holland, Amsterdam, Vol. 2, 1961, p. 89.

2 Eshelby, J. D., "The Determination of the Elastic Field of an Ellipsoidal Inclusion, and Related Problems," *Proc. Roy. Soc.*, Series A, Vol. 241, 1957, pp. 376-396.

3 Chiu, Y. P., "On The Stress Field Due to Initial Strains in a Cuboid Surrounded by an Infinite Elastic Space," ASME JOURNAL OF APPLIED MECHANICS, Vol. 44, 1977, pp. 587-590.

4 Mindlin, R. D., "Force at a Point in the Interior of a Semi-Infinite Solid," *Physics*, Vol. 7, 1936, pp. 195-202.

5 Mindlin, R. D., and Cheng, D. H., "Thermoelastic Stress in the Semi-Infinite Solid," *Journal of Applied Physics*, Vol. 21, 1950, pp. 931-933.

6 Seo, K., and Mura, T., "The Elastic Field in a Half Space Due to Ellipsoidal Inclusions With Uniform Dilatational Eigenstrains," ASME JOURNAL OF APPLIED MECHANICS, Vol. 46, 1979, pp. 568-572.

7 Chiu, Y. P., "On the Stress Field and Surface Deformation in a Half Space With a Cuboidal Zone in Which Initial Strains are Uniform," ASME JOURNAL OF APPLIED MECHANICS, Vol. 45, 1978, pp. 302-306.

Design of an Adhesive Lap Joint

P. Czarnocki[1] and K. Piekarski[1]

One of the problems facing engineers in the aircraft industry is the task of the reduction of the total weight of an aircraft and thus, the increase of its pay load.

The efficiency of the adhesive joint can be measured by the ratio of its load capacity to the joint's surface area. Increase in this ratio reduces the weight of the joint and thus the total weight of the structure. An example of a joint to be considered is shown in Fig. 1.

Previous investigators [1, 2], showed that the shear stress is distributed uniformly across the thickness of the adhesive at approximately 92 percent of the length of the joint. The sharp changes occur only at the end zone, for approximately 3 percent of the joint length. Therefore, for the calculation of the load capacity, for the whole joint, the shear stress can be considered as being approximately constant across the thickness of the adhesive [1] and the shear strain in it can be expressed by the relative displacements of the corresponding points of the lap's and plate's surfaces. Therefore, shear stresses τ_{xz} and τ_{yz} in the adhesive layer can be calculated according to the following formulas:

$$\tau_{xzj} = \frac{G}{h}\,(U_j^L - U_j^M)$$

$$\tau_{yzj} = \frac{G}{h}\,(V_j^L - V_j^M) \qquad (1)$$

where U_j^M U_j^M V_j^M V_j^L total displacements of the corresponding points of the membrane and the lap in x and y directions, respectively, G = shear modulus of the adhesive, and h = thickness of the adhesive layer.

These displacements, for the membrane, were obtained by an analytical method using Airy's Stress Functions. The functions for semi-infinite membrane were the combination of the known solution for an infinite membrane loaded at its interior point by a unit force and additional expressions that

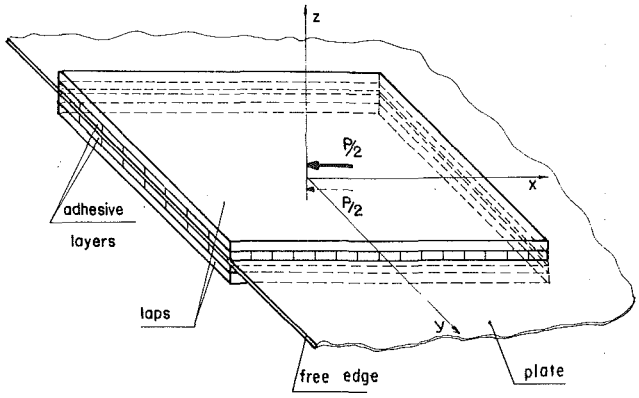


Fig. 1 Adhesive joint in which the load *P* is applied to the laps and transferred through the layers to the semi-infinite plate

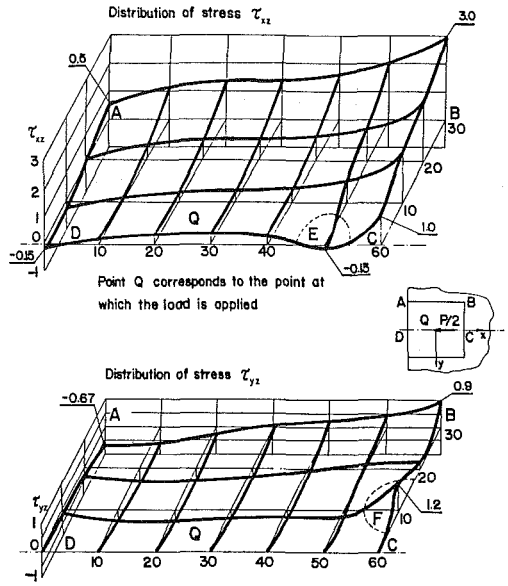


Fig. 2 Distribution of the relative shear stress in the adhesive layer

were derived in such a way that they satisifed the boundary conditions for the semi-infinite membrane. Values of the displacements, for the plane stress-state were calculated by integration of the stress-strain relationships:

$$u(^Px) = \frac{1}{E}\left[\int \frac{\partial^2\phi(^Px)}{\partial y^2}\,dx - \nu\frac{\partial\phi(^Px)}{\partial x}\right] + C_1$$

$$v(^Px) = \frac{1}{E}\left[\int \frac{\partial^2\phi(^Px)}{\partial x^2}\,dy - \nu\frac{\partial\phi(^Px)}{\partial y}\right] + C_2$$

$$u(^Py) = \frac{1}{E}\left[\int \frac{\partial^2\phi(^Py)}{\partial y^2}\,dx - \nu\frac{\partial\phi(^Py)}{\partial x}\right] + C_3$$

$$v(^Py) = \frac{1}{E}\left[\int \frac{\partial^2\phi(^Py)}{\partial x^2}\,dy - \nu\frac{\partial\phi(^Py)}{\partial y}\right] + C_4 \qquad (2)$$

where $\phi(P_x)$, $\phi(P_y)$ = Airy's Stress Functions for the force P_x (perpendicular to the free edge) and P_y (parallel to the free edge), $u(P_x)$, $u(P_y)$ = displacement in the x direction (perpendicular to the free edge) caused by forces P_x and P_y respectively; $v(P_x)$, $v(P_y)$ = displacement in the y direction (parallel to the free edge) caused by forces P_x and P_y, respectively; E = Young modulus; and ν = Poisson's ratio. Displacements in the lap were calculated by the finite element method.

[1] PhD. Student and Professor, respectively, Department of Mechanical Engineering, University of Waterloo, Waterloo, Ontario Canada.

Manuscript received by ASME Applied Mechanics Division, October, 1983; final revision, June, 1984.

Downloaded 02 May 2010 to 171.66.16.54. Redistribution subject to ASME license or copyright; see http://www.asme.org/terms/Terms_Use.cfm

Acknowledgment

The authors would like to thank Professor J. C. M. Li for valuable discussions. They also thank Mr. F. T. Lin for checking some numerical results.

References

1 Eshelby, J. D., *Progress in Solid Mechanics*, North Holland, Amsterdam, Vol. 2, 1961, p. 89.

2 Eshelby, J. D., "The Determination of the Elastic Field of an Ellipsoidal Inclusion, and Related Problems," *Proc. Roy. Soc.*, Series A, Vol. 241, 1957, pp. 376-396.

3 Chiu, Y. P., "On The Stress Field Due to Initial Strains in a Cuboid Surrounded by an Infinite Elastic Space," ASME JOURNAL OF APPLIED MECHANICS, Vol. 44, 1977, pp. 587-590.

4 Mindlin, R. D., "Force at a Point in the Interior of a Semi-Infinite Solid," *Physics*, Vol. 7, 1936, pp. 195-202.

5 Mindlin, R. D., and Cheng, D. H., "Thermoelastic Stress in the Semi-Infinite Solid," *Journal of Applied Physics*, Vol. 21, 1950, pp. 931-933.

6 Seo, K., and Mura, T., "The Elastic Field in a Half Space Due to Ellipsoidal Inclusions With Uniform Dilatational Eigenstrains," ASME JOURNAL OF APPLIED MECHANICS, Vol. 46, 1979, pp. 568-572.

7 Chiu, Y. P., "On the Stress Field and Surface Deformation in a Half Space With a Cuboidal Zone in Which Initial Strains are Uniform," ASME JOURNAL OF APPLIED MECHANICS, Vol. 45, 1978, pp. 302-306.

Design of an Adhesive Lap Joint

P. Czarnocki[1] and K. Piekarski[1]

One of the problems facing engineers in the aircraft industry is the task of the reduction of the total weight of an aircraft and thus, the increase of its pay load.

The efficiency of the adhesive joint can be measured by the ratio of its load capacity to the joint's surface area. Increase in this ratio reduces the weight of the joint and thus the total weight of the structure. An example of a joint to be considered is shown in Fig. 1.

Previous investigators [1, 2], showed that the shear stress is distributed uniformly across the thickness of the adhesive at approximately 92 percent of the length of the joint. The sharp changes occur only at the end zone, for approximately 3 percent of the joint length. Therefore, for the calculation of the load capacity, for the whole joint, the shear stress can be considered as being approximately constant across the thickness of the adhesive [1] and the shear strain in it can be expressed by the relative displacements of the corresponding points of the lap's and plate's surfaces. Therefore, shear stresses τ_{xz} and τ_{yz} in the adhesive layer can be calculated according to the following formulas:

$$\tau_{xzj} = \frac{G}{h}\,(U_j^L - U_j^M)$$

$$\tau_{yzj} = \frac{G}{h}\,(V_j^L - V_j^M) \qquad (1)$$

where U_j^M U_j^M V_j^M V_j^L total displacements of the corresponding points of the membrane and the lap in x and y directions, respectively, G = shear modulus of the adhesive, and h = thickness of the adhesive layer.

These displacements, for the membrane, were obtained by an analytical method using Airy's Stress Functions. The functions for semi-infinite membrane were the combination of the known solution for an infinite membrane loaded at its interior point by a unit force and additional expressions that

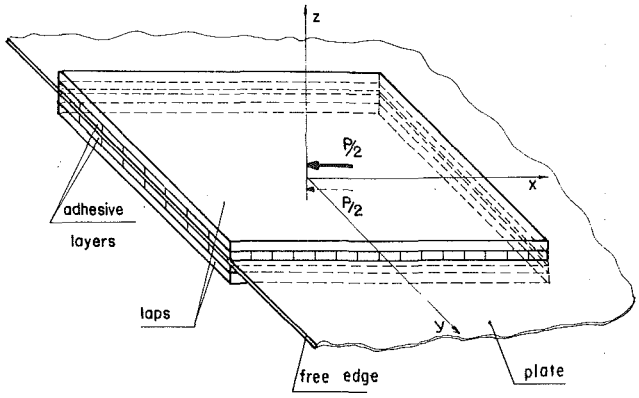


Fig. 1 Adhesive joint in which the load P is applied to the laps and transferred through the layers to the semi-infinite plate

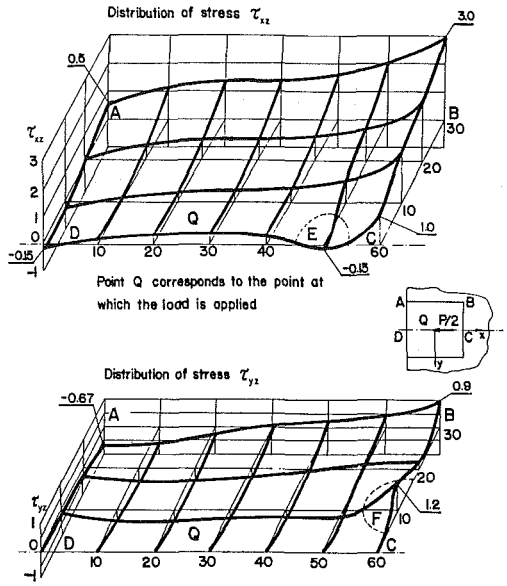


Fig. 2 Distribution of the relative shear stress in the adhesive layer

were derived in such a way that they satisifed the boundary conditions for the semi-infinite membrane. Values of the displacements, for the plane stress-state were calculated by integration of the stress-strain relationships:

$$u(^Px) = \frac{1}{E}\left[\int \frac{\partial^2\phi(^Px)}{\partial y^2}\,dx - \nu\frac{\partial\phi(^Px)}{\partial x}\right] + C_1$$

$$v(^Px) = \frac{1}{E}\left[\int \frac{\partial^2\phi(^Px)}{\partial x^2}\,dy - \nu\frac{\partial\phi(^Px)}{\partial y}\right] + C_2$$

$$u(^Py) = \frac{1}{E}\left[\int \frac{\partial^2\phi(^Py)}{\partial y^2}\,dx - \nu\frac{\partial\phi(^Py)}{\partial x}\right] + C_3$$

$$v(^Py) = \frac{1}{E}\left[\int \frac{\partial^2\phi(^Py)}{\partial x^2}\,dy - \nu\frac{\partial\phi(^Py)}{\partial y}\right] + C_4 \qquad (2)$$

where $\phi(P_x)$, $\phi(P_y)$ = Airy's Stress Functions for the force P_x (perpendicular to the free edge) and P_y (parallel to the free edge), $u(P_x)$, $u(P_y)$ = displacement in the x direction (perpendicular to the free edge) caused by forces P_x and P_y respectively; $v(P_x)$, $v(P_y)$ = displacement in the y direction (parallel to the free edge) caused by forces P_x and P_y, respectively; E = Young modulus; and ν = Poisson's ratio. Displacements in the lap were calculated by the finite element method.

[1] PhD. Student and Professor, respectively, Department of Mechanical Engineering, University of Waterloo, Waterloo, Ontario Canada.

Manuscript received by ASME Applied Mechanics Division, October, 1983; final revision, June, 1984.

Copyright © 1985 by ASME
Downloaded 02 May 2010 to 171.66.16.54. Redistribution subject to ASME license or copyright; see http://www.asme.org/terms/Terms_Use.cfm

Results

The preceding method was used for the determination of shear stresses τ_{xz} and τ_{yz} in the adhesive for the joint shown in Fig. 1. The obtained solution (Fig. 2) shows that:

1. Distribution of shear stresses τ_{xz} and τ_{yz} is not uniform.
2. Resultant shear stress (i.e., sum of shear stresses τ_{xz} and τ_{yz}) is noticeably higher than the shear stress τ_{xz}.
3. The highest values of shear stress τ_{xz} occur at the corners of the joint (corners B and C) and along the edges AB, BC (see Fig. 2).
4. Shear stress τ_{xz} reverses its sign close to the free edge of the membrane (region AD) and between the point at which the load is applied and the edge BC in the region of point E.
5. Shear stress, τ_{yz}, caused by the different flexibility of the adherends, changes its sign also. The maximum value of the stress occurs at the inner part of the joint in the region of point F.

Conclusions

1. Shear stress τ_{yz} has a significant effect on the strength of the joint.
2. Shear stress τ_{yz} and τ_{xz} produce lateral normal stresses.
3. To improve the distribution of stress, τ_{xz}, the shape of the lap should be changed. The lap should be shorter in the direction of the applied load and longer in the transverse direction. The corners at which the peaks of the shear stress occur should be rounded, thus the shape of the lap would tend to resemble an ellipse.

References

1 Ishai, O., and Gali, S., "Two-Dimensional Interlaminar Stress Distribution Within the Adhesive Layer of a Symmetrical Doubler Model," *Journal of Adhesion*, Vol. 8, 1977, pp. 301–312.

2 Pirvice, J., "Two Dimensional Displacement-Stress Distribution in Adhesive Bonded Composite Structures," *Journal of Adhesion*, Vol. 6, 1979, pp. 207–228.

Stability of Short Columns Subjected to Distributed Axial Loads

B. P. Shastry[1] and G. Venkateswara Rao[1]

Introduction

Stability of columns of various geometries subjected to a variety of loadings are discussed in reference [1]. The secondary effects like shear deformation play an important role when the columns are short. In reference [1] this effect is considered in studying the stability behavior of Euler columns subjected to a concentrated axial load. In references [2] and [3] the effect of shear deformation on the stability of Beck's and Leipholz's columns are discussed. However, the stability of short columns subjected to more complex loadings, like a uniformly distributed axial load or a linearly varying axial load, has not received much attention in the literature. Such loadings are of common occurrence for structural members subjected to constant or varying acceleration fields, as in the case a rocket in flight or a structural member in a centrifuge, respectively. The aim of this Note is to present critical loads of columns of various slenderness ratios with various end conditions subjected to (*i*) a uniformly distributed axial load and (*ii*) a linearly varying axial load. The versatile finite element method [4] is used for the analysis.

[1] Scientist/Engineer, Aerospace Structures Division, Vikram Sarabhai Space Centre, Trivandrum-695 022, India.

Manuscript received by ASME Applied Mechanics Division, October, 1983; final revision, August, 1984.

Finite Element Formulation

The strain energy U, of an element of length 1 is given by [5]

$$U=\frac{1}{2}\int_0^1 [EI\psi_x^2+k\{EA/2(1+\nu)\}\gamma^2]dx \tag{1}$$

where k is the shear coefficient (in the present study k is taken as 5/6), E is Young's modulus, I is the moment of inertia, A is the area of the cross section, ν is Poisson's ratio (taken as 0.3), ψ_x is the curvature, δ is the shear rotation, and x is the axial coordinate.

The work done, W, by the external axial compressive load is given by

$$W=\frac{1}{2}\int_0^1 Q(x)\left(\frac{dw}{dx}\right)^2 dx \tag{2}$$

where $Q(x)$ is the axial load distribution in an element and w is the lateral displacement.

The element matrices are derived employing cubic displacement distributions for w and γ over an element from U and W.

Following the standard procedure [4] of stability problems, the governing matrix equation

$$[K]\{\delta\}-\lambda[G]\{\delta\}=0 \tag{3}$$

is solved to obtain λ, where $[K]$ is the assembled stiffness matrix, $[G]$ is the assembled geometric stiffness matrix, λ is the eigenvalue, and $\{\delta\}$ is the eigenvector.

Numerical Results

The critical loads of columns of various L/r ratios (where L is the length of the column and r is the radius of gyration), ranging from 10 to 500, are obtained for various boundary conditions subjected to (*i*) a uniformly distributed axial load and (*ii*) a linearly varying axial load. The number of elements (of equal length) employed in idealizing the column are different for different types of boundary conditions to obtain convergence of λ.

Tables 1 and 2 give the stability load parameters for columns in the presence of shear deformation ($\lambda=qL^3/EI$ where q is the intensity of axial loading per unit length) covering L/r ratios from 10 to 500 for the two types of loading considered with different end conditions. The results of reference [1] for slender cantilever columns agree very well with the present results for $L/r = 500$. In these tables the results obtained from two finite element idealizations to yield less than 1 percent error in successive idealizaitons are given and the idealizations are not common for all the boundary conditions considered. Also, it can be seen from these tables that convergence for simply supported and cantilever columns is very good even for $L/r = 10$ and the convergence is rather slow for other boundary conditions, especially for a clamped column with $L/r = 10$. Convergence is also slow when the clamped end is on the higher, loaded side.

References

1 Timoshenko, S. P., and Gere, J. M., *Theory of Elastic Stability*, McGraw-Hill, New York, 1961.

2 Sundararamaiah, V., and Venkateswara Rao, G., "Effect of Shear Deformation and Rotary Inertia on the Stability of Beck's and Leipholz's Columns," *AIAA Journal*, Vol. 18, 1980, pp. 124–125.

3 Sundararamaiah, V., and Venkateswara Rao, G., Stability of Short Beck and Leipholz Columns on Elastic Foundation," *AIAA Journal*, Vol. 21, 1983, pp. 1053–1055.

4 Zienkiewiez, O. C., *Finite Element Method in Engineering Science*, McGraw-Hill, New York, 1971.

5 Venkateswara Rao, G., Raju, I. S., and Kanaka Raju, K., "Nonlinear Vibration of Beams Considering Shear Deformation and Rotary Inertia," *AIAA Journal*, Vol. 14, 1976, pp. 685–687.

Downloaded 02 May 2010 to 171.66.16.54. Redistribution subject to ASME license or copyright; see http://www.asme.org/terms/Terms_Use.cfm

Results

The preceding method was used for the determination of shear stresses τ_{xz} and τ_{yz} in the adhesive for the joint shown in Fig. 1. The obtained solution (Fig. 2) shows that:

1. Distribution of shear stresses τ_{xz} and τ_{yz} is not uniform.
2. Resultant shear stress (i.e., sum of shear stresses τ_{xz} and τ_{yz}) is noticeably higher than the shear stress τ_{xz}.
3. The highest values of shear stress τ_{xz} occur at the corners of the joint (corners B and C) and along the edges AB, BC (see Fig. 2).
4. Shear stress τ_{xz} reverses its sign close to the free edge of the membrane (region AD) and between the point at which the load is applied and the edge BC in the region of point E.
5. Shear stress, τ_{yz}, caused by the different flexibility of the adherends, changes its sign also. The maximum value of the stress occurs at the inner part of the joint in the region of point F.

Conclusions

1. Shear stress τ_{yz} has a significant effect on the strength of the joint.
2. Shear stress τ_{yz} and τ_{xz} produce lateral normal stresses.
3. To improve the distribution of stress, τ_{xz}, the shape of the lap should be changed. The lap should be shorter in the direction of the applied load and longer in the transverse direction. The corners at which the peaks of the shear stress occur should be rounded, thus the shape of the lap would tend to resemble an ellipse.

References

1 Ishai, O., and Gali, S., "Two-Dimensional Interlaminar Stress Distribution Within the Adhesive Layer of a Symmetrical Doubler Model," *Journal of Adhesion*, Vol. 8, 1977, pp. 301–312.

2 Pirvice, J., "Two Dimensional Displacement-Stress Distribution in Adhesive Bonded Composite Structures," *Journal of Adhesion*, Vol. 6, 1979, pp. 207–228.

Stability of Short Columns Subjected to Distributed Axial Loads

B. P. Shastry[1] and G. Venkateswara Rao[1]

Introduction

Stability of columns of various geometries subjected to a variety of loadings are discussed in reference [1]. The secondary effects like shear deformation play an important role when the columns are short. In reference [1] this effect is considered in studying the stability behavior of Euler columns subjected to a concentrated axial load. In references [2] and [3] the effect of shear deformation on the stability of Beck's and Leipholz's columns are discussed. However, the stability of short columns subjected to more complex loadings, like a uniformly distributed axial load or a linearly varying axial load, has not received much attention in the literature. Such loadings are of common occurrence for structural members subjected to constant or varying acceleration fields, as in the case a rocket in flight or a structural member in a centrifuge, respectively. The aim of this Note is to present critical loads of columns of various slenderness ratios with various end conditions subjected to (*i*) a uniformly distributed axial load and (*ii*) a linearly varying axial load. The versatile finite element method [4] is used for the analysis.

[1] Scientist/Engineer, Aerospace Structures Division, Vikram Sarabhai Space Centre, Trivandrum-695 022, India.

Manuscript received by ASME Applied Mechanics Division, October, 1983; final revision, August, 1984.

Finite Element Formulation

The strain energy U, of an element of length 1 is given by [5]

$$U=\frac{1}{2}\int_0^1 [EI\psi_x^2+k\{EA/2(1+\nu)\}\gamma^2]dx \tag{1}$$

where k is the shear coefficient (in the present study k is taken as 5/6), E is Young's modulus, I is the moment of inertia, A is the area of the cross section, ν is Poisson's ratio (taken as 0.3), ψ_x is the curvature, δ is the shear rotation, and x is the axial coordinate.

The work done, W, by the external axial compressive load is given by

$$W=\frac{1}{2}\int_0^1 Q(x)\left(\frac{dw}{dx}\right)^2 dx \tag{2}$$

where $Q(x)$ is the axial load distribution in an element and w is the lateral displacement.

The element matrices are derived employing cubic displacement distributions for w and γ over an element from U and W.

Following the standard procedure [4] of stability problems, the governing matrix equation

$$[K]\{\delta\}-\lambda[G]\{\delta\}=0 \tag{3}$$

is solved to obtain λ, where $[K]$ is the assembled stiffness matrix, $[G]$ is the assembled geometric stiffness matrix, λ is the eigenvalue, and $\{\delta\}$ is the eigenvector.

Numerical Results

The critical loads of columns of various L/r ratios (where L is the length of the column and r is the radius of gyration), ranging from 10 to 500, are obtained for various boundary conditions subjected to (*i*) a uniformly distributed axial load and (*ii*) a linearly varying axial load. The number of elements (of equal length) employed in idealizing the column are different for different types of boundary conditions to obtain convergence of λ.

Tables 1 and 2 give the stability load parameters for columns in the presence of shear deformation ($\lambda=qL^3/EI$ where q is the intensity of axial loading per unit length) covering L/r ratios from 10 to 500 for the two types of loading considered with different end conditions. The results of reference [1] for slender cantilever columns agree very well with the present results for $L/r = 500$. In these tables the results obtained from two finite element idealizations to yield less than 1 percent error in successive idealizaitons are given and the idealizations are not common for all the boundary conditions considered. Also, it can be seen from these tables that convergence for simply supported and cantilever columns is very good even for $L/r = 10$ and the convergence is rather slow for other boundary conditions, especially for a clamped column with $L/r = 10$. Convergence is also slow when the clamped end is on the higher, loaded side.

References

1 Timoshenko, S. P., and Gere, J. M., *Theory of Elastic Stability*, McGraw-Hill, New York, 1961.

2 Sundararamaiah, V., and Venkateswara Rao, G., "Effect of Shear Deformation and Rotary Inertia on the Stability of Beck's and Leipholz's Columns," *AIAA Journal*, Vol. 18, 1980, pp. 124–125.

3 Sundararamaiah, V., and Venkateswara Rao, G., Stability of Short Beck and Leipholz Columns on Elastic Foundation," *AIAA Journal*, Vol. 21, 1983, pp. 1053–1055.

4 Zienkiewiez, O. C., *Finite Element Method in Engineering Science*, McGraw-Hill, New York, 1971.

5 Venkateswara Rao, G., Raju, I. S., and Kanaka Raju, K., "Nonlinear Vibration of Beams Considering Shear Deformation and Rotary Inertia," *AIAA Journal*, Vol. 14, 1976, pp. 685–687.

Copyright © 1985 by ASME
Downloaded 02 May 2010 to 171.66.16.54. Redistribution subject to ASME license or copyright; see http://www.asme.org/terms/Terms_Use.cfm

Table 1 Stability parameter λ for short column subjected to uniformly distributed axial load

BOUNDARY CONDITIONS	L/r					SLENDER COLUMN REF(1)
	10	25	50	100	500	
	13·34 (8)+ 13·34 (12)	17·59 17·53	18·39 18·32	18·61 18·53	18·68 18·60	—
	7·017(8) 7·010(12)	7·711 7·700	7·819 7·807	7·847 7·834	7·857 7·843	7·84
	17·22(8) 17·20 (12)	27·07 26·93	29·41 29·24	30·07 29·88	30·29 30·09	—
	25·97 (12) 25·85 (16)	45·92 45·78	50·91 50·76	52·31 52·15	52·77 52·60	—
	29·37(12) 29·12(16)	61·33 61·04	71·24 70·92	74·18 73·86	75·17 74·84	—

+ NUMBERS IN BRACKETS REPRESENT THE ELEMENTS EMPLOYED FOR FINITE ELEMENTS IDEALIZATION FOR THE VARIOUS L/r VALUES GIVEN IN THIS TABLE.

Table 2 Stability parameter λ for short columns subjected to linearly varying axial load

BOUNDARY CONDITIONS	L/r					SLENDER COLUMN REF·(1)
	10	25	50	100	500	
	31·95 (4) + 31·94 (8)	43·50 43·48	45·74 45·69	46·35 46·28	46·56 46·47	—
	26·86 (4) 26·86 (8)	31·27 31·26	31·97 31·96	32·16 32·14	32·21 32·20	32·2
	40·04 (8) 40·01 (12)	65·17 65·15	71·26 71·25	72·95 72·95	73·52 73·51	—
	64·66(8) 64·39(12)	133·4 133·4	151·3 151·2	156·3 156·2	158·0 157·9	—
	67·36(12) 66·79(16)	169·9 169·8	202·5 202·4	212·3 212·2	215·6 215·5	—

+ NUMBERS IN BRACKETS REPRESENT THE NUMBER OF ELEMENTS EMPLOYED FOR FINITE ELEMENT IDEALIZATION FOR THE VARIOUS L/r VALUES GIVEN IN THIS TABLE.

Response Cell Probabilities for Nonlinear Random Systems

T. T. Soong[1] and L. L. Chung[1]

Introduction

In a series of papers [1–3], Hsu has considered a cell state space concept for the study of global properties of deterministic dynamic systems. It is the purpose of this Note to show that this concept is directly adaptable to the study of a class of nonlinear random systems, i.e., nonlinear systems with random external excitations and/or random parametric variations. For this class of systems, the cell state space concept provides an efficient solution algorithm for generating their response probability densities by solving a system of *linear* deterministic differential equations. The dimension of this system of equations, however, is large but its solution is facilitated by the fact that its coefficient matrix is generally quite sparse.

The Random System

Consider random systems characterized by a system of random differential equations

$$\dot{\mathbf{X}}(t)=\mathbf{f}(\mathbf{X}(t),\mathbf{Y}(t),t), \quad \mathbf{X}(0)=\mathbf{X}_0 \tag{1}$$

where $\mathbf{X}(t)$ is the system state vector and $\mathbf{Y}(t)$ is a vector stochastic process whose component processes enter (1) either as inhomgeneous terms (external excitation) or as coefficient processes (parameters). For generality, the initial condition $\mathbf{X}_0$ is also considered a random vector with a prescribed distribution. In this Note, random quantities will be denoted by capital letters.

In our development, the random systems of interest are those where $\mathbf{Y}(t)$ can be modeled by a vector stochastic process with finite degrees of randomness, i.e., the randomness enters $\mathbf{Y}(t)$ through a finite dimensional random vector $\mathbf{A}$ in the form

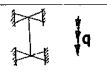
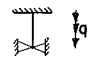
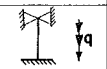
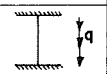
$$\mathbf{Y}(t)=\mathbf{Y}(\mathbf{A},t) \tag{2}$$

[1]Professor and Research Assistant, respectively, Department of Civil Engineering, State University of New York at Buffalo, Buffalo, New York 14260.

Manuscript received by ASME Applied Mechanics Division, June, 1984; final revision, September, 1984.

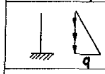
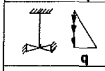
Downloaded 02 May 2010 to 171.66.16.54. Redistribution subject to ASME license or copyright; see http://www.asme.org/terms/Terms_Use.cfm

Table 1 Stability parameter λ for short column subjected to uniformly distributed axial load

BOUNDARY CONDITIONS	L/r					SLENDER COLUMN REF(1)
	10	25	50	100	500	
	13·34 (8)+ 13·34 (12)	17·59 17·53	18·39 18·32	18·61 18·53	18·68 18·60	—
	7·017(8) 7·010(12)	7·711 7·700	7·819 7·807	7·847 7·834	7·857 7·843	7·84
	17·22(8) 17·20 (12)	27·07 26·93	29·41 29·24	30·07 29·88	30·29 30·09	—
	25·97 (12) 25·85 (16)	45·92 45·78	50·91 50·76	52·31 52·15	52·77 52·60	—
	29·37(12) 29·12(16)	61·33 61·04	71·24 70·92	74·18 73·86	75·17 74·84	—

+ NUMBERS IN BRACKETS REPRESENT THE ELEMENTS EMPLOYED FOR FINITE ELEMENTS IDEALIZATION FOR THE VARIOUS L/r VALUES GIVEN IN THIS TABLE.

Table 2 Stability parameter λ for short columns subjected to linearly varying axial load

BOUNDARY CONDITIONS	L/r					SLENDER COLUMN REF·(1)
	10	25	50	100	500	
	31·95 (4) + 31·94 (8)	43·50 43·48	45·74 45·69	46·35 46·28	46·56 46·47	—
	26·86 (4) 26·86 (8)	31·27 31·26	31·97 31·96	32·16 32·14	32·21 32·20	32·2
	40·04 (8) 40·01 (12)	65·17 65·15	71·26 71·25	72·95 72·95	73·52 73·51	—
	64·66(8) 64·39(12)	133·4 133·4	151·3 151·2	156·3 156·2	158·0 157·9	—
	67·36(12) 66·79(16)	169·9 169·8	202·5 202·4	212·3 212·2	215·6 215·5	—

+ NUMBERS IN BRACKETS REPRESENT THE NUMBER OF ELEMENTS EMPLOYED FOR FINITE ELEMENT IDEALIZATION FOR THE VARIOUS L/r VALUES GIVEN IN THIS TABLE.

Response Cell Probabilities for Nonlinear Random Systems

T. T. Soong[1] and L. L. Chung[1]

Introduction

In a series of papers [1–3], Hsu has considered a cell state space concept for the study of global properties of deterministic dynamic systems. It is the purpose of this Note to show that this concept is directly adaptable to the study of a class of nonlinear random systems, i.e., nonlinear systems with random external excitations and/or random parametric variations. For this class of systems, the cell state space concept provides an efficient solution algorithm for generating their response probability densities by solving a system of *linear* deterministic differential equations. The dimension of this system of equations, however, is large but its solution is facilitated by the fact that its coefficient matrix is generally quite sparse.

The Random System

Consider random systems characterized by a system of random differential equations

$$\dot{\mathbf{X}}(t)=\mathbf{f}(\mathbf{X}(t),\mathbf{Y}(t),t),\quad \mathbf{X}(0)=\mathbf{X}_0 \tag{1}$$

where $\mathbf{X}(t)$ is the system state vector and $\mathbf{Y}(t)$ is a vector stochastic process whose component processes enter (1) either as inhomgeneous terms (external excitation) or as coefficient processes (parameters). For generality, the initial condition $\mathbf{X}_0$ is also considered a random vector with a prescribed distribution. In this Note, random quantities will be denoted by capital letters.

In our development, the random systems of interest are those where $\mathbf{Y}(t)$ can be modeled by a vector stochastic process with finite degrees of randomness, i.e., the randomness enters $\mathbf{Y}(t)$ through a finite dimensional random vector $\mathbf{A}$ in the form

$$\mathbf{Y}(t)=\mathbf{Y}(\mathbf{A},t) \tag{2}$$

[1]Professor and Research Assistant, respectively, Department of Civil Engineering, State University of New York at Buffalo, Buffalo, New York 14260.

Manuscript received by ASME Applied Mechanics Division, June, 1984; final revision, September, 1984.

Copyright © 1985 by ASME
Downloaded 02 May 2010 to 171.66.16.54. Redistribution subject to ASME license or copyright; see http://www.asme.org/terms/Terms_Use.cfm

With $\mathbf{Y}(t)$ given by equation (2), equation (1) can be written as

$$\dot{\mathbf{X}}(t) = \mathbf{g}(\mathbf{X}(t), \mathbf{A}, t), \quad \mathbf{X}(0) = \mathbf{X}_0 \tag{3}$$

The representation given by (2) is widely used to simulate both stationary and nonstationary processes. For example, consider a stationary stochastic process $Y(t)$ with mean zero and power spectral density $S_Y(\omega)$ specified in the region $|\omega| \leq \omega_u < \infty$. Defining $\Delta\omega = \omega_u/n$, the process $Y(t)$ can be simulated by [4]

$$Y(t) = \sum_{i=1}^{n} (2S_Y(\omega_i)\Delta\omega)^{1/2} \cos(\omega_i t + \Phi_i) \tag{4}$$

where Φ_i are independent random phase angles uniformly distributed between 0 and 2π and $\omega_i = (i - \frac{1}{2})\Delta\omega$. Equation (4) has also been used to simulate nonstationary processes by replacing $S_Y(\omega_i)$ in (4) by $S_Y(t, \omega_i)$, the evolutionary power spectral density of a nonstationary process.

It should be mentioned that there are physical problems in which the components of $\mathbf{Y}(t)$ are simply random constants themselves, i.e.,

$$\mathbf{Y}(t) = \mathbf{A} \tag{5}$$

Cell State Space Approach

Our basic interest is to obtain the joint probability density of the response $\mathbf{X}(t)$ at any t when $\mathbf{X}(t)$ is governed by (3). Following Hsu, an n-vector state space represented by $\mathbf{X}(t)$ is partitioned into a collection of n-dimensional cells, in each of which a certain amount of probability lies. The evolution of probability distribution of $\mathbf{X}(t)$ can then be determined by examining the flow of probabilities between cells as a function of time.

The basic ideas in treating a random system described by (3) are given in the following for a one-dimensional system. The procedure developed by Hsu for multidimensional systems is equally applicable here in the multidimensional random system case.

Consider a scalar differential equation of the form

$$\dot{X} = g(X, \mathbf{A}, t), \quad X(0) = X_0 \tag{6}$$

where the random vector $\mathbf{A}$ is characterized by its joint probability density $f_{\mathbf{A}}(\mathbf{a})$. If X_0 is also random, it is assumed that X_0 is specified by its density function $f_{X_0}(x_0)$ and it is independent of $\mathbf{A}$.

Let us partition the range space of $X(t)$ into sufficiently small cells $z_1, z_2, \ldots, z_m$. A cell z_i is defined to be one that contains all values of X satisfying $x_i^- \leq X < x_i^+$ with

$$x_i^- = \left(z_i - \frac{1}{2}\right)h \quad \text{and} \quad x_i^+ = \left(z_i + \frac{1}{2}\right)h \tag{7}$$

where h is the cell size. The cells z_i and z_m are boundary cells and the rest are interior cells. Our aim is to determine $p(z_i, t)$, the probability of finding the system in cell z_i at time t for all $i = 1, \ldots, m$. The knowledge of $p(z_i, t)$, $i = 1, \ldots, m$, gives an approximation of the probability distribution of $X(t)$. An important property of this approximation is that its accuracy can be improved with a decrease in cell size, although it necessitates more computational labor.

The proposed procedure for finding $p(z_i, t)$ consists of the following two steps:

(*a*) Determine $p_{\mathbf{a}}(z_i, t)$, the probability $p(z_i, t)$ *conditional upon* $\mathbf{A} = \mathbf{a}$.

(*b*) Determine $p(z_i, t)$ by, using the total probability theorem, $p(z_i, t) = \int \ldots \int p_{\mathbf{a}}(z_i, t) f_{\mathbf{A}}(\mathbf{a}) d\mathbf{a}$ (8)

For step (*a*), it is recognized that, given that $\mathbf{A} = \mathbf{a}$ has been realized, the random system reduces to a deterministic system, and the cell state space formulation can be directly applied to establish the cell probability equations for $p_{\mathbf{a}}(z_i, t)$. Briefly, consider a typical cell z_i. If the cell size h is sufficiently small, $p_{\mathbf{a}}(z_i, t)$ can be considered uniformly distributed over $x_i^- \leq x < x_i^+$ at each t. Over an infinitesimal interval dt, it is seen from (6) that $p_{\mathbf{a}}(z_i, t)$ either increases, decreases, or remains unchanged according to the signs of $g(x, \mathbf{a}, t)$ at cell boundaries $x = x_i^-$ and $x = x_i^+$. We thus have

$$\dot{p}_{\mathbf{a}}(z_i, t) = \frac{1}{h}\left[g(x_i^-, \mathbf{a}, t)\,\xi - g(x_i^+, \mathbf{a}, t)\,\eta\right] \tag{9}$$

where, for interior cells ($i = 2, \ldots, m-1$),

$$\begin{aligned} \xi &= p_{\mathbf{a}}(z_i, t) && \text{if} \quad g(x_i^-, \mathbf{a}, t) < 0 \\ &= 0 && \text{if} \quad g(x_i^-, \mathbf{a}, t) = 0 \\ &= p_{\mathbf{a}}(z_{i-1}, t) && \text{if} \quad g(x_i^-, \mathbf{a}, t) > 0 \end{aligned} \tag{10}$$

and

$$\begin{aligned} \eta &= p_{\mathbf{a}}(z_{i+1}, t) && \text{if} \quad g(x_i^+, \mathbf{a}, t) < 0 \\ &= 0 && \text{if} \quad g(x_i^+, \mathbf{a}, t) = 0 \\ &= p_{\mathbf{a}}(z_i, t) && \text{if} \quad g(x_i^+, \mathbf{a}, t) > 0 \end{aligned} \tag{11}$$

For boundary cell z_1, equation (11) stays unaltered with $i = 1$ but (10) becomes $\xi \equiv 0$. Similarly, for boundary cell z_m, equation (10) stays unaltered with $i = m$ and (11) becomes $\eta \equiv 0$.

Let $\mathbf{p}_{\mathbf{a}}(\mathbf{z}, t)$ be a column m-vector with components $p_{\mathbf{a}}(z_i, t)$, $i = 1, \ldots, m$. Equation (9), together with (10) and (11), can be represented by a linear vector-matrix differential equation

$$\dot{\mathbf{p}}_{\mathbf{a}}(\mathbf{z}, t) = Q(t)\,\mathbf{p}_{\mathbf{a}}(\mathbf{z}, t) \tag{12}$$

with initial condition $\mathbf{p}_{\mathbf{a}}(\mathbf{z}, 0)$, whose ith element is determined from

$$p_{\mathbf{a}}(z_i, 0) = \int_{x_i^-}^{x_i^+} f_{X_0}(x_0) dx_0 \tag{13}$$

The "rate matrix" $Q(t)$ in (12) takes the form

$$Q(t) = \begin{bmatrix} x & x & 0 & 0 & 0 & \ldots & 0 \\ x & x & x & 0 & 0 & \ldots & 0 \\ 0 & x & x & x & 0 & \ldots & 0 \\ \cdot & & & & & & \cdot \\ \cdot & & & & & & \cdot \\ \cdot & & & & & & \cdot \\ 0 & \ldots & & x & x & x & 0 \\ 0 & \ldots & & 0 & x & x & x \\ 0 & \ldots & & 0 & 0 & x & x \end{bmatrix} \tag{14}$$

In the foregoing, the positions marked by x are the only possible nonzero elements of $Q(t)$. For a given $\mathbf{a}$, it is seen from (10) and (11) that $Q(t)$ is at most a function of t. Furthermore, $Q(t)$ has the following properties:

(*a*) Each row has at most two nonzero elements;

(*b*) Each column has at most three nonzero elements; and

(*c*) $Q(t)$ is an intensity matrix, that is, all off-diagonal elements are nonnegative, all diagonal elements are nonpositive, and each column has a zero sum.

In so far as the conditional probability vector $\mathbf{p}_{\mathbf{a}}(\mathbf{z}, t)$ is concerned, it is interesting to note that, while the dynamic system represented by (6) can be highly nonlinear, the cell probability equation (12) is *linear* and *homogeneous*. Even with large dimensions, the coefficient matrix $Q(t)$ is sparse and efficient solution algorithms can be constructed.

The important difference between the random system problem addressed here and the deterministic problem considered by Hsu is that, while (12) gives the desired cell probabilities for the deterministic problem, it only gives the *conditional* cell probabilities in the random case. Step (*b*) or the integral given by (8) must now be carried out and this requires that (12) be solved for as many values of $\mathbf{a}$ as necessary in order that (8) can be evaluated, resulting in the desired cell probabilities $p(z_i, t)$.

Downloaded 02 May 2010 to 171.66.16.54. Redistribution subject to ASME license or copyright; see http://www.asme.org/terms/Terms_Use.cfm

An Alternate Formulation

Another look at the additional computation required for the random system problem can be gleaned from a slightly different problem formulation.

Consider again equation (3). If we define

$$\mathbf{W}(t) = \begin{bmatrix} \mathbf{X}(t) \\ \mathbf{A} \end{bmatrix} \tag{15}$$

then $\mathbf{W}(t)$ satisfies

$$\dot{\mathbf{W}}(t) = \mathbf{h}(\mathbf{W}(t), t), \quad \mathbf{W}(t) = \mathbf{W}_0 \tag{16}$$

where

$$\mathbf{h} = \begin{bmatrix} \mathbf{f} \\ \mathbf{0} \end{bmatrix} \quad \text{and} \quad \mathbf{W}_0 = \begin{bmatrix} \mathbf{X}_0 \\ \mathbf{A} \end{bmatrix} \tag{17}$$

Now, let $\mathbf{W}(t)$ be the state vector of the augmented system. Equation (16) defines a deterministic system with only random initial conditions. The cell state space approach given by Hsu thus applies directly to the new system and cell probabilities for $\mathbf{W}(t)$ can be found. The effect of $\mathbf{A}$ on the solution algorithm is the addition of extra dimensions to the original system – one extra dimension for each random variable in $\mathbf{A}$.

Concluding Remarks

Great difficulties exist in analyzing response behavior of nonlinear random systems. It is shown that, for systems involving stochastic processes with finite degrees of randomness, the cell state space formulation leads to an efficient method of generating response probability distributions.

A distinctive advantage associated with the cell state space approach is that one deals only with a system of *linear* and *homogeneous* differential equations. While the dimension involved can be quite large, this linearity property, coupled with sparseness of the coefficient matrix, makes the technique more manageable than other methods of solutions such as Monte Carlo simulation, the Liouville equation approach [5], and other numerical techniques [6].

Acknowledgments

This work was supported in part by the National Science Foundation under Grant Nos. CEE-8010891 and CEE-8311879.

References

1 Hsu, C. S., "A Theory of Cell-to-Cell Mapping for Dynamical Systems," ASME JOURNAL OF APPLIED MECHANICS, Vol. 47, 1980, pp. 931–939.

2 Hsu, C. S., "A Generalized Theory of Cell-to-Cell Mapping for Nonlinear Dynamical Systems," ASME JOURNAL OF APPLIED MECHANICS, Vol. 48, 1981, pp. 634–642.

3 Hsu, C. S., "A Probabilistic Theory of Nonlinear Dynamical System Based on the Cell State Space Concept," ASME JOURNAL OF APPLIED MECHANICS, Vol. 49, 1982, pp. 895–902.

4 Shinozuka, M., and Jan, C. M., "Digital Simulation of Random Processes and Its Applications," *J. Sound Vibration*, Vol. 25, 1972, pp. 111–128.

5 Soong, T. T., and Chuang, S. N., "Solutions of a Class of Random Differential Equations," *SIAM J. Appl. Math.*, Vol. 24, 1973, pp. 449–459.

6 Bharucha-Reid, A. T., ed., *Approximate Solutions of Random Equations*, North Holland, Amsterdam, 1979.

Stability of Wide Strips Under Locally Distributed Forces

G. Baker[1] and M. N. Pavlović[2]

Introduction

Consider the problem shown in Fig. 1, which depicts a rectangular plate, simply supported throughout its edges, and subject to locally distributed forces along two opposite sides. The stability of the system was studied in a previous publication [1] for different values of the loaded-length ratio $\gamma\,(=l/b)$. Those results, however, referred primarily to values of the aspect ratio $\phi\,(=a/b)$ in excess of unity, corresponding to the range of geometries encompassing square to "long" plates.

The aim of the present Note is to complement the existing information for $\phi \gtrsim 1$ by studying the stability of "wide" plates, that is, of those elements for which the relative geometry lies in the range $0 \le \phi \le 1$. Representative values of the buckling stress are given throughout the whole of this range of ϕ's, and, in particular, it is shown that the asymptotic values for the critical patch loads acting on an infinitely wide strip ($\phi = 0$) take on a very simple form. In addition, attention is drawn to the existence of a finite range of plate geometries for which a somewhat abrupt drop in buckling load may take place.

Results and Discussion

The details of the analysis, which uses the exact distribution of in-plane stresses and a suitable infinite series for the transverse buckled shape, can be found in reference [1].

Figure 2 shows the variation of the buckling coefficient K_1 with γ for several representative values of ϕ for wide plates. K_1 is defined as

$$K_1 = k\gamma\phi \tag{1}$$

where k is the buckling coefficient associated with the load intensity N (force per unit length), and hence is given by the well-known expression [2, 3]:

$$k = \frac{Nb^2}{\pi^2 D} \tag{2}$$

in which D is the flexural rigidity of the plate. It is clear from Fig. 2 that, in general, K_1 decreases almost linearly with γ, since it tends to the asymptotic value γ/ϕ provided γ is not too small. The accuracy of this asymptotic approximation increases as the plate becomes wider: thus, as shown in Fig. 2, the difference between the actual values of K_1 and the straight lines γ/ϕ (shown dotted) decreases fairly rapidly as $\phi \to 0$.

The foregoing asymptotic approximation, however, no longer holds for small γ's. Instead, the K_1 values cluster together in the vicinity of $K_1 = 1.455$, which corresponds to the buckling coefficient of an infinitely wide plate ($\phi = 0$) under the action of a point load ($\gamma = 0$) [1]. What is the value of γ below which a patch load can be approximated to a point load? As shown in reference [1], any $\gamma < 0.1$ can be treated as a point load provided $\phi > 1$. On the other hand, when $\phi < 1$, the condition under which such an approximation is acceptable becomes more stringent as ϕ decreases [4]. For the problem under consideration, a rough rule of thumb can be obtained for small ϕ's (say $\phi < 0.05$) by using the point of intersection of the asymptote $K_1 = \gamma/\phi$ with the horizontal

[1]Department of Civil Engineering, Heriot-Watt University, Riccarton, Edinburgh, EH14 4AS, England.

[2]Department of Civil Engineering, Imperial College of Science and Technology, University of London, London, SW7 2BU, England.

Manuscript received by ASME Applied Mechanics Division, June, 1984; final revision, September, 1984.

Downloaded 02 May 2010 to 171.66.16.54. Redistribution subject to ASME license or copyright; see http://www.asme.org/terms/Terms_Use.cfm

An Alternate Formulation

Another look at the additional computation required for the random system problem can be gleaned from a slightly different problem formulation.

Consider again equation (3). If we define

$$\mathbf{W}(t) = \begin{bmatrix} \mathbf{X}(t) \\ \mathbf{A} \end{bmatrix} \tag{15}$$

then $\mathbf{W}(t)$ satisfies

$$\dot{\mathbf{W}}(t) = \mathbf{h}(\mathbf{W}(t), t), \quad \mathbf{W}(t) = \mathbf{W}_0 \tag{16}$$

where

$$\mathbf{h} = \begin{bmatrix} \mathbf{f} \\ \mathbf{0} \end{bmatrix} \quad \text{and} \quad \mathbf{W}_0 = \begin{bmatrix} \mathbf{X}_0 \\ \mathbf{A} \end{bmatrix} \tag{17}$$

Now, let $\mathbf{W}(t)$ be the state vector of the augmented system. Equation (16) defines a deterministic system with only random initial conditions. The cell state space approach given by Hsu thus applies directly to the new system and cell probabilities for $\mathbf{W}(t)$ can be found. The effect of $\mathbf{A}$ on the solution algorithm is the addition of extra dimensions to the original system – one extra dimension for each random variable in $\mathbf{A}$.

Concluding Remarks

Great difficulties exist in analyzing response behavior of nonlinear random systems. It is shown that, for systems involving stochastic processes with finite degrees of randomness, the cell state space formulation leads to an efficient method of generating response probability distributions.

A distinctive advantage associated with the cell state space approach is that one deals only with a system of *linear* and *homogeneous* differential equations. While the dimension involved can be quite large, this linearity property, coupled with sparseness of the coefficient matrix, makes the technique more manageable than other methods of solutions such as Monte Carlo simulation, the Liouville equation approach [5], and other numerical techniques [6].

Acknowledgments

This work was supported in part by the National Science Foundation under Grant Nos. CEE-8010891 and CEE-8311879.

References

1 Hsu, C. S., "A Theory of Cell-to-Cell Mapping for Dynamical Systems," ASME JOURNAL OF APPLIED MECHANICS, Vol. 47, 1980, pp. 931–939.

2 Hsu, C. S., "A Generalized Theory of Cell-to-Cell Mapping for Nonlinear Dynamical Systems," ASME JOURNAL OF APPLIED MECHANICS, Vol. 48, 1981, pp. 634–642.

3 Hsu, C. S., "A Probabilistic Theory of Nonlinear Dynamical System Based on the Cell State Space Concept," ASME JOURNAL OF APPLIED MECHANICS, Vol. 49, 1982, pp. 895–902.

4 Shinozuka, M., and Jan, C. M., "Digital Simulation of Random Processes and Its Applications," *J. Sound Vibration*, Vol. 25, 1972, pp. 111–128.

5 Soong, T. T., and Chuang, S. N., "Solutions of a Class of Random Differential Equations," *SIAM J. Appl. Math.*, Vol. 24, 1973, pp. 449–459.

6 Bharucha-Reid, A. T., ed., *Approximate Solutions of Random Equations*, North Holland, Amsterdam, 1979.

Stability of Wide Strips Under Locally Distributed Forces

G. Baker[1] and M. N. Pavlović[2]

Introduction

Consider the problem shown in Fig. 1, which depicts a rectangular plate, simply supported throughout its edges, and subject to locally distributed forces along two opposite sides. The stability of the system was studied in a previous publication [1] for different values of the loaded-length ratio $\gamma\,(=l/b)$. Those results, however, referred primarily to values of the aspect ratio $\phi\,(=a/b)$ in excess of unity, corresponding to the range of geometries encompassing square to "long" plates.

The aim of the present Note is to complement the existing information for $\phi \gtrsim 1$ by studying the stability of "wide" plates, that is, of those elements for which the relative geometry lies in the range $0 \le \phi \le 1$. Representative values of the buckling stress are given throughout the whole of this range of ϕ's, and, in particular, it is shown that the asymptotic values for the critical patch loads acting on an infinitely wide strip ($\phi = 0$) take on a very simple form. In addition, attention is drawn to the existence of a finite range of plate geometries for which a somewhat abrupt drop in buckling load may take place.

Results and Discussion

The details of the analysis, which uses the exact distribution of in-plane stresses and a suitable infinite series for the transverse buckled shape, can be found in reference [1].

Figure 2 shows the variation of the buckling coefficient K_1 with γ for several representative values of ϕ for wide plates. K_1 is defined as

$$K_1 = k\gamma\phi \tag{1}$$

where k is the buckling coefficient associated with the load intensity N (force per unit length), and hence is given by the well-known expression [2, 3]:

$$k = \frac{Nb^2}{\pi^2 D} \tag{2}$$

in which D is the flexural rigidity of the plate. It is clear from Fig. 2 that, in general, K_1 decreases almost linearly with γ, since it tends to the asymptotic value γ/ϕ provided γ is not too small. The accuracy of this asymptotic approximation increases as the plate becomes wider: thus, as shown in Fig. 2, the difference between the actual values of K_1 and the straight lines γ/ϕ (shown dotted) decreases fairly rapidly as $\phi \to 0$.

The foregoing asymptotic approximation, however, no longer holds for small γ's. Instead, the K_1 values cluster together in the vicinity of $K_1 = 1.455$, which corresponds to the buckling coefficient of an infinitely wide plate ($\phi = 0$) under the action of a point load ($\gamma = 0$) [1]. What is the value of γ below which a patch load can be approximated to a point load? As shown in reference [1], any $\gamma < 0.1$ can be treated as a point load provided $\phi > 1$. On the other hand, when $\phi < 1$, the condition under which such an approximation is acceptable becomes more stringent as ϕ decreases [4]. For the problem under consideration, a rough rule of thumb can be obtained for small ϕ's (say $\phi < 0.05$) by using the point of intersection of the asymptote $K_1 = \gamma/\phi$ with the horizontal

[1]Department of Civil Engineering, Heriot-Watt University, Riccarton, Edinburgh, EH14 4AS, England.

[2]Department of Civil Engineering, Imperial College of Science and Technology, University of London, London, SW7 2BU, England.

Manuscript received by ASME Applied Mechanics Division, June, 1984; final revision, September, 1984.

Copyright © 1985 by ASME
Downloaded 02 May 2010 to 171.66.16.54. Redistribution subject to ASME license or copyright; see http://www.asme.org/terms/Terms_Use.cfm

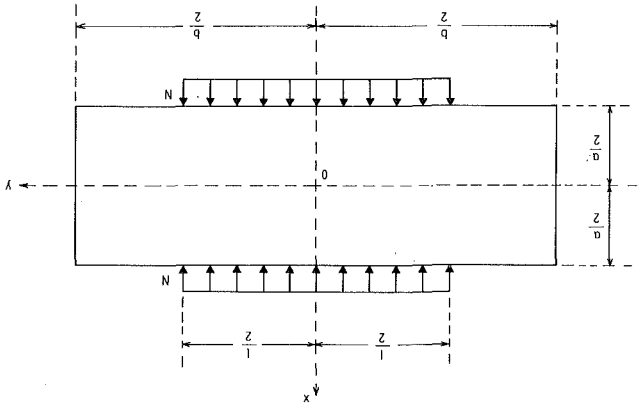


Fig. 1 Thin plate under the action of two equal and opposite, uniformly distributed loads

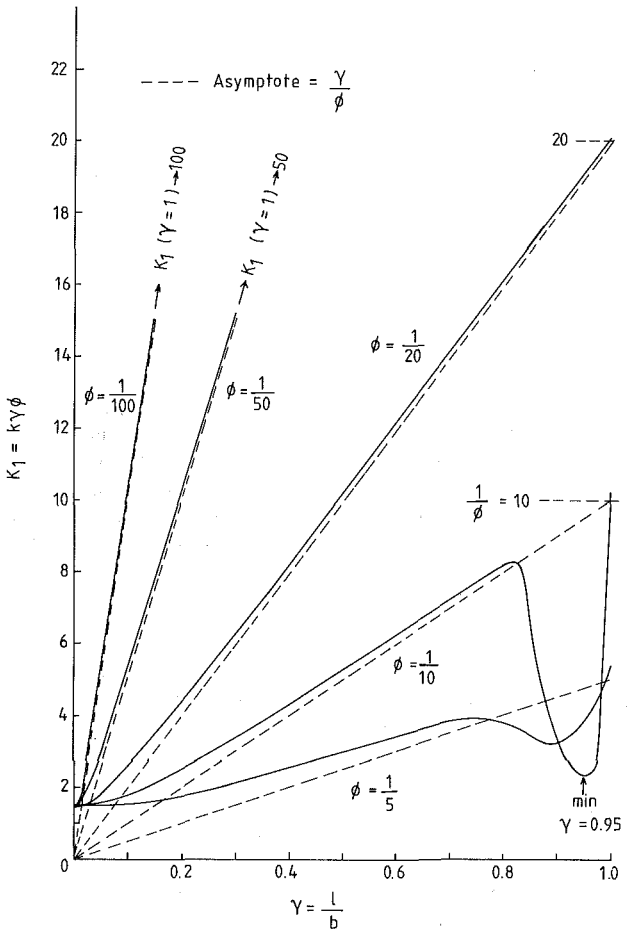


Fig. 2 K_1 versus γ plots for different values of ϕ

Table 1 Numerical values of K_2 for various ϕ and γ

$\gamma\backslash\phi$	0.1	0.3	0.5	0.7	0.9	1.0
0.1	0.181	0.454	0.717	1.059	1.671	2.144
0.3	0.343	0.542	0.777	1.129	1.770	2.265
0.5	0.530	0.677	0.886	1.268	1.975	2.514
0.7	0.723	0.813	1.045	1.500	2.318	2.926
0.9	0.309	0.960	1.327	1.907	2.877	3.565
1.0	1.020	1.188	1.563	2.220	3.276	4.000

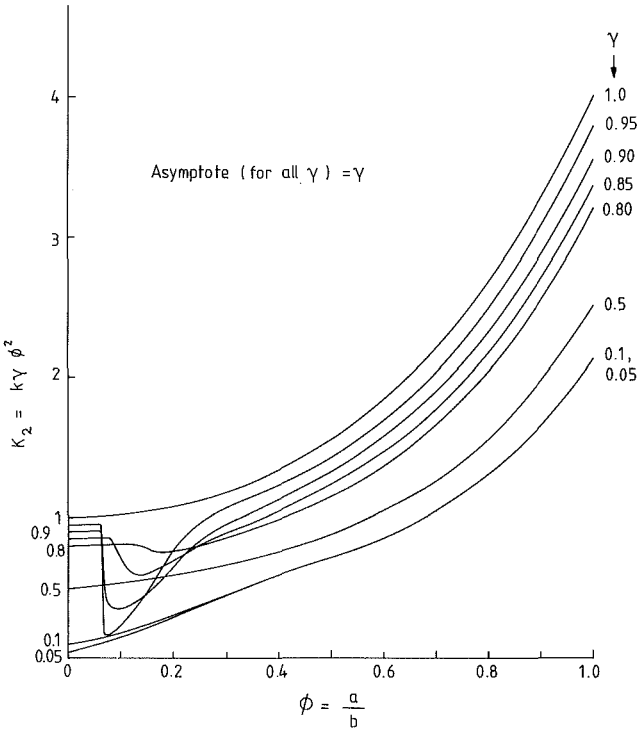


Fig. 3 K_2 versus ϕ plots for different values of γ

line $K_1 = 1.455$: the latter value of K_1, corresponding to a concentrated load, may then be used in all cases for which $\gamma < 1.455\ \phi$.

The variation of the buckling coefficient K_2 with aspect ratio, for different γ values, appears in Fig. 3. K_2 is defined as

$$K_2 = K_1 \phi \tag{3}$$

Such a definition is convenient since it shows quite clearly the asymptotic value $K_2 = \gamma$, for all γ's, as $\phi \to 0$. Furthermore, this definition ensures that the new buckling coefficient is finite for all values of γ and ϕ. In particular, at $\gamma = 1$, $K_2 \to 1$ for very wide plates, while both expressions (1) and (2) become infinite for this case ($k \to 1/\phi^2$ and $K_1 \to 1/\phi$, as $\phi \to 0$). On the other hand, $K_2 \to 0$ as both ϕ and γ approach zero while, as stated earlier, the alternative definition gives $K_1 = 1.455$. It may also be interesting to note that, for $\phi < 1$ and $\gamma = 0$, the K_1 versus ϕ characteristic is oscillatory about its asymptote [1], but that this is not the case in the corresponding K_2 versus ϕ plot.

Figure 3 shows clearly the range of aspect ratios around $\phi \sim 0.1$ where the otherwise smooth K_2 versus ϕ characteristics experience a sudden drop, which may result in a very drastic loss of buckling-load capacity (as high as 90 percent). This "dip" of the K_2 versus ϕ plot around $\phi \sim 0.1$ has already been observed in the study of the stability of wide plates subject to a series of discrete in-plane loads [4], and can be attributed, primarily, to the very complex stress distribution in this range of aspect ratios. It is significant that, when the stress distribution becomes more predictable (as, for example, in the extreme cases $\gamma = 1$ and $\gamma = 0$), the sudden drop in K_2 does not occur so that the K_2 versus ϕ characteristic is then smooth throughout the whole range of plate geometries. Numerical studies permit a more precise determination of those widths of the patch load for which the drop does occur: the resultant values of γ lie in the range $0.75 < \gamma < 1.0$. Therefore, for $\gamma \leq 0.75$, values of K_2 may safely be interpolated from those given in Fig. 3.

Finally, as the results of the present analysis may be considered to be "exact" [1], they can be used as reference data

Downloaded 02 May 2010 to 171.66.16.54. Redistribution subject to ASME license or copyright; see http://www.asme.org/terms/Terms_Use.cfm

for approximate and/or numerical models such as, for example, the finite element technique. For this reason, Table 1 is appended, giving vlaues of K_2 (correct to three decimal places) for various ϕ's and γ's.

References

1 Baker, G., and Pavlović, M. N., "Elastic Stability of Simply Supported Rectangular Plates Under Locally Distributed Edge Forces," ASME JOURNAL OF APPLIED MECHANICS, Vol. 49, 1982, pp. 177–179.

2 Timoshenko, S. P., and Gere, J. M., *Theory of Elastic Stability*, McGraw-Hill, New York, 1961.

3 Bulson, P. S., *The Stability of Flat Plates*, Chatto and Windus, London, 1970.

4 Baker, G., and Pavlović, M. N., "Rectangular Plates Compressed by a Series of In-Plane Loads: Stability and Stress Distribution," *The Aeronautical Journal*, Vol. 87, 1983, pp. 183–188.

A Pathological Situation in Micropolar Elasticity

R. S. Lakes[1]

The case of zero coupling number N *in micropolar elasticity is considered. This situation has been examined by several investigators to simplify the analysis of micropolar materials. We show that the case of $N=0$ is pathological and present a physical example.*

Introduction

Micropolar elasticity is a continuum theory that allows degrees of freedom not present in classical elasticity. The extra degrees of freedom are thought to describe some aspects of the deformation of materials with microstructure. The constitutive equations for a linear, isotropic micropolar solid are [1]:

$$t_{kl} = \lambda e_{rr}\delta_{kl} + (2\mu+\kappa)e_{kl} + \kappa\, e_{klm}(r_m - \phi_m) \tag{1}$$

$$m_{kl} = \alpha\, \phi_{r,r}\delta_{kl} + \beta\, \phi_{k,l} + \gamma\, \phi_{l,k} \tag{2}$$

in which t is the asymmetric force stress, m is the couple stress, $e_{kl} = \frac{1}{2}(u_{k,l} + u_{l,k})$ is the small strain, u is the displacement, ϕ is the microrotation, and e_{klm} is the permutation symbol. $r_k = \frac{1}{2}e_{klm}u_{m,l}$ is the macrorotation, which is kinematically distinct from the microrotation. α, β, γ, and κ are micropolar elastic constants; when they vanish, classical elasticity is recovered as a special case.

Significance of κ

Following [2, 3] we define the coupling number N: $N^2 = \kappa/2(\mu+\kappa)$. N is dimensionless and its range of permitted values is [0, 1], based on energy considerations [2]. N is a measure of the intensity of coupling between the microrotation and macrorotation fields. When $N = 1$, these fields become perfectly coupled, so the microrotation ceases to be an independent kinematical degree of freedom. This special case corresponds to the indeterminate couple stress theory [4]. For this case, many of the effects predicted to occur in a micropolar solid, e.g., stiffening of thin rods in bending [3] and in torsion [5], and reduction of the stress concentration around a hole [2], are maximum.

Several authors have considered the special case $\kappa=0$, or equivalently, $N=0$. This special case may considerably simplify problems for which it is difficult to obtain an explicit solution [6] or may be used to explore limiting behavior of solutions of micropolar problems [7]. The solutions to some problems are observed to coincide with classical elasticity, if $N=0$, [2, 1].

A Torsion Problem

The problem of quasistatic torsion of a long circularly cylindrical rod of an isotropic, micropolar medium has been solved by Gauthier and Jahsman [5]. In this Note we explore solutions to this problem for the case of zero coupling number. In the general torsion problem, the displacement and microrotation fields are uniquely specified by the applied torque and by the assumption of translational symmetry in the axial direction. For the case of zero coupling number N we observe a different situation: a given value of applied torque can be realized in more than one way.

Specifically, the case of zero applied torque may be realized by either of the following displacement fields:

$$\begin{Bmatrix} u_r = 0 \\ u_\theta = C_1 rz \\ u_z = 0 \end{Bmatrix} \quad \begin{Bmatrix} \phi_r = C_2(-\alpha/(2\alpha+\beta+\gamma))r \\ \phi_\theta = 0 \\ \phi_z = C_2 z \end{Bmatrix} \tag{3}$$

in which $C_2 = -C_1[(R^2/2)(\mu/[(\beta+\gamma)+\alpha(1-\alpha/(2\alpha+\beta+\gamma))])]$, R is the cylinder radius and C_1 is any number of dimension 1/length; and

$$\begin{Bmatrix} u_r = 0 \\ u_\theta = 0 \\ u_z = 0 \end{Bmatrix} \quad \begin{Bmatrix} \phi_r = 0 \\ \phi_\theta = 0 \\ \phi_z = 0 \end{Bmatrix} \tag{4}$$

In field (3), there arise opposing, nonzero states of force stress and couple stress that result in zero net torque upon the end surfaces. In keeping with the boundary conditions, there must be a prescribed self-equilibrated distribution of force stress and couple stress upon the end surfaces, or the displacement and microrotation must be prescribed on these surfaces. For the case $N\neq 0$, by contrast it is not possible to achieve the displacement and microrotation field (3) since the difference between the macrorotation and microrotation gives rise to an antisymmetric contribution to the force stress by virtue of (1) for $\kappa\neq 0$. This contribution makes it impossible to satisfy the equilibrium equations, therefore for $N\neq 0$, field (4) is the unique displacement and microrotation field associated with zero end torque (and zero end force).

For the special case $N=0$, the constitutive equations (1) and (2) may be used to show that field (3) satisfies the equilibrium equations and boundary conditions. Field (3) also must automatically satisfy the micropolar compatibility conditions [1] since the displacement-rotation field, rather than the strain field, has been prescribed. This may be verified by using the tensorial form of the compatibility conditions to obtain an expanded form for cylindrical coordinates. The expanded form given in [8] must be viewed with caution since this version has been specialized under the implicit assumption that the micropolar strain $\epsilon_{kl} = e_{kl} + e_{klm}(r_m - \phi_m)$ has no z dependence. This assumption does not apply to field (3), therefore the full compatibility conditions given in [1] must be considered. In field (3), the conventional strain e_{kl} is, however, independent of z and, with $N = 0$, the stresses are also independent of z.

Discussion and Conclusion

The case $N=0$ does not correspond to a failure of uniqueness in the usual sense, since different local boundary tractions are associated with the displacement and

Department of Biomedical Engineering and Department of Mechanical Engineering, University of Iowa, Iowa City, Iowa 52242.

Manuscript received by ASME Applied Mechanics Division, November, 1982; final revision, October, 1984.

Downloaded 02 May 2010 to 171.66.16.54. Redistribution subject to ASME license or copyright; see http://www.asme.org/terms/Terms_Use.cfm

for approximate and/or numerical models such as, for example, the finite element technique. For this reason, Table 1 is appended, giving vlaues of K_2 (correct to three decimal places) for various ϕ's and γ's.

References

1 Baker, G., and Pavlović, M. N., "Elastic Stability of Simply Supported Rectangular Plates Under Locally Distributed Edge Forces," ASME JOURNAL OF APPLIED MECHANICS, Vol. 49, 1982, pp. 177–179.

2 Timoshenko, S. P., and Gere, J. M., *Theory of Elastic Stability*, McGraw-Hill, New York, 1961.

3 Bulson, P. S., *The Stability of Flat Plates*, Chatto and Windus, London, 1970.

4 Baker, G., and Pavlović, M. N., "Rectangular Plates Compressed by a Series of In-Plane Loads: Stability and Stress Distribution," *The Aeronautical Journal*, Vol. 87, 1983, pp. 183–188.

A Pathological Situation in Micropolar Elasticity

R. S. Lakes[1]

The case of zero coupling number N *in micropolar elasticity is considered. This situation has been examined by several investigators to simplify the analysis of micropolar materials. We show that the case of $N=0$ is pathological and present a physical example.*

Introduction

Micropolar elasticity is a continuum theory that allows degrees of freedom not present in classical elasticity. The extra degrees of freedom are thought to describe some aspects of the deformation of materials with microstructure. The constitutive equations for a linear, isotropic micropolar solid are [1]:

$$t_{kl} = \lambda e_{rr}\delta_{kl} + (2\mu+\kappa)e_{kl} + \kappa\, e_{klm}(r_m - \phi_m) \tag{1}$$

$$m_{kl} = \alpha\, \phi_{r,r}\delta_{kl} + \beta\, \phi_{k,l} + \gamma\, \phi_{l,k} \tag{2}$$

in which t is the asymmetric force stress, m is the couple stress, $e_{kl} = \frac{1}{2}(u_{k,l} + u_{l,k})$ is the small strain, u is the displacement, ϕ is the microrotation, and e_{klm} is the permutation symbol. $r_k = \frac{1}{2}e_{klm}u_{m,l}$ is the macrorotation, which is kinematically distinct from the microrotation. α, β, γ, and κ are micropolar elastic constants; when they vanish, classical elasticity is recovered as a special case.

Significance of κ

Following [2, 3] we define the coupling number N: $N^2 = \kappa/2(\mu+\kappa)$. N is dimensionless and its range of permitted values is [0, 1], based on energy considerations [2]. N is a measure of the intensity of coupling between the microrotation and macrorotation fields. When $N = 1$, these fields become perfectly coupled, so the microrotation ceases to be an independent kinematical degree of freedom. This special case corresponds to the indeterminate couple stress theory [4]. For this case, many of the effects predicted to occur in a micropolar solid, e.g., stiffening of thin rods in bending [3] and in torsion [5], and reduction of the stress concentration around a hole [2], are maximum.

Several authors have considered the special case $\kappa=0$, or equivalently, $N=0$. This special case may considerably simplify problems for which it is difficult to obtain an explicit solution [6] or may be used to explore limiting behavior of solutions of micropolar problems [7]. The solutions to some problems are observed to coincide with classical elasticity, if $N=0$, [2, 1].

A Torsion Problem

The problem of quasistatic torsion of a long circularly cylindrical rod of an isotropic, micropolar medium has been solved by Gauthier and Jahsman [5]. In this Note we explore solutions to this problem for the case of zero coupling number. In the general torsion problem, the displacement and microrotation fields are uniquely specified by the applied torque and by the assumption of translational symmetry in the axial direction. For the case of zero coupling number N we observe a different situation: a given value of applied torque can be realized in more than one way.

Specifically, the case of zero applied torque may be realized by either of the following displacement fields:

$$\left\{\begin{matrix} u_r = 0 \\ u_\theta = C_1 rz \\ u_z = 0 \end{matrix}\right\} \qquad \left\{\begin{matrix} \phi_r = C_2(-\alpha/(2\alpha+\beta+\gamma))r \\ \phi_\theta = 0 \\ \phi_z = C_2 z \end{matrix}\right\} \tag{3}$$

in which $C_2 = -C_1[(R^2/2)(\mu/[(\beta+\gamma) + \alpha(1 - \alpha/(2\alpha+\beta+\gamma))])]$, R is the cylinder radius and C_1 is any number of dimension 1/length; and

$$\left\{\begin{matrix} u_r = 0 \\ u_\theta = 0 \\ u_z = 0 \end{matrix}\right\} \qquad \left\{\begin{matrix} \phi_r = 0 \\ \phi_\theta = 0 \\ \phi_z = 0 \end{matrix}\right\} \tag{4}$$

In field (3), there arise opposing, nonzero states of force stress and couple stress that result in zero net torque upon the end surfaces. In keeping with the boundary conditions, there must be a prescribed self-equilibrated distribution of force stress and couple stress upon the end surfaces, or the displacement and microrotation must be prescribed on these surfaces. For the case $N\neq 0$, by contrast it is not possible to achieve the displacement and microrotation field (3) since the difference between the macrorotation and microrotation gives rise to an antisymmetric contribution to the force stress by virtue of (1) for $\kappa\neq 0$. This contribution makes it impossible to satisfy the equilibrium equations, therefore for $N\neq 0$, field (4) is the unique displacement and microrotation field associated with zero end torque (and zero end force).

For the special case $N=0$, the constitutive equations (1) and (2) may be used to show that field (3) satisfies the equilibrium equations and boundary conditions. Field (3) also must automatically satisfy the micropolar compatibility conditions [1] since the displacement-rotation field, rather than the strain field, has been prescribed. This may be verified by using the tensorial form of the compatibility conditions to obtain an expanded form for cylindrical coordinates. The expanded form given in [8] must be viewed with caution since this version has been specialized under the implicit assumption that the micropolar strain $\epsilon_{kl} = e_{kl} + e_{klm}(r_m - \phi_m)$ has no z dependence. This assumption does not apply to field (3), therefore the full compatibility conditions given in [1] must be considered. In field (3), the conventional strain e_{kl} is, however, independent of z and, with $N = 0$, the stresses are also independent of z.

Discussion and Conclusion

The case $N=0$ does not correspond to a failure of uniqueness in the usual sense, since different local boundary tractions are associated with the displacement and

Department of Biomedical Engineering and Department of Mechanical Engineering, University of Iowa, Iowa City, Iowa 52242.

Manuscript received by ASME Applied Mechanics Division, November, 1982; final revision, October, 1984.

Copyright © 1985 by ASME
Downloaded 02 May 2010 to 171.66.16.54. Redistribution subject to ASME license or copyright; see http://www.asme.org/terms/Terms_Use.cfm

microrotation fields (3), (4). The total macroscopic load, however, is the same at the end, which may be arbitrarily far from the region of interest. The different stress distributions at the end in fields (3) and (4) are therefore equivalent in the sense of Saint-Venant. In this sense, the case $N=0$ is pathological. For some specific problems, the solution for $N=0$ is found to coincide with the solution for classical elasticity. This case is not equivalent to classical elasticity, however; the microstructural degrees of freedom remain. Classical elasticity is recovered as a special case of micropolar elasticity only if α, β, γ, and κ all vanish.

A physical example that exhibits some features of the situation just considered is as follows. Consider a long rod of a composite material made of parallel stiff fibers embedded in a compliant matrix. Fiber orientation is random, so macroscopic properties are isotropic. The spatial average of force per unit area upon fibers and matrix may be regarded as the force stress, and the corresponding spatial average of couple upon each individual fiber, per unit area, may be regarded as the couple stress. At each end of the rod, we may macroscopically twist the end by a given angle, and microscopically twist the end of each fiber in the opposite direction until the net end torque is zero. If the interface between fiber and matrix is perfectly lubricated, the effect of the end displacements and rotations may be expected to propagate an arbitrary distance down the rod. This situation is analogous to the continuum case $N=0$ considered in the foregoing. Significant end effects may also occur in classical elasticity of highly anisotropic materials [9]; by contrast the preceding example depends on micromechanical degrees of freedom rather than anisotropy.

Micropolar elasticity has been found to be useful in the interpretation of recent experiments upon solids with fibrous [10] and cellular [11] structures. Nonzero values of N were inferred from these experiments. No structures corresponding to the preceding physical example, however, were studied.

To conclude, the special case $N=0$ in micropolar elasticity is pathological in that specification of the macroscopic end load on a rod does not uniquely determine the displacement and microrotation fields far from the end. The dependence of these fields on remote, localized distributions of self-equilibrated load calls into question the applicability of Saint-Venant's principle for such solids.

References

1 Eringen, A. C., "Theory of Micropolar Elasticity," in: *Fracture*, Liebowitz, M., ed., Vol. 2, Academic Press, New York, 1968, pp. 621-729.

2 Cowin, S. C., "An Incorrect Inequality in Micropolar Elasticity Theory," *J. Appl. Math, Phys. (ZAMP)*, Vol. 21, 1970, pp. 494-497.

3 Krishna Reddy, G. V., and Venkatasubramanian, N. K., "On the Flexural Rigidity of a Micropolar Elastic Circular Cylinder," ASME JOURNAL OF APPLIED MECHANICS, Vol. 45, 1978, pp. 429-431.

4 Mindlin, R. D., and Tiersten, H. F., "Effects of Couple Stresses in Linear Elasticity," *Arch. Rat. Mech. Anal.*, Vol. 11, 1962, pp. 415-448.

5 Gauthier, R. D., and Jahsman, W. E., "A Quest for Micropolar Elastic Constants," ASME JOURNAL OF APPLIED MECHANICS, Vol. 42, 1975, pp. 369-374.

6 Willson, A. J., "The Micropolar Elastic Vibrations of a Circular Cylinder," *Int. J. Eng. Sci.*, Vol. 10, 1972, pp. 17-22.

7 Gauthier, R. D., and Jahsman, W. E., "Bending of a Curved Bar of Micropolar Elastic Material," ASME JOURNAL OF APPLIED MECHANICS, Vol. 43, 1976, pp. 502-503.

8 Gauthier, R. D., "Experimental Investigations on Micropolar Media," in: *Mechanics of Micropolar Media*, Brulin, O., and Hsieh, R. K. T., eds., World Scientific, Singapore, 1982.

9 Horgan, C. O., "On Saint-Venant's Principle in Plane Anisotropic Elasticity," *J. Elasticity*, Vol. 2, 1972, pp. 169-180.

10 Yang, J. F. C., and Lakes, R. S., "Experimental Study of Micropolar and Couple Stress Elasticity in Bone in Bending," *J. Biomechanics*, Vol. 15, 1982, pp. 91-98.

11 Lakes, R. S., "Experimental Microelasticity of Two Porous Solids," *Int. J. Solids and Structures*, in press.

Effect of Debonding on the Stability of Fiber-Reinforced Composites

J. Barber[1] and N. Triantafyllidis[1]

1 Introduction

In this work we present some analytical solutions to a model problem in order to elucidate the effects of a preexisting debonding between fiber and matrix on the stability properties of reinforced composites.

Our analysis is motivated by some recent experimental [1] and theoretical investigations [2, 3] on delamination buckling of fiber-reinforced and laminated composites subjected to compressive loads along the reinforcing direction. Of particular interest is the effect of the debonded length on the critical buckling load which is investigated here for two extreme cases of the fiber-to-matrix relative stiffness. By ignoring fiber interaction effects and using a simple model for our problem, we are able to obtain closed-form analytical solutions.

More specifically, we consider a beam on two elastic type foundations. The effect of debonding in a certain region is modeled by the local exclusion of tensile lateral forces. Realistic buckling loads and eigenmodes have been found for all the cases considered and all critical loads were of the same order of magnitude as that for the fully bonded composite. Our results at this stage are preliminary in nature, but they indicate the possibility of solution of some more complicated but more realistic delamination buckling problems.

2 Fiber Buckling in a Soft Matrix

To study the effects of debonding in the fiber buckling of a soft matrix composite, the matrix material on each side of the fiber is idealized as an elastic foundation of modulus k. Two cases will be considered. In the first case the entire fiber is assumed to be debonded from the matrix material so that tensile stresses at the matrix-fiber interface are nowhere allowed. In the second case debonding will be assumed only in a finite zone of length $2a$.

2.1 Fully Debonded Fiber (Debonded Zone $-\infty \le x \le +\infty$). In the case of full debonding, every point of the fiber will be in contact with one of the two foundations (the one corresponding to a compressive distrbuted load). Consequently, the problem is equivalent to the buckling (under a lateral force P) of a continuous beam resting on only one elastic foundation of modulus k. The critical load for this case is well known (see, for example, Timoshenko and Gere [4]) and is

$$P_d = (4\ k\ EI)^{1/2} \tag{2.1}$$

where EI is the fiber's bending stiffness. For the fully bonded fiber, of course, both the elastic foundations on each side of the fiber will be active at buckling, and the total effective foundation stiffness will be $2k$. Therefore the corresponding lateral buckling load P_b should be given by

$$P_b = (8\ K\ EI)^{1/2} \tag{2.2}$$

For the partially bonded fiber to be analyzed subsequently, the corresponding critical load P_p is expected to satisfy $P_d \le P_p \le P_b$.

2.2 Partially Debonded Fiber (Debonded Zone $-a \le x \le a$). If $u(x)$ is the lateral displacement of the fiber due to

[1] Department of Mechanical Engineering and Applied Mechanics, and Department of Aerospace Engineering, respectively, The University of Michigan, Ann Arbor, Mich. 48109.

Manuscript received by ASME Applied Mechanics Division, August, 1984.

Downloaded 02 May 2010 to 171.66.16.54. Redistribution subject to ASME license or copyright; see http://www.asme.org/terms/Terms_Use.cfm

microrotation fields (3), (4). The total macroscopic load, however, is the same at the end, which may be arbitrarily far from the region of interest. The different stress distributions at the end in fields (3) and (4) are therefore equivalent in the sense of Saint-Venant. In this sense, the case $N=0$ is pathological. For some specific problems, the solution for $N=0$ is found to coincide with the solution for classical elasticity. This case is not equivalent to classical elasticity, however; the microstructural degrees of freedom remain. Classical elasticity is recovered as a special case of micropolar elasticity only if α, β, γ, and κ all vanish.

A physical example that exhibits some features of the situation just considered is as follows. Consider a long rod of a composite material made of parallel stiff fibers embedded in a compliant matrix. Fiber orientation is random, so macroscopic properties are isotropic. The spatial average of force per unit area upon fibers and matrix may be regarded as the force stress, and the corresponding spatial average of couple upon each individual fiber, per unit area, may be regarded as the couple stress. At each end of the rod, we may macroscopically twist the end by a given angle, and microscopically twist the end of each fiber in the opposite direction until the net end torque is zero. If the interface between fiber and matrix is perfectly lubricated, the effect of the end displacements and rotations may be expected to propagate an arbitrary distance down the rod. This situation is analogous to the continuum case $N=0$ considered in the foregoing. Significant end effects may also occur in classical elasticity of highly anisotropic materials [9]; by contrast the preceding example depends on micromechanical degrees of freedom rather than anisotropy.

Micropolar elasticity has been found to be useful in the interpretation of recent experiments upon solids with fibrous [10] and cellular [11] structures. Nonzero values of N were inferred from these experiments. No structures corresponding to the preceding physical example, however, were studied.

To conclude, the special case $N=0$ in micropolar elasticity is pathological in that specification of the macroscopic end load on a rod does not uniquely determine the displacement and microrotation fields far from the end. The dependence of these fields on remote, localized distributions of self-equilibrated load calls into question the applicability of Saint-Venant's principle for such solids.

References

1 Eringen, A. C., "Theory of Micropolar Elasticity," in: *Fracture*, Liebowitz, M., ed., Vol. 2, Academic Press, New York, 1968, pp. 621-729.

2 Cowin, S. C., "An Incorrect Inequality in Micropolar Elasticity Theory," *J. Appl. Math, Phys. (ZAMP)*, Vol. 21, 1970, pp. 494-497.

3 Krishna Reddy, G. V., and Venkatasubramanian, N. K., "On the Flexural Rigidity of a Micropolar Elastic Circular Cylinder," ASME JOURNAL OF APPLIED MECHANICS, Vol. 45, 1978, pp. 429-431.

4 Mindlin, R. D., and Tiersten, H. F., "Effects of Couple Stresses in Linear Elasticity," *Arch. Rat. Mech. Anal.*, Vol. 11, 1962, pp. 415-448.

5 Gauthier, R. D., and Jahsman, W. E., "A Quest for Micropolar Elastic Constants," ASME JOURNAL OF APPLIED MECHANICS, Vol. 42, 1975, pp. 369-374.

6 Willson, A. J., "The Micropolar Elastic Vibrations of a Circular Cylinder," *Int. J. Eng. Sci.*, Vol. 10, 1972, pp. 17-22.

7 Gauthier, R. D., and Jahsman, W. E., "Bending of a Curved Bar of Micropolar Elastic Material," ASME JOURNAL OF APPLIED MECHANICS, Vol. 43, 1976, pp. 502-503.

8 Gauthier, R. D., "Experimental Investigations on Micropolar Media," in: *Mechanics of Micropolar Media*, Brulin, O., and Hsieh, R. K. T., eds., World Scientific, Singapore, 1982.

9 Horgan, C. O., "On Saint-Venant's Principle in Plane Anisotropic Elasticity," *J. Elasticity*, Vol. 2, 1972, pp. 169-180.

10 Yang, J. F. C., and Lakes, R. S., "Experimental Study of Micropolar and Couple Stress Elasticity in Bone in Bending," *J. Biomechanics*, Vol. 15, 1982, pp. 91-98.

11 Lakes, R. S., "Experimental Microelasticity of Two Porous Solids," *Int. J. Solids and Structures*, in press.

Effect of Debonding on the Stability of Fiber-Reinforced Composites

J. Barber[1] and N. Triantafyllidis[1]

1 Introduction

In this work we present some analytical solutions to a model problem in order to elucidate the effects of a preexisting debonding between fiber and matrix on the stability properties of reinforced composites.

Our analysis is motivated by some recent experimental [1] and theoretical investigations [2, 3] on delamination buckling of fiber-reinforced and laminated composites subjected to compressive loads along the reinforcing direction. Of particular interest is the effect of the debonded length on the critical buckling load which is investigated here for two extreme cases of the fiber-to-matrix relative stiffness. By ignoring fiber interaction effects and using a simple model for our problem, we are able to obtain closed-form analytical solutions.

More specifically, we consider a beam on two elastic type foundations. The effect of debonding in a certain region is modeled by the local exclusion of tensile lateral forces. Realistic buckling loads and eigenmodes have been found for all the cases considered and all critical loads were of the same order of magnitude as that for the fully bonded composite. Our results at this stage are preliminary in nature, but they indicate the possibility of solution of some more complicated but more realistic delamination buckling problems.

2 Fiber Buckling in a Soft Matrix

To study the effects of debonding in the fiber buckling of a soft matrix composite, the matrix material on each side of the fiber is idealized as an elastic foundation of modulus k. Two cases will be considered. In the first case the entire fiber is assumed to be debonded from the matrix material so that tensile stresses at the matrix-fiber interface are nowhere allowed. In the second case debonding will be assumed only in a finite zone of length $2a$.

2.1 Fully Debonded Fiber (Debonded Zone $-\infty \le x \le +\infty$). In the case of full debonding, every point of the fiber will be in contact with one of the two foundations (the one corresponding to a compressive distrbuted load). Consequently, the problem is equivalent to the buckling (under a lateral force P) of a continuous beam resting on only one elastic foundation of modulus k. The critical load for this case is well known (see, for example, Timoshenko and Gere [4]) and is

$$P_d = (4\ k\ EI)^{1/2} \tag{2.1}$$

where EI is the fiber's bending stiffness. For the fully bonded fiber, of course, both the elastic foundations on each side of the fiber will be active at buckling, and the total effective foundation stiffness will be $2k$. Therefore the corresponding lateral buckling load P_b should be given by

$$P_b = (8\ K\ EI)^{1/2} \tag{2.2}$$

For the partially bonded fiber to be analyzed subsequently, the corresponding critical load P_p is expected to satisfy $P_d \le P_p \le P_b$.

2.2 Partially Debonded Fiber (Debonded Zone $-a \le x \le a$). If $u(x)$ is the lateral displacement of the fiber due to

[1] Department of Mechanical Engineering and Applied Mechanics, and Department of Aerospace Engineering, respectively, The University of Michigan, Ann Arbor, Mich. 48109.

Manuscript received by ASME Applied Mechanics Division, August, 1984.

Copyright © 1985 by ASME

Downloaded 02 May 2010 to 171.66.16.54. Redistribution subject to ASME license or copyright; see http://www.asme.org/terms/Terms_Use.cfm

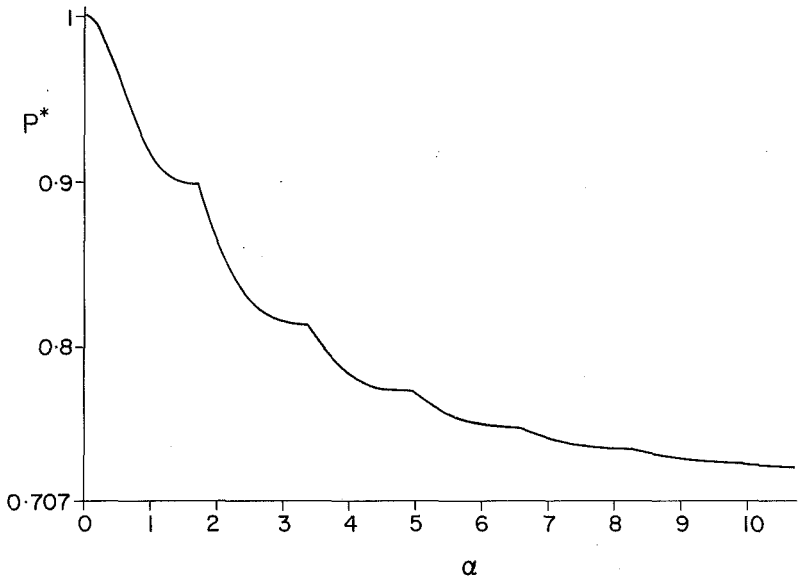


Fig. 1 Nondimensionalized load P^* versus crack length parameter α for a partially debonded fiber in a soft matrix

an axial load P_p, the governing equation for the fiber buckling is

$$EI\frac{d^4u}{dx^4}+P_p\frac{d^2u}{dx^2}+ku=0 \quad \text{in debonded zone} \quad |x|\le a$$
$$EI\frac{d^4u}{dx^4}+P_p\frac{d^2u}{dx^2}+2\,ku=0 \quad \text{in bonded zone} \quad |x|\ge a \tag{2.3}$$

As mentioned earlier, only solutions in the range $P_d \le P_p \le P_b$ are of interest here, and thus the general solutions to (2.3) can be put in the form

$$u(x)=\begin{cases} [C_1^- \cos(\omega(x-a))+C_2^- \sin(\omega(x-a))] \\ \exp(-\lambda\,(x-a)): x\ge a \\ A_1^- \sin(\omega_1(x-a))+A_2^- \sin(\omega_2(x-a)) \\ +A_1^+ \sin(\omega_1(x+a))+A_2^+ \sin(\omega_2(x+a)): \ |x|\le a \\ [C_1^+ \cos(\omega(x+a))+C_2^+ \sin(\omega(x+a))] \\ \exp(\lambda(x+a)): x\le -a \end{cases} \tag{2.4}$$

where ω_1, ω_2, ω, λ, and P^* are given by

$$\left.\begin{aligned} \omega_1&=(P^*+(P^{*2}-\tfrac{1}{2})^{1/2})^{1/2}(2k/EI)^{1/4}, \\ \omega_2&=(P^*-(P^{*2}-\tfrac{1}{2})^{1/2})^{1/2}(2k/EI)^{1/4} \\ \omega&=((1+P^*)/2)^{1/2}(2k/EI)^{1/4}, \\ \lambda&=((1-P^*)/2)^{1/2}(2k/EI)^{1/4}, P^*=P_p/P_b \end{aligned}\right\} \tag{2.5}$$

The eight continuity conditions (four at $x=+a$ and four at $x=-a$) for $u(x)$ and its first three derivatives – following from the displacement, slope, moment and shear continuity requirements for the fiber – provide a linear homogeneous system of eight equations for the eight unknowns A_i^+, A_i^-, C_i^+, C_i^- $(i=1,2)$. After considerable manipulations one can show that a nontrival solution to the aforementioned system is possible if and only if

$$F(\lambda,\omega,\omega_1,\omega_2;\ \tan(.))F(\lambda,\omega,\omega_1,\omega_2;-\cot(.))=0 \tag{2.6}$$

where $F(\lambda,\omega,\omega_1,\omega_2;g(.))$ is given by

$$\begin{aligned} F \equiv\ & 2\lambda(\omega_2^2-\omega_1^2)(\lambda^2+\omega^2+\omega_1\omega_2 g(\omega_1 a)g(\omega_2 a)) \\ & +\omega_1 g(\omega_1 a)(\omega_1^2(\lambda^2+\omega^2) \\ & +\omega_2^2(\omega^2-3\lambda^2)-(\lambda^2+\omega^2)^2-\omega_1^2\omega_2^2) \\ & +\omega_2 g(\omega_2 a)(\omega_1^2\omega_2^2+(\lambda^2+\omega^2)^2 \\ & -\omega_2^2(\lambda^2+\omega^2)-\omega_1^2(\omega^2-3\lambda^2)) \end{aligned} \tag{2.7}$$

It can also be shown that $F(\ldots;\tan(.))=0$ corresponds to a symmetric eigenmode while $F(\ldots;\ -\cot\ (.))=0$ corresponds to an antisymmetric one with respect to the origin $x=0$.

The results giving the lowest value of P^* satisfying (2.6) as a function of $\alpha\equiv a(k/EI)^{1/4}$ (a properly nondimensionalized debonded zone size) are presented in Fig. 1. Note that, for fixed material properties, as the zone size α increases from 0 (fully bonded fiber) to ∞ (fully debonded fiber), the nondimensionalized critical load P^* decreases montonically from 1 to $1/\sqrt{2}=0.707$.

3 Fiber Buckling in a Stiff Matrix

In the previous solution, the contact region(s) between the fiber and the matrix extend over a full half wave of the bifurcation eigenmode. In practice, a much more restricted contact area is anticipated in view of the nonlocal pressure-displacement relation for the elastic matrix. A limiting case of some interest is that in which the contact area is sufficiently localized for the pressure exerted by the matrix to be considered as a system of point forces. This will be the case if the stiffening effect of adjacent fibers is sufficiently weak for rigid body displacement of the matrix to dominate the localized elastic deformation. The problem can then be idealized as an elastic beam constrained between two parallel rigid beams on elastic foundations. The magnitude of each (normal) point force on the fiber is proportional to the local displacement and to the wavelength of the corresponding buckling mode say $4a$ i.e.,

$$F=4\,a\,k\,u(a) \tag{3.1}$$

with $u(a)$ the eigenmode's maximum amplitude.

It is sufficient to consider the governing (buckling) equation for one quarter wavelength, namely

$$EI\frac{d^2u}{dx^2}+P(u)=Fx/2 \quad 0\le x\le a \tag{3.2}$$

with boundary conditions

$$u=0 \quad \text{at} \quad x=0, \quad \frac{du}{dx}=0 \quad \text{at} \quad x=a \tag{3.3}$$

Downloaded 02 May 2010 to 171.66.16.54. Redistribution subject to ASME license or copyright; see http://www.asme.org/terms/Terms_Use.cfm

For no interpenetration between fiber and support, u is additionally required to satisfy

$$\frac{d^2u}{dx^2} < 0 \quad \text{at} \quad x = a \tag{3.4}$$

The solution to (3.2), and (3.3) is thus found to be

$$u(x) = Fx/2P - F\,a\,\sin(\eta x/a)/2P\eta\,\cos\,\eta;(\eta \equiv a(P/EI)^{1/2}) \tag{3.5}$$

which, upon taking into consideration (3.1) and (3.4) yields

$$P/P_b = [\eta(\eta - \tan\eta)]^{1/2}/2, \quad \text{with} \quad (2n-1)\pi \le \eta \le n\pi;\ n \epsilon I\!N \tag{3.6}$$

One can easily show from (3.6) that the minimum possible buckling load P corresponds to an η-satisfying

$$2\eta = \tan 2\eta,\ \pi/2 < \eta < \pi \quad \text{i.e.,} \quad \eta = 2.2467$$

and hence the corresponding critical value for the nondimensionalized critical load is $P^* = P/P_b = 1.4008$ (almost twice the value of the fully debonded fiber in the soft matrix $P^* = 0.707$).

4 Conclusions

In an attempt to investigate the effects of fiber debonding on the critical load for delamination-type buckling in fiber-reinforced composites, we have constructed some simpler models for sparingly reinforced composites under plane strain conditions. It was found that the buckling load varies between 1.4008 and 0.707 of that for the fully bonded fiber, with the upper limit corresponding to a highly rigid matrix and the lower one corresponding to a very soft matrix. These preliminary results indicate that considerable critical load variations can occur in a fiber-reinforced composite, depending on the fiber to matrix relative stiffness, and on the size of the debonded zone.

References

1 Knauss, W. B., Babcock, C. D., and Chai, H., "Visualization of Impact Damage of Composite Plates by Means of the Moire Technique," NASA-CR 159261, Apr. 1980.

2 Chai, H., Babcock, C. D., and Knauss, W. G., "One Dimensional Modelling of Failure in Laminated Plates by Delamination Buckling," *Int. J. Solids Structures*, Vol. 17, 1981, pp. 1069–1083.

3 Bottega, W. J., and Meawall, A., "Delamination Buckling and Growth in Laminates," ASME JOURNAL OF APPLIED MECHANICS, Vol. 50, 1983, pp. 184–189.

4 Timoshenko, S. P., and Gere, J. M., *Theory of Elastic Stabililty*, 2nd ed., McGraw-Hill, New York, 1961.

Crack Growth Prediction of Subsurface Crack in Yielded Material

D. Y. Tzou[1] and G. C. Sih[2]

1 Introduction

The problem of wear delamination by the growth of a subsurface crack subjected to compressive and shear loading was discussed in [1]. The objective of this Note is to show that the direction of crack growth can be determined by application of the strain-energy density criterion even though the surroundiong material undergoes plastic deformation.

In what follows, the subsurface crack problem will be resolved by application of the incremental theory of plasticity and the strain-energy density criterion. The modified version of the PAPST finite element program [2] will be used to determine the first increments of crack growth at the left and right tips of the crack. The values of the strain-energy density function dW/dV at the nodes and Gaussian points in Fig. 1 are first obtained. The Lagrangian method of interpolation is then applied to find the stationary values of dW/dV. Referring to the finite element grid pattern in Figs. 1 and 2, 1/9 and 4/9 intermediate nodes are introduced at elements adjacent to the crack tips ensuring the required $1/r$ singularity of the strain-energy density field[3]. The physical dimensions and loads in Fig. 2 correspond to those in [1]. Outlined in Table 1 are the material properties with the available critical strain-energy density $(dW/dV)_c^*$ defined as

$$\left(\frac{dW}{dV}\right)_c^* = \left(\frac{dW}{dV}\right)_c - \left(\frac{dW}{dV}\right)_p \tag{1}$$

in which $(dW/dV)_p$ pertains to that portion of the energy density dissipated by plastic deformation being no longer available during the growth of macrocrack. The variations of dW/dV as a function of θ are calculated for a fixed radius of $r \simeq 0.25$ μm centered at the right and left tips of the crack. Displayed graphically in Fig. 3 are the results. Note that the dW/dV curves indeed possess minima near $\theta = 0$ deg. They correspond to crack initiation angles of approximately 6 deg at the right tip and 0 deg at the left tip. According to the strain-energy density criterion [3], which remains valid when yielding occurs, the subsurface crack extends almost parallel

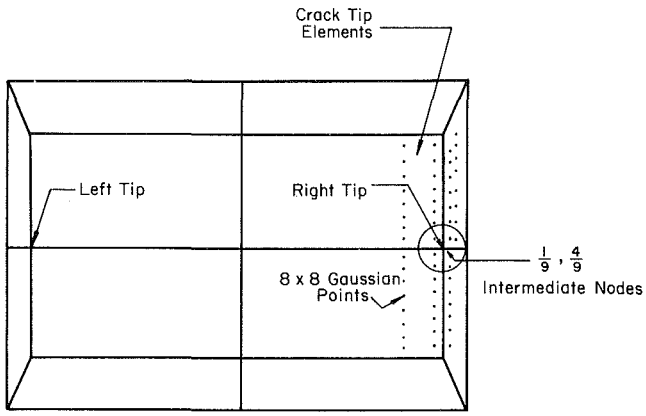


Fig. 1 Crack tip elements and Gaussian points

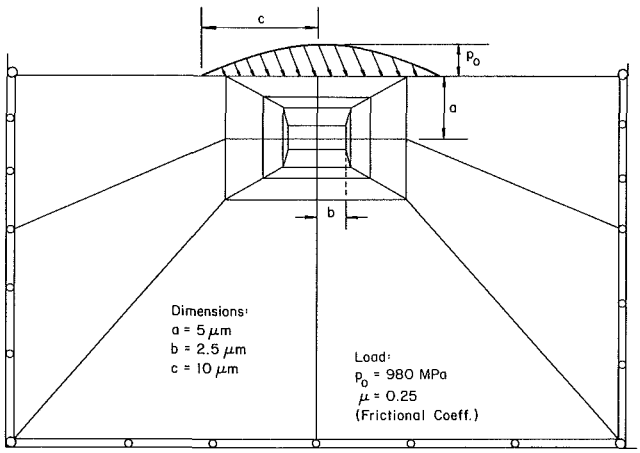


Fig. 2 Finite element grid pattern and load applied

Table 1 Mechanical properties of material in subsurface crack problem

Young's modulus E (MPa)	Tangent modulus E_T (MPa)	Poisson's ratio ν	Critical available strain-energy density $(dW/dV)_c^*$ (MPa)
1.96×10^5	19.6	0.28	1.638

[1] Research Assistant, Department of Mechanical Engineering and Mechanics, Lehigh University, Bethlehem, Pa. 18015.

[2] Professor of Mechanics and Director of Institute of Fracture and Solid Mechanics, Lehigh University, Bethlehem, Pa. 18015. Fellow, ASME

[3] The $1/r$ singular behavior of the strain energy density function holds for all material and is independent of loading and crack type.

Manuscript received by ASME Applied Mechanics Division, August, 1984.

Downloaded 02 May 2010 to 171.66.16.54. Redistribution subject to ASME license or copyright; see http://www.asme.org/terms/Terms_Use.cfm

For no interpenetration between fiber and support, u is additionally required to satisfy

$$\frac{d^2u}{dx^2} < 0 \quad \text{at} \quad x = a \tag{3.4}$$

The solution to (3.2), and (3.3) is thus found to be

$$u(x) = Fx/2P - F\,a\,\sin(\eta x/a)/2P\eta\,\cos\,\eta;(\eta \equiv a(P/EI)^{1/2}) \tag{3.5}$$

which, upon taking into consideration (3.1) and (3.4) yields

$$P/P_b = [\eta(\eta - \tan\eta)]^{1/2}/2, \quad \text{with} \quad (2n-1)\pi \le \eta \le n\pi;\ n \epsilon I\!N \tag{3.6}$$

One can easily show from (3.6) that the minimum possible buckling load P corresponds to an η-satisfying

$$2\eta = \tan 2\eta,\ \pi/2 < \eta < \pi \quad \text{i.e.,} \quad \eta = 2.2467$$

and hence the corresponding critical value for the nondimensionalized critical load is $P^* = P/P_b = 1.4008$ (almost twice the value of the fully debonded fiber in the soft matrix $P^* = 0.707$).

4 Conclusions

In an attempt to investigate the effects of fiber debonding on the critical load for delamination-type buckling in fiber-reinforced composites, we have constructed some simpler models for sparingly reinforced composites under plane strain conditions. It was found that the buckling load varies between 1.4008 and 0.707 of that for the fully bonded fiber, with the upper limit corresponding to a highly rigid matrix and the lower one corresponding to a very soft matrix. These preliminary results indicate that considerable critical load variations can occur in a fiber-reinforced composite, depending on the fiber to matrix relative stiffness, and on the size of the debonded zone.

References

1 Knauss, W. B., Babcock, C. D., and Chai, H., "Visualization of Impact Damage of Composite Plates by Means of the Moire Technique," NASA-CR 159261, Apr. 1980.

2 Chai, H., Babcock, C. D., and Knauss, W. G., "One Dimensional Modelling of Failure in Laminated Plates by Delamination Buckling," *Int. J. Solids Structures*, Vol. 17, 1981, pp. 1069–1083.

3 Bottega, W. J., and Meawall, A., "Delamination Buckling and Growth in Laminates," ASME JOURNAL OF APPLIED MECHANICS, Vol. 50, 1983, pp. 184–189.

4 Timoshenko, S. P., and Gere, J. M., *Theory of Elastic Stabililty*, 2nd ed., McGraw-Hill, New York, 1961.

Crack Growth Prediction of Subsurface Crack in Yielded Material

D. Y. Tzou[1] and G. C. Sih[2]

1 Introduction

The problem of wear delamination by the growth of a subsurface crack subjected to compressive and shear loading was discussed in [1]. The objective of this Note is to show that the direction of crack growth can be determined by application of the strain-energy density criterion even though the surroundiong material undergoes plastic deformation.

In what follows, the subsurface crack problem will be resolved by application of the incremental theory of plasticity and the strain-energy density criterion. The modified version of the PAPST finite element program [2] will be used to determine the first increments of crack growth at the left and right tips of the crack. The values of the strain-energy density function dW/dV at the nodes and Gaussian points in Fig. 1 are first obtained. The Lagrangian method of interpolation is then applied to find the stationary values of dW/dV. Referring to the finite element grid pattern in Figs. 1 and 2, 1/9 and 4/9 intermediate nodes are introduced at elements adjacent to the crack tips ensuring the required $1/r$ singularity of the strain-energy density field[3]. The physical dimensions and loads in Fig. 2 correspond to those in [1]. Outlined in Table 1 are the material properties with the available critical strain-energy density $(dW/dV)_c^*$ defined as

$$\left(\frac{dW}{dV}\right)_c^* = \left(\frac{dW}{dV}\right)_c - \left(\frac{dW}{dV}\right)_p \tag{1}$$

in which $(dW/dV)_p$ pertains to that portion of the energy density dissipated by plastic deformation being no longer available during the growth of macrocrack. The variations of dW/dV as a function of θ are calculated for a fixed radius of $r \simeq 0.25$ μm centered at the right and left tips of the crack. Displayed graphically in Fig. 3 are the results. Note that the dW/dV curves indeed possess minima near $\theta = 0$ deg. They correspond to crack initiation angles of approximately 6 deg at the right tip and 0 deg at the left tip. According to the strain-energy density criterion [3], which remains valid when yielding occurs, the subsurface crack extends almost parallel

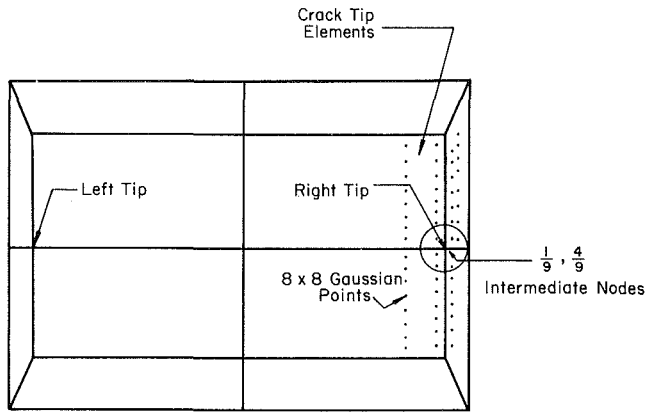


Fig. 1 Crack tip elements and Gaussian points

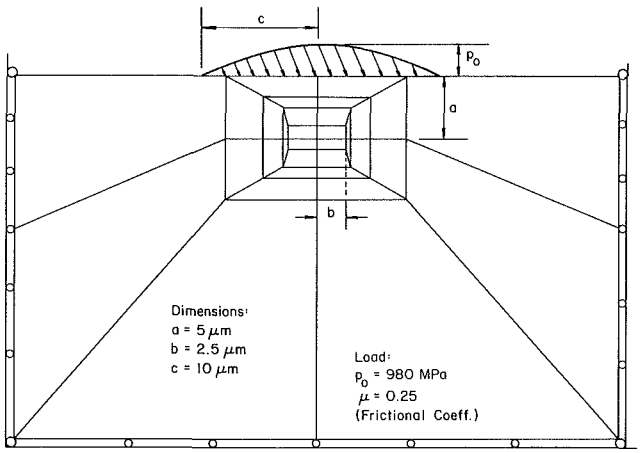


Fig. 2 Finite element grid pattern and load applied

Table 1 Mechanical properties of material in subsurface crack problem

Young's modulus E (MPa)	Tangent modulus E_T (MPa)	Poisson's ratio ν	Critical available strain-energy density $(dW/dV)_c^*$ (MPa)
1.96×10^5	19.6	0.28	1.638

[1] Research Assistant, Department of Mechanical Engineering and Mechanics, Lehigh University, Bethlehem, Pa. 18015.

[2] Professor of Mechanics and Director of Institute of Fracture and Solid Mechanics, Lehigh University, Bethlehem, Pa. 18015. Fellow, ASME

[3] The $1/r$ singular behavior of the strain energy density function holds for all material and is independent of loading and crack type.

Manuscript received by ASME Applied Mechanics Division, August, 1984.

Copyright © 1985 by ASME
Downloaded 02 May 2010 to 171.66.16.54. Redistribution subject to ASME license or copyright; see http://www.asme.org/terms/Terms_Use.cfm

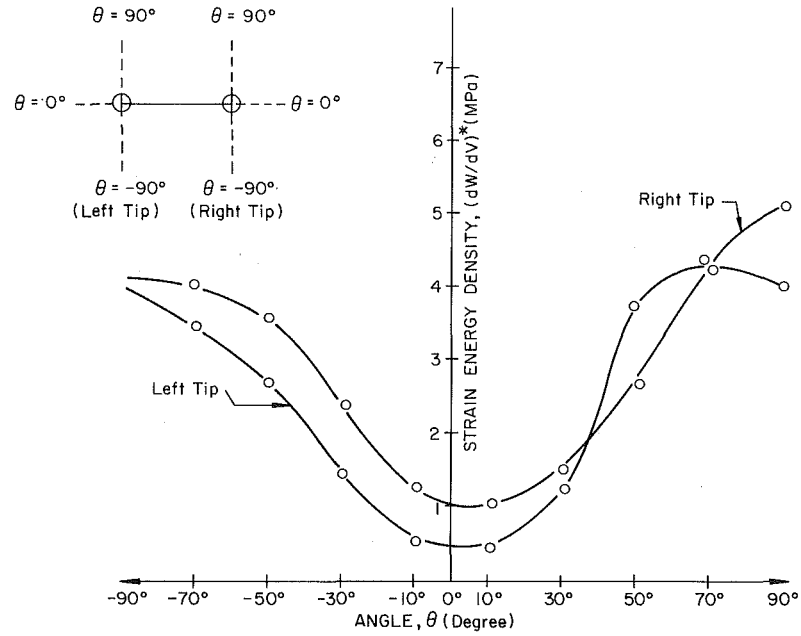


Fig. 3 Variation of strain-energy density of circle with $r = 0.25\mu m$

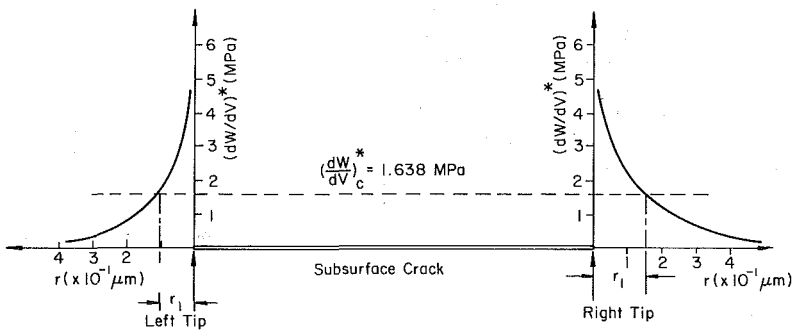


Fig. 4 Determination of first increments of crack propagation at right and left tips

to the surface. The first increment of crack growth r_1 can also be predicted from the intersection of the $(dW/dV)^*$ versus r curve with $(dW/dV)_c^* = 1.638$ MPa line. This is illustrated in Fig. 4 which yields values of $r_1 = 0.100$ and 0.165 μm at the left and right crack tip, respectively. The subsurface crack therefore tends to grow more in the direction of the angle loading. The crack growth procedure can be repeated for each load increment in accordance with

$$\left(\frac{dW}{dV}\right)_c^* = \frac{S_1}{r_1} = \frac{S_2}{r_2} = \cdots = \frac{S_j}{r_j} = \cdots = \frac{S_c^*}{r_c^*} \tag{2}$$

for obtaining the rate at which the material is being damaged. Several examples on subcritical crack growth in different material and loading conditions can be found in [4–6]. Whether the final event of material separation is catastrophic depends on the critical strain-energy density factor S_c^* and the size of the last ligament of crack growth r_c^*.

To conclude, it should be emphasized that failure criteria must necessarily be independent of the complexity of loading and material type. It is not difficult to concoct failure criteria so that the results agree with experiments. Examples are widespread in today's literature [7–10]. This prevails even in situations where the credibility of failure criteria were questioned as a result of obvious errors made in the stress analysis [7,8]. The test of any failure criterion must therefore be directed at its generality, versatility, and usefulness. The agreement with experiments is necessary but hardly sufficient.

References

1 Sih, G. C., and Tzou, D. Y., Discussion on "Subsurface Crack Propagation Due to Surface Traction in Sliding Wear," by H. C. Sin and N. P. Suh, ASME Journal of Applied Mechanics, Vol. 52, 1984, pp. 239–240.

2 Gifford, L. N., and Hilton, P. D., "Preliminary Documentation of PAPST—Nonlinear Fracture and Analysis by Finite Elements," NSRDC—Preliminary Document, 1981.

3 Sih, G. C., ed., *Mechanics of Fracture*, Introductory Chapters Vol. I–VII, Martinus Nijhoff, The Hague, pp. 1972–1982.

4 Sih, G. C., and Madenci, E., "Crack Growth Resistance Characterized by the Strain Energy Density Function," *Journal of Engineering Fracture Mechanics*, Vol. 18, 1983, pp. 1159–1171.

5 Sih, G. C., and Tzou, D. Y., "Crack-Extension Resistance of Polycarbonate Material," *Journal of Theoretical and Applied Fracture Mechanics*, Vol. 2, No. 3, in press.

6 Sih, G. C., and Tzou, D. Y., "Mechanics of Nonlinear Crack Growth: Effect of Specimen Size and Loading Step," *Proceedings on Modeling Problems in Crack Tip Mechanics*, Pindera, J. T., ed., Martinus Nijhoff, The Hague, 1984.

7 Sih, G. C., and Tzou, D. Y., "Discussion on Criteria for Brittle Fracture in Biaxial Tension by S. K. Maiti and R. A. Smith ," *Journal of Engineering Fracture Mechanics*, in press.

8 Sih, G. C., and Madenci, E., Discussion on "A Further Examination on the Application of the Strain Energy Density Theory to the Angled Crack Problem," by K. J. Chang, ASME Journal of Applied Mechanics, Vol. 50, 1983, pp. 234–236.

9 Sih, G. C., and Gdoutos, E. E., Discussion on "A Modified Strain-Energy Density Criterion Applied to Crack Propagation," by P. S. Theocaris and N. P. Andrianopoulos, ASME Journal of Applied Mechanics, Vol. 49 , 1982, pp. 678–679.

10 Sih, G. C., Moyer, E. T., Jr., and Gdoutos, E. E., "Discussion on The Mises Elastic-Plastic Boundary as the Core Region in Fracture Criteria by P. S. Theocaris and N. P. Andrianopoulos," *Engineering Fracture Mechanics*, Vol. 18, No. 3, 1983, pp. 731–734.

Downloaded 02 May 2010 to 171.66.16.54. Redistribution subject to ASME license or copyright; see http://www.asme.org/terms/Terms_Use.cfm

Journal of Applied Mechanics

Discussion

Subsurface Crack Propagation Due to Surface Traction in Sliding Wear[1]

G. C. Sih[2] and D. Y. Tzou[3]. The authors attempt to model the problem of wear delamination by the growth of a subsurface crack subjected to compressive and shear loading. The ADINA finite element program was adopted for calculating the elastic-plastic stress and displacement fields. A major issue raised by the authors was that linear elastic fracture mechanics (LEFM) cannot be applied to the problem at hand as a result of extensive plastic flow of the cracked layer. And yet, they employed the maximum shear stress criterion involving the stress intensity factors K_I and K_{II} in LEFM for determining the direction of crack initiation. This was based on the argument that the plastic stress components are proportional to the corresponding elastic stress components associated with τ_{max} in equation (1). It is well known, however, that the qualitative character and functional form of the plastic stress components near the crack depends on the strain hardening coefficients while the near-field elastic stress components depend only on the space variables[4] and are independent of load history. The difference becomes more and more pronounced as the plastic deformation intensifies. This being the case of subsurfae cracking invalidates the authors' argument.

In the opinion of the discussers, the authors have not only failed to achieve the three objectives outlined as (*a*), (*b*) and (*c*) in the Introduction, but have made numerous unsupported statements concerning the probem as a whole. To reiterate what has been said earlier, the authors unknowingly contradicted objective (*a*) in applying LEFM to explain crack initiation in materials experiencing gross yielding. Their attempts to investigate the various criteria for crack growth as part of objective (*b*) resulted in a number of misinterpretations that require clarification. First of all, there is no need to *prove* that the path-independent *J*-integral cannot be used in conjunction with the incremental theory of plasticity. This is known by definition. The authors' claim that the maximum principal stress criterion led to unrealistic predictions of crack extending[5] 110 deg at the left tip and 70 deg at the right tip referred to Fig. 1 of [1] is irrevelant because these results pertain to applied normal stress loading only and pure elastic deformation. Neither of these situations prevailed in the problem under discussion. Their remarks with reference to the strain energy density criterion are therefore also invalid. In fact, it has been shown [2] that the strain energy density criterion indeed does predict crack growth nearly parallel to the surface. Objective (*c*) refers to predicting the rate of crack propagation from the crack-tip sliding displacement (CTSD) in equation (2). The authors then assume that CTSD could be tied in with a fracture strain criterion but, at the same time, admit their inability to associate these quantities with crack growth rate.

[1] Sin, H. C., and Suh, N. P., and published in the June 1984 issue of the ASME JOURNAL OF APPLIED MECHANICS, Vol. 51, pp. 317-323.

[2] Professor of Mechanics and Director of Institute of Fracture and Solid Mechanics, Lehigh University, Bethlehem, Pa. 18015. Fellow ASME.

[3] Research Assistant, Department of Mechanical Engineering and Mechanics, Lehigh University, Bethlehem, Pa. 18015.

[4] This applies to the situation when the crack tip lies in an isotropic and homogeneous material.

[5] Crack growth is symmetric with reference to the normal load and extends toward the surface at both tips.

References

1 Sin, H. C., and Suh, N. P., "Subsurface Crack Propagation Due to Surface Traction in Sliding Wear," ASME JOURNAL OF APPLIED MECHANICS, Vol. 51, 1984, pp. 317-323.

2 Tzou, D. Y., and Sih, G. C., "Crack Growth Prediction of Subsurface Crack in Yielded Material," ASME JOURNAL OF APPLIED MECHANICS, Vol. 52, 1985, pp. 237-238.

Authors' Closure

The authors appreciate the comments of Dr. Sih and Mr. Tzou. Indeed, it is well known that the plastic stress components near the crack tip depend on the strain-hardening coefficients and are different from the elastic near-field stress components. However, the dominance of the near-field shear component under the combined shear and compression loading changes insignificantly for the problem under consideration when plastic deformation occurs. In fact, the stresses predicted by the ADINA finite element program indicate that the shear stress at the tip is near the maximum in the direction parallel to the surface. The LEFM results are presented to show that the state of plastic stresses can be related to the yielding history since the FEM results gave the stresses only at the integration points. The discussers should note that the 110 deg and 70 deg predictions were made for the combined normal and tangential stress loading, rather than the pure, normal loading case.

The strain energy density criterion may lead to the right prediction of the crack propagation direction when all the necessary information for this complicated plastic stress field is properly considered. Since the reference cited by the discussers is not available at this time, it is difficult to respond adequately to their claim.

Finally, the path-independent *J*-integral obviously cannot be used in conjunction with the incremental theory of plasticity. Therefore, the crack-tip sliding displacement (CTSD) was used, which gives an estimate of the crack propagation rate. Crack-tip sliding displacement and fracture strain to crack growth rate cannot be related to each other definitively at this time because of the dependence of fracture strain on microstructure. However, assuming that crack-tip

Copyright © 1985 by ASME
Downloaded 02 May 2010 to 171.66.16.54. Redistribution subject to ASME license or copyright; see http://www.asme.org/terms/Terms_Use.cfm

sliding displacement is a reasonable estimate of the crack propagation rate, experimentally observed delamination wear rates could be predicted.

| Dynamics of Gyroelatic Continua[1]

C. W. Bert[2]. The authors have presented an interesting analysis of gyroelastic continua, which should be quite important in connection with control of large, flexible space structures. According to Dimentberg [1], the first analytical treatment of distributed gyroscopic behavior, as distinct from the more familiar discrete behavior, is due to Grammel [2] in 1920. This work was concerned with dynamics of a rotating shaft. More recently, in 1978 Padovan [3] presented an analysis of three-dimensional gyroelastic continua. However, in that work, the possibility of separately controlled gyroscopic action was not considered and thus it was not quite as general as the present paper.

[1] By G. M. T. D'Eleuterio and P. C. Hughes, and published in the June, 1984 issue of the ASME JOURNAL OF APPLIED MECHANICS, Vol. 51, pp. 415-422.

[2] Benjamin H. Perkinson Professor of Engineering, School of Aerospace, Mechanical and Nuclear Engineering, The University of Oklahoma, Norman, Okla. 73019. Fellow ASME.

References

1 Dimentberg, F. M., *Flexural Vibrations of Rotating Shafts*, English translation, Butterworths, London, 1961.

2 Grammel, R., "Kritische Drehzahl und Kreiselwirkung," *Zeitschrift des Vereines Deutscher Ingenieur*, Vol. 64, 1920, pp. 911-914.

3 Padovan, J., "On Gyroscopic Problems in Elasticity," *International Journal of Engineering Science*, Vol. 16, 1978, pp. 1061-1074.

Authors' Closure

The authors appreciate Professor Bert's interest in their paper and his information on earlier literature. It should be reiterated, however, that the focus of the paper was a separately specified distribution of gyricity. In the work of Grammel and Padovan, the gyric effects were due to a single spinning body.

Downloaded 02 May 2010 to 171.66.16.54. Redistribution subject to ASME license or copyright; see http://www.asme.org/terms/Terms_Use.cfm

sliding displacement is a reasonable estimate of the crack propagation rate, experimentally observed delamination wear rates could be predicted.

| Dynamics of Gyroelatic Continua[1]

C. W. Bert[2]. The authors have presented an interesting analysis of gyroelastic continua, which should be quite important in connection with control of large, flexible space structures. According to Dimentberg [1], the first analytical treatment of distributed gyroscopic behavior, as distinct from the more familiar discrete behavior, is due to Grammel [2] in 1920. This work was concerned with dynamics of a rotating shaft. More recently, in 1978 Padovan [3] presented an analysis of three-dimensional gyroelastic continua. However, in that work, the possibility of separately controlled gyroscopic action was not considered and thus it was not quite as general as the present paper.

[1] By G. M. T. D'Eleuterio and P. C. Hughes, and published in the June, 1984 issue of the ASME JOURNAL OF APPLIED MECHANICS, Vol. 51, pp. 415-422.

[2] Benjamin H. Perkinson Professor of Engineering, School of Aerospace, Mechanical and Nuclear Engineering, The University of Oklahoma, Norman, Okla. 73019. Fellow ASME.

References

1 Dimentberg, F. M., *Flexural Vibrations of Rotating Shafts*, English translation, Butterworths, London, 1961.

2 Grammel, R., "Kritische Drehzahl und Kreiselwirkung," *Zeitschrift des Vereines Deutscher Ingenieur*, Vol. 64, 1920, pp. 911-914.

3 Padovan, J., "On Gyroscopic Problems in Elasticity," *International Journal of Engineering Science*, Vol. 16, 1978, pp. 1061-1074.

Authors' Closure

The authors appreciate Professor Bert's interest in their paper and his information on earlier literature. It should be reiterated, however, that the focus of the paper was a separately specified distribution of gyricity. In the work of Grammel and Padovan, the gyric effects were due to a single spinning body.

Copyright © 1985 by ASME
Downloaded 02 May 2010 to 171.66.16.54. Redistribution subject to ASME license or copyright; see http://www.asme.org/terms/Terms_Use.cfm

Journal of Applied Mechanics

Book Reviews

Boundary Element Techniques. Theory and Applications in Engineering. By C. A. Brebbia, J. C. F. Telles, and L. C. Wrobel. Springer Verlag, New York, 1984. 464 pages. Price $78.

REVIEWED BY S. MUKHERJEE[1]

Although the boundary element method (BEM) is rooted in classical integral equation formulation of problems, numerical implementation of the method, with applications to various branches of engineering, is of relatively recent vintage. The past decade, however, has witnessed a great deal of activity in this area of research as evidenced by many publications in journals and several recent books on the subject. The method has now been established as a strong competitor to the more widely used finite element method, both in terms of range of applicability to different kinds of problems and with regard to computational efficiency.

This book by Brebbia, Telles, and Wrobel is a very welcome addition to the literature on BEM applications in the general areas of solid and fluid mechanics and heat transfer. It is a comprehensive text on the subject which covers the entire field from the fundamental mathematical formulations to the latest research results. The subject matter is presented clearly throughout the text.

The book is divided into 14 chapters. It starts with a discussion of an unifying approach to approximate methods of analysis (such as finite difference, finite elements, and boundary elements) based on weighted residual methods. This is followed by a discussion of potential problems. Next comes a discussion of different kinds of interpolation functions that are necessary in order to reduce the governing integral equations to a system of algebraic ones.

The book then addresses itself to diffusion and then several topics in solids mechanics such as elastostatics, elastoplasticity, viscoplasticity, and plate bending. This is followed by chapters on elastodynamics, vibrations, and a brief discussion on applications in fluid mechanics. The concluding chapters present a discussion of coupling of the BEM with other methods such as the finite element method (FEM), followed by a computer program for two-dimensional elastostatics. Three appendices complete the book.

The fact that the authors of this book are well-recognized researchers in the field is clearly in evidence throughout the book. I very much liked the attention to mathematical detail and the discussions of numerical implementations of the various integral equations. While, in my opinion, all the different topics are adequately treated here, the chapters on solid mechanics are particularly strong. Careful attention to the differentiated versions of the displacement integral equations – those that deliver the strains and stresses pointwise inside a solid body – is particularly useful. These equations often have strongly singular kernels and one must be very careful in dealing with them. Another attractive feature of the book is the discussion of exterior problems in infinite and semi-infinite domains. It is in these problems that the BEM is often more efficient than domain type techniques. Finally, the authors do a good job in pointing out how in certain problems a coupling of the BEM and FEM can lead to the two methods complementing each other so that the particular strengths of each can be exploited to advantage.

In summary, I feel that this text by Brebbia, Telles, and Wrobel will be very useful to researchers in computational mechanics. It can be used as an introductory text by readers unfamiliar with boundary element methods. It is also an excellent reference volume for others who are already familiar with this powerful, general purpose analytical/computational technique.

Elastic Instability Phenomena. By J. M. T. Thompson and G. W. Hunt. Wiley-Interscience, New York, 1984. 209 Pages. Price $32.95.

REVIEWED BY V. TVERGAARD[2]

This book treats the elastic buckling of structures with a strong emphasis on interpretations in terms of the mathematical topological theory, known as catastrophe theory. The book is restricted to conservative systems, and it can be seen as a complement to the earlier book *A general Theory of Elastic Stability*, Wiley (1973), by the same authors. The book is intended for undergraduate and postgraduate courses in civil, mechanical, marine, and aerospace engineering.

In Chapter 1 fundamental principles of equilibrium and stability are introduced for an n-degree-of-freedom conservative mechanical system. Discretizations by a modal expansion or a finite element method, leading to n-degree-of-freedom approximations, are illustrated in Chapter 2 for vibrations and buckling of beams and struts.

[1] Associate Professor, Department of Theoretical and Applied Mechanics, Cornell University, Ithaca, N.Y. 14853. Mem. ASME.

[2] Department of Solid Mechanics, Technical University of Denmark, Lyngby, Denmark DK-2800.

Copyright © 1985 by ASME
Downloaded 02 May 2010 to 171.66.16.54. Redistribution subject to ASME license or copyright; see http://www.asme.org/terms/Terms_Use.cfm

Loads and imperfections are introduced as control parameters in the potential energy, in Chapter 3. Limit points, asymmetric and symmetric bifurcation points are discussed, leading to an introduction of expressions for the seven "elementary" catastrophes which much of the book centers on. Four of these expressions relate to a single critical mode, and the remaining three relate to two simultaneous modes.

Chapter 4 treats single-mode buckling phenomena at distinct critical points. Simple rigid bar-spring models are used to illustrate the "fold catastrophe," which corresponds to snap-buckling at a limit point or to an asymmetric bifurcation point. The "cusp catastrophe" corresponds to symmetric postbifurcation behavior. Furthermore, the two higher-order unimodal singularities, the "swallowtail catastrophe" and the "butterfly catastrophe" are briefly discussed. As an example of the cusp singularity, a two-mode Rayleigh-Ritz analysis of a shallow arch is carried out in Chapter 5. The symmetric postbifurcation behavior corresponding to an asymmetric mode, the imperfection-sensitivity, and the influence of prestress are illustrated in this example, and the results are compared with experiments.

In Chapter 6 some simple rigid bar-spring models, and a structural model of an eccentrically stiffened panel, all with simultaneous (or nearly simultaneous) bifurcation in two modes, are used to illustrate the "elliptic, hyperbolic, or parabolic umbilic catastrophes." Routes through these umbilic catastrophes are explored. Chapter 7, on the other hand, is not directly oriented toward the catastrophe theory viewpoint, but gives a systematic treatment of bifurcation problems with many simultaneous bifurcation modes.

The last chapter gives a discussion of some engineering buckling problems, including plates, axially compressed cylindrical shells, and spherical shells under external pressure. Results are discussed, without showing many equations, and some relations to catastrophe theory are emphasized.

From the point of view of structural buckling this book treats a special selection of topics. The continuum mechanics approach to elastic postbuckling theory developed by W. T. Koiter (1945), and many later contributions in this area by B. Budiansky, J. W. Hutchinson, and others, is not given much prominence here. Nor are the many numerical investigations of elastic buckling phenomena; see *Buckling of Bars, Plates and Shells* by D. O. Brush and B. O. Almroth, McGraw-Hill (1975).

For the audience interested in the connexion between the elastic stability theory and catastrophe theory the present book will provide a good, broad introduction to the area.

Problems of Mixed Mode Crack Propagation. By E. E. Gdoutos. Martinus Nijhoff, The Hague, 1984. 204 Pages.

REVIEWED BY L. M. BROCK[3]

This book is the second in a new series entitled *Engineering Applications of Fracture Mechanics*, edited by G. C. Sih. Sih also edits the long-standing series *Mechanics of Fracture*, and there are similarities between the two: both series highlight the strain-energy density criterion of linear-elastic fracture mechanics, and both give compendia of often previously published fracture analyses. However, as exemplified by this book, the new series is aimed at the applications-oriented researcher and engineer.

In keeping with the theme of mixed-mode fracture, many of the problems treated in the book involve asymmetries in the alignments of crack path, geometry, and loading. After an introductory chapter on the strain density criterion, these problems are categorized into eight separate chapters and discussed in view of this criterion. The categories are: general two-dimensional crack problems; branched, interacting, and arc-shaped cracks; cracks radiating from holes or inclusions; cracks in composites and plates and shells; and three-dimensional crack problems. Crack propagation in the book does not refer to actual crack motion, so that all the problems treated are quasistatic. Moreover, except in the last chapter, they are all essentially two-dimensional in nature.

Each chapter includes expressions for crack-edge stress fields, strain-energy densities, predicted critical stresses, and parameters of particular importance in the given category, e.g., branching angles in the branched crack problems. Little developmental material is given, but the results are well (if not exhaustively) referenced.

The problem geometries are also clearly illustrated, and numerous parameter graphs are included, as well as, in some cases, illustrations of theoretical-experimental data comparisons.

Mixed-mode fracture is a somewhat controversial topic, since some commonly used fracture criteria, such as the maximum normal stress criterion, see a symmetry between a crack plane and the applied loading. In this book, the author meets the controversy head-on by pointing out situations in which mixed-mode fracture could occur, and by treating idealizations of such situations in view of a criterion that does not require such symmetry.

Indeed, he states that the book's main purpose is to illustrate the utility of the strain-energy density criterion, not to present large numbers of problems. Nevertheless, the number of problems, along with the consideration of crack path-geometry-loading alignment asymmetry and the large number of references given, is sufficient in itself to make the book a useful contribution. Researchers in fracture mechanics as well as the author's targeted audience will find the book a good information source.

Numerical Simulation of Non-Newtonian Flow. By M. J. Crochet, A. R. Davies, and K. Walters. Elsevier, New York, 1984, 352 Pages. Price $65.50

REVIEWED BY R. I. TANNER[4]

The volume under review is one of the first in this rapidly growing area. Due to the nonlinear history-dependent relations between stress and kinematic quantities, the field of non-Newtonian fluid mechanics needs good numerical methods urgently, and the present book is therefore timely.

The first two chapters review physical motivation and describe the equations to be solved. Several rival schools have developed in the description of materials with memory and the present treatment is conciliatory, fair, and ultimately pragmatic in this respect. The description of numerical methods deals both with the finite-difference approach and the finite-element approach. As the former has its greatest number of adherents among fluid dynamicists and the latter

[3] Professor L. M. Brock, Department of Engineering Mechanics, University of Kentucky, Lexington, Ky. 40506.

[4] Professor, Department of Mechanical Engineering, University of Sydney, New South Wales, Australia, Mem. ASME.

Copyright © 1985 by ASME
Downloaded 02 May 2010 to 171.66.16.54. Redistribution subject to ASME license or copyright; see http://www.asme.org/terms/Terms_Use.cfm

has a large following in solid mechanics, while our substances lie somewhat between viscous fluids and elastic solids, this is a fair balance of attention. The main finite-difference method described is the classical stream-function (ψ) - vorticity (ω) method, augmented by the stress components as unknowns in the non-Newtonian case. The difficulties in obtaining convergent numerical solutions in cases where the elastic stresses are of the same order of magnitude as the viscous stresses are frankly discussed. The (ψ, ω) method runs into some basic problems in these flows. For example, it is extremely difficult to recover the pressure field. It should be emphasized that the efforts the authors have made to get this scheme to work are heroic and anyone contemplating writing a finite-difference progam to solve nonlinear viscoelastic problems should read this account first.

The second half of the book deals with various finite-element aproaches. An ingenious set of mixed methods, in which the velocity components, (u,v) the pressure (p), and the stress components are solved for simultaneously, is described. Thus the pressure recovery problem and the problems of fitting irregular fluid domains and free boundary conditions are all solved in these approaches, but the computations are very expensive.

The one problem that seems to be independent of computing method is the blow-up or lack of convergence when the ratio of elastic forces to viscous forces (the Weissenberg number) exceeds about one or two. Several suggestions are made in the final section as to how this problem may be overcome. Since the computations on elastic fluids in this book were mostly made with the so-called convected Maxwell and Oldroyd-B models, I believe that the best suggestion as to the cause of lack of convergence is that there is *no* stable solution to many of these problems using these fluid models. Evidence on this point follows from the recent stability analysis of Phan-Thien ((*J. Non-Newtonian Fluid Mechanics*, Vol. 13, 1983, p. 325) and recent computing experiences.

I recommend this as a valuable, scholarly book for those wishing to enter this rapidly developing field; one sees how far one has progressed from the simple idea of letting the viscosity vary with shear rate, and how much further there is yet to go.

Computer Aided Analysis and Optimization of Mechanical System Dynamics. Edited by E. J. Haug. Springer-Verlag, New York, 1984, 700 Pages. Price $49.50

REVIEWED BY R. L. HUSTON[5]

This volume contains the proceedings of a conference held in Iowa City last year. The title defines the subject matter, which in the book is divided into five parts: Analytical Methods; Computer Aided Formulation of Equations of Dynamics; Numerical Methods in Dynamics; Interdisciplinary Problems; and Synthesis and Optimization.

Each of these parts contains apporoximately four papers written by leading researchers in the respective areas. The first part contains contributions by B. Paul, J. Wittenberg, and R. A. Wehage with an emphasis upon quaternion algebra and computer analysis. In the second part, W. O. Schliehlen, M. A. Chace, P. E. Nikravesh, M. A. Hussain, and B. Noble discuss various approaches to computer-aided formulations of dynamics equations for large systems. In the third part, W. H. Enright, C. W. Gear, and P. E. Nikravesh discuss various numerical procedures for solving systems of differential equations and combined systems of differential and algebric equations. In the fourth part, K. van der Wertf, M. Vanderploeg, and G. P. Ostermeyer et al., discuss the feasibility of combining finite-element methods, feedback control theory, and numerical techniques in the analysis of large mechanical system. Finally, in the last part I. H. Rankers, E. J. Huag, C. Fleury, and P. E. Gill, et al. consider design and optimization of mechanical systems. Iterative procedures with large computer codes are discussed.

This reviewer believes the book could be useful reference for those interested in machine dynamics and in large mechanical system. Although the subject matter of many of the papers is availble elsewhere, the collection represents a good summary of the state of the art of computational mechanical systems. Students and researchers alike should benefit from the many ideas discussed in the book.

[5]Professor, Department of Mechanical and Industrial Engineering, University of Cincinnati, Cincinnatti, Ohio 45221-0072.

Copyright © 1985 by ASME
Downloaded 02 May 2010 to 171.66.16.54. Redistribution subject to ASME license or copyright; see http://www.asme.org/terms/Terms_Use.cfm